Experimentelle Physik

Second-Order Weak Decays in XENON1T and Future Xenon Time Projection Chambers

Inaugural-Dissertation
zur Erlangung des Doktorgrades (Dr. rer. nat.)
der Naturwissenschaften im Fachbereich Physik
der Mathematisch-Naturwissenschaftlichen Fakultät
der Westfälischen Wilhelms-Universität Münster

vorgelegt von
Christian Wittweg
aus Höxter
–2021–

WWU
MÜNSTER

Dekan: **Prof. Dr. Michael Rohlfing**

Erster Gutachter: **Prof. Dr. Christian Weinheimer**

Zweiter Gutachter: **Prof. Dr. Anton Andronic**

Tag der mündlichen Prüfung: ______________________________

Tag der Promotion: ______________________________

Time feels differently reckoned after the mine: further deepened, further folded. My sense of nature feels differently reckoned, too: further disturbed, further entangled. Somewhere to my east, men are at work a mile below the moors, half a mile under the sea, cutting tunnels through the salt-ghost of an ocean to harvest its energy for crops as yet ungrown. A Time Projection Chamber is waiting for signals from Cygnus, the Swan, that might tell something of the birth of the universe, 13.8 billion years earlier. A labyrinth of drift is slowly closing up, lizard-machines and Ford Transits are being sealed into their tombs of salt – and through it all is passing a particle wind of WIMPs and neutrinos, to which this world is as mere mist and silk.

Robert Macfarlane, *Underland – A Deep Time Journey*

Erratum

1st July 2021

A central result of this dissertation is the two-neutrino double-electron capture half-life $T_{1/2}^{\text{KK+KL+LL}}$ of the isotope ^{124}Xe that was determined for captures from the K- and L-shells, KK-, KL- and LL-capture, using data from the XENON1T experiment. In this study, a double-electron capture was detected for the first time with a significance larger than 5σ. The value of $T_{1/2}^{\text{KK+KL+LL}} = (1.13 \pm 0.18_{\text{stat}} \pm 0.05_{\text{sys}}) \cdot 10^{22}$ yr was interpreted as the total half-life $T_{1/2}^{2\nu\text{ECEC}}$ of ^{124}Xe in chapters 4 and 7 as well as in the abstracts. The direct conversion of $T_{1/2}^{\text{KK+KL+LL}}$ to $T_{1/2}^{2\nu\text{ECEC}}$ followed references [1] and [2] where only captures from the K- and L1- shells are considered. These are the decays that were directly accessible to XENON1T. In a discussion connected to the doctoral exam and during the preparation of a publication it was found that captures from the higher M-, N- and O-shells contribute to the decay rate to a small degree. Due to the high precision of the result, they should be taken into account. With this, the central value of $T_{1/2}^{\text{KK+KL+LL}}$ determined in the thesis remains unchanged, but the total half-life derived from that value by theoretical input is reduced by approximately 6 % to $T_{1/2}^{2\nu\text{ECEC}} = 1.06 \cdot 10^{22}$ yr.

Due to the uncertainty associated with the contributions from higher-shell captures, the total half-life is connected with a larger systematic uncertainty and, after rounding to the first digit, is given as $T_{1/2}^{2\nu\text{ECEC}} = (1.1 \pm 0.2_{\text{stat}} \pm 0.1_{\text{sys}}) \cdot 10^{22}$ yr. Equations (1) and (3) in the English and German abstracts, equation (4.38) and figure 4.13 in section 4.4, and equation (7.4) in chapter 7 have to be updated with this value. Moreover the relative capture fractions in section 1.2.4, as well as in table 4.4 and the caption of figure 4.9 in section 4.3 are updated according to the discussion below.

The effect of higher-shell captures is estimated by determining the associated change in the relative fraction of KK-, KL- and LL-captures $f_{\text{KK+KL+LL}} = f_{2\nu\text{KK}} + f_{2\nu\text{KL}} + f_{2\nu\text{LL}}$. Considering only the overlap of the electron wave functions with the nucleus and using the normalised values of the squared radial wave functions of the K- to N5-shells at the nucleus [3], $f_{\text{KK+KL+LL}}$ reduces from 100 % to 93.8 % ($f_{2\nu\text{KK}} = 72.4\,\%$, $f_{2\nu\text{KL}} = 20.0\,\%$, $f_{2\nu\text{KM}} = 4.3\,\%$, $f_{2\nu\text{KN}} = 1.0\,\%$, $f_{2\nu\text{LL}} = 1.4\,\%$, $f_{\text{other}} = 0.8\,\%$). No literature values for the O-shell are available, but its inclusion is estimated to cause an additional $\mathcal{O}(0.1)$ % absolute reduction of $f_{\text{KK+KL+LL}}$. It should be noted that considering only wave function overlap is a simplified approach. For instance, captures from shells with higher orbital angular momenta could be suppressed as in allowed vs. forbidden single-electron captures [4], so capture rates from higher shells would be reduced. Taking into account only s-shell electrons with K1-, L1-, M1- and N1-captures leads to $f_{\text{KK+KL+LL}} = 94.3\,\%$. Accordingly, the updated $f_{\text{KK+KL+LL}} = 93.8\,\%$ represents a lower limit.

The changes outlined above do not have an impact on the consistency checks that were carried out in section 4.5 since these focused on the KK-capture half-lives. Moreover, the goodness of fit and significance of the 2νECEC signal, discussed in section 4.4, are not expected to change notably due to the dominance of the KK- and KL-peaks in the fit. A comprehensive study with a fit of an updated signal model is presently conducted by the author of this work for a XENON collaboration paper.

[1] M. Doi and T. Kotani, Progress of Theoretical Physics 87, 1207 (1992).

[2] J. Suhonen, Journal of Physics G40, 075102 (2013).

[3] R. B. Firestone, C. M. Baglin (editor) and S. Y. F. Chu (editor), *Table of isotopes: 1999 Update*, 8th edition, Wiley (1999).

[4] W. Bambynek *et al.*, Review of Modern Physics 49, 77 (1977).

Abstract

The nature of Dark Matter, the mechanism generating the neutrino masses and the origin of the matter-antimatter symmetry in the Universe are among the great unanswered questions of particle physics. The quest for the direct detection of particle Dark Matter has led to the development of dual-phase xenon time projection chambers with ever increasing target masses and ever decreasing experimental backgrounds. Among these, XENON1T was the most sensitive experiment for a multitude of Dark Matter candidate particles to date. It was also a capable observatory for neutrino physics, especially with regard to neutrinoless second-order weak decays in xenon. An observation of these hypothetical decays would indicate that neutrinos are Majorana particles and would give access to the neutrino mass scale. Moreover, it would demonstrate lepton number violation and help to explain the matter-antimatter symmetry in the Universe.

The interpretation of neutrinoless double-weak decays in terms of neutrino masses relies on theoretical nuclear structure calculations. These calculations are informed by experimental measurements of related Standard Model decays such as the two-neutrino double-electron capture of ^{124}Xe. Compared to the widely-measured double-β^- decays, indications for double-electron capture only exist in three isotopes – ^{78}Kr, ^{130}Ba and ^{124}Xe – and no detection above the 5σ discovery threshold has been achieved to date. A measurement of such a decay would provide nuclear theorists with a data point from the proton-rich side of the nuclide chart.

This work describes the analysis that lead to the first observation of ^{124}Xe double-electron capture in XENON1T with a significance of 4.4σ. It then presents an improved analysis with a larger exposure that achieves a significant detection of the decay at 6.8σ and measured the total half-life from KK-, KL- and LL-electron captures at

$$T_{1/2}^{2\nu\mathrm{ECEC}} = (1.13 \pm 0.18_{\mathrm{stat}} \pm 0.05_{\mathrm{sys}}) \cdot 10^{22}\ \mathrm{yr}. \tag{1}$$

The isotope ^{124}Xe can undergo two more two-neutrino decay modes, the electron capture with positron emission and double-positron emission, that have not been measured in any isotope. The same is true for the neutrinoless counterparts of these decays as well as for the neutrinoless double-electron capture of ^{124}Xe. Using simulations and a newly developed coincidence-based reconstruction algorithm the detection prospects of these five decay modes in future xenon-based detectors are investigated. The two-neutrino and neutrinoless electron capture with positron emission emerge as the most promising decays for future detection.

Due to the more favourable phase-space and the larger natural isotopic abundance of ^{136}Xe compared to ^{124}Xe, the neutrinoless double-β decay of ^{136}Xe is regarded as the most promising window to lepton number violation and Majorana neutrinos in xenon-based detectors. On the grounds of a simulation-based background model that is fitted to data, the sensitivity of XENON1T to this decay is investigated. The sensitivity for setting a lower limit on the half-life is found at

$$T_{1/2}^{0\nu\beta\beta} > 1.7 \cdot 10^{24}\ \mathrm{yr} \quad (90\,\%\ \mathrm{C.\,L.}). \tag{2}$$

This is the best sensitivity to this process achieved by a xenon-based Dark matter detector to date.

Zusammenfassung

Die Natur der Dunklen Materie, der physikalische Mechanismus zur Erzeugung der Neutrinomassen und der Ursprung der Asymmetrie zwischen Materie und Antimaterie im Universum gehören zu den großen ungelösten Fragen der Teilchenphysik. Die Suche nach Dunkler Materie hat zur Entwicklung von Xenon-Zweiphasen-Zeitprojektionskammern mit stetig wachsenden Detektormassen und dabei abnehmenden experimentellen Untergründen geführt. XENON1T war in den letzten Jahren das empfindlichste Experiment dieser Art für eine Vielzahl möglicher Kandidaten von Teilchen der Dunklen Materie. Zudem war es ein sensitives Experiment für die Neutrinophysik, speziell im Hinblick auf neutrinolose schwache Zerfälle zweiter Ordnung in Xenon. Eine Beobachtung dieser hypothetischen Zerfälle würde zeigen, dass Neutrinos Majoranateilchen sind, und es würde einen Zugang zur Massenskala der Neutrinos ermöglichen. Darüber hinaus würde sie die Verletzung der Leptonenzahl zeigen, was in Zusammenhang mit der Asymmetrie von Materie und Antimaterie im Universum steht.

Die Interpretation neutrinoloser schwacher Zerfälle zweiter Ordnung im Hinblick auf Neutrinomassen erfordert theoretische Berechnungen von Kernmatrixelementen. Experimentelle Befunde zu Verwandten Standardmodellzerfällen fließen in diese Berechnungen ein. Ein Beispielzerfall ist der Zwei-Neutrino Doppel-Elektroneneinfang von ^{124}Xe. Im Vergleich zu den weitgehend vermessenen Zwei-Neutrino Doppelbetazerfällen existieren Hinweise für den Zwei-Neutrino Doppel-Elektroneneinfang nur bei drei Isotopen: ^{78}Kr, ^{130}Ba und ^{124}Xe. Eine Detektion oberhalb der 5σ Entdeckungsschwelle ist bislang nicht vermeldet worden. Die Messung der Halbwertszeit eines solchen Zerfalls würde Kerntheoretikern einen Datenpunkt von der protonenreichen Seite der Nuklidkarte liefern.

Die vorliegende Arbeit beschreibt eine Analyse, die zur ersten Beobachtung des Zwei-Neutrino Doppelelektroneneinfangs von ^{124}Xe im XENON1T Detektor mit einer Signifikanz von 4.4σ geführt hat. Im folgenden wird eine verbesserte Analyse auf einem vergrößerten Datensatz präsentiert, die eine mit 6.8σ signifikante Detektion dieses Zerfalls ermöglicht. Unter Berücksichtigung von KK-, KL- und LL-Elektroneneinfängen wird die Halbwertszeit des Zerfalls angegeben mit

$$T_{1/2}^{2\nu\mathrm{ECEC}} = (1.13 \pm 0.18_{\mathrm{stat}} \pm 0.05_{\mathrm{sys}}) \cdot 10^{22}\ \mathrm{yr}. \tag{3}$$

Weitergehend kann ^{124}Xe auch über den Zwei-Neutrino Elektroneneinfang mit Positronenemission und die Zwei-Neutrino Doppel-Positronenemission zerfallen. Alle drei Standarmodellzerfälle mit zwei Neutrinos haben hypothetische neutrinolose Gegenstücke. Die Aussichten für die Detektion dieser Zerfälle in zukünftigen Xenondetektoren wird unter der Nutzung von Simulationen zusammen mit einem neu entwickelten Koinzidenzrekonstruktionsalgorithmus untersucht. Der Zwei-Neutrino Elektroneneinfang mit Positronenemission und sein neutrinoloses Gegenstück stellen sich hier als die vielversprechendsten Kandidaten für eine zukünftige Detektion heraus.

Aufgrund des größeren Phasenraums und wegen der größeren natürlichen Isotopenhäufigkeit von ^{136}Xe im Vergleich zu ^{124}Xe wird der neutrinolose Doppelbetazerfall von ^{136}Xe als aussichtsreichster Kandidat für die Beobachtung von Majorananeutrinos und Leptonenzahlverletzung in Xenondetektoren angesehen. Mit einem simulationsbasierten Untergrundmodell, das an die Daten angepasst wird, wird die Sensitivität von XENON1T für diesen Zerfall untersucht. Die Sensitivität zur Angabe einer unteren Schranke auf die Halbwertszeit ist

$$T_{1/2}^{0\nu\beta\beta} > 1.7 \cdot 10^{24}\ \mathrm{yr} \quad (90\,\%\ \mathrm{C.\,L.}). \tag{4}$$

Damit hat XENON1T die höchste Sensitivität für diesen Prozess, die bisher von einem xenonbasierten Experiment zur Suche nach Dunkler Materie erreicht wurde.

Contents

Introduction

The rise of the Standard Model of particle physics (SM) is one of the major scientific achievements of the 20th century [1]. It provides a consistent framework for the description of fundamental physical interactions and its predictions have overwhelmingly been confirmed experimentally culminating in the discovery of the Higgs boson in 2012 [2, 3]. However, experimental and observational evidence have shown that the Standard Model is incomplete, as it does not provide a candidate particle for Dark Matter. This yet undetected form of matter amounts to 26.4 % of the energy density of the Universe according to ΛCDM cosmology [4]. Theories beyond the Standard Model such as supersymmetry (SUSY) [5, 6] predict the existence of massive and stable particles that only undergo minimal interactions with baryonic matter. The weakly interacting massive particle (WIMP) is just one in a plethora of candidate particles from several extensions of the SM. Axions which solve the strong CP problem are another popular class of Dark Matter candidates [7]. Searches for Dark Matter production at accelerators, their indirect detection through annihilation products and the direct detection of Dark Matter via the measurement of WIMP scattering on SM matter are aimed to determine the nature of particle Dark Matter [8].

In the past decade, liquid xenon dual-phase time projection chambers (TPCs) have emerged as the leading technology in the direct search for WIMP Dark Matter [9]. Owed to their increasing target masses, successful background avoidance and reduction, and the progress in analysis techniques, their experimental sensitivity to WIMP-nucleus scattering has grown steadily [10]. The XENON1T Dark Matter experiment was operated at Laboratori Nazionali del Gran Sasso in Italy from 2016 to 2018. It achieved the lowest background rate of any xenon-based Dark Matter experiment and placed the currently most stringent limits on a multitude of Dark Matter particles and their interactions [11–16]. The next generation of detectors with LZ and XENONnT is currently in commissioning [17, 18]. The large targets and low backgrounds also make xenon dual-phase TPCs increasingly suited for other rare event searches beyond Dark Matter direct detection. The neutrinoless second-order weak decays of ^{124}Xe and ^{136}Xe are of particular interest. These isotopes are contained within the detectors' xenon targets and allow to investigate physics beyond the SM.

The discovery of neutrino oscillations by the SNO and Super-Kamiokande experiments proved that neutrinos have a finite mass [19, 20]. Since then the neutrino mixing angles and differences of the squared neutrino masses have been measured with increasing precision [4]. Yet, only upper limits on the masses of the neutrino flavour eigenstates exist and the SM does not provide an explanation for the presence and smallness of these masses [21, 22]. Hypothetical neutrinoless second-order weak decays provide an experimental test if neutrinos are Majorana particles, i.e. their own antiparticles. This would, in turn, give indications on the physical mechanism that generates the neutrino masses [23]. Moreover, an observation of this lepton number violating process could help to explain the asymmetry between matter and antimatter in the universe by means of leptogenesis [24].

Due to the more favourable phase-space and ~ 10 times larger natural isotopic abundance compared to ^{124}Xe, searches for neutrinoless double-weak decays in xenon commonly focus on neutrinoless double-β^- decays ($0\nu\beta^-\beta^-$) of ^{136}Xe [23].The current lower limit on the $0\nu\beta^-\beta^-$ half-life is $1.07 \cdot 10^{26}$ yr at 90 % confidence level [25]. Even longer half-lives are expected for the neutrinoless decays of ^{124}Xe which would energetically allow three different neutrinoless decay modes: double-electron capture, electron capture with positron emission and double-positron emission [26, 27]. The observation of any of these decay modes in conjunction with an observation of a neutrinoless double-weak decay in another isotope could allow to reveal the interaction that mediates the double-weak nuclear decay [28].

The interpretation of the results of neutrinoless double-weak decay experiments relies on theoretically calculated nuclear matrix elements. These theory calculations are informed by experimental measurements of related decays, such as the two-neutrino double-weak decays of the same isotopes [29, 30]. Especially on the neutron-rich side of the nuclide chart, the two-neutrino double-β^- decays have widely been observed [30]. However, for the proton-rich side no detection of two-neutrino double-electron capture , electron capture with positron emission or double-positron emission that exceeds the 5σ discovery threshold has been achieved to date [31]. Therefore, a significant measurement of either process in ^{124}Xe would provide nuclear theorists with a new experimental constraint from the proton-rich side of the nuclide chart.

This work leverages the world-record low background of XENON1T for a significant detection of two-neutrino double-electron capture in ^{124}Xe. Moreover, it illustrates the physics potential and detection prospects of the remaining five two-neutrino and neutrinoless decay modes of ^{124}Xe in future detectors. And lastly, it uses XENON1T as an example of how xenon-based Dark Matter detectors become competitive in searches of ^{136}Xe neutrinoless double-β decay.

The first chapter contextualises neutrino physics and Dark Matter direct detection. Theoretical and experimental considerations for direct Dark Matter and double-Weak decay searches are presented. A discussion of coherent elastic neutrino-nucleus scattering as a background for direct Dark Matter searches and a probe for physics beyond the SM concludes this chapter. Chapter two introduces the xenon dual-phase TPC as an instrument for rare event searches. Signal generation and measurement are described and an overview of the XENON1T experiment is given. The third chapter describes the analysis that lead to the first observation of two-neutrino double-electron capture in ^{124}Xe with XENON1T. Chapter four extends this work using a larger dataset and improved analysis techniques. The detection prospects for the neutrinoless decays of ^{124}Xe as well as the yet undetected positronic two-neutrino decay modes in future xenon detectors are investigated in chapter 5. The sixth chapter is devoted to a study of XENON1T's sensitivity to the neutrinoless double-β decay of ^{136}Xe. The final chapter summarises the analyses and provides an outlook on future studies and experiments.

Neutrino Physics in the Context of Dark Matter Direct Detection

1

Dark Matter direct detection experiments are critically dependent on reducing background sources and maximising target masses. The progress in these two disciplines within recent years has enabled experiments to reach unprecedented sensitivities for the exclusion of multiple Dark Matter candidate particles' parameter space. It has also highlighted the presence of irreducible neutrino backgrounds and rare signals that arise from long-lived isotopes undergoing second-order weak decays with or – potentially – without neutrino emission. This chapter will summarise the evidence for Dark Matter and motivate direct detection efforts. It will then discuss ultra-rare second-order weak decays that can be probed in these experiments as a window to new physics. It will conclude with a discussion of irreducible backgrounds from neutrinos for the next generation of direct Dark Matter searches and their possible exploitation as a probe for new physics.

1.1 Dark Matter evidence and direct detection

The concept of Dark Matter has been introduced in the early 20th century by astronomers, among them Kapteyn and Oort [32, 33], as a means of describing the motions of astronomical objects. Studying nebulae in the Coma cluster via their red shift, Fritz Zwicky observed that under the assumption of the Virial theorem the velocities of these nebulae could not be explained taking only the gravitational interactions of visible matter into account [34]. Since this observation in 1933, the body of evidence at all scales for the existence of weakly interacting, massive and non-baryonic matter has grown steadily and stimulated a broad effort for its experimental detection [8, 10].

1.1.1 Evidence for Dark Matter

Forty years after the pioneering observations, Vera Rubin found that stars' orbital velocities v_o within multiple spiral galaxies approach a constant value with increasing distance r to the respective galactic centre [35]. From the distribution of visible mass and Newtonian mechanics a $v_o \propto 1/\sqrt{r}$ dependence would be expected at large r. Since the original observation this behaviour has been shown to hold up even further from the galactic centre using the 21 cm hydrogen line [36]. The deviation can be explained by the introduction of a uniformly distributed dark matter halo with a $\rho \propto 1/r^2$ density profile [37, 38].

Gravitational lensing of light from luminous objects by aggregations of invisible Dark Matter augments the evidence from rotation curves [39]. The distortion of space-time caused by the Dark Matter in the foreground results in multiple images (strong lensing) or a deformation (weak lensing) of the image of an object in the background. The gravitational

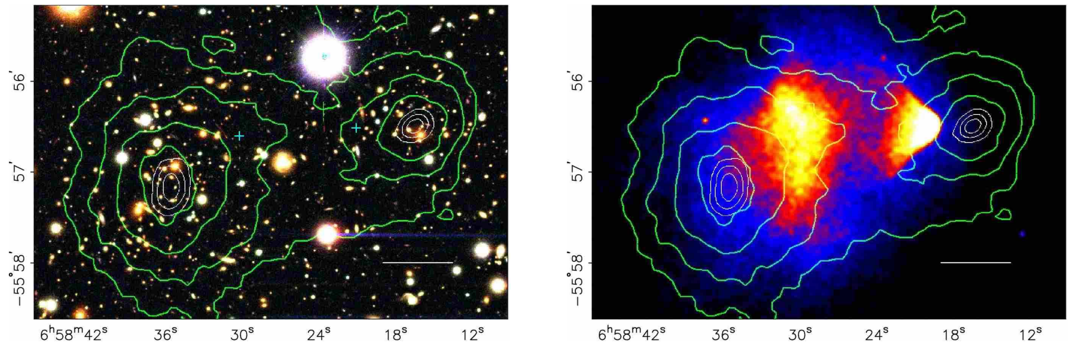

Figure 1.1: Left: Colourisation of Magellan images of the merging cluster 1E0657-558 (*bullet cluster*). The white bar indicates 200 kpc at the distance of the cluster. Green contours indicate the mass distribution of the clusters inferred from weak lensing. The white contours show the position uncertainties of the lensing peaks and correspond to 68.3 %, 95.5 %, and 99.7 % confidence levels. Cyan crosses mark the centre of gravity of the heated gas clouds from the right image. Right: Chandra X-ray image of the hot gas clouds constituting the bulk of baryonic matter in the image. A clear offset from the centre of mass is visible. Taken from [39].

potential of the deflecting Dark Matter can then be reconstructed from the degree of image deformation. The *bullet cluster* is a prominent example that extends the observational scales from galaxies to galaxy clusters [39]. The optical observations by the Magellan probe and X-ray observations by the Chandra satellite are shown together in figure 1.1. The visible light image allows to infer the mass distribution of two colliding galaxy clusters from gravitational lensing. The bulk of baryonic matter in both clusters is constituted by the colliding gas clouds that glow in X-rays. The offset of the centre of mass and these clouds is clearly visible. Accordingly, the main contribution of the cluster masses must come from non-luminous matter that can pass through the baryonic matter unperturbed.

The cosmic microwave background (CMB) and large scale structure (LSS) of the Universe are evidence at the largest observable scales [8, 10]. The CMB represents a snapshot of the era in cosmic evolution when photons decoupled from the electron-proton plasma of the early Universe, about 380,000 years after the Big Bang. Its near perfect black body spectrum with a temperature of 2.725 K has been studied by multiple satellite missions such as WMAP [40] and Planck [41]. Precision analyses of their data show temperature anisotropies with a relative intensity of 10^{-5}. These are an imprint of density and temperature fluctuations at the time of the CMBs origin and they are driven by the gravitational potential of inhomogeneously distributed baryonic[1] and Dark Matter. The inhomogeneities themselves are assumed to have originated from quantum fluctuations during the period of inflation. An exemplary power spectrum of the fluctuations, i.e. the strength of the fluctuations as a function of their angular scale, is shown in figure 1.2. The dashed black line shows the most recent fit to the Planck data [41]. The underlying six-parameter ΛCDM model describes the measured data well. It assumes that the energy content of the Universe is described by the cosmological constant or Dark Energy Λ, cold Dark Matter (CDM) and

---

[1] In this section baryonic matter refers to all matter in the Standard Model, baryons as well as leptons.

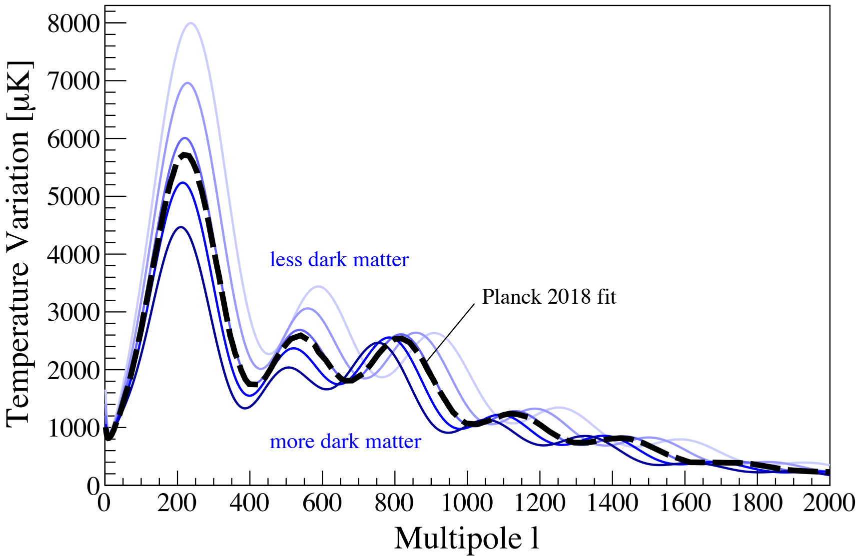

Figure 1.2: Temperature power spectrum of the CMB with a varying cold Dark matter density contribution and all other ΛCDM parameters kept constant. Values between $\Omega_{\mathrm{CDM}} = 0.11$ and $\Omega_{\mathrm{CDM}} = 0.43$ are indicated by solid blue lines with increasing saturation. The best fit of the ΛCDM model to Planck data [41] is shown as a dashed black line. Small multipoles correspond to large angular scales and vice versa. Taken from [10].

baryonic matter with the relative contributions [42]

$$\begin{aligned} \Omega_\Lambda &= 0.6911(62), \\ \Omega_{\mathrm{CDM}} &= 0.2589(57), \\ \Omega_{\mathrm{baryon}} &= 0.0486(10). \end{aligned} \tag{1.1}$$

As can be seen in figure 1.2 the amount of Dark Matter in the model modifies the peaks' positions and relative amplitudes [10]. The formation of large scale structure ($\gtrsim 10\,\mathrm{kpc}$) in the further evolution of the Universe is commonly studied employing N-body simulations of baryonic matter and Dark Matter [43]. These simulation outcomes can then be compared to astronomical observations, e.g. galaxy surveys [44,45]. Relativistic hot Dark Matter would disperse LSS, but this does not match the observed clustering scale of galaxies. This further adds to the CMB postulate of dominantly cold Dark Matter and discourages light neutrinos as Dark Matter particles [8].

The discussion of selected Dark Matter evidence is concluded with an example from an earlier stage in the evolution of the Universe in the first minutes after the Big Bang. Changing the baryon density in the phase of primordial nucleosynthesis modifies the expected relative abundances of light elements that can still be measured today [46]. Observed abundances of ^{2}H, ^{3}He, ^{4}He and ^{7}Li reflect the theoretical expectations for Ω_{baryon} values that match the precision analyses of the CMB [47]. Thus, they further motivate the existence of Dark Matter and exclude baryonic matter as an explanation. Accordingly, particle Dark Matter is composed of massive, neutral, non-baryonic and non-relativistic particles exhibiting weak self-interaction. However, the precise nature of this Dark Matter is yet to be determined and multiple candidate particles have been proposed.

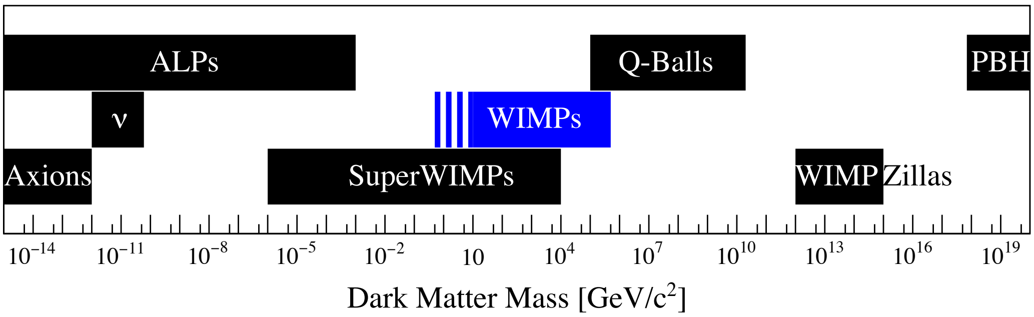

Figure 1.3: Mass range of proposed Dark Matter candidate particles. WIMP Dark Matter is displayed as a solid blue bar for masses above 10 GeV/c² and as a dashed blue bar for masses below. Taken from [10].

1.1.2 Weakly interacting massive particles and axions as Dark Matter candidates

Under the assumption that Dark Matter is made up of one or more particles[2], these cannot be part of the Standard Model of particle physics (SM). The proposed candidate particles span a wide mass range as seen in figure 1.3. At the low mass end of the mass spectrum one finds heavy right-handed neutrinos, axions and axion-like particles (ALPs) [7, 10]. Axions were initially proposed to resolve the smallness of CP violation in quantum chromodynamics (QCD) [8]. They are non-relativistic particles, are constrained by astrophysical and cosmological observations, and could account for the full Ω_{CDM}. Recently, XENON1T observed an excess of low-energy events that could be explained by interactions of solar axions or ALPs inside the detector [14]. However, these results are in strong tension with astrophysical constraints. Alternative explanations include unknown backgrounds or an enhancement of solar neutrino interaction rate due to a finite neutrino magnetic moment.

Weakly interacting massive particles (WIMPs) arise in various theories beyond the SM (BSM) where they constitute the lightest particles that cannot decay further due to the conservation of a new quantum number [5, 6, 8, 10, 48]. One example is the neutralino χ in supersymmetric theories that can act as the WIMP [49]. WIMPs are usually assumed to be in a mass range from a few GeV/c² for asymmetric Dark Matter models [50], over 100 GeV/c² for supersymmetry, and ultimately up to 100 TeV/c². The interaction cross-sections range from 10^{-41} cm^2 to 10^{-51} cm^2 [49]. WIMPs would have been thermally produced in the early Universe making them cold Dark Matter and leading to the so-called *WIMP miracle*: Assuming weak-scale thermal production cross-sections leads to a relic abundance in concordance with the measured Ω_{CDM} almost irrespective of the WIMP mass [10, 51]. Consequently, there is a broad scientific effort for their detection.

1.1.3 Direct Dark Matter searches

Three complementary approaches are employed in the search for Dark Matter: its production at colliders, indirect searches for signals from Dark Matter particles annihilating into SM particles, and direct searches for the scattering of Dark Matter particles off ordinary matter. The corresponding couplings to ordinary matter are depicted in figure 1.4. Direct detection relies on measuring the energy depositions of particle Dark Matter with an earth-

---

[2] For the sake of brevity we do not discuss massive compact halo objects (MACHOS) and primordial black holes (PBH) as Dark Matter candidates. Moreover, modifications of the laws of gravity are omitted in the discussion. All of these items have largely been excluded [10].

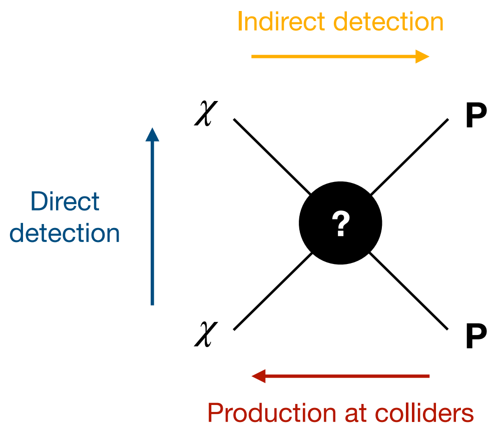

Figure 1.4: Schematic couplings of Dark Matter to ordinary matter and the respective detection channels. Adapted from [8].

bound target in an ultra-low-background detector. For WIMP searches the scattering with nuclei is of interest due to the similar masses while lighter Dark Matter particles such as axions would be detected via interactions with electrons, such as the axioelectric effect [8]. In the following the elastic scattering of WIMPs with target nuclei will be discussed. These interactions produce nuclear recoils (NRs) in the range of $(1-100)$ keV. The measurement of these events requires their discrimination from backgrounds. The interpretation of an eventual signal then relies on assumptions about the nuclear response as well as on astrophysical considerations. The latter include assumptions regarding the local Dark Matter density at Earth and its velocity distribution in the Milky Way [52].

The expected WIMP scattering rate R off a target nucleus with mass m_A is given by [8, 10, 52]

$$\frac{\mathrm{d}R}{\mathrm{d}E_{\mathrm{nr}}} = \frac{\rho_0 M}{m_A m_\chi} \int_{v_{\mathrm{min}}}^{v_{\mathrm{esc}}} v f(v) \frac{\mathrm{d}\sigma}{\mathrm{d}E_{\mathrm{nr}}} dv \tag{1.2}$$

with the nuclear recoil energy E_{nr}, the WIMP mass m_χ, the detector target mass M, and the local Dark Matter density ρ_0. Direct detection results are usually interpreted using $\rho_0 = 0.3\ \mathrm{GeV/c^2 cm^3}$ and assuming no substructure of the halo. Recent measurements indicate that this value could be increased by 50 % [10], but as long as all experiments follow the same convention this merely changes the normalisation of experimental results in direct detection. The integral over the product of WIMP velocity v, the velocity distribution $f(v)$, and the differential scattering cross-section $\frac{d\sigma}{dE_{\mathrm{nr}}}$ is calculated from the minimum WIMP velocity that can induce a nuclear recoil

$$v_{\mathrm{min}} = \sqrt{\frac{E_{\mathrm{nr}} m_A}{2\mu^2}}, \tag{1.3}$$

where the reduced mass of the WIMP-nucleus system is

$$\mu = \frac{m_A + m_\chi}{m_A m_\chi}. \tag{1.4}$$

The upper bound is given by the escape velocity $v_{\mathrm{esc}} = 544\ \mathrm{km/s}$ where WIMPs are no longer gravitationally bound in the galaxy. The actual 90 % confidence range of possible values is $498-608\ \mathrm{km/s}$ and the above number is used by convention [53]. The baseline assumption for the Dark Matter halo [10] is derived from the solution of the Boltzmann equation for collisionless particles: an isotropic isothermal sphere with a Maxwellian velocity distribution

$$f(\vec{v}) = N \cdot \exp\left(-\frac{3|\vec{v}|^2}{2\sigma^2}\right) \tag{1.5}$$

that does not rotate with the galactic disk. Here, $N \propto v^2$ is the normalisation constant and $\sigma(r) = \sqrt{\frac{3}{2}}\, v_c(r)$ is the velocity dispersion following the average orbital velocity $v_c(r)$ of objects at a distance r from the galactic centre. For an earthbound experiment [10] one has $v_c(r = 8\,\text{kpc}) = 220\,\text{km/s}$ from the solar orbital motion. The additional motion of Earth orbiting the Sun induces an annual modulation of the relative WIMP velocity distribution with respect to Earth's reference frame [8, 10]. Accordingly, the scattering rate measured in a terrestrial experiment would be modulated with a relative strength of ~ 5 % and an expected rate maximum on June 2nd. Moreover, this would induce a directional dependence of WIMP signals which would apparently come out of the direction of the constellation of Cygnus [10]. As background sources are neither expected to have a similarly modulated rate nor a specific direction, these would be telltale signatures of WIMP scattering.

As indicated in figure 1.4 the interaction mechanism between WIMPs and ordinary matter is unknown. In principle the interaction could be expressed by a scalar, vector or axial-vector effective Lagrangian [10]. The former two would describe interactions independent of the nuclear spin (SI) while the latter would describe a spin-dependent (SD) interaction:

$$\frac{d\sigma}{dE_\text{nr}} = \frac{m_A}{2v^2\mu^2}\left(\sigma_\text{SI}F^2_\text{SI}(E_\text{nr}) + \sigma_\text{SD}F^2_\text{SD}(E_\text{nr})\right). \tag{1.6}$$

Due to small de Broglie wavelength associated with the few tens of keV momentum transfer

$$|\mathbf{q}| = \sqrt{2m_A E_\text{nr}} \tag{1.7}$$

WIMPs would scatter coherently with the whole nucleus. The form factors $F^2_\text{SI}(E_\text{nr})$ and $F^2_\text{SD}(E_\text{nr})$ describe the loss of coherence at larger momentum transfers leading to larger recoil energies. The expected scattering rate decrease at higher $|\mathbf{q}|$ becomes relevant for heavier nuclei such as ^{131}Xe shown in figure 1.5 for SI interactions. The Helm parametrisation of the form factor [52, 54]

$$F(|\mathbf{q}|) = \frac{3J_1\left(\frac{|\mathbf{q}|R_A}{\hbar \text{c}}\right)\hbar\text{c}}{|\mathbf{q}|R_A} \cdot e^{-\frac{\mathbf{q}^2 s^2}{2\hbar^2\text{c}^2}} \tag{1.8}$$

is commonly used for the evaluation of the SI cross-section. Here, $R_A \approx 1.23 \cdot A^{\frac{1}{3}}$ fm is the nuclear radius of the respective isotope, $s \approx 0.9$ fm is the skin thickness, and $J_1(x)$ is the spherical Bessel function of the first kind. The exact parameters of the function have to be determined for each nucleus [10]. More recent large-scale nuclear structure calculations provide alternative nuclear responses that would have implications on the interpretation of Dark Matter direct detection results in case of a signal [55]. Assuming that the WIMP-proton coupling f_p is the same as the WIMP-neutron coupling f_n one can relate the total spin-independent WIMP-nucleus cross-section σ_SI to the WIMP-nucleon cross section σ_n using

$$\sigma_\text{SI} = \sigma_\text{n}\frac{\mu^2 \cdot (f_p Z + f_n(A - Z))^2}{\mu^2_\text{n}} = \sigma_\text{n}\frac{\mu^2}{\mu^2_\text{N}}A^2, \tag{1.9}$$

where μ_n is introduced as the reduced mass of the WIMP-nucleon system [10] and μ is defined as in equation (1.6). This quantity can be used to compare results from experiments using different target nuclei. The interplay of A^2-dependence and $|\mathbf{q}|$ implies that

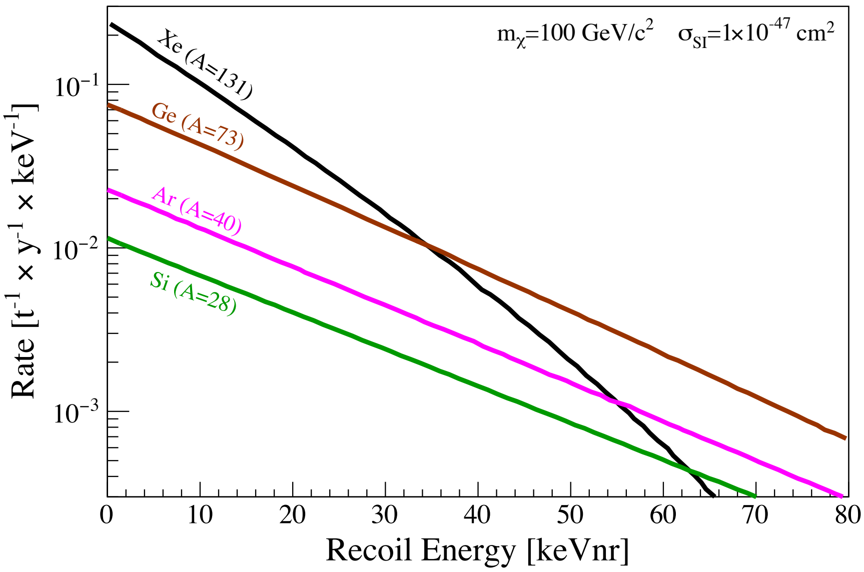

Figure 1.5: Nuclear recoil energy (E_{nr}) spectra for SI scattering of a WIMP with a mass $m_\chi = 100$ GeV/c². The assumed cross-section is $\sigma_{\mathrm{SI}} = 10^{-47}$ cm^2. At $E_{\mathrm{nr}} = 0$ the rate scales with the squared number of target nucleons A^2. At larger recoil energies the loss of coherence leads to a decrease of scattering rate, especially for heavier nuclei. Taken from [10].

experiments using heavier nuclei profit from the cross-section enhancement and can probe smaller cross-sections for heavier 50 – 100 GeV/c² WIMPs while lighter WIMPs require a low energy threshold due to the smaller $|\mathbf{q}|$.

Spin-dependent interactions assume that WIMPs are fermions that couple to unpaired nuclear spins. Accordingly, a detection requires even-odd nuclei in the target. These are discussed in detail in [10], but will not be further outlined in the scope of this work. The SI and SD interactions discussed above represent a subset of general effective field theories and other interaction mechanisms could be present, e.g. a coupling of WIMPs to nuclear exchange pions [15, 56, 57]. WIMPs could also scatter off nuclei inelastically, which would allow to distinguish between a spin-independent and spin-dependent main interaction mechanism [58].

In summary, the shape and rate of the recoil spectrum are driven by the interaction model with its associated nuclear structure effects, and the kinematics of the interaction [10]. SI scattering rates of $\mathcal{O}(1)$ events/tonne/year would be expected in the current generation of experiments factoring in current limits on σ_{n} and the local Dark Matter density ρ_0. The expected recoil energies are $E_{\mathrm{nr}} = \mathcal{O}(1 - 100)$ keV. Accordingly, a WIMP detector should feature a large target mass, high A for maximum cross-section enhancement, a low energy threshold and an ultra-low background. The impact of these requirements is reflected in current upper limits on σ_{n} as a function of m_χ [4]. These are shown in figure 1.6. For high WIMP masses large, ultra-low background time projection chambers using xenon targets such as XENON1T [12], LUX [59] and PandaX-II [60] provide the strongest limits. At low m_χ the limit curves are driven up by the energy threshold of these detectors. At high WIMP masses one expects a linear relation of cross-section and m_χ due to the decreasing number of WIMPs with increasing mass, but a fixed local Dark Matter density (cf. equation (1.2)). Semiconductor detectors, e.g. CDMSLite [61], and bolometers, e.g. CRESST [62], can probe lower m_χ due to their lower energy thresholds. However, the difficulty of achieving large target masses leads to worse upper limits. Recently noble gas experiments such as

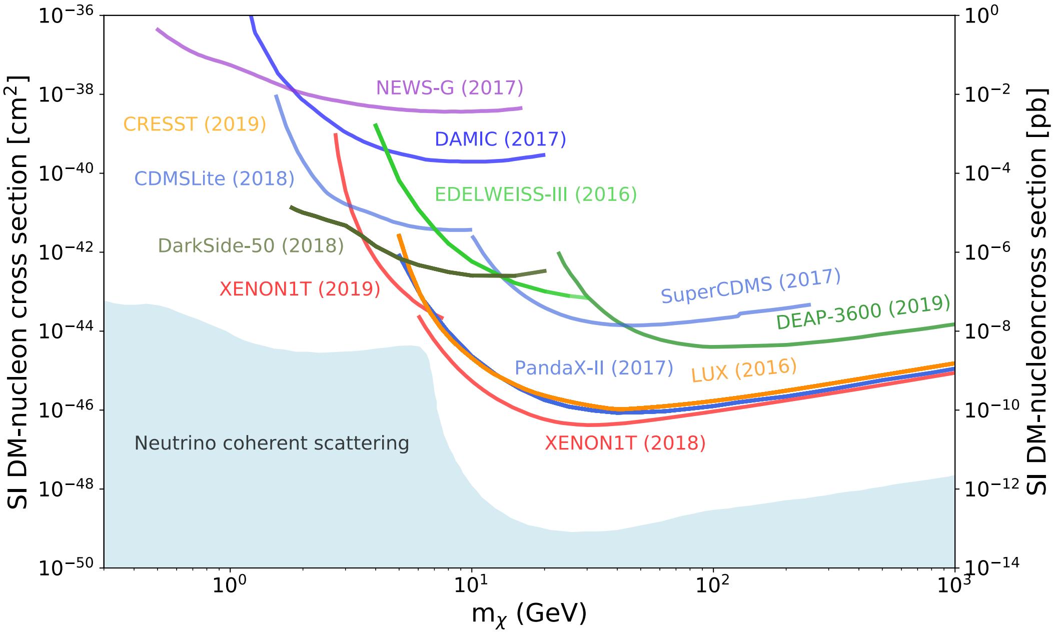

Figure 1.6: Current upper limits on the SI WIMP-nucleon cross-section σ_n from different experiments indicated as solid coloured lines. The parameter space where the coherent scattering of solar, atmospheric and diffuse supernova background neutrinos represent a sizeable part of the NR background is illustrated as a pale blue patch. Taken from [4].

DarkSide-50 and XENON1T have started to probe lower mass WIMPs by decreasing their energy threshold in data analysis [63, 64]. This is achieved by reconstructing events based on their ionisation signal only at the expense of background rejection capability.

The backgrounds in Dark Matter direct detection experiments can be divided into three categories: electronic recoil, nuclear recoil and instrumental backgrounds [18, 65, 66]. The latter category is detector-specific and can hardly be generalised. Among these backgrounds are wrongly reconstructed events, accidental coincidences of multiple interactions within a detector, and electronic noise [11].

In an electronic recoil (ER) event a radiogenic γ-ray or β-electron interacts with the electron shell of a target atom [67]. The source of these quanta are radioactive contaminants in the vicinity of the detector, in detector materials or within the target itself. External backgrounds can be mitigated by using appropriate absorbers as radiation shields. In order to minimize this background from the outset, low-activity detector construction materials are selected in extensive radioassay campaigns [68, 69]. The ever-increasing target mass of detectors coupled with a reconstruction of event positions also enables self-shielding [70]. Here, the outer layers of a detector's target are used as an active radiation shield. Backgrounds that are intrinsic to the target have to be reduced and mitigated in a different fashion. If they are not produced inside the target continuously, they can be removed by purification before data taking starts. This has been applied for the reduction of anthropogenic ^{85}Kr in the XMASS and XENON Dark Matter searches using cryogenic distillation [71–73]. However, radon is emanated into any target continuously from materials. The β-decays of its daughter isotopes represent the main background for most direct detection experiments [65, 66]. Material selection, surface treatments and detector construction in clean rooms with reduced radon-concentration in air are common reduction strategies [74–76]. Since radon is emanated from material surfaces, an increase in detector volume also reduces background by increasing the volume to surface ratio. Purification of the target is only viable if it can be applied continuously, e.g. by cryogenic distillation [77].

A discrimination of ER from WIMP NR signals can be achieved by exploiting the different energy deposition mechanisms in the target, namely the generation of scintillation light, ionisation charges and heat [8, 67]. The measurement of these three signal channels and the resulting measured signal shapes are different in general. The total signals from ER and NR then feature different relative contributions from those signal channels. This will be discussed in detail for xenon dual-phase time projection chambers (TPCs) in chapter 2. A general discussion of different detector types and signal channels can be found in [8] and [10].

The α-decays of radioactive contaminants can usually be vetoed easily due to the large energy deposition or distinct pulse shape of their signals in a given detector [11]. Still, a low α-activity has to be achieved in direct detection experiments since (α, n)-reactions can produce radiogenic neutrons. These undergo nuclear recoils within a detector and can mimic WIMP signals [18, 66]. Since a WIMP will only interact once in a given detector, a part of the resulting background can be rejected by identifying multiple interactions of the same neutron within a detector [11]. The same is true for muon induced neutrons where a muon interacts with a nucleus in the vicinity of a detector and produces a free neutron that can scatter inside the detector. In order to reduce the muon flux, experiments are located deep underground with shielding powers equivalent to several kilometres of water [10]. This also prevents cosmogenic activation of detector materials that can lead to additional electronic recoil backgrounds [78]. Auxiliary detectors further aid neutron mitigation. Neutrons that leave the WIMP detector after a single interaction can be tagged using gadolinium- or boron-loaded veto detectors surrounding the main WIMP detector [79–81]. Such an assembly can then be encapsulated in a muon-veto system that detects crossing muons using scintillation or Cherenkov light [82]. Any events in coincidence with a muon would be excluded from analysis.

With increasing sensitivity the coherent elastic scattering of solar, atmospheric and supernova neutrinos on target nuclei arises as an irreducible NR background. These interactions exactly mimic the coherent scattering signals of WIMP Dark Matter [83]. While current experiments are not yet sensitive enough to measure coherent elastic neutrino-nucleus scattering (CEνNS), it could limit the reach of future experiments [83, 84]. CEνNS is discussed in detail in section 1.3.

1.1.4 The XENON Dark Matter project

The XENON Dark Matter project is aimed at the direct detection of Dark Matter with xenon dual-phase TPCs that measure a dual light and charge signal. This detector type in general and the XENON1T experiment in particular will be discussed in detail in chapter 2. The XENON experiments have been constructed and are operated at Laboratori Nazionali del Gran Sasso (LNGS) by an international collaboration of ~ 160 scientists from 29 institutions.

The XENON10 detector was constructed in 2005 and used an active xenon target of 14 kg that was instrumented with photosensors [85]. It demonstrated stable long-term operation of a xenon dual-phase TPC, a low energy threshold of < 10 keV for nuclear recoils, novel energy reconstruction techniques, and it set limits on WIMP-nucleon interactions [86]. The successor experiment XENON100 increased the total xenon mass tenfold with 161 kg where 62 kg constituted the active target and 99 kg were used as an active veto. Due to the lowered background and threshold, larger target mass, and longer exposure of ultimately 48 kg-yr, an upper limit on the WIMP nucleon cross-section of $1.1 \cdot 10^{-45}$ cm^2 could be set for SI interactions with $m_\chi = 50$ Gev/c^2 at 90 % C.L. An SD WIMP-nucleon cross-section upper limit

Figure 1.7: The XENON1T experiment at hall B of LNGS in March 2018. The support building containing the gas handling and storage, data acquisition, xenon purification and cryogenic systems can be seen in the foreground. The cylindrical water tank in the background acted as passive shielding and active water Cherenkov muon veto. The detector was immersed in the water tank as shown on the poster covering the tank.

of $2 \cdot 10^{-40}$ cm^2 could be set at the same WIMP mass[3] and confidence level [87]. It was operated from January 2010 to January 2014 and superseded by XENON1T.

XENON1T was the first tonne-scale xenon dual-phase TPC for Dark Matter direct detection [88]. The technical aspects of the experiment will be presented in detail in section 2.2. A picture of LNGS hall B with the water tank, acting as passive shield and active water Cherenkov muon veto, containing the detector in the background, and the support building with the experimental infrastructure in the foreground is shown in figure 1.7. XENON1T was operated from November 2016 to February 2018 taking data in three science campaigns, referred to as science runs 0, 1 and 2 (SR0, SR1, SR2). All experimental data that is analysed in the scope of this work is taken from SR1 and SR2. Using the data acquired in SR0 and SR1 the XENON collaboration set world-leading upper limits on SI and SD WIMP nucleon cross-sections over a wide mass range [12, 13]. It also set the first limits on interactions of WIMPs with nuclear exchange pions [15]. The sensitivity at low WIMP masses could be enhanced by using ionisation signals for the analysis and discarding the scintillation signal as the main driver of a higher energy threshold [64]. Moreover, light Dark Matter searches were conducted searching for interactions enhanced by the Migdal effect or bremsstrahlung [16]. The SI limits are shown in figure 1.8.

All the above searches are centred around interactions of Dark Matter with a xenon nucleus. As an extension of the NR physics program, XENON1T searched for ER interactions of axions, axion-like particles and bosonic Dark matter. Owed to an unprecedentedly low ER background rate of 76 ± 2 events/t/yr below 30 keV ER energy, previously unexplored

---

[3] The limits here are given for the minimum of the cross-section vs. WIMP mass curve, where the strongest upper limits on the cross-sections were achieved.

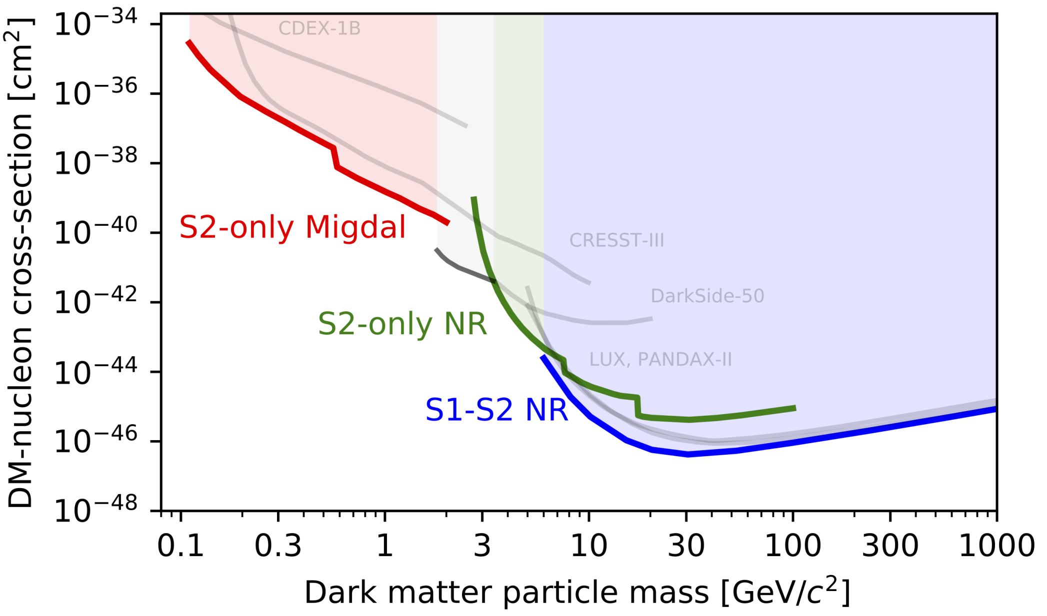

Figure 1.8: Upper limits on SI Dark Matter-nucleon interactions as a function of Dark Matter particle mass derived from XENON1T data (coloured) and selected other experiments (grey). The blue limit is from the main analysis using the scintillation and ionisation signals [12]. The solid red and green lines are from the analysis based on the ionisation signal only [64]. The red line uses the Migdal effect signal model, and the green line assumes elastic nuclear scattering [16]. Figure by the XENON collaboration.

parameter space could be probed. An excess of events at electronic recoil energies below 7 keV was observed [14]. This excess is compatible with all aforementioned signals as well as with an enhancement of the solar neutrino-electron interaction rate by means of a neutrino magnetic moment. Most notably solar axions are preferred over the background-only hypothesis at 3.5σ significance. However, the signal could also be attributed to previously unknown backgrounds such as the β-decay of tritium inside the xenon target – on its own with a significance of 3.2σ. Both, the solar axion and tritium hypothesis best fits, are shown in figure 1.9. The axion signal consists of three contributions from the ABC, Primakoff and ^{57}Fe solar axion production mechanisms. Even though the solar axion signal model is still preferred over the tritium background, its significance is reduced to 2.1σ. All signal models are in strong tension with experimental stellar constraints. A final verdict on the origin of this excess will be possible with XENONnT.

XENONnT is currently under commissioning and will increase the active target mass to 5.9 tonnes xenon with a target exposure of 20 t-yr[4] after 5 years of operation [18]. It expanded and reuses existing XENON1T infrastructure such as the water-tank, support building, cryogenic systems, and krypton distillation column. Additional systems including liquid purification and radon-distillation will allow for a higher chemical and radiopurity. The resulting seven-fold ER background reduction will enable up to two orders of magnitude larger sensitivity for SI WIMP-nucleon interactions [18]. For $\sigma_{\mathrm{n}} \geq 10^{-48}$ cm^2 a 5σ discovery would be within reach.

All XENON experiments used and still use natural xenon targets. One of the merits of

---

[4] In the following the shorthand t-yr and kg-d will be used for tonne · years and kilogram · days when referring to exposures.

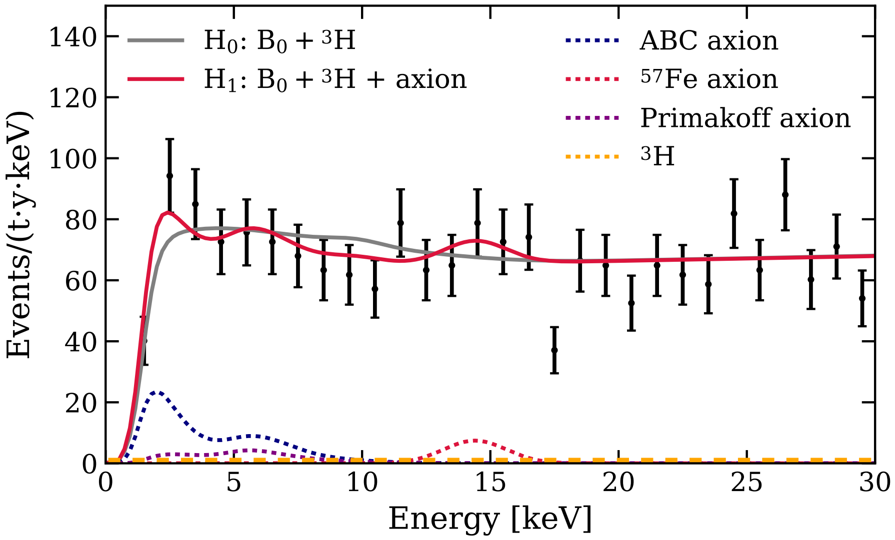

Figure 1.9: Low-energy ER data from XENON1T SR1 with fits of two models. The solid grey line indicates the best-fit of a nominal background B_0 and tritium (^{3}H). The solid red line also includes B_0 and ^{3}H, but adds a three-component solar axion model. The ABC, ^{57}Fe and Primakoff contributions of the red model are shown as the dashed blue, red and purple lines, respectively. The dashed orange line for tritium is scaled to zero in the best-fit of the ^{3}H+axion model. The solar axion significance for this model is 2.1σ. The tritium-only significance without an axion signal is 3.2σ compared to 3.5σ for an axion-only model without ^{3}H in the background model. Adapted from figure 7 in [14].

natural xenon is that it contains virtually no radioactive isotopes. The only background-producing isotopes undergo double-weak decays that feature half lives exceeding the age of the universe by a factor of 10^9 [30]. These decays are interesting for SM and BSM physics themselves and, with increasing detector size and specialised analyses, they become signals of interest.

1.2 Double weak decays

In a double weak process, such as the Double-β decay first theorised by Maria Goeppert-Mayer in 1935 [29], a double-even nucleus assumes a lower mass state along an isobar by the simultaneous conversion of two nucleons [30]. This occurs when no energetically favourable states are reachable by single β-decay. Such second-order weak processes exhibit half-lives in excess of $10^{17} - 10^{25}$ years. It is illustrated in figure 1.10 following the semi-empirical Bethe-Weizsäcker formula for nuclear masses where double-even nuclei have lower masses than double-odd nuclei due to the pairing term. Accordingly, either two neutrons are simultaneously converted into two protons or vice versa. The Q-value of the decay is given by the mass difference of the initial and final nuclei:

$$Q_{\beta\beta} = (M(A,Z) - M(A,Z\pm 2))\cdot c^2. \tag{1.10}$$

Due to charge conservation two electrons ($\beta^-\beta^-$) or positrons ($\beta^+\beta^+$) are emitted in the process. It is also possible that one (ECβ^+) or both positron emissions (ECEC) are substituted with captures of atomic electrons by the nucleus [26, 89]. In the SM weak interaction lepton number L is conserved and parity is violated, so the electronic decay mode is accompanied by the emission of two right-handed electron antineutrinos, $\bar{\nu}_e$,

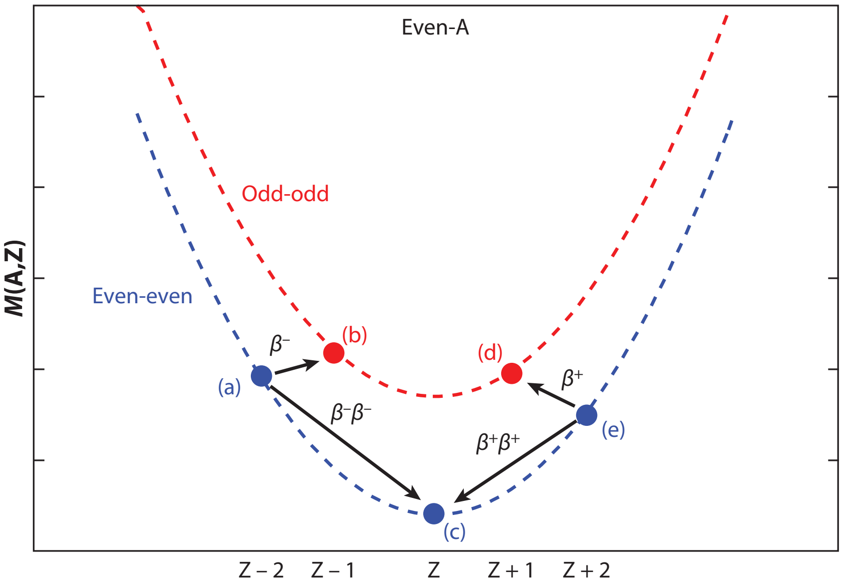

Figure 1.10: Mass parabolas according to the semi-empirical Bethe-Weizsäcker formula for nuclear isobars with even A. Due to the pairing term double-even nuclei have lower masses than double-odd nuclei. Accordingly, a single β^--decay from (a) to (b) is not possible. So is the positronic counterpart from (e) to (d). Accordingly, only direct double-weak transitions from (a) to (c), or (e) to (c) can occur. Taken from [30].

while the positronic decay mode is accompanied by the emission of left-handed electron neutrinos, ν_e:

$$\begin{aligned}
2\nu\beta^-\beta^-: &\quad (A,Z) \rightarrow (A,Z+2) + 2e^- + 2\bar{\nu}_e,\\
2\nu\beta^+\beta^+: &\quad (A,Z) \rightarrow (A,Z-2) + 2e^+ + 2\nu_e,\\
2\nu EC\beta^+: &\quad (A,Z) + e^- \rightarrow (A,Z-2) + e^+ + 2\nu_e,\\
2\nu ECEC: &\quad (A,Z) + 2e^- \rightarrow (A,Z-2) + 2\nu_e. \qquad (1.11)
\end{aligned}$$

However, theories beyond the SM (BSM) predict possible neutrinoless decays that can be written as in equation (1.11), but without the neutrinos. These would imply that neutrinos are their own antiparticles [90] and that lepton number is violated with $\Delta L = 2$. An observation of such a neutrinoless double-β decay would give insights into the neutrino mass scale [91] and could unravel the origin of the matter-antimatter asymmetry in the Universe by means of leptogenesis [24].

1.2.1 Two-neutrino double-β decay

The half-life for a two-neutrino double-β decay[5] can be expressed as

$$T_{1/2}^{2\nu} = (G_{2\nu}|M_{2\nu}|^2)^{-1} \qquad (1.12)$$

with the phase-space factor (PSF) $G_{2\nu}$ and the nuclear matrix element (NME) $M_{2\nu}$ [30]. In this factorisation, the PSF contains the kinematic part of the decay, i.e. the phase-space of the emitted leptons. The PSF is obtained by integrating over all possible emission energies

---

[5] In the following two-neutrino double-β decay refers to all second-order weak decay modes introduced in equation (1.11).

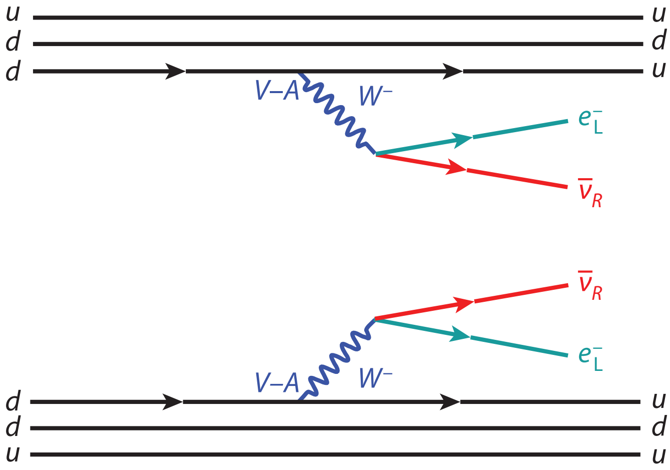

Figure 1.11: Feynman diagram for $2\nu\beta^-\beta^-$. Two left-handed electrons and two right-handed electron antineutrinos are emitted in the conversion of to neutrons to protons. On the particle-level two down-quarks are converted into up-quarks in a charged-current reaction. $V-A$ signifies the vector and axial couplings involved in the weak interaction. Taken from [30].

and angles of the emitted leptons and can be exactly calculated under consideration of relativistic wave functions and effects originating from finite nuclear size [92–97]. With four leptons the PSF has a

$$G_{2\nu} \propto Q^{11} \tag{1.13}$$

proportionality to the Q-value [98] and is usually given in units of $10^{-17} - 10^{-25}\,\mathrm{yr}^{-1}$ depending on the decay mode. The shape of the emitted electrons' spectra and angular distributions is to first order determined by the PSF while the NME only has a minor impact and primarily determines the total transition probability [30]. Since there are between two (2νECEC) and four ($2\nu\beta^\pm\beta^\pm$) leptons, and a nucleus in the final state, the emitted leptons exhibit a continuous energy distribution. Since the neutrinos usually leave experiments without an interaction, only electrons, positrons, their annihilation γ-rays, and X-rays as well as Auger electrons deposit energy inside detectors. The endpoint of the summed energy spectrum of these quanta is the Q-value of the decay. For the two electrons from $2\nu\beta^-\beta^-$ an example summed energy spectrum is illustrated in figure 1.12.

The NME describes the transition probability from the initial to the final nucleus [30] and is usually given as a number $\lesssim 7$ (cf. figure 1.17 for $0\nu\beta^-\beta^-$). With both nuclei being complex bound many-body systems that can undergo a multitude of transitions, the calculation is a complex task and many different approaches exist. The transition between the initial and final even-even nuclei progresses via a virtual odd-odd nucleus. This is schematically shown in figure 1.13 for ^{100}Mo. The initial ^{100}Mo nucleus in its ground state with the spin and parity configuration $J^P = 0^+$ transitions to a 0^+ state of ^{100}Ru via 1^+ states of a virtual ^{100}Tc nucleus. The NME then contains the initial (0^+_i), intermediate (1^+_m) and final (0^+_f) state wave functions as well as the operator ($\tau^+\sigma$) connecting them [30]. Due to isospin conservation only the Gamow-Teller matrix element contributes in the two-neutrino decay:

$$M^{2\nu}_{\mathrm{GT}} = \sum_{\mathrm{m}} \frac{\langle 0^+_\mathrm{f}|\tau^+\sigma|1^+_\mathrm{m}\rangle\langle 1^+_\mathrm{m}|\tau^+\sigma|0^+_\mathrm{i}\rangle}{E_\mathrm{m} - {}^{(M_\mathrm{i}+M_\mathrm{f})}/_2}. \tag{1.14}$$

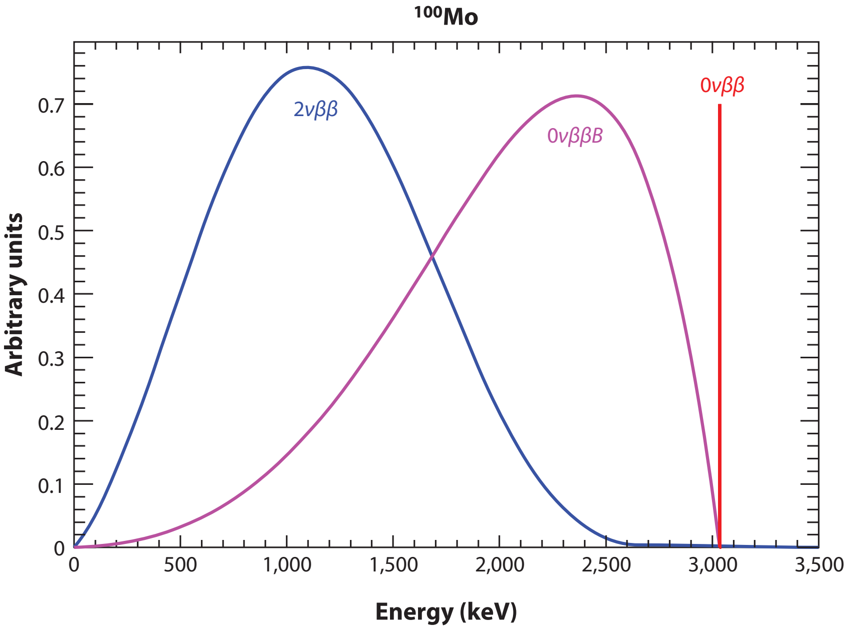

Figure 1.12: Example spectra for ^{100}Mo double beta decay for $2\nu\beta^-\beta^-$ (blue), $0\nu\beta^-\beta^-$ (red) and $0\nu\beta^-\beta^-B$ that involves the emission of a light or massless Goldstone Boson, a majoron B (purple). The latter decay mode is not discussed in this work. Taken from [30].

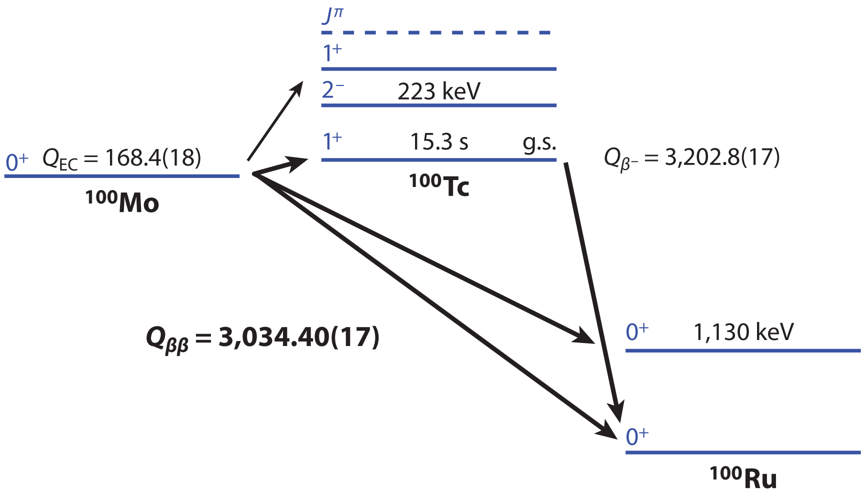

Figure 1.13: Level diagram for the $2\nu\beta^-\beta^-$ decay of ^{100}Mo to ^{100}Ru via a virtual ^{100}Tc nucleus. Taken from [30].

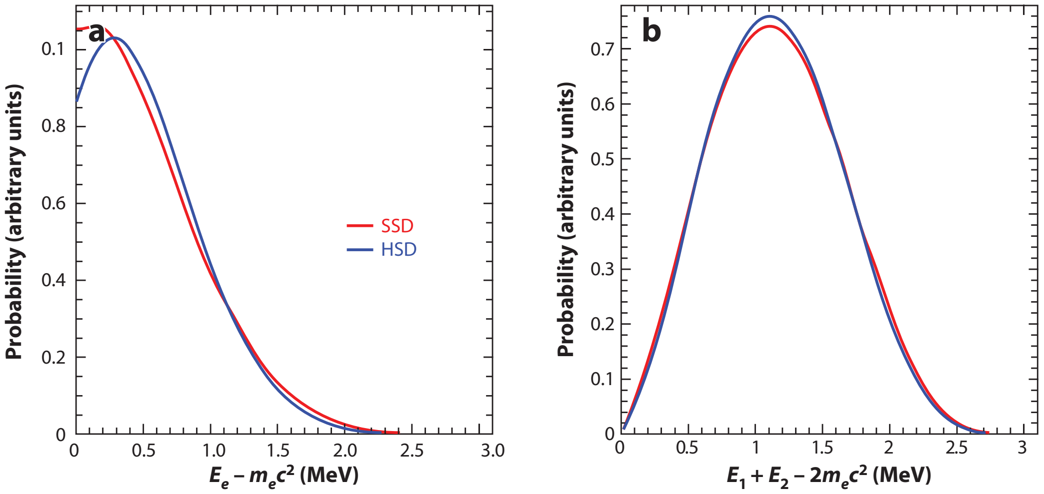

Figure 1.14: Example single electron (a) and summed two-electron (b) kinetic energy spectra for the $2\nu\beta^-\beta^-$ of ^{100}Mo under the SSD (red) and HSD (blue) hypotheses. Taken from [30].

The summation then goes over all 1^+ states of the intermediate nucleus with the energy E_m. The relative contributions of the individual intermediate states is a central question for the theoretical evaluation of nuclear matrix elements [30]. The hypothesis that the lowest-lying or ground 1^+ state dominates the decay is denoted as single-state dominance (SSD). A preference for the higher-lying 1^+ states is referred to as higher-state dominance (HSD). Both hypotheses impact decay rate and the shape of the single as well as the summed two-electron energy spectra as shown in figure 1.14. Measurements of the single electron spectra of $2\nu\beta^-\beta^-$ in ^{82}Se by NEMO-3 show clear evidence for a preference of SSD over HSD [99]. KamLAND-Zen has also started to investigate the shape of the two-electron spectra for ^{136}Xe[6] [100].

Common methods for the theoretical evaluation of nuclear matrix elements include the interacting boson model (IBM), the quasiparticle random phase approximation (QRPA) and the nuclear shell model (NSM). In the IBM [101] collective states in even-even nuclei are described by a set of interacting bosons that are formed by proton and neutron pairs and that are characterised by their angular momentum. IBM calculations are available for all double-weak decay modes of ^{124}Xe and ^{136}Xe that are discussed below [96, 102, 103].

In the NSM [30, 104] the NME is evaluated using a set of valence single-particle states. The interactions between these states is described by an effective Hamiltonian that is based on free nucleon-nucleon interactions, but modified by effective nuclear interactions. These adjustments are informed by information from nuclear spectroscopy such as transition probabilities and energy levels. The NSM is limited by the number of single-particle states that can be incorporated given computational constraints. The effects from these states are then replaced by effective operators which introduce uncertainties in the calculations. Full ab initio NSM calculations are – to date – only available for light nuclei, but effective NSM NME calculations for heavier xenon nuclei exist and agree with existing experimental data [105, 106].

In the QRPA [30, 107] complexity is reduced by limiting the amount correlations between

---

[6] Since the two-electron spectra exhibit less discrimination power and large liquid xenon-based experiments cannot resolve the individual electron spectra, the spectral shape effects of the SSD and HSD hypotheses will only become apparent in the next generation of xenon Dark Matter detectors where the $2\nu\beta^-\beta^-$ spectrum is not dominated by material backgrounds.

single-particle states rather than by truncating states. Another difference compared to the NSM approach is the use of phenomenological repulsive and attractive interactions rather than free nucleon-nucleon interactions. The experimental results on the two-neutrino NMEs can be reproduced by tuning of the phenomenological interactions' parameters [108–111].

The Gamow-Teller matrix element is approximately proportional to the squared axial coupling constant g_A^2 [23]. Due to shortcomings of the individual calculation approaches, modifications of the nuclear matrix elements are necessary in order to reconcile half-life measurements and theoretical predictions. Agreement is commonly achieved by reducing $g_A^2 = 1.27^2$ with the quenching factor q:

$$g_{A,\mathrm{eff}}^2 = q \cdot g_A^2. \tag{1.15}$$

Possible origins of this apparent quenching are different among the calculation methods and can include the incomplete treatment of nuclear medium effects, many-body currents and inherent shortcomings of the nuclear many-body models [23]. It has recently been shown for single β-decay that the apparent quenching arises largely from the coupling of the weak force to two nucleons and from nuclear correlations [112]. Accordingly, a reduction of the systematic uncertainty associated with subsuming model imperfections in a quenching factor could be realised in future calculation approaches.

It was established that there are two main benchmarks for nuclear matrix element calculations: Decay rate (half-life) and spectral shape of the emitted charged leptons. Experimental data from several isotopes and decay modes can be used in order to evaluate and refine the calculations. Even though the two-neutrino NMEs are not directly connected to their neutrinoless counterparts the evaluation of the underlying calculation methods is essential: Precise NME calculations are a prerequisite for extracting new physics from an eventual detection of neutrinoless double-β decay. Therefore, the measurement of new two-neutrino decay modes will help to validate calculations and to reduce systematic uncertainties associated with g_A^2-quenching.

1.2.2 Neutrinoless double-β decay and neutrino masses

Neutrinoless double-β[7] decay requires BSM physics where the two-neutrino emission is replaced by a different interaction [23]. In general the half-life of this process can be written as

$$T_{1/2}^{0\nu} = (G_{0\nu}\,|M_{0\nu}|^2\,|F_{0\nu}|^2)^{-1} \tag{1.16}$$

with the neutrinoless decay versions of the PSF $G_{0\nu} \propto Q^5$, the NME $M_{0\nu}$ and the BSM decay mechanism term $F_{0\nu}$. Multiple such mechanisms have been suggested and the light neutrino exchange will be presented here as a popular example. The Feynman diagram of the $0\nu\beta\beta$ process is shown in figure 1.15. The right handed $\bar{\nu}_e$ emitted at the upper vertex is absorbed as a left-handed $\bar{\nu}_e$ at the lower vertex. This is equivalent to the emission of a left-handed ν_e that occurs in the two-neutrino decay. Three requirements have to be met in order to allow this process: lepton number must be violated, neutrinos must be Majorana fermions, i.e. their own antiparticles, and neutrino masses must be finite in order to allow the change of neutrino helicity between the two vertices.

Lepton number violation (ΔL) can be fulfilled since no fundamental SM symmetry requires lepton number conservation. It is a common ingredient in grand unified theories (GUTs) that often require new neutral fermions, e.g. right-handed neutrinos. Detecting

---

[7] In the following, neutrinoless double-β decay refers to the neutrinoless analogues of all decay modes that were introduced in equation (1.11).

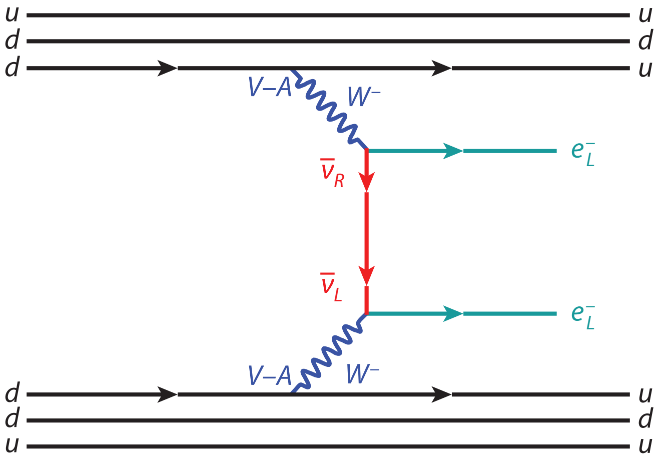

Figure 1.15: Feynman diagram for $0\nu\beta^-\beta^-$ mediated by light neutrino exchange. A right-handed antineutrino $\bar{\nu}_R$ emitted at the upper vertex is absorbed at the lower vertex as a left-handed neutrino ν_L. For Majorana neutrinos one has $\bar{\nu}_L = \nu_L$. Taken from [30].

neutrinoless double-weak processes would offer insights on the strength of the violation and open a window to the GUT energy scale [23]. The matter-antimatter asymmetry in the Universe is a further motivation for ΔL searches. It signifies that a mechanism creating more matter than antimatter must exist with a possible candidate being leptogenesis [24].

The concept of neutrinos as Majorana fermions [90] and the origin of neutrino masses are strongly interconnected. Since the observation of atmospheric and solar neutrino oscillations by Super-Kamiokande [19, 113] and SNO [20, 114], respectively, it is evident that neutrinos are massive. In the SM Lagrangian fermion mass terms occur as Yukawa couplings to the Higgs boson [4]

$$\mathscr{L} = \frac{f\upsilon}{\sqrt{2}} \bar{\psi}_{\mathrm{L}} \psi_{\mathrm{R}} + \mathrm{h.c.} \cong m_f \tag{1.17}$$

with the coupling $f\upsilon/\sqrt{2}$, the left-handed spinor of the antifermion $\bar{\psi}_{\mathrm{L}}$, and the right-handed spinor of the fermion ψ_{R}. However, there are no right-handed neutrinos in the SM. Moreover, cosmological and direct measurements of the neutrino masses show that they – and the respective couplings – are at least six orders of magnitude smaller than for the other fermions. This motivates a different mechanism generating the neutrino masses. One such possibility is adding an arbitrary number m of sterile neutrinos $\nu_{\mathrm{s,i}}$ that can be right-handed. Maintaining the gauge symmetry and renormalisability of the SM one can introduce two operators that lead to so-called Dirac (m_D) and Majorana (m_{RR}) mass terms [4]. The resulting $3+m$ mass eigenstates can be described by a $3+m$ dimensional vector ν of neutrino spinors. The charge ($\hat{C}$), parity ($\hat{P}$), and left- and right-handed projection operators ($\hat{P}_{L,R}$) act on this vector with

$$\begin{aligned} \nu^C &= \hat{C}\hat{P}\nu = \bar{\nu}, \\ \nu_L &= \hat{P}_L \nu. \end{aligned} \tag{1.18}$$

Assuming that neutrinos are Majorana particles with $\nu^C = \nu$, the Dirac and Majorana mass terms for a simplified 1+1 model with one active and one sterile neutrino can be written as

$$\begin{aligned}\mathscr{L} &= m_D\,(\bar{\nu}_L\nu_R + (\bar{\nu}_R)^C(\nu_L)^C) + m_{RR}\bar{\nu}_R(\nu_R)^C + \text{h.c.}\\ &= (\bar{\nu}_L,\,(\bar{\nu}_R)^C)\cdot\mathscr{M}\cdot\begin{pmatrix}(\nu_L)^C\\ \nu_R\end{pmatrix} + \text{h.c.}\end{aligned} \tag{1.19}$$

with the matrix

$$\mathscr{M} = \begin{pmatrix}0 & m_D\\ m_D & m_{RR}\end{pmatrix}. \tag{1.20}$$

Above $\mathscr{M}_{11} = m_{LL} = 0$ has already been set to zero since ν_L is in the same weak isospin doublet as the left-handed projection of the electron spinor e^-_L. This is not an issue for the right-handed singlet ν_R. The neutrino masses can be obtained by diagonalising $\mathscr{M}$:

$$m_{\nu_{1,2}} = \frac{m_{RR}}{2} \pm \sqrt{\frac{m_{RR}^2}{4} + m_D^2}. \tag{1.21}$$

For $m_{RR} \gg m_D$ the fraction ${m_D^2}/{m_{RR}}$ becomes very small. In this case neutrino masses would be pushed to low values due to a large m_{RR}. With m_D on the MeV-scale associated with the SM light fermion masses, the BSM m_{RR} would have to reach the TeV scale in order to obtain eV neutrino masses. The underlying so-called seesaw mechanism could be realised in various sub-types that will not be discussed in the scope of this work [4, 115]. In the 3+3 Majorana neutrino case, with 6 masses and 6 corresponding Majorana spinors, $\mathscr{M}$ now becomes a 6 × 6 matrix. One has

$$\mathscr{L} = (\bar{\nu}_L,\,(\bar{\nu}_R)^C)\cdot\begin{pmatrix}0_{3\times 3} & M_D\\ M_D & M_{RR}\end{pmatrix}\cdot\begin{pmatrix}(\nu_L)^C\\ \nu_R\end{pmatrix} + \text{h.c.}, \tag{1.22}$$

where M_D and M_{RR} are 3 × 3 matrices and $\nu_{L,R}$ each have three components. Here, the three sterile neutrinos' masses are of the order of the eigenvalues of M_{RR}. The masses of the active e, μ and τ neutrino flavor eigenstates are connected to the neutrino mass eigenstates by the neutrino mass matrix [23]

$$\begin{aligned}M_\nu &= M_D\cdot M_{RR}^{-1}\cdot M_D^T\\ &= U\cdot\begin{pmatrix}m_1 & 0 & 0\\ 0 & m_2 & 0\\ 0 & 0 & m_3\end{pmatrix}\cdot U^T,\end{aligned} \tag{1.23}$$

where $m_{1,2,3}$ are the real positive neutrino masses and U is the Pontecorvo-Maki-Nakagawa-Sakata (PMNS) matrix. This matrix contains three mixing angles $\theta_{12,23,13}$, one Dirac CP phase δ_{CP} and two Majorana CP phases $\eta_{1,2}$. One can write

$$\begin{aligned}U = &\begin{pmatrix}1 & 0 & 0\\ 0 & c_{23} & s_{23}\\ 0 & -s_{23} & c_{23}\end{pmatrix}\cdot\begin{pmatrix}c_{13} & 0 & s_{13}e^{-i\delta_{\text{CP}}}\\ 0 & 1 & 0\\ -s_{13}e^{i\delta_{\text{CP}}} & 0 & c_{13}\end{pmatrix}\cdot\\ &\begin{pmatrix}c_{12} & s_{12} & 0\\ -s_{12} & c_{12} & 0\\ 0 & 0 & 1\end{pmatrix}\cdot\begin{pmatrix}e^{i\eta_1} & 0 & 0\\ 0 & e^{i\eta_2} & 0\\ 0 & 0 & 1\end{pmatrix}\end{aligned} \tag{1.24}$$

using the shorthand $c_{\text{ij}} = \cos\theta_{\text{ij}}$ and $s_{\text{ij}} = \sin\theta_{\text{ij}}$. The mixing angles and the closely related squared-mass differences $\Delta m^2_{\text{ij}} = m^2_{\text{i}} - m^2_{\text{j}}$ of the mass eigenstates have been measured to great precision by neutrino oscillation experiments probing neutrinos from nuclear reactors

(θ_{13}), particle accelerators (θ_{23}, δ_{CP}), the sun (θ_{12}), and the atmosphere [4]. Moreover, evidence for CP violation has been observed by the T2K collaboration [116].

For light neutrino exchange the BSM factor from equation (1.16) becomes

$$|F_{0\nu}(m_\mathrm{i}, U_\mathrm{ei})| = \frac{\langle m_{\beta\beta}\rangle}{m_\mathrm{e}} = \frac{|\sum_\mathrm{i}(U_\mathrm{ei}^2 m_\mathrm{i})|}{m_\mathrm{e}}. \tag{1.25}$$

Here, a linear combination of the light neutrino masses m_i and elements of the PMNS mixing matrix U_ei leads to the effective neutrino mass $\langle m_{\beta\beta}\rangle$ [102, 117]. This coherent sum can contain phase-cancellations with

$$\langle m_{\beta\beta}\rangle = |m_1 c_{12}^2 c_{13}^2 + m_2 s_{12}^2 c_{13}^2 e^{i\eta_1} + m_3 s_{13}^2 e^{i\eta_2}|, \tag{1.26}$$

so it can assume a zero value despite non-zero physical neutrino masses. Accordingly, neutrinoless double-weak decays are not a direct probe of neutrino masses and $\langle m_{\beta\beta}\rangle$ differs from the direct kinematic observable

$$m_\beta = \sqrt{\sum_\mathrm{i} |U_\mathrm{ei}|^2 m_\mathrm{i}^2} < 1.1\,\mathrm{eV/c^2},\ 90\,\%\ \mathrm{C.L.} \tag{1.27}$$

probed by KATRIN [21]. The effective mass also differs from the model-dependent cosmological observable [23]

$$\Sigma = m_1 + m_2 + m_3. \tag{1.28}$$

with current limits from Planck satellite data also depending on the neutrino mass ordering [118]:

$$\Sigma < \begin{cases} 0.15\,\mathrm{eV/c^2},\ 95\,\%\ \mathrm{C.L.} & \mathrm{(NO)} \\ 0.17\,\mathrm{eV/c^2},\ 95\,\%\ \mathrm{C.L.} & \mathrm{(IO)} \end{cases} \tag{1.29}$$

The lightest neutrino mass m_β, the sum of all neutrino masses Σ and neutrino mass hierarchy are still unknown [4, 23]. In figure 1.16 $\langle m_{\beta\beta}\rangle$ is shown as a function of m_β and Σ for the normal (NO) and inverted (IO) mass orderings. The bands originate from varying the neutrino oscillation parameters within the 3σ ranges of a global fit to oscillation data. In the NO case $\langle m_{\beta\beta}\rangle$ is in the meV range and can vanish while in the IO case a minimum value of approximately 0.013 meV/c² exists [23, 120]. Even though current global fits of neutrino oscillation data show a preference for NO over IO with a significance of more than 3σ [121], this does not automatically require small values of $\langle m_{\beta\beta}\rangle$. In turn, searches for neutrinoless weak decays remain feasible even with NO [122].

As shown in equation (1.16), connecting the experimental observable $T_{1/2}^{0\nu}$ with $\langle m_{\beta\beta}\rangle$ requires theoretically calculated PSFs and NMEs for the neutrinoless process. Similar to the two-neutrino decays, the PSFs can in principle be precisely calculated while there is a multitude of calculation approaches for the NME. In general, the NME for neutrinoless double-weak decays is given by

$$M_{0\nu} = M_{\mathrm{GT}}^{0\nu} - \frac{g_V^2}{g_A^2} M_\mathrm{F}^{0\nu} + M_\mathrm{T}^{0\nu} \tag{1.30}$$

with the Gamow-Teller ($M_{\mathrm{GT}}^{0\nu}$), Fermi ($M_\mathrm{F}^{0\nu}$) and tensor ($M_\mathrm{T}^{0\nu}$) matrix elements, as well as the squared vector (g_V^2) and axial (g_A^2) coupling constants [23]. The challenges for the different calculation approaches are similar to those for the two-neutrino decays, but there is no one to one correspondence between the matrix elements for two-neutrino and neutrinoless processes. Due to the variety of calculation approaches, among them IBM, QRPA and NSM

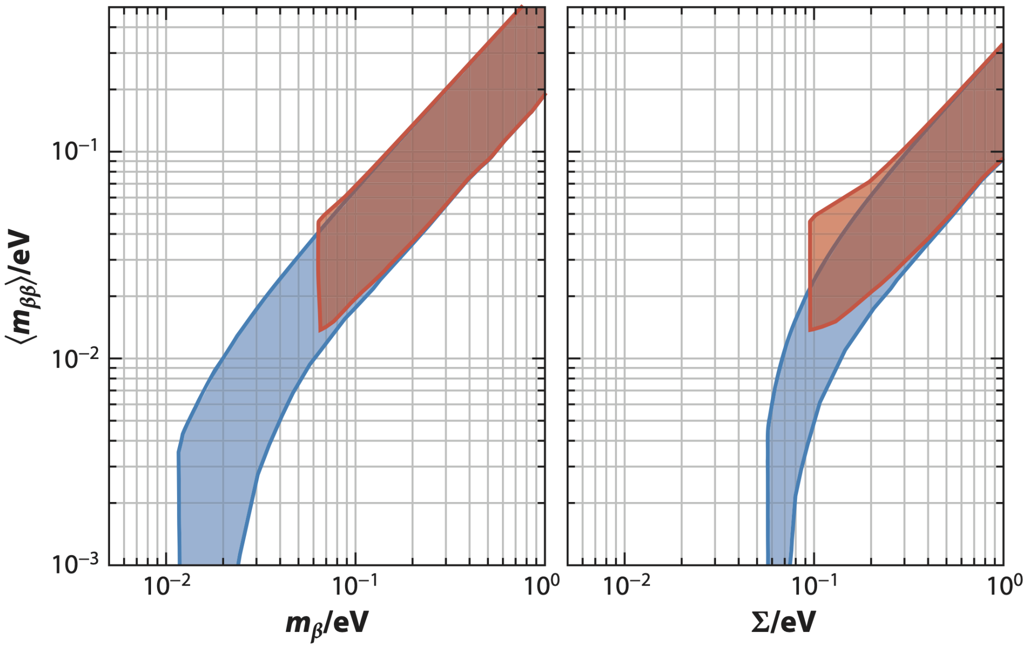

Figure 1.16: Effective neutrino mass $\langle m_{\beta\beta}\rangle$ versus the kinematic (m_β) and cosmological (Σ) neutrino mass observables for inverted (red) and normal (blue) mass orderings. The bands originate from varying neutrino oscillation parameters within 3σ intervals of a global fit to oscillation data. Taken from [23].

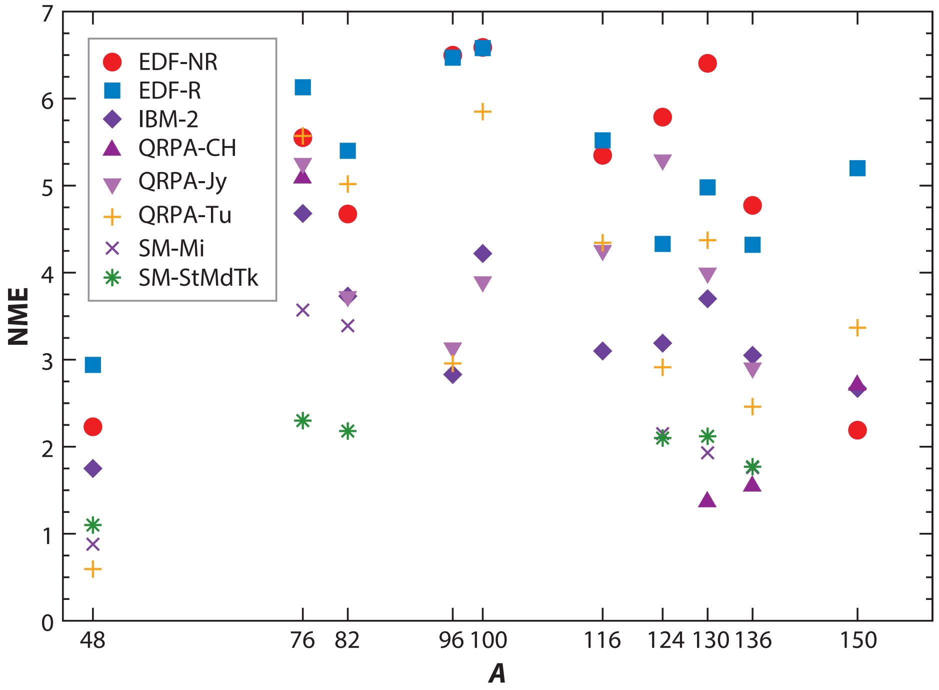

Figure 1.17: Nuclear matrix elements for several $0\nu\beta^-\beta^-$-nuclei with different calculation approaches. Three QRPA methods, the IBM-2 interacting boson model method and two shell-model (SM) approaches are included. All NMEs are given for $g_{A,\mathrm{eff}} = g_A = 1.27$. Taken from [23] with original data from [119].

as illustrated in figure 1.17, an uncertainty of about an order of magnitude exists for the connection of $T_{1/2}^{0\nu}$ and $\langle m_{\beta\beta}\rangle$.

Moreover, it is unknown if the apparent quenching of the axial coupling constant (cf. equation (1.15)) associated with the Gamow-Teller matrix element is the same among the two-neutrino and neutrinoless double-weak decays. The momentum transfer in two-neutrino processes is $\mathcal{O}(1)$ MeV while for neutrinoless processes it is $\mathcal{O}(100)$ MeV, where model deficiencies might boost the relative strength of the Gamow-Teller contribution [23]. The $g_{A,\text{eff}}^4$ dependence of the half-life induces an additional systematic uncertainty when deriving constraints on $\langle m_{\beta\beta}\rangle$ from lower limits on neutrinoless double-weak decay half-lives within a given NME calculation framework.

In conclusion the eventual detection of a neutrinoless double-weak decay would give an insight into how neutrinos acquire their minuscule masses even though a direct determination of the neutrino mass would not be within reach. Although several possible interactions could mediate neutrinoless double-weak processes, a detection would signify that neutrinos are Majorana particles because any Feynman diagram that can mediate the process will inadvertently generate light neutrino Majorana mass terms [123]. Moreover, an observation of the process would indicate Lepton number violation that could help to explain the matter-antimatter asymmetry in the Universe and give access to the energy scale of GUTs.

1.2.3 Experimental considerations and status of neutrinoless double-weak decay searches

There are 35 known isotopes that can undergo double-weak decays [124] and most experimental efforts have been made in the search for $0\nu\beta^-\beta^-$ [23]. The total energy deposit in neutrinoless decays occurs around $Q_{\beta\beta}$ that can be measured with great precision in Penning traps [27, 125, 126] (cf. equation (1.10)). Accordingly, experiments can define a narrow search region of interest (ROI) around the Q-value that is determined by the energy resolution of a detector. The number $N_{0\nu}$ of observed decays in the ROI is

$$N_{0\nu} = \ln(2)\frac{N_\text{A}\eta_{0\nu}\epsilon\cdot mt}{M_A T_{1/2}^{0\nu}} \tag{1.31}$$

with Avogadro's number N_A, the molar mass of the source containing the decaying isotope M_A, and the isotopic abundance of the isotope in the source $\eta_{0\nu}$. In order to compensate for the long half-life $T_{1/2}^{0\nu}$, experiments usually aim for large detection efficiency ϵ and exposure given by the livetime t, i.e. the time an experiment effectively records data, and source mass m. Moreover, the sources can be enriched in the double-weak decaying isotope leading to an increase in $\eta_{0\nu}$ [127]. Apart from the choice of a narrow ROI due to the wider spectra, these and the following experimental considerations also apply to measurements of two-neutrino decays. The half-life sensitivity of an experiment then depends on the number of signal and background events in the ROI [23]. A figure of merit is given by

$$T_{1/2}^{0\nu} \propto \begin{cases} \eta_{0\nu}\epsilon\cdot mt & \text{(background-free)} \\ \eta_{0\nu}\epsilon\sqrt{\frac{mt}{B\cdot\Delta E}} & \text{(with background)} \end{cases} \tag{1.32}$$

with the background index B and ΔE as the width of the ROI. Accordingly, reduction of background is paramount and the strategies follow the general low-background experiment considerations also applied in Dark Matter direct detection (cf. section 1.1.3). Notable backgrounds in the MeV range imposed by $Q_{\beta\beta}$ are γ-rays from ^{60}Co at 2.506 MeV as well as from the ^{232}Th and ^{238}U chains in detector materials – most notably from ^{214}Bi at various energies around 2 MeV and ^{208}Tl at 2.615 MeV [23]. These isotopes can also be mixed with

Table 1.1: Current status of $0\nu\beta^-\beta^-$ decay searches. Limits on $T^{0\nu}_{1/2}$ are given at 90 % C.L. MAJORANA refers to the MAJORANA demonstrator [129].

Isotope	**Experiment**	$\mathbf{T^{0\nu}_{1/2}}$ **[$\mathbf{10^{25}}$ yr]**	$\langle \mathbf{m_{\beta\beta}} \rangle$ **[eV/$\mathbf{c^2}$]**
^{48}Ca	ELEGANT-IV [130]	$> 5.8 \cdot 10^{-3}$	$< 3.5 - 22$
^{76}Ge	GERDA [131]	> 18	$< 0.079 - 0.180$
	MAJORANA [129]	> 1.9	$< 0.24 - 0.52$
^{82}Se	NEMO-3 [132]	$> 3.6 \cdot 10^{-1}$	$< 0.89 - 2.43$
^{96}Zr	NEMO-3 [133]	$> 9.2 \cdot 10^{-4}$	$< 7.2 - 19.4$
^{100}Mo	NEMO-3 [134]	$> 1.1 \cdot 10^{-1}$	$< 0.33 - 0.62$
^{116}Cd	Aurora [135]	$> 2.2 \cdot 10^{-2}$	$< 1.0 - 1.7$
^{128}Te	Arnaboldi et al. [136]	$> 1.1 \cdot 10^{-2}$	-
^{130}Te	CUORE [137]	> 3.2	$< 0.075 - 0.350$
^{136}Xe	KamLAND-Zen [25]	> 10.7	$< 0.061 - 0.165$
	EXO-200 [138]	> 3.5	$< 0.078 - 0.239$
^{150}Nd	NEMO-3 [139]	$> 2.0 \cdot 10^{-3}$	$< 1.6 - 5.3$

the target itself. In detectors ^{222}Rn is continuously emanated into the target and the ^{214}Bi daughter isotope emitting a β-electron with an endpoint energy of 3.270 MeV becomes relevant. Depending on the energy resolution of a detector a $0\nu\beta\beta$ signal can be mimicked by the two electrons from $2\nu\beta\beta$.

Ideally an isotope with $Q_{\beta\beta}$ above the energy range of common backgrounds is chosen. As a larger Q-value also increases available phase-space, the theoretical half-lives are shorter and easier to probe in general. However, the natural abundance of an isotope might make it difficult to accumulate enough target isotope in the source without resorting to costly enrichment or a massive source. One example is ^{48}Ca with $Q_{\beta\beta} = 4.263$ MeV, but just $\eta_{0\nu} = 0.187\,\%$ isotopic abundance [128]. In general, experimental searches for double-weak decays go beyond simple counting experiments within a predefined energy region. Their sensitivity is increased by leveraging more observables, such as time coincidences and general event topolgy, pulse-shape discrimination, spatial information, as well as simulated spectral shapes of signal and background. The specific strategy largely depends on the detector technology, the target isotope and the decay mode of interest. A detailed discussion of the search strategies for all ^{124}Xe decay modes and the $0\nu\beta\beta$ decay of ^{136}Xe will be given in chapters 5 and 6 of this work. A general discussion of detector technologies and analysis strategies can be found in [23].

An overview of the current status of $0\nu\beta^-\beta^-$ decay searches is given in table 1.1. The strongest current bounds on $\langle m_{\beta\beta} \rangle$ come from the GERDA and KamLAND-Zen collaborations that probe half-lives exceeding 10^{26} yr of ^{76}Ge and ^{136}Xe, respectively. The GERDA collaboration [131, 140, 141] achieves this with ^{76}Ge-enriched high purity germanium semiconductor detectors with an energy resolution of between (3.0 ± 0.1) keV and (3.6 ± 0.1) keV at full-width half maximum depending on the exact detector type. It uses low-radioactivity materials, an active Ar-based veto system and pulse-shape discrimination techniques to reach a background index of $\sim 5.2 \cdot 10^{-4}$ counts/keV/kg/yr [131]. The total exposure recorded by GERDA is 127.2 kg-yr [131]. This low background, high energy resolution and moderate exposure approach is markedly different from the strategy employed by KamLAND-Zen. It uses xenon-loaded liquid scintillator contained in a nylon balloon that is suspended in a larger liquid scintillator balloon within an 18 meter diameter non-scintillating oil buffer [23, 25]. Using 320 kg of xenon enriched in ^{136}Xe, an exposure of 504 kg · yr was accumulated. This allowed to set competitive limits even with larger background and a lower energy resolution compared to GERDA [25]. Other detector technologies include bolometers such as CUORE [142], tracking calorimeters that aim to individually reconstruct both β-electrons such as NEMO-3 [132], and time projection chambers such as EXO-200 that use technology similar to the XENON detectors discussed in section 2.1. The next generation of experiments will further evolve existing technologies, reduce backgrounds, and scale up exposures in order to probe the effective neutrino mass scale of the inverted hierarchy [23]. In the process xenon-based detectors will play a central role [143].

1.2.4 Double-β decay in xenon

Natural xenon contains four isotopes that can undergo second-order weak decays, namely ^{124}Xe and ^{126}Xe as proton-rich isotopes, as well as ^{134}Xe and ^{136}Xe as neutron-rich isotopes [124]. While two-neutrino decays to the ground state of the respective daughter nuclei have been detected for ^{136}Xe [144] and ^{124}Xe [31], only limits exist for ^{126}Xe [145] and ^{134}Xe [146] due to their lower Q-values and correspondingly smaller PSFs. The Q-values, allowed decay modes, abundances and measured half-lives – or limits in absence of a measurement – of these isotopes are shown in table 1.2. It is evident that no experimental constraints exist for most of the ^{124}Xe decays. Due to the low Q-value and thus unfavourable phase-space no second order weak decays haven been observed in ^{126}Xe and ^{134}Xe to date. The currently leading experiments with respect to measurements of $T_{1/2}^{2\nu\beta^-\beta^-}$ and lower limits on $T_{1/2}^{0\nu\beta^-\beta^-}$ are EXO-200 [138, 147–149] and KamLAND-Zen [25, 100] which both use targets enriched in ^{136}Xe. While KamLAND-Zen is continuously increasing its target mass, EXO-200 has been decommissioned to be superseded by nEXO [127, 150]. Due to their increasing total mass and decreasing background the next generation of Dark Matter experiments using non-enriched xenon could achieve competitive sensitivities [151, 152]. In this case a 50 tonne natural xenon detector such as DARWIN would achieve a similar exposure as the 5 tonne enriched xenon detector nEXO.

Decay modes of ^{124}Xe

At (2856.73 ± 0.12) keV [27], the Q-value of ^{124}Xe energetically allows three two-neutrino and neutrinoless decay modes: double-electron capture (0νECEC and 2νECEC), double-positron emission ($0\nu\beta^+\beta^+$ and $2\nu\beta^+\beta^+$) and single electron-capture with coincident positron emission ($0\nu\mathrm{EC}\beta^+$ and $2\nu\mathrm{EC}\beta^+$) [89]. In the following the decay modes are grouped by the number of emitted positrons. Each emitted positron will lead to the emission of at least two γ-rays and reduce the energy that is initially available for the positrons and neutrinos by twice the positron mass. Each of the 0ν decays will exhibit a mono-energetic total energy deposition while the 2ν decays have continuous spectra due to the neutrinos leaving the detector without further interaction. Furthermore, only decays to the ground state of the daughter nucleus are considered for the positronic decay modes. A special treatment is required for 0νECEC, as only decays which resonantly populate an excited state of ^{124}Te may be accessible to experiments [8].

---

[8] This section has to a large extent been published in [155].

Table 1.2: Xenon isotopes that can undergo second-order weak decays with their isotopic abundances, Q-values, decay modes and experimentally determined half-lives. Lower limits on half-lives are given at 90 % C.L.

Isotope	**Abundance** **[%]** [153]	**Q-value** **[keV]**	**Decay** **mode**	**Experimental** **half-life [yr]**
^{124}Xe	0.095(5)	2856.73(12) [27]	2νECEC	$(1.8 \pm 0.5_{\text{stat}} \pm 0.1_{\text{sys}}) \cdot 10^{22}$ (2νKK) [31]
			0νECEC	–
			2νECβ^+	–
			0νECβ^+	–
			$2\nu\beta^+\beta^+$	–
			$0\nu\beta^+\beta^+$	–
^{126}Xe	0.089(3)	918.3(3.4) [128]	2νECEC	$> 1.9 \cdot 10^{22}$ [145]
			0νECEC	–
^{134}Xe	10.436(35)	824.1(0.3) [128]	$2\nu\beta^-\beta^-$	$> 8.7 \cdot 10^{20}$ [146]
			$0\nu\beta^-\beta^-$	$> 1.1 \cdot 10^{23}$ [146]
^{136}Xe	8.857(72)	2458.7(0.6) [154]	$2\nu\beta^-\beta^-$	$(2.18 \pm 0.05) \cdot 10^{21}$ [144]
			$0\nu\beta^-\beta^-$	$> 1.07 \cdot 10^{26}$ [25]

2νECEC

In the 2νECEC two electrons from the atomic shell are captured by the nucleus [26]. Two protons are converted into neutrons under the emission of two electron-neutrinos:

$$^{124}\text{Xe} + 2\text{e}^- \rightarrow {}^{124}\text{Te} + 2\nu_\text{e} + \text{X}_{2\text{k}}. \tag{1.33}$$

In this decay, the measurable signal is constituted by the atomic deexcitation cascade of X-rays and Auger electrons $\text{X}_{2\text{k}}$ that occurs when the vacancies of the captured electrons are refilled. A schematic of the decay is shown in figure 1.18. For the capture of two K-shell electrons that occurs in 76.5 % of all decays [89]

$$E_{2\text{k}} = (64.457 \pm 0.012)\,\text{keV} \tag{1.34}$$

is the energy of the double-electron hole [27]. It is slightly larger than twice the energy of a single K-electron hole [156]. The double K-electron capture has recently been measured with the XENON1T Dark Matter detector [31]. At $T_{1/2}^{2\nu\text{KK}} = (1.8 \pm 0.5_{\text{stat}} \pm 0.1_{\text{sys}}) \times 10^{22}$ yr the measurement agrees well with recent theoretical predictions [106, 108, 110] and is the longest directly measured half-life to date. As a part of this work the measurement will be discussed in chapter 3.

Electron captures from higher shells, e.g. the L-shell, are also possible, but less likely due to the smaller overlap of the electron wave functions with the nucleus. Mixed KL- or LL-captures can occur with relative frequencies of 22.0 % and 1.5 %, respectively[9] [89, 145]. Other than for $E_{2\text{k}}$ there are currently no calculations for the corresponding double-hole

---

[9] These numbers are obtained from the wave function normalisations of the low-lying shells in ^{124}Xe from [89]. The Dirac solutions assuming a homogeneous charge-distribution in the nucleus are used and solely

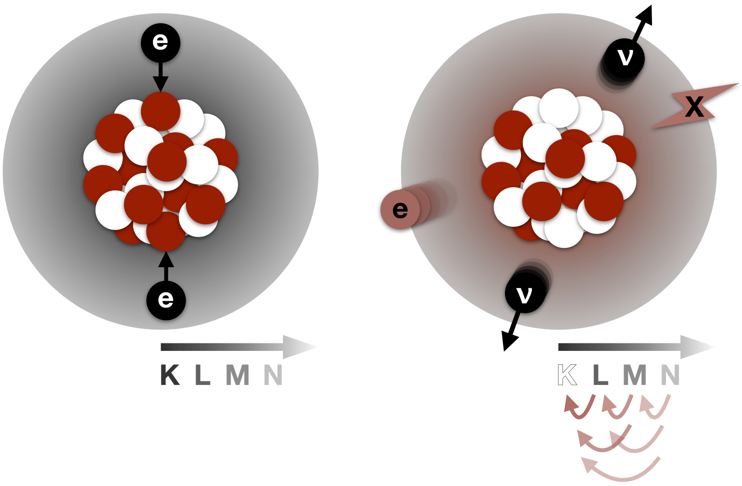

Figure 1.18: In the 2νECEC process the nucleus captures two atomic shell electrons (black) and simultaneously converts two protons (red) to neutrons (white). The electrons are most likely captured from the K-shell. Two neutrinos carrying most of the decay energy (black) are emitted from the nucleus. The atomic shell is left in an excited state with two holes and a cascade of X-rays (red X) and Auger electrons (red e) are emitted in its relaxation. Here, the lower shells are refilled from the higher ones (arrows). Taken from [31].

energies E_{kl} and E_{ll}. They can be approximated by viewing the double-electron capture as two subsequent single electron captures. The K- and L1-electrons in the intermediate ^{124}I nucleus are bound more strongly than in the final ^{124}Te nucleus. This approximation can be tested on the KK-capture where one would add the K-edge energies of iodine and tellurium [156]

$$\begin{aligned} E_{\mathrm{k,\,I}} &= 33.16969(89)\ \mathrm{keV}, \\ E_{\mathrm{k,\,Te}} &= 31.8150(12)\ \mathrm{keV}, \end{aligned} \tag{1.35}$$

yielding

$$\tilde{E}_{2\mathrm{k}} = E_{\mathrm{k,\,I}} + E_{\mathrm{k,\,Te}} = 64.99\ \mathrm{keV}, \tag{1.36}$$

which is larger than the result from the oversimplified $2 \cdot E_{\mathrm{k,\,Te}} = 63.63$ keV, but would overestimate $E_{2\mathrm{k}}$. Since the mean of $2 \cdot E_{\mathrm{k,\,Te}}$ and $\tilde{E}_{2\mathrm{k}}$ at $\overline{E}_{2\mathrm{k}} = 64.31$ keV is reasonably close to the theoretical value of $E_{2\mathrm{k}}$, $\overline{E}_{\mathrm{kl}}$ and $\overline{E}_{\mathrm{ll}}$ are calculated in the same fashion[10]. The relevant L1-edge energies [156] are

$$\begin{aligned} E_{\mathrm{l,\,I}} &= 5.18838(81)\ \mathrm{keV}, \\ E_{\mathrm{l,\,Te}} &= 4.93965(99)\ \mathrm{keV} \end{aligned} \tag{1.37}$$

---

captures from the L1 shell are taken into account. Captures from the L2 and L3 shell are suppressed by an order of magnitude when compared to the L1 shell, so they are not taken into account here. Note that the numbers have been rounded to the first decimal place. In order to not exceed 100 %, the LL-fraction was scaled down from 1.6 %.

[10] Since the experimental energy resolutions relevant in this work are $\mathcal{O}(1\ \mathrm{keV})$ one can safely disregard the uncertainties of the X-ray energy reference values.

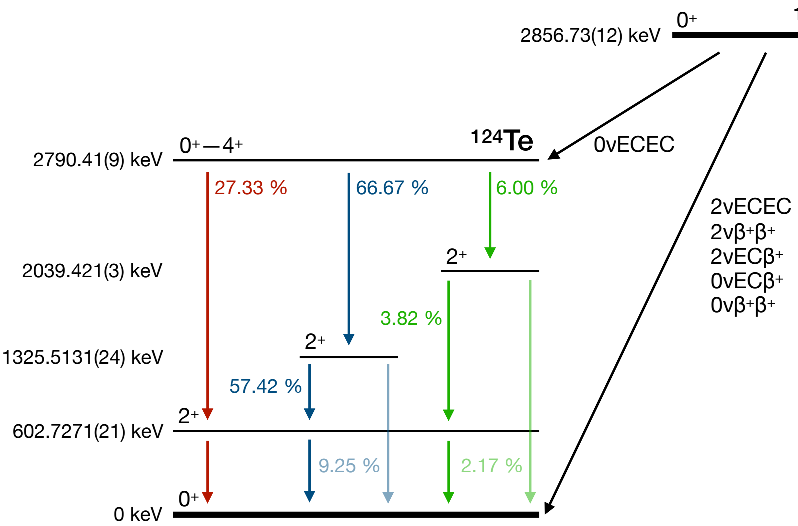

Figure 1.19: Decay scheme of ^{124}Xe. While $0/2\nu EC\beta^+$, $0/2\nu\beta^+\beta^+$ and 2νECEC most likely occur to the ground state of ^{124}Te, 0νECEC resonantly populates an excited state at (2790.41 ± 0.09) keV. There are five different known γ-cascades along three different intermediate states. The energy level and J^P are given for each state and the γ-intensities $I_{\gamma,\mathrm{i}}$ for the transitions have been normalised, such that $\sum_\mathrm{i} I_{\gamma,\mathrm{i}} = 100\,\%$ [157]. Taken from [155].

and lead to

$$\begin{aligned} \overline{E}_\mathrm{kl} &= 37.29^{+0.82}_{-0.53}\,\mathrm{keV}, \\ \overline{E}_\mathrm{ll} &= (10.01 \pm 0.13)\,\mathrm{keV}. \end{aligned} \tag{1.38}$$

The uncertainty for the LL capture is given by the difference of $\overline{E}_\mathrm{ll}$ and $\tilde{E}_\mathrm{ll}$. The asymmetric uncertainties on E_kl stem from the fact that the sequence of captures can either be KL or LK, so the mean has to be calculated from the input values $\tilde{E}_\mathrm{kl}$, $\tilde{E}_\mathrm{lk}$ and $E_\mathrm{k,Te} + E_\mathrm{l,Te}$. The uncertainties are then given by the largest differences between $\overline{E}_\mathrm{kl}$ and the input values.

Resonant 0νECEC

In contrast to the two-neutrino decay mode, no initial quanta are emitted from the nucleus in the 0νECEC. For a double-K capture one only has the atomic deexcitation cascade X_2k. In order to conserve energy and momentum the energy released in the 0νECEC decay has to be transferred to a matching excited nuclear state of the $^{124}\mathrm{Te}^*$ daughter isotope:

$$\begin{aligned} {}^{124}\mathrm{Xe} + 2\mathrm{e}^- &\rightarrow {}^{124}\mathrm{Te}^* + \mathrm{X}_\mathrm{2k}, \\ {}^{124}\mathrm{Te}^* &\rightarrow {}^{124}\mathrm{Te} + \text{ multiple } \gamma. \end{aligned} \tag{1.39}$$

The corresponding energy match has to be exact within uncertainties, so the excitation energy $E_\mathrm{exc,res}$ of the state $^{124}\mathrm{Te}^*$ has to fulfil the resonance condition

$$\begin{aligned} E_\mathrm{exc,res} &= Q - E_\mathrm{2k} \\ &= (2856.73 \pm 0.12)\,\mathrm{keV} - (64.457 \pm 0.012)\,\mathrm{keV} \\ &= (2792.27 \pm 0.13)\,\mathrm{keV}. \end{aligned} \tag{1.40}$$

The resonance is approximately realised with a positive parity nuclear state at an energy of $E_{\mathrm{exc}} = (2790.41 \pm 0.09)\,\mathrm{keV}$ and a corresponding deviation of $\Delta E_{\mathrm{exc,res}} = (1.86 \pm 0.15)\,\mathrm{keV}$ from the resonance[11] [27, 157]. The angular momentum of this state is not precisely known, but 0^+ to 4^+ are possible J^P configurations. The level scheme relevant to the decay is shown in figure 1.19. There are five different γ-cascades that are either $\geq 0^+ \to 2^+ \to 0^+$ or $\geq 0^+ \to 2^+ \to 2^+ \to 0^+$ for two- and three-γ transitions, respectively. As a considerable decay rate is only expected to 0^+ and 1^+ states [27], in the following it is assumed that the resonantly populated state is 0^+. The dominant $0^+ \to 2^+ \to 2^+ \to 0^+$ transition occurs in 57.42 % of all decays.

$0/2\nu\mathrm{EC}\beta^+$

The electron capture with coincident positron emission can be written as

$$^{124}\mathrm{Xe} + \mathrm{e}^- \to {}^{124}\mathrm{Te} + \mathrm{e}^+ (+2\nu_\mathrm{e}) + \mathrm{X_k}, \tag{1.41}$$

where the Standard Model decay features the emission of two electron-neutrinos (ν_e) in addition to the positron (e^+). We assume the most-likely case of an electron capture from the K-shell. This will produce a cascade of X-rays and Auger electrons ($\mathrm{X_k}$) with a total energy of (31.8115 ± 0.0012) keV [156]. The total available energy for the e^+ and the two ν_e is then given by

$$\begin{aligned} E_\mathrm{e}(+E_{2\nu}) &= Q - 2m_\mathrm{e}\mathrm{c}^2 - E_\mathrm{k} \\ &= (2856.73 \pm 0.12)\,\mathrm{keV} - 1022.00\,\mathrm{keV} - 31.81\,\mathrm{keV} \\ &= (1802.92 \pm 0.12)\,\mathrm{keV}, \end{aligned} \tag{1.42}$$

where one has a mono-energetic positron for the neutrinoless decay and a β-like spectrum for the two-neutrino decay. Upon thermalisation the e^+ annihilates with an atomic electron resulting in two back-to-back 511 keV γ-rays[12].

$0/2\nu\beta^+\beta^+$

The reaction equation for the $\beta^+\beta^+$-decay to the ground state is

$$^{124}\mathrm{Xe} \to {}^{124}\mathrm{Te} + 2\mathrm{e}^+ (+2\nu_\mathrm{e}). \tag{1.43}$$

The energy available for the two e^+ and the two ν_e is given by

$$\begin{aligned} E_{2\mathrm{e}}(+E_{2\nu}) &= Q - 4m_\mathrm{e}\mathrm{c}^2 \\ &= (2856.73 \pm 0.12)\,\mathrm{keV} - 2043.99\,\mathrm{keV} \\ &= (812.74 \pm 0.12)\,\mathrm{keV}, \end{aligned} \tag{1.44}$$

where one has a continuous spectrum for the energies of the two positrons for the two-neutrino decay and a peak for the neutrinoless decay. Upon thermalisation the positrons annihilate to at least four 511 keV γ-rays emitted as back-to-back pairs. The angular correlation of the positrons is not discussed in the scope of this work, as their thermalisation range is smaller than the spatial resolution in existing and planned experiments.

---

[11] The authors of [27] recommend to perform at least one more independent measurement of the $^{124}\mathrm{Xe} \to {}^{124}\mathrm{Te}$ Q-value in order to resolve discrepancies between existing measurements. In addition a determination of J^P of the (2790.41 ± 0.09) keV excited state would be helpful in order to further assess the feasibility of this decay mode.

[12] The subdominant uncertainties of the electron mass (44 ppb) and the K-shell X-ray energy are neglected in the above calculations. Moreover, the 2γ-annihilation is by far the most likely case for positronium, but more γ-rays are possible.

1.3 Coherent elastic neutrino-nucleus scattering

CEνNS was investigated in depth as a theory project within the graduate programme of the research training group GRK 2149 *Strong and weak interactions – from hadrons to dark matter*. To this end a collaboration with the nuclear theory colleagues A. Schwenk, M. Hoferichter and J. Menéndez was initiated in order to investigate the potential of CEνNS as a signal in Dark Matter direct detection experiments. While no results are presented in this work, an active collaboration on this project persists. This section describes the theoretical foundations of CEνNS, illustrates its potential as a probe of interactions beyond the standard model and introduces it as a background for direct Dark Matter searches.

1.3.1 Theoretical description and formalism

Although it was theorised in 1974 [158], CEνNS has eluded detection until 2017 when it was observed in CsI by the COHERENT collaboration [159]. While the measurement of CEνNS cross-sections was initially proposed as a probe of the weak current of the SM, it also bears potential for the investigation of BSM physics. As in direct Dark Matter detection (cf. equation (1.6)), the response of the nucleus is crucial for the interpretation of the cross-section. A general formalism based on the large-scale nuclear shell model for this response – typically subsumed in the weak form factor $F_W(\mathbf{q}^2)$ – for SM and BSM interactions can be found in [160]. The results build on the nuclear structure factors for Dark Matter direct detection [55]. As in the case of the Dark Matter nuclear responses, the new calculations present an alternative to the simplified Helm form factor that was introduced in equation (1.8) and that is commonly used in the interpretation of experimental CEνNS results [159, 161–163].

In the framework from [160], the CEνNS cross-section is decomposed into Wilson coefficients of effective operators, hadronic matrix elements and nuclear structure factors. In the SM the effective operators describe the Z-boson exchange. In turn, the SM Wilson coefficients contain the short-range physics at the particle level. For the standard model the interactions are described by the so-called dimension-6 Lagrangian [160]

$$\mathscr{L}^{(6)} = \sum_q \left(C_q^V \bar{\nu}\gamma^\mu P_L \nu \bar{q}\gamma_\mu q + C_q^A \bar{\nu}\gamma^\mu P_L \nu \bar{q}\gamma_\mu\gamma_5 q \right), \tag{1.45}$$

where the sum goes over all quarks q, γ_μ denotes the Dirac matrices, and C_q^V and C_q^A are the vector and axial-vector Wilson coefficients. Only left-handed neutrinos ν are considered with the left-handed projector $P_L = (1-\gamma_5)/2$. Neutrino indices are suppressed since no flavour changes are assumed to occur in the interactions. For Z-exchange the SM Wilson coefficients for $q = u, d, s$ are

$$\begin{aligned} C_u^V &= -\frac{G_F}{\sqrt{2}}\left(1 - \frac{8}{3}\sin^2\theta_W\right), \\ C_d^V = C_s^V &= \frac{G_F}{\sqrt{2}}\left(1 - \frac{4}{3}\sin^2\theta_W\right), \\ C_u^A = -C_d^A = -C_s^A &= \frac{G_F}{\sqrt{2}} \end{aligned} \tag{1.46}$$

with the Fermi constant G_F and the weak mixing angle θ_W [160]. This treatment can be extended by the introduction of new operators for BSM interactions, for example in dimension-5 and dimension-7 operators. Moreover, an additional tensor contribution can be added to the SM dimension-6 operator. The full SM and BSM operator basis for CEνNS can be found in [160]. Moreover, the SM Wilson coefficients could be modified due to non-standard interactions. A common notation introduces the deviations $\epsilon_{\mathrm{ee}}^{qV}$ and $\epsilon_{\mathrm{ee}}^{qA}$ of the BSM Wilson coefficients $C_{q,\mathrm{BSM}}^{V}$ and $C_{q,\mathrm{BSM}}^{A}$ from the SM values [163]:

$$\begin{aligned} C_{q,\mathrm{BSM}}^{V} - C_{q}^{V} &= -\sqrt{2} G_F \epsilon_{\mathrm{ee}}^{qV}, \\ C_{q,\mathrm{BSM}}^{A} - C_{q}^{A} &= \sqrt{2} G_F \epsilon_{\mathrm{ee}}^{qA}. \end{aligned} \tag{1.47}$$

In this notation, the subscript ee indicates that the non-standard interaction would only affect ν_{e}. However, the modification of the Wilson coefficients can be extended to ν_{μ} and ν_{τ} as well as to flavour changes [163–165].

The hadronic form factors extend the scope to the single-nucleon level. These have to be calculated for each operator and set of Wilson coefficients. Nuclear structure factors consider the many-body nuclear matrix element of the single-nucleon currents by convolving the nucleon level matrix elements with the nuclear states [160]. The most relevant contributions to the nuclear responses are given by the structure factors of the charge operator $\mathscr{F}_{\pm}^{M}(\mathbf{q}^2)$, the structure factor $\mathscr{F}_{\pm}^{\Phi''}$, which can be interpreted in terms of spin-orbit corrections, and the spin-dependent responses from the axial vector operator S_{ij}. Only the charge operator nuclear response is fully coherent and the spin-orbit correction receives some coherent enhancement in heavy nuclei, but vanishes at zero momentum transfer $\mathbf{q}^2 = 0$. The axial-vector contribution is not coherent, but remains finite at $\mathbf{q}^2 = 0$ [160]. Since the coherent part of the nuclear response contains four different structure factor contributions, a modification of the weak form factor and weak charge is required if BSM effects are allowed in the Wilson coefficients [160].

Combining effective operators, hadronic matrix elements and nuclear structure factors in the SM case yields the weak form factor $F_W(\mathbf{q}^2)$. Then, the differential SM CEνNS cross section

$$\frac{\mathrm{d}\sigma_A}{\mathrm{d}T} = \left.\frac{\mathrm{d}\sigma_A}{\mathrm{d}T}\right|_{\mathrm{coherent}} + \left.\frac{\mathrm{d}\sigma_A}{\mathrm{d}T}\right|_{\mathrm{SD}} \tag{1.48}$$

consists of the fully coherent contribution and the spin-dependent (SD) axial-vector contribution [160]. With the nuclear recoil energy T, the incoming neutrino energy E_ν, the nuclear mass m_A and the weak charge Q_W, the coherent contribution can be written as

$$\left.\frac{\mathrm{d}\sigma_A}{\mathrm{d}T}\right|_{\mathrm{coherent}} = \frac{G_F^2 m_A}{4\pi}\left(1 - \frac{m_A T}{2E_\nu^2} - \frac{T}{E_\nu}\right) Q_W^2 |F_W(\mathbf{q}^2)|^2. \tag{1.49}$$

The nuclear recoil energy is connected to the energies of the incoming and outgoing neutrino energies E_ν and $E_\nu^{'}$ with

$$T = E_\nu - E_\nu' = \frac{\mathbf{q}^2}{2m_A}, \tag{1.50}$$

where $\mathbf{q}^2$ is the squared momentum transfer. Natural units with $\hbar = \mathrm{c} = m_{\mathrm{e}} = \varepsilon_0 = 1$ are employed throughout this section [4]. The momentum transfer $\mathbf{q}$ is defined as

$$\mathbf{q} = \mathbf{k}' - \mathbf{k} = \mathbf{p} - \mathbf{p}'. \tag{1.51}$$

Here, $\mathbf{k}$ and $\mathbf{k}'$ are the in- and outgoing neutrino four-momenta, and $\mathbf{p}$ and $\mathbf{p}'$ are the in- and outgoing nucleus four-momenta. Accordingly, $\mathbf{q}^2$ is an invariant. The maximum nuclear recoil energy for a neutrino scattering angle $\theta = \pi$ is

$$T_{\max} = \frac{2E_\nu^2}{m_A + 2E_\nu}. \tag{1.52}$$

The actual coherent enhancement in the cross-section originates from the presence of the factor Q_W^2 which has been separated from $F_W(\mathbf{q}^2)$ [160,163]. With the nuclear charge Z, the neutron number N and the weak charges of the proton Q_W^p and neutron Q_W^n it is commonly written as

$$Q_W = ZQ_W^p + NQ_W^n \tag{1.53}$$

with

$$\begin{aligned} Q_W^p &= 1 - 4\sin^2\theta_W, \\ Q_W^n &= -1. \end{aligned} \tag{1.54}$$

The authors of [160] note that Q_W^2 does not fully factorise from $F_W(\mathbf{q}^2)$. Moreover, there are process-dependent radiative corrections on Q_W^p and Q_W^n. These are not available for CEνNS at this point. For now the corrections from parity violating electron scattering, the scattering of spin-polarised electrons on unpolarised nuclei, are used. This model interaction is chosen since it also involves left-handed leptons scattering off nuclei and is mediated by short-range Z-exchange in the SM [4,160]. With the fine-structure constant α one has [166]

$$\begin{aligned} Q_W^p &\to (Q_W^p - 0.00010)\left(1 - \frac{\alpha}{2\pi}\right) = 0.0712, \\ Q_W^n &\to (Q_W^n - 0.00012)\left(1 - \frac{\alpha}{2\pi}\right) = -0.9890. \end{aligned} \tag{1.55}$$

Thus, similar to SI WIMP scattering with its A^2 dependence, the coherent contribution of the cross-section is approximately proportional to N^2. The axial-vector contribution can be written as

$$\left.\frac{\mathrm{d}\sigma_A}{\mathrm{d}T}\right|_{\mathrm{SD}} = \frac{G_F^2 m_A}{4\pi}\left(1 + \frac{m_A T}{2E_\nu^2} - \frac{T}{E_\nu}\right) F_A(\mathbf{q}^2), \tag{1.56}$$

where $F_A(\mathbf{q}^2)$ is the axial-vector analog of the weak form factor [160]. With this, the full SM CEνNS cross-section is

$$\begin{aligned} \left.\frac{\mathrm{d}\sigma_A}{\mathrm{d}T}\right|_{\mathrm{SM}} &= \frac{G_F^2 m_A}{4\pi}\left(1 - \frac{m_A T}{2E_\nu^2} - \frac{T}{E_\nu}\right) Q_W^2 |F_W(\mathbf{q}^2)|^2 \\ &+ \frac{G_F^2 m_A}{4\pi}\left(1 + \frac{m_A T}{2E_\nu^2} - \frac{T}{E_\nu}\right) F_A(\mathbf{q}^2). \end{aligned} \tag{1.57}$$

In the BSM case with modified vector and axial-vector dimension-6 operators, the expression of the differential cross-section does not change substantially. The weak charge and weak form factor are replaced by their BSM counterparts $\tilde{Q}_W$, taking in $G_F/\sqrt{2}$, and $\tilde{F}_W(\mathbf{q}^2)$. Moreover, the axial vector form factor $\tilde{F}_A(\mathbf{q}^2)$ is modified [160]:

$$\begin{aligned} \left.\frac{\mathrm{d}\sigma_A}{\mathrm{d}T}\right|_{\mathrm{BSM}} &= \frac{m_A}{2\pi}\left(1 - \frac{m_A T}{2E_\nu^2} - \frac{T}{E_\nu}\right) \tilde{Q}_W^2 |\tilde{F}_W(\mathbf{q}^2)|^2 \\ &+ \frac{m_A}{2\pi}\left(1 + \frac{m_A T}{2E_\nu^2} - \frac{T}{E_\nu}\right) \tilde{F}_A(\mathbf{q}^2). \end{aligned} \tag{1.58}$$

The BSM form factors change the shape and normalisation of the cross-section with respect to the SM. Additionally the modified $\tilde{Q}_W$ shifts the whole coherent cross-section upwards or downwards. Accordingly, non-standard interactions can be probed by measuring the rate as well as the shape of the CEνNS nuclear recoil spectrum. The dipole operator is introduced as example for an operator not present in the standard model [160]. It arises from the dimension-5 Lagrangian

$$\mathscr{L}^{(5)} = C_F \bar{\nu} \sigma^{\mu\nu} P_L \nu F_{\mu\nu} \tag{1.59}$$

with the coupling constant C_F, the photon field strength tensor $F_{\mu\nu}$, and

$$\sigma^{\mu\nu} = -\frac{i}{4}\left(\gamma^\mu \gamma^\nu - \gamma^\nu \gamma^\mu\right) \tag{1.60}$$

consisting of the Dirac matrices γ^μ and γ^ν. After the full treatment with hadronic matrix elements and contraction with the nuclear structure factors, the cross section

$$\left.\frac{\mathrm{d}\sigma_A}{\mathrm{d}T}\right|_{\mathrm{dipole}} = \frac{4\alpha C_F^2}{T} Z^2 |F_{\mathrm{ch}}(\mathbf{q}^2)|^2 \tag{1.61}$$

is obtained [160] with the nuclear charge form factor F_{ch} and the nuclear charge Z. Due to the absence of interference terms with the SM the dipole operator causes a new long-range interaction [160]. In contrast to the other BSM operators discussed in [160] it is divergent for $T \to 0$, so the largest contribution to the CEνNS nuclear recoil rate would be expected at low nuclear recoil energies. Moreover, it is independent of the incoming neutrinos' energies while the other operators' cross-sections scale with $1/E_\nu^2$. This could lead to an experimentally accessible increase in the NR cross-section. The physical interpretation of such a long-range interaction would be a finite neutrino magnetic moment [164]. XENON1T recently observed an ER rate excess that could be explained by such an interaction [14]. An NR signal from the same interaction could serve as a cross-check.

The BSM modifications of the CEνNS cross-section and the resulting physics potential in xenon-based Dark Matter detectors will be further investigated in the ongoing collaboration with the theory colleagues. The focus is now placed on SM interactions and the role of CEνNS as a background in direct Dark Matter searches.

1.3.2 SM form factors and cross-sections for xenon

A programme for the calculation of the weak and axial-vector form factors in the SM and BSM cases has been obtained from the authors of [160]. Figure 1.20 shows the squared SM weak form factors and axial-vector form factors of the xenon isotopes with natural abundances larger than 1 %. They are given as a function of the absolute value of the momentum transfer $|\mathbf{q}|$. The axial-vector form factors are only present for the odd-numbered ^{129}Xe and ^{131}Xe because they have unpaired nucleon spins. Their theoretical uncertainty bands arise mainly from two-body contributions to the nuclear structure factor [160]. In absolute value $F_A(\mathbf{q}^2)$ are below $F_W^2(\mathbf{q}^2)$ by down to an order of magnitude at zero momentum transfer. With increasing momentum transfer both form factors can go to zero, similarly as in nuclear charge form factors that approximately correspond to Fourier transforms of the charge distributions in nuclei [98]. The decrease of coherence with increasing momentum transfer is clearly visible for the weak form factors. While one has $F_W^2(\mathbf{q}^2 = 0) \approx 1$, the squared form factor rapidly decreases for larger $|\mathbf{q}|$. Therefore, the cross-section for an incoming neutrino with $E_\nu = 10$ MeV obtains approximately a factor 10 larger coherent enhancement than that of a neutrino with $E_\nu = 50$ MeV.

These two example energies are typical neutrino energies in CEνNS experiments. Future xenon-based Dark Matter detectors will mostly be sensitive to solar neutrinos with energies up to 16 MeV [83], while reactor-neutrino experiments such as CONUS operate in the few MeV range [161]. The accelerator-based experiment COHERENT measures neutrinos with energies in the 10–50 MeV range from proton interactions in a mercury target [159]. Note

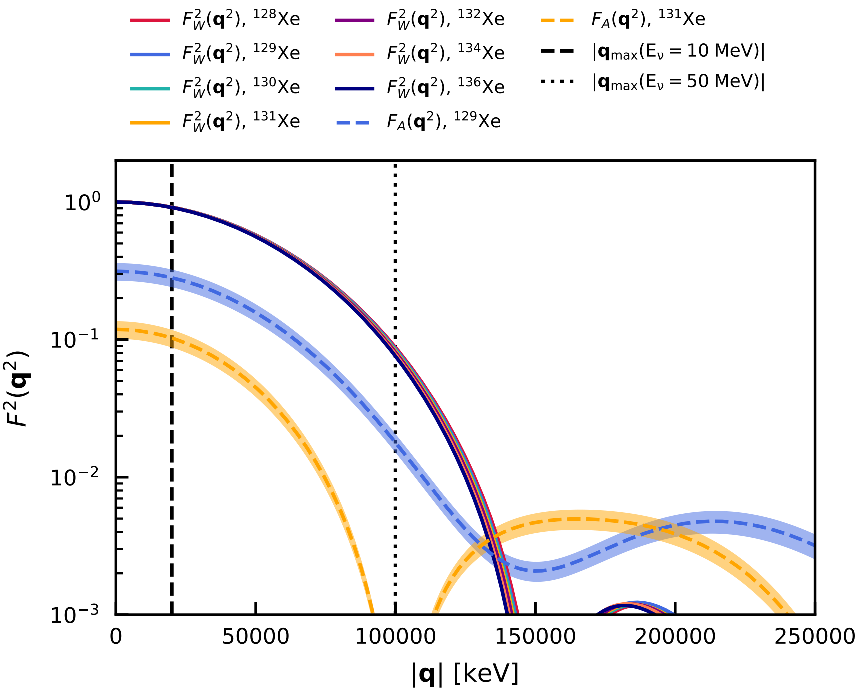

Figure 1.20: Squared weak form factors $F_W^2(\mathbf{q}^2)$ and axial-vector form factors $F_A(\mathbf{q}^2)$ for xenon isotopes with natural abundances larger than 1 % as a function of the momentum transfer $|\mathbf{q}|$. The axial-vector form factors for ^{129}Xe and ^{131}Xe have associated theory uncertainty bands. The maximum momentum transfers $|\mathbf{q}_{\text{max}}|$ for incoming neutrino energies $E_\nu = 10$ MeV and $E_\nu = 50$ MeV in a natural xenon target are indicated by the dashed and dotted black lines, respectively.

that COHERENT and CONUS do not use xenon targets, but the general trends observed for the xenon nuclear structure factors and cross-sections also apply to these experiments.

One can now compare the large-scale nuclear structure $F_W^2(\mathbf{q}^2)$ to the commonly used Helm parametrisation $F_H^2(\mathbf{q}^2)$ in order to assess the impact of this choice on experimental results. Figure 1.21 shows the relative differences of the updated weak form factors and their respective Helm parametrisations for xenon. In all cases, the squared Helm form factor is larger than the form factor from large-scale nuclear structure calculations. Again comparing the benchmark neutrino energies of 10 and 50 MeV, the difference between the form factors increases with the momentum transfer. While the relative difference is ~ 2 % for a 10 MeV neutrino, it is ~ 20 % for a 50 MeV neutrino. Moreover, the difference is larger for heavier nuclei with the spread between nuclei also increasing at larger momentum transfers. Accordingly, a xenon-based experiment at an accelerator would see a strong impact on the results depending on the chosen form factor, while this would be less-relevant for a xenon experiment measuring solar neutrinos.

Figure 1.22 shows the differential CEνNS cross-sections as a function of the nuclear recoil energy T for scattering on ^{131}Xe with $E_\nu = 10$ MeV and $E_\nu = 50$ MeV. The maximum nuclear recoil energies are 1.5 keV and 38.2 keV, respectively. This illustrates the reason why it took 43 years in order to measure CEνNS: While the CEνNS cross-section is relatively large compared to other MeV neutrino interactions such as CC-scattering and inverse β-decay [159], the nuclear recoil energies require a low energy threshold of a given detector. The relative contribution of the axial-vector part to the CEνNS cross-section is almost five orders of magnitude below the coherent contribution. This is owed to the enhancement of

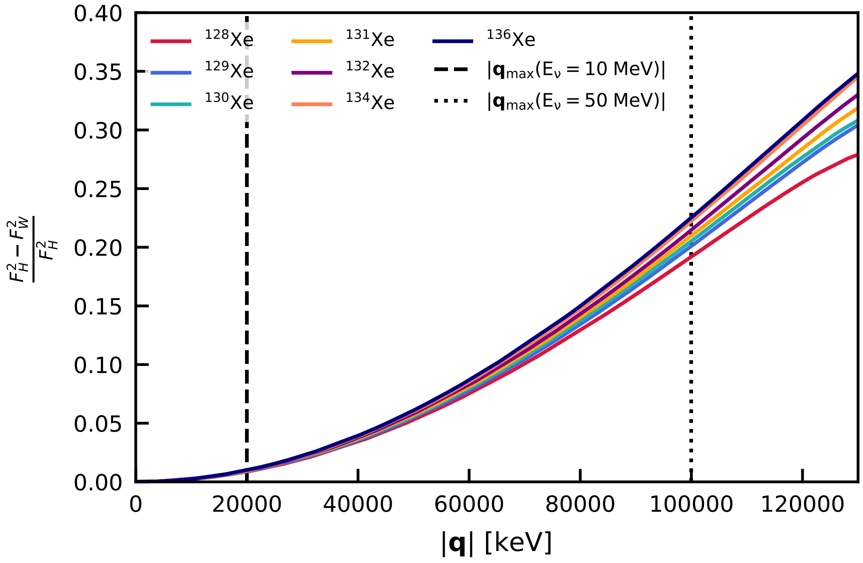

Figure 1.21: Relative differences of squared large-scale nuclear structure and Helm weak form factors for xenon isotopes with natural abundances larger than 1 % as a function of the momentum transfer |**q**|. The maximum momentum transfers $|\mathbf{q}_{\text{max}}|$ for incoming neutrino energies E_ν = 10 MeV and E_ν = 50 MeV in a natural xenon target are indicated by the dashed and dotted black lines, respectively.

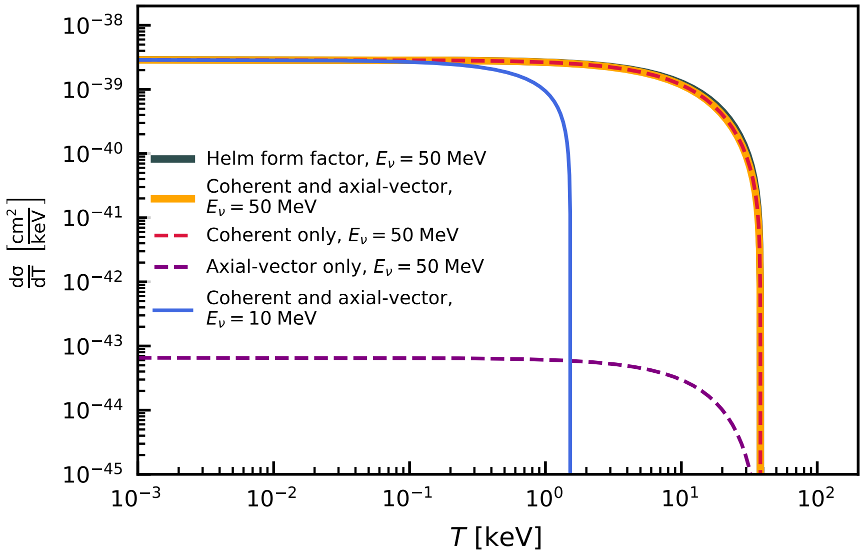

Figure 1.22: Differential CEνNS cross-sections on ^{131}Xe for E_ν = 10 MeV (solid blue) and E_ν = 50 MeV (solid orange) for the weak and axial-vector form factors from [160]. The differential cross-section using the Helm parametrisation of the form factor is indicated by the solid grey line for E_ν = 50 MeV. For this energy, the individual contributions of the weak and the axial-vector form factors are illustrated by the dashed red and purple lines, respectively.

the cross-section with N^2 in the weak nuclear charge. Therefore, it will not be relevant for experiments in the foreseeable future and it will not be discussed further. Since the nuclear recoil energy is proportional to the square of the momentum transfer, the difference in the cross-sections between the form factors from [160] and the Helm parametrisation starts to become visible at larger T. At the maximum momentum transfer, the relative difference of the differential cross-section is $\sim 20\,\%$ for $E_\nu = 50$ MeV while it is $\sim 2\,\%$ for $E_\nu = 10$ MeV.

1.3.3 CEνNS as a background for Dark Matter direct detection experiments

Since it produces low-energy nuclear recoils, CEνNS can become a background in direct Dark Matter search experiments [83]. There are three relevant sources of neutrinos with energies from $\mathcal{O}(100)$ keV up to 1 GeV: solar neutrinos from nuclear fusion processes in the sun, atmospheric neutrinos from cosmic ray collisions in Earth's atmosphere and the diffuse supernova neutrino background (DSNB) [83, 167]. The neutrino flux at Earth as a function of the neutrino energy is shown in figure 1.23 [167]. The majority of the solar neutrino flux from the primary pp-reactions and CNO cycle – recently measured for the first time by Borexino [168] – features $E_\nu < 10$ MeV. Accordingly Dark Matter direct detection experiments with an energy threshold of $T = \mathcal{O}(1)$ keV are not sensitive to the bulk of the solar neutrino flux. The main components that are relevant here are ^{8}B and hep neutrinos from the reactions:

$$\begin{aligned} {}^8\mathrm{B} &\rightarrow {}^8\,\mathrm{Be} + \mathrm{e}^+ + \nu_\mathrm{e}\ ({}^8\mathrm{B}), \\ {}^3\mathrm{He} + \mathrm{p} &\rightarrow {}^4\,\mathrm{He} + \mathrm{e}^+ + \nu_\mathrm{e}\ (hep). \end{aligned} \tag{1.62}$$

While the ^{8}B flux was among the first to be measured in real-time [20] and is known with a relative precision of $\sim 10\,\%$, no detection of hep neutrinos has been achieved to date [167, 169, 170]. The relative hep flux uncertainty of $\sim 30\,\%$ originates from the flux prediction uncertainties of the high-metallicity standard solar model [171]. Models with high core-metallicity appear to be preferred by recent measurements of the ^{8}B and CNO fluxes [167, 168, 170].

Although the ^{8}B component is the most accessible to experiments due to its comparatively high energy, it features the most complex spectrum. While the other continuous neutrino spectra follow the shape of an allowed β-decay spectrum[13], the ^{8}B does not have a sharp cut-off. This is due to the fact that the ^{8}Be daughter nucleus is 2α-unstable with an extremely short half-life of $8.19(37) \cdot 10^{-17}$ s [167]. Recent measurements, where the ν_e spectrum is inferred from the measured α and β^+ spectra, show a fair agreement with the commonly used theoretical spectra by Bahcall et al. [173, 174]. This spectral shape is of interest for Dark Matter experiments since the proximity of the maximum recoil energy $T_\mathrm{max} \propto E_\nu^2$ to the detector threshold makes these experiments sensitive to the endpoint energy of the spectrum.

The atmospheric neutrino flux originates from cosmic ray collisions in the atmosphere. It has been measured by a multitude of experiments, most notably in the discovery of neutrino oscillations by Super-Kamiokande [19, 83, 167]. In contrast to direct Dark Matter detection experiments, these experiments featured directional sensitivity. It is the dominant flux component at $E_\nu > 25$ MeV and the flux uncertainty below 100 MeV is $\sim 20\,\%$. The uncertainties are larger for the yet undetected DSNB at $\sim 50\,\%$ [167]. This background is expected to be a sizable contribution on the terrestrial neutrino flux between 10 and 25 MeV [167]. It is composed of the neutrino flux from all past supernovae in the Universe. Accordingly, the flux at Earth is a convolution of the core-collapse supernova rate as a function of the red-shift with the per-supernova neutrino flux spectra [83].

---

[13] These spectra are commonly adjusted with final-state corrections and thermal initial-state distributions [172].

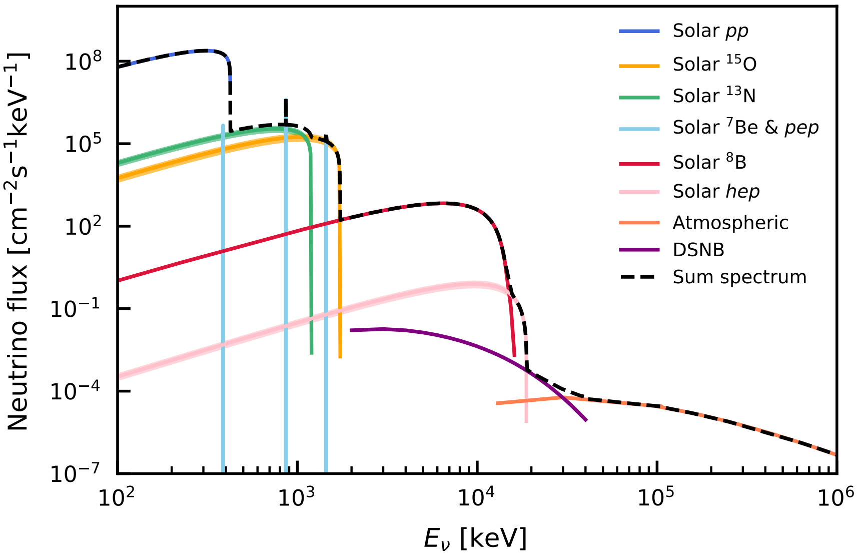

Figure 1.23: Solar, atmospheric and DSNB neutrino fluxes at Earth as a function of the neutrino energies regardless of the neutrino flavour. Flux spectra and their uncertainties were taken from [167]. For atmospheric and DSNB neutrinos, the fluxes of neutrinos and anti-neutrinos have been summed. The sum of all flux-components is indicated by the dashed black line.

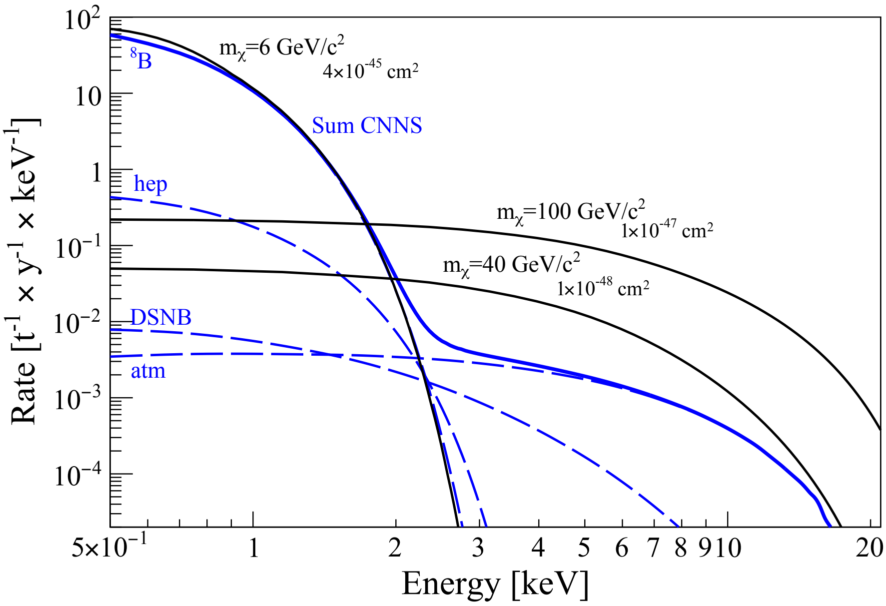

Figure 1.24: Recoil rates in xenon as a function of the recoil energy for CEνNS (solid blue) and for WIMPs of different masses m_χ (solid black) at different WIMP-nucleon cross-sections. The solar ^{8}B and *hep*, as well as the atmospheric and DSNB components of the neutrino background are indicated by the dashed blue lines. The NR recoil energy has been converted to ER energy equivalent for the sole measurement of a scintillation light signal (cf. figure 2.8 and section 2.1.1). A 50 % NR acceptance is assumed. Taken from [10].

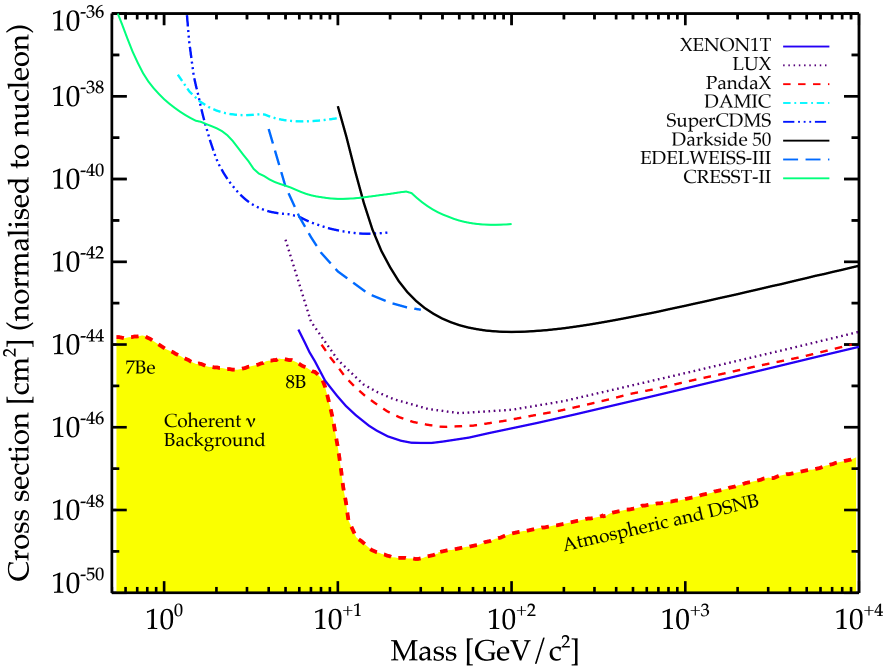

Figure 1.25: WIMP discovery limit due to CEνNS of solar, atmospheric and DSNB neutrinos in xenon as defined in [83]. Recent experimental limits on the SI WIMP-nucleon cross-section are indicated by the solid and dashed coloured lines. Taken from [177].

Figure 1.24 shows the expected NR scattering rates in xenon as a function of the recoil energy for WIMPs with different masses and cross-sections. These rates are contrasted with the CEνNS rates from the sources discussed above. The largest exposure of any xenon-based Dark Matter experiment has been obtained by the XENON1T detector at 1 t-yr. Under the assumption of the a 50 % NR acceptance as in the figure and with a 2 keV scintilliation-only ER energy threshold it would have recorded $\mathcal{O}(1)$ event from ^{8}B neutrinos. A reduction of the threshold by a factor two would allow the measurement of tens of events [10]. A recent XENON1T study using a 0.6 t-yr exposure with an NR energy threshold of 1.6 keV for combined scintillation and ionisation signals found no significant excess of ^{8}B-like events [175]. However, future experiments such as XENONnT and DARWIN will have significantly larger exposures [18, 84, 176] and likely measure CEνNS of solar ^{8}B neutrinos for the first time. This presents the interesting opportunity of an independent measurement of these neutrinos via the neutral current that has until now only been achieved by SNO [169]. Such a measurement is of interest because it measures the total solar ^{8}B flux regardless of matter-enhanced and vacuum neutrino oscillations as is the case for neutrino-electron scattering experiments [170]. A sizeable ^{8}B rate would also allow to probe the non-standard neutrino interactions discussed in section 1.3.1.

However, the main concern for now is the presence of CEνNS as a background to Dark Matter direct detection experiments [83]. From figure 1.24 it is evident that CEνNS from solar neutrinos would mimic the signal from a $m_\chi = 6\,\mathrm{GeV/c^2}$ WIMP at a SI WIMP-nucleon cross-section of $4 \cdot 10^{-45}$ cm^2. Due to the higher attainable recoil energies, but lower fluxes and loss of coherence, CEνNS from atmospheric and DSNB neutrinos would mimic interactions of higher mass WIMPs at cross sections that are two to four orders of magnitude below 10^{-45} cm^2 [10]. The misidentification of CEνNS as WIMP events limits the discovery potential of future experiments. The WIMP discovery limit as defined in [83] is shown in figure 1.25. As stated above the discovery potential is limited by coherent interactions of solar neutrinos at WIMP masses below the few GeV/c^2 range and by atmospheric as well as DSNB neutrinos at larger masses. The WIMP sensitivity of DARWIN is projected to cross the solar neutrino floor and to approach the atmospheric and DSNB limit [84].

It should be noted that the actual WIMP discovery limit is strongly dependent on the experimental setting with regard to the detector threshold as well as the NR background at the relevant recoil energies. Several techniques have been suggested in order to alleviate the otherwise irreducible CEνNS background. These exploit the different directionality of the WIMP and neutrino signals as well as their distinct temporal event rate modulations [10]. While time-modulation analyses are commonly employed in xenon-based detectors already [178, 179], new concepts are needed in order to measure directionality in xenon. Finally, the discovery limit assumes the same nuclear response, the Helm form factor, for SI WIMP interactions as well as for CEνNS. As shown in [57] different WIMP-nucleus response functions could be discriminated in future xenon Dark Matter detectors. Consequently, a difference in coherent WIMP-nucleus and neutrino-nucleus responses could also allow a discrimination of WIMP signal and CEνNS background. This highlights the further questions that could be addressed in the theory collaboration that was initiated in the scope of this work: How is the WIMP discovery potential affected by CEνNS under the assumptions of different nuclear responses for WIMPs and neutrinos? Could future xenon Dark Matter experiments probe non-standard neutrino interactions with solar neutrinos? And would it be possible to cross-check ER evidence of a neutrino magnetic moment with NR interactions via an enhancement of the CEνNS cross-section by the interaction associated with the dipole operator?

Xenon Dual-Phase Time Projection Chambers 2

Xenon dual-phase TPCs are the currently leading technology for Dark Matter direct detection over a broad energy range and for multiple candidate particles [12–16]. They are also used successfully in $0\nu\beta^-\beta^-$ and other double-weak decay searches [31, 138]. This chapter will present the signal generation mechanism in liquid xenon and the working principle of this detector type. It will then discuss practical aspects of signal detection and introduce the XENON1T experiment.

2.1 The xenon dual-phase TPC for Dark Matter detection

Xenon is a popular target for several types of radiation detectors and offers manifold merits for Dark Matter direct detection and double-weak decay searches [9]. It features the highest shielding capability against ionising radiation of all noble liquids owed to its atomic number $Z = 54$ and high density of 2.862 $\mathrm{g/cm^3}$ at a liquid temperature of $-96°\,\mathrm{C}$ [180]. This means that self-shielding is highly effective when applying fiducialisation, i.e. the definition of a low radioactivity inner analysis volume exploiting the position reconstruction capability of a detector [11, 70]. The aforementioned operating temperature is relatively easy to achieve with cryogenic systems. Furthermore, monolithic liquid xenon targets can be scaled up more easily when compared to crystalline detectors that are limited in size by the growth process. Xenon features even and odd isotopes in its natural composition, so xenon detectors are sensitive to both SI and SD interactions. The molar mass $M_A = 131.293(3)$ $\mathrm{g/mol}$ [180] makes them most sensitive to WIMPs in the mass range of about 10 $\mathrm{GeV/c^2}$ to a few hundred $\mathrm{GeV/c^2}$.

The xenon absorption coefficients for X-rays and γ-rays are shown in figure 2.1 for the photoelectric effect, Compton-scattering, and pair-production. Between 200 and 300 keV Compton scattering starts to dominate over photoelectric absorption [181]. It stays the dominant mechanism up to approximately 6 MeV where it is surpassed by pair-production. Therefore, common γ-rays from ^{60}Co, ^{214}Bi and ^{208}Tl contained in detector construction materials and with energies between 1.1 and 2.6 MeV predominantly undergo Compton-scattering in a xenon-filled detector [182–184].

Natural xenon – in the absence of cosmogenic activation underground – does not contain radioactive isotopes that would constitute a background. Only double-weak decays of ^{124}Xe and ^{136}Xe can present a significant background contribution – that can also be viewed as a physics channel – in tonne-scale targets for Dark Matter detection [151, 152]. Internal radioactive backgrounds such as the anthropogenic ^{85}Kr or the continuously emanated ^{222}Rn can be removed by cryogenic distillation [71–73, 77]. Finally, one can achieve an exceptional chemical purity by constant online purification [185]. This is needed to extract the maximum amount of signal from a particle interaction within a detector.

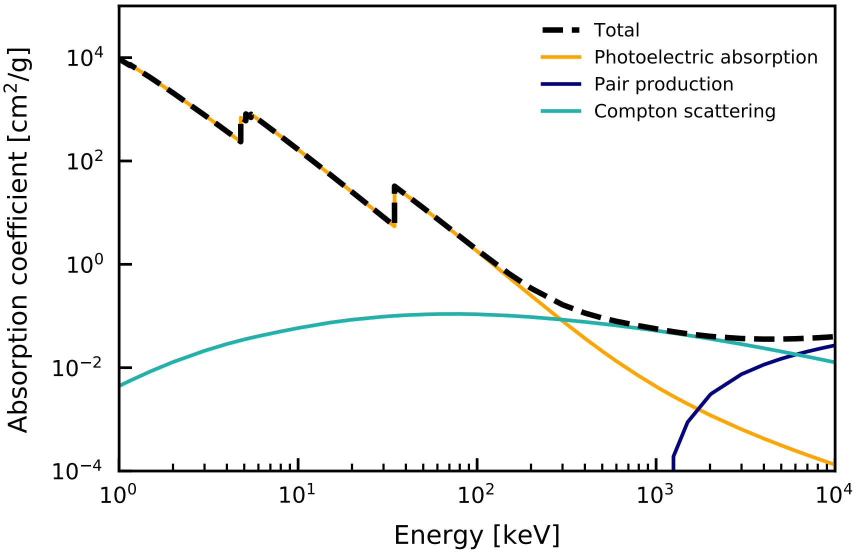

Figure 2.1: Xenon γ- and X-ray absorption coefficient (dashed black). Individual contributions are shown for the photoelectric effect (orange), Compton-scattering (teal), and pair production in the nuclear and electron electric fields (blue). Values taken from [181].

2.1.1 Signal generation in xenon

An energy deposition in xenon gas or liquid produces excited as well as ionised xenon atoms [9]. The direct excitation and recombination of electrons with xenon ions produces scintillation light $h\nu$ by the formation of excited Xe_2^* dimers. For the excited Xe^* atoms one has

$$\begin{aligned} \mathrm{Xe}^* + \mathrm{Xe} + \mathrm{Xe} &\rightarrow \mathrm{Xe}_2^* + \mathrm{Xe}, \\ \mathrm{Xe}_2^* &\rightarrow 2\mathrm{Xe} + h\nu. \end{aligned} \tag{2.1}$$

For Xe^+ ions recombination and the associated deexcitation are also relevant:

$$\begin{aligned} \mathrm{Xe}^+ + \mathrm{Xe} &\rightarrow \mathrm{Xe}_2^+, \\ \mathrm{Xe}_2^+ + \mathrm{e}^- &\rightarrow \mathrm{Xe}^{**} + \mathrm{Xe}, \\ \mathrm{Xe}^{**} &\rightarrow \mathrm{Xe}^* + \mathrm{heat}, \\ \mathrm{Xe}^* + \mathrm{Xe} + \mathrm{Xe} &\rightarrow \mathrm{Xe}_2^* + \mathrm{Xe}, \\ \mathrm{Xe}_2^* &\rightarrow 2\mathrm{Xe} + h\nu. \end{aligned} \tag{2.2}$$

Since it is emitted by dimers, xenon is transparent to its own scintillation light with a wavelength of 178 nm [9]. The scintillation yield is comparable to that of common NaI(Tl) scintillators, albeit with a faster time response [9]. The excited dimers can be in singlet or triplet states with a deexcitation time of a few to tens of nanoseconds. The population of these states can differ with regard to ER and NR interactions, but pulse-shape discrimination of different interactions is challenging due to the nanosecond time resolution of commonly used photosensors and digitisers [186].

Still, a discrimination between ER and NR can be achieved by treating scintillation and ionisation as separate signal channels. For this purpose, recombination has to be partly suppressed by an electric field that separates the electrons from the ions. In this case, the numbers of electron-ion pairs and scintillation photos, N_i and N_γ, become anti-correlated

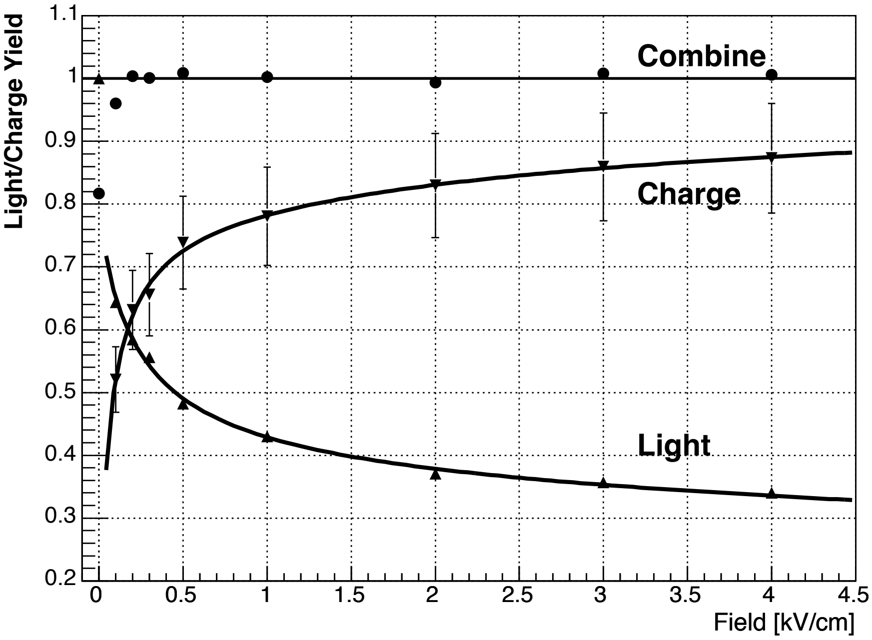

Figure 2.2: Light and charge yield as a function of the applied electric drift field for 661.2 keV γ-rays from ^{137}Cs. Yields are given relative to the light-yield without an electric field applied. At a given electric field a higher light yield is paired with a lower charge yield and vice versa. The combined yield is constant. Taken from [9].

for a given energy deposition [187–189]. This is illustrated in figure 2.2. For an energy deposition E that generates N_γ scintillation photons and N_i electron ion pairs with a negligible amount of energy going into non-usable signal channels, commonly referred to as heat, one may write

$$E = W \cdot (N_i + N_\gamma). \tag{2.3}$$

The average energies W_i and W_γ to produce an electron-ion pair or an excited xenon atom, respectively, are different for the two processes [9]. Yet, it is common to assume a mean value of both with $W = 13.7\,\text{eV}$, so on average 73 quanta are generated per keV [190].

At the low energies E relevant for Dark Matter search and a drift field of the strength $\mathscr{E}$ the combined probability P for generating N_γ photons and N_e escaping electrons can be approximated by two independent Poisson processes [191]:

$$P(N_\gamma, N_\text{e} | E_u, \mathscr{E}) \approx \text{Poi}(N_\gamma | n_\gamma) \cdot \text{Poi}(N_\text{e} | n_\text{e}). \tag{2.4}$$

The expectation values for the numbers of photons and electrons, $n_\gamma(E_u, \mathscr{E})$ and $n_\text{e}(E_u, \mathscr{E})$, respectively, depend on the deposited energies, the interaction type with $u = \text{nr}$ for NR and $u = \text{er}$ for ER interactions, and the electric field. The effective W-values again denote the average energies needed for quanta generation. The field dependence is factorised by $S_u(\mathscr{E})$ for the field quenching of scintillation and $T_u(\mathscr{E})$ for recombination charge loss. One has $S_u(\mathscr{E} \to 0) = 1$ for zero field and $T_u(\mathscr{E} \to \infty) = 1$ for an infinite field strength. Then, the expectation values can be written as

$$n_\gamma(E_u, \mathscr{E}) \approx \frac{E_u}{W_\gamma(E_u, \mathscr{E} = 0)} \, S_u(\mathscr{E}), \tag{2.5}$$

$$n_\text{e}(E_u, \mathscr{E}) \approx \frac{E_u}{W_\text{e}(E_u, \mathscr{E} \to \infty)} \, T_u(\mathscr{E}). \tag{2.6}$$

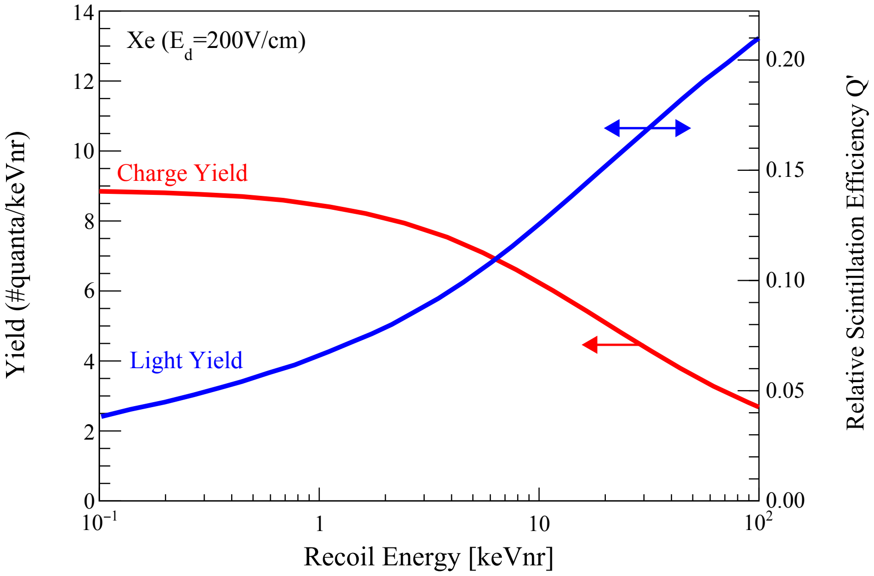

Figure 2.3: Light and charge yields of nuclear recoils (left y-axis) as a function of recoil energy. Yields are given by the NEST model [190] and drawn as solid blue and red lines, respectively. The model assumes a xenon detector with a 200 V/cm electric field. The right y-axis compares the NR light yield to that of a 32.1 keV ER interaction via a relative quenching factor Q'. Model uncertainties are not shown, but are on the order 20 – 30 % at 1 keV$_{\mathrm{NR}}$. Taken from [10].

The scintillation and ionisation yields per unit energy are different for ER and NR at the same field [67]. In fact the expected total signal from an NR interaction is smaller than an ER one for the same energy deposition. This signal quenching is caused by the different energy deposition mechanism of the two interactions. For NR a larger amount of energy goes into the aforementioned unusable heat signal [10]. Accordingly, a larger NR energy deposition is needed in order to produce a measurable signal. The absolute NR quenching

$$Q(E_{\mathrm{nr}}) = \frac{E_{\mathrm{nr}}}{E_{\mathrm{er}}} \tag{2.7}$$

is energy-dependent and an intrinsic property of the target used in an experiment [10]. While it is possible to calculate the quenching analytically for some target materials, this has not been achieved for xenon-based detectors [10, 192]. Instead semi-analytic approaches such as the Noble Element Simulation Technique (NEST) are applied [190]. These approaches rely heavily on experiments specifically designed to measure the absolute and relative ionisation and scintillation efficiencies for nuclear recoils [193, 194].

Figure 2.3 shows the NEST output for the light- and charge-yields of nuclear recoils in xenon as a function of energy in a detector with a 200 V/cm electric field. Again, one can identify the anticorrelation of the light and charge yields indicated as the solid blue and red lines, respectively. The model uncertainties are not shown, but are on the order of 20 – 30 % at 1 keV$_{\mathrm{NR}}$. This is a result of the NEST model's tuning to reproduce measured light and charge yields from multiple experiments at different electric fields. The systematic differences between these measurements can be even larger than the model uncertainty [10]. The light yield of NRs in xenon has been measured down to 1 keV$_{\mathrm{NR}}$. For the charge yield measurements exist down to 0.3 keV$_{\mathrm{NR}}$ [195]. In the above plot the most recent measurements of the charge yield had not yet been incorporated into the model and the charge yield was set to a constant value at sub-keV energies. More recent measurements indicating that the charge yield approaches zero at sub-keV energies [194] have been incorporated in the newest NEST version [196].

An alternative parametrisation of the quenching is presented on the right y-axis of figure 2.3. Here, the NR light yield is given relative to that of a 32.1 keV reference ER interaction from a $^{83\mathrm{m}}$Kr isomeric transition. A notable example for this parametrization is the relative scintillation efficiency $\mathscr{L}_{\mathrm{eff}}$ of nuclear recoils with respect to the reference γ-line at zero field. It is needed to convert the electronic recoil equivalent energy E_{er} to the nuclear recoil energy E_{nr}. For zero field and at a fixed electronic recoil reference energy E_{ref}, e.g. the 122 keV γ-line of ^{57}Co, it can be expressed as [191]

$$\mathscr{L}_{\mathrm{eff}}(E_{\mathrm{nr}}, \mathscr{E} = 0) = \frac{W_\gamma(E_{\mathrm{er}} = E_{\mathrm{ref}}, \mathscr{E} = 0)}{W_\gamma(E_{\mathrm{nr}}, \mathscr{E} = 0)}. \tag{2.8}$$

It was used in past analyses [197] to reconstruct the NR energy scale since the NR ionization yields were not known to low enough energies. This highlights a central conclusion of this section, namely that the energy reconstruction represents a major systematic uncertainty in the interpretation of nuclear recoil signals in xenon-based detectors. Although the different yields and quenching add further complications to WIMP searches, they can also be taken advantage of: the ratio of the ionisation and scintillation signals enables the discrimination between ER and NR interactions. This can be applied in a xenon dual-phase TPC.

2.1.2 Dual-phase TPC working principle

The working principle of a dual-phase TPC is schematically shown in figure 2.4. The cylindrical detector features photodetector arrays at the top and bottom. The photodetectors in this example are arranged in concentric circles at the and in a hexagonal pattern at the bottom. Current and planned Dark Matter direct detection experiments use photomultiplier tubes (PMTs) [79, 85] while avalanche photodiodes and silicon photomultipliers are used or planned for use in neutrinoless double-β decay experiments [127, 147]. Several wires and meshes apply electric drift and extraction fields. The detector walls are usually clad with PTFE which is highly reflective at 178 nm and maximises light collection [198, 199].

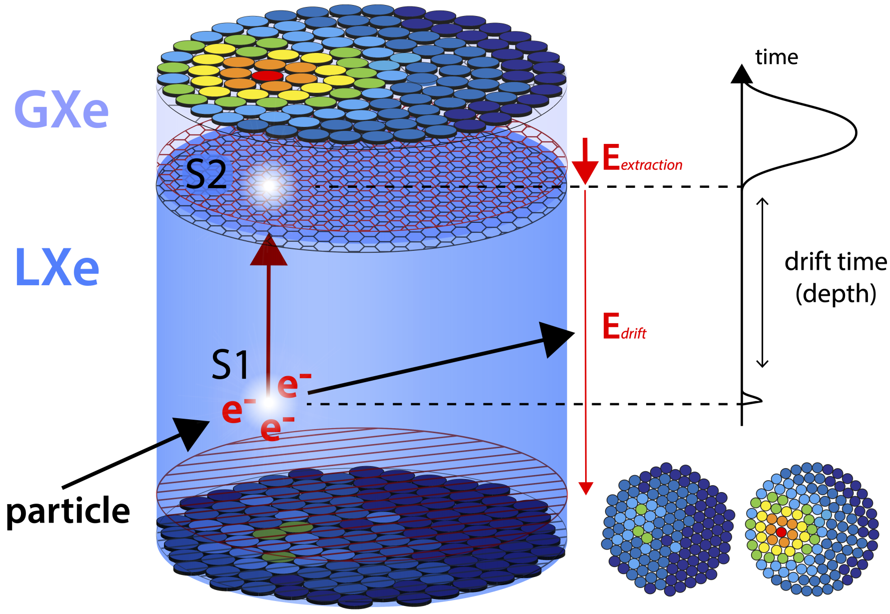

Figure 2.4: Schematic of a dual-phase TPC's working principle. Taken from [200].

When a particle interacts inside the liquid xenon target and deposits energy it can either be fully absorbed or escape before a further energy deposition. An energy deposition produces scintillation light and ionisation charges. Multiple interactions of the same particle, e.g. a neutron or high-energy γ-ray undergoing Compton scattering before full absorption, will produce multiple scintillation light pulses and ionisation charge clusters. The sum of prompt scintillation light pulses is registered simultaneously. This prompt signal is called S1. Due to total internal reflection at the liquid-gas interface, it is mainly registered by the bottom photodetector array. The charges from the single or multiple charge clusters are drifted upwards by an electric drift field. They are accelerated into a thin gas layer at the top of the detector by a stronger extraction field and generate one or multiple secondary scintillation signals measured principally by the top PMT array. This amplified signal is denoted as S2. The S2 hit pattern can be used to infer the horizontal x-y position of an interaction. The time delay between S1 and S2 then gives the vertical z position of an interaction site. If the charge clusters do not overlap, one can resolve multiple S2s. Due to the detector dimensions, time-resolution and short photon travel times, only the summed S1 signal can be measured.

The above discussion mostly applies to Dark Matter detectors that need to achieve single-photon detection for a low S1 detection threshold. This threshold usually dominates the S2 detection threshold since the latter signal is amplified in dual-phase TPCs [201]. Detectors such as EXO-200 or nEXO measure dual signals, but only use a liquid phase of xenon. In the case of EXO-200, the drift-field is applied between a center electrode and the end caps of the cylindrical detector. Charges are drifted to the end caps where the ionisation signal is read out using a wire grid. The application of charge sensitive tiles is planned for nEXO [127, 147]. The absence of S2 amplification leads to a higher energy threshold, but a better x-y-z resolution can be achieved for the rejection of multi-site interactions.

The identification of multi-site events is important for Dark Matter detectors in order to reject neutron NR backgrounds. In neutrinoless double-β decay searches, γ-rays at MeV energies produce multi-site events when they undergo Compton scattering. The capability to fully reconstruct coincident interactions at multiple sites can also be of interest in order to identify coincidence signatures. An example for this is discussed in chapter 5 for the second-order weak decays of ^{124}Xe. Position reconstruction can also be used for background reduction by fiducialisation. Events from an inner volume of the detector can be selected for analysis while events from the outer layers of the target are discarded. Accordingly, the self-shielding of the detector reduces the total measured rate of α-, β- and γ-backgrounds that are mostly absorbed in the outer layers of the detector. In a dual-phase TPC, backgrounds can be further reduced by the discrimination of ER from NR signals.

The discrimination of ER and NR signals is achieved through the difference of their S2/S1 ratio at a given energy. This is a direct consequence of the different scintillation and ionisation yields discussed in section 2.1.1. Figure 2.5 shows the S1 vs. the S2 of individual events (black dots) in two calibration datasets and one Dark Matter dataset from XENON1T's first science run, SR0 [202]. Only the fraction of the S2 signal recorded by the bottom PMT array was used for reconstruction of the signal magnitude since it features more homogeneous light collection. The axis labels also highlight that both signals have been corrected for detector effects that will be discussed in section 2.1.3. Signals with a corrected S1 below 3 photoelectrons were excluded from analysis and do not appear in the plot. The top panel shows events from ^{220}Rn calibration data. The short-lived ($T_{1/2} = 55$ s) α-emitter is an intrinsic calibration source [203]. At energies of few to tens of keV – the electronic recoil energy equivalents (keV$_{\mathrm{ee}}$) are indicated by grey lines – events originate from the ^{212}Pb daughter isotope undergoing ground-state to ground-state β-decay. Accordingly, the signals are exclusively low-energy electronic recoils. The median and $\pm 2\sigma$ quantiles of the so-called ER band are indicated by the solid and dotted blue

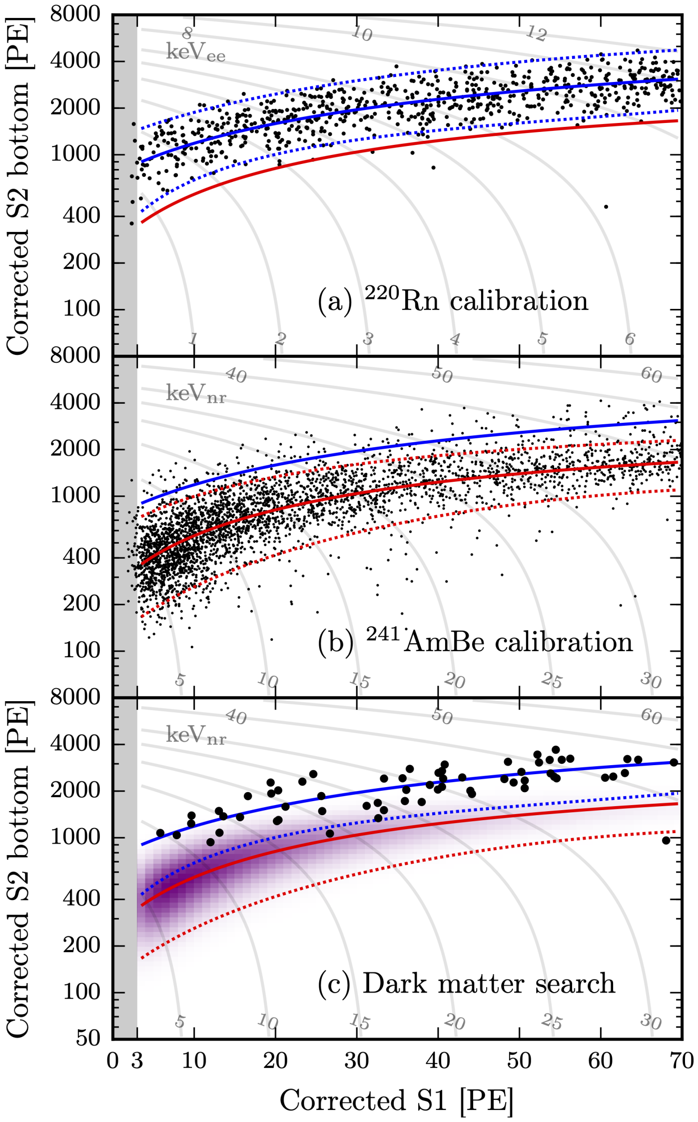

Figure 2.5: Illustration of ER and NR bands in XENON1T calibration and Dark Matter search data. Solid and dotted lines show the band medians and $\pm 2\sigma$ quantiles of the ER band in blue and NR band in red. The bands have been identified using ^{220}Rn and ^{241}AmBe calibration data. The grey lines in the plots show the respective ER and NR energies. The bottom panel shows individual events from the first XENON1T Dark Matter search campaign. Most events fall into the ER band. The expected signal contour from 50 GeV/c^2 WIMP interactions is shown in purple. Data below a corrected S1 signal of 3 photoelectrons was excluded from the analysis. Taken from [202].

lines, respectively[1]. The solid red line indicates the median of the NR band. This band has been identified using data from an external ^{241}AmBe neutron source that is shown in the middle panel. Neutrons are produced in (α, n) reactions of α-particles emitted by ^{241}Am on ^{7}Be. The signals in the detector are predominantly nuclear recoils with the nuclear recoil energy equivalent energies (keV$_{\mathrm{nr}}$) shown as grey lines. The offset between the two band medians is clearly visible. In the bottom plot data from the first XENON1T Dark Matter science campaign is shown. The signal contour for a 50 GeV/c^2 WIMP is shown in purple. Most events are centred around the ER band median and no background events, except for an outlier around 70 photoelectrons, can be found below the NR median. In general ER rejection efficiencies of 99.9 % can be achieved at an NR acceptance of ~ 30 % [10]. The efficiency of the discrimination is field-dependent [67] and it should be noted that background rejection and signal acceptance are always a compromise. However, rather than relying on cut-based analyses with fixed efficiencies, most experiments nowadays employ sophisticated profile-likelihood analyses. There, signal and background are modeled with respect to interaction and detector physics and are fitted to the full measured data [11].

In a dual-phase TPC, the energy of an interaction can be reconstructed from the magnitude of either the S1, the S2 or the combination of both signals. If only one signal is used, recombination fluctuations negatively impact the achievable energy resolution: Apart from the Poisson fluctuations in the light or charge generation themselves, a part of the measurable signal goes into the respective other channel. Measuring both signals at once, the Poisson fluctuations in the recombination process that affect one of the two signal channels are absorbed by the other. Accordingly, the anti-correlation of the signals is used to improve the energy resolution of detectors. This is crucial for high-energy double-weak decay searches and enables energy resolutions of ~ 1 % at the ^{136}Xe Q-value [138, 201]. The fact that the total deposited energy in an event is a linear combination of the S1 and S2 signal magnitudes can be illustrated by rewriting equation (2.3) to [9]

$$E = W \cdot \left(\frac{cS1}{g_1} + \frac{cS2_{\mathrm{b}}}{g_2} \right). \tag{2.9}$$

Here g_1 is the photon detection efficiency and g_2 is the charge amplification factor. These detector-specific quantities relate the number of primary photons and ionisation charges to the measured signal areas. In a detector such as XENON1T that reads out both S1 and S2 as light with PMTs they are given in photoelectrons (pe) per photon (pe/ph) and photoelectrons per electron (pe/e). Even though the linear combination of both signals can be associated with a fixed energy – if the interaction type is known – the individual yields are non-linear. This is illustrated for the case of low-energy NR in figure 2.3, but similarly true for ER. Usually, multiple ER sources of a known energy, mostly γ- or conversion electron-emitters, are used to determine g_1 and g_2. These parameters can then be applied for the ER energy calibration. Together with emission models like NEST one can then derive the corresponding NR energy scale. This can be applied both for single-site and multi-site interactions. For the latter one uses the single S1 and sum of all S2 signals measured in an event [201]. Note that $cS1$ and $cS2_{\mathrm{b}}$ in equation (2.9) are the measured areas of the signals in pe that have already been corrected for detector effects. These corrections and the measurement process will be discussed now.

2.1.3 Measurement and corrections of S1 and S2 signals

In the XENON detectors, S1 and S2 signals are measured by PMTs. An incident photon can free an electron when hitting the photocathode of the PMT. This electron is accelerated

---

[1] The bands are the median and $\pm 2\sigma$ quantiles from simulated ER and NR data that have been fitted to calibration data.

and multiplied along the increasing potential of the dynodes. The incident photoelectron is amplified by a gain factor on the order of 10^6 to obtain a charge pulse that can be measured. The pulses are digitised for data processing based on the signal amplification and PMT gain [191]. The data processing for XENON1T will be discussed further in section 2.2.1. The contribution $s1_i$ of each PMT to the area of the measured S1 signal can be written as:

$$s1_i(\vec{r}) \approx n_\gamma(E_u, \mathscr{E})\mu_i(\vec{r}). \tag{2.10}$$

The individual PMT light detection efficiencies for an S1 at an x-y-z position $\vec{r}$ are denoted as $\mu_\mathrm{i}(\vec{r})$. They include the PMTs quantum efficiencies, i.e. the fraction of incident photons producing a photoelectron, and the position-dependent light-collection efficiency. The total light-detection efficiency $\mu(\vec{r})$ is given by the sum of the individual PMTs' light-detection efficiencies. Then, the expectation value for the area of the total S1 signal of a nuclear recoil with the interaction position $\vec{r}$ is given by

$$s1(\vec{r}) = \sum_\mathrm{i} s1_\mathrm{i}(\vec{r}) \approx n_\gamma(E_\mathrm{nr}, \mathscr{E})\mu(\vec{r}). \tag{2.11}$$

Similarly it can be obtained for an ER signal with the respective n_γ. In order to achieve a uniform signal inside the whole detector $s1$ is usually corrected using the spatial average of the light detection efficiency $\langle\mu\rangle$:

$$cS1 = s1(\vec{r})\frac{\langle\mu\rangle}{\mu(\vec{r})}. \tag{2.12}$$

Using the definitions from equation (2.5) one can now define the light yield at a given ER equivalent energy E_er as

$$L_y(E_\mathrm{er}, \mathscr{E}, \vec{r}) = \frac{S_\mathrm{er}(\mathscr{E}) \cdot \mu(\vec{r})}{W_\gamma(E_\mathrm{er}, \mathscr{E} = 0)}. \tag{2.13}$$

With equations 2.5, 2.8, and 2.13 one obtains $cS1$ as a function of the nuclear recoil energy E_nr:

$$cS1 = E_\mathrm{er}\langle L_y(E_\mathrm{ref}, \mathscr{E})\rangle \cdot \mathscr{L}_\mathrm{eff}(E_\mathrm{nr}, \mathscr{E} = 0)\frac{S_\mathrm{nr}(\mathscr{E})}{S_\mathrm{er}(\mathscr{E})}, \tag{2.14}$$

where $\langle L_y\rangle$ is the detector-averaged light yield at a given electric field $\mathscr{E}$ and an ER reference energy E_ref.

The measured S2 signals are determined by additional factors. During the drift towards the liquid gas interface that occurs within the drift time t_d, ionisation charges are lost due to an attachment to electronegative impurities in the liquid. This attachment process can be described by a characteristic electron-lifetime τ_e that is a function of xenon purity [70]. The electron extraction yield κ and the proportional scintillation amplification factor Y depend on the strength of the extraction field $\mathscr{E}_\mathrm{extraction}$ at the top of the detector. The gas density ρ and the width of the gas gap h_g also influence the amplification. Then, the expectation values for the individual PMTs' contributions $s2_\mathrm{i}$ to the full S2 signal with an interaction position $\vec{r}$ are given by [191]:

$$s2_\mathrm{i}(\vec{r}) \approx n_\mathrm{e}(E_u, \mathscr{E}) \cdot e^{\frac{-t_d}{\tau_e}} \cdot \kappa(\mathscr{E}_\mathrm{extraction}) \cdot Y\left(\frac{\mathscr{E}_\mathrm{extraction}}{\rho}, h_g\right) \cdot \beta_\mathrm{i}(x, y)\eta_\mathrm{i}. \tag{2.15}$$

The width of the gas gap h_g is usually position-dependent due to an unoavoidable warping of the meshes or sagging of the wires that apply the electric field. An inclined liquid level can have a similar effect. The efficiency of the light detection is parametrised by $\beta_\mathrm{i}(x, y)$, the probability for a photon created at (x, y) to reach the PMT photocathode, and η_i, the product of the PMT's quantum and light collection efficiencies. The sum over the PMT-wise products of $\delta_i = \kappa Y \beta_i \eta_i$ has to be measured with calibration sources and is denoted as $\delta(x,y)$. Then, the expectation value for the full S2 area $s2$ of a nuclear recoil is [191].

$$s2(\vec{r}) = \sum_{\mathrm{i}} s2_{\mathrm{i}}(\vec{r}) = E_{\mathrm{nr}} \cdot Q_y(E_{\mathrm{nr}}) \cdot e^{\frac{-t_d}{\tau_e}} \delta(x,y). \tag{2.16}$$

Here, Q_y is the charge yield for a nuclear recoil in electrons per $\mathrm{keV_{nr}}$ following equation (2.5):

$$Q_y = \frac{T_{\mathrm{nr}}(\mathscr{E})}{W_e(E_{\mathrm{nr}}, \mathscr{E}_{\mathrm{ref}})}. \tag{2.17}$$

The ER S2 is obtained in a similar fashion with the respective light yield measured with calibration sources. Again, the spatial average $\langle\delta\rangle$ of $\delta(x,y)$ is used in practice to obtain a spatially uniform corrected signal $cs2$ via [191].

$$cS2 = s2(\vec{r}) \cdot e^{\frac{t_d}{\tau_e}} \frac{\langle\delta\rangle}{\delta(x,y)}. \tag{2.18}$$

As the S2 signal is highly localised at the top of the detector, the light collection is concentrated on a few PMTs. This is important for position reconstruction, but can be problematic for energy reconstruction if signals are recorded in regions of low-gain or defective PMTs. At the larger energy depositions expected for double-β decay, this concentration of signal can lead to a saturation of the PMT itself or of the digitiser down the signal chain [201]. Accordingly, one commonly uses only the fraction of the S2 that has been recorded by the PMTs at the bottom of the detector. This signal is referred to as $cS2_{\mathrm{b}}$.

2.2 The XENON1T experiment

The XENON1T detector [88] used 3.2 t of ultra-pure liquid xenon (LXe) with 2 t inside the sensitive volume of the TPC making it the first tonne-scale liquid xenon dual-phase TPC. A drawing of the detector is shown in figure 2.6. The TPC was a cylinder of 96 cm diameter and 97 cm drift length. The top and bottom PMT arrays were instrumented with 127 PMTs arranged in concentric circles and 121 PMTs arranged in a hexagonal pattern, respectively. This choice was made in order to improve S2-based position reconstruction at the top of the detector while maximising S1 light collection efficiency at the bottom. The Hamamatsu R11410-21 3 inch PMTs were jointly developed by Hamamatsu and the XENON collaboration [204]. They featured a quantum efficiency between 28 % to 42 % for xenon scintillation light with the highest quantum efficiency PMTs located in the centre of the bottom array. PMTs with less quantum efficiency were generally placed at the edges of the detector. The copper holding structures of the arrays were equipped with reflective PTFE surfaces between the PMT photocathodes. These minimised photoionisation and increased light collection. The TPC walls were made of highly-reflective PTFE panels backed by 74 oxygen free high thermal conductivity copper field-shaping electrodes. These ensured homogeneity of the electric drift field. The electric drift and acceleration fields were applied by 5 high transparency electrodes: The cathode and screening mesh protecting the bottom PMTs were realised as gold-plated stainless steel wires of 216 µm diameter and 7.75 mm pitch. The distance between the two sets of wires was 48 mm. The gate electrode, which together with the cathode marked the drift region of the detector, was realised as an etched hexagonal stainless steel mesh. Its centre marked the origin of the detector coordinate system. The anode and top screening mesh were also etched hexagonal meshes. The liquid xenon level in operation had to be levelled within the 5 mm gap between the gate and

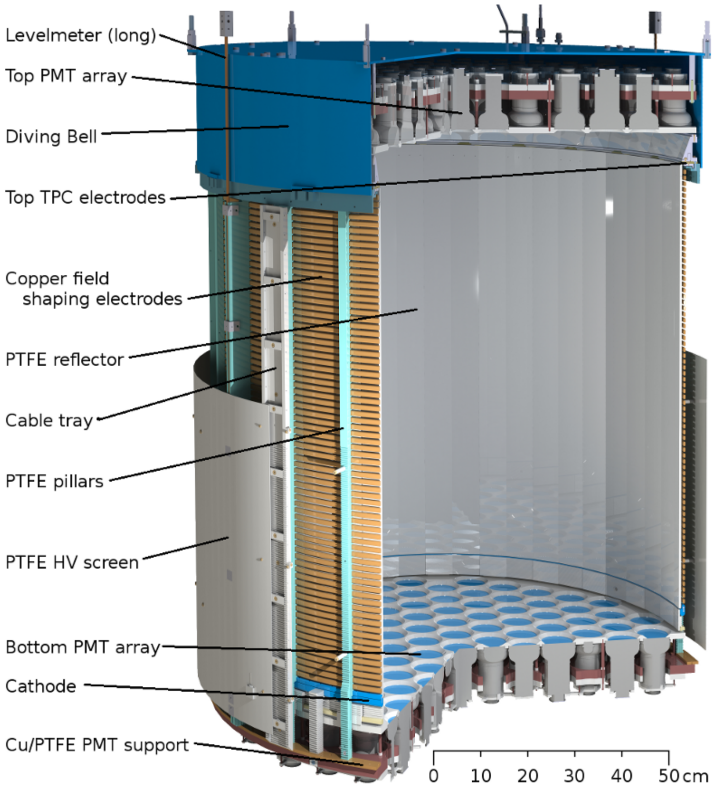

Figure 2.6: Drawing of the XENON1T TPC. Taken from [88].

anode. This was aided by the diving bell at the top of the detector. Multiple level meters were deployed in order to measure the liquid level. All materials were screened and selected for their low intrinsic radioactivity [68].

The TPC was housed within a stainless steel double-walled cryostat that itself was immersed in a water shield of 10 meter diameter and height. This setup is shown in figure 2.7. It is located in hall B of LNGS at a depth of 3600 m water equivalent. The cryostat sat in the centre of the tank and was anchored to the bottom of the tank in order to compensate for its buoyancy. Otherwise the detector was freely suspended from its triangular levelling system at the top of the support structure shown in dark yellow. The belt systems for the deployment of external ^{137}Cs and ^{228}Tl γ-sources are indicated in red and blue. These were also used in order to deploy a ^{241}AmBe (n, α) neutron source. In addition, a deuterium-deuterium fusion neutron generator (NG) could be deployed next to the cryostat from the top of the water tank. When not in use, it was stored at the top of the water tank, so the detector was shielded from eventual γ-radiation by several metres of water. The walls of the tank were equipped with reflective foil and 84 PMTs. This way the tank could be used as an active water Cherenkov muon veto [82]. Two pipes connected the cryostat with the systems in the support building next to the water tank. The large pipe at the top was vacuum-insulated and contained all the liquid and gaseous xenon pipes as well as all PMT and other sensor cables. The smaller pipe indicated in orange had the sole purpose of delivering the cathode high voltage.

The support building contained the xenon storage, purification, and cryogenic systems. These and their interconnections are shown in figure 2.8 and more details on all systems can be found in [88]. Here, the focus lies on three systems that are specifically referred to in the following analysis chapters: the gas analytics system, the purification system and the cryogenic distillation column. The gas analytics system was built around an Inficon Transpector H200M residual gas analyser (RGA) and can be used to monitor xenon-

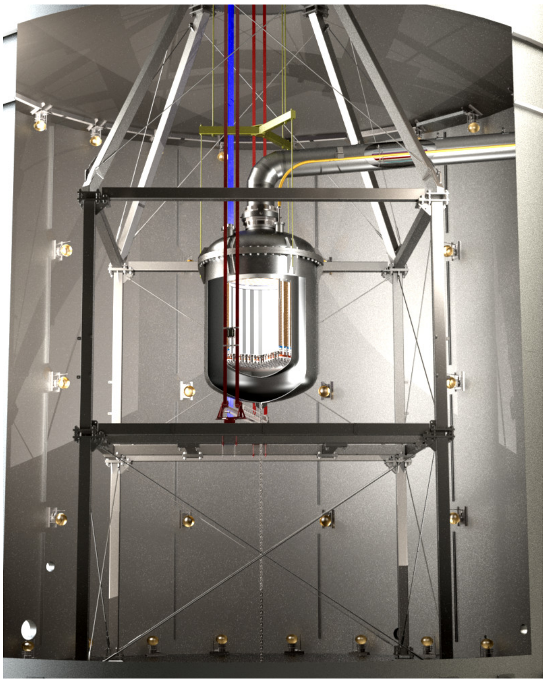

Figure 2.7: Drawing of the XENON1T cryostat inside the water tank. The drawing also shows the support structure, belt system for calibration sources, umbilical pipe and PMTs of the water Cherenkov muon veto. Taken from [88].

purity [205]. Notably, it could measure $^{\mathrm{nat}}$Kr contaminations to a certain extent. However, at the sub-ppt krypton concentrations that were required for the XENON1T background goals, a dedicated rare gas mass spectrometry (RGMS) system at MPIK Heidelberg was required in order to infer the contamination level during the science campaigns [206]. The on-site RGA system was also used in order to determine the isotopic composition of XENON1T's target [207]. It was found that the isotopic composition was close to the natural one with a slight depletion towards heavier isotopes and the corresponding enrichment at lower masses. This is in line with a single bottle of ^{136}Xe-depleted xenon in the total 3.2 tonne xenon inventory. With respect to the double-weak decaying ^{124}Xe it was found that the abundance was $\eta^{^{124}\mathrm{Xe}}_{\mathrm{meas}} = (9.94 \pm 0.14_{\mathrm{stat}} \pm 0.15_{\mathrm{sys}}) \cdot 10^{-4}$ mol/mol [31, 207]. This is 4 % larger than the natural abundance of $\eta^{^{124}\mathrm{Xe}}_{\mathrm{nat}} = (9.52 \pm 0.03) \cdot 10^{-4}$ mol/mol [153]. For ^{136}Xe the measured abundance was $\eta^{^{136}\mathrm{Xe}}_{\mathrm{meas}} = (8.49 \pm 0.04_{\mathrm{stat}} \pm 0.13_{\mathrm{sys}}) \cdot 10^{-2}$ mol/mol [207]. Accordingly, the measured abundance is 4 % smaller than the natural abundance $\eta^{^{136}\mathrm{Xe}}_{\mathrm{nat}} = (8.8573 \pm 0.0044) \cdot 10^{-2}$ mol/mol [153].

The cryogenic distillation column was designed to remove $^{\mathrm{nat}}$Kr from the liquid xenon inventory [72, 73]. This was necessary since $^{\mathrm{nat}}$Kr contains the anthropogenic β-emitter ^{85}Kr at the $2 \cdot 10^{-11}$ level [88]. Commercially available high-purity xenon gas usually has a $^{\mathrm{nat}}$Kr/Xe concentration of less than 2 ppm, which was enough to make ^{85}Kr the primary background source for Dark Matter search in XENON1T. Using the factor 10.8 larger vapour pressure of krypton and operating stably at a xenon throughput of 6.5 kg/h the full xenon target could have been purified within 3 weeks in order to reach the design goal of $^{\mathrm{nat}}\mathrm{Kr}/\mathrm{Xe} <$ 0.2 ppt. However, a different operation mode was chosen in order to purify while already taking data in a fully operational detector. By continuously purifying the ~ 20 kg gas layer at the top of the TPC with the distillation column, the krypton particle equilibrium inside the cryostat was disturbed steadily. This lead to the continuous migration of krypton into the gas-phase where it could be removed from the detector permanently [73]. With this an

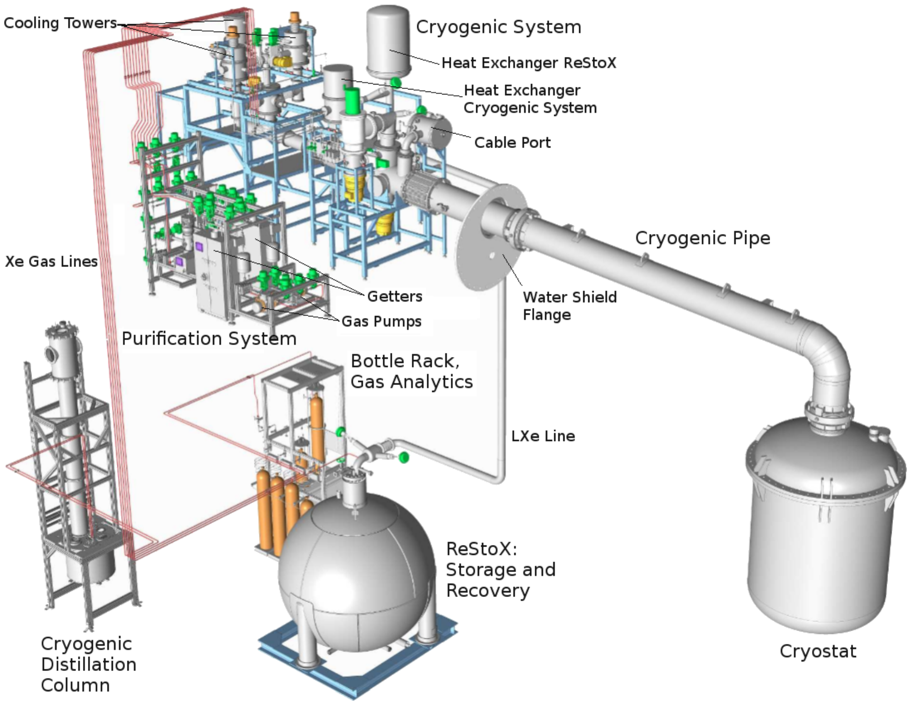

Figure 2.8: The xenon handling system of XENON1T. The cryogenic system was responsible for cooling and liquefying xenon gas. The purification system was required for the online removal of electronegative impurities from xenon gas that was continuously extracted from and re-fed into the detector. The ReStoX could be used for the recovery of liquid xenon in an emergency, but could also be used for storage and filling. The bottle rack housed xenon gas. A gas analytics system with a residual gas analyser was also available on site. The cryogenic distillation column could remove ^{85}Kr from the xenon inventory and could further be used for the continuous distillation of ^{222}Rn from the detector. Taken from [88].

average krypton concentration of $^{\mathrm{nat}}\mathrm{Kr}/\mathrm{Xe} = (0.66 \pm 0.11)$ ppt was achieved for SR1 [12].

At this krypton level the dominant ER background comes from the emanation of ^{222}Rn. Exploiting the smaller radon vapour pressure, a reverse online radon-distillation was demonstrated using the cryogenic distillation column [73, 77]. Figure 2.9 shows the activity concentrations over time of ^{222}Rn and the daughter isotope ^{218}Po as inferred from measuring the α-decay rate inside the detector [76]. For the XENON1T SR0 and SR1 average activity concentrations of $(13.3 \pm 0.5)\ \mu\mathrm{Bq/kg}$ and $(12.7 \pm 0.5)\ \mu\mathrm{Bq/kg}$ were found for ^{222}Rn and ^{218}Po, respectively. For SR2 the ^{222}Rn activity concentration could be further reduced to $(6.7 \pm 0.1)\ \mu\mathrm{Bq/kg}$ by exchanging the purification system's QDrive pumps – a major contributor to the XENON1T radon budget – for a single magnetically coupled piston pump with lower radon emanation [208]. Continuous cryogenic distillation further reduced the ^{222}Rn activity concentration by $\sim 20\,\%$ and ultimately $(4.5 \pm 0.1)\ \mu\mathrm{Bq/kg}$ were reached at the end of SR2 [76].

The purification system removed electronegative impurities adversely affecting S1 and S2 signals by absorbing scintillation light and capturing drifting electrons [88, 185]. The latter leads to a characteristic electron-lifetime τ_e as defined in equation (2.16). The impurities are constantly added to the xenon by outgassing from all detector components. Two redundant purification loops could be run in parallel and remove electronegative impurities by circulating xenon gas over high-temperature rare gas purifiers, so-called getters of the type SAES PS4-MT50-R. These zirconium-based getters form chemical bonds with oxide,

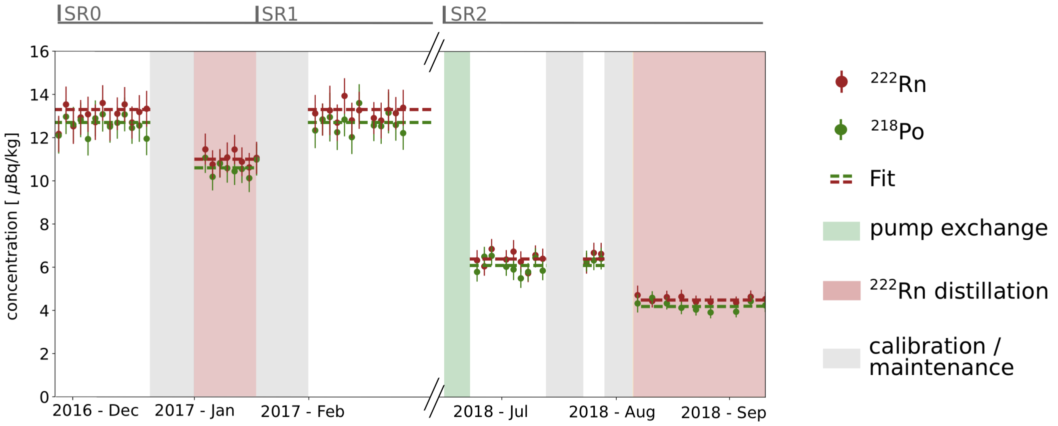

Figure 2.9: Activity concentration evolutions of ^{222}Rn (red) and ^{218}Po (green) inside the XENON1T TPC inferred from measured α-decay rates. Grey areas mark calibration and maintenance periods. During the red periods the activity concentrations of both isotopes were decreased owed to continuous cryogenic distillation. The green area indicates the exchange of the purification system's QDrive pumps with a single magnetic piston pump with lower radon emanation. Taken from [76].

carbide and nitrite impurities from the circulated xenon and trap the impurities in the porous material. Moreover, they should remove halogens such as iodine effectively. For the circulation each loop was equipped with two CHART QDrive pumps and an MKS 1579A mass flow controller. At a purification flow of 425 kg/d (50 slpm) the total cycle time of the detector inventory was ~ 7.5 d. In June 2018 the QDrive pumps were removed from the system and substituted with a single magnetically coupled piston pump. This allowed to increase the purification flow to ~ 700 kg/d (80 slpm) [208].

Figure 2.10 shows the evolution of τ_e in XENON1T. An electron lifetime of 650 µs was achieved at the end of the SR1. This is approximately the drift time of an electron over the whole length of the TPC at the applied drift field of 81 V/cm [12, 88]. Drops in electron lifetime are associated with maintenance operations or power failures in the laboratory. The electron lifetime model takes into account purification and outgassing. It was first fitted to electron lifetime values that were found for different ^{222}Rn progeny by using the S2s from α-decays at a known energy. Since the energy was fixed, the size of the S2 should have been the same over the whole range of t_d. The depth dependence of the S2 at a given energy that was induced by electronegative impurities capturing drift electrons could then be used to determine τ_e with an exponential fit. The electron lifetime model was then scaled to the electron lifetime values that were found for the S2 from a total 41.5 keV energy deposition of the internal ^{83m}Kr calibration source at different t_d. The calibrations are indicated by the pale red areas in the plot. The scaling was necessary since it was observed that using the electron lifetime from α-decays lead to a systematic underestimation of the electron lifetime from low- as well as high-energy ER signals (see appendix section A1). After the purification upgrade in SR2, an electron lifetime $\tau_e \approx 1$ ms was achieved.

In addition to purification, calibration sources can be injected directly into the liquid xenon target via the gas circulation loop. The available calibration isotopes are ^{220}Rn, ^{83m}Kr and ^{37}Ar. The latter was not used in the scope of this work, but application examples of ^{37}Ar can be found in [209, 210]. The isotope ^{220}Rn is emanated from a ^{228}Th calibration source. Its ^{212}Pb progeny were homogeneously distributed inside the TPC during calibrations. It undergoes β-decays with an endpoint energy of 569.9(19) keV and a half-life of 10.64 h [211].

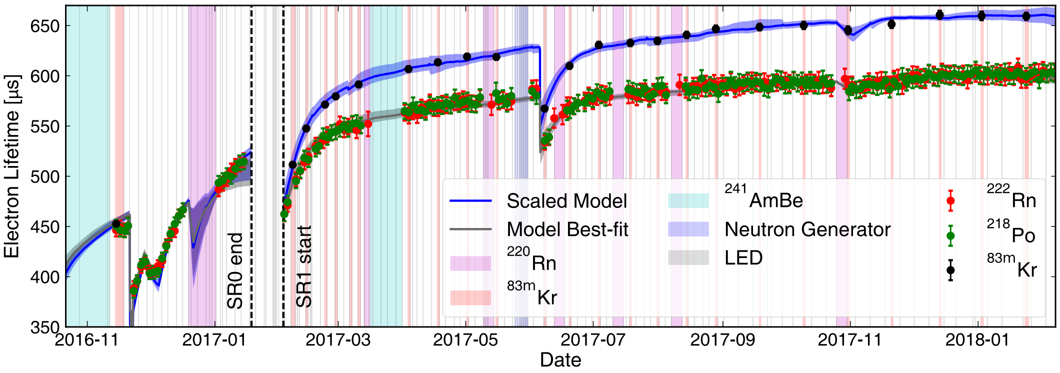

Figure 2.10: Evolution of the electron lifetime in XENON1T SR0 and SR1. The blue line is the electron lifetime model scaled to fit $^{83\mathrm{m}}$Kr electron lifetime data points (black). The model had initially been fitted to the electron lifetime values from α-decays (solid black line) of ^{222}Rn progeny (red and green markers). The pale blue band around the model indicates the 68 % credible region of the Bayesian Markov Chain Monte Carlo fit of the electron lifetime model. Calibration periods with $^{83\mathrm{m}}$Kr and other calibrations sources are indicated by the coloured areas. The end of SR0 and the start of SR1 are indicated by the vertical dashed black lines. Taken from [70].

The decay can be accompanied by γ-ray emission, so the resulting signals are similar to the expected ER background (see section 3.2). Accordingly the ^{220}Rn source can used for calibration and cut acceptance studies over a wide energy range. Owed to the relatively short half-life, normal data taking operation can be resumed in less than a week after calibration.

The isotope $^{83\mathrm{m}}$Kr is a common calibration source for different detector types [212, 213]. In XENON1T it is emanated from zeolite beads containing ^{83}Rb [88]. The ^{83}Rb decays to excited states of its ^{83}Kr daughter isotope via electron capture with a half-life of 86.2 d. Nuclear transitions in ^{83}Kr then populate the metastable state at 41.5575(7) keV [214] and the total branching ratio for the decay to $^{83\mathrm{m}}$Kr is 77.9 % [213]. The decay scheme for the internal transitions to the ground-state is shown in figure 2.11. It proceeds in two steps, both of which are highly converted [214]. The first step dominates the half-life at $T_{1/2} = 1.83$ h and the total emitted energy of the γ-rays and conversion electrons is 32.1 keV. Due to their short range and fast timing, the individual conversion electrons cannot be resolved in XENON1T. The second step has a half-life of 154 ns and a total energy deposition of 9.4 keV. While the first step almost exclusively proceeds via internal conversion (IC) with the coincident emission of Auger electrons and X-rays, the second step has a small branching fraction of 5 % for γ-emission. Due to the intrinsic few-µs width of the S2 signals, both transitions would always be merged into a single S2 peak in XENON1T. Narrower S1s of both transitions could be distinguished, so the S1 coincidence could be used for efficient event selection. The effective $T_{1/2} = 1.83$ h allowed a homogeneous distribution of $^{83\mathrm{m}}$Kr inside the detector, but prevented a long-term contamination. Due to its relatively low total energy deposition it could be used as a model for WIMP and low-energy ER signals. Accordingly it was used to infer light and charge yields, to benchmark the position reconstruction algorithms, and to derive position-dependent corrections for S1 and S2 [70].

The last system housed in the support building was the data acquisition (DAQ) [215]. The signals from the TPC's PMTs were amplified by a factor of 10 with Phillips Scientific 776 amplifiers and digitised by 100 MHz CAEN V1724 flash ADC boards. These boards featured 14 bit resolution, a bandwidth of 40 MHz, and a 2.25 V dynamic range. The DAQ

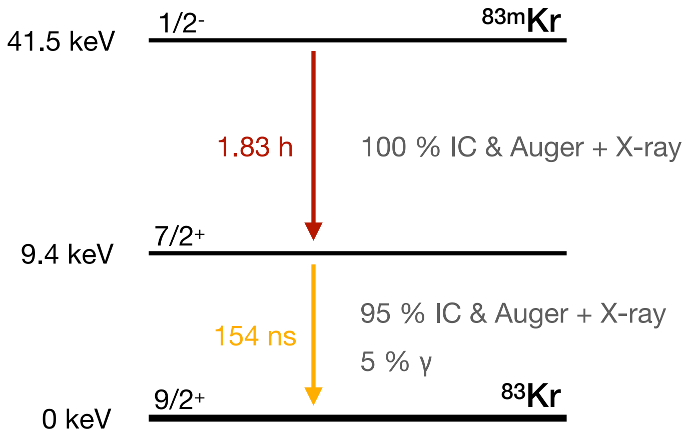

Figure 2.11: Simplified decay scheme of $^{83\text{m}}$Kr. Adapted from [212] with additional data on the J^P configurations of the nuclear states from [214].

was operated in a triggerless mode: Independently for each channel, every pulse above an approximate 0.3 pe digitisation threshold was read out and the baseline between pulses was not digitised (zero suppression). The 32 ADC boards – the muon veto used the same ADCs, but did not rely on signal amplification – were read out in parallel by six reader computers at a maximum data rate of 300 MB/s. This corresponded to an event rate of ~ 100 events/s during calibrations. The digitised pulses were stored in a database with basic pulse information such as the timestamp and PMT channel. Another computer, the acquisition monitor, continuously read out the sum signal of all bottom array PMTs together with the busy information of the digitisers and eventual veto signals. This was used for determining the measurement deadtime. Trigger decisions about the occurence of an actual particle interaction were made by a software event builder in real time. It scanned the pulse database and grouped causally connected pulses into events that were stored in a raw data file. The standard trigger was based on S2 signals and achieved a ≥ 99 % trigger efficiency for raw, i.e. uncorrected, S2s of 200 pe corresponding to a signal from ~ 7 electrons. After temporary underground storage the raw data was transferred to different data processing and storage sites in Europe and the United States [88].

2.2.1 The PAX raw data processor

The Processor for Analysing Xenon (PAX) [216, 217] is used to extract event properties such as signal areas, timings and widths from the raw data. It is based on Python with mathematics handled by NumPy [218] and data handling by Pandas [219]. For the output it also has a ROOT interface [220]. As an open source program it can be customised for use on other TPCs than XENON1T and has been benchmarked on XENON100 data [221]. Physical events are processed by passing through a series of plugins sharing a common structure. The PAX processing chain as used in XENON1T is illustrated in figure 2.12. The blue tiles in the figure signify the objects that are stored in the output ROOT file. These contain measured properties. With each step, the new objects incorporate higher level information from the preceding processing steps. The steps represent the series of processor plugins and are depicted as purple tiles. Going from the high to the low level objects, a physical *event* in PAX contains multiple *peaks*. Pairs of these *peaks* are the result of physical *interactions* inside the detector. According to the positions of the interactions, corrections on S1 and S2 can be applied and the main interaction, i.e. the interaction with the largest energy

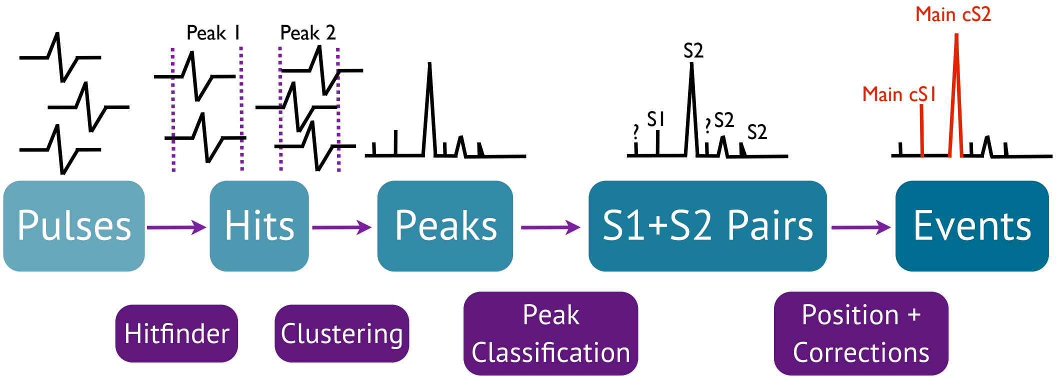

Figure 2.12: General working principle of PAX. PAX objects (blue tiles) are generated by passing data through a series of plugins (purple tiles). With each step, the objects contain a higher order of information from the previous processing steps. Taken from [221].

deposition, within an event is identified. *Peaks* are the sum of coincident PMT *hits* among several channels. The hits directly originate from *pulses* out of the raw data file that were saved by the DAQ. A *hit* then is a pulse with a sufficient excursion above the waveform's baseline.

Figure 2.13 shows an example waveform from a single PMT channel (recreated from [221]) in XENON100 data reconstructed with PAX. Although XENON100 used different PMTs, the per PMT waveforms in XENON1T are similar enough to use the same hitfinding logic which is outlined in the following. The sample size of the ADCs is 10 ns. This waveform snapshot is treated as a single *pulse* by PAX. It is processed in three steps: First, the baseline is calculated from samples at the beginning and end of the *pulse*. The higher of the two values is used. Then two hitfinder thresholds are set depending on the standard deviation of the baseline. Once a sample exceeds the lower threshold at 1 standard deviation over the baseline mean, the hitfinder will calculate the sum of all consecutive samples above the lower threshold. In a third step, the sum is stored as a *hit* under the condition that one of the samples in the window exceeds the high threshold at five standard deviations. One *pulse* may contain multiple *hits*. The pulse areas in pe are calculated from the ADC counts by applying the PMT gain values. The aggregation of coincident *hits* to *peaks* starts with a rough clustering based on the gaps between hits. Then, a recursive natural breaks algorithm carries out the finer clustering of the rough chunks of hits. Should a channel exhibit a lone *hit* that is not coincident with any other, it is marked as suspicious. This classification suppresses a large amount of signals that do not originate from particle interactions such as noise or PMT dark counts. The uncorrected *peak* area A in pe is then calculated as the sum of all contributing *hits*. The *peak* clustering is followed by a classification step. *Peaks* are classified according to their area, width and coincidence level. In general wider peaks of few μs and areas of few thousands to millions of photoelectrons, depending on the interaction type and energy, are identified as S2s. Smaller peaks of few tens of ns width are S1s. One notable classification criterion is the requirement of a three-PMT coincidence for S1s. This criterion reduces the rate of accidental coincidences of small signals in the Dark Matter search. It is the main driver of the S1 energy threshold since signals of $\mathcal{O}(1\text{ keV})$ are likely to be seen by three PMTs or less. Special cases are present for *peaks* that cannot be classified.

The pairing of S1s and S2s builds *interactions* that are attributed to the same physical origin. A physical pairing requires that the S1 precedes the S2. Each causally meaningful interaction is saved in the processor output. The first S1+S2 pair in the output array is the main *interaction*. It contains the largest area S1 and S2 in the event. For each *interaction*

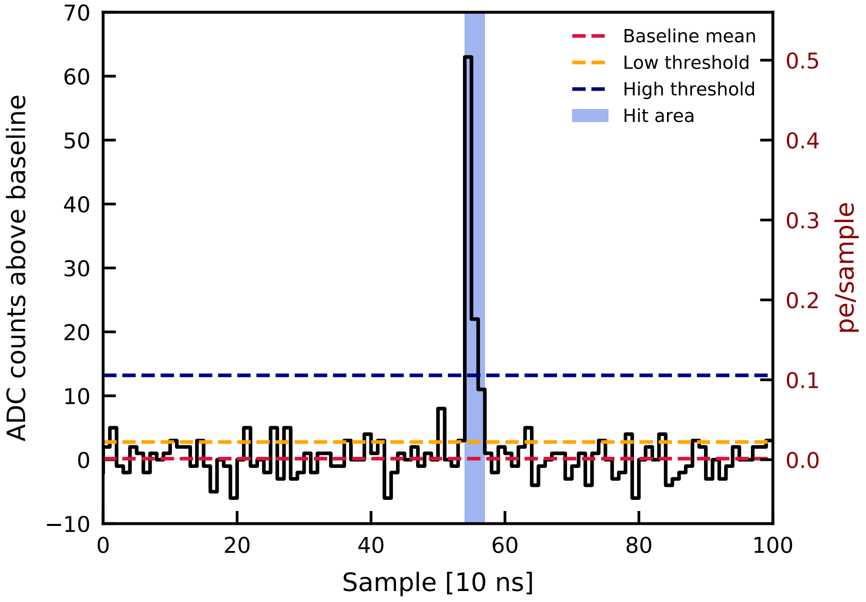

Figure 2.13: Example waveform recreated from the first event of a XENON100 raw data file as in [221]. The y-axis on the left gives ADC counts above the mean baseline. These are converted into pe/sample using the PMT gain. The x-axis shows the sample number of the waveform. The sample size is 10 ns. The dashed red line indicates the mean baseline. The lower threshold, one standard deviation above the baseline, is the dashed orange line. The five standard deviation higher threshold is shown as the dashed blue line. The blue-shaded area marks the full *hit*.

the x-y-z position can be reconstructed from the S2 hit pattern and the S1-S2-delay. The main reconstruction algorithm is based on a neural network that is trained on Monte Carlo simulations of the light response of the top PMT array. A secondary hit pattern fit algorithm can be used for cross-checks and cuts on misreconstructed events [70]. The reconstructed positions and their associated signal corrections for calculating $cS1$ and $cS2_\mathrm{b}$ are saved for all pairings. The final *event* is built from all *interactions* occurring in a time window of 2 ms and contains the information from the whole processing chain down to the *pulse* level. An exemplary waveform of a WIMP-candidate event from XENON1T is shown in figure 2.14. The four panels in the top row show, from left to right, the sum waveforms of the main S1 and S2, the S1 hit pattern on the bottom PMT array, and the S2 hit pattern on the top PMT array. The red cross marks the reconstructed interaction position. The middle panel shows the summed waveform of all PMTs. In addition to the main S1 and S2 multiple smaller peaks can be identified. These are usually attributed to afterpulses in individual PMTs, noise or dark counts. They are not classified as physical peaks. In some cases an S2 signal will be followed by smaller S2 signals, a so-called electron train. Here, single electrons that are created by photoionisation or extracted with a time delay due to yet unknown reasons can cause follow-up signals. In the bottom panel the timing of the individual pulses is indicated for all 248 PMT channels. The pulse area is given by the size of the red dot. The multi-channel coincidence for the S1 and S2 can be identified clearly while the smaller unclassified peaks consist of isolated pulses. The waveform was processed with version 6.8.0 of PAX, which is also used for the analysis in chapter 3. A high energy waveform like it would be expected in a $0\nu\beta^-\beta^-$ decay search has several unique features that distinguish it from this low-energy example. These include multiple interactions, saturation effects and

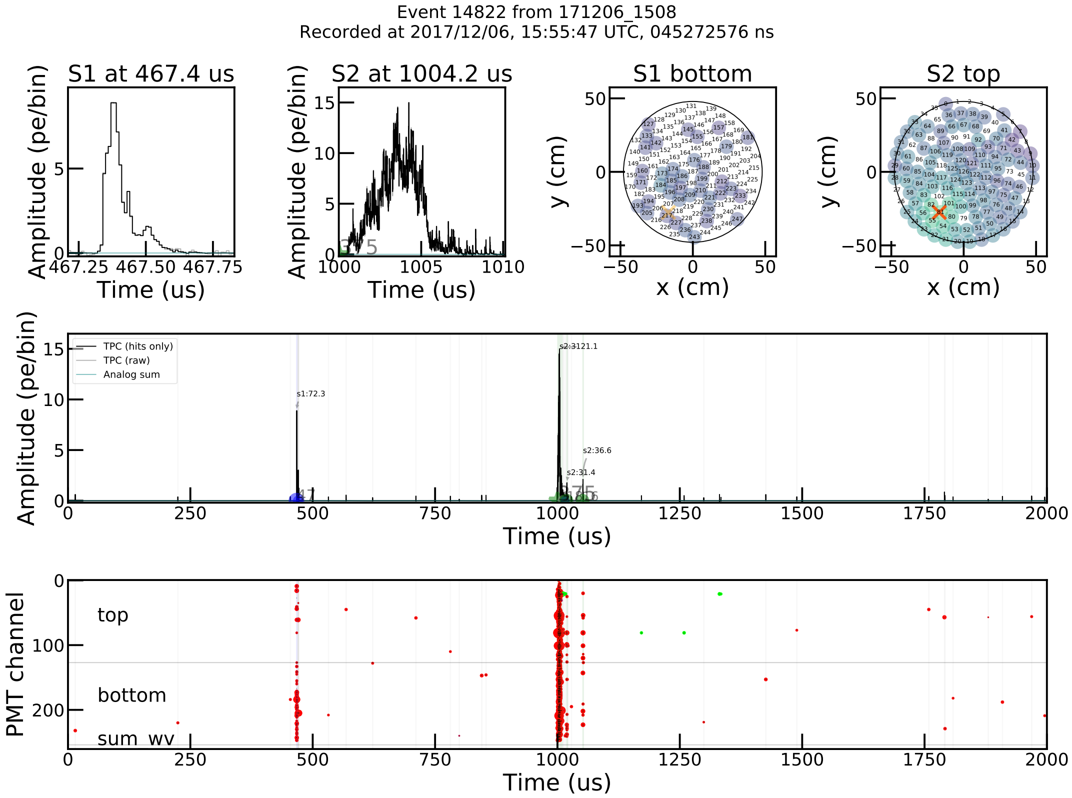

Figure 2.14: Example waveform from one of the WIMP candidate events in [12] recorded on 6th December 2017. The top row shows the sum waveforms of the main S1 and S2 signals as well as the S1 and S2 hit patterns on the bottom and top PMT arrays, respectively. The middle panel gives the amplitude of the sum waveform over time. The bottom panel shows the pulse timing of all 248 PMT channels. The size of the red dots indicates the pulse area.

single-electron trains of few 100 µs length. Several high-energy improvements of PAX for the analysis of such signals were implemented after XENON1T SR1. These are discussed in section 6.1. The PAX version with these improvements is 6.10.1, which is used for the analyses in chapters 4 and 6.

Observation of ^{124}Xe Two-Neutrino Double-Electron Capture in XENON1T

3

XENON1T achieved the first direct observation of two-neutrino double-electron capture in ^{124}Xe. This chapter will present the analysis that led to the 4.4σ observation of the double-K capture (2νKK) that features the longest half-life measured to date. The results that are presented in this chapter have been obtained in collaboration with A. Fieguth. A preliminary version of the results has been published in his PhD thesis [207]. The final analysis has been published as a XENON collaboration paper [31] with A. Fieguth and the author of this work as the corresponding authors. This chapter will be based on that paper. A. Fieguth contributed the signal model, data selection criteria, fiducial volume, and analysed the ^{124}Xe abundance measurements. The main contributions in the scope of this work were the energy calibration of the detector, the quantitative model of the ^{125}I background, and the full background model based on Monte Carlo simulations. The latter model was fitted to the data and was used for calculating the significance of the double-K electron capture peak.

3.1 Data selection, energy calibration and fiducial volume

The data analysed in this chapter was recorded between 2nd February 2017 and 8th February 2018 as part of XENON1T SR1. Details on the detector conditions and signal corrections can be found in the original publications [11, 12, 70]. While fixing the data quality criteria, fiducial volume and background model, the data in the energy region of interest around the 64.3 keV peak of the 2νKK was blinded. This means, the energy region from 56 keV to 72 keV was inaccessible for analysis. Datasets recorded directly after detector calibrations with an external ^{241}AmBe neutron source or the deuterium-deuterium-fusion NG were removed in order to reduce the impact of radioactive ^{125}I which will be discussed in section 3.3. It is produced by thermal neutron capture on ^{124}Xe during neutron calibrations and removed from the detector by the purification system. A pre-unblinding quantification of this removal using short-term calibration data from SR2 led to a first reduction of the dataset to 214.3 days [207]. This data was used for fixing the background model. After unblinding, the long-term activity evolution of ^{125}I could be quantified. This led to a further removal of datasets yielding a final live-time of 177.7 days. This live-time includes corrections for detector deadtime and cut-induced live-time losses.

3.1.1 Data quality criteria

Most of the data selection and quality criteria – commonly referred to as cuts – have been adopted from the SI WIMP search in [12], but in order to maximise signal acceptance, cuts that only target low-energy nuclear recoils have been discarded. This signifies the change of philosophy in the cut selection compared to the Dark Matter search [207]. While it is crucial to veto single background events in a Dark Matter search with $\mathcal{O}(1)$ signal and background events in the NR band, in the 2νKK search one expects few hundreds of background events in the ER band regardless of cuts. At the XMASS lower half-life limit of $T_{1/2} > 2.1 \cdot 10^{22}$ yr (90% C.L.) [145], the signal expectation is $\mathcal{O}(100)$ events. The main drivers of the achievable signal significance are the magnitude of the 2νKK signal itself and the $\sqrt{N}$ Poisson fluctuations of the physical β- and γ-background. For single-site interactions, these background contributions cannot be cut without compromising the signal due to their similar ER signatures. Thus, the cut selection focuses on the removal of unphysical backgrounds and multi-site interactions. Accordingly, a few percent larger signal acceptance at the cost of a smaller cut efficiency, i.e. the survival of more unphysical or multi-site background events, would still lead to a favourable signal to background ratio.

The data quality criteria employed in this analysis are summarised in table 3.1. The right column provides a short description of the functioning and purpose of the cut. A detailed description can be found in [207]. The centre column gives the method employed for the derivation of the cut acceptance. Essentially three different methods are applied in XENON1T analysis depending on the definition of the cut. Live-time cuts such as the DAQ veto and S2 tails cuts remove fixed time periods of data. Accordingly, their acceptance can be corrected by giving an effective live-time of the data that is smaller than the real time of data taking. The analytic method can be used where the bulk of a signal-like event population can be distinguished from the background-like population in data. The S2 width cut is an example for this. Due to diffusion of the electron cloud, the width of the S2 signal will increase with interaction depth. The signal-like population follows the diffusion behaviour while unphysical background events appear as outliers. The cut boundary is set as the 98 % quantile of the signal-like population. Consequently, this is the analytic acceptance of the cut. If the underlying physics process is unknown or does not allow to clearly discriminate the signal and background populations, the $N-1$ and iterative methods have to be applied. The $N-1$ acceptance of a cut then is the number of events remaining after applying all N cuts divided by the number of events after applying all cuts, but the one under consideration ($N-1$). Since the relative numbers of signal and background events removed by the cut under consideration are unknown, all removed background events are regarded as signal events. In turn, the $N-1$ acceptance can be regarded as a lower limit on the cut acceptance. The iterative methods is similar to the $N-1$ treatment, but uses different combinations within all N cuts in order to identify eventual correlations between cuts and obtain an estimate of the final acceptance that is closer to the actual value. The $N-1$ and iterative acceptances are either determined on unblinded energy sidebands of the background data, i.e. the same data as for the physics search, or on independent ^{220}Rn calibration data.

The total cut acceptance was determined in 1 keV bins in the 20–200 keV energy interval by a bin-wise multiplication of the individual cuts' acceptances. Binomial uncertainties were used in order to account for the fact that for a unity acceptance there can only be a lower uncertainty bound. The acceptance data points were then parametrised by the energy-dependent linear function $\epsilon_{\mathrm{XENON1T}}(E)$ [207]:

$$\epsilon_{\mathrm{XENON1T}}(E) \geq [(-1.48 \cdot 10^{-2} \cdot E + 94.28) \pm 0.73]\,\%. \tag{3.1}$$

Since the acceptance variation over the ROI is smaller than the uncertainty, the lower limit

Table 3.1: Data quality criteria for the 2νKK search with their acceptance derivation method and short description. Adapted from [207].

Cut name	Acceptance derivation	Description
DAQVeto	Live-time	Correct for DAQ deadtime
S2Tails	Live-time	Remove high rate periods following large S2s
ERband	Analytic	Remove NR events from ER data
S2Width	Analytic	Correlate S2 signal width and interaction depth
InteractionPeaksBiggest	Analytic	Check if largest peak is in main interaction
PreS2Junk	$N-1$ (background)	Remove noise
S2SingleScatter	$N-1$ (background)	Remove multi-site events
S2AreaFractionTop	$N-1$ (^{220}Rn)	Remove events with anomalous relative PMT array contributions to the S2
S1AreaFractionTop	Iterative (^{220}Rn)	Remove evens with anomalous relative PMT array contributions to the S1
S1PatternLikelihood	Iterative (^{220}Rn)	S1 signal distribution among PMTs
S1SingleScatter	Iterative (^{220}Rn)	Remove signals with multiple S1s from consecutive nuclear decays or pileup

on the 2νKK signal acceptance $\epsilon_{2\nu\mathrm{KK}}$ is given as a constant value [207] from the fit of a function constant in energy:

$$\epsilon_{2\nu\mathrm{KK}} \geq (93.4 \pm 0.7)\,\%. \tag{3.2}$$

This constant acceptance assumption was initially applied in the fit of the background model to the measured data. In the course of the analysis it was found that the assumption of a constant acceptance could not be upheld.

Between 200 and 300 keV the absorption coefficient for Compton-scattering becomes the dominant γ-energy loss mechanism in xenon (cf. figure 2.1). Moreover, γ-rays from TPC construction materials can penetrate the xenon target further at higher energies. Accordingly, above 200 keV the fraction of multi-site interactions increases exponentially. A large fraction of multi-site interactions is removed by the S2 single scatter cut. This cut removes waveforms with multiple physical S2s. However, if two scatters are sufficiently close in z their S2s will be merged leading to a single widened S2. Accordingly, above 200 keV the shape of the S2 width distribution changes and actual single-site interactions cannot be distinguished from unresolved multi-site interactions anymore. Consequently, the cut

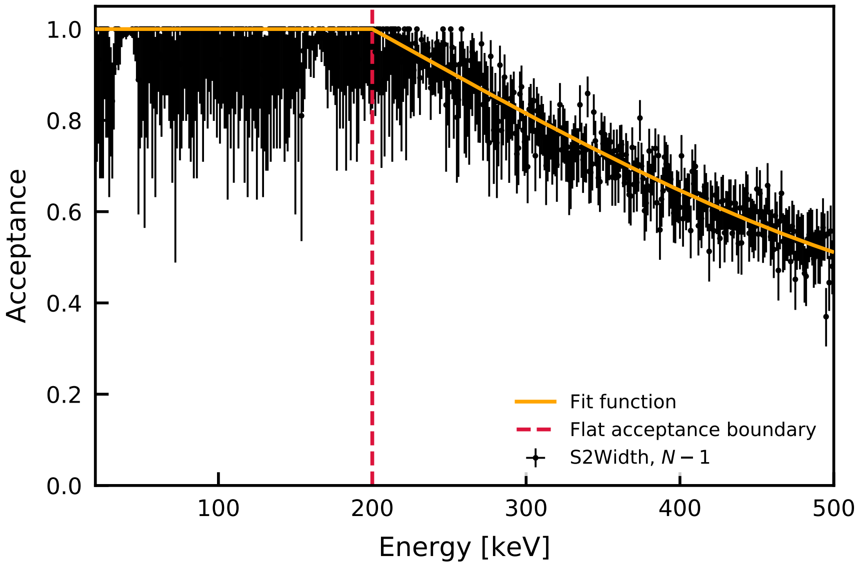

Figure 3.1: The $N-1$ acceptance of the S2 width cut as a function of energy in bins of 1 keV width between 10 and 500 keV. All other event selections for the 2νKK search have been applied in a 1 tonne fiducial volume. Binomial uncertainties are shown for the data points. The dashed red line indicates the 200 keV energy up to which the flat acceptance had been determined earlier. The orange line indicates the fit function used to model the flat behaviour up to this point and the subsequent acceptance decrease.

had only been defined up to 200 MeV. For energies above this threshold, the acceptance treatment had to be changed from the analytic approach to $N-1$. Figure 3.1 shows the $N-1$ acceptance of the S2Width cut within the cylindrical 1 tonne fiducial volume used in [12]. While the acceptance is approximately unity up to 200 keV, beyond it decreases down to ~ 50 % at 500 keV. This behaviour was parametrised as unity below a freely fitted threshold energy E_{var} and with the phenomenological function

$$\epsilon_{\text{S2Width}} = \begin{cases} 1 & \text{for } E \leq E_{\text{var}}, \\ (E-E_{\text{var}})\cdot a + (E-E_{\text{var}})^3 \cdot b & \text{for } E > E_{\text{var}}. \end{cases} \tag{3.3}$$

In a χ^2 fit using the mean symmetrised uncertainty one obtains

$$\begin{aligned} E_{\text{var}} &= (200 \pm 1)\ \text{keV}, \\ a &= (1.88 \pm 0.04)\cdot 10^{-3}, \\ b &= (2.8 \pm 0.6)\cdot 10^{-9} \end{aligned} \tag{3.4}$$

with $\chi^2/\text{ndf} = 0.71$. This points to an overestimation of the uncertainty that can be associated with the symmetrisation. Since the signal and background fractions in the removed events are not known, the function gives a lower limit on the acceptance. For the same reason, this lower limit is not associated with a statistical confidence level. The true acceptance can assume any value between the fit function and unity. Therefore, an overestimation of the uncertainties is not an issue for the further analysis steps.

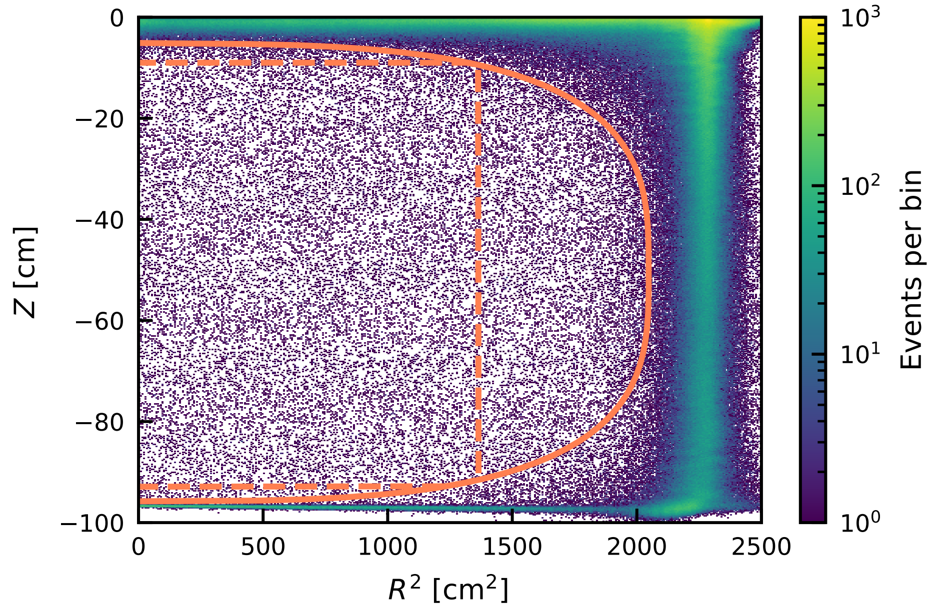

Figure 3.2: Spatial distribution of events as a histogram in interaction depth Z vs. squared radius R^2. The energy range of the events is 80 keV–140 keV. High density areas can be found close to the edges of the TPC where the majority of external β- and γ-radiation is absorbed. The 1502 kg fiducial volume is indicated by the solid coral line. The further segmentation into an inner (1.0 t) and outer (0.5 t) volume is marked by the dashed coral line. Modified from [31].

3.1.2 Fiducial volume

As the number of 2νKK events is proportional to the number of ^{124}Xe nuclei, the signal strength grows linearly with the xenon mass m_{volume} inside the detector volume selected for analysis. At the same time, distinguishing background from signal depends on the Poisson uncertainty $\Delta N_{\mathrm{background}} = \sqrt{N_{\mathrm{background}}}$ on the number of background events. The volume-dependent sensitivity S_{vol} is then proportional to the contained xenon mass divided by the background uncertainty:

$$S_{\mathrm{vol}} \propto \frac{m_{\mathrm{volume}}}{\sqrt{N_{\mathrm{background}}}}. \tag{3.5}$$

The sensitivity parameter was optimised by iterating over cylindrical and superellipsoidal volumes of different dimensions and identifying the volume that featured the largest value of S_{vol} [31]. A superellipsoid of 1502 kg mass was found to offer the optimal sensitivity. Since the signal region was blinded, an energy sideband from 80 keV to 140 keV was used for the optimisation. In order to include spatial information to the background and signal model fit and for consistency checks, the superellipsoid was segmented into an inner and outer volume. The segmentation is indicated in figure 3.2. Intrinsic background sources mixed with the xenon, solar neutrinos, and the 2νKK signal should appear at the same rate in both volumes. However, the material background contribution is strongest near the detector walls and PMT arrays. Accordingly, a simultaneous fit should provide better background constraints and a higher sensitivity compared to a single monolithic volume. Moreover, the inner volume has been studied extensively since it was used for the first Dark Matter results from XENON1T [202].

The finite resolution of the position reconstruction in XENON1T leads to an uncertainty on the fiducial mass. This was quantified by contrasting the analytically calculated mass, derived from the fiducial volume geometry and LXe density of 2.862 g/cm^3 at −96.1 °C [180], with $^{83\text{m}}$Kr data. Since the calibration isotope is homogeneously distributed inside the detector, the fiducial mass is the total liquid xenon mass in the TPC multiplied with the fraction of $^{83\text{m}}$Kr events in the fiducial volume. Then, the fiducial mass is $m = (1502 \pm 9_{\text{sys}})$ kg. The segmentation was found to yield a 1052 kg inner volume an outer 448 kg volume, each with a 1 % systematic uncertainty on its mass [207].

3.1.3 Energy calibration

The energy calibration of the detector takes advantage of the anti-correlation of light (S1) and charge (S2) signals in the XENON1T dual phase TPC as outlined in equation (2.9). This leads to mono-energetic γ-lines appearing as rotated ellipses when plotting $cS1$ against $cs2_\text{b}$. The rotated ellipses are shown in figure 3.3 for the full energy range and for the ellipses from the $^{83\text{m}}$Kr, $^{131\text{m}}$Xe and $^{129\text{m}}$Xe peaks in the inner 1 t fiducial volume. For $^{83\text{m}}$Kr the peak corresponds to the total 41.5 keV energy deposition when both S1s and S2s were merged to a single signal (cf. figure 2.11). The metastable $^{131\text{m}}$Xe (163.9 keV) and $^{129\text{m}}$Xe (236.2 keV) were activated by inelastic neutron scattering during calibration campaigns with the NG or the ^{241}AmBe source [222]. They decay with half-lives of 11.86 d and 8.88 d, respectively [223, 224]. These lines as well as the 1173.2 keV and 1332.5 keV γ-transition lines of ^{60}Co [182], which is present in the stainless steel detector components such as the cryostat, are used for the energy calibration. Moreover, the 1460.8 keV line of ^{40}K is used [225]. Higher energy lines are excluded due to missing high-energy optimisations of the signal reconstruction which were only available for the analyses in chapters 4 and 6.

In the calibration procedure, the $cS1$-$cS2_\text{b}$ distribution is projected onto the energy axis. Along the tilt axis, the width of the ellipses is minimal, so a projection along this axis yields the optimal energy resolution[1] [188]. In a first step all lines were fitted using rotated two-dimensional Gaussian functions of the form

$$A(cS1, cS2_\text{b}) = A_0 \cdot e^{-\frac{f_1(cS1, cS2_\text{b})^2}{2a^2} - \frac{f_2(cS1, cS2_\text{b})^2}{2b^2}} + B_0. \tag{3.6}$$

The parameters a and b in the denominators of the exponent contain the rotated standard deviations in $cS1$ and $cS2_\text{b}$. They determine the ellipticity of the lines. The parameter B_0 is added as an approximately constant background contribution within the fit window. With the peak amplitude A_0, the mean $cS1$ value μ_{S1}, mean $cS2_\text{b}$ value μ_{S2} and the ellipse rotation angle θ, the enumerators of the exponent are

$$\begin{aligned} f_1(cS1, cS2_\text{b}) &= ((cS1 - \mu_{\text{S1}}) \cdot \cos\theta - (cS2_\text{b} - \mu_{\text{S2}}) \cdot \sin\theta), \\ f_2(cS1, cS2_\text{b}) &= ((cS1 - \mu_{\text{S1}}) \cdot \sin\theta + (cS2_\text{b} - \mu_{\text{S2}}) \cdot \cos\theta). \end{aligned} \tag{3.7}$$

The fit function is illustrated in the bottom panel of figure 3.3 and exemplary fits can be found in section A2 of the appendix. The peak means (μ_{S1}, μ_{S2}) are extracted from the individual fits of the six lines. Dividing them by the energy gives the light and charge yields L_y and Q_y, respectively:

$$\begin{aligned} L_y &= \frac{\mu_{\text{S1}}}{E}, \\ Q_y &= \frac{\mu_{\text{S2}}}{E}. \end{aligned} \tag{3.8}$$

---

[1] The $^{83\text{m}}$Kr peak exhibits a slightly different rotation compared to the metastable xenon lines. This can be attributed to its double-decay signature paired with the non-linearity of the light and charge yields as a function of energy (cf. figure 2.3).

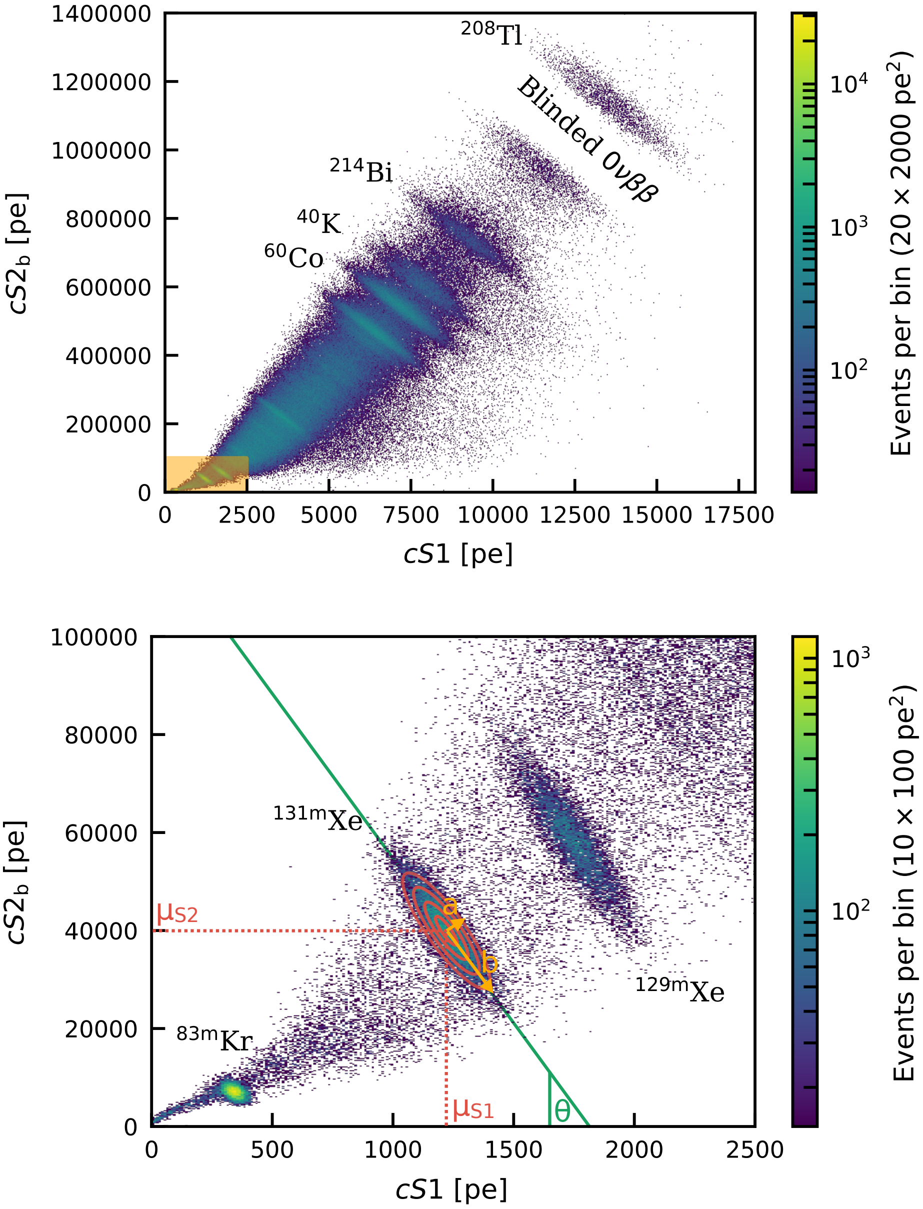

Figure 3.3: Histograms of $cS1$ vs. $cS2_\mathrm{b}$ for data from XENON1T SR1 after all analysis cuts. Only single-site events are shown, and the plots have been produced after unblinding of the double-electron capture region. The $0\nu\beta\beta$ region is still blinded. The final run selection has not been applied to this data in order to have a higher rate of the metastable xenon peaks, associated with neutron calibrations, for illustration. **Top:** Full energy range with high energy lines of ^{60}Co, ^{40}K, ^{214}Bi and ^{208}Tl. The band connecting the peaks is the result of β-decays and Compton scattering of higher energy γ-rays. The region shaded in orange is the low-energy cutout in the bottom plot. **Bottom:** Lines of $^{83\mathrm{m}}$Kr, $^{131\mathrm{m}}$Xe and $^{129\mathrm{m}}$Xe from bottom left to top right. The elliptical fit function with the mean $cS1$ value μ_{S1} and mean $cS2_\mathrm{b}$ value μ_{S2} is shown above the $^{131\mathrm{m}}$Xe line. The angle angle θ gives the ellipse rotation while a and b determine the ellipticity. The amplitude is indicated by the concentric red ellipses. The projection onto the energy axis is carried out along the green main axis of the ellipse.

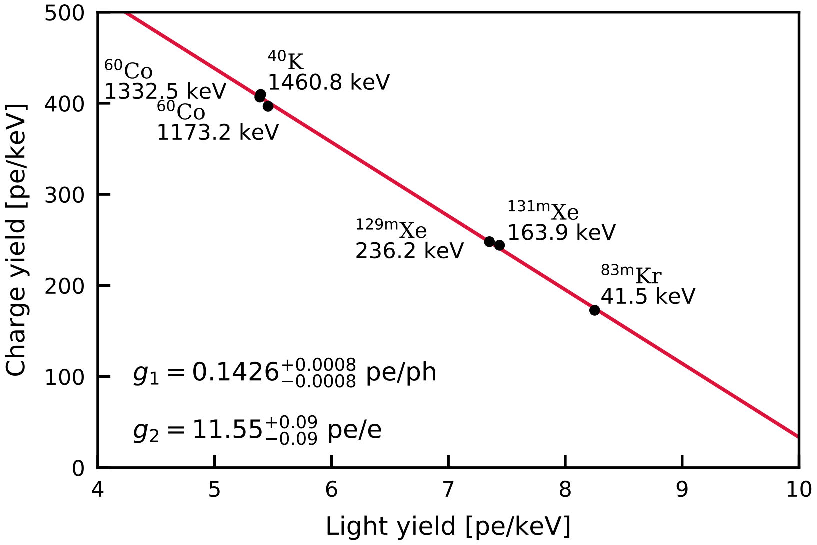

Figure 3.4: Fit of light and charge yields of selected γ-lines in order to obtain the energy calibration parameters g_1 and g_2 in the 1 t inner fiducial volume. The statistical uncertainties of the data points have been scaled with $\sqrt{\chi^2/\mathrm{ndf}} = \sqrt{657/4}$ in order to account for systematic uncertainties from the elliptical line fits. Still, the uncertainties are too small to be visible in the plot. Modified from [207].

Now one can rearrange equation (2.9) to obtain a fit function

$$Q_y = -\frac{g_2}{g_1} \cdot L_y + \frac{g_2}{W}, \tag{3.9}$$

along which the individual light and charge yield data points are arranged. The fit parameters are g_1 and g_2. The result from a χ^2-fit to the data points in the inner 1 t fiducial volume is shown in figure 3.4 [207]. In an initial fit only the statistical uncertainties of L_y and Q_y were considered and yielded $\chi^2/\mathrm{ndf} \approx 657/4$ even though the points clearly follow the expected linear trend. This can be explained by the systematic uncertainties that arise from the fit method: The choice of the $cS1$-$cS2_\mathrm{b}$ window influences the shape of the background that is only approximately flat. As discussed in [221], it is desirable to choose a small energy window for background suppression, but a too small window will truncate the peak and bias the fit. Especially at the higher energies of ^{60}Co and ^{40}K additional peaks are present that cannot be resolved and individually fit in $cS1$ vs. $cS2_\mathrm{b}$. These will shift the peak mean upwards and downwards if they are situated above or below the peak of interest. As a consistent treatment of this systematic uncertainty was challenging for each individual peak and assumed to have only a minor impact on overall result for the central values of g_1 and g_2, a simplified method was applied: The uncertainties on the data points were scaled with $\sqrt{\chi^2/\mathrm{ndf}} = \sqrt{657/4}$ in order to estimate the systematic uncertainty and to obtain realistic uncertainties on g_1 and g_2. While the χ^2/ndf of the fit with the increased uncertainty is unity, the uncertainties of the data points are still too small to be visible in the plot. The energy calibration parameters

$$\begin{aligned} g_1 &= (0.1426 \pm 0.0008)\ \mathrm{pe/ph}, \\ g_2 &= (11.55 \pm 0.09)\ \mathrm{pe/e} \end{aligned} \tag{3.10}$$

that were determined in this work were applied in the signal and background modelling for the SI WIMP search in XENON1T [12] as outlined in [11].

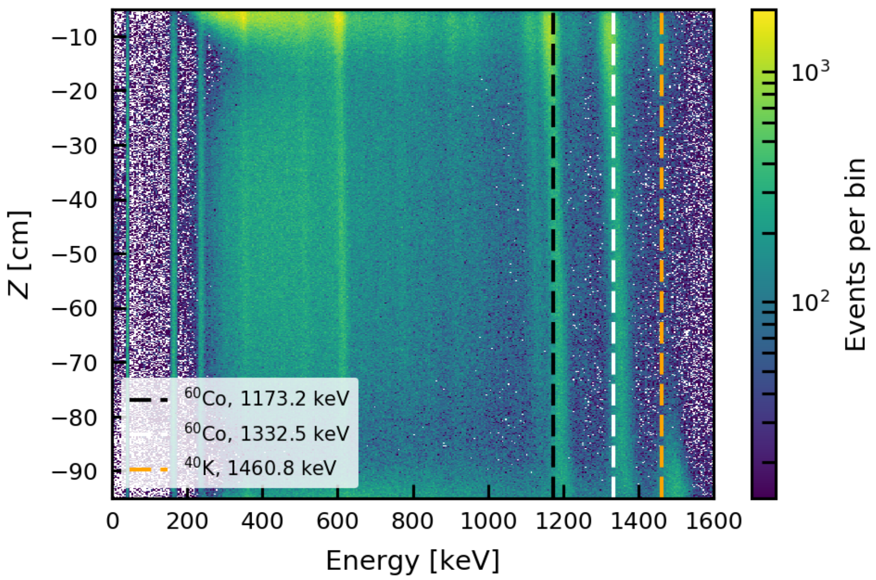

Figure 3.5: Energy vs. interaction depth of single-site events after all data selections in the 1.5 t superellipsoid. The energy was reconstructed using g_1 and g_2 from (3.10). Mono-energetic peaks of ^{60}Co at 1173.2 keV and 1332.5 keV are indicated by dashed black and white lines, respectively. The 1460.8 keV peak of ^{40}K is marked by the dashed orange line. Note that the ^{40}K signals are mostly found at the top and bottom of the TPC as they originate from the PMTs. All peaks show a tilt, so energies are shifted towards larger values with increasing interaction depth.

Figure 3.5 shows the interaction depth Z against the reconstructed energy E with the ^{60}Co and ^{40}K indicated by dashed lines. These lines exhibit a visible tilt: at lower depth the reconstructed energy is smaller than the mean energy while it is larger deeper in the TPC. A similar phenomenon was observed when S2 signals were corrected with the electron lifetime derived from α-lines. Since this electron lifetime was systematically lower than that determined from ^{83m}Kr the correction factor would be larger. This led to a similar, but stronger tilt (cf. section A1 in the appendix). The origin of the residual tilt is not known, but could be related to the α-^{83m}Kr discrepancy: Due to charge accumulation at the detector walls over time, the electric drift field inside the TPC was deformed. Since the field affects recombination depending on the energy and type of an interaction, this can introduce an additional S2 size dependence [226]. As an ER, the interaction type of ^{83m}Kr is the same as for the other lines, in contrast to α-decays, but the energy deposition is more than an order of magnitude smaller than, for example, ^{60}Co[2]. Accordingly, its recombination would be affected differently and the electron lifetime derived from its S2 signal could be systematically higher or lower than that of higher energy lines. In order to test this hypothesis, reliable recombination models and field maps of the detector would have been needed. Only preliminary studies existed for the field maps at the time of the analysis and the reliability of the NEST emission model was unknown at high energy. Therefore, it was decided to apply a phenomenological correction to the data by defining $g_1(z)$ and $g_2(z)$ as depth-dependent parameters. The calibration procedure was carried out in ten slices along

---

[2] Moreover, ^{83m}Kr undergoes a two-step decay with multiple energy depositions that are merged to a single S1+S2 pair. However, for ^{60}Co multiple energy depositions can also occur when individual Compton scatters are close enough in space to have their S2s and S1s merged to a single interaction pair. This illustrates the complexity of these considerations and the difficulty inherent to the modelling of these processes.

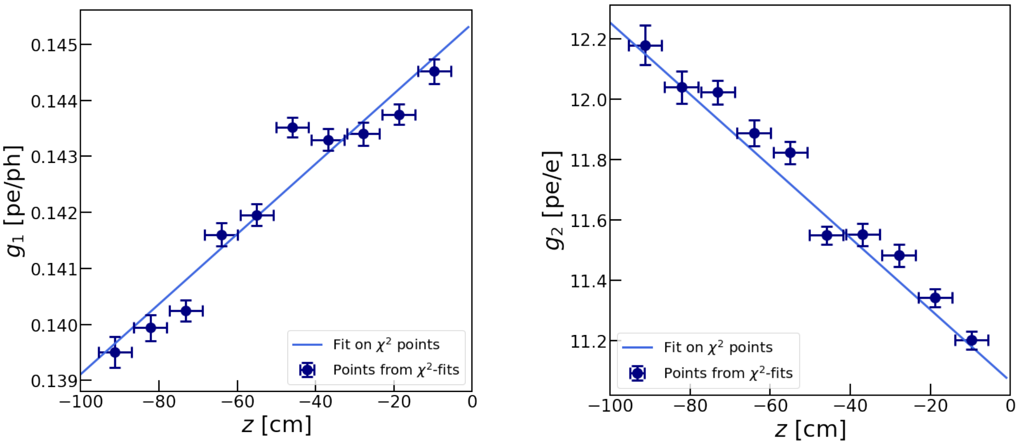

Figure 3.6: Linear fits to g_1 (**left**) and g_1 (**right**) data points determined in 10 horizontal slices of the 1.5 t superellipsoid. The uncertainties in the z direction are the widths of the slices. The g_1 and g_2 uncertainties are given by the best-fit uncertainties of the linear fits to L_y and Q_y of five mono-energetic lines. Taken from [207].

the central axis of the 1.5 t super-ellipsoid. For each slice g_1 and g_2 were determined on the aforementioned mono-energetic lines with the exception of ^{40}K. As this line originated from the PMTs, it was localised at the top and bottom of the detector. Thus, it could not be found in the central slices of the fiducial volume (cf. figure 3.5). A linear fit to the g_1 and g_2 data points in figure 3.6 yielded [207]:

$$\begin{aligned} g_1(z) &= (0.1454 \pm 0.0002)\,\frac{\text{pe}}{\text{ph}} + z \cdot (6.3 \pm 0.3) \cdot 10^{-5}\,\frac{\text{pe}}{\text{ph} \cdot \text{cm}}, \\ g_2(z) &= (11.10 \pm 0.03)\,\frac{\text{pe}}{\text{e}} - z \cdot (1.20 \pm 0.05) \cdot 10^{-2}\,\frac{\text{pe}}{\text{e} \cdot \text{cm}}. \end{aligned} \tag{3.11}$$

The variations over the whole detector are ~ 4 % and ~ 9 % of the mean g_1 and g_2, respectively. The larger variation in S2 supports the assumption that the residual variation is connected to S2 corrections. However, the g_1 variation cannot be explained by this. Figure 3.7 shows that the mono-energetic peaks now appear as straight lines when shown against the interaction depth, both at low and high energies.

The energy resolution resulting from the depth-dependent energy reconstruction is shown in figure 3.8 as a function of the energy. It was determined from the reconstructed energy spectrum by fitting Gaussian functions with the mean μ_E and standard deviation σ_E to mono-energetic peaks of the calibration sources ($^{83\text{m}}$Kr, $^{131\text{m}}$Xe, $^{129\text{m}}$Xe) and radioactive isotopes in the TPC materials (^{214}Pb, ^{208}Tl) up to 510.8 keV. The relative resolution $sigma_E/\mu_E$ for all peaks was parametrised with a phenomenological function

$$\frac{\sigma_E}{\mu_E} = \frac{a}{\sqrt{E}} + b. \tag{3.12}$$

The best-fit energy resolution parameters

$$\begin{aligned} a &= (0.3098 \pm 0.0043)\ \text{keV}^{1/2}, \\ b &= 0.0037 \pm 0.0003 \end{aligned} \tag{3.13}$$

yield $\sigma_E/\mu_E = (4.1 \pm 0.4)$ % for the KK-capture [207]. This result is similar to the one achieved in the LUX experiment [227] and superior to XENON100 [197]. The energy reconstruction in [201] is also based on the z-dependent calibration method developed in this work.

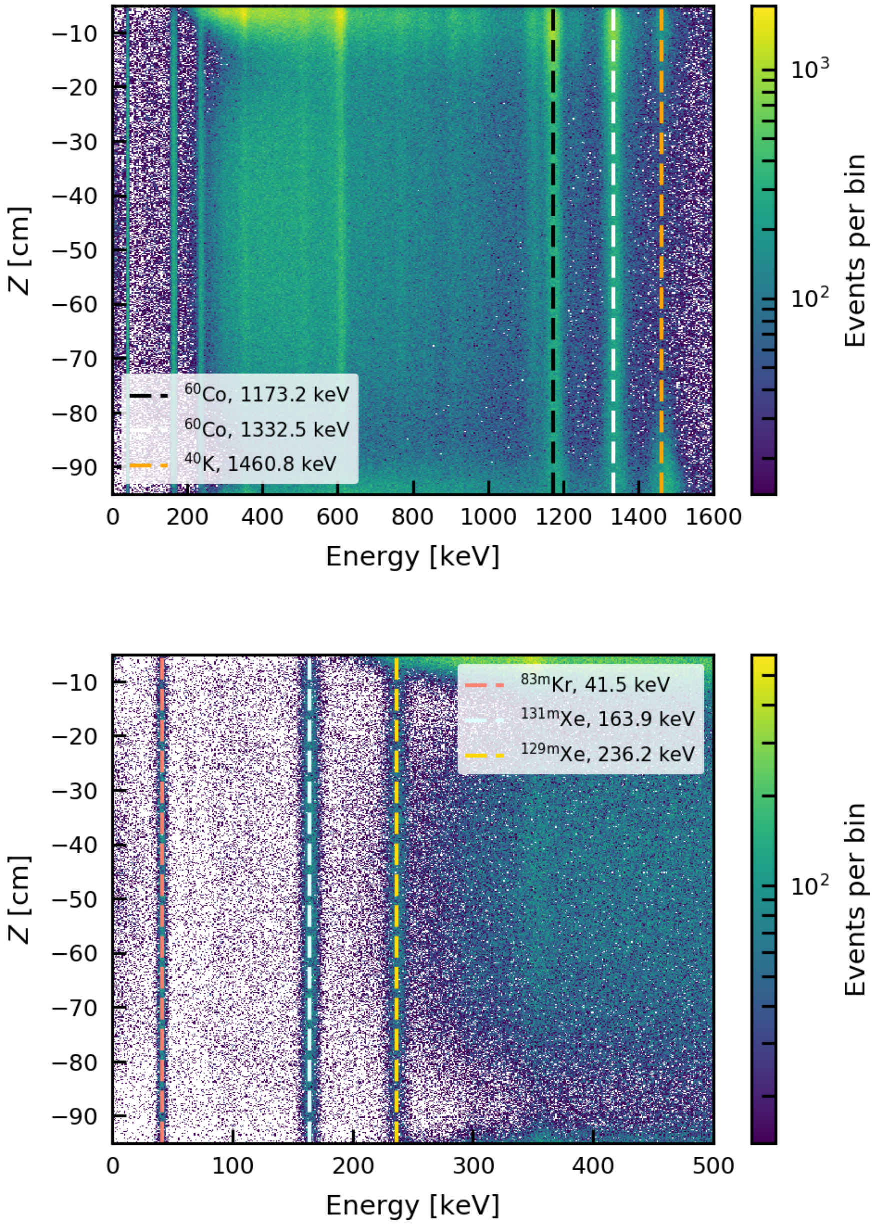

Figure 3.7: Energy vs. interaction depth of single-site events after all data selections in the 1.5 t superellipsoid over the full (**top**) and double-electron capture (**bottom**) energy ranges. The energy was reconstructed using $g_1(z)$ and $g_2(z)$ from (3.11). Mono-energetic peaks are indicated by dashed lines.

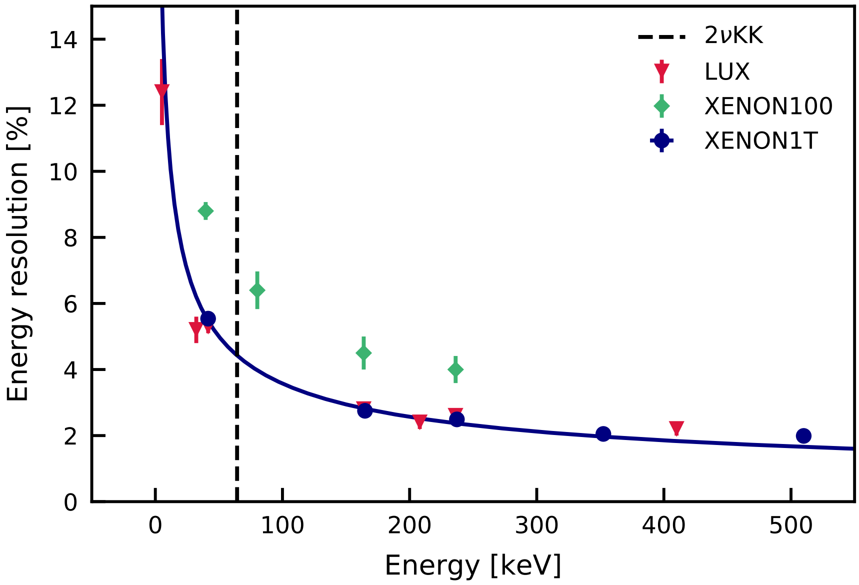

Figure 3.8: Energy resolution of low energy mono-energetic lines for selected liquid xenon Dark Matter experiments [197, 227] and the XENON1T detector in the 1.5 t fiducial superellipsoid. The relative resolution is defined as $\sigma_\mathrm{E}/\mu_\mathrm{E}$ of the Gaussian lines and fitted using a phenomenological function (solid blue line). For XENON1T the data points are $^{83\mathrm{m}}$Kr (41.5 keV), $^{131\mathrm{m}}$Xe (163.9 keV), $^{129\mathrm{m}}$Xe (236.2 keV), ^{214}Pb (351.9 keV) and ^{208}Tl (510.8 keV). Only statistical uncertainties are shown for XENON1T which are too small to be visible. The energy of the 2νKK peak is indicated by the black dashed line. Modified from [31].

3.2 Signal and background models

As established in section 1.2.4, the measured signal for 2νKK originates from the atomic deexcitation cascade after the capture of two K-shell electrons. Atomic X-rays and Auger electrons cannot be resolved individually in XENON1T due to their sub-millimetre range and the fast atomic processes. Thus, the experimental signature is a single S1 + S2 pair which will be reconstructed as a mono-energetic peak at $E_{2\nu\mathrm{KK}} = (64.3 \pm 0.6)$ keV. The uncertainty on $E_{2\nu\mathrm{KK}}$ reflects the energy reconstruction uncertainty as well as the uncertainty from the correction for sub-excitation quanta [31, 207]. These quanta from the deexcitation cascade are too low in energy to create photons or ions in LXe, so the total measurable energy is smaller than the double hole energy $E_{2\mathrm{k}} = (64.457 \pm 0.012)$ keV. The sub-excitation contribution has been determined with the RELAX code [207, 228]. At the lower limit on the half-life of $2.1 \cdot 10^{22}$ yr (90 % C.L.) [145] the expected KK-capture event rate is $(151 \pm 27)\ \mathrm{t}^{-1}\mathrm{yr}^{-1}$ assuming unity acceptance and the measured ^{124}Xe abundance. The uncertainty stems from the uncertainties of the abundance and the fiducial mass. The expected peak is shown in figure 3.9. In comparison the background rate is expected to be similar to the low-energy ER background from the SI WIMP search at $\sim 80\ \mathrm{t}^{-1}\mathrm{yr}^{-1}\mathrm{keV}^{-1}$ in a 1 t fiducial volume [12]. Thus, in a symmetric 10 keV window ($\sim 4\sigma_E$) around the peak mean one would expect ~ 600 events in the same exposure with a $\sqrt{N}$ uncertainty of ~ 25 events. In order to observe the 2νKK an understanding of this background is paramount. From the early XENON1T sensitivity studies [66] it is expected that three classes of background contribute to the energy spectrum: solar neutrino ER interactions, intrinsic radioactive isotopes and radioactive contaminations within the detector materials.

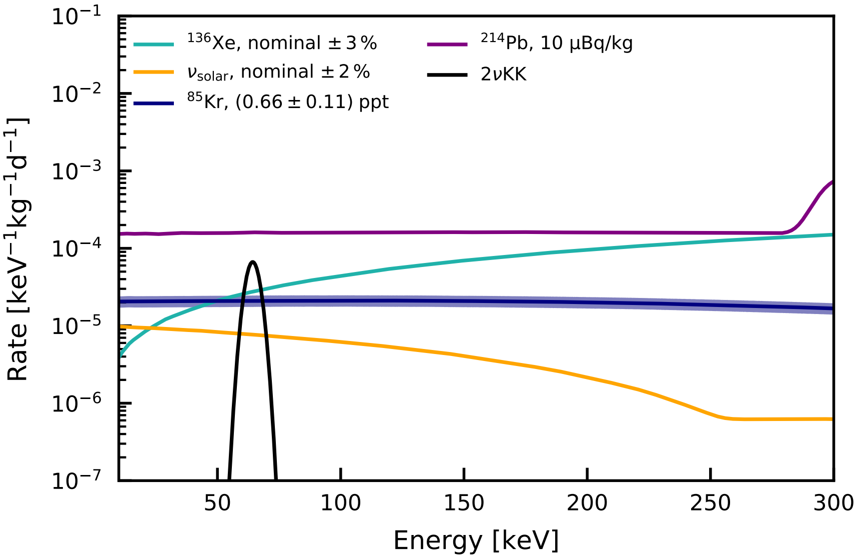

Figure 3.9: Simulated spectra of solar neutrinos (gold) and intrinsic backgrounds from ^{136}Xe (green), ^{85}Kr (blue), and ^{214}Pb (purple) within the inner 1 t fiducial volume in the energy range from 10 to 300 keV. All spectra are scaled according to their expected rates from external measurements. Except for ^{214}Pb, indicate the 1σ range of the expectation. For reference the 2νKK signal is shown at $T_{1/2} = 2.1 \cdot 10^{22}$ yr.

3.2.1 Solar neutrino and intrinsic backgrounds

The solar neutrino and intrinsic backgrounds are summarised in table 3.2. Solar neutrinos undergo elastic scattering on atomic electrons in LXe [229]:

$$\nu_{e,\mu,\tau} + e^- \rightarrow \nu_{e,\mu,\tau} + e^- . \tag{3.14}$$

While ν_e can interact by charged and neutral current interactions, $\nu_{\mu,\tau}$ can only interact via the neutral current. The spectral shape of this background is well constrained by solar physics, scattering kinematics, neutrino-electron cross-sections and neutrino oscillation parameters. This analysis uses the spectrum parametrization from [66] that assumes an electron neutrino survival probability of $P_{ee} = 0.55$. After convolving the fluxes with the cross-sections, 92 % of the solar neutrino rate can be attributed to pp-neutrinos, 7 % to ^{7}Be neutrinos, and the remaining 1 % originates from all other solar neutrino fluxes. The parametrisation of the solar neutrino ER energy spectrum is

$$(9.155 - 0.036 \cdot \frac{E}{\mathrm{keV}}) \cdot 10^{-6}\,\mathrm{keV}^{-1}\mathrm{kg}^{-1}\mathrm{d}^{-1}. \tag{3.15}$$

With an average background rate of $8.9 \cdot 10^{-6}$ keV^{-1}kg^{-1}d^{-1} in the 1–12 keV energy window and the steady decrease of rate with higher energy, this background component is subdominant. The uncertainty on the normalisation of the spectrum is 2 % from the uncertainties on the neutrino fluxes and oscillation parameters [66]. The expected rate from a simulated energy spectrum is shown as the solid gold line in figure 3.9 alongside the intrinsic backgrounds and the expected 2νKK signal at $2.1 \cdot 10^{22}$ yr. More details on the simulations in general will be given in section 3.2.3. In order to obtain the solar neutrino spectrum, electrons with an energy distribution following the expected elastic neutrino-electron scattering spectrum were simulated. The kink at ~ 250 keV marks the end of the pp and the onset of the ^{7}Be part of the spectrum.

Table 3.2: Solar neutrino and intrinsic ER background contributions to the 2νKK search energy spectrum.

Source	**Origin**	**Properties**
Solar ν	pp (92 %), other (7 %)	Subdominant, 2 % uncertaity
^{136}Xe	$2\nu\beta^-\beta^-$	$\eta_{\text{meas}}^{^{136}\text{Xe}} = (8.49 \pm 0.14) \cdot 10^{-2}$ mol/mol [207] $T_{1/2}^{^{136}\text{Xe}} = (2.165 \pm 0.061) \cdot 10^{21}$ yr [147]
^{214}Pb	^{222}Rn emanation	~ 10 µBq/kg from α-acitivity of ^{222}Rn,^{218}Po and ^{214}BiPo [76]
^{85}Kr	Anthropogenic, present in xenon from air	$^{\text{nat}}$Kr/Xe concentration $(0.66 \pm 0.11) \cdot 10^{-12}$ mol/mol [12] measured with RGMS
$^{83\text{m}}$Kr	Calibration, ^{83}Rb contamination	Rate decreases with $T_{1/2}^{^{83}\text{Rb}} = 86.2$ d [213]
$^{131\text{m}}$Xe	Inelastic neutron scattering	$T_{1/2}^{^{131}\text{Xe}} = 11.86$ d [224]
$^{129\text{m}}$Xe	Inelastic neutron scattering	$T_{1/2}^{^{129}\text{Xe}} = 8.88$ d [223]
^{133}Xe	Thermal neutron capture	$T_{1/2}^{^{133}\text{Xe}} = 5.25$ d [230]
^{125}Xe	Thermal neutron capture	$T_{1/2}^{^{125}\text{Xe}} = 16.8$ h [231]
^{125}I	^{125}Xe EC	$T_{1/2}^{^{125}\text{Xe}} = 59.4$ d [231]

The main intrinsic background components are β-decays of ^{214}Pb, the two-neutrino double β-decay of ^{136}Xe, and the β-decay of ^{85}Kr. Figure 3.10 shows the decay chain of ^{222}Rn with the dominant α- or β-decay modes for each isotope. The radon is continuously emanated from surfaces in contact with xenon. As a result, all daughter isotopes are present in the detector. Owed to their high energy and small S2/S1 ratio, α-decays do not affect the ER band. Among the β-emitters, the long lived ^{210}Pb was found to plate out on the PTFE surfaces of the TPC, so this isotope and its progeny do not contribute to the ER background in the fiducial volume [11]. The β-decay of ^{214}Bi is directly followed by the ^{214}Po α-decay with a half-life of 162 µs which is well within the time window of a XENON1T event. These so-called BiPo events feature two S1 signals, so they are almost fully rejected by the S1 single scatter cut.

The only significant background contribution from a ^{222}Rn daughter comes from ^{214}Pb. It is the dominant ER background source for virtually all XENON1T physics searches up to its Q-value of 1.019(11) MeV. The naked β-decay to the ^{214}Pb ground state produces the flat low-energy part of the ^{214}Pb spectrum in figure 3.9. The branching ratio for this decay is 11.0(10) % [184]. In most other cases a lower energy β-electron is accompanied by γ-rays with total energies of 295.2 keV (40.2(6) %) or 351.9 keV (45.9(9) %) [184]. If the β and γ are merged, the β-spectra are shifted upwards by the γ-energy. This causes the kink around 295.2 keV in figure 3.9. The activity concentration of ^{214}Pb can be constrained by measuring the α-activities of ^{222}Rn, ^{218}Po, and the rate of ^{214}BiPo delayed coincidence events. Due to the slightly shorter ^{214}Bi half-life both isotopes should be in a transient equilibrium. Since

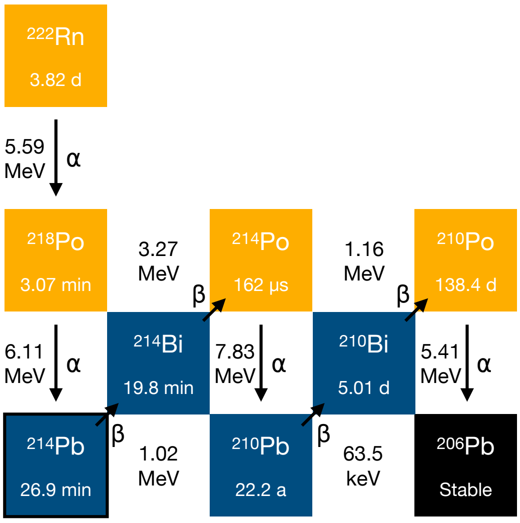

Figure 3.10: The ^{222}Rn decay chain. Only the dominant decay mode, either α-decay in yellow or β^--decay in blue, is indicated for each isotope. The Q-value and decay type are stated next to the arrows. The boxes contain the isotope designation and the half-life. Data taken from [184, 233–235].

the ^{214}Pb half-life is longer than the ^{218}Po parent's, no equilibrium can be assumed. Still, ^{222}Rn and ^{218}Po activity concentrations represent an upper bound on that of ^{214}Pb. The mean measured activity concentrations in SR1 are [76, 232]:

$$\begin{aligned} A_{^{222}\mathrm{Rn}} &= (13.3 \pm 0.5)\ \mathrm{\mu Bq/kg}, \\ A_{^{218}\mathrm{Po}} &= (12.7 \pm 0.5)\ \mathrm{\mu Bq/kg}, \\ A_{^{214}\mathrm{BiPo}} &= (5.1 \pm 0.5)\ \mathrm{\mu Bq/kg}. \end{aligned} \tag{3.16}$$

While ^{222}Rn and ^{218}Po show the expected equilibrium within uncertainties, the ^{214}BiPo activity concentration is less than half of the other two. The reason is that ^{214}Pb and ^{214}Bi have a long enough half-lives to plate out on the detector walls where a part of their decay signal is absorbed outside of the sensitive LXe volume. Accordingly, the ^{214}Pb activity concentration in the fiducial volume is expected fall between the measured values for ^{222}Rn and ^{214}BiPo.

The fission product ^{85}Kr decays with a half-life of 10.739(14) yr and is present in earth's atmosphere as a byproduct of nuclear arms tests and nuclear reprocessing [236]. Since commercially available xenon is produced by air liquefaction, it contains trace amounts of ^{85}Kr. The β-decay of ^{85}Kr to ^{85}Rb can occur directly to the ground state with a relative frequency of 99.463(10) % or to an excited state at 514.0(20) keV in 0.434(10) % of all decays. The total Q-value is 687.0(20) keV [237]. With a half-life of 1.015 µs a delayed coincidence analysis of the excited state decays allowed to infer the ^{85}Kr abundance at $^{\mathrm{nat}}\mathrm{Kr}/^{85}\mathrm{Kr} = 1.65^{+0.41}_{-0.28} \cdot 10^{-11}\,\mathrm{mol/mol}$ [238]. In XENON1T SR1, the average concentration of all krypton isotopes was reduced to $^{\mathrm{nat}}\mathrm{Kr/Xe} = (0.66 \pm 0.11)$ ppt by cryogenic distillation (cf. section 2.2), so the expected activity concentration is $A_{^{85}\mathrm{Kr}} = 0.102^{+0.031}_{-0.024}\ \mathrm{\mu Bq/kg}$. The expected flat spectrum from the ground-state decays is shown in figure 3.9.

The ^{136}Xe decay rate can be calculated from the measured abundance $\eta^{^{136}\mathrm{Xe}}_{\mathrm{meas}} = (8.49 \pm 0.14) \cdot 10^{-2}\ \mathrm{mol/mol}$ [207] and the $2\nu\beta^-\beta^-$ half-life $T^{^{136}\mathrm{Xe}}_{1/2} = (2.165 \pm 0.061) \cdot 10^{21}$ yr measured by EXO-200 [147]. With this the total activity concentration is $A_{^{136}\mathrm{Xe}} = (3.95 \pm 0.13)\ \mathrm{\mu Bq/kg}$. In the simulations of this background the theoretical two-electron energy spectra and angular distributions from [239] were used [240]. The resulting spectrum of the merged energy depositions of the two electrons is shown in figure 3.9.

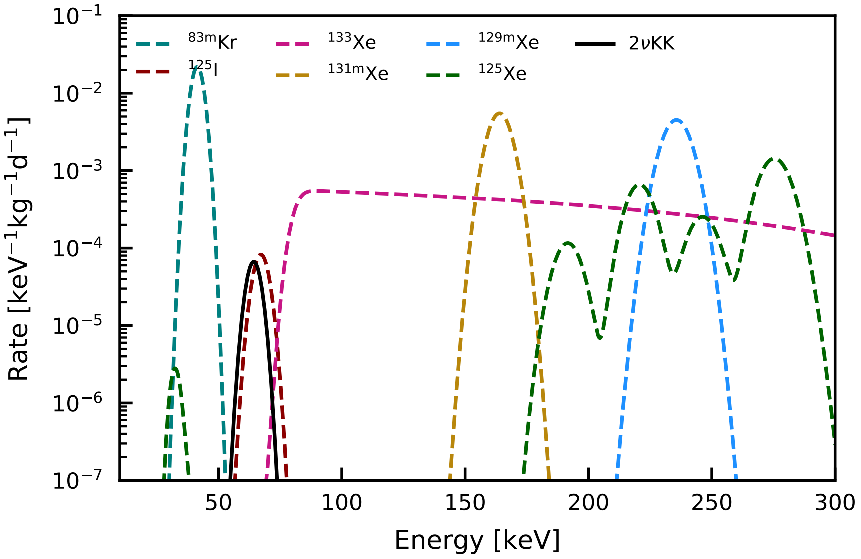

Figure 3.11: Simulated spectra of backgrounds that are not constant in time within the inner 1 t fiducial volume in the energy range between 10 to 300 keV. For reference the 2νKK signal is shown at $T_{1/2} = 2.1 \cdot 10^{22}$ yr. All other scalings are arbitrary since the expected scaling strongly depends on data selection. The ^{125}I spectrum (dashed brown) is scaled to a similar activity as the 2νKK. The ^{83m}Kr (teal), ^{131m}Xe (dashed gold) and ^{129m}Xe (dashed blue) peaks are scaled to a factor 100 higher activity. The ^{133}Xe (dashed magenta) and ^{125}Xe spectra are scaled to a total activity concentration of 1 µBq/kg.

In addition to the intrinsic background components that exhibit a stable rate over time, multiple time-dependent intrinsic backgrounds are present in the spectrum. The ^{83m}Kr peak is present at all times due to a contamination of the detector with ^{83}Rb that occurred during a calibration. The measured rate of this peak decreases with the 86.2 d half-life of ^{83}Rb [14]. The data that is used in this analysis also exhibits a processing artefact with regard to ^{83m}Kr. If the two S1 signals from the consecutive isomeric transitions can be resolved, these events are removed by the S1 single scatter cut. However, in a considerable fraction of krypton events, the secondary S1 is misidentified as an S2 signal. This secondary S2 signal, in turn, is too small to be removed by the S2 single scatter cut. This manifests itself as a second ^{83m}Kr peak at 32.1 keV, the energy of the higher energy transition (cf. figure 3.14). The presence of the two high rate ^{83m}Kr peaks makes the search for the KL-capture of ^{124}Xe at $E_{\mathrm{kl}} = 37.29^{+0.82}_{-0.53}$ keV unfeasible (cf. section 1.2.4).

The xenon target itself is activated during neutron calibrations either by inelastic neutron scattering (^{131m}Xe and ^{129m}Xe, cf. section 3.1) or thermal neutron capture. The latter produces ^{125}Xe and ^{133}Xe. The activation

$$^{124}\mathrm{Xe} + \mathrm{n} \rightarrow {}^{125}\mathrm{Xe} + \gamma \tag{3.17}$$

leads to the presence of ^{125}I in the detector [145, 231]. This isotope presents a major background for the 2νKK search and will be discussed separately in section 3.3. ^{133}Xe decays to ^{133}Cs via β^--decay with a half-life of 5.2475(5) d [230]. It almost exclusively emits β-electrons with an endpoint energy of 346.4(24) keV that are accompanied by an 81 keV γ-ray. Due to the short range of both quanta, their S1 and S2 signals are merged and appear as a β-spectrum starting at 81 keV. This can be seen in 3.11 where all time-variable sources are shown together with the 2νKK peak for reference.

Table 3.3: Activity concentrations of radioisotopes in detector construction materials. Taken from [66]. The isotope ^{137}Cs and the ^{235}U chain are not considered because no significant activity was measured in the screening. All values are given in mBq/kg except for the PMT bases and PMTs where they are given in mBq/unit. In case of decay chains, the activity concentration refers to the parent isotope. Shell and flanges are the respective parts of the cryostat. The stainless steel components in the TPC such as the bell are denoted as *steel.* The PMT bases are referred to as *bases.*

	^{238}U	**^{226}Ra**	**^{232}Th**	**^{228}Th**	**^{60}Co**	**^{40}K**
Shell	2.4 ± 0.7	< 0.64	0.21 ± 0.06	< 0.36	9.7 ± 0.8	< 2.7
Flanges	1.4 ± 0.4	< 4.0	0.21 ± 0.06	4.5 ± 0.6	37.3 ± 0.9	< 5.6
PTFE	< 0.25	< 0.12	< 0.041	< 0.065	< 0.027	< 0.34
Copper	< 1.2	< 0.033	< 0.043	< 0.034	0.21 ± 0.02	< 0.28
Steel	2.4 ± 0.7	< 0.064	0.21 ± 0.06	< 0.36	9.7 ± 0.8	< 2.7
Bases	0.82 ± 0.30	0.32 ± 0.02	0.20 ± 0.03	0.153 ± 0.013	< 0.0052	0.36 ± 0.08
PMTs	8 ± 2	0.5 ± 0.1	0.5 ± 0.1	0.50 ± 0.06	0.71 ± 0.03	13 ± 2

3.2.2 Material backgrounds

The remaining background components originate from radioactive contaminations of the detector construction materials with ^{60}Co, ^{40}K and ^{137}Cs as well as with isotopes from the ^{238}U, ^{235}U and ^{232}Th decay chains. These emit ionising radiation from within their respective detector components, but only γ-rays are energetic enough to reach the fiducial volume. The activity concentrations for each isotope and detector component can be constrained by screening measurements [68]. Table 3.3 summarises the values from screening used in this work. These are based on the XENON1T material radioassay results used for the WIMP sensitivity projections in [66]. The contributions of ^{137}Cs and the ^{235}U chain are not considered because no significant activity could be measured in the screening. The measured activity concentrations now have to be translated into background rate expectations by the means of Monte Carlo (MC) simulations.

All known background sources were simulated with Geant4 [241–243] using the detector model developed for [66]. Except for ^{136}Xe, new simulations for each background component with a factor 10-100 larger numbers of events compared to [66] were generated. The numbers of simulated events for the material backgrounds are given in table 3.4. The cryostat was simulated as a single component, but can be subdivided into shell and flanges using the primary positions of the simulated events. The ^{238}U and ^{232}Th decay chains were split at ^{226}Ra and ^{228}Th, respectively, in order to account for possible decay chain disequilibrium. The simulated spectra are shown in figure 3.12. As they consist mostly of single Compton scatters where the γ-ray left the detector before another energy deposition, the spectrum is featureless below 200 keV for the dominant ^{60}Co and ^{226}Ra background contributions. In total, the expected material background contribution is an order of magnitude smaller than the one from the dominant ^{214}Pb background. Due to low simulation statistics, the subdominant components exhibit unphysical features that will be addressed in the background fit.

Intrinsic backgrounds were either exclusively simulated in the active volume or also in the uninstrumented LXe shell around the TPC. The latter approach produces a large overhead of events that do not penetrate the active volume of the detector. Accordingly, shell events

Table 3.4: Number of simulated events for radioisotopes in detector construction materials. The stainless steel components in the TPC such as the bell are denoted as *TPC steel.* The bell and flanges of the *cryostat* have been simulated as a single component, but can be divided by origin into shell and flanges later.

	^{238}U	^{226}Ra	^{232}Th	^{228}Th	^{60}Co	^{40}K
Cryostat	$9.965 \cdot 10^8$	10^9	$9.9 \cdot 10^8$	$9.962 \cdot 10^8$	10^9	$9.965 \cdot 10^8$
PTFE	10^8	$5 \cdot 10^7$	$9.996 \cdot 10^8$	10^8	10^8	$2 \cdot 10^7$
Copper	10^8	$5 \cdot 10^7$	10^9	10^8	10^8	$2 \cdot 10^7$
TPC Steel	$5 \cdot 10^7$	$5 \cdot 10^7$	$9.999 \cdot 10^8$	10^8	$5 \cdot 10^7$	$2 \cdot 10^7$
PMT bases	$3.8 \cdot 10^7$	$5 \cdot 10^7$	10^9	10^8	$5 \cdot 10^7$	$2 \cdot 10^7$
PMTs	10^9	10^8	$9.93 \cdot 10^8$	10^8	10^8	$9.93 \cdot 10^8$

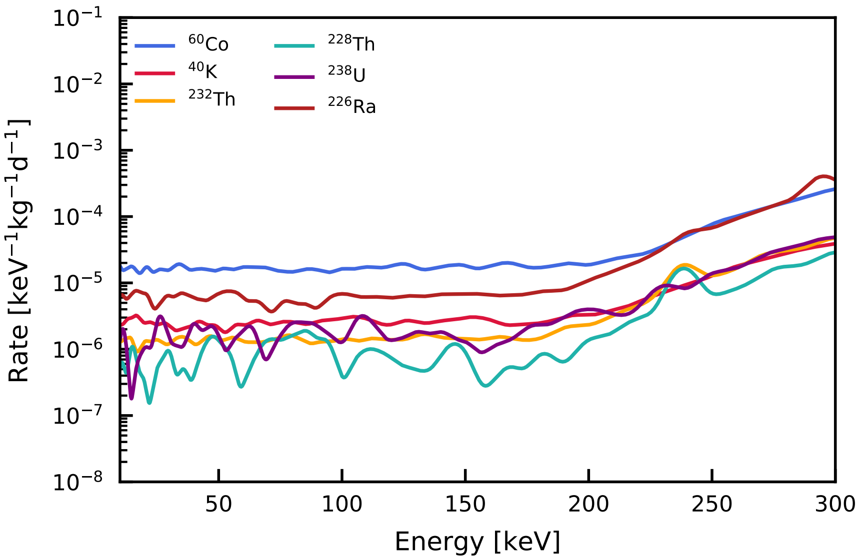

Figure 3.12: Simulated spectra of material backgrounds from ^{60}Co (blue), ^{40}K (red), ^{232}Th (orange), ^{228}Th (green), ^{238}U (purple) and ^{226}Ra (brown) between 10 and 300 keV in the inner 1 t fiducial volume. The total activity of each isotope is the sum of the individual component activities from table 3.3. Upper limits were treated as central values.

Table 3.5: Number of simulated events for solar neutrinos and intrinsic background sources. If a sizable contribution of γ-rays penetrating the TPC from the uninstrumented outer LXe shell was expected, the sources were also simulated there. Otherwise the primary event positions were simulated solely in the active volume of the TPC.

	Solar ν	^{214}Pb	^{85}Kr	^{125}Xe	^{133}Xe	^{136}Xe
TPC	10^8	–	10^8	–	10^8	$1.8 \cdot 10^8$
TPC + shell	–	$4.99 \cdot 10^7$	–	10^7	–	–

were only simulated if a sizeable fraction of γ-rays penetrating the detector was expected[3]. The numbers of simulated events for the intrinsic background sources are given in table 3.5

3.2.3 Fit of the MC background model

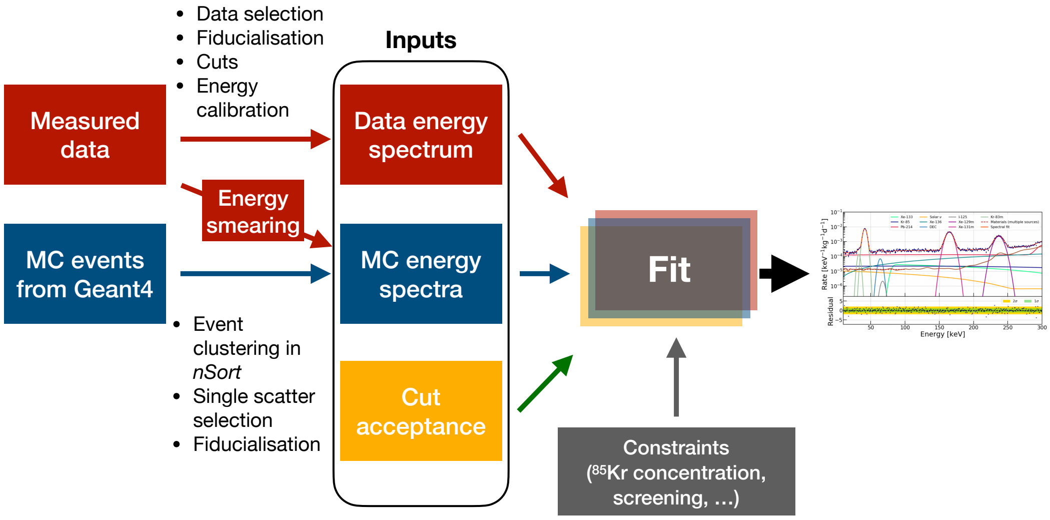

Figure 3.13: Data flow of the background modelling.

The data flow of the simulations and measured data in the background model fit is illustrated in figure 3.13. In order to mimic the detector resolution for individual interactions, the energy depositions from Geant4 were clustered in space, time and energy using the so-called *nSort* algorithm developed by the XENON collaboration. Its event clustering depends on the interaction depth because S2 signals, which allow to identify multiple coincident interactions, are broadened by diffusion. Accordingly, the overlap for multiple signals from greater depth is larger and individual interactions cannot be resolved. The opposite is true for multiple interactions at lower depth. Events with single energy depositions in the active volume are selected from the MC data and the resulting spectra for all components are convolved with the energy resolution from measured data. Peak-like sources are not simulated, but modeled using Gaussian functions. Then, the background model is constructed by fitting the weighted sum of all background components to the measured energy spectrum. In the fit above 200 keV and 160 keV of the inner and outer volume, respectively, the MC spectra are scaled with the cut acceptance from data in order to obtain the correct spectral shape and scaling.

The scaling parameters of the spectra and the properties of the Gaussian peaks make up the fit parameters $\vec{p}$. The fit is carried out as a χ^2 minimisation with the cost functions

$$\chi^2_{\mathrm{n}}(\vec{p}) = \sum_{\mathrm{i}}^{\mathrm{bins}} \frac{\left(R_{\mathrm{i,n}} - f_{\mathrm{n}}(E_{\mathrm{i,n}}, \vec{p})\right)^2}{(\Delta R_{\mathrm{i,n}})^2}, \tag{3.18}$$

with n = [inner, outer] for the inner and outer volumes. Here, $R_{\mathrm{i,n}}$ is the measured event rate in the energy bin E_{i} and $f_{\mathrm{n}}(E_{\mathrm{i}}, \vec{p})$ is the background fit function in the respective volume. At energies below 100 keV, low statistics of simulated backgrounds from detector construction materials require an interpolation of the simulated spectra in order to avoid

---

[3] Although ^{214}Pb is not expected to produce a large amount of γ-background it was found after the simulation that the TPC + shell setting had been selected. As the sole purpose of simulating just inside the TPC is saving computing resources and since it has no impact on the analysis, the spectrum was not simulated again.

over-fitting of the expected featureless spectrum from single Compton scatters. Thus, the sum of the material contributions is linearly interpolated up to 100 keV. The fit function is then written as

$$\begin{aligned} f_\mathrm{n}(E_\mathrm{i,n}, \vec{p}) = &\left[\sum_\mathrm{k}^\mathrm{material} p_\mathrm{k} R_\mathrm{k}(E_\mathrm{i,n})\right]_\mathrm{interpolated < 100\,keV} \\ &+ \sum_\mathrm{l}^\mathrm{intrinsic} p_\mathrm{l} R_\mathrm{l}(E_\mathrm{i,n}) \\ &+ \sum_\mathrm{m}^\mathrm{peaks} \mathrm{Gaussian_m}\,(\vec{p}_\mathrm{m}, E_\mathrm{i,n}), \end{aligned} \tag{3.19}$$

where the sums correspond to the (interpolated) material component, the intrinsic sources plus solar neutrinos, and the mono-energetic peaks with the fit parameters $p_\mathrm{k,l,m} \in \vec{p}$. From table 3.3 it is evident that the material backgrounds alone would introduce six scaling parameters for each of the 7 simulated components, so 42 parameters in total [244]. In order to limit the number of fit parameters, the relative contributions of each detector component to the total activity per isotope are fixed. With k = [^{60}Co, ^{40}K, ...] denoting the isotopes and u = [Cryostat, PMTs, ...] signifying the components, the rate per isotope is

$$R_\mathrm{k}(E_\mathrm{i}) = \sum_\mathrm{u}^\mathrm{components} \tilde{R}_\mathrm{k,u}(E_\mathrm{i}) \cdot s_\mathrm{k,u}. \tag{3.20}$$

The weighting factors $s_\mathrm{k,u}$ for fixing the ratios are taken from table 3.1. In cases where only an upper limit on the activity is available, the limit is interpreted as a central value. The contributions of the cryostat flanges and shell are subsumed in a single component. The MC spectra of the materials have been normalised in the same fashion as in [66]. The fit parameters p_k then scale the total backgrounds from each isotope as shown in equation (3.19). This treatment can be motivated by the fact that, apart from the volume segmentation, no spatial information is used in the fit. In turn, the spectra from the same isotope in different components are largely degenerate.

The sum over the constraints incorporates knowledge from external measurements. They include the ^{85}Kr concentration measurement, the solar neutrino expectation, as well as the ^{136}Xe abundance and half-life. The fit constraints have the form

$$\mathrm{constraint_j} = \frac{(p_\mathrm{j} - p_\mathrm{expected,j})^2}{(\Delta p_\mathrm{j})^2}. \tag{3.21}$$

with the expectation value $p_\mathrm{expected,j}$ and the uncertainty Δp_j. A deviation of the fit parameter p_j by $n \cdot \Delta p_\mathrm{j}$ from the expectation increases the value of the cost function by n^2. When including the signal, the 2νKK peak is constrained to the expected position $\mu_{2\nu\mathrm{KK}}$ and width $\sigma_{2\nu\mathrm{KK}}$. Finally, the systematic uncertainties of the cut acceptance and fiducial mass are included as constrained fit parameters $\vec{\kappa}$ and $\vec{V}$, respectively. These are the only parameters that are fitted independently in the inner and outer detector volume. The full χ^2 function can then be written as

$$\chi^2_\mathrm{combined}(\vec{p}, \vec{V}, \vec{\kappa}) = \sum_\mathrm{n}^\mathrm{volumes} \chi^2_\mathrm{n}(\vec{p}, V_\mathrm{n}, \kappa_\mathrm{n}) + \sum_\mathrm{j}^\mathrm{constraints} \mathrm{constraint_j}. \tag{3.22}$$

The sum over j now includes all constraints on scalings of simulated spectra, widths and positions of peaks, fiducial volume masses and cut acceptances. The volume uncertainties are implemented as multipliers on $f_\mathrm{n}(E_\mathrm{i,n}, \vec{p})$ constrained to $V_\mathrm{n} = 1 \pm 0.01$. The cut acceptance is implemented using the parametrisation from equation (3.3) as a lower limit $a_\mathrm{n,min}(E)$

Table 3.6: Fit parameters of the background model. The additional fit parameters from the ^{124}Xe signal and ^{125}I background are given at the bottom of the table.

Parameter	**Description**	**Constraint/limit**	**Unit**
Solar ν	external	1.00 ± 0.03	$1.8 \cdot 10^{-8}\,\mathrm{s^{-1}kg^{-1}}$
^{136}Xe	intrinsic	1.00 ± 0.02	3.96 μBq/kg
^{85}Kr	intrinsic	6.6 ± 1.1	0.1 ppt
^{214}Pb	intrinsic	–	μBq/kg
^{125}Xe	neutron activation	–	μBq/kg
^{133}Xe	neutron activation	–	μBq/kg
^{238}U	materials	positive	scaling
^{226}Ra	materials	positive	scaling
^{232}Th	materials	positive	scaling
^{228}Th	materials	–	scaling
^{60}Co	materials	positive	scaling
^{40}K	materials	positive	scaling
$A_{^{83\mathrm{m}}\mathrm{Kr}}$	^{83}Rb contamination	–	$\mathrm{kg^{-1}d^{-1}}$
$\mu_{^{83\mathrm{m}}\mathrm{Kr}}$	peak mean	41.5 ± 0.6	keV
$\sigma_{^{83\mathrm{m}}\mathrm{Kr}}$	peak width	–	keV
$A_{^{83\mathrm{m}}\mathrm{Kr,\,misID}}$	misidentified	–	$\mathrm{kg^{-1}d^{-1}}$
$\mu_{^{83\mathrm{m}}\mathrm{Kr,\,misID}}$	peak mean	32.1 ± 0.6	keV
$\sigma_{^{83\mathrm{m}}\mathrm{Kr,\,misID}}$	peak width	–	keV
$A_{^{131\mathrm{m}}\mathrm{Xe}}$	neutron activation	–	$\mathrm{kg^{-1}d^{-1}}$
$\mu_{^{131\mathrm{m}}\mathrm{Xe}}$	peak mean	163.9 ± 0.6	keV
$\sigma_{^{131\mathrm{m}}\mathrm{Xe}}$	peak width	–	keV
$A_{^{129\mathrm{m}}\mathrm{Xe}}$	neutron activation	–	$\mathrm{kg^{-1}d^{-1}}$
$\mu_{^{129\mathrm{m}}\mathrm{Xe}}$	peak mean	236.2 ± 0.6	keV
$\sigma_{^{129\mathrm{m}}\mathrm{Xe}}$	peak width	–	keV
V_{inner}	fiducial mass	1.00 ± 0.01	1052 kg
V_{outer}	fiducial mass	1.00 ± 0.01	448 kg
κ_{inner}	acceptance	$\frac{2}{3} \pm \frac{1}{3}$	scaling
κ_{outer}	acceptance	$\frac{2}{3} \pm \frac{1}{3}$	scaling
$N_{^{125}\mathrm{I}}$	neutron activation	10 ± 7	events
$\mu_{^{125}\mathrm{I}}$	peak mean	67.3 ± 0.6	keV
$\sigma_{^{125}\mathrm{I}}$	peak width	2.8 ± 0.5	keV
$N_{2\nu\mathrm{KK}}$	signal	–	events
$\mu_{2\nu\mathrm{KK}}$	peak mean	64.33 ± 0.58	keV
$\sigma_{2\nu\mathrm{KK}}$	peak width	2.64 ± 0.24	keV

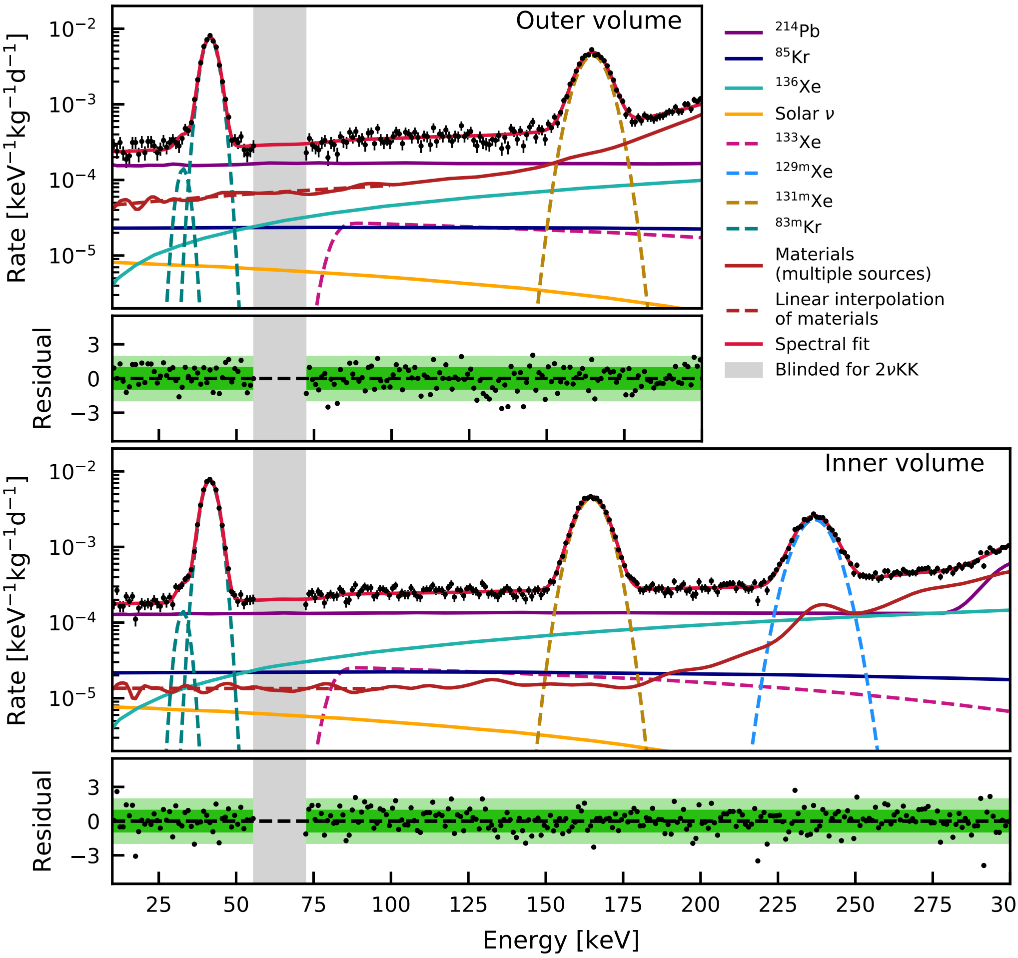

Figure 3.14: Combined fit of the background energy spectra in the inner (**bottom**) and outer (**top**) subvolume of the 1.5 t superellipsoid with residuals for both volumes. Backgrounds constant in time are indicated by solid lines while backgrounds varying with time are shown as dashed lines. One obtains $\chi^2/\text{ndf} = 448/431 \approx 1.04$ with 28 fit parameters, 11 of them constrained.

on the cut acceptance for each volume n. The parametrisation for the outer volume can be found in the appendix in section A3. In the fit, the cut acceptance $a_\text{n}(E_\text{i, n})$ is allowed to vary between $a_\text{n, min}(E_\text{i, n})$ and unity by defining it as

$$a_\text{n}(E_\text{i, n}) = \kappa_\text{n} \cdot a_\text{n, min}(E_\text{i, n}) + (1 - \kappa_\text{n}). \tag{3.23}$$

The acceptance scaling parameters for both volumes are constrained to $\kappa_\text{n} = \frac{2}{3} \pm \frac{1}{3}$. This only affects the energy range above the transition points around ~ 200 keV for the inner volume and ~ 160 keV for the outer volume since the flat acceptance is assumed to be unity below. Including the volume and cut acceptance parameters, the background fit function is modified to its final definition

$$\tilde{f}_\text{n}(E_\text{i, n}, \vec{p}, V_\text{n}, \kappa_\text{n}) = f_\text{n}(E_\text{i, n}, \vec{p}) \cdot V_\text{n} \cdot a_\text{n}(E_\text{i, n}). \tag{3.24}$$

The fit parameters, including those of the later signal fit, are summarised in table 3.6.

The background model was fitted to the data with the ROI still blinded. The fit used the preliminary data selection of 214.3 d in the 1.5 t fiducial volume that was segmented into

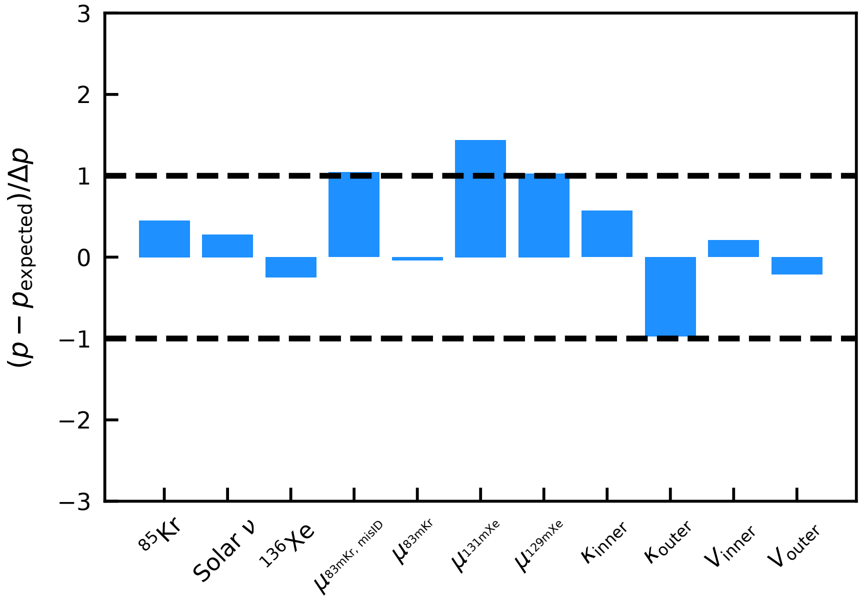

Figure 3.15: Parameter pulls of the 11 constrained parameters from the fit to the blinded data in the segmented 1.5 t fiducial volume and 214.3 d of data.

an inner 1052 kg cylinder and an outer 448 kg shell. For the inner volume a fit range from 10 to 300 keV was chosen while for the outer volume it was limited to 200 keV. The fit result is shown in figure 3.14. The fit describes the data well with $\chi^2/\mathrm{ndf} = 448/431 \approx 1.04$. No structures can be discerned in the residuals. Of the 28 fit parameters, 11 are constrained. The parameter pulls from the expected value are shown in figure 3.15. No anomalous pulls above $2\Delta p$ were observed. Accordingly, the fit method was fixed and the data was unblinded.

3.3 Modelling additional background from ^{125}I

The isotope ^{125}I produces a background peak at 67.3 keV close to $E_{2\nu\mathrm{KK}} = 64.33$ keV [145, 231, 245]. It can be present in liquid xenon detectors as a consequence of thermal neutron activation [145]. The thermal neutrons are captured by ^{124}Xe transmuting it to ^{125}Xe:

$$^{124}\mathrm{Xe} + \mathrm{n} \rightarrow {}^{125}\mathrm{Xe} + \gamma. \tag{3.25}$$

With a half-life of 16.9 h, ^{125}Xe undergoes electron capture to ^{125}I [231]:

$$\begin{aligned} {}^{125}\mathrm{Xe} &\xrightarrow[\mathrm{EC}]{16.9\,\mathrm{h}} {}^{125}\mathrm{I}^{*} + \nu_e, \\ {}^{125}\mathrm{I}^{*} &\xrightarrow{<1\,\mathrm{ns}} {}^{125}\mathrm{I} + \gamma + \mathrm{X}. \end{aligned} \tag{3.26}$$

The X-rays and Auger electrons from the atomic relaxation after the electron capture are denoted by X. The ^{125}I then undergoes electron capture to ^{125}Te with a 59.4 d half-life [231]:

$$\begin{aligned} {}^{125}\mathrm{I} &\xrightarrow[\mathrm{EC}]{59.4\,\mathrm{d}} {}^{125}\mathrm{Te}^{*} + \nu_e, \\ {}^{125}\mathrm{Te}^{*} &\xrightarrow{1.48\,\mathrm{ns}} {}^{125}\mathrm{Te} + \gamma + \mathrm{X}. \end{aligned} \tag{3.27}$$

The decays of ^{125}Xe and ^{125}I, populate short-lived excited nuclear states of ^{125}I and ^{125}Te. Due to the short range and fast timing of the atomic relaxation quanta, the γ-transitions can be merged with the atomic relaxation signals following the electron capture. The tellurium X-ray from K-electron capture, which occurs with a relative frequency of 80.11(17) % [245], is always merged with a 35.5 keV nuclear transition [231] leading to a Gaussian line centred around 67.3 keV.

In XENON1T, two sources of thermal neutrons lead to the presence of ^{125}I in the detector: artificial activation by neutrons from the deuterium-deuterium fusion neutron generator or the ^{241}AmBe source during calibrations, and activation in the purification loop outside of the water shield by environmental thermal neutrons [31]. The rate equations for the activation are

$$\begin{aligned}
\frac{\mathrm{d}N_{^{125}\mathrm{Xe}}}{\mathrm{d}t} &= \mathscr{A}_\mathrm{s} - \lambda_{^{125}\mathrm{Xe}} N_{^{125}\mathrm{Xe}}(t), \\
\frac{\mathrm{d}N_{^{125}\mathrm{I}}}{\mathrm{d}t} &= \lambda_{^{125}\mathrm{Xe}} N_{^{125}\mathrm{Xe}}(t) - \lambda_{^{125}\mathrm{I}} N_{^{125}\mathrm{I}}(t), \\
\frac{\mathrm{d}N_{^{125}\mathrm{Xe}}}{\mathrm{d}t} &= \lambda_{^{125}\mathrm{I}} N_{^{125}\mathrm{I}}(t).
\end{aligned} \tag{3.28}$$

Here, $\lambda_{^{125}\mathrm{Xe/I}}$ are the respective decay constants, $N_{^{125}\mathrm{Xe/I/Te}}$ are the numbers of the respective nuclei, and $\mathscr{A}_\mathrm{s}$ is the ^{125}Xe activation rate with the sources s = [nat, ^{241}AmBe, NG]. For environmental neutrons n_nat literature values from flux measurements at LNGS are used to estimate the activation [246–249]. The measurements have been taken at different locations in the laboratory and none of them agree within the quoted uncertainties. In [250] this is attributed to varying water levels in the rock over time that cause a different moderation of radiogenic neutrons. For this study, the average and standard deviation of all measurements are used as the thermal neutron flux

$$\Phi_\mathrm{n} = (1.00 \pm 0.67) \cdot 10^{-6}\,\mathrm{cm}^{-2}\mathrm{s}^{-1}. \tag{3.29}$$

The natural activation rate

$$\mathscr{A}_\mathrm{nat} = \Phi_\mathrm{n} \cdot \frac{m_\mathrm{out} \cdot N_A \cdot \eta_\mathrm{meas}^{^{124}\mathrm{Xe}}}{M_A} \cdot \sigma_{^{124}\mathrm{Xe}} \tag{3.30}$$

is then given by the product of the thermal neutron flux, the thermal neutron capture cross-section $\sigma_{^{124}\mathrm{Xe}} = (165 \pm 11) \cdot 10^{-24}\,\mathrm{cm}^{-2}$ [251] and the number of ^{124}Xe nuclei. The latter is calculated with an estimated xenon mass $m_\mathrm{out} \approx 10$ kg outside of the water tank, and the measured abundance, Avogadro constant and xenon molar mass. While m_out could not be determined precisely, 10 kg can be regarded as an upper limit from the dimensions of the cryogenic and purification systems. A more aggressive approach would yield a value of ≈ 5 kg [207]. The activation rate under the conservative assumption of a larger mass is

$$\mathscr{A}_\mathrm{nat} \approx (0.65 \pm 0.44)\,\mathrm{d}^{-1}. \tag{3.31}$$

Due to the 16.8 h half life, it is likely that the ^{125}Xe nuclei are refed into the detector before decaying, but are diluted in the total xenon mass of 3.2 t. Far higher activation rates directly inside the active target were reached during neutron calibrations. In dedicated studies of ^{241}AmBe and NG data

$$\begin{aligned}
\mathscr{A}_{^{241}\mathrm{AmBe}} &\approx (60 \pm 7)\,\mathrm{t}^{-1}\mathrm{d}^{-1}, \\
\mathscr{A}_\mathrm{NG} &\approx (411 \pm 35)\,\mathrm{t}^{-1}\mathrm{d}^{-1}
\end{aligned} \tag{3.32}$$

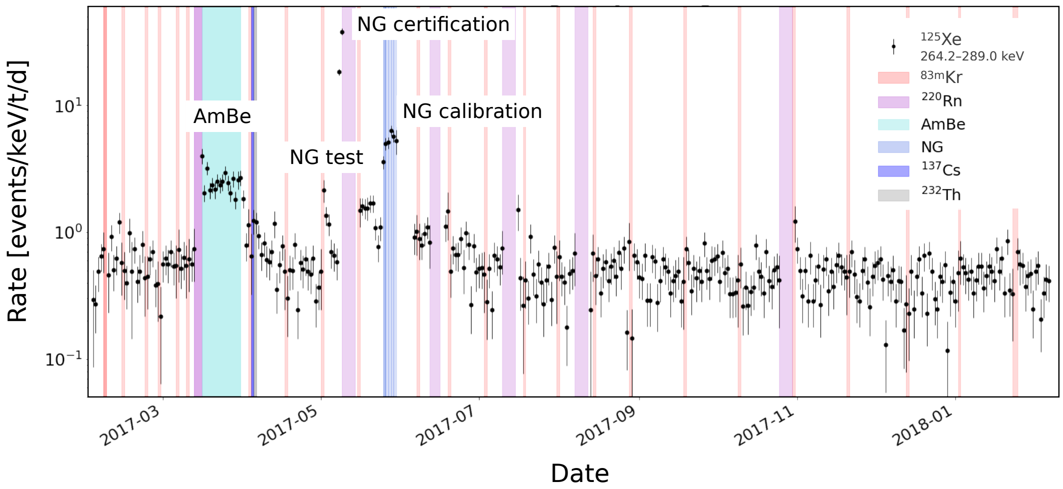

Figure 3.16: Measured ^{125}Xe event rate over time in 1-day bins within the inner 1-tonne fiducial volume after the application of all data selection criteria. The energy range in which the rate was determined is 264.2 to 289.0 keV, a symmetric $2\sigma_E$ energy resolution interval around the 276.6 keV ^{125}Xe peak. Calibration periods are shown as coloured areas in the plot. Poisson uncertainties are assumed for the rate. All bins are corrected for live-time loss from cuts.

were found. These studies are detailed in section A4 of the appendix. In both, post-AmBe and post-neutron generator data, fewer iodine decays than expected from the decay of the parent isotope ^{125}Xe were observed [207]. This is attributed to the removal of ^{125}I during the continuous purification of the detector's xenon inventory by circulation over hot zirconium getters. A study using five days of neutron generator data quantified the short-term behaviour of the removal and lead to a pre-unblinding reduction of the whole SR1 dataset to 214.3 live days. This study is detailed in [207]. However, due to the blinding of the signal region containing the ^{125}I peak, the long-term behaviour of the removal could only be assessed after unblinding.

Since every ^{125}Xe decay in the detector results in an ^{125}I nucleus, a model for the expected iodine decay rate from artificial activation was constructed from the measured decay rate of ^{125}Xe in close collaboration with C. Weinheimer. With a branching ratio of 66.4 % ^{125}Xe decays into an excited state of ^{125}I with a half-life of 0.23 ns [231]. The emitted γ-ray with an energy of 243.378(5) keV [231] is predominantly merged with the 33.1672(13) keV K-shell cascade from ^{125}I that occurs in 88.2 % of all cases [252]. The resulting line at 276.6 keV in the measured energy spectrum is sufficiently far away from the ^{129m}Xe line for tracking the decay of this isotope without significant background. The rate evolution within a symmetric $2\sigma_E$ window around the peak mean is shown in figure 3.16 for SR1. The data is shown in 1-day bins corrected for live-time loss from cuts. Calibration periods are signified by coloured areas in the plot. Rate increases can be clearly be attributed to the ^{241}AmBe calibration in March 2017 as well as to the NG calibration in May/June 2017. Neutron generator tests and a certification run at full power, causing the largest rate increase observed, are not marked in colour, but indicated in the plot. After calibrations the rate returns to the background level within a few days.

The ^{125}Xe data is background-subtracted using a linear fit of data sufficiently far away from calibration periods. Details on the background subtraction can be found in section A5 of the appendix. In a second step, the measured rates are scaled up by the nuclear and atomic branching fractions [231], as well as by the statistical 95.4 % coverage of the $2\sigma_E$ energy interval around the peak centre. The resulting rate corresponds to the total ^{125}Xe

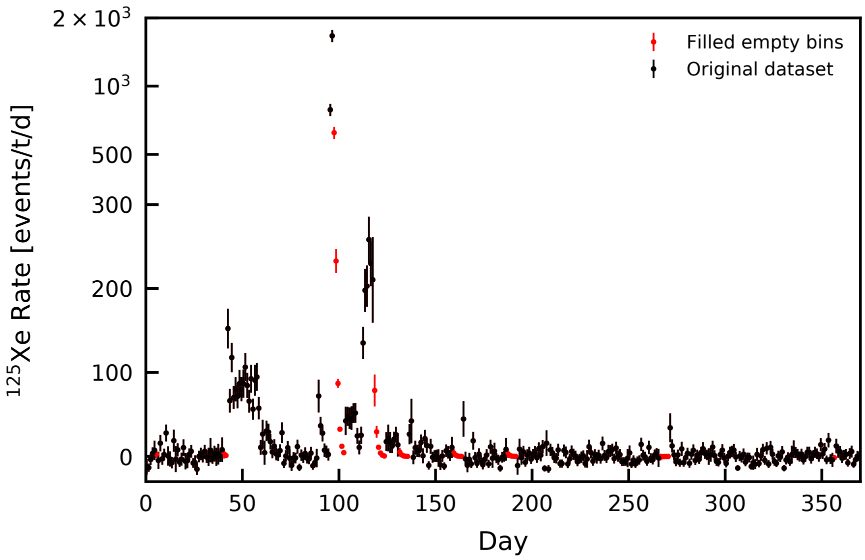

Figure 3.17: Rate evolution of ^{125}Xe data after background subtraction, upscaling and filling of empty bins. Measured data bins are denoted by black markers and Poisson uncertainties are assumed. These have been scaled with the same correction as the rate. Filled empty bins are marked in red and their uncertainties correspond to the propagated Poisson uncertainties of the last preceding bin containing measured data. This is also true for filled bins that are preceded by another filled bin. The y-axis for the rate is linear up to 300 events/t/d and logarithmic above in order to show the few highest rate points. The x-axis shows the time in days since the start of data-taking for SR1.

decay rate inside the detector. Due to calibrations and periods without data taking empty bins are present during periods without activation. These are filled using the rate from preceding bins and the ^{125}Xe half-life. The Poisson uncertainties from the preceding bins are propagated from the respective last bin containing measured data. The resulting ^{125}Xe rate with filled empty bins is presented in figure 3.17. Here, only data points from SR1 are shown although a dedicated calibration run for the assessment of ^{125}I removal from SR2 was included in the model. The SR2 data will be discussed in detail in chapter 4.

The model is then constructed by integrating the background-subtracted ^{125}Xe rate over time in one-day steps. The number of decays in the preceding ^{125}Xe bin adds this number of ^{125}I nuclei according to equation (3.28). The multiplication of the current number of ^{125}I nuclei with the decay constant yields the decay rate in the current time bin. In order to obtain a continuous fit function, the binned model was linearly interpolated. Equation (3.28) had to be modified with a purification term in order to account for the observed removal of ^{125}I before its decay:

$$\frac{\mathrm{d}N_{^{125}\mathrm{I}}}{\mathrm{d}t} = \lambda_{^{125}\mathrm{Xe}} N_{^{125}\mathrm{Xe}}(t) - \lambda_{\mathrm{eff}} N_{^{125}\mathrm{I}}(t) \tag{3.33}$$

The effective decay constant is

$$\lambda_{\mathrm{eff}} = \lambda_{^{125}\mathrm{I}} + \lambda_{\mathrm{pur}} \tag{3.34}$$

and its inverse is the effective time constant

$$\tau_{\mathrm{eff}} = \left(\frac{1}{\tau_{^{125}\mathrm{I}}} + \frac{1}{\tau_{\mathrm{pur}}} \right)^{-1} . \tag{3.35}$$

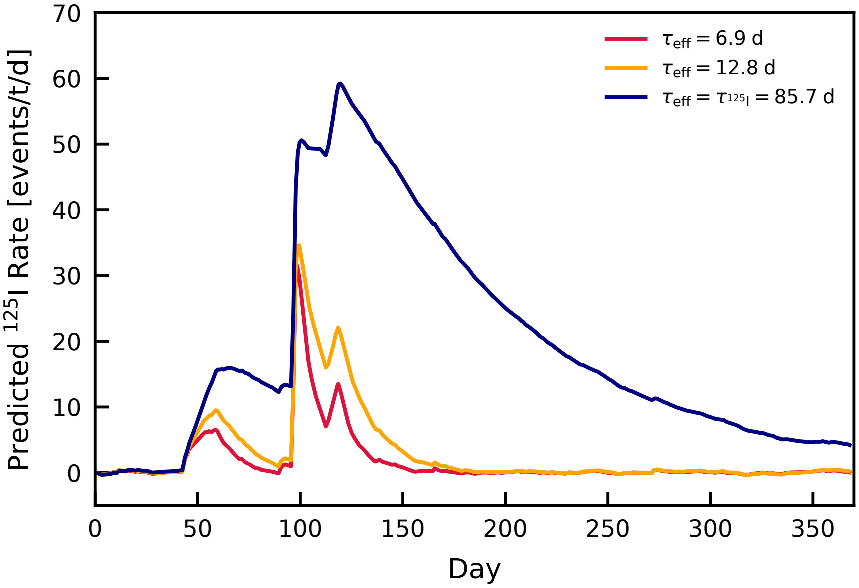

Figure 3.18: Predicted ^{125}I decay rates according to the summed and decay-constant convolved ^{125}Xe data. The solid blue line would be realised in the absence of iodine removal. The red and orange lines showcase the predicted rate evolution for $\tau_{\mathrm{eff}} = 6.9$ d ($\tau_{\mathrm{pur}} = 7.5$ d) and $\tau_{\mathrm{eff}} = 12.8$ d ($\tau_{\mathrm{pur}} = 15.0$ d), respectively. All curves are scaled with $\lambda_{^{125}\mathrm{I}}$.

If ^{125}I is solely removed by the purification system and if the removal is 100 % efficient, $\tau_{\mathrm{pur}} \rightarrow 7.5$ d approaches the purification cycle time of the detector with the resulting $\tau_{\mathrm{eff}} \rightarrow 6.9$ d. The resulting ^{125}I predictions for three τ_{eff} are shown in figure 3.18. The solid blue line would be realised in the absence of iodine removal. The red and orange lines showcase the predicted rate evolutions for $\tau_{\mathrm{pur}} = 7.5$ d and $\tau_{\mathrm{pur}} = 15.0$ d, respectively. All curves are scaled with $\lambda_{^{125}\mathrm{I}}$, so τ_{eff} affects the area under the curves, i.e. the number of measured events, by determining the slope and the maximum amplitude of the decay rate.

The model was fitted to the measured ^{125}I rate evolution in a $2\sigma_E$ interval around the peak (61.7 keV to 72.9 keV) with three free parameters: model scaling, τ_{eff} and linear background. The ^{125}I data is upscaled in a similar fashion as the ^{125}Xe data with the respective K-shell fraction and 95.4 % interval coverage. A best-fit $\tau_{\mathrm{eff}} = (9.1 \pm 2.6)$ d was found. This is in agreement with the expected decay constant from efficient iodine removal by the purification system. Since the model was constructed directly from data with underlying Poisson uncertainties, a special uncertainty propagation method had to be devised. The ^{125}Xe rate uncertainties are propagated by drawing artificial toy datasets from the measured ^{125}Xe data. The rate in each toy dataset bin is drawn from a Poisson distribution with the measured number of events as the expectation value. An ^{125}I model is made for each toy ^{125}Xe dataset and fitted to the ^{125}I rate evolution. The best fit to the measured ^{125}I rate over time in 10-day bins and the uncertainty band derived from an ensemble of 10^3 toy data fits are shown in Fig 3.19. The final ensemble distributions can be found in section A6 of the appendix. In order to investigate if the binning in time introduced bias, different binnings of the ^{125}I data between 1 and 14 days were tested with χ^2 and log-likelihood fits and yielded consistent results. For the final 2νKK search, only datasets with a decay rate at the non-activated background level were selected. The data range of this selection is shown as the red area in Fig. 3.19 and contains 177.7 live-days. The expected number of ^{125}I decays from artificial activation $N_{^{125}\mathrm{I,art}}$ is obtained by integrating the best fit model

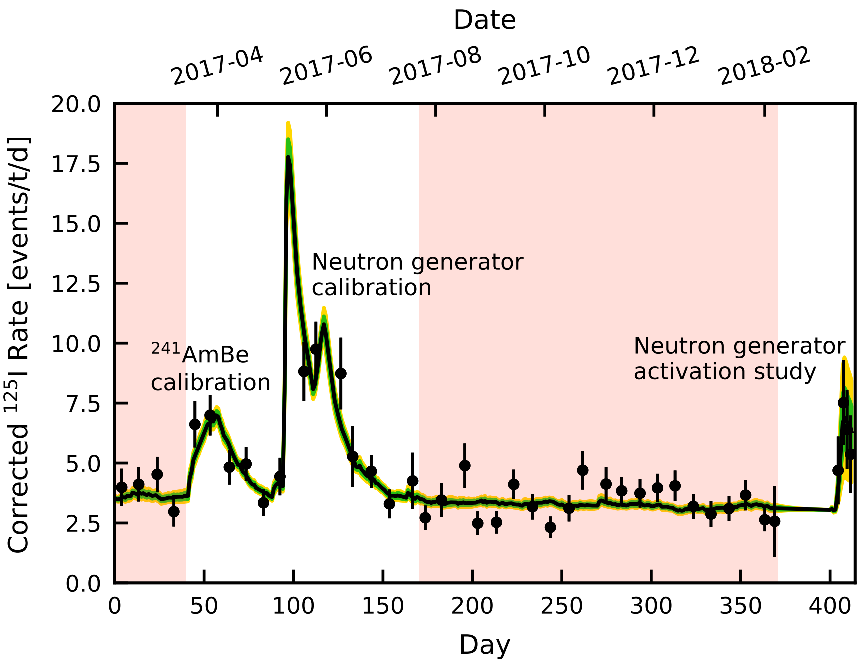

Figure 3.19: Fit of the ^{125}I model to the measured rate over time in a $2\sigma_E$ interval around the ^{125}I peak mean in 10-day bins. Periods with increased rate originate from artificial activation during neutron calibrations, equipment tests, and a dedicated activation study. The best-fit effective iodine decay constant is $\tau_{\mathrm{eff}} = 9.1$ d. The corresponding fit curve is shown as a black line. The green and yellow bands mark the 1σ and 2σ model uncertainties, respectively. The final data selection for the 2νKK search is indicated in pale red. Taken from [31].

over the actual data taking periods. The ensemble distribution of $N_{^{125}\mathrm{I,art}}$ from the toy data fits allows to extract both a central value and uncertainties. With this one has

$$N_{^{125}\mathrm{I,art}} = 6 \pm 6 \text{ events} \tag{3.36}$$

in the 177.7 d dataset and a 1.5 t fiducial volume. The thermal component is not included here due to the background subtraction, but can be calculated as

$$N_{^{125}\mathrm{I,nat}} = 4 \pm 3 \text{ events} \tag{3.37}$$

using equations (3.28) and (3.34) with $\mathscr{A}_{\mathrm{nat}} = (0.65 \pm 0.44)\ \mathrm{d}^{-1}$ and $\tau_{\mathrm{eff}} = (9.1 \pm 2.6)$d. Together these yield

$$N_{^{125}\mathrm{I}} = 10 \pm 7 \text{ events} \tag{3.38}$$

as a fit constraint on the total number of ^{125}I events in the analysis dataset.

3.4 First direct observation of 2νKK

After unblinding of the signal region the background model with the added 2νKK signal and ^{125}I background peaks was again fitted to the data. The resulting spectra of the event rate in both subvolumes are shown in figure 3.20. The best-fit parameters are summarised in table 3.7. Although $\chi^2/\mathrm{ndf} = 527.3/462 \approx 1.14$ is marginally larger than for the fit on the 214.3 d dataset before unblinding, the data is still described well. Looking at the residuals in figure 3.20 the deterioration in goodness of fit is driven by individual outlier points. Only at energies close to the upper energy bound in the outer volume the data is systematcially higher than the fit, but still within the 2σ band of the data. The parameter pulls are shown in figure 3.21 and exhibit the same trend as those of the background-only fit prior to unblinding (cf. figure 3.15). The only pull above $2\Delta p$ is observed for the mean position of the $^{131\mathrm{m}}$Xe peak. This was already the largest positive pull before the unblinding and reduction of the dataset. Therefore, the larger pull in the reduced dataset after unblinding is attributed to the reduction in statistics. No anomalous pulls are observed for the mean positions and standard deviations of the constrained signal and ^{125}I peaks. The same is true for the $^{83\mathrm{m}}$Kr peak with higher statistics.

A clear peak at $E_{2\nu\mathrm{KK}}$ was identified. The mean energy and peak width obtained from the spectral fit to the unblinded data are $\mu_{2\nu\mathrm{KK}} = (64.2 \pm 0.5)$ keV and $\sigma_{2\nu\mathrm{KK}} = (2.6 \pm 0.3)$ keV, respectively. Converting the fit to a total event count yields $N_{^{125}\mathrm{I}} = (9 \pm 7)$ events from the decay of ^{125}I and $N_{2\nu\mathrm{KK}} = (126 \pm 29)$ events from 2νKK. Compared to the null hypothesis the $\sqrt{\Delta\chi^2}$ of the best-fit is 4.4 [31]. The χ^2 profile for $N_{2\nu\mathrm{KK}}$ is shown in figure 3.22. A significance of 4.4σ is derived from the $\sqrt{\Delta\chi^2}$ between the best-fit and a null result.

Several consistency checks were carried out in the scope of [207]. It was verified that the signal is homogeneously distributed in space and that it accumulates linearly with the exposure. The linearity of the energy calibration is verified by identifying the ^{125}I activation peak at its expected position in background-subtracted data that was recorded directly after a neutron calibration. This is illustrated in the bottom panel of figure 3.23. The top panel shows a zoom on the ROI with a tonne-year scale on the vertical axis. The middle panel shows the symmetric residuals in this energy region.

Considering the systematic uncertainties on fiducial mass, elemental abundance and cut acceptance, the observed number of $N_{2\nu\mathrm{KK}} = (126 \pm 29)$ events is converted into a half-life. Rearranging equation (1.31) gives the half-life as a function of the measured events with

$$T_{1/2}^{2\nu\mathrm{KK}} = \ln(2)\frac{\epsilon\eta N_A m t}{M_\mathrm{A} N_{2\nu\mathrm{KK}}}, \tag{3.39}$$

where $M_A = 131.293(3)$ g/mol [180] is the mean molar mass of xenon[4], N_A is Avogadro's constant, and $t = 177.7$ d is the live-time of the measurement. The acceptance of the data selection criteria between 55 keV and 75 keV is constant within the uncertainties at $\epsilon = 0.967 \pm 0.007_\mathrm{stat} \pm 0.033_\mathrm{sys}$. The additional systematic uncertainty accounts for the fact that for a few data selection criteria only a lower limit on the acceptance was measurable. With the measured ^{124}Xe isotopic abundance $\eta_\mathrm{meas}^{^{124}\mathrm{Xe}} = (9.94 \pm 0.14_\mathrm{stat} \pm 0.15_\mathrm{sys}) \times 10^{-4}$ mol/mol and the fiducial mass $m = (1502 \pm 9_\mathrm{sys})$ kg, the half-life is

$$T_{1/2}^{2\nu\mathrm{KK}} = (1.8 \pm 0.5_\mathrm{stat} \pm 0.1_\mathrm{sys}) \times 10^{22}\ \mathrm{yr}. \tag{3.40}$$

This is the longest half-life measured directly to date. Indications of a similarly-long half-life for 2νKK were reported for ^{78}Kr [253]. Within their uncertainties the half-lives are on the same level, but the uncertainty of the result for ^{124}Xe in this work is a factor two smaller.

---

[4] The minor deviations from the natural abundances assumed in this number can be neglected here, but would have to be taken care of in experiments using targets enriched in ^{124}Xe or ^{136}Xe.

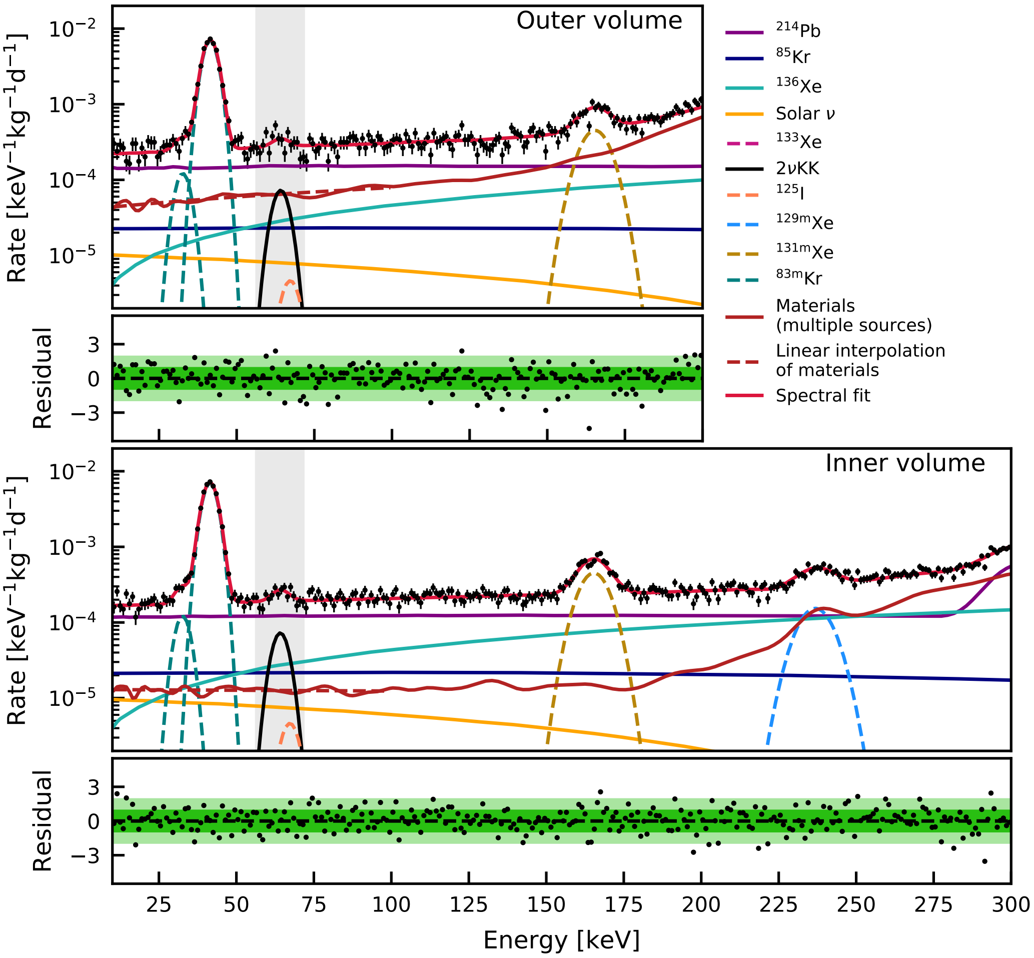

Figure 3.20: Fit of the signal and background models to the measured energy spectrum after unblinding of the data. Uncertainties on the data points are symmetric $\sqrt{N}$ Poisson uncertainties. The final exposure is 177.7 d in the 1.5 t fiducial volume, which is segmented into inner (**bottom panel**) and outer (**top panel**) subvolumes that were fitted simultaneously. The sum spectrum is indicated by the solid red line with $\chi^2/\mathrm{ndf} = 527.3/462 \approx 1.14$. The residuals are shown individually for each volume. Background sources constant in time are shown as solid lines while those that vary over time are shown as dashed lines. The material interpolation below 100 keV is indicated by a dashed brown line. The formerly blinded region is signified by the grey band and includes the 2νKK signal peak (solid black) and the ^{125}I background peak (dashed coral). Modified from [31].

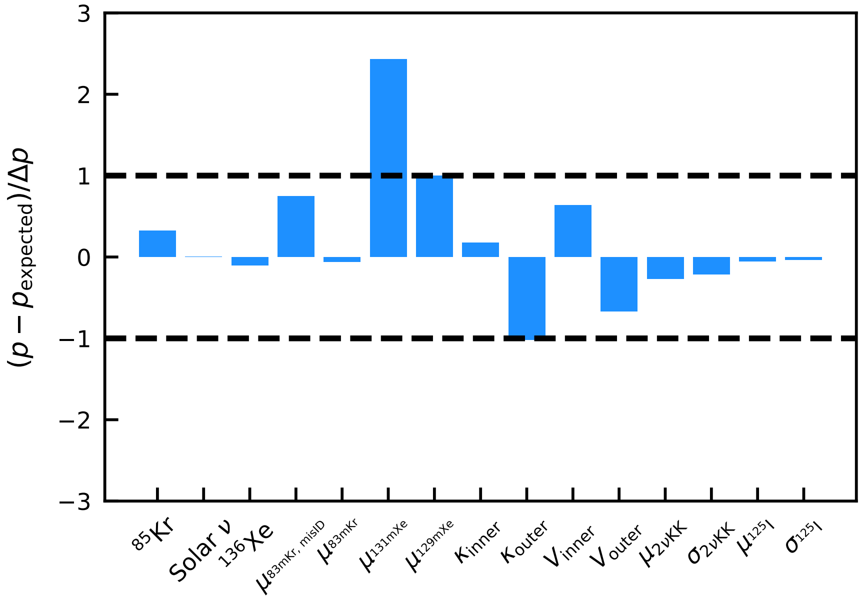

Figure 3.21: Parameter pulls of the 15 constrained parameters from the fit to the unblinded data in the segmented 1.5 t fiducial volume and 177.7 d of data.

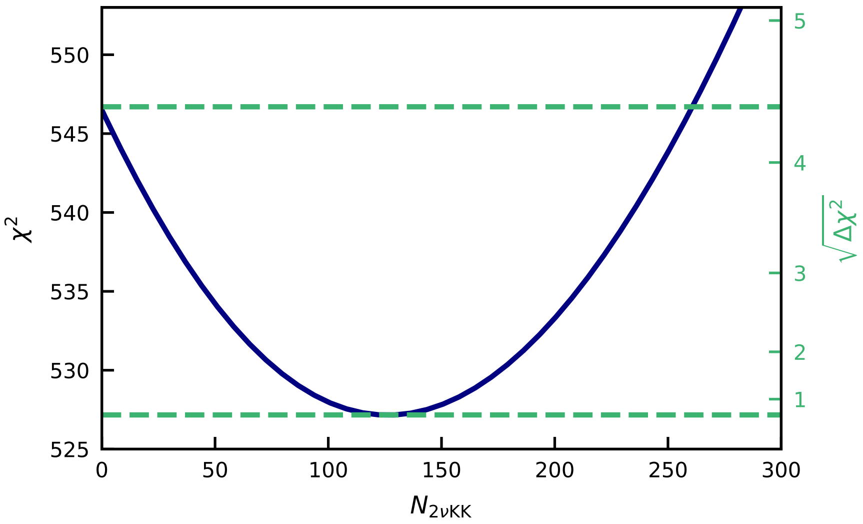

Figure 3.22: χ^2 profile for $N_{2\nu\mathrm{KK}}$ (solid blue). The minimum and the zero-intersect are marked by dashed green lines. The intersect for $N_{2\nu\mathrm{KK}}$ occurs at $\sqrt{\Delta\chi^2} = 4.4$. Modified from [31].

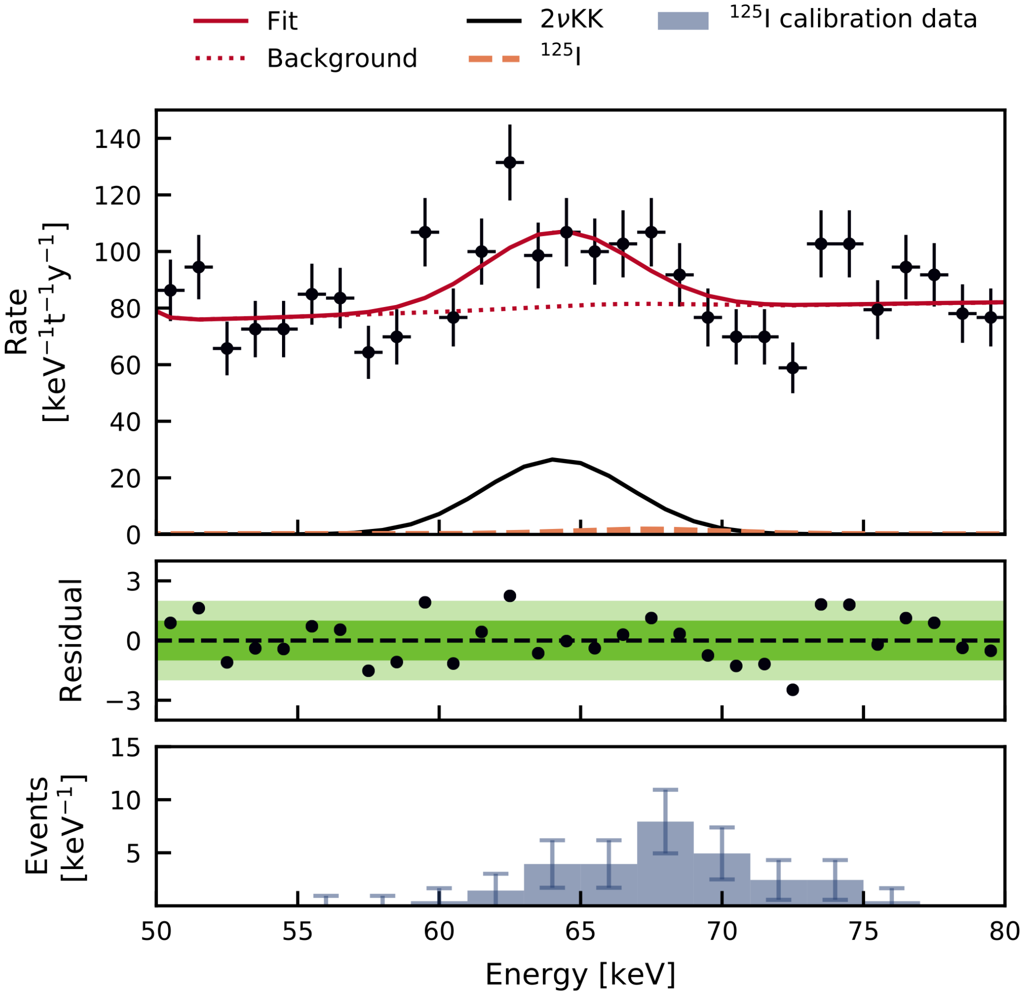

Figure 3.23: Zoom on the fit in the ROI for 2νKK in ^{124}Xe. The 2νKK best-fit peak with $N_{2\nu\mathrm{ECEC}} = 126$ events is indicated by the solid black line. The full spectral fit is shown as the solid red line. The peak from ^{125}I with $N_{^{125}\mathrm{I}} = 9$ events is identified by the the dashed coral line. It is clear that the background-only model without the 2νKK peak, shown in dotted red, cannot describe the measured data. Residuals for the best fit are given in the central panel. The bottom panel shows a histogram of the background-subtracted ^{125}I activation peak. The peak was found in 6 d of data after a dedicated NG calibration. The peak is identified at its expected mean position at 67.3 keV. Modified from [31].

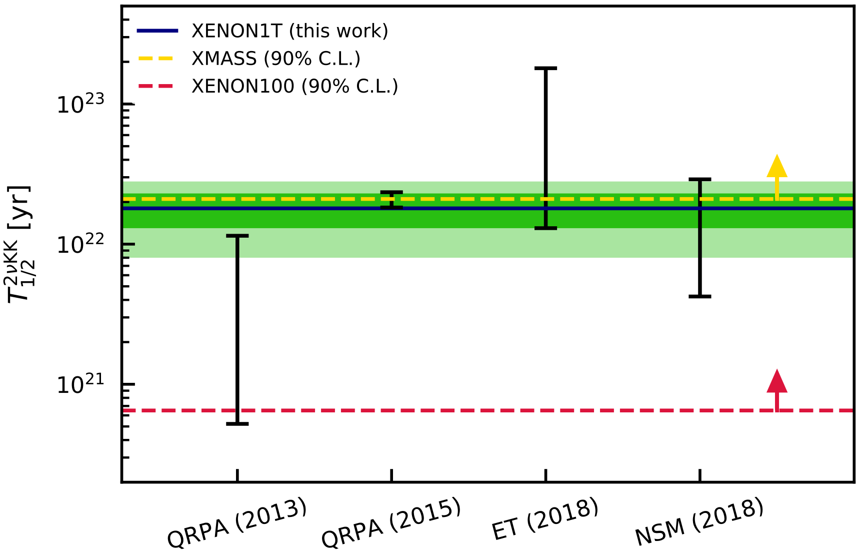

Figure 3.24: Comparison of the 2νKK half-life from this work with theoretical predictions and the experimental 90 % C.L. lower limits from XMASS [145] (dashed yellow) and XENON100 [254] (dashed red). The measured half-life (solid blue) with the 1σ and 2σ statistical uncertainty bands indicated in green and light green, respectively, is compared to results from nuclear structure calculations [106, 108, 110]. An agreement is found for all measurements. The theoretical half-lives from the quasiparticle random-phase approximation (QRPA) were calculated for the KK capture as well as for captures from higher electron shells which have not been observed yet. Accordingly, they have been scaled up by the KK-fraction $f_{2\nu KK} = 0.765$ of the decay [89]. This was not necessary for the effective theory (ET) and nuclear shell model (NSM) half-lives already given for 2νKK. Modified from [31].

Moreover, it is found that the result is compatible with the lower limit from XMASS [145]. This is presented in figure 3.24 alongside theoretical predictions of the 2νKK half-life from nuclear structure calculations. These calculations used the QRPA [108, 110] approach, a novel effective theory [106], and the NSM [106]. The QRPA half-lives had to be scaled with the KK-capture fraction $f_{2\nu KK} = 0.765$ [89] since they were given for all double-electron captures, but only the double-K capture was observed. Overall, the calculation results match the observed half-life well, but stretch over more than two orders of magnitude. Still, a systematic analysis of several nuclei in the mass range from $A = 100$–130, QRPA (2015) states the smallest uncertainty and at the same time matches the observed half-life best.

While it is still below the 5σ threshold, this first direct observation of 2νECEC in ^{124}Xe showcases the potential of xenon-based Dark Matter search experiments for nuclear and neutrino physics. With the increased target mass and world-leading ER background level of XENON1T, the direct observation of a previously inaccessible process could be achieved. The next generation detectors XENONnT [18], LZ [17] and PandaX-4T [255] are either under construction or in commissioning and will be able to probe the 2νKK with precision. Yet, the potential of the existing XENON1T data is not exhausted at this point.

Table 3.7: Best-fit parameters on the 177.7 d dataset in the segmented 1.5 t fiducial volume.

Parameter	**Fit result**	**Constraint/limit**	**Unit**
Solar ν	1.00 ± 0.02	1 ± 0.02	$1.8 \cdot 10^{-8}\ \mathrm{s^{-1}kg^{-1}}$
^{136}Xe	0.995 ± 0.029	1.00 ± 0.03	3.96 μBq/kg
^{85}Kr	7.0 ± 1.1	6.6 ± 1.1	0.1 ppt
^{214}Pb	7.8 ± 0.4	–	μBq/kg
^{125}Xe	-0.025 ± 0.016	–	μBq/kg
^{133}Xe	-0.003 ± 0.012	–	μBq/kg
^{238}U	0.2 ± 0.5	positive	scaling
^{226}Ra	0.000 ± 0.009	positive	scaling
^{232}Th	124 ± 25	positive	scaling
^{228}Th	-8 ± 14	–	scaling
^{60}Co	0.046 ± 0.023	positive	scaling
^{40}K	0.001 ± 0.004	positive	scaling
$A_{^{83\mathrm{m}}\mathrm{Kr}}$	$(4.05 \pm 0.05) \cdot 10^{-2}$	–	$\mathrm{kg^{-1}d^{-1}}$
$\mu_{^{83\mathrm{m}}\mathrm{Kr}}$	41.466 ± 0.025	41.5 ± 0.6	keV
$\sigma_{^{83\mathrm{m}}\mathrm{Kr}}$	2.306 ± 0.021	–	keV
$A_{^{83\mathrm{m}}\mathrm{Kr,\,misID}}$	$(7.2 \pm 1.5) \cdot 10^{-4}$	–	$\mathrm{kg^{-1}d^{-1}}$
$\mu_{^{83\mathrm{m}}\mathrm{Kr,\,misID}}$	32.6 ± 0.4	32.1 ± 0.6	keV
$\sigma_{^{83\mathrm{m}}\mathrm{Kr,\,misID}}$	2.4 ± 0.6	–	keV
$A_{^{131\mathrm{m}}\mathrm{Xe}}$	$(5.26 \pm 0.23) \cdot 10^{-3}$	–	$\mathrm{kg^{-1}d^{-1}}$
$\mu_{^{131\mathrm{m}}\mathrm{Xe}}$	165.36 ± 0.21	163.9 ± 0.6	keV
$\sigma_{^{131\mathrm{m}}\mathrm{Xe}}$	4.65 ± 0.19	–	keV
$A_{^{129\mathrm{m}}\mathrm{Xe}}$	$(2.06 \pm 0.30) \cdot 10^{-3}$	–	$\mathrm{kg^{-1}d^{-1}}$
$\mu_{^{129\mathrm{m}}\mathrm{Xe}}$	236.8 ± 0.5	236.2 ± 0.6	keV
$\sigma_{^{1291\mathrm{m}}\mathrm{Xe}}$	5.4 ± 0.8	–	keV
V_{inner}	1.007 ± 0.009	1.00 ± 0.01	1052 kg
V_{outer}	0.993 ± 0.009	1.00 ± 0.01	448 kg
κ_{inner}	0.7 ± 0.21	$\frac{2}{3} \pm \frac{1}{3}$	scaling
κ_{outer}	0.33 ± 0.32	$\frac{2}{3} \pm \frac{1}{3}$	scaling
$N_{^{125}\mathrm{I}}$	9 ± 7	10 ± 7	events
$\mu_{^{125}\mathrm{I}}$	67.3 ± 0.5	67.3 ± 0.6	keV
$\sigma_{^{125}\mathrm{I}}$	2.8 ± 0.5	2.8 ± 0.5	keV
$N_{2\nu\mathrm{KK}}$	126 ± 29	–	events
$\mu_{2\nu\mathrm{KK}}$	64.2 ± 0.4	64.33 ± 0.58	keV
$\sigma_{2\nu\mathrm{KK}}$	2.59 ± 0.21	2.64 ± 0.24	keV

Extended Search for Two-Neutrino Double-Electron Capture with XENON1T

4

The original search for the two-neutrino double-electron capture in ^{124}Xe used a conservative data selection in order to largely avoid background from ^{125}I. Owed to the detailed modelling of this background it is possible to use additional exposure. Moreover, while background from misidentified $^{83\text{m}}$Kr events limited the original study to simultaneous captures of two K-shell electrons, an improved signal selection also allows the search for the simultaneous capture of a K- and an L-shell electron, the KL-capture. This section will describe the extended analysis.

4.1 Additional data

The XENON1T low-energy ER analysis [14] demonstrated that it was possible to analyse a larger portion of the SR1 data than was conservatively used for the double-electron capture analysis [31]. In the first data selection step of the low-energy ER analysis, data taking runs within 24 h of $^{83\text{m}}$Kr and ^{220}Rn calibrations were removed in order to avoid the background from residual calibration isotopes in the detector. After this selection, the total live-time corrected for cut-related exposure reductions is 226.9 d [14]. In a second step, the data was subdivided into two categories, which are referred to as the *clean* and *dirty* data. *Clean* data is at least 50 d of real time away from NG or AmBe neutron calibrations. Accordingly, it exhibits a lower background from neutron-activated xenon isotopes and especially lower background from ^{125}I. The total live-time of this data is 171.2 d. The remaining 55.8 d of *dirty* data contain larger background contributions from neutron-activation. The clean SR1 data contains 164.3 d of data from the 177.7 d dataset used in [31]. The dirty partition of SR1 contains only data that has not been investigated in the former analysis.

Figure 4.1 shows the distribution of the science and calibration data over SR1. The clean data is located at the start of the science run up to mid-March 2017 and then starts again in mid-July 2017 extending to the end of the science run. The dirty data is located in between these two blocks of clean data and contains a two-week AmBe calibration as well as shorter NG calibration runs. The remaining calibration data is evenly distributed over the science run.

On top of the SR1 data, 24.3 live days of data from SR2, recorded between 7th February 2018 and 24th September 2018, can be used. This is clean data 50 d away from neutron calibrations that was used for a cross-check of the low-energy ER result [14]. Due to frequently changing detector conditions associated with hardware tests and modifications, the total amount of usable data in this research and development run is smaller than for

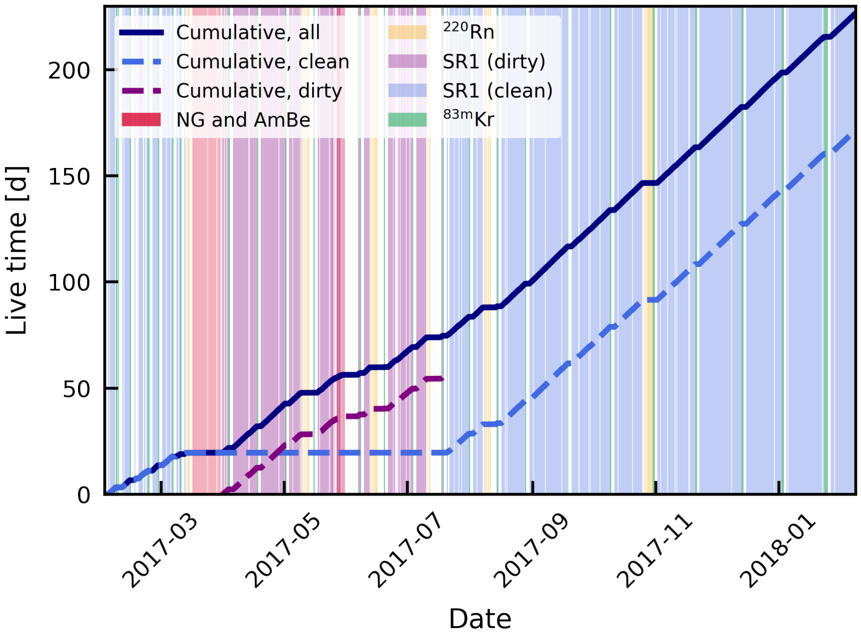

Figure 4.1: Data distribution over SR1. The clean and dirty science data periods are indicated by the blue- and purple-coloured areas, respectively. Calibration data is indicated in red for NG and Ambe, orange for ^{220}Rn and green for ^{83m}Kr. The cumulative live-time corrected for losses due to cuts is indicated by the dashed light blue line for the clean data, the dashed purple line for the dirty data and the solid dark blue line for all science data.

the Dark Matter SR1. The relative amount of clean data is also smaller in SR2 due to more frequent and longer NG calibrations as well as an extended ^{83m}Kr calibration. No dirty data has been selected for SR2 due to the large amount of expected background from ^{125}I (cf. section 4.2) and ^{83m}Kr.

The distribution of data over SR2 is shown in figure 4.2. Here, the clean data is mainly distributed in three blocks in early March, late May and September 2018. Data with the NG was taken twice in March for approximately two weeks in total and again in mid-July for four days. Notably, the last calibration campaign was followed up immediately with ^{220}Rn calibration data. In April it was decided to leave the ^{83m}Kr source open in order to allow for continuous calibration. Two notable operations are also indicated in the plot. In June the QDrive pumps of the gas purification system were exchanged for a new magnetically coupled piston pump [208]. This lead to two changes of detector conditions relevant for the analysis presented here: Since those pumps were among the largest contributors to the XENON1T ^{222}Rn budget the associated background was reduced as shown in figure 2.9. Moreover, the larger purification flow is expected to impact the time constant of the ^{125}I removal. This will be further examined in section 4.2. In late July 2018 the Kr-distillation column was operated in a specialised radon distillation mode [73, 77] further reducing the ^{222}Rn activity concentration to $(4.5 \pm 0.1\ \mu\mathrm{Bq/kg})$ [76]. The amount of clean SR2 data with radon reduction from the MagPump and distillation is 36.2 %. Assuming that in the remaining data the ^{222}Rn activity concentration is the same as in SR1 with $(13.3 \pm 0.5\ \mu\mathrm{Bq/kg})$, the time-averaged ^{222}Rn activity concentration in the clean SR2 data is $(10.1 \pm 0.3\ \mu\mathrm{Bq/kg})$. This is $(76 \pm 1)\,\%$ of the SR1 mean. Assuming that the ^{214}Pb background follows the ^{222}Rn activity concentration one would expect a corresponding background reduction.

Due to hardware operations it is possible that ambient air – and with it ^{85}Kr – was in-

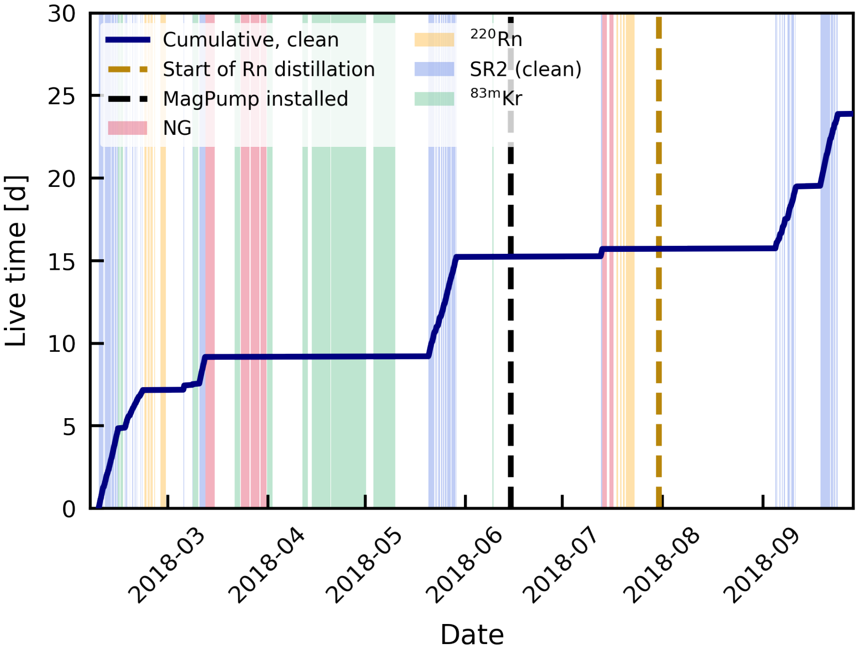

Figure 4.2: Data distribution over SR2. The clean science data periods are indicated by the blue-coloured areas. Calibration data is indicated in red for NG, orange for ^{220}Rn and green for ^{83m}Kr. The cumulative live-time corrected for losses due to cuts is indicated by the solid dark blue line. The completion of the MagPump installation and the start of the Rn distillation are shown as the vertical dashed black and gold lines, respectively.

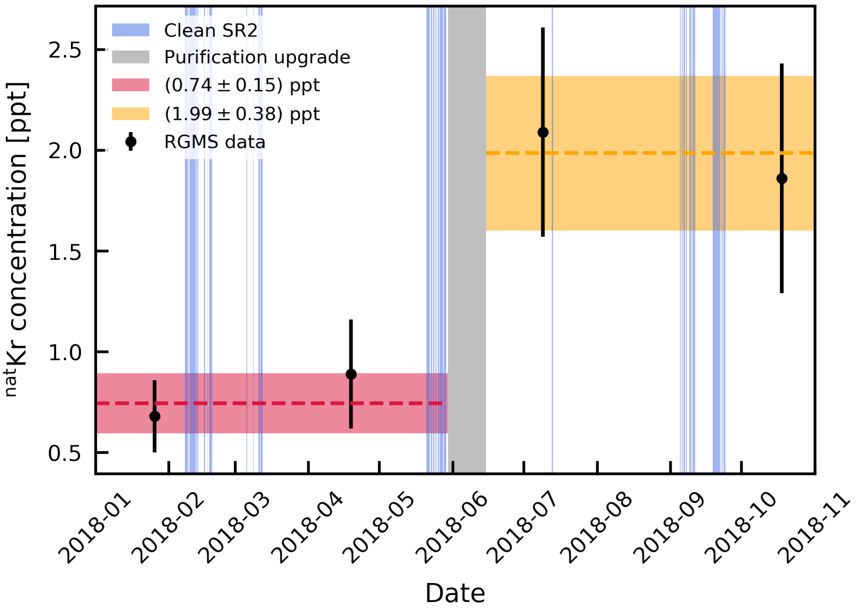

Figure 4.3: Concentration of ^{nat}Kr in xenon during SR2. Four RGMS data points are available (black markers) with the error bars containing both statistical and systematic uncertainties [256]. Clean data periods are indicated in blue. The fitted average concentration before the MagPump installation is $^{nat}\mathrm{Kr}/\mathrm{Xe} = (0.74 \pm 0.15)$ ppt (red), while it is $^{nat}\mathrm{Kr}/\mathrm{Xe} = (1.99 \pm 0.38)$ ppt (orange) after.

troduced to the detector. Moreover, it was observed over SR1 that the ^{85}Kr level increased over time which would be compatible with a minor air leak in the system [238]. Figure 4.3 shows the behaviour of the $^{\mathrm{nat}}$Kr concentration in xenon over SR2 based on four RGMS data points [256]. The fitted average concentration before the MagPump installation is $^{\mathrm{nat}}\mathrm{Kr}/\mathrm{Xe} = (0.74 \pm 0.15)$ ppt (red), while it is $^{\mathrm{nat}}\mathrm{Kr}/\mathrm{Xe} = (1.99 \pm 0.38)$ ppt (orange) after[1]. This indicates a negligible increase compared to the $^{\mathrm{nat}}\mathrm{Kr}/\mathrm{Xe} = (0.66 \pm 0.11)$ ppt in SR1. In the data with reduced ^{222}Rn level, the ^{85}Kr background is expected to be thrice as high as in the SR1 data[2]. The exposure-weighted average concentration in the clean SR2 data is $^{\mathrm{nat}}\mathrm{Kr}/\mathrm{Xe} = (1.19 \pm 0.17)$ ppt.

It was decided to use the data processed with PAX version 6.10.1 as used in [14] since it offered various benefits over version 6.8.0 [216] used in [31]. First, it enables the use of the improved position and energy reconstruction from [201] (cf. section 6.1). With this, the energy resolution in SR1 is

$$\frac{\sigma_E}{E} = \frac{(0.313 \pm 0.007)\ \mathrm{keV}^{1/2}}{\sqrt{E}} + (0.0017 \pm 0.0002). \tag{4.1}$$

While the published energy calibration parameters can be used for SR1, they had to be derived anew for SR2. Following the method outlined in section 3.1 the depth-dependent calibration parameters

$$\begin{aligned} g_1(z) &= (0.146 \pm 0.027)\ \frac{\mathrm{pe}}{\mathrm{ph}} + z \cdot (6.3 \pm 0.8) \cdot 10^{-5}\ \frac{\mathrm{pe}}{\mathrm{ph} \cdot \mathrm{cm}}, \\ g_2(z) &= (10.8 \pm 2.1)\ \frac{\mathrm{pe}}{\mathrm{e}} - z \cdot (1.54 \pm 0.20) \cdot 10^{-2}\ \frac{\mathrm{pe}}{\mathrm{e} \cdot \mathrm{cm}} \end{aligned} \tag{4.2}$$

were found [257]. These are compatible with the SR1 parameters from [201]. The energy resolution [257] σ_E for SR2 was parametrised with

$$\frac{\sigma_E}{E} = \frac{(0.339 \pm 0.005)\ \mathrm{keV}^{1/2}}{\sqrt{E}} + (0.0023 \pm 0.0008). \tag{4.3}$$

As a second benefit, the analysis can take advantage of redefined cuts with higher acceptances as well as newly developed cuts. These include a cut that removes the low-energy shoulder of the $^{83\mathrm{m}}$Kr peak (cf. figure 3.14) – enabling the search for the KL double-electron capture in addition to the KK-capture. The cuts will be discussed in the following.

4.1.1 Cuts for the extended double-electron capture analysis

The cuts applied in this analysis are for the most part the same as in [14]. Most of these cuts are updated versions of those in [31]. Only notable differences will be outlined here together with the determination of the combined acceptance for both science runs. The cuts are summarised in table 4.1.

The *S1MaxPMT* cut was removed from the low-energy ER cut list. This cut removes all events with $Z < -92.9$ cm which is the lower boundary of the fiducial volume used in [14]. Since the superellipsoid for the double-electron capture analysis stretches further towards the cathode, it was not possible to use the cut. The new PAX version uses a lower two-PMT coincidence threshold for S1 signals compared to the former three-PMT coincidence in order to achieve a lower energy threshold. For the low-energy ER analysis the old coincidence criterion was recreated with the *S1PMT3fold* cut. In this analysis, the

---

[1] A goodness of fit discussion is forgone for two data points each with the given uncertainties.

[2] In part this will negate the benefits of the radon distillation in this data. In XENONnT the krypton will be removed from the xenon inventory as for XENON1T SR1. This way XENONnT will take full advantage of the reduced radon level [18] from distillation and other reduction techniques.

cut is also applied, but should not affect the data of interest since only events above 10 keV are selected. At this energy, S1 coincidences below 3 PMTs do not occur. In addition to the *ERband* cut from chapter 3 the *SimpleSurfaceCut* and *S2Threshold* cuts remove inwards-reconstructed events from radon progeny decays occuring on the PTFE wall that feature anomalously small S2s. Owed to a redefinition, the *S2PatternLikelihood* featured a larger acceptance than the version studied for [31], so it could be applied in this analysis. The *MisIDS1SingleScatter* cut is central to the extended double-electron capture analysis since it removes the low-energy shoulder on the $^{83\mathrm{m}}$Kr peak that was still present in the former analysis at all times of SR1. This shoulder obscured the expected KL-capture peak from ^{124}Xe. Events fell into this shoulder when the secondary S1 from the two-step $^{83\mathrm{m}}$Kr decay was misidentified as an S2. Such an event would not be removed by the *S1SingleScatter* cut. The new cut targets the largest S2 before the main S2. It removes this event population down to the 10^{-4} level compared to the main peak (cf. section A10 of the appendix) while having 100 % acceptance for all other ER events in this energy region [258].

Two cuts were redefined for SR2 by A. Bismark: *CS2AreaFractionTopExtendedSR2* and *S2PatternLikelihoodSR2*. Both cuts use the PMT hit patterns and were affected by the deactivation of PMTs during SR2 due to deteriorating PMT performance. The resulting time-dependence of the cut acceptance could be overcome by the redefinition of the cuts in a time-dependent fashion [259, 260]. A second notable change for SR2 is the omission of the *PosDiff* cut. This cut compares the reconstructed interaction positions from two different position reconstruction algorithms, the neural network and the top pattern fit. Since only the new neural network from [201] was updated for the changes in the PMT configuration in SR2, the top pattern fit algorithm does not produce meaningful results in this data. Accordingly, the position difference cannot be used for a cut.

As in section 3.1.1, multiple methods are used in order to derive the combined cut acceptance. The live-time reductions are again taken into account at the stage of the exposure calculation. The acceptance of all analytic cuts is expected to be unity. Following the analysis in [14] the $N-1$ method is used on ^{220}Rn data to derive a lower limit on the acceptance for the remaining 8 cuts in SR1 and 7 remaining cuts in SR2. Figure 4.4 shows the combined cut acceptance for SR1. The superellipsoid fiducial volume has been subdivided into an inner cylinder (black markers) and an outer shell (gold markers) as in [31]. The combined acceptances in both volumes are shown in the energy range from 0 to 210 keV in 2 keV bins. The uncertainties on the data points have been derived in the same fashion as in [14]. For the individual $N-1$ acceptances they represent Bayesian 68.3 % credible intervals [261]. These are in general asymmetric because the efficiency can neither exceed unity nor go below zero. However, for less extreme cases and in the presence of large statistics, they become symmetric. The final combined acceptance uncertainties are the separately Gaussian-propagated upper and lower uncertainties of the individual cuts. In figure 4.4 they are mostly symmetric due to the large available statistics from all ^{220}Rn calibrations over SR1.

Both fiducial volumes exhibit a sudden acceptance loss at larger energies as observed in section 3.1.1. Again this is caused by the removal of true multi-site events by way of the *S2Width* and *S2SingleScatter* cuts. While in the former analysis, this acceptance loss was modeled, it was decided to exclude this data from the extended analysis, so the fit ranges are chosen as 10 to 200 keV for the inner and 10 to 160 keV for the outer volume. The excluded data is indicated in light and dark green, for the inner and outer volume respectively. Data below 10 keV (orange patch) is excluded in order to stay clear from the low-energy ER excess found in [14]. The data excluded at high energy is far from the signal region and the only benefit from a larger fit range are stronger constraints on material backgrounds which start to dominate around 200 keV. In the previous analysis these stronger constraints from data were needed, since the material background constraints in the fit were relative constraints

Table 4.1: Data quality criteria for the 2νECEC search with their acceptance derivation method, the science run they are applied in, and a short description. The cuts marked with an asterisk were redefined for SR2.

Cut name	**Acceptance derivation**	**Science run**	**Description**
DAQVeto	Live-time	1, 2	Correct for DAQ deadtime
S2Tails	Live-time	1, 2	Remove high rate periods following large S2s
Flash	Live-time	1, 2	Remove events after isolated large light signals from muons
ERband	Analytic	1, 2	Remove NR events
InteractionExists	Analytic	1, 2	Check if event has a valid S1+S2 pair
InteractionPeaksBiggest	Analytic	1, 2	Check if largest peak is in main interaction
S2Threshold	Analytic	1, 2	Main S2 > 200 pe
S1PMT3fold	Analytic	1, 2	Threefold PMT coincidence for main S1
SimpleSurfaceCut	Analytic	1, 2	Remove PTFE surface events
MisIdS1SingleScatter	Analytic	1, 2	Remove low-energy shoulder of ^{83m}Kr peak
PosDiff	$N-1$ (^{220}Rn)	1	Remove events where PMT pattern fit and neural network reconstructed positions differ
S1SingleScatter	$N-1$ (^{220}Rn)	1, 2	Remove signals with multiple S1s from consecutive nuclear decays or pileup
CS2AreaFractionTopExtended(SR2)	$N-1$ (^{220}Rn)	1, 2*	Remove events with aberrant relative PMT array contributions to the S2
S1PatternLikelihood	$N-1$ (^{220}Rn)	1, 2	S1 signal distribution among PMTs
S1AreaFractionTop	$N-1$ (^{220}Rn)		Remove events with aberrant relative PMT array contributions to the S1
S2PatternLikelihood(SR2)	$N-1$ (^{220}Rn)	1, 2*	S2 signal distribution among PMTs
S2Width	$N-1$ (^{220}Rn)	1, 2	Correlate S2 signal width and interaction depth
S2SingleScatter	$N-1$ (^{220}Rn)	1, 2	Remove multi-site events

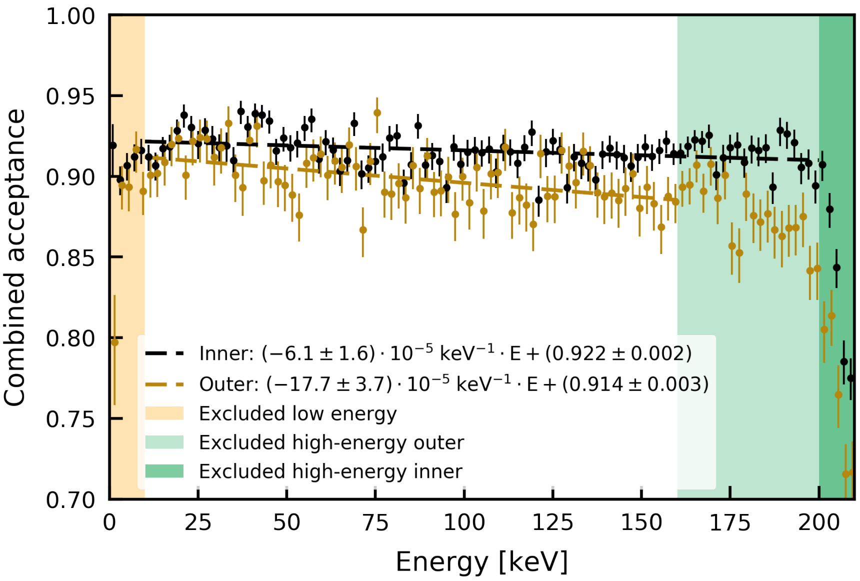

Figure 4.4: Combined cut acceptance in SR1 for the inner (black markers) and outer (gold markers) sub-volumes of the superellipsoid fiducial volume. The uncertainties are the Gaussian-propagated Bayesian 68.3 % credible intervals from the individual cuts' $N-1$ acceptances. The linear fit functions are indicated by the dashed black and gold lines for the inner and outer volume, respectively. The excluded energy region containing the low-energy ER excess is coloured in orange. The excluded high-energy regions are shown in light green for the outer volume and dark green for the inner volume.

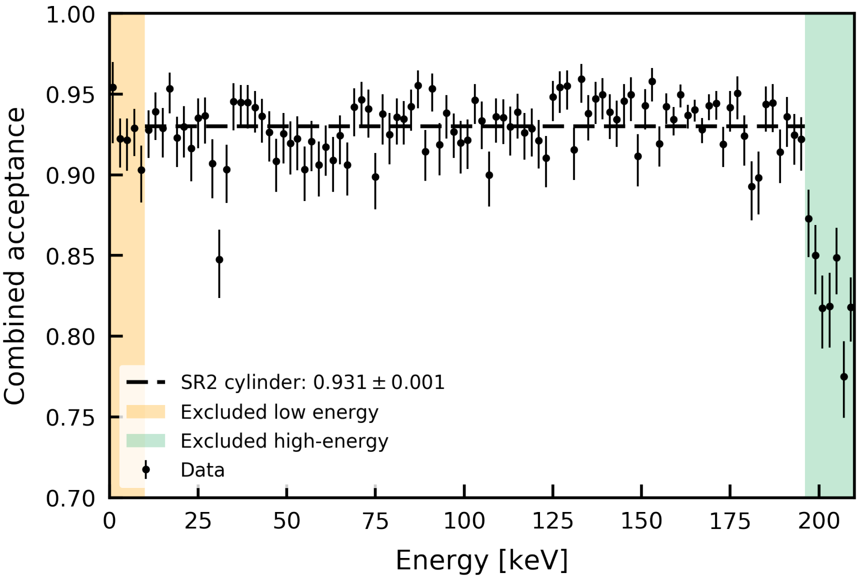

Figure 4.5: Combined cut acceptance in SR2 for the 1-tonne fiducial cylinder (black markers). The uncertainties are the Gaussian-propagated Bayesian 68.3 % credible intervals from the individual cuts' $N-1$ acceptances. The constant fit function is shown as the dashed black line. The excluded energy region containing the low-energy ER excess is coloured in orange. The excluded high-energy region is coloured green.

only. The absolute scaling required data with a sizeable material background contribution. This analysis uses the absolute screening constraints that will be discussed in detail in section 6.2.1 for the neutrinoless double-β decay search, so as in [14] a smaller fit range can be chosen. For the outer volume the markers indicate that an extension of the data range to 200 keV would have been possible. However, a conservative 160 keV upper fit bound was chosen in order to avoid an eventual γ-background from the NG that will be discussed in section 6.1.2 since it is more relevant for the neutrinoless double-β decay analysis.

The acceptances in both volumes are parametrised by fitting linear functions in the respective fit ranges. The asymmetric uncertainties are considered by defining an asymmetric test statistic

$$\chi^2_{\mathrm{asym}} = \chi^2_{\mathrm{up}} + \chi^2_{\mathrm{low}}. \tag{4.4}$$

The summands are calculated indepently for points above and below the fit function

$$\begin{aligned} \chi^2_{\mathrm{up}} &= \sum_{\mathrm{i}} \frac{(f_{\mathrm{acc}}(E_{\mathrm{i}}) - a_{\mathrm{i}})^2}{\sigma^2_{\mathrm{i,\,up}}} \quad \forall f_{\mathrm{acc}}(E_{\mathrm{i}}) - a_{\mathrm{i}} \geq 0, \\ \chi^2_{\mathrm{low}} &= \sum_{\mathrm{j}} \frac{(f_{\mathrm{acc}}(E_{\mathrm{j}}) - a_{\mathrm{j}})^2}{\sigma^2_{\mathrm{j,\,low}}} \quad \forall f_{\mathrm{acc}}(E_{\mathrm{j}}) - a_{\mathrm{j}} < 0. \end{aligned} \tag{4.5}$$

with the fit function $f_{\mathrm{acc}}(E_{\mathrm{i,j}})$, the energies of the tested bins $E_{\mathrm{i,j}}$ and the acceptance values $a_{\mathrm{i,j}}$. The upper and lower uncertainties are $\sigma_{\mathrm{i,\,up}}$ and $\sigma_{\mathrm{j,\,low}}$, respectively. With linear fits of the acceptance, the parametrisations $f_{\mathrm{acc}}(E)$ for both volumes are obtained as

$$\begin{aligned} f_{\mathrm{acc,\,inner}}(E) &= (-6.1 \pm 1.6) \cdot 10^{-5}\,\mathrm{keV}^{-1} + (0.922 \pm 0.002), \\ f_{\mathrm{acc,\,outer}}(E) &= (-17.7 \pm 3.7) \cdot 10^{-5}\,\mathrm{keV}^{-1} + (0.914 \pm 0.003). \end{aligned} \tag{4.6}$$

The fits yield $\chi^2_{\mathrm{asym,\,inner}}/\mathrm{ndf} = 143.1/93.0$ from 10 to 200 keV and $\chi^2_{\mathrm{asym,\,outer}}/\mathrm{ndf} = 72.5/74.0$ from 10 to 160 keV. This indicates a better description of the data in the outer volume. Since the fit function for the inner volume is neither systematically lower nor higher than the data and since a more complex, but arbitrary function could induce overfitting, the linear model is accepted in both volumes for the further analysis. At 10 keV the lower limits on the acceptance are (92.1 ± 0.2) %) for the inner volume and (91.2 ± 0.3) %) for the outer volume. The respective acceptance reductions from 10 keV to the end of the fit energy ranges are (1.2 ± 0.3) % and (2.7 ± 0.5) %.

The combined SR2 acceptance from 0 to 210 keV in the inner 1 t cylinder as used in [14] is shown in figure 4.5. As before, the bin size is 2 keV, but the 68.3 % credible intervals on the data are more asymmetric and considerably larger due to smaller available statistics. As observed before, at around 200 keV the acceptance starts to drop due to the onset of true multi-site background that is cut by the *S2Width* and *S2SingleScatter* cuts. The first data point with a significantly lower acceptance is just above 196 keV, so this is set as the upper analysis boundary. The lower boundary is again set at 10 keV in order to avoid the low-energy excess region [14]. For a constant fit from 10 to 196 keV one obtains a constant acceptance of

$$f_{\mathrm{acc,\,SR2}} = 0.931 \pm 0.001. \tag{4.7}$$

with $\chi^2_{\mathrm{asym,\,SR2}}/\mathrm{ndf} = 130.0/92.0$. A linear fit yielded a slope compatible with zero without an improvement in reduced χ^2, so the simpler constant model was chosen. The acceptance of (93.1 ± 0.1) % is similar to that in the inner volume of the SR1 superellipsoid. The ~ 1 % larger acceptance over the whole energy range can be attributed to the omission of the *PosDiff* cut.

4.1.2 Reassessment of fiducial volume mass uncertainty

Since this analysis uses the updated position reconstruction algorithm, the systematic uncertainty on the superellipsoid fiducial volume for SR1 has to be revised. Moreover, the inclusion of SR2 requires the choice of a fiducial volume and the assessment of the systematic uncertainty. The analysis of SR1 uses the fiducial volume described in section 3.1.2 with the same inner and outer segmentation. For SR2 the cylindrical volume with

$$\begin{aligned} R &\leq 36.94\,\mathrm{cm}, \\ -92.9\,\mathrm{cm} \leq Z &\leq -9.0\,\mathrm{cm} \end{aligned} \tag{4.8}$$

from [14] is used since all SR2 cuts have been optimised for and tested in this volume. The method outlined in section 3.1.2 is used for deriving the systematic uncertainty on the fiducial volumes. A time-dependent correction for the altered drift path of ionisation electrons due to charge-up of the PTFE walls is applied on the reconstructed positions [70]. With this it is possible that the position reconstruction would reconstruct events into and out of the fiducial volumes in a time dependent fashion. Since this would affect the clean and dirty partitions of SR1 differently, their fiducial mass uncertainties are calculated independently. To this end, $^{83\mathrm{m}}$Kr data within both partitions of the data is used for this study. For SR2 all available $^{83\mathrm{m}}$Kr data is used.

Table 4.2 summarises the results for the inner and outer volumes in the clean and dirty SR1 data as well as for the cylindrical volume in the SR2 data. The uncertainties are the result of the counting uncertainties on the numbers of $^{83\mathrm{m}}$Kr events contained in each volume and the uncertainty on the total LXe mass in the active volume $m_{\mathrm{active}} = (2003.8 \pm 5.2)$ kg. The uncertainty on m_{active} results from two other uncertainties: the LXe density at −96° C with $\rho_{\mathrm{Xe}}(-96°\,\mathrm{C}) = (2.862 \pm 0.004)\,\mathrm{g/cm^3}$ [180] and the uncertainty on the true dimensions of the detector at the millimetre level. The analytically calculated masses of the inner and outer volumes are $m_{\mathrm{inner}} = (1029.4 \pm 1.4)$ kg and $m_{\mathrm{outer}} = (464.3 \pm 0.7)$ kg with the uncertainties solely from ρ_{Xe}. The inner volume has, except for its curved edges, the same dimensions as the cylinder used for the SR2 analysis. Accordingly, both feature the same mass. The central values and systematic uncertainties on the fiducial masses then are:

$$\begin{aligned} m_{\mathrm{clean,\,inner}} &= (1031.5 \pm 2.9_{\mathrm{stat}} \pm 2.1_{\mathrm{sys}})\ \mathrm{kg}, \\ m_{\mathrm{clean,\,outer}} &= (460.4 \pm 3.4_{\mathrm{stat}} \pm 1.9_{\mathrm{sys}})\ \mathrm{kg}, \\ m_{\mathrm{dirty,\,inner}} &= (1029.1 \pm 3.1_{\mathrm{stat}} \pm 0.3_{\mathrm{sys}})\ \mathrm{kg}, \\ m_{\mathrm{dirty,\,outer}} &= (460.0 \pm 1.5_{\mathrm{stat}} \pm 4.3_{\mathrm{sys}})\ \mathrm{kg}, \\ m_{\mathrm{SR2}} &= (1033.6 \pm 3.1_{\mathrm{stat}} \pm 4.2_{\mathrm{sys}})\ \mathrm{kg}. \end{aligned} \tag{4.9}$$

The central value is the mean of the two different mass values per volume from table 4.2. The semi-difference between the central value and the two base values is taken as the systematic uncertainty. Due to the correlated statistical uncertainties between the Kr-derived masses and the analytic masses, only the former were taken into account. For SR1 the result is compatible with that in section 3.1.2. The systematic uncertainty for all investigated volumes is $< 1\,\%$. The results for the clean and dirty partitions are compatible within the statistical uncertainties alone, so there is no significant drift of the position reconstruction over time. The same is true when comparing the inner volumes of both SR1 partitions with the inner volume from SR2.

Figure 4.6 shows the distribution of $^{83\mathrm{m}}$Kr events in the Z- and R^2- (top) as well as the X- and Y-directions inside the active volume for the clean partition of SR1. The physical dimensions of the active volume in the XENON1T coordinate system are indicated by the dashed black rectangle in the upper panel and the dashed black circle in the lower panel.

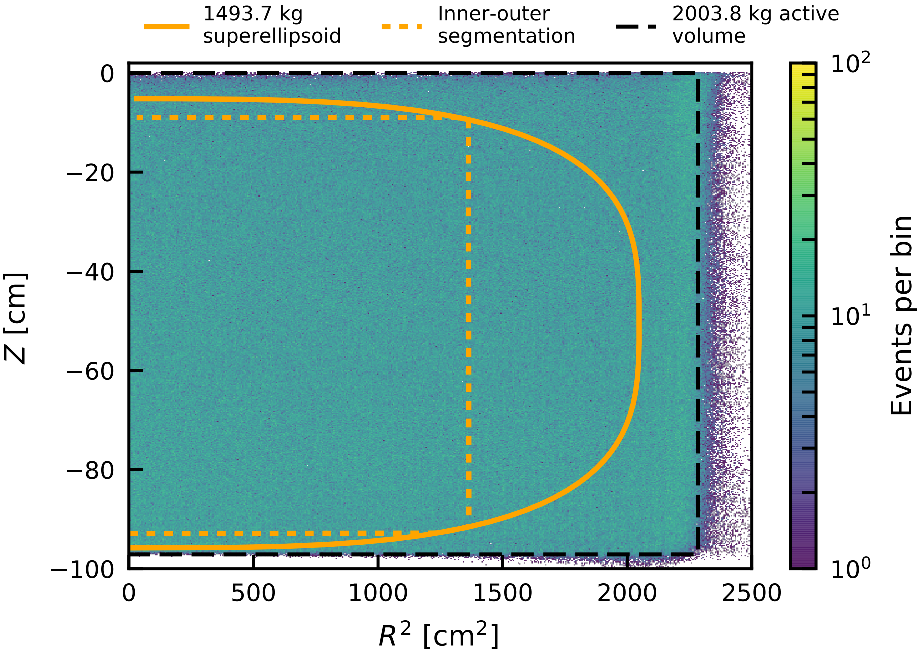

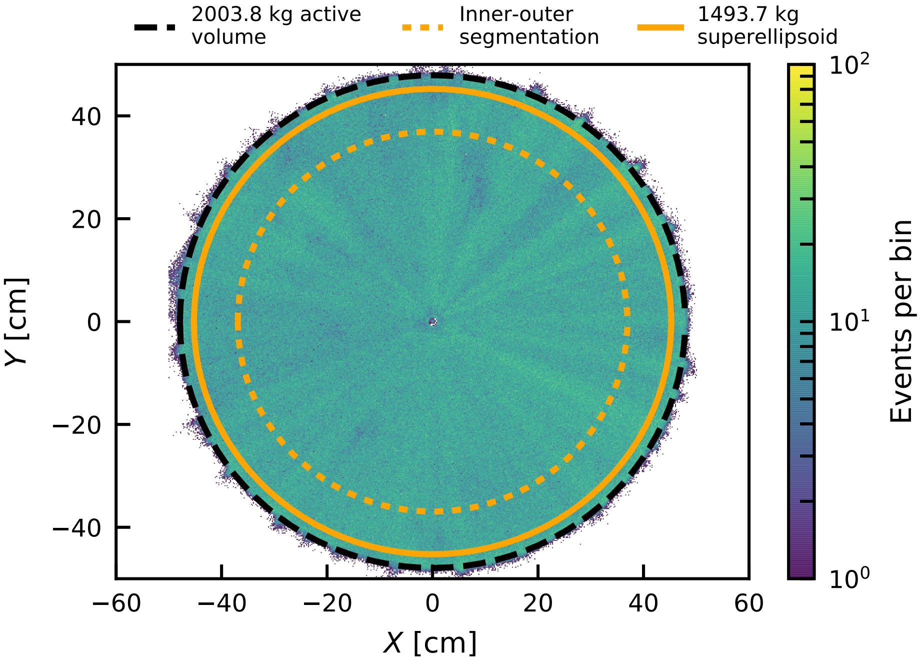

Figure 4.6: **Top:** Distribution of ${}^{83\mathrm{m}}$Kr events in the squared radial and axial directions of the active volume after cuts. With 500 bins in both directions, the volume of each bin is 1 cm^3. **Bottom:** Distribution for the top view onto the TPC for the same data. The area of each bin with 500 bins in both directions is 0.04 cm^2. All data is from the clean partition of SR1 with all analysis cuts applied. The 41.5 keV line was selected in $cS1$-$cS2_\mathrm{b}$ space. The edges of the active volume are marked by the dashed black line. The superellipsoid fiducial volume is indicated by the solid orange line. The dotted orange line marks the segmentation between the inner and outer sub-volumes of the superellipsoid.

Table 4.2: Fiducial masses for SR1 and SR2 from $^{83\mathrm{m}}$Kr and an analytic calculation.

Volume	**Contained $^{83\mathrm{m}}$Kr [%]**	**Mass from $^{83\mathrm{m}}$Kr [kg]**	**Analytic mass [kg]**
Clean SR1			
Full active	100 %	-	2003.8 ± 5.2
Superellipsoid	(74.37 ± 0.08) %	1490.1 ± 3.9	1493.7 ± 1.6
Inner	(51.58 ± 0.06) %	1033.6 ± 2.9	1029.4 ± 1.4
Outer	(22.78 ± 0.04) %	456.5 ± 1.4	464.3 ± 0.7
Dirty SR1			
Full active	100 %	-	2003.8 ± 5.2
Superellipsoid	(74.08 ± 0.11) %	1484.4 ± 4.4	1493.7 ± 1.6
Inner	(51.34 ± 0.08) %	1028.8 ± 3.1	1029.4 ± 1.4
Outer	(22.74 ± 0.05) %	455.6 ± 1.5	464.3 ± 0.7
SR2			
Full active	100 %	-	2003.8 ± 5.2
Cylinder	(51.78 ± 0.08) %	1037.7 ± 3.7	1029.4 ± 1.4

The superellipsoid is shown as the solid orange line and the inner volume is indicated by the dotted orange line. All SR1 cuts have been applied to the data and the 41.5 keV line was selected with cuts in $cS1$-$cS2_\mathrm{b}$ space. The data is homogeneously distributed inside the active volume and the edges of the active volume are smeared out due to the uncertainty of the position reconstruction. The same plots for the dirty partition and SR2 can be found in section A7 of the appendix.

Only the inner fiducial volume of the dirty SR1 data will be used in the following analysis, since the outer volume with the increased background would not offer added sensitivity to 2νECEC. With this, the exposure is 0.93 t-yr. The main factor driving this decision is the increased ^{125}I background level expected for the dirty partition. The detailed ^{125}I background expectation will be discussed in the next section.

4.2 Extended ^{125}I model

Since an increased background contribution of ^{125}I is expected in the dirty partition of SR1, the ^{125}I predictions from the model derived in section 3.3 have to be updated for the new data selections. Moreover, the inclusion of SR2 with its multiple neutron calibrations requires the construction of a second ^{125}I model for this data. First, ^{125}I predictions are derived for the clean and dirty partitions of SR1 by integrating the model derived in section 3.3 over the clean and dirty data periods. The uncertainties from the ^{125}Xe data points and the best-fit model are propagated in the same fashion as in that section. The distributions for the numbers of predicted ^{125}I decays from ^{125}Xe toy datasets can be found in section A8 of the appendix. For the artificial activation by neutron calibrations one obtains

$$
\begin{aligned}
N^{^{125}\mathrm{I}}_{\text{art, clean}} &= (5.2 \pm 4.5)\ ^{\text{events}}/_{\text{t}}, \\
N^{^{125}\mathrm{I}}_{\text{art, dirty}} &= (102.7 \pm 18.8)\ ^{\text{events}}/_{\text{t}}
\end{aligned}
\tag{4.10}
$$

With thermal neutron components for activation in the purification loop outside of the water tank

$$\begin{aligned} N^{^{125}\mathrm{I}}_{\mathrm{nat,\,clean}} &= (5.1 \pm 2.9)\ \mathrm{events/t}, \\ N^{^{125}\mathrm{I}}_{\mathrm{nat,\,dirty}} &= (1.7 \pm 0.9)\ \mathrm{events/t} \end{aligned} \tag{4.11}$$

the total expectations for ^{125}I events in both partitions are

$$\begin{aligned} N^{^{125}\mathrm{I}}_{\mathrm{clean}} &= (10 \pm 5)\ \mathrm{events/t}, \\ N^{^{125}\mathrm{I}}_{\mathrm{dirty}} &= (104 \pm 19)\ \mathrm{events/t}. \end{aligned} \tag{4.12}$$

In the last step, the numbers have been rounded to full events. These are the total numbers of ^{125}I K-, L- and M-electron captures per tonne of xenon in the respective data partition[3]. A preliminary version of these predictions has also been used in [14].

For SR2 the model has to be made from scratch using the measured rate in the 276.6 keV line of ^{125}Xe over time. Figure 4.7 shows the measured event rate in a $2\sigma_E$ interval from 264.0 to 289.2 keV around the peak mean in the cylindrical SR2 fiducial volume. The data during the three NG calibrations and 35.2 d of dirty background data were used in addition to the clean SR2 data. Clear rate increases are identified during the NG calibrations. For the NG data in July an ad-hoc energy calibration was required since a part of this data was taken at an anode voltage of 3 kV instead of the nominal 4 kV during SR2. Accordingly, smaller S2s were observed in this data. The adjustment of the energy calibration is summarised in section A8 of the appendix together with the further data preparation steps for the ^{125}I model and the uncertainty propagation. As in section 3.3, the ^{125}Xe data was background-subtracted, scaled up by the branching fraction and the coverage of the $2\sigma_E$ interval, and empty bins were filled using the exponential decay of ^{125}Xe.

For the construction of the SR2 ^{125}I model two notable changes have been made with respect to SR1. First, after the installation of the magnetic pump, the constant background level in the energy range of the ^{125}I peak is changed due to the reduction in ^{222}Rn and the increase in ^{85}Kr. Therefore, the model is divided into two parts with different background levels separated by the date of the MagPump installation[4]. Second, the new pump allowed for a higher purification flow which should lead to a faster ^{125}I removal by purification. Starting with equations (3.34) and (3.35) and assuming that the iodine removal is proportional to the purification flow one can introduce the flow-specific purification constant $\dot{\lambda}_0$ with

$$\lambda_{\mathrm{pur,\,k}} = \dot{\lambda}_0 \cdot f_{\mathrm{k}}. \tag{4.13}$$

Here, f_{k} is the constant purification flow in the respective time period under investigation with k = 1 before the MagPump installation and k = 2 thereafter. In principle this model can be generalised to be continuous in time. However, in the data periods under consideration the flows do not change significantly, so it is sufficient to derive time-averaged quantities. For the purification constants in both periods one finds that the purification constant is determined by the purification flow ratio r_{flow} with

$$\frac{\lambda_{\mathrm{pur,\,2}}}{\lambda_{\mathrm{pur,\,1}}} = \frac{f_2}{f_1} = r_{\mathrm{flow}}. \tag{4.14}$$

---

[3] Note that in section 3.3 the the ^{125}I predictions were given for K-captures only in the full superellipsoid and 177.7 d of data.

[4] The change in background level at the start of the radon distillation is not taken into account since the additional reduction with respect to the initial reduction by the MagPump is small compared to the total background level (cf. figure 2.9).

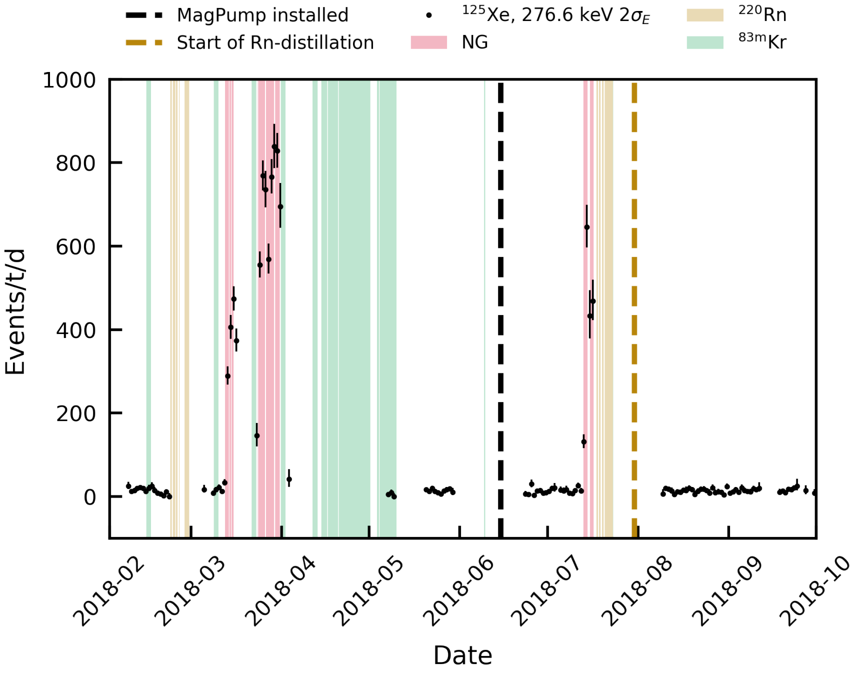

Figure 4.7: Measured event rate over SR2 in a $2\sigma_E$ interval (264.0 to 289.2 keV) around the 276.6 keV peak of ^{125}Xe. The black markers show the rate before background-subtraction. The data from the cylindrical SR2 fiducial volume after cuts has been corrected by the live-time per bin. Uncertainties are based on Feldman & Cousins 68.3 % confidence intervals [262]. NG, ^{83m}Kr and ^{220}Rn calibration data are shaded in red, green and gold, respectively. Data points outside these regions are from clean and dirty SR2 background data. The data points inside the May 2018 krypton data are isolated dirty background runs. The MagPump installation is indicated by the dashed black line. The start of the radon distillation is indicated by the gold dashed line.

The purification time constants are linked as

$$\tau_{\text{pur},2} = \frac{\tau_{\text{pur},1}}{r_{\text{flow}}}. \tag{4.15}$$

With this, r_{flow} and $\tau_{\text{pur},1}$ are used in order to express $\tau_{\text{pur},2}$ in the ^{125}I model after the installation of the MagPump. By using the mean purification flows and their standard deviations from the XENON1T slow control in both periods one obtains

$$r_{\text{flow}} = 1.59 \pm 0.08, \tag{4.16}$$

which is used as a constraint in the fit of the ^{125}I model. With this, the six fit parameters of the ^{125}I model in SR2 are the constant background levels before and after the installation of the MagPump, the model scaling amplitudes in both periods, the purification time constant in the first period, and the purification flow ratio connecting the time constant in both periods.

For the ^{125}I data points events in a $2\sigma_E$ interval around the 67.3 keV K-capture peak, 61.4 to 73.2 keV, are selected from the same data as the ^{125}Xe. The points are scaled up by the live-time per bin and the statistical coverage of the $2\sigma_E$ interval. The lower data density compared to SR1 does not allow time bins of 14-days with sufficient statistics for a χ^2 fit.

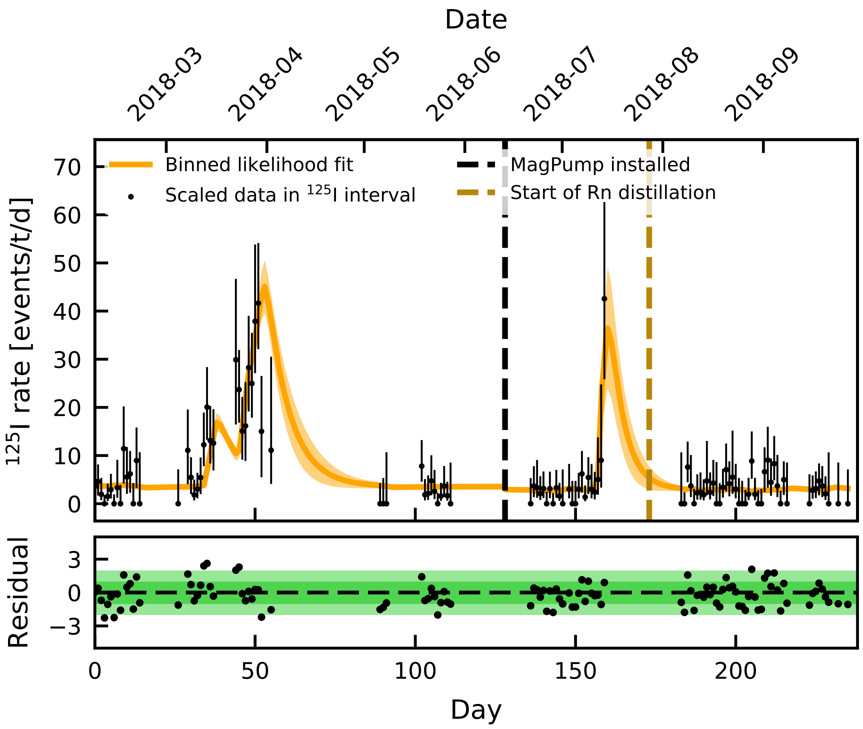

Figure 4.8: Fit of the ^{125}I model to data with $\chi^2_\lambda/\mathrm{ndf} = 138/108$. The data from a $2\sigma_E$ interval around 67.3 keV is subdivided into 1-day bins shown by the black markers. The rate has been corrected for statistical coverage and live-time. The uncertainties are based on Feldman & Cousins 68.3 % confidence intervals [262] and are for illustration only. The 1σ model uncertainty is shown as an orange band around the solid orange line for the best fit. The installation of the MagPump, indicated by the dashed black line, marks the separation point of the model into two periods. The start of the radon distillation is shown by the dashed gold line. The residuals in the bottom panel are given by the square-roots of the χ^2_λ [263] summands. The 1σ and 2σ intervals for symmetric residuals are indicated by the dark and light green bands.

Instead, 1-day bins are used with a binned χ^2_λ Poisson likelihood that is normalised such that it can be interpreted in the same fashion as a χ^2 fit [263]. It is defined as:

$$\chi^2_\lambda = 2\sum_{\mathrm{i}}^{\mathrm{bins}} \lambda_\mathrm{i}(\vec{p}) - y_\mathrm{i} + y_\mathrm{i}\ln\left(\frac{y_\mathrm{i}}{\lambda_\mathrm{i}(\vec{p})}\right). \tag{4.17}$$

Here, the expectation value $\lambda_\mathrm{i}(\vec{p})$ is given by the value of the fit function $f(\vec{p}, x_\mathrm{i})$ at x_i for the best fit parameters $\vec{p}$. The sum goes over the number of bins with y_i counts per bin[5]. As for a χ^2 fit, the square-roots of the summands can be used as residuals. The sign of each residual is given by the sign of $\lambda_\mathrm{i} - y_\mathrm{i}$. It should be noted that these residuals are only expected to be symmetric for bin counts $\gtrsim 10$ since Poisson statistics lead to asymmetric confidence intervals below.

Figure 4.8 shows the fit of the ^{125}I model to the data and the best-fit parameters are presented in table 4.3. With $\chi^2_\lambda/\mathrm{ndf} = 138/108 \approx 1.28$ the goodness of fit is comparable to

---

[5] In the code implementation the second term in the sum has to be treated differently for empty bins with $y_\mathrm{i} = 0$ because those would lead to the undefined expression $\ln 0$. Therefore, the second term is set to zero in such cases.

Table 4.3: Fit parameters of the ^{125}I model in SR2 with their best-fit values, constraints and units.

Parameter	Fit value	Constraint	Unit
$\tau_{\mathrm{pur},1}$	7.3 ± 2.7	-	d
r_{flow}	1.59 ± 0.07	1.59 ± 0.08	-
$\mathrm{background}_1$	3.6 ± 0.5	-	$\mathrm{t}^{-1}\mathrm{d}^{-1}$
$\mathrm{background}_2$	2.9 ± 0.3	-	$\mathrm{t}^{-1}\mathrm{d}^{-1}$
scale_1	0.5 ± 0.1	-	$\lambda_{^{125}\mathrm{I}}$
scale_2	1.2 ± 0.5	-	$\lambda_{^{125}\mathrm{I}}$

the SR1 model. The calibration campaigns in March 2018 are well described and single outlier points in the residuals are present above and below zero. Two data points right after day 50 are below the model by approximately 2σ. These would suggest a faster purification, but this is constrained by the more numerous data points during the phase of increasing rate associated with the two preceding neutron calibrations. For the neutron calibration in July 2018 only three data points are available during the activation period and all are well described by the model. Due to a ^{220}Rn calibration and the start of the radon distillation directly after the NG runs, no data is available for two weeks after the end of the neutron calibration. The first available data points are already back at the constant background level. According to the fit, the background in the second model period is reduced by 19.4 %, which is expected from the reduced radon and elevated krypton levels. The purification time constant $\tau_{\mathrm{pur},1} = (7.3 \pm 2.7)$ d is compatible with the 7.5 d turnaround interval of the full detector. Translated to $\tau_{\mathrm{eff},1} = (6.7 \pm 2.3)$ d it agrees with the value of $\tau_{\mathrm{eff}} = (9.1 \pm 2.6)$ d found in section 3.3 within the uncertainty. The constrained flow ratio is reproduced by the fit and leads to $\tau_{\mathrm{pur},2} = (4.6 \pm 1.7)$ d. The scaling parameters of both data periods agree within their uncertainties. Since the scaling parameter $\mathrm{scale}_2 = (1.2 \pm 0.5)\lambda_{^{125}\mathrm{I}}$ for the second period is constrained by a single data point, the uncertainty is relatively large. As in section 3.3 the scaling parameters are different from unity since they incorporate cut acceptances and single scatter reconstruction efficiencies.

The number of expected ^{125}I events is obtained by integrating the model over the clean data periods of SR2. The statistical uncertainty associated with the fit of the model results from the integration of the uncertainty bands. For the uncertainties arising from the ^{125}Xe data underlying the model, toy datasets are drawn, fitted and integrated in the same fashion as in section 3.3. For the artificial activation by the NG in SR2 one obtains

$$N^{^{125}\mathrm{I}}_{\mathrm{art,\,SR2}} = (1.9 \pm 1.4)\ \mathrm{events/t}. \tag{4.18}$$

Here, the statistical uncertainty $\Delta N_{\mathrm{stat}} = 1.0$ events/t and the ^{125}Xe uncertainty $\Delta N_{^{125}\mathrm{Xe}} = 1.0$ events/t have been added in quadrature. With thermal neutron components for activation in the purification loop outside of the water tank

$$N^{^{125}\mathrm{I}}_{\mathrm{nat,\,SR2}} = (1 \pm 1)\ \mathrm{events/t} \tag{4.19}$$

the total expectation for ^{125}I events in SR2 is

$$N^{^{125}\mathrm{I}}_{\mathrm{SR2}} = (3 \pm 2)\ \mathrm{events/t}. \tag{4.20}$$

With the same calculation one obtains an expectation of $N^{^{125}\mathrm{I}}_{\mathrm{SR2,\,dirty}} = (76 \pm 38)$ events/t for the dirty 35.2 d of data. This outweighs the expected $\mathcal{O}(10)$ events/t for signal by far, so this data is not sensitive to the decay. Accordingly, it was not used in the analysis.

Table 4.4: Relative probabilities of KK-, KL- and LL-captures for all 2νECEC decays. The values have been obtained using the normalisations of the K- and L1-electron wave functions in ^{124}Xe. These can be found in [89] (table V therein) for the Dirac solutions of a finite size nucleus with homogeneous charge distribution as well as for the Schrödinger solution of a point nucleus. The L2 and L3 electrons have not been considered here since their normalisations are an order of magnitude smaller than for the L1 shell.

Decay fraction	**Dirac solution [%]**	**Schrödinger solution [%]**	**Absolute difference [%]**
$f_{2\nu\mathrm{KK}}$	76.5	79.1	2.6
$f_{2\nu\mathrm{KL}}$	22.0	19.7	2.3
$f_{2\nu\mathrm{LL}}$	1.6	1.2	0.4

4.3 Changes to signal model, background model and fit method

The KL- and LL-capture peaks are added to the signal model in order to maximise sensitivity. With this, the 2νECEC signal model consists of three Gaussian peaks. The decay energies from sections 1.2.4 and 3.2 determine the peak positions at

$$\begin{aligned}\mu_{2\nu\mathrm{KK}} &= (64.33 \pm 0.13)\ \mathrm{keV},\\ \mu_{2\nu\mathrm{KL}} &= (37.29 \pm 0.68)\ \mathrm{keV},\\ \mu_{2\nu\mathrm{LL}} &= (10.01 \pm 0.13)\ \mathrm{keV}.\end{aligned} \tag{4.21}$$

For the KL- and LL-peaks no calculations for the double-hole energies in ^{124}Xe are available in the existing literature. Accordingly, these values are assigned uncertainties as outlined in section 1.2.4. The energy uncertainty for the KL capture has been symmetrised by taking the mean of the upper and lower uncertainties. The energy resolutions at the respective energies follow from the parametrisations for SR1 and SR2 in equations (4.1) and (4.3).

The relative fractions of the KK-, KL- and LL-captures, denoted as $f_{2\nu\mathrm{KK}}$, $f_{2\nu\mathrm{KL}}$ and $f_{2\nu\mathrm{LL}}$, give the relative scaling of the peaks for a total decay rate $A_{2\nu\mathrm{KK}}$. In absence of a secondary source for the relative probabilities of the different captures, no meaningful theory uncertainty can be derived. However, the authors of [89] provide two solutions for the wave function normalisations of the low-lying electron shells in ^{124}Xe: the solution of the Dirac equation for a finite size nucleus with a homogeneous charge distribution and the solution of the Schrödinger equation for a point nucleus. The respective relative probabilities are given in table 4.4. Here, only electron captures from the L1 shell have been considered since the wave function normalisations of the L2 and L3 shells are an order of magnitude smaller. The largest discrepancy when comparing both solutions is found for the KK-capture with an absolute difference of 2.6 %. Taking the semi-difference between both values as a systematic uncertainty would likely overestimate the actual theory uncertainty because the Schrödinger solution for a point nucleus represents the most extreme case of an approximation. Moreover, with $\gtrsim 10\,\%$ relative uncertainties on the measured event rate, XENON1T would not be sensitive to uncertainties on the KK- vs. KL-ratio on this level. Accordingly, the relativistic Dirac solutions for a finite size nucleus are considered further without assuming an uncertainty on these values. The absolute scaling of the signal is given by the half-life according to equation (1.31).

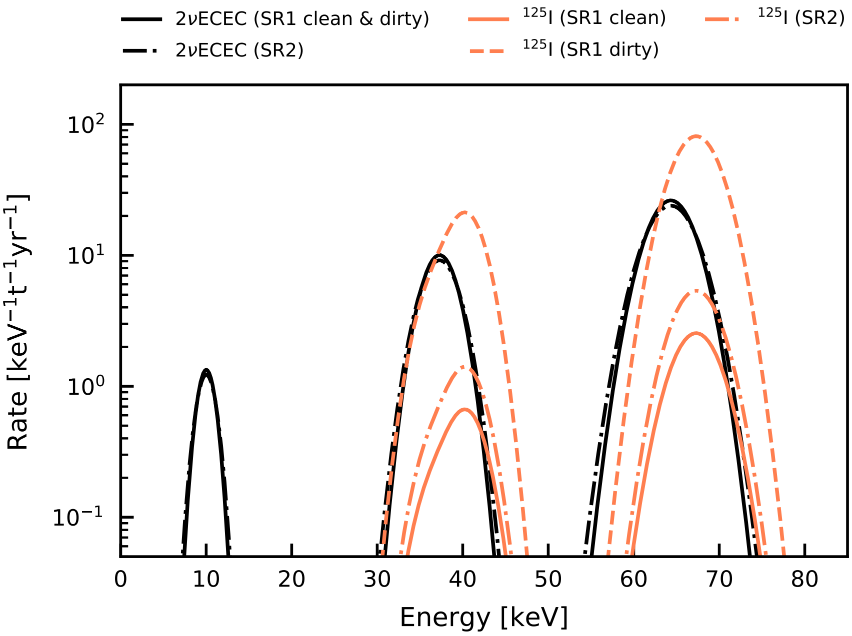

Figure 4.9: Double-electron capture signal and ^{125}I background peaks for SR1 and SR2. The signal peaks in SR1 are indicated by the solid black lines, those for SR2 by the dash-dotted black lines. The common scaling of all three peaks is given by the KK-decay rate from section 3.4 divided by $f_{2\nu\text{KK}} = 0.765$. All peak widths are governed by equation 4.1 for SR1 and equation 4.3 for SR2. The amplitudes of the ^{125}I peaks in the clean (solid coral) and dirty (dashed coral) partitions of SR1 as well as in SR2 (dash-dotted coral) follow the central values of the ^{125}I predictions from section 4.2.

4.3.1 Additional ^{125}I peaks

Additional ^{125}I peaks have to be considered together with the added signal peaks, namely those arising from L- and M-shell electron captures whose atomic deexcitation cascades are merged with the ^{125}Te 35.5 keV γ-ray [231, 245]. Accordingly, the ^{125}I background model also consists of three Gaussian peaks. The relative fractions of K-, L-, and M-shell electron captures [245] are

$$\begin{aligned} f_{^{125}\text{I,K}} &= 80.11(17)\,\%, \\ f_{^{125}\text{I,L}} &= 15.61(13)\,\%, \\ f_{^{125}\text{I,M}} &= 3.49(7)\,\%. \end{aligned} \tag{4.22}$$

Opposed to the double-electron capture peaks uncertainties are given. However, they are at the sub-percent level, so they can be safely neglected given that $\mathcal{O}(100)$ events are expected in the XENON1T data. The peak positions are obtained by adding the 35.5 keV γ-energy to the energies of the atomic relaxations [156, 264]:

$$\begin{aligned} \mu_{^{125}\text{I,K}} &= 67.3\,\text{keV}, \\ \mu_{^{125}\text{I,L}} &= 40.4\,\text{keV}, \\ \mu_{^{125}\text{I,M}} &= 36.5\,\text{keV}. \end{aligned} \tag{4.23}$$

The uncertainties on the X-ray transition energies are on the eV-level far below the XENON1T energy resolution, so they are not quoted here. The peak widths are again given by the energy resolutions in both science runs. The expected rates and their uncertainties are given as the fit constraints summarised in table 4.6.

The 2νECEC signal and ^{125}I background models are illustrated in figure 4.9. The peaks have been smeared using the energy resolutions for SR1 and SR2. The slightly worse energy resolution leads to lower amplitude, but wider double-electron capture peaks in SR2 (dash-dotted black) than in SR1 (solid black). The area contained under the curves is the same. Here, the KK decay rate from section 3.4 has been used and divided by $f_{2\nu\mathrm{KK}} = 0.765$ in order to obtain the total decay rate. The ^{125}I peaks are shown for the clean partition of SR1 (solid coral), the dirty partition of SR1 (dashed coral) and SR2 (dash-dotted coral). The scaling of the peaks was performed according to the predicted decay rates from section 4.2 taking into account the exposure of the respective datasets. The uncertainties associated with the peak scaling, the peak positions and the peak widths are not shown in order to keep the plot readable. It is evident that the clean partition of SR1 provides the best signal to background ratio with regard to ^{125}I. While there is still more expected signal for SR2 than ^{125}I background this is not the case for the dirty partition of SR1. The added L- and M-capture peaks of ^{125}I mainly affect the ^{124}Xe KL-capture. The LL-capture is not affected by ^{125}I background. Still, only 3 ± 1 events are expected in the 0.93 t-yr exposure, so this peak cannot be detected on its own. Moreover, half of the peak is removed by the 10 keV analysis threshold. As discussed in section 4.1.1 this threshold was introduced in order to avoid the choice of a signal model for the low-energy excess [14]. Such choice would introduce additional fit parameters for the excess components and it could affect fit parameters such as the dominant ^{214}Pb background. Since this would introduce a risk of biasing the KK- and KL-capture peaks while offering no potential for detecting the LL-capture, the 10 keV threshold of the fit is not lowered, but the LL-peak is kept in the model for completeness. With better knowledge of the low-energy ER spectrum in future experiments, the LL-capture will offer an event sample independent of ^{125}I modelling [18].

4.3.2 Updated fit method

Conceptually, the fit method is the same as the one outlined in section 3.2.3. Several detail changes will be discussed in this section. Technically, the framework for handling measured and MC data, cut acceptances, constraints and fitting was generalised and implemented as a python package with specific modules for each task. The resulting Modular Matching (*MoMa*) package takes care of all the steps outlined in figure 3.13 and provides auxiliary functions for uncertainty propagation, toy-MC generation and fit diagnostics. The package was made available to the XENON collaboration and has since been used for background model cross-checks in [14]. It will also be used for the ^{136}Xe neutrinoless double-β decay search in chapter 6.

As in equation (3.22) the combined cost function for the signal and background fit is the sum of the individual cost functions of the respective datasets with the constraints added on top:

$$\chi^2_{\lambda,\mathrm{combined}}(\vec{p},\vec{\kappa}) = \sum_{\mathrm{n}}^{\mathrm{datasets}} \chi^2_{\lambda,\mathrm{n}}(\vec{p}_\mathrm{n},\vec{\kappa}_\mathrm{n}) + \sum_{\mathrm{j}}^{\mathrm{constraints}} \mathrm{constraint}_\mathrm{j}. \tag{4.24}$$

The fit parameters $\vec{p}_\mathrm{n}$ and the systematic uncertainty parameters for the cut acceptances $\vec{\kappa}_\mathrm{n}$ are again included in the fit function. The fit parameters are summarised in table 4.5 for parameters that are shared among all datasets, and in table 4.6 for parameters that are exclusive to a single dataset or only shared among a fraction of the datasets. Due the decreased fit ranges the volume systematic parameters V_n as used in section 3.2.3 would have been degenerate with the background components that are now flat over the whole fit range, such as the scaling of the ^{214}Pb background. Therefore, they are not considered in the fit. Instead, the systematic uncertainties on the fiducial masses will be included in the calculation of the 2νECEC half-life. A notable difference to the definition in equation (3.22) is the summation variable n. In the original analysis the combined χ^2 was the sum of the individual χ^2 functions of the inner and outer volumes in 177.7 d of data. The extended analysis consists of four datasets: the inner and outer volume of the clean SR1 data, the inner volume of the dirty SR1 data, and the SR2 data in a single cylindrical fiducial volume. Second, the cost function has been changed from χ^2 to a generalised χ^2_λ binned Poisson likelihood [263]. This is owed to the fact that the dirty SR1 and SR2 data feature limited statistics. For each of the datasets one has:

$$\chi^2_{\lambda,\mathrm{n}} = 2\sum_{\mathrm{i}}^{\mathrm{bins}} \lambda_{\mathrm{i,n}}(\vec{p}_\mathrm{n}, \vec{\kappa}_\mathrm{n}) - N_{\mathrm{i,n}} + N_{\mathrm{i\,n}} \ln\left(\frac{N_{\mathrm{i,n}}}{\lambda_{\mathrm{i,n}}(\vec{p}_\mathrm{n}, \vec{\kappa}_\mathrm{n})}\right). \tag{4.25}$$

Here, $N_{\mathrm{i,n}}$ is the number of events in each bin. For empty bins, the logarithmic term is set to zero. The expectation value $\lambda_{\mathrm{i,n}}$ for each energy bin $E_{\mathrm{i,n}}$ is obtained with the fit functions f_n and $\tilde{f}_\mathrm{n}$ defined in equations (3.19) and (3.24):

$$\begin{aligned} \lambda_{\mathrm{i,n}}(\vec{p}_\mathrm{n}, \vec{\kappa}_\mathrm{n}) &= c_\mathrm{n} \cdot \tilde{f}_\mathrm{n}(E_{\mathrm{i,n}}, \vec{p}_\mathrm{n}, \vec{\kappa}_\mathrm{n}), \\ &= c_\mathrm{n} \cdot f_\mathrm{n}(E_{\mathrm{i,n}}, \vec{p}) \cdot \tilde{a}_\mathrm{n}(E_{\mathrm{i,n}}, \vec{\kappa}_\mathrm{n}). \end{aligned} \tag{4.26}$$

Since the fit function is defined as an event rate, the normalisation factor

$$c_\mathrm{n} = t_\mathrm{n} \cdot m_\mathrm{n} \cdot \Delta E_\mathrm{n} \tag{4.27}$$

with the live-time t_n, the fiducial mass m_n and the energy bin size ΔE_n is needed for a conversion to events per bin in each dataset.

For the acceptance parameters it was found that in general the acceptance can no longer be assumed constant at low energy with a high-energy polynomial tail (cf. section 4.1.1 and section 3.1.1). It now has to be accounted for over the whole fit range. Therefore, the acceptance treatment is modified using the acceptance parametrisations f_acc from equation (4.4) for the inner and outer volumes of SR1 and from equation (4.5) for SR2. Since these represent lower limits on the cut acceptance, any value between f_acc and unity can in principle be assumed. Using the acceptance parametrisation at the lower limit as the acceptance in the fit would be prone to a systematic underestimation of the true acceptance. This in turn would lead to a systematic overestimation of the 2νECEC decay rate. Therefore, the acceptance scaling function in the fit is defined as the mean value of f_acc and unity:

$$\tilde{a}_\mathrm{n}(E_{\mathrm{i,n}}, \vec{\kappa}_\mathrm{n}) = \frac{f_{\mathrm{acc,n}}(E_{\mathrm{i,n}}, \vec{\kappa}_\mathrm{n}) + 1}{2}. \tag{4.28}$$

The parameters $\vec{\kappa}_\mathrm{n} = (\kappa_{\mathrm{const,n}}, \kappa_{\mathrm{slope,n}})$ contain the acceptance constant and slope from the linear parametrisations in the case of SR1 datasets and just the constant for SR2. The acceptance fit parameters are summarised in table 4.6. The systematic uncertainty associated with this acceptance parametrisation is obtained in the same fashion as earlier. The difference between the mean best-fit acceptance and unity yields the upper bound of the relative systematic uncertainty on the fitted 2νECEC amplitude. The relative difference between the mean best-fit acceptance and the lower limit from the respective parametrisation $f_{\mathrm{acc,n}}$ yields the lower bound of the relative systematic uncertainty.

Energy resolution and reconstruction uncertainties are handled differently than in the analysis presented in chapter 3. The energy resolution for each dataset is determined by the parametrisations for SR1 and SR2 in equations (4.1) and (4.3). While the MC simulated spectra for materials and intrinsic backgrounds are smeared before the fit, the width

σ_E of the mono-energetic peaks centred around μ_E can vary in the fit by including the parametrization

$$\sigma_E = a_{\text{res}} \cdot \sqrt{\mu_E} + b_{\text{res}} \cdot \mu_E. \tag{4.29}$$

The resolution parameters a_{res} and b_{res} are independent for each of the three SR1 datasets and the SR2 dataset. The respective constraints are given in table 4.6.

The treatment of the energy reconstruction uncertainty was also updated. In the original analysis an energy reconstruction uncertainty was assigned to the Gaussian peaks by allowing their mean positions μ_E to move within constraints. The MC simulated spectra, on the other hand, were fixed in energy. This had two drawbacks. First, it only accounted for energy reconstruction uncertainties for the peaks. Second, the treatment mixed theoretical uncertainties on the true peak positions, such as the ones present for the KK-, KL- and LL-peaks, with systematic uncertainties on the energy reconstruction. In order to disentangle these sources of uncertainty and in order to account for reconstruction uncertainty for the full signal and background model, the treatment is changed. First, all peaks without theoretical uncertainties are now fixed to their theoretical positions. Peaks with theoretical uncertainties on μ_E are still allowed to move within the corresponding constraints. Then, the fitted energy E_{fit} for each signal and background component can be shifted from the simulated energy E by adding an energy dependent shift $\Delta E(E)$ in the fit:

$$E_{\text{fit}}(E) = E + \Delta E(E). \tag{4.30}$$

The energy shift is parametrised as

$$\Delta E(E) = a_{\text{shift}} \cdot (E - b_{\text{shift}}). \tag{4.31}$$

This linear parametrisation is taken from the high-energy analysis in chapter 6 where it has been shown that the deviations of peak positions from their expected energies are well described by a linear function. Therefore, the same treatment is applied here. The technical details on the application of the shift in the fit are described in section 6.2.3. The energy reconstruction shifts are applied independently for all datasets. This allows to account for a spatial dependence, i.e. a difference of the energy reconstruction in the inner and outer volume of the detector, as well as for an eventual temporal drift. This is obvious for SR2 where the energy reconstruction and resolution parameters are different from those determined for SR1. For SR1, the time partitions and the inner and outer volume have to be treated separately. The SR1 energy calibration was only carried out in the inner 1 t detector volume [201]. Accordingly, the energy reconstruction parameters for the outer volume could be different. Moreover, time-dependent effects of the energy reconstruction are averaged by using the full SR1 background data in order to determine g_1 and g_2 [201]. If the time-dependent corrections, such as the electron lifetime, were slightly imperfect, this would lead to a temporal drift of the energy reconstruction. Therefore, the energy reconstructions could differ for the clean and dirty partitions of SR1. Since no independent calibration data is available over the whole duration of SR1 that could be used to formulate constraints a_{shift} and b_{shift} are left unconstrained for all datasets.

In the spectral fit function f_{n} from equation (3.19) the linear interpolation at low energy has been removed. This is justified by improved absolute material background constraints from screening. The relative contributions of the different detector components to the background of each isotope are fixed as in the original analysis, but the normalisations of the simulations were changed in order to derive absolute rather than relative constraints for the material backgrounds. These constraints are discussed in detail in section 6.2.1. They show that in areas with limited MC statistics the absolute background rate from

Table 4.5: Fit parameters of the signal and background model that are shared among all four datasets, namely the inner and outer volume of the clean SR1 data, the inner volume of the dirty SR1 data and the SR2 data in the cylindrical fiducial volume.

Shared parameters

Parameter	**Description**	**Constraint**	**Unit**
Solar ν	external	1.00 ± 0.03	$1.8 \cdot 10^{-8}\,\mathrm{s^{-1}kg^{-1}}$
^{136}Xe	intrinsic	1.00 ± 0.02	$3.96\,\mu\mathrm{Bq/kg}$
^{238}U	materials	1.00 ± 0.58	scaling
^{226}Ra	materials	1.00 ± 0.48	scaling
^{232}Th	materials	1.00 ± 0.59	scaling
^{228}Th	materials	0 ± 0.59	scaling
^{60}Co	materials	1.00 ± 0.42	scaling
^{40}K	materials	1.00 ± 0.26	scaling
$\mu_{^{83m}\mathrm{Kr,misID}}$	peak mean	32.1 ± 0.6	keV
$\sigma_{^{83m}\mathrm{Kr,misID}}$	peak width	1.3 ± 0.2	keV
$f_{^{83m}\mathrm{Kr,misID}}$	peak fraction	$(2.6 \pm 0.4) \cdot 10^{-4}$	-
$\mu_{2\nu\mathrm{KK}}$	peak mean	64.33 ± 0.15	keV
$\mu_{2\nu\mathrm{KL}}$	peak mean	36.74 ± 0.48	keV
$\mu_{2\nu\mathrm{LL}}$	peak mean	9.86 ± 0.13	keV
$A_{2\nu\mathrm{ECEC}}$	peak area	-	events/kg·d

detector construction materials is low enough to not affect the fit even when only limited statistics are available. This has been tested and confirmed by applying the new fit method outlined here to the data from chapter 3. The results of the validation fits can be found in section A9 of the appendix. The origins of the constraints for the remaining fit parameters are presented in the next section.

4.3.3 Fit parameters, parameter assignment to datasets and updated constraints

The definition of the total likelihood for the signal and background model includes 54 fit parameters. Of these, 32 parameters are constrained. Fifteen parameters are shared among all datasets. They are summarised in table 4.5. The shared parameters include the background sources that are constant in time such as detector construction material backgrounds, solar neutrinos and $2\nu\beta\beta$ of ^{136}Xe. The latter two backgrounds use the constraints from section 3.2. For the material backgrounds the updated absolute constraints are used. These are discussed in detail in section 6.2 where detector materials represent the dominant background source.

Although it is reduced to the 10^{-4} level by the *MisIDS1SingleScatter* cut, a residual low-energy shoulder of misidentified ^{83m}Kr events persists in the 41.5 keV peak. Data from calibration runs over the full SR1 have shown that the fraction of remaining events compared to the area of the main peak $f_{^{83m}\mathrm{Kr,misID}}$ is the same in the inner and outer detector volume. Moreover, the residual events can be described by a Gaussian peak where the

Table 4.6: Fit parameters of the signal and background model that are exclusive to SR1 and SR2. The parameters in the first horizontal section of the table are shared among both fiducial volumes in the clean and dirty partitions of SR1. Together with the parameters from SR2 they add 4 parameters to the fit. The second section contains parameters that are shared among both volumes in SR1, but that are different for the clean and dirty partitions. Together with the SR2 parameters this section of the table adds 10 parameters to the fit. The third section contains the acceptance parameters that are the same in the clean and dirty partitions, but not shared among fiducial volumes. In total these are 5 parameters. The last section of the table contains fit parameters that are individual for each of the three SR1 datasets and the SR2 dataset. This adds 20 parameters to the fit. Parameters that are not present in the respective dataset for a given line of the table are marked as non-applicable (n. a.).

SR1 and SR2 exclusive parameters				
Parameter	**Description**	**Constraint SR1**	**Constraint SR2**	**Unit**
Shared among time partitions and volumes				
^{85}Kr	intrinsic	6.6 ± 1.1	11.9 ± 1.7	0.1 ppt
^{214}Pb	intrinsic	-	-	µBq/kg
Shared among volumes				
$^{125}\text{Xe}_{\text{dirty}}$	intrinsic	-	n. a.	µBq/kg
$^{133}\text{Xe}_{\text{clean}}$	intrinsic	-	n. a.	µBq/kg
$^{133}\text{Xe}_{\text{dirty}}$	intrinsic	-	n. a.	µBq/kg
$^{133}\text{Xe}_{\text{SR2}}$	intrinsic	n. a.	-	µBq/kg
$A_{^{125}\text{I, clean}}$	peak area	$(5.8 \pm 2.9) \cdot 10^{-5}$	n. a.	events/kg·d
$A_{^{125}\text{I, dirty}}$	peak area	$(1.8 \pm 0.3) \cdot 10^{-3}$	n. a.	events/kg·d
$A_{^{125}\text{I, SR2}}$	peak area	n. a.	$(1.2 \pm 0.8) \cdot 10^{-4}$	events/kg·d
$A_{^{131\text{m}}\text{Xe, clean}}$	peak area	-	n. a.	events/kg·d
$A_{^{131\text{m}}\text{Xe, dirty}}$	peak area	-	n. a.	events/kg·d
$A_{^{131\text{m}}\text{Xe, SR2}}$	peak area	n. a.	-	events/kg·d
Shared among time partitions				
$\kappa_{\text{const, inner}}$	acceptance	92.2 ± 0.2	n. a.	%
$\kappa_{\text{slope, inner}}$	acceptance	-6.1 ± 1.6	n. a.	10^{-3} %/keV
$\kappa_{\text{const, outer}}$	acceptance	91.4 ± 0.3	n. a.	%
$\kappa_{\text{slope, outer}}$	acceptance	-17.7 ± 3.7	n. a.	10^{-3} %/keV
$\kappa_{\text{const, SR2}}$	acceptance	n. a.	93.1 ± 0.1	%
Individual for each dataset				
$A_{^{83\text{m}}\text{Kr}}$	peak area	-	-	events/kg·d
a_{res}	resolution	0.313 ± 0.007	0.339 ± 0.010	$\text{keV}^{1/2}$
b_{res}	resolution	$(1.7 \pm 0.2) \cdot 10^{-3}$	$(2.3 \pm 1.5) \cdot 10^{-3}$	-
a_{shift}	energy shift	-	-	-
b_{shift}	energy shift	-	-	keV

constraints for the mean $\mu_{^{83\mathrm{m}}\mathrm{Kr,\,misID}}$ and standard deviation $\sigma_{^{83\mathrm{m}}\mathrm{Kr,\,misID}}$ have been derived using said calibration data. Since this peak does not follow the energy resolution parametrisation anymore after the cut, its standard deviation has to be treated differently than for the other peaks. The study on calibration data can be found in section A10 of the appendix.

The mean positions of the mono-energetic peaks from the 2νECEC of ^{124}Xe are also shared among all datasets. The uncertainties on the means are given by the theoretical uncertainties on the expected peak positions. As a last shared parameter, the 2νECEC decay rate in the form of the peak area $A_{2\nu\mathrm{ECEC}}$ is shared among all datasets.

The remaining 39 parameters that are not shared among all datasets can be grouped into four different categories that correspond to the four sections of table 4.6. The first category includes the parameters that are different for SR1 and SR2, so they are exclusively applied to datasets in either science run. Among the three SR1 datasets, the clean and dirty time partitions in the inner volume and the clean time partition in the outer volume, these parameters are shared. These four parameters – 2 per row – include backgrounds that are not constant in time, but can be time-averaged over the whole science run. Due to the purification upgrade and radon distillation outlined in section 4.1, the ^{85}Kr level averaged over SR2 is expected to be increased by a factor 1.80 ± 0.40 when compared to SR1. While the quantitative constraints from RGMS measurements can be applied to ^{85}Kr in SR1 and SR2, for ^{214}Pb only the α-activity concentrations of the ^{222}Rn and ^{218}Po parent isotopes have been measured. Their time-averaged activity concentration in SR2 is reduced by a factor of 0.76 ± 0.01 compared to SR1. It was observed in [31] and [14] that the ^{214}Pb activity concentration is not in equilibrium with the activity concentrations of the α-emitters. The reason for this disequilibrium is not fully understood, but a fraction of daughter nuclei after the α-decays could be ionised. The ions would then drift to the cathode and their decays would not occur in the fiducial volume. Plate-out of daughter isotopes on the inner detector surfaces as observed for ^{210}Pb [11] could also play a role. Accordingly, it is unclear if the reduction in ^{222}Rn for SR2 can be translated directly to a corresponding reduction in ^{214}Pb. Therefore, the ^{214}Pb fit components for both, SR1 and SR2, are left free in the fit.

The second category contains background parameters that cannot be averaged over the whole science run. This is the case for the decay rates of the neutron-activated peaks of ^{125}I and $^{131\mathrm{m}}$Xe, as well as for the spectra of ^{125}Xe and ^{133}Xe. As they are connected to calibrations, they are highly time-dependent. Therefore, they are different for the clean and dirty SR1 as well as for the SR2 data periods. Yet, they are shared between the inner and outer fiducial volume of the clean SR1 data since the neutron-activated isotopes are long-lived enough to distribute uniformly within the detector. Due to its 16.9 h half-life ^{125}Xe can only be present in datasets that are close in time to neutron calibrations. Accordingly, it is only included in the fit of the dirty SR1 data. This category adds one fit parameter per row, so 10 fit parameters in total.

The third category contains the acceptance parameters. These are assumed to be constant over time, but differ in the inner and outer volumes of the detector according to section 4.1.1. This category adds 5 parameters to the fit.

The fourth and last category consists of parameters that are both time- and position-dependent. Accordingly, they are fitted individually for each dataset. This has already been discussed for the energy-resolution and the energy-shift parameters in the preceding section. For the $^{83\mathrm{m}}$Kr decay rate $A_{^{83\mathrm{m}}\mathrm{Kr}}$ the time dependence originates from the decay of ^{83}Rb that contaminated the detector leading to the presence of $^{83\mathrm{m}}$Kr in the first place. In the first half of SR1, where most of the dirty data was taken, the decay rate is higher than in second half where most of the clean data was recorded. In SR2 the rate had further decreased with the ^{83}Rb half-life of 86.2 d [14, 213]. The spatial dependence is a feature of the event reconstruction. Since $^{83\mathrm{m}}$Kr undergoes a two-step decay, events only appear in the 41.5 keV peak if the S1s and S2s from both the 32.1 keV and the subsequent 9.4 keV isomeric transitions are merged by the data processor. While the S2s are usually merged in any case due to their μs width, the S1s can be distinguished depending on their separation in time, usually 3-4 half-lives, and the decay position in the TPC. For the same $^{83\mathrm{m}}$Kr activity in the inner and outer volumes of the TPC this leads to a different area of the 41.5 keV peak in both volumes. This consideration is not necessary for the remaining peak sources since they do not exhibit the same double-decay structure with a rather long lived second state at $T_{1/2} = 154$ ns [212–214]. This last category adds four parameters per row of the table, one for each dataset, which adds up to 20 parameters in total.

4.4 Discovery of 2νECEC

The combined background and signal model is fitted to all four datasets simultaneously by minimising the value of χ^2_λ from equation (4.24). The minimisation is carried out with the MIGRAD minimiser in iMinuit [265]. The resulting best-fit background model, components and data spectra are shown in figure 4.10. Each of the four panels shows the result for one dataset: the clean inner, clean outer and dirty inner SR1 data, as well as the SR2 data. The panels are segmented into the spectrum, best-fit components and full fit function at the top and the residuals from square-roots of the χ^2_λ summands at the bottom. The clean inner and outer spectra of SR1 are shown and fitted with a 1 keV binning while the dirty inner SR1 and SR2 datasets use a 2 keV binning owed to the lower exposure and statistics[6]. The uncertainties on the data points are 68.3 % Feldman & Cousins confidence intervals on the counts per bin. These have been converted to the rate on the y-axis and are only used for illustration.

The spectra in the inner and outer volumes of the clean SR1 partition are featureless except for the mono-energetic peaks from the 2νECEC signal, the $^{83\mathrm{m}}$Kr peak and the neutron-activation peaks. The spectrum in the outer volume has a larger slope owed to the larger material background contribution in this data. The dirty and SR2 spectra exhibit the expected larger contributions of neutron-activated peaks as well as the step from the merged $\beta + \gamma$ signature of ^{133}Xe. Due to the selection of datasets at least 50 d away from neutron calibrations, the SR2 ^{133}Xe step is at a lower level. Overall, the neutron activation contribution in SR2 is lower than in the dirty SR1 data, but higher than in the clean SR1 data. Notably, the SR2 data exhibits the smallest $^{83\mathrm{m}}$Kr peak of all datasets since the ^{83}Rb contamination had decreased with its 86.2 d half-life [14, 213]. The low-energy shoulder of the 41.5 keV peak is not visible since these events have been largely cut from the data. The fit describes the data well with

$$\frac{\chi^2_\lambda}{\mathrm{ndf}} = \frac{517.9}{508} \approx 1.02. \tag{4.32}$$

The standard deviation of a χ^2 distribution with 508 degrees of freedom would be $\sigma_{\chi^2} = \sqrt{2/\mathrm{ndf}} = 0.06$. The above goodness of fit measure includes the contributions of the constraints

$$\Sigma = \sum_{\mathrm{j}}^{\text{constraints}} \text{constraint}_\mathrm{j} = 7.8 \tag{4.33}$$

that will be discussed below. Without considering the constraints in the calculations of χ^2_λ and ndf, the quality of the fit can be quantified solely on the deviation between the best-fit

---

[6] Different binnings of 0.5 keV, 1.0 keV, 1.5 keV and 2.0 keV were tested for all datasets, but these did not significantly affect the fit results. Relative differences in the calculated 2νECEC half-lives were of $\mathcal{O}(1)$ %.

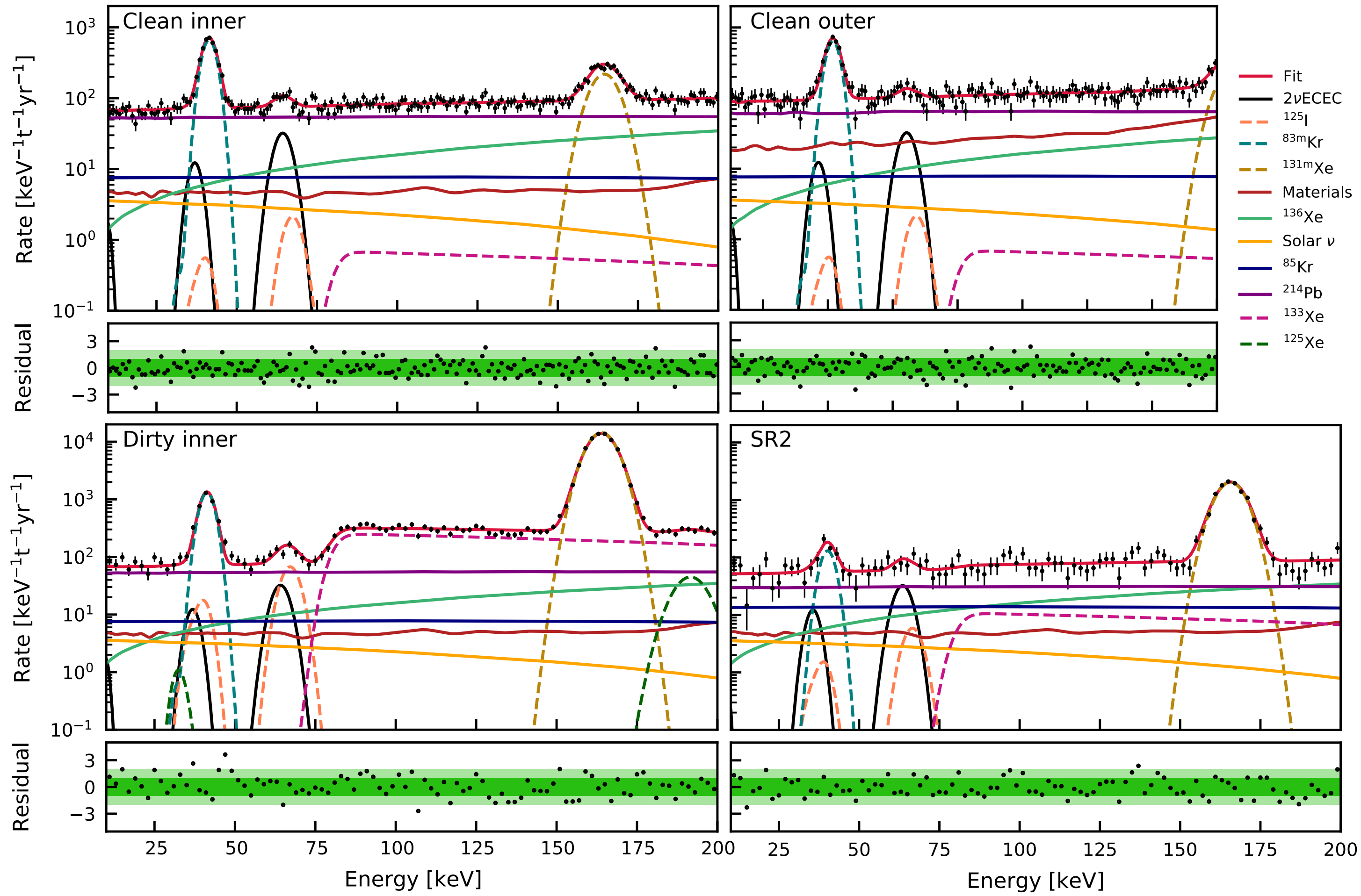

Figure 4.10: Fit of the signal and background models to the measured energy spectra. Uncertainties on the data points are. 68.3 % Feldman & Cousins confidence intervals [262] on the number of counts per bin scaled with the exposure. The final exposure of 0.93 t-yr is partitioned into the clean inner (**top left**), clean outer (**top right**) and dirty inner (**bottom left**) datasets of SR1 as well as the clean data of SR2 (**bottom right**). The four datasets were fitted simultaneously. The sum spectrum is indicated by the solid red line with $\chi^2_\lambda/\mathrm{ndf} = 517.9/508 \approx 1.02$. The residuals from the square-roots of the χ^2_λ summands are shown individually for each volume. Background sources constant in time are shown as solid lines while those that vary over time are shown as dashed lines. The 2νECEC signal peaks are indicated by solid black lines.

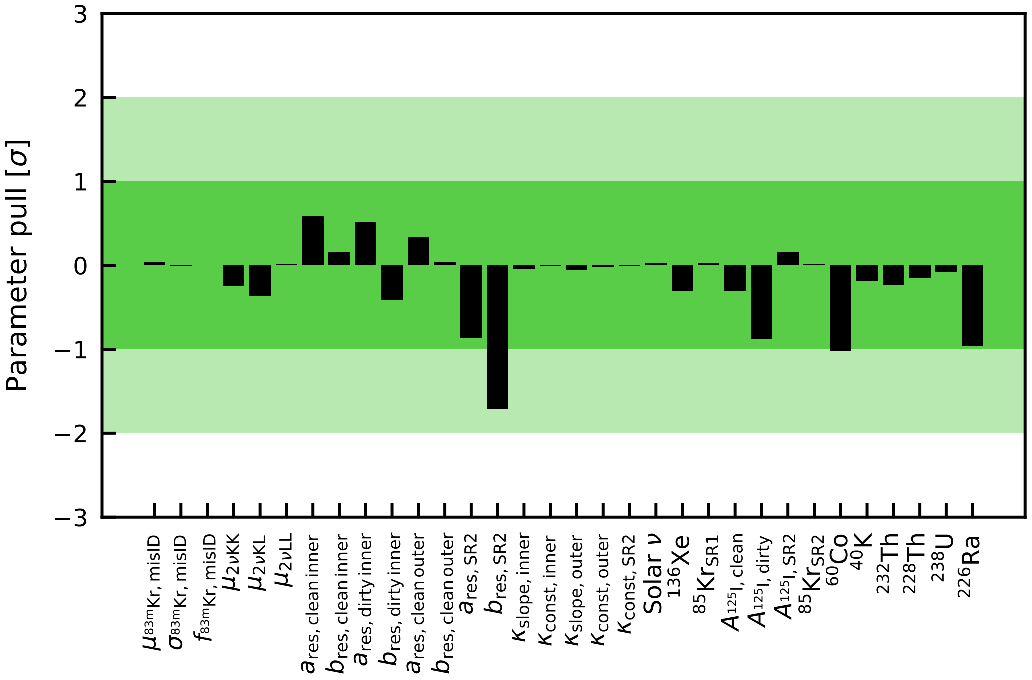

Figure 4.11: Parameter pulls of the 32 constrained parameters from the fit to the four datasets from SR1 and SR2 in the respective fiducial volumes and time partitions. The pulls are defined in equation (4.35).

model and the data. With the number of data points n_{data} and the number of fit parameters n_{par} this yields

$$\frac{\chi^2_\lambda - \Sigma}{n_{\mathrm{data}} - n_{\mathrm{par}}} = \frac{510.1}{476} \approx 1.07. \tag{4.34}$$

The standard deviation of the corresponding χ^2 distribution would be $\tilde{\sigma}_{\chi^2} = 0.06$, so the data is still well described. The residuals for all datasets are symmetrically distributed around zero and do not exhibit distinct features.

The parameter pulls of the fit are shown in figure 4.11. The pulls are defined as the deviation of the fitted parameter $p_{\mathrm{fit,\,j}}$ from the expected value $p_{\mathrm{expected,\,j}}$ normalised by the uncertainty Δp_{j} of the respective constraint[7] with

$$\mathrm{pull_j} = \frac{(p_{\mathrm{fit,\,j}} - p_{\mathrm{expected,\,j}})}{\Delta p_{\mathrm{j}}}. \tag{4.35}$$

The squares of the pulls correspond to the constraints from the combined χ^2_λ binned likelihood in equation (4.24), so one has

$$\Sigma = \sum_{\mathrm{j}} \mathrm{pull}^2_{\mathrm{j}} = \sum_{\mathrm{j}} \mathrm{constraint_j}. \tag{4.36}$$

None of the 32 pulls exceed 2σ and the sum of the squared pulls is $\Sigma = 7.8$. For n_{pull} pulls where Δp_{j} originate from symmetric 68.3 % confidence intervals one would expect the pulls to follow a normal distribution leading to $\Sigma \cong n_{\mathrm{pull}}$. This could indicate that the fit has not converged to the global minimum or that the uncertainties in the pull terms have

---

[7] While the pulls are unitless, in the plots they are given in units of $\sigma = \Delta p_{\mathrm{j}}$.

Table 4.7: Best-fit parameters of the signal and background model that are shared among all datasets with their fit constraints and units.

Parameter	**Value**	**Constraint**	**Unit**
Solar ν	1.00 ± 0.02	1.00 ± 0.02	scaling
^{136}Xe	0.99 ± 0.03	1.00 ± 0.03	scaling
^{238}U	0.96 ± 0.39	1.00 ± 0.58	scaling
^{226}Ra	0.54 ± 0.15	1.00 ± 0.48	scaling
^{232}Th	0.86 ± 0.42	1.00 ± 0.59	scaling
^{228}Th	-0.06 ± 0.38	0.00 ± 0.59	scaling
^{60}Co	0.57 ± 0.18	1.00 ± 0.42	scaling
^{40}K	0.95 ± 0.21	1.00 ± 0.26	scaling
$\mu_{^{83\mathrm{m}}\mathrm{Kr,misID}}$	32.1 ± 0.6	32.1 ± 0.6	keV
$\sigma_{^{83\mathrm{m}}\mathrm{Kr,misID}}$	1.3 ± 0.2	1.3 ± 0.2	keV
$f_{^{83\mathrm{m}}\mathrm{Kr,misID}}$	$(2.6 \pm 0.4) \cdot 10^{-4}$	$(2.6 \pm 0.4) \cdot 10^{-4}$	-
$\mu_{2\nu\mathrm{KK}}$	64.30 ± 0.13	64.33 ± 0.13	keV
$\mu_{2\nu\mathrm{KL}}$	37.04 ± 0.63	37.29 ± 0.68	keV
$\mu_{2\nu\mathrm{LL}}$	10.01 ± 0.13	10.01 ± 0.13	keV
$A_{2\nu\mathrm{ECEC}}$	$(7.67 \pm 1.24) \cdot 10^{-4}$	-	events/kg·d

been overestimated. A convergence failure was excluded by examining the χ^2_λ profiles of all variables, by lowering the threshold for the estimated distance to the cost function minimum in iMinuit, and by varying the optimisation strategy. The smallness of Σ can be explained by taking a closer look at the individual pulls. First, for some parameters Δp_j does not correspond to a statistical confidence interval from a measurement. This is the case for the uncertainties on the double-electron capture peak positions $\mu_{2\nu\mathrm{KK}}$, $\mu_{2\nu\mathrm{KL}}$, $\mu_{2\nu\mathrm{LL}}$ as well as for the solar neutrino scaling. These are barely moved away from their expected values. For other parameters, the fit is more sensitive to the constraint than it is to the change of the fit function by that parameter. This is the case for the parameters that describe the remaining part of the misidentified $^{83\mathrm{m}}$Kr peak. Since the total area of the peak is more than two order of magnitude below the signal rate, changes in its parameters change the constraint terms more strongly than the residuals. Thus, the best-fit parameter is at the expected value of the constraint. This is also the case for constrained background components that have the same shape as an unconstrained background component. This is the case for the SR1 and SR2 ^{85}Kr parameters. In the chosen fit range, the spectrum of this constrained background has almost the same shape as the unconstrained ^{214}Pb spectrum. Accordingly, the fit stays at the expected parameter value and manages the residuals by modifying the ^{214}Pb parameter. The same argument can be made for the acceptance parameters as well as for the ^{136}Xe background scaling. Therefore, the smallness of Σ does not indicate a problem with the fit.

The best-fit parameters are given in table 4.7 for the shared parameters and in table 4.8 for the exclusive parameters. No unexpected parameter values are observed and a subset of parameters is discussed in particular. For one, the amplitudes of the ^{125}I peaks correspond to the expectations. While in the clean and dirty partitions of SR1 14 % and 11 % lower rates are measured than expected, this is well within the uncertainties. For SR2 the best-fit rate is 17 % larger than expected, but also within the 67 % relative uncertainty. The best-

Table 4.8: Best-fit parameters of the signal and background model that are not shared among all datasets or exclusive to one dataset with their fit constraints and units.

Parameter	**Value**	**Constraint**	**Unit**
$^{214}\mathrm{Pb}_{\mathrm{SR1}}$	9.4 ± 0.3	-	μBq/kg
$^{214}\mathrm{Pb}_{\mathrm{SR2}}$	5.3 ± 0.6	-	μBq/kg
$^{85}\mathrm{Kr}_{\mathrm{SR1}}$	6.6 ± 1.0	6.6 ± 1.1	0.1 ppt
$^{85}\mathrm{Kr}_{\mathrm{SR2}}$	11.9 ± 1.4	11.9 ± 1.7	0.1 ppt
$^{125}\mathrm{Xe}_{\mathrm{dirty}}$	1.05 ± 0.35	-	μBq/kg
$^{133}\mathrm{Xe}_{\mathrm{clean}}$	$(3.4 \pm 9.5) \cdot 10^{-3}$	-	μBq/kg
$^{133}\mathrm{Xe}_{\mathrm{dirty}}$	1.24 ± 0.03	-	μBq/kg
$^{133}\mathrm{Xe}_{\mathrm{SR2}}$	0.05 ± 0.02	-	μBq/kg
$A_{^{125}\mathrm{I,clean}}$	$(5.0 \pm 2.8) \cdot 10^{-5}$	$(5.8 \pm 2.9) \cdot 10^{-5}$	events/kg·d
$A_{^{125}\mathrm{I,dirty}}$	$(1.6 \pm 0.2) \cdot 10^{-3}$	$(1.8 \pm 0.3) \cdot 10^{-3}$	events/kg·d
$A_{^{125}\mathrm{I,SR2}}$	$(1.4 \pm 0.8) \cdot 10^{-4}$	$(1.2 \pm 0.8) \cdot 10^{-4}$	events/kg·d
$A_{^{131}\mathrm{Xe,clean}}$	$(6.5 \pm 0.3) \cdot 10^{-3}$	-	events/kg·d
$A_{^{131}\mathrm{Xe,dirty}}$	$(4.26 \pm 0.03) \cdot 10^{-1}$	-	events/kg·d
$A_{^{131}\mathrm{Xe,SR2}}$	$(5.9 \pm 0.2) \cdot 10^{-2}$	-	events/kg·d
$\kappa_{\mathrm{slope,inner}}$	$(-6.2 \pm 1.5) \cdot 10^{-5}$	$(-6.1 \pm 1.6) \cdot 10^{-5}$	keV^{-1}
$\kappa_{\mathrm{const,inner}}$	0.922 ± 0.002	0.922 ± 0.002	
$\kappa_{\mathrm{slope,outer}}$	$(-17.8 \pm 3.7) \cdot 10^{-5}$	$(-17.7 \pm 3.7) \cdot 10^{-5}$	keV^{-1}
$\kappa_{\mathrm{const,outer}}$	0.914 ± 0.003	0.914 ± 0.003	-
$\kappa_{\mathrm{const,SR2}}$	0.931 ± 0.001	0.931 ± 0.001	-
$A_{^{83m}\mathrm{Kr,clean\ inner}}$	$(9.7 \pm 0.3) \cdot 10^{-3}$	-	events/kg·d
$A_{^{83m}\mathrm{Kr,clean\ outer}}$	$(9.1 \pm 0.4) \cdot 10^{-3}$	-	events/kg·d
$A_{^{83m}\mathrm{Kr,dirty\ inner}}$	$(1.90 \pm 0.06) \cdot 10^{-2}$	-	events/kg·d
$A_{^{83m}\mathrm{Kr,SR2}}$	$(1.9 \pm 0.4) \cdot 10^{-3}$	-	events/kg·d
$a_{\mathrm{res,clean\ inner}}$	0.317 ± 0.005	0.313 ± 0.007	$\mathrm{keV}^{1/2}$
$b_{\mathrm{res,clean\ inner}}$	$(1.7 \pm 0.2) \cdot 10^{-3}$	$(1.7 \pm 0.2) \cdot 10^{-3}$	-
$a_{\mathrm{res,clean\ outer}}$	0.315 ± 0.006	0.313 ± 0.007	$\mathrm{keV}^{1/2}$
$b_{\mathrm{res,clean\ outer}}$	$(1.7 \pm 0.2) \cdot 10^{-3}$	$(1.7 \pm 0.2) \cdot 10^{-3}$	-
$a_{\mathrm{res,dirty\ inner}}$	0.317 ± 0.002	0.313 ± 0.007	$\mathrm{keV}^{1/2}$
$b_{\mathrm{res,dirty\ inner}}$	$(1.6 \pm 0.1) \cdot 10^{-3}$	$(1.7 \pm 0.2) \cdot 10^{-3}$	-
$a_{\mathrm{res,SR2}}$	0.330 ± 0.006	0.339 ± 0.010	$\mathrm{keV}^{1/2}$
$b_{\mathrm{res,SR2}}$	$(-3.1 \pm 5.5) \cdot 10^{-4}$	$(2.3 \pm 1.5) \cdot 10^{-3}$	-
$a_{\mathrm{shift,clean\ inner}}$	$(5.5 \pm 2.1) \cdot 10^{-3}$	-	-
$b_{\mathrm{shift,clean\ inner}}$	56.7 ± 12.1	-	keV
$a_{\mathrm{shift,clean\ outer}}$	$(-1.6 \pm 3.1) \cdot 10^{-3}$	-	-
$b_{\mathrm{shift,clean\ outer}}$	59.3 ± 60.6	-	keV
$a_{\mathrm{shift,dirty\ inner}}$	$(1.8 \pm 0.6) \cdot 10^{-3}$	-	-
$b_{\mathrm{shift,dirty\ inner}}$	137.2 ± 15.4	-	keV
$a_{\mathrm{shift,SR2}}$	$(2.5 \pm 0.2) \cdot 10^{-2}$	-	-
$b_{\mathrm{shift,SR2}}$	93.7 ± 4.7	–	keV

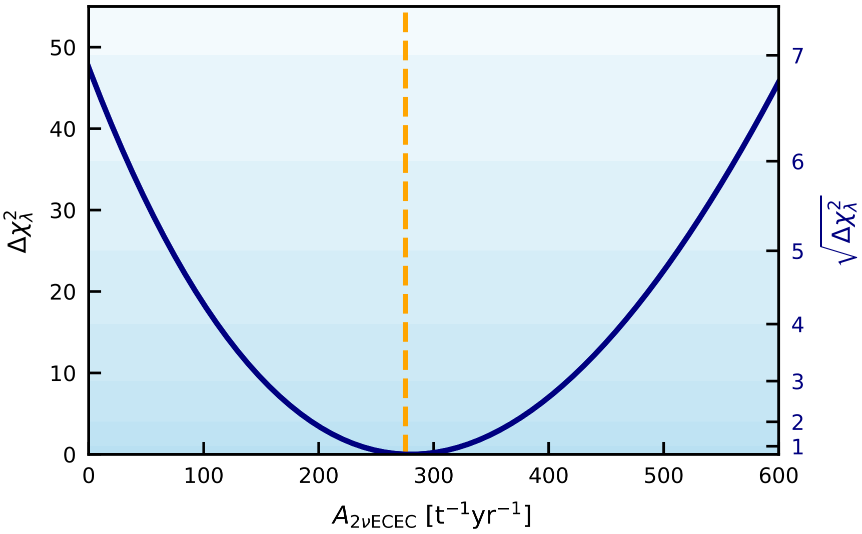

Figure 4.12: The χ^2_λ profile of the double-electron capture decay rate $A_{2\nu\mathrm{ECEC}}$ (solid blue). The minimum at $A_{2\nu\mathrm{ECEC}} = 280$ events/t·yr is indicated by the dashed orange line. The left y-axis gives the $\Delta\chi^2_\lambda$ between the best-fit rate at the minimum and the respective value of $A_{2\nu\mathrm{ECEC}}$ on the x-axis. The right y-axis marks the significance level from the comparison to a null-result. The integer significance steps are marked by the blue-shaded areas. The significance according to the profile is 6.8σ.

fit ^{214}Pb activity concentration in SR1 is close to the expected 10 µBq/kg with $^{214}\mathrm{Pb}_{\mathrm{SR1}} = (9.4 \pm 0.3)$ µBq/kg. For SR2 the best-fit activity concentration is $^{214}\mathrm{Pb}_{\mathrm{SR2}} = (5.3 \pm 0.6)$ µBq/kg, so the ratio between SR2 and SR1 is 0.56 ± 0.07. This is in tension with the expected 0.76 ± 0.01, but as stated before, a reduction in the ^{222}Rn activity concentration inside the detector does not necessarily translate to the same reduction in the activity concentration of ^{214}Pb. Moreover, there is the aforementioned degeneracy with the constrained ^{85}Kr component in the fit. If this component were overestimated, it would reduce the best-fit ^{214}Pb level.

The significance of the 2νECEC signal is derived from the χ^2_λ profile of $A_{2\nu\mathrm{ECEC}}$ as shown in figure 4.12. The best-fit double-electron capture rate $A_{2\nu\mathrm{ECEC}}$ from the KK-, KL- and LL-capture peaks is

$$\begin{aligned} A_{2\nu\mathrm{ECEC}} &= (7.67 \pm 1.24) \cdot 10^{-4}\ \mathrm{events/kg{\cdot}d} \\ &\approx (280 \pm 45)\ \mathrm{events/t{\cdot}yr}. \end{aligned} \tag{4.37}$$

The difference $\Delta\chi^2_\lambda \approx 46.9$ between the best-fit rate and a null result yields a significance of 6.8σ for the presence of a double-electron capture signal. This marks the first significant detection of a two-neutrino double-electron capture in any isotope that exceeds the 5σ discovery threshold [4]. Moreover, it is the first measurement of this process in any isotope that leverages the signatures of the KL- and LL-captures.

A total of $N_{2\nu\mathrm{ECEC}} = (260 \pm 42)$ events is found in the 0.93 t-yr exposure. This is inserted into equation (3.39) in order to calculate the 2νECEC half-life

$$T_{1/2}^{2\nu\mathrm{ECEC}} = (1.13 \pm 0.18_{\mathrm{stat}} \pm 0.05_{\mathrm{sys}}) \cdot 10^{22}\ \mathrm{yr}. \tag{4.38}$$

Here, $M_A = 131.293$ g/mol [180], $\eta^{^{124}\mathrm{Xe}}_{\mathrm{meas}} = (9.94 \pm 0.14_{\mathrm{stat}} \pm 0.15_{\mathrm{sys}}) \cdot 10^{-4}$ [207], and the respective fiducial masses and live-times from section 4.1.2 were used. Since the acceptance is

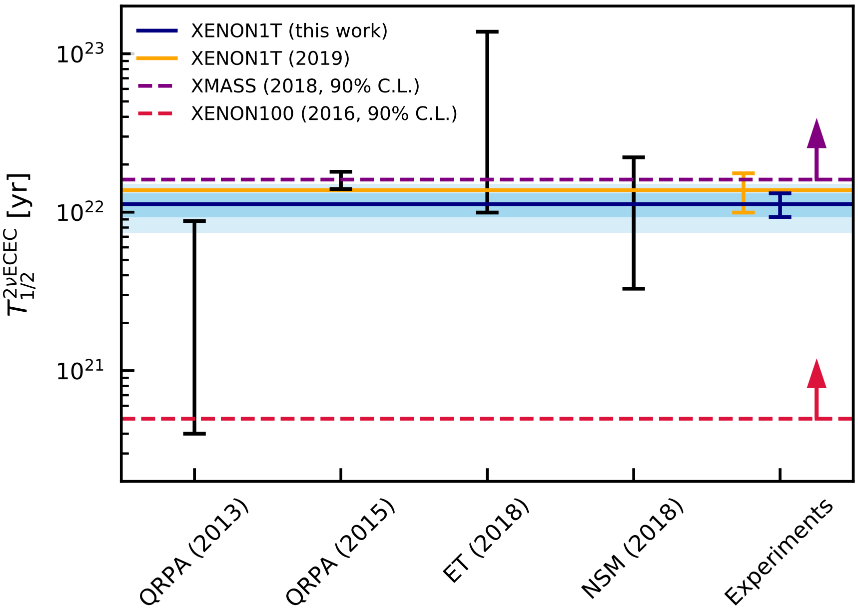

Figure 4.13: Comparison of the 2νECEC half-life from this work with theoretical predictions and the experimental 90 % C.L. lower limits from XMASS [145] (dashed purple) and XENON100 [254] (dashed red). The published result from the previous XENON1T analysis is indicated by the solid orange line [31]. The value was scaled down by $f_{2\nu\mathrm{KK}}$ [89]. The uncertainty is given by the error bars on the right of the plot. The updated central value of the measured half-life is shown as the solid blue line. The 1σ and 2σ uncertainty bands are indicated in blue and light blue, respectively. Four results from nuclear structure calculations [106, 108, 110] are indicated by the black uncertainty bars. An agreement within 2σ is found for all measurements.

already included in the fit function, $\epsilon = 1$ was used. For comparison with the result from chapter 3 the fractional KK-capture half life is calculated using $f_{2\nu\mathrm{KK}}$. The resulting half-life is

$$T_{1/2}^{2\nu\mathrm{KK}} = (1.47 \pm 0.24_{\mathrm{stat}} \pm 0.07_{\mathrm{sys}}) \cdot 10^{22}\ \mathrm{yr}. \tag{4.39}$$

The systematic uncertainty on the half-life has three individual contributions, namely the cut acceptance, exposure and the ^{124}Xe isotopic abundance. The respective uncertainty contributions are obtained by Gaussian uncertainty propagation with equation 3.39. The uncertainty on the acceptance is obtained by calculating the average acceptance over the whole energy range for each dataset. The difference of the exposure weighted sum of these average values from unity is taken as the systematic uncertainty $\Delta\epsilon$. The uncertainty on the exposure Δmt is obtained from the fiducial volume uncertainties of each dataset that are multiplied with the corresponding live-times and added in quadrature. For $\Delta\eta$ the statistical and systematic uncertainties of η are added in quadrature as in [31, 207]. With this the individual contributions to the systematic uncertainties on $T_{1/2}^{2\nu\mathrm{KK}}$ are:

$$\begin{aligned} \Delta T_{1/2,\epsilon}^{2\nu\mathrm{KK}} &= 0.05 \cdot 10^{22}\ \mathrm{yr}, \\ \Delta T_{1/2,mt}^{2\nu\mathrm{KK}} &= 0.003 \cdot 10^{22}\ \mathrm{yr}, \\ \Delta T_{1/2,\eta}^{2\nu\mathrm{KK}} &= 0.02 \cdot 10^{22}\ \mathrm{yr}. \end{aligned} \tag{4.40}$$

The total systematic uncertainty is obtained by adding the individual components in quadrature. The systematic uncertainty contributions for $T_{1/2}^{2\nu\mathrm{ECEC}}$ can be calculated by multiplying the values for $T_{1/2}^{2\nu\mathrm{KK}}$ with $f_{2\nu\mathrm{KK}}$.

In figure 4.13, the half-life is compared with the results from the same four theoretical approaches as in section 3.4. These still are the most recent theory results. Due to the shorter half-life compared to the former analysis, the agreement with the QRPA (2013) calculation is improved [108]. At the same time the new half-life value is 2σ below the lower bound of the QRPA (2015) result [110] . Both, the ET and the NSM calculations are compatible with the updated half-life [106]. Here, the result from this work is at the lower bound of the ET half-life range, while for the NSM it is in the upper half of the range.

While the central value of the first XENON1T result was less than 1σ below the 90 % C.L. lower limit of XMASS, the updated result is more than 2σ below the XMASS limit. Accounting for the statistical and systematic uncertainties, there is considerable tension between both results. A wrongly estimated cut-acceptance in either analysis would lead to such a discrepancy, yet this is already included in this analysis. Given that the fit in this work reproduces the expected background levels of all components, this is unlikely and small discrepancies are accounted for in the systematic uncertainty. Another source of the discrepancy could be an overestimation of the ^{125}I background in the XMASS analysis. While the double-K capture peak of ^{124}Xe and the K+γ peak of ^{125}I are separated by more than $1\sigma_E$ in XENON1T, this is not the case in XMASS. Here, both peaks almost fully overlap, so the background fit relies heavily on the ^{125}Xe production rate. If this rate were overestimated, for example due to an overestimated thermal neutron flux at the experimental site, this would lead to an overestimation of the ^{125}I decay rate. Due to the degeneracy of both peaks this would push the fitted double-electron capture rate down leading to an apparently longer half-life. Due to the better energy resolution and peak separation in XENON1T the fit in this work is less susceptible to this. A final verdict on the matter will be possible with an independent detection by an upcoming next-generation xenon TPC such as LZ [151] or XENONnT [18].

4.5 Consistency with the published XENON1T result

In the previous section the updated result on $T_{1/2}^{2\nu\mathrm{ECEC}}$ and $T_{1/2}^{2\nu\mathrm{KK}}$ was compared to theoretical values and limits from other experiments. This section discusses if the current result

$$T_{1/2,\mathrm{updated}}^{2\nu\mathrm{KK}} = (1.47 \pm 0.24_{\mathrm{stat}} \pm 0.07_{\mathrm{sys}}) \cdot 10^{22}\ \mathrm{yr} \tag{4.41}$$

is consistent with the published result from [31]:

$$T_{1/2,\mathrm{published}}^{2\nu\mathrm{KK}} = (1.8 \pm 0.5_{\mathrm{stat}} \pm 0.1_{\mathrm{sys}}) \cdot 10^{22}\ \mathrm{yr}. \tag{4.42}$$

These two values cannot be compared in terms of their statistical uncertainties, because the majority of the underlying data taking runs is shared between both analyses. The total overlap contains a live-time of 164.3 d in the full 1.5 t superellipsoid which amounts to a 0.68 t-yr exposure, while the total exposures are 0.93 t-yr for the updated analysis and 0.73 t-yr for the published analysis, respectively. Therefore, both results are partly correlated from the data selection alone.

However, there is no full correlation even in the overlapping exposure since both analyses use different versions of the PAX raw data processor, a different energy and position reconstruction for individual events, and different cuts on the data. The differences are summarised in table 4.9. The changes to the PAX 6.10.1 data processor are mostly relevant for analyses in the MeV energy range [201] and will be discussed in chapter 6. Since the

Table 4.9: Comparison of the datasets in the published double-electron capture analysis from [31], discussed in chapter 3, and the updated analysis.

	Published	**Updated**
PAX version	6.8.0	6.10.1
Live time	177.7 d (SR1)	171.2 d (clean SR1), 55.8 d (dirty SR1), 24.3 d (SR2)
Fiducial volume	1.5 t superellipsoid	1.5 t superellipsoid (clean SR1), 1 t cylinder (dirty SR1, SR2)
Cuts	Subset from [12], table 3.1	Subset from [14], table 4.1
Position reconstruction	Neural network [12]	Updated neural network [201]
Energy reconstruction	z-dependent g_1 and g_2 [31]	z-dependent g_1 and g_2 with reconstruction improvements [201]

energy calibration of the updated analysis relies on γ-lines at MeV-energies such as those from ^{60}Co, improvements on the energy reconstruction in the 100 keV range of this analysis are also expected. At the event-level this means that the same events can be reconstructed at different energies, e.g. inside or outside a double-electron capture peak. In turn, this impacts the degree of correlation between both datasets. The same argument holds for the different position reconstruction algorithms that can reconstruct the same event inside the fiducial volume in one dataset, but outside in the other. The newer and optimised set of cuts for the updated analysis [14] leads to different cut acceptances in both datasets. At the event level this means that events present in one dataset do not appear in the other, again reducing the degree of correlation.

In a first step, the effect of the new model on the old PAX 6.8.0 data is investigated. For this the validation fits of the new signal and background model from the updated analysis on the data from the published analysis can be used. These are summarised in section A9 of the appendix. A half-life of

$$T^{2\nu\mathrm{KK}}_{1/2,\mathrm{validation}} = (1.72 \pm 0.42_{\mathrm{stat}} \pm 0.07_{\mathrm{sys}}) \cdot 10^{22}\ \mathrm{yr} \tag{4.43}$$

was found, so the updated method yields a lower half-life than the old method on the same data. It was found that removing the KL- and LL-signal peaks leads to

$$T^{2\nu\mathrm{KK}}_{1/2,\mathrm{validation,\,KK\text{-}only}} = (1.77 \pm 0.45_{\mathrm{stat}} \pm 0.07_{\mathrm{sys}}) \cdot 10^{22}\ \mathrm{yr}, \tag{4.44}$$

which is the same result as in the original analysis before rounding to the first decimal. This does not only validate the new fit method, but also shows that not including the KL- and LL-capture peaks in the model leads to an overestimation of the half-life by $0.05 \cdot 10^{22}$ yr in the published analysis. Since the half-life of the ^{124}Xe double-electron capture was not known at the time of the published analysis, it was assumed that XENON1T would have no sensitivity to the KL- and LL-captures due to their lower relative frequencies. Moreover, due to the misidentified $^{83\mathrm{m}}$Kr events on the left flank of the 41.5 keV peak it was expected that these events would be fully obscured.

After accounting for this systematic effect, a $0.25 \cdot 10^{22}$ yr difference between the published and updated results remains. The origin of this difference is further investigated by quantifying the correlation of the old and new datasets. In a first step, the two datasets are

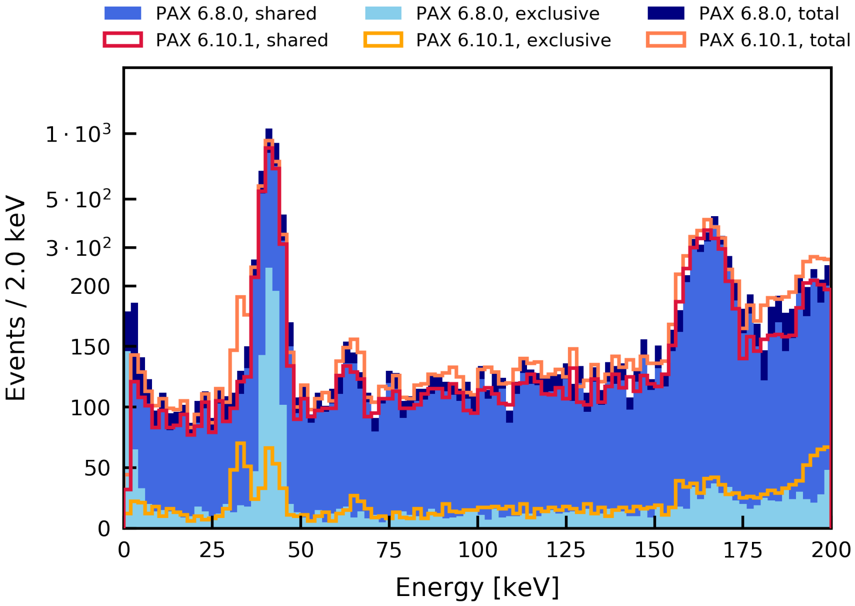

Figure 4.14: Energy histograms for PAX 6.8.0 and PAX 6.10.1 data from the overlapping data-taking runs that are used in the published analysis [31] as well as in this work. Only events in the 1.5 t fiducial superellipsoid are selected. The solid dark blue histogram and the coral line histogram show the full data in PAX 6.8.0 and PAX 6.10.1, respectively. The events that are present in the old and new data are shown in medium blue and red. The events that are exclusively contained in either dataset are shown in light blue and orange.

reduced to the overlapping data-taking runs, i.e. the data taking runs used in both analyses, in SR1 within the 1.5 t fiducial superellipsoid. Figure 4.14 shows the energy histograms from 0 to 200 keV in these datasets for the old PAX 6.8.0 and new PAX 6.10.1 data. For better comparability the *MisIDS1SingleScatter* cut has not been applied to the PAX 6.10.1 data. The histograms for events contained in both datasets and for events contained only in either dataset are also shown.

There are several notable differences between the datasets. For instance, there are less 41.5 keV $^{83\mathrm{m}}$Kr events in the PAX 6.10.1 data while more events are misreconstructed into the low-energy shoulder of the peak. This can be explained by the tuning of the peak clustering in the newer PAX version that leads to less merging of subsequent S1s. Accordingly fewer events appear in the merged 41.5 keV peak. On the other hand, the larger number of 9.4 keV S1s that can be separated allow for more misidentification of these signals as S2s, so the low-energy shoulder of the 41.5 keV peak becomes more peak-like. In general, the events that are exclusively found in the newer data appear more peak-like, also in the KK-capture/^{125}I region. This hints at the improved energy reconstruction and energy resolution in PAX 6.10.1. As an example, the $^{131\mathrm{m}}$Xe peak at 163.9 keV is shifted to higher energies in the PAX 6.8.0 data while for the PAX 6.10.1 data it is found at the expected energy. Even though features in the older data appear smoother, the LowER excess from [14] is present in both datasets. Since the cuts below 10 keV are less stringent in the PAX 6.8.0 data, the exclusive dataset contains more low-energy events from nuclear recoils and misreconstructed ^{210}Pb decays from the PTFE surfaces [11].

Most importantly, except for the energy region below 10 keV and the $^{83\mathrm{m}}$Kr peak, there are less events in the PAX 6.8.0 data. According to the parametrisations in equations (3.1)

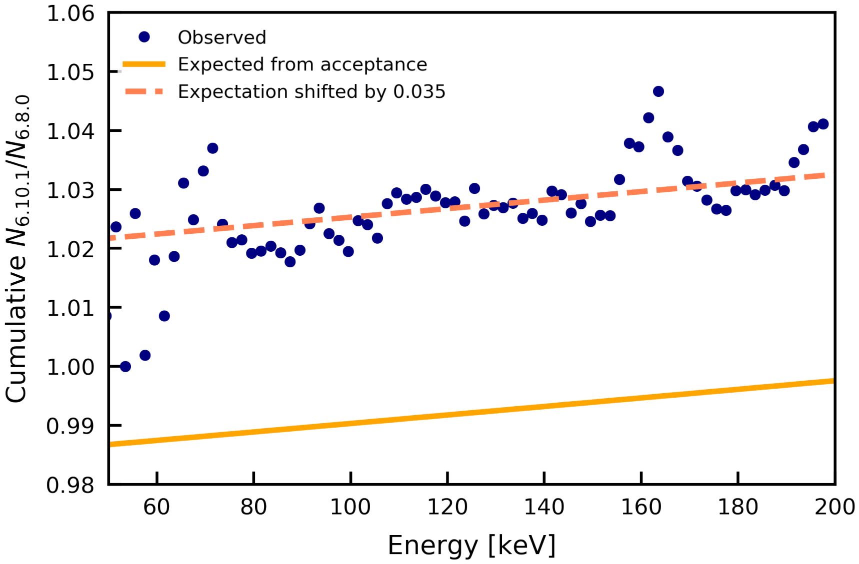

Figure 4.15: Ratio of the cumulative histograms of overlapping PAX 6.10.1 and PAX 6.8.0 data in the 1.5 t fiducial superellipsoid (blue markers). The energy range is 50 to 200 keV in 5 keV bins. The expected ratio from the cut acceptance parametrisations in equations (3.1) and (4.6) is indicated by the solid orange line. This needs to be shifted upwards by 3.5 % in order to describe the data (dashed coral line). No uncertainties are shown.

and (4.6) a higher acceptance is expected in the PAX 6.8.0 data. This observation is quantified by making cumulative histograms of the full overlapping PAX 6.8.0 and PAX 6.10.1 datasets starting at 50 keV in order to avoid a bias from the $^{83\mathrm{m}}$Kr peak. The ratio of both histograms is shown in figure 4.15 together with the expected ratio from the acceptances. In order to describe the observed ratio, the expected ratio has to be shifted upwards by ~ 3.5 %. This indicates a lower cut acceptance in the PAX 6.8.0 data. Since the acceptance parametrisations resemble lower limits the difference can be explained by the true acceptance in the PAX 6.10.1 data just being further away from the lower limit. This is accounted for by the 3.4 % relative systematic uncertainty on the half-life in equation (4.40).

In order to remove the effect of cut acceptances in a next step only events that appear in the PAX 6.8.0 data as well as in the PAX 6.10.1 data are considered. This removes approximately 12.5 % of the data in the PAX 6.10.1 dataset. In the following it is assumed that the exposure in both datasets is reduced accordingly. The energy spectra of the overlapping events are fitted with the updated signal and background model. The fit results are summarised in table 4.10. The full spectra, χ^2_λ profiles, pull-plots and best-fit parameters can be found in section A11 of the appendix. Note that the PAX 6.8.0 data requires fewer fit parameters since the energy calibration, resolution and cut acceptance have been derived for the full 1.5 t superellipsoid in this data. Accordingly, the inner and outer spectra share the respective fit parameters. This is not the case for the PAX 6.10.1 data where the individual fit of the acceptance, resolution and energy shift adds six parameters.

The trends that were already observed in the full datasets are reproduced in the event-overlap. First, the goodness of fit, both with and without considering the pull terms, is better in the PAX 6.10.1 data. Comparing the raw χ^2_λ yields a difference of

$$\chi^2_{\lambda,6.8.0} - \chi^2_{\lambda,6.10.1} = 29 \tag{4.45}$$

while the difference in degrees of freedom (fit parameters) is 2 (6). Therefore, the updated fit

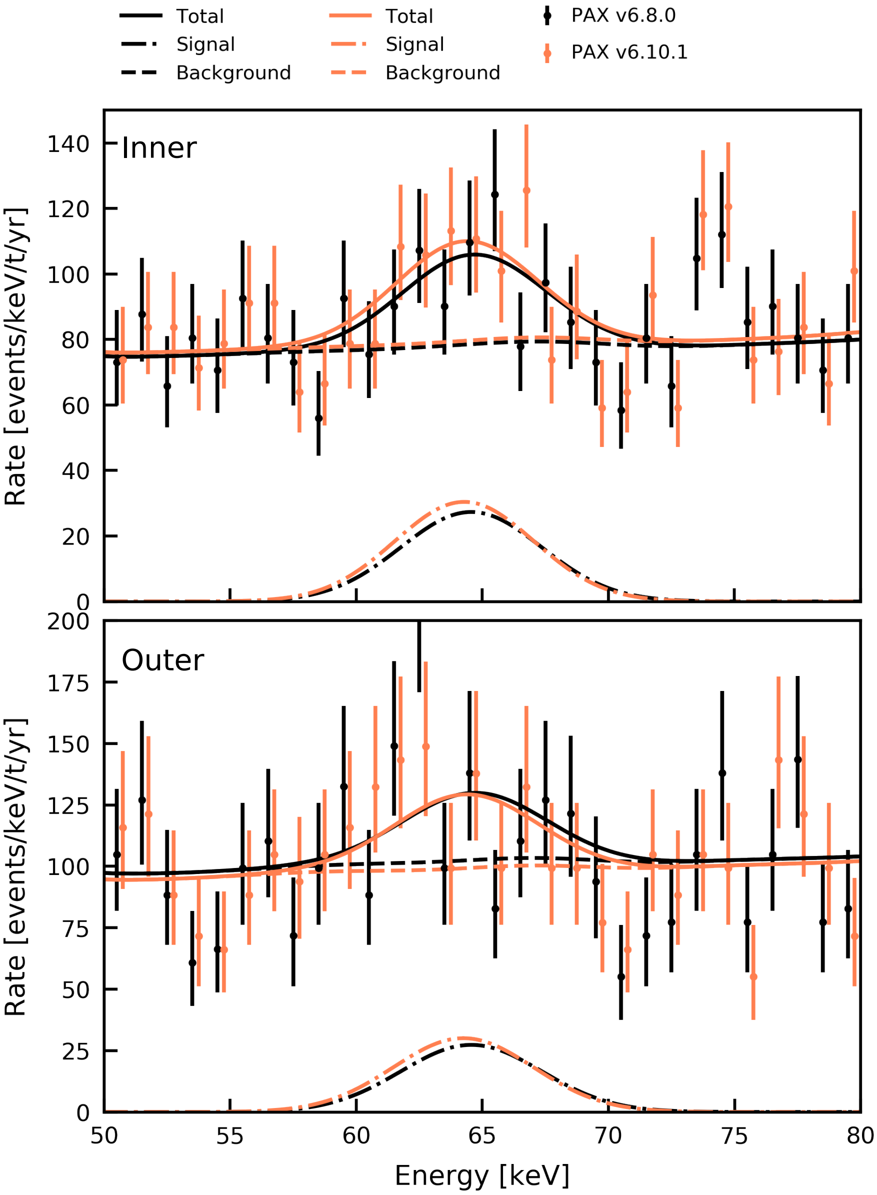

Figure 4.16: Energy spectra between 50 and 80 keV for the fit of the overlap in events between the published PAX 6.8.0 data (black markers) from [31] and the updated PAX 6.10.1 data (orange markers) from this work. Spectra are shown separately for the inner (**top**) and outer (**bottom**) sub-volumes of the 1.5 t fiducial superellipsoid. The best-fit total spectra for the PAX 6.8.0 and the PAX 6.10.1 data are indicated by the solid black and orange lines, respectively. The background-only spectrum and the KK-peak are indicated by the dashed and dash-dotted lines of the same color. Uncertainties on the data points resemble 68.3 % Feldman & Cousins confidence intervals and are used for illustration only.

Table 4.10: Fit results for the fit of the overlap in events between the published PAX 6.8.0 data from [31] and the updated PAX 6.10.1 data from this work.

	Published (PAX 6.8.0)	**Updated (PAX 6.10.1)**
$\mathbf{n_{data}}$	340	340
$\mathbf{n_{par}}$	29	35
$\mathbf{n_{constrained}}$	18	22
ndf	329	327
χ^2_λ	333.5	304.5
$\sqrt{\frac{\mathbf{2}}{\mathbf{ndf}}}$	0.08	0.08
Σ	6.7	8.4
$\frac{\chi^2_\lambda}{\mathbf{ndf}}$	1.01	0.93
$\frac{\chi^2_\lambda-\Sigma}{\mathbf{n_{data}}-\mathbf{n_{par}}}$	1.05	0.97
$\sqrt{\Delta\chi^2_\lambda}$	4.8	5.3
$\mathbf{N_{2\nu ECEC}}$ [**events**]	146 ± 37	161 ± 32
$\mathbf{T^{2\nu ECEC}_{1/2}}$ [10^{22} **yr**]	$1.28\pm0.32_{\mathrm{stat}}\pm0.05_{\mathrm{sys}}$	$1.16\pm0.23_{\mathrm{stat}}\pm0.06_{\mathrm{sys}}$
$\mathbf{T^{2\nu KK}_{1/2}}$ [10^{22} **yr**]	$1.68\pm0.42_{\mathrm{stat}}\pm0.07_{\mathrm{sys}}$	$1.51\pm0.30_{\mathrm{stat}}\pm0.07_{\mathrm{sys}}$

describes the data significantly better. From the χ^2_λ profile on the double-electron capture decay rate, the significance and number of events is higher in the PAX 6.10.1 data with (161 ± 32) events at 5.3σ vs. (146 ± 37) events at 4.8σ. The fits of the overlapping spectra reproduce the trend found in the full datasets where the PAX 6.10.1 half-life is 10 % shorter than the one found with PAX 6.8.0. For the KK-capture one obtains

$$\begin{aligned} T^{2\nu\mathrm{KK}}_{1/2,6.8.0} &= (1.68\pm0.42_{\mathrm{stat}}\pm0.07_{\mathrm{sys}})\cdot10^{22}\,\mathrm{yr},\\ T^{2\nu\mathrm{KK}}_{1/2,6.10.1} &= (1.51\pm0.30_{\mathrm{stat}}\pm0.07_{\mathrm{sys}})\cdot10^{22}\,\mathrm{yr}. \end{aligned} \tag{4.46}$$

It should be noted that the systematic uncertainties originating from exposure and cut acceptance are independent for the PAX 6.8.0 and PAX 6.10.1 datasets. Disentangling the shared abundance uncertainty from the independent uncertainties one obtains

$$\begin{aligned} T^{2\nu\mathrm{KK}}_{1/2,6.8.0} &= (1.68\pm0.42_{\mathrm{stat}}\pm0.07_{\mathrm{sys,\,6.8.0}}\pm0.02_{\mathrm{sys,\,shared}})\cdot10^{22}\,\mathrm{yr},\\ T^{2\nu\mathrm{KK}}_{1/2,6.10.1} &= (1.51\pm0.30_{\mathrm{stat}}\pm0.06_{\mathrm{sys,\,6.10.1}}\pm0.03_{\mathrm{sys,\,shared}})\cdot10^{22}\,\mathrm{yr}. \end{aligned} \tag{4.47}$$

Even though the $\Delta\eta$ systematic uncertainty is the same for both datasets, the central values of the exposure and cut acceptance in the calculation differ. Together with the rounding this leads to different respective values of the shared systematic uncertainty for both PAX versions although the source of the uncertainty is the same. The independent systematic uncertainties further reduce the observed discrepancy between the half-lives.

The difference in fitted events in both datasets is visible by eye in figure 4.16. The figure shows the data and fit result in both fiducial volumes for the 50 to 80 keV energy region that contains the KK-capture peak. Here, the best-fit peak in both volumes is visibly larger for the newer PAX version. The background level in the inner volume is nearly the same as before while in the outer volume it is lower which is caused by the lower assumed cut acceptance in

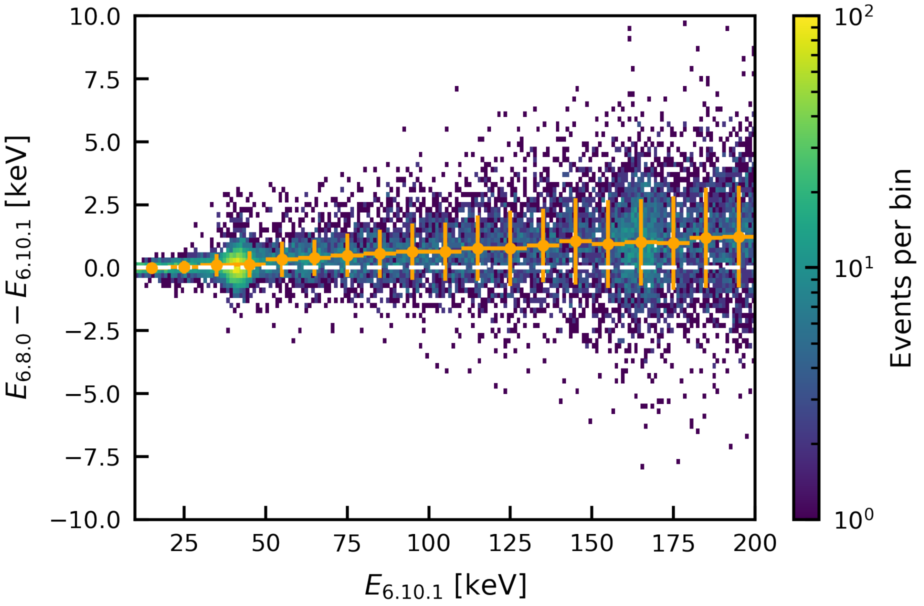

Figure 4.17: Event-wise energy-difference between the overlapping PAX 6.8.0 and PAX 6.10.1 data as a function of the energy reconstructed with PAX 6.10.1 (2D histogram). The orange markers and error bars show the arithmetic means and standard deviations in 10 keV energy intervals. The zero difference is indicated by the dashed white line.

the fit. Compared to the PAX 6.8.0 data the PAX 6.10.1 data points appear more peak-like in the KK-capture region. For the black markers there is more fluctuation around the best-fit sum spectrum. Moreover, the peaks in PAX 6.8.0 are shifted towards higher energies. Since both datasets contain the same events, the fluctuations and the shift illustrate the difference in both energy reconstructions. Together with the persistent difference in the best-fit half-lives, this suggests that the principal difference of the published analysis and this work must originate in the energy reconstruction. Differences in exposure and cut-acceptance have been removed by selecting the overlap and also the independent systematic uncertainties can only explain a part of the difference.

4.6 Dataset correlation and energy reconstruction

Due to the differences in the energy reconstruction the datasets containing the same events are not fully correlated. This section illustrates the impact of the different energy reconstructions in both PAX versions on the reconstructed half-lives using toy-MC simulations. The analysis was performed with help from C. Weinheimer. Figure 4.17 shows the 2D distribution of the event-wise energy difference between PAX 6.10.1 and PAX 6.8.0 as a function of the reconstructed energy from PAX 6.10.1. One can clearly see that the orange markers, which indicate the arithmetic mean of the differences in a 10 keV interval, exhibit a positive offset from the zero-line. Moreover, the standard deviations of the differences, shown by the orange bars, increase with energy.

This behaviour is expected since the reconstruction improvements in PAX 6.10.1 [201] yield a significantly better energy resolution than in PAX 6.8.0. Both resolution parametrisations are shown in figure 4.18. It can be assumed that the energy resolution in either PAX version is determined by the physical processes in the signal generation and measure-

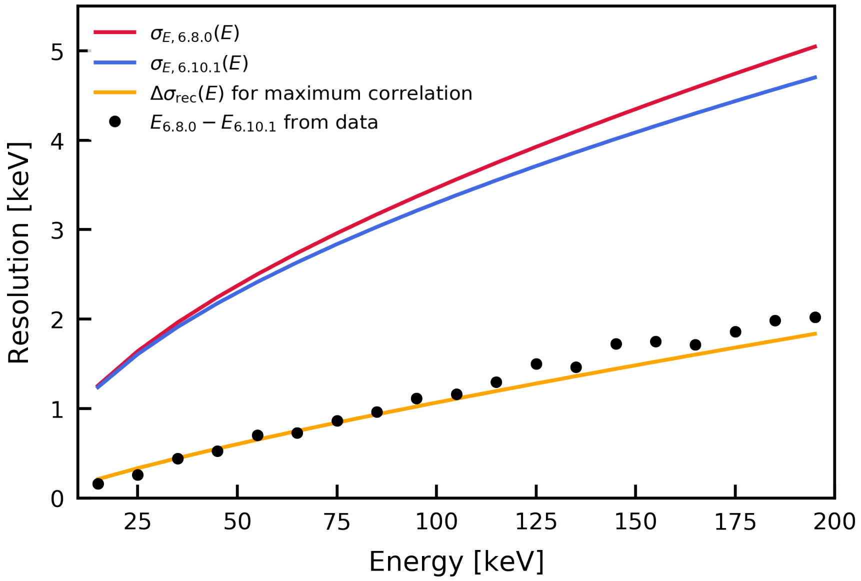

Figure 4.18: Energy resolutions for PAX 6.8.0 ($\sigma_{E,6.8.0}$, solid red) and PAX 6.10.1 ($\sigma_{E,6.10.1}$, solid blue) from equations (3.8) and (4.1). The solid orange line shows the difference of both parametrisations $\Delta\sigma_{\mathrm{rec}}$. The mean difference of reconstructed energies determined from the data in figure 4.17 is shown by the black markers.

ment leading to $\sigma_0(E)$ and by the reconstruction leading to $\Delta\sigma_{E,6.8.0}(E)$ and $\Delta\sigma_{E,6.10.1}(E)$, respectively[8]. The energy resolutions can then be rewritten as.

$$\begin{aligned}\sigma_{E,6.8.0} &= \sqrt{\sigma_0^2 + \Delta\sigma_{E,6.8.0}^2},\\ \sigma_{E,6.10.1} &= \sqrt{\sigma_0^2 + \Delta\sigma_{E,6.10.1}^2}.\end{aligned} \tag{4.48}$$

Assuming that the distribution of event-wise energy differences $E_{6.8.0} - E_{6.10.1}$ can be described by a Gaussian distribution with the standard deviation $\Delta\sigma_{\mathrm{rec}}$ three different cases present themselves. For $\sigma_0 = 0$ both energy reconstructions would be fully uncorrelated with

$$\Delta\sigma_{\mathrm{rec,\,max}} = \sqrt{\sigma_{E,6.8.0}^2 + \sigma_{E,6.10.1}^2}. \tag{4.49}$$

In this unphysical case the processes of signal generation and measurement would not have an impact on the energy resolution and the correlation would be minimal with $\Delta\sigma_{\mathrm{rec}} = \Delta\sigma_{\mathrm{rec,\,max}}$ at its maximum value. For $\sigma_0 = \sigma_{E,6.10.1}$, the energy reconstruction by PAX 6.8.0 would add $\Delta\sigma_{E,6.8.0}$ yielding the maximum possible correlation with

$$\Delta\sigma_{\mathrm{rec,\,min}} = \Delta\sigma_{E,6.8.0} = \sqrt{\sigma_{E,6.8.0}^2 - \sigma_{E,6.10.1}^2}. \tag{4.50}$$

In this case of maximum correlation $\Delta\sigma_{\mathrm{rec}} = \Delta\sigma_{\mathrm{rec,\,min}}$ assumes its smallest value. In the third case one would have $0 < \sigma_0 < \sigma_{E,6.10.1}$ and

$$\Delta\sigma_{\mathrm{rec,\,min}} < \Delta\sigma_{\mathrm{rec}} < \Delta\sigma_{\mathrm{rec,\,max}}. \tag{4.51}$$

The means of $E_{6.8.0} - E_{6.10.1}$ from figure 4.17 are are overlaid with $\Delta\sigma_{\mathrm{rec,\,max}}$ in figure 4.18. The fact that the difference in reconstructed energies is well described by $\Delta\sigma_{\mathrm{rec,\,max}}$ suggests

---

[8] In the following the energy dependence is not explicitly stated for better readability.

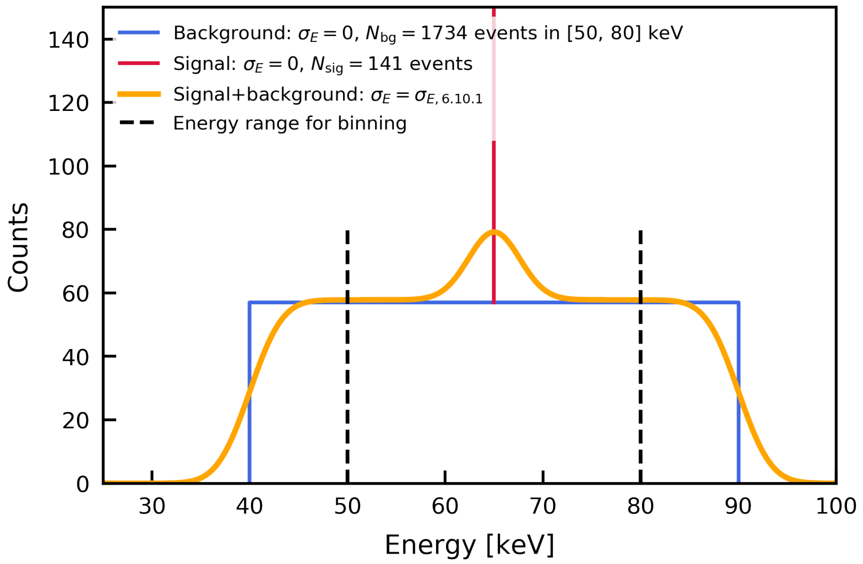

Figure 4.19: Setup of the toy-MC simulations. The signal is simulated as a sharp line containing $N_{\mathrm{sig}} = 141$ events (solid red). The background is simulated as a box containing $N_{\mathrm{bg}} = 1437$ events between 50 and 80 keV (solid blue). The signal+background spectrum is smeared with $\sigma_{E,6.10.1}$ (solid orange).

a maximum correlation between both energy reconstructions. Above 100 keV the data points show larger differences than expected for maximum correlation. This indicates that at higher energies the correlation is reduced due to the missing high-energy optimisations in PAX 6.8.0.

In the next step simulations of PAX 6.8.0 and PAX 6.10.1 toy datasets are made under the assumption of full correlation. Figure 4.19 shows the setup of the simulations. For the signal and background a sharp line at 65 keV and a box-spectrum are used. The numbers of simulated signal and background events in the full 1.5 t fiducial volume are taken from best-fit parameters of the PAX 6.10.1 data from figure 4.16. In the energy interval from 50 to 80 keV, $N_{\mathrm{sig}} = 141$ events and $N_{\mathrm{bg}} = 1437$ events are expected. The background spectrum is extended beyond the bounds of the energy ROI in order to avoid artefacts from the energy smearing. To this end, the N_{bg} in the box is increased accordingly. Then, 1000 toy datasets are drawn from the signal and background distributions. In the next step, the spectra are smeared with $\sigma_0 = \sigma_{E,6.10.1}$. This yields the PAX 6.10.1 energy spectrum. The PAX 6.8.0 spectrum is obtained by a convolution of this spectrum with $\Delta\sigma_{\mathrm{rec,\,max}}$. For each simulation, both spectra are fitted with a constant function and a Gaussian peak with constrained position and width. The reproduction of the input parameters in the fits has been tested and the distribution of fitted peak areas $A_{\mathrm{fit},6.10.1}$ and $A_{\mathrm{fit},6.8.0}$ for both toy dataset ensembles are shown in figure 4.20. The number of injected signal events is reproduced in both toy ensembles and both distributions have a similar width. The difference $\Delta A_{\mathrm{fit}} = A_{\mathrm{fit},6.8.0} - A_{\mathrm{fit},6.10.1}$ of the fitted areas in both ensembles is shown in figure 4.21. The resulting distribution is fitted with a Gaussian peak with a standard deviation of $\sigma_{\Delta A} = 10.9$ events.

Considering $N_{\mathrm{sig}} = 141$ events this simplified toy model shows that for the same underlying data and a maximally correlated energy reconstruction a relative deviation in the number of reconstructed signal events larger than 7.7 % can occur with a relative frequency of 31.7 %. For a half-life of $T_{1/2}^{2\nu\mathrm{KK}} = 1.51 \cdot 10^{22}$ yr this translates to $\Delta T_{1/2,\,\mathrm{rec}}^{2\nu\mathrm{KK}} = 0.12 \cdot 10^{22}$ yr. Together with the independent systematic uncertainties that account for a half-life difference of $\Delta T_{1/2,\,\mathrm{sys},\,6.10.1}^{2\nu\mathrm{KK}} = 0.06 \cdot 10^{22}$ yr, the results from the event-wise overlap of the PAX

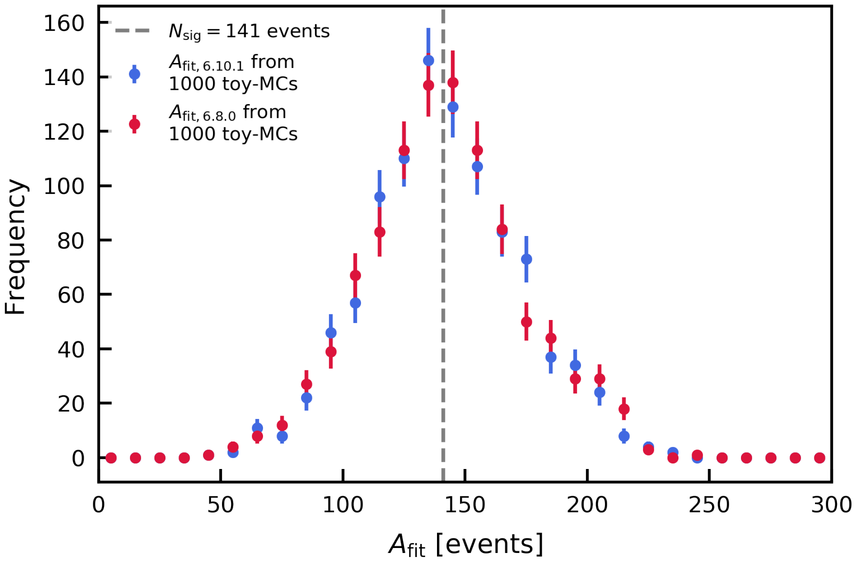

Figure 4.20: Distribution of fitted areas $A_{\mathrm{fit,6.8.0}}$ (red) and $A_{\mathrm{fit,6.10.1}}$ (blue) from 1000 toy-MC datasets with the PAX 6.8.0 and PAX 6.10.1 energy resolutions, respectively. The error bars correspond to simplified $\sqrt{N}$ counting uncertainties. The number of injected signal events in the toys $N_{\mathrm{sig}} = 141$ events is indicated by the dashed grey line.

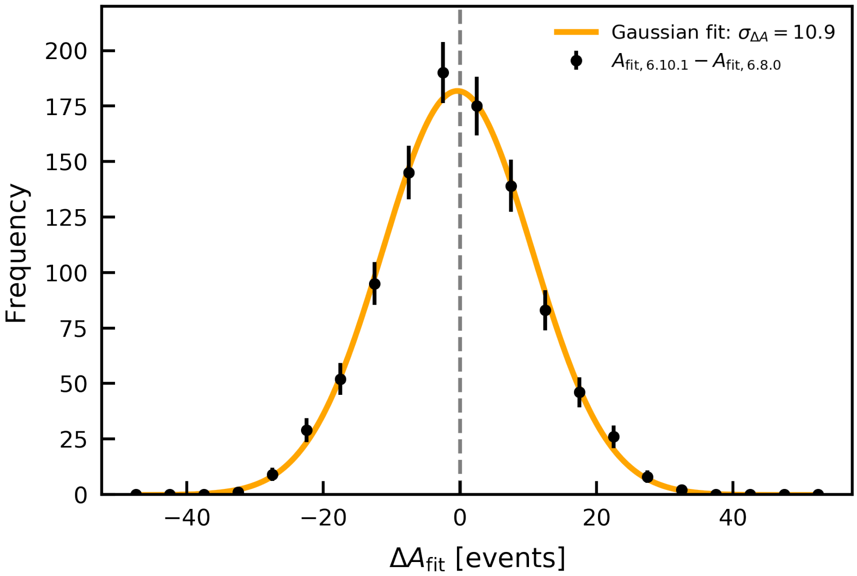

Figure 4.21: Distribution of $\Delta A_{\mathrm{fit}} = A_{\mathrm{fit,6.8.0}} - A_{\mathrm{fit,6.10.1}}$ from 1000 toy-MC datasets with the PAX 6.8.0 and PAX 6.10.1 energy resolutions (black markers). The error bars correspond to simplified $\sqrt{N}$ counting uncertainties. The solid orange line marks a Gaussian fit of the data with $\sigma_{\Delta A} = 10.9$ events.

6.10.1 and PAX 6.8.0 data are compatible. Further differences in the full datasets arise from the larger cut acceptance in PAX 6.10.1, the inclusion of the KL- and LL-peaks in the signal model, and the 33 % larger exposure of the full dataset in the extended analysis.

Finally, it can be concluded that the published XENON1T result [31] from chapter 3 and the updated result presented here are consistent. The significant detection of 2νECEC in ^{124}Xe at 6.8σ has been achieved. The half-life is $T_{1/2}^{2\nu\mathrm{ECEC}} = (1.13 \pm 0.18_{\mathrm{stat}} \pm 0.05_{\mathrm{sys}}) \cdot 10^{22}$ yr. Future xenon-based detectors with lower backgrounds and larger exposures will further probe this decay in order to obtain constraints on NME calculations from the proton-rich side of the nuclide chart. At $A_{2\nu\mathrm{ECEC}} = 280$ events/t·yr XENONnT would measure 5600 double-electron capture events in its projected 20 t-yr exposure. With a reduction in background by a factor of ~ 7 [18] the half-life could be measured with a precision at the few-percent level. Moreover, with more exposure and less background the remaining two-neutrino and hypothetical neutrinoless decays of ^{124}Xe could become accessible. Their detection prospects are discussed in the next chapter.

Detection Prospects for the Second-Order Weak Decays of ^{124}Xe 5

The Q-value of ^{124}Xe allows for three two-neutrino and neutrinoless double-weak decay modes. With the two-neutrino double-electron capture only one of these has been observed experimentally. Neither the two-neutrino nor the neutrinoless modes of the double-positron emission or electron capture with coincident positron emission have been detected yet. The same is true for the neutrinoless double-electron capture. This section will outline the detection prospects of the remaining decays in future experiments. To this end it will present the expected half-lives and signals, outline their simulation and reconstruction and discuss experimental backgrounds. Finally it will give the sensitivity of future multi-tonne xenon detectors and discuss the complementarity of ^{124}Xe searches and double-β decays in other isotopes. The results presented in this chapter have been published in [155]. The main contributions in the scope of this work are the half-life calculations for the two-neutrino decays, the neutrinoless decay half-life calculations in close cooperation with C. Weinheimer, the signal simulation that required an enhancement of the DECAY0 event generator, and the conception of the reconstruction algorithm in close collaboration with A. Fieguth. The reconstruction efficiencies were evaluated by A. Fieguth while the background sources and left-right symmetric constraints were evaluated by B. Lenardo.

5.1 Half-life estimates for two-neutrino and neutrinoless decays

Following equation (1.12), the half-lives for the two-neutrino decay modes are calculated from

$$(T_{1/2}^{2\nu})^{-1} = G_{2\nu}|M_{2\nu}|^2, \tag{5.1}$$

with the PSF $G_{2\nu}$ and the NME $|M_{2\nu}|^2$. While the PSF is different among the decay modes [89,96,97], the NME differs only slightly between 2νECEC and 2νECβ^+. It is about a factor of two smaller for $2\nu\beta^+\beta^+$ [108, 110]. Since the relative uncertainty on the measured 2νECEC half-life is still large at $\sim 29\,\%$ [31], it outweighs the NME differences. One can assume

$$M_{2\nu\mathrm{ECEC}} = M_{2\nu\mathrm{EC}\beta^+} = 2\cdot M_{2\nu\beta^+\beta^+} \tag{5.2}$$

and use the existing 2νECEC measurement to constrain $M_{2\nu\mathrm{ECEC}}$. The half-life value[1] for the double-K capture from [31] has to be scaled by its branching fraction $f_{2\nu\mathrm{KK}} = 0.765$ [89]

---

[1] The analysis presented in chapter 4 had not been finished at the time of this study. Therefore, all calculations for two-neutrino decays are based on the half-life from [31].

Table 5.1: The different 2ν decay modes of ^{124}Xe with the corresponding PSFs, the assumptions of the corresponding NMEs according to equation (5.2), and the measured or predicted half-lives according to equation (5.3) and equation (5.4), respectively. The PSF values were taken from the review [97] which summarizes work by the reviewers and from [89, 117]. Therefore, a range of PSF values is given. For predicting the half-lives of the decay modes $2\nu\text{EC}\beta^+$ and $2\nu\beta^+\beta^+$ the central value of this range is used as the most probable PSF value with the half-range as the uncertainty. Taken from [155].

Decay	$\mathbf{G_{2\nu}}$ **[yr^{-1}]**	$\mathbf{M_{2\nu}}$ **(5.2)**	**Half-life [yr]**	
			Measured (5.3)	**Predicted (5.4)**
2νECEC	$(1.5-2.0)\cdot 10^{-20}$	$M_{2\nu\text{ECEC}}$	$(1.4\pm 0.4)\cdot 10^{22}$	
$2\nu\text{EC}\beta^+$	$(1.2-1.7)\cdot 10^{-21}$	$M_{2\nu\text{ECEC}}$		$(1.7\pm 0.6)\cdot 10^{23}$
$2\nu\beta^+\beta^+$	$(4.3-4.9)\cdot 10^{-26}$	$\frac{1}{2}\cdot M_{2\nu\text{ECEC}}$		$(2.2\pm 0.7)\cdot 10^{28}$

in order to obtain the total half-life[2]:

$$T_{1/2}^{2\nu\text{ECEC}} = (1.4\pm 0.4)\cdot 10^{22}\ \text{yr}. \tag{5.3}$$

The literature values for the PSFs and $T_{1/2}^{2\nu\text{ECEC}}$ can now be inserted into equation (1.12) and solved for the unknown half-lives yielding

$$\begin{aligned} T_{1/2}^{2\nu\text{EC}\beta^+} &= \frac{G_{2\nu\text{ECEC}}}{G_{2\nu\text{EC}\beta^+}}\cdot T_{1/2}^{2\nu\text{ECEC}}, \\ T_{1/2}^{2\nu\beta^+\beta^+} &= \frac{4\cdot G_{2\nu\text{ECEC}}}{G_{2\nu\beta^+\beta^+}}\times T_{1/2}^{2\nu\text{ECEC}}. \end{aligned} \tag{5.4}$$

The resulting expected half-lives for $2\nu\text{EC}\beta^+$ and $2\nu\beta^+\beta^+$ are summarised in table 5.1 [155]. Due to the smaller available phase-space, the $2\nu\text{EC}\beta^+$ half-life is about one order of magnitude larger than $T_{1/2}^{2\nu\text{ECEC}}$. The PSF difference is more drastic for $2\nu\beta^+\beta^+$, where the half-life is approximately six orders of magnitude longer. In turn, $2\nu\text{EC}\beta^+$ could be within reach of next-generation experiments such as LZ or XENONnT while the measurement of $2\nu\beta^+\beta^+$ will pose a considerable challenge.

The half-lives for the neutrinoless decays are calculated according to equation (1.16) with the BSM-factor from equation (1.25) for light neutrino exchange:

$$(T_{1/2}^{0\nu})^{-1} = G_{0\nu}|M_{0\nu}|^2\left|\frac{\langle m_{\beta\beta}\rangle}{m_\text{e}}\right|^2. \tag{5.5}$$

Here the effective neutrino mass

$$\langle m_{\beta\beta}\rangle = \sum_{\text{i=light}}(U_{\text{ei}}^2 m_\text{i}) \tag{5.6}$$

has already been included as a linear combination of the light neutrino masses m_i and elements of the PMNS mixing matrix U_ei [102, 117] with $\text{i} = 1,2,3$. The PSFs and NMEs are different from their two-neutrino counterparts as established in section 1.2.2. For 0νECEC a resonance factor R has to be added to equation (5.5):

$$(T_{1/2}^{0\nu\text{ECEC}})^{-1} = G_{0\nu}|M_{0\nu}|^2\left|\frac{\langle m_{\beta\beta}\rangle}{m_\text{e}}\right|^2\cdot R. \tag{5.7}$$

---

[2] At the time of this analysis, the extended double-electron capture analysis from chapter 4 had not been finished. Therefore, the published half-life values from [31] were used here.

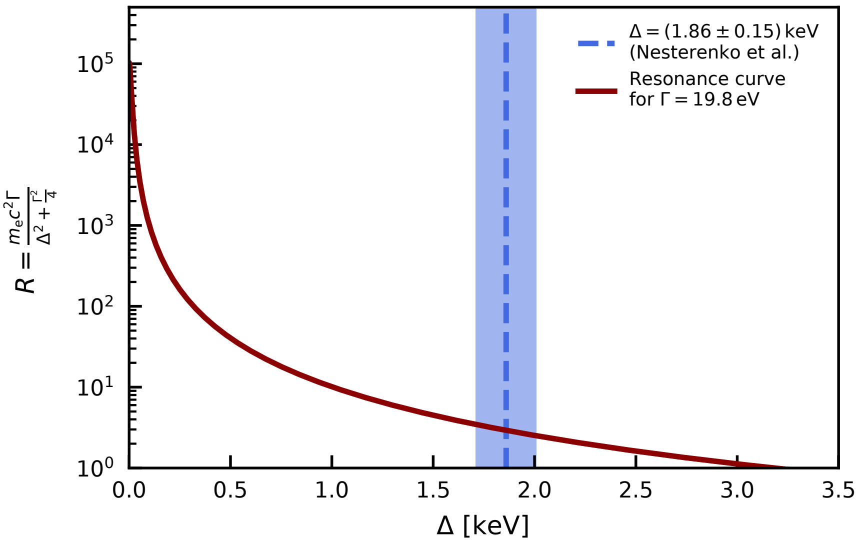

Figure 5.1: Resonance factor R for 0νECEC as a function of the energy mismatch between the decay surplus energy and the excited ^{124}Te daughter state $\Delta = |Q - E_{2k} - E_{exc}|$ (solid dark red) for $\Gamma = 0.0198$ keV. The currently most precise value of $\Delta = (1.86 \pm 0.15)$ keV [27] for double-K capture is indicated by the dashed blue line with the uncertainty as the light blue patch.

This factor describes the availability of a suitable excited state of the daughter nucleus that the decay can proceed to under the conservation of energy and momentum. It is mainly driven by the mismatch $\Delta = |Q - E_{2k} - E_{exc}| = (1.86 \pm 0.15)$ keV between the available energy and the energy level of the daughter nucleus in the excited state E_{exc} [27]. With the two-hole width $\Gamma = 0.0198$ keV [102] it is

$$R = \frac{m_e c^2 \Gamma}{\Delta^2 + \Gamma^2/4} = 2.92 \pm 0.47\,. \tag{5.8}$$

The resonance factor R is plotted as a function of Δ in figure 5.1. If the resonance were realised with $\Delta = 0$, the decay rate would be boosted by almost five orders of magnitude. Although this is unlikely given the present value from [27], the authors recommend an independent validation measurement of their results. Such a measurement would enable a verdict on the experimental feasibility of a search for 0νECEC in ^{124}Xe.

A source of uncertainty for the neutrinoless decay half-lives arises from the fact that the NMEs have not been measured for any neutrinoless decay. Moreover, the effective neutrino mass is unknown. For these half-life ingredients, different experimental constraints and theory calculations have to be put to use. In order to account for the latter, two distinct sets of experimental constraints are used to get lower limits for the expected half-lives of neutrinoless double-weak decays of ^{124}Xe. First, the most recent result from the KATRIN experiment is used, which set the most stringent, direct, and model-independent limit on $m_{\nu_e} < 1.1$ eV (90% C.L.) [22]. This limit is then combined with a global fit to neutrino oscillation results [266]. The result is an upper limit range – corresponding to the uncertainties in the Majorana and CP-phases of the PMNS matrix – on the effective neutrino mass:

$$\langle m_\nu \rangle < 0.3 - 1.1\,\mathrm{eV/c^2} \quad (90\%\ \mathrm{C.L.}). \tag{5.9}$$

The resulting half-life estimates for neutrinoless ^{124}Xe decays are listed under *Constraints 1* in table 5.2.

The second set of constraints is informed by the most stringent limits from searches for $0\nu\beta^-\beta^-$ decay. The experiments CUORE [137], EXO-200 [138], GERDA [131], KamLAND-Zen [25] and the MAJORANA demonstrator [267] use the isotopes ^{130}Te, ^{136}Xe, and ^{76}Ge. For their respective isotopes they quote lower limits of $\mathcal{O}(10^{26})$ yr on the $0\nu\beta^-\beta^-$ half-life. These can be translated into upper limits of $\mathcal{O}(0.1)$ eV/c^2 on the effective neutrino mass considering the different NMEs and neutrino mixing angles. Since the KAMLAND-Zen result [25] with a half-life limit of $T^{0\nu}_{1/2} > 1.07 \cdot 10^{26}$ yr (90 % C.L.) for ^{136}Xe, provides the strongest constraints on the effective neutrino mass with

$$\langle m_{\beta\beta} \rangle < 0.061 - 0.165\,\mathrm{eV/c^2} \tag{5.10}$$

this range is used in the half-life calculations. The resulting half-life estimates for ^{124}Xe are listed in table 5.2 under *Constraints 2*. The two different sources of experimental constraints, namely the direct neutrino mass measurements vs. $0\nu\beta^-\beta^-$ searches, provide different information: The former are model-independent, but less constraining. Accordingly, the resulting half-life lower limits are smaller. The latter are more constraining, but require additional assumptions.

In equations (5.5) and (5.7) three available sets of calculations were taken into account. The first set is based on the quasi-random phase approximation (QRPA) and was calculated in [108]. The second comes from the interacting boson model (IBM) [102, 103]. The third set is based on nuclear shell model (NSM) calculations as performed for the two-neutrino case [106] and is limited by lower and upper values of the full shell model similar to normal neutrinoless double-β decay as shown in [104] and [268]. Both the QRPA and NSM calculations provided good predictions of $T_{1/2}$ for 2νECEC while there were no 2ν-predictions for IBM. The relevant PSF- and NME-values are summarised together with the resulting lower half-life limits in table 5.2. Limits are given for the range of $\langle m_\nu \rangle$ from equation (5.9) [22, 266] and from equation (5.10) [25]. The PSFs ($G_{0\nu}$) were taken from [102], and the review [97] which summarises work by the reviewers and from [96, 269]. We use the central value of the PSF-range as the most probable value and half of this range as the uncertainty. The same is done for the NMEs ($M_{0\nu}$) in all cases were a range of values is given in the original publication. For 0νECEC the NMEs values from QRPA [108] and IBM [102] were used. The NME for IBM is obtained by taking the single value given in the publication and assuming an axial vector coupling constant $g_A = 1.269$. The NME-range for QRPA stems from the smallest and largest NME value for $g_A = 1.25$ under the assumption of different bases and short-range correlations. For the $0\nu\text{EC}\beta^+$ and the $0\nu\beta^+\beta^+$ QRPA [108], NSM (calculated in [270] as in [106]), and IBM [103] NMEs were considered. The range of NMEs for QRPA and the value for IBM are obtained as above. However, for the latter an uncertainty is given in the publication instead of a value range. For the NSM the NME-range is given by different model configurations, and the most probable value and uncertainty are derived in the same fashion as for QRPA. All uncertainties are propagated by drawing 10^6 independent samples from the parameter distributions and multiplying with the upper limit on $\langle m_{\beta\beta} \rangle$. Then the 90 % C.L. upper limit on $T^{-1}_{1/2}$ is determined from the resulting distribution and inverted to obtain the corresponding lower limit on $T_{1/2}$.

As for the two-neutrino decays, the mixed mode decay $0\nu\text{EC}\beta^+$ is expected to have the shortest half-life. In turn, it is the most promising candidate for an eventual experimental observation. The other decay modes, $0\nu\beta^+\beta^+$ and resonant 0νECEC, exhibit considerably longer half-lives. This is owed to unfavourable phase-space for the double-positron mode, while the neutrinoless double electron capture appears unfeasible due to a lack of resonance enhancement R. As expected, the half-life limits calculated with the first set of constraints are systematically lower than the ones for the second. The capability to observe any of the described decay channels is not only governed by the theoretical predictions on their half-lives, but also by the detection efficiencies in a given experiment. In the following

Table 5.2: Predicted lower limits on the half-life of the 0ν decay modes of ^{124}Xe according to equation (5.5) using equation (5.9) for constraints 1 (upper table) and equation (5.10) for constraints 2 (lower table). The $\langle m_\nu \rangle$ limits are given in units of eV/c^2. Modified from [155].

Constraints 1

Decay	**$G_{0\nu}$ $[10^{-18}\ \mathrm{yr}^{-1}]$**	**$M_{0\nu}$**	**Model**	**Predicted lower $T_{1/2}$ limit [yr] (90% C.L.)**	
				$\langle m_\nu \rangle < 1.1$	**$\langle m_\nu \rangle < 0.3$**
0νECEC	0.26	1.080 – 1.298	QRPA	$1.8 \cdot 10^{29}$	$2.4 \cdot 10^{30}$
		0.478	IBM	$1.2 \cdot 10^{30}$	$1.6 \cdot 10^{31}$
0νECβ^+	17 – 23	4.692 – 6.617	QRPA	$8.7 \cdot 10^{25}$	$1.2 \cdot 10^{27}$
		7.63(1.23)	IBM	$4.8 \cdot 10^{25}$	$6.5 \cdot 10^{26}$
		2.22 – 4.77	NSM	$1.6 \cdot 10^{26}$	$2.2 \cdot 10^{27}$
0ν$\beta^+\beta^+$	1.1 – 1.2	4.692 – 6.617	QRPA	$1.5 \cdot 10^{27}$	$2.1 \cdot 10^{28}$
		7.63(1.23)	IBM	$8.6 \cdot 10^{26}$	$1.2 \cdot 10^{28}$
		2.22 – 4.77	NSM	$2.9 \cdot 10^{27}$	$3.9 \cdot 10^{28}$

Constraints 2

Decay	**$G_{0\nu}$ $[10^{-18}\ \mathrm{yr}^{-1}]$**	**$M_{0\nu}$**	**Model**	**Predicted lower $T_{1/2}$ limit [yr] (90% C.L.)**	
				$\langle m_\nu \rangle < 0.165$	**$\langle m_\nu \rangle < 0.061$**
0νECEC	0.26	1.080 – 1.298	QRPA	$8.0 \cdot 10^{30}$	$5.8 \cdot 10^{31}$
		0.478	IBM	$5.4 \cdot 10^{31}$	$3.9 \cdot 10^{32}$
0νECβ^+	17 – 23	4.692 – 6.617	QRPA	$3.9 \cdot 10^{27}$	$2.8 \cdot 10^{28}$
		7.63(1.23)	IBM	$2.2 \cdot 10^{27}$	$1.6 \cdot 10^{28}$
		2.22 – 4.77	NSM	$7.3 \cdot 10^{27}$	$5.3 \cdot 10^{28}$
0ν$\beta^+\beta^+$	1.1 – 1.2	4.692 – 6.617	QRPA	$6.8 \cdot 10^{28}$	$5.0 \cdot 10^{29}$
		7.63(1.23)	IBM	$3.8 \cdot 10^{28}$	$2.8 \cdot 10^{29}$
		2.22 – 4.77	NSM	$1.3 \cdot 10^{29}$	$9.3 \cdot 10^{29}$

sections, the detection prospects for the yet unobserved decay modes are discussed for future experiments which could have significantly larger samples of ^{124}Xe.

5.2 Signal signatures, simulations and reconstruction algorithm

As established in chapter 2.1.2, the energy and position of an energy deposition are reconstructed in a liquid xenon dual-phase TPC using ionisation and scintillation signals. Absolute position resolutions of few millimetres and relative energy resolutions of < 1 % at $Q = 2.8$ MeV can be achieved [201]. Paired with low backgrounds, large target masses and 1 kg of ^{124}Xe per tonne of natural xenon, this makes these detectors ideally suited to search for ^{124}Xe decays. We now investigate how the above signatures of 2νECβ^+, 2ν$\beta^+\beta^+$, 0νECEC, 0νECβ^+ and 0ν$\beta^+\beta^+$ can be detected in multi-tonne xenon TPCs. The following discussion assumes a TPC with a dual signal readout of S1 and S2, but is not restricted to Dark Matter detectors such as XENON1T [88], XENONnT [18], LZ [79] or DARWIN [84]. Detectors with alternative light and charge readouts, by SiPMs and charge-sensitive tiles,

Table 5.3: Signatures of the different decay modes of ^{124}Xe. Taken from [155].

Decay mode	**Emitted quanta**	**Coincidence**
$2\nu EC\beta^+$	X-rays/e_{Auger}, e^+, 2ν	X-rays/e_{Auger} + e^+ and 2γ from (e^++e^-)
$0\nu EC\beta^+$	X-rays/e_{Auger}, e^+	X-rays/e_{Auger} + e^+ and 2γ from (e^++e^-)
$2\nu\beta^+\beta^+$	$2e^+$, 2ν	$2e^+$ and 4γ from ($2e^+$+$2e^-$)
$0\nu\beta^+\beta^+$	$2e^+$	$2e^+$ and 4γ from ($2e^+$+$2e^-$)
$0\nu ECEC$	X-rays/e_{Auger}, $2-3\gamma$	X-rays/e_{Auger} and 3γ

such as nEXO [150] could also be capable of measuring the decays of ^{124}Xe. However, due to the planned > 90 % enrichment in ^{136}Xe and the associated depletion in ^{124}Xe for nEXO, the isotopic composition of the xenon inventory would have to be changed.

The yet unobserved ^{124}Xe decays provide distinct signatures. These can be measured by the coincidence and magnitude of energy depositions when they are contained in a detector. The expected coincidence signatures are summarised in table 5.3. All decays involving positrons would produce coincidence signatures from multiple γ-rays on top of the energy deposited by the positrons. The one- or two-positron energy spectrum is continuous for two-neutrino decays and monoenergetic for the neutrinoless decays. Those decays involving electron captures additionally feature the keV-range energy depositions from the atomic deexcitation. The resonant 0νECEC is characterized by the emission of multiple γ-rays (cf. figure 1.19). In order to fully exploit these coincidence signatures, it is required that the individual energy depositions can be resolved.

The S1 signals from multiple energy depositions are usually merged, so a single scintillation pulse is measured for the entire event. The individual interactions sites can only be resolved by the individual S2 signals arriving at the charge readout at different positions and times. A schematic of the expected $0/2\nu EC\beta^+$ decay signature is shown in figure 5.2. Five different S2s are measured in this example: The X-ray cascade from the refilling of the atomic shells after the electron capture generates an S2 close to the position of the decayed nucleus. In addition, the positron produces a short track of ionised xenon atoms that forms a single S2. The remaining S2s are produced by the γ-rays from the annihilating positrons. One of these undergoes Compton scattering before photoabsorption. Note that the timing of the measured S2s does not represent the time order of the interactions, but the depth (z-coordinate) at which they occured. With sufficient position and energy resolution, one can use this information to classify events and perform particle identification. This way backgrounds can be separated from the signal of interest.

Multiple factors influence a detector's capability to resolve to individual interaction sites: the time resolution in the charge channel, the width of the S2 signals, and the x-y resolution of the charge readout. These properties depend on the specific readout techniques in each experiment. Furthermore, each S2 has to exceed the detector's charge energy threshold. In this work, the detection efficiency ϵ for the various decay modes of ^{124}Xe is investigated as a function of the x-y- and z-position resolution using MC simulations of the signals. The dependence on the energy threshold is also checked. This provides efficiency estimates that represent a possible range for existing and future experiments.

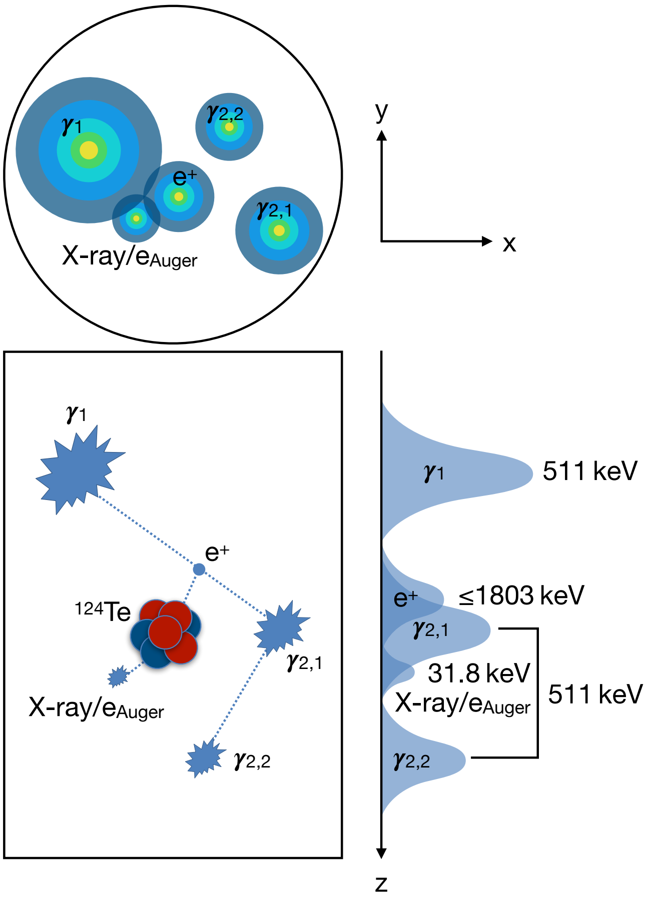

Figure 5.2: Schematic of a $0/2\nu EC\beta^+$-decay signature inside a xenon time projection chamber. As shown in the bottom panel, an initial positron and atomic excitation quanta are emitted and deposit their energy close to the nucleus. Two secondary γ-rays are emitted after the annihilation of the positron. One of those is directly absorbed and the other Compton-scatters before photo-absorption. On the z-axis the ionisation signals of γ_1, $\gamma_{2,1}$ and $\gamma_{2,2}$ can be distinguished from one another by their timing. The positron and atomic deexcitation signals are merged with $\gamma_{2,1}$ in this example. The top panel shows the corresponding hit-pattern of the ionisation signal. In x-y-coordinates the individual scatters of γ_2 can clearly be distinguished from γ_1, while the discrimination of the atomic deexcitation quanta and the positron from γ_1 is not trivial. The scintillation signal is merged for all energy depositions and is not shown in the figure. The sizes of the scintillation signals in x-y and z-coordinates roughly correspond to the magnitudes of the energy depositions. Taken from [155].

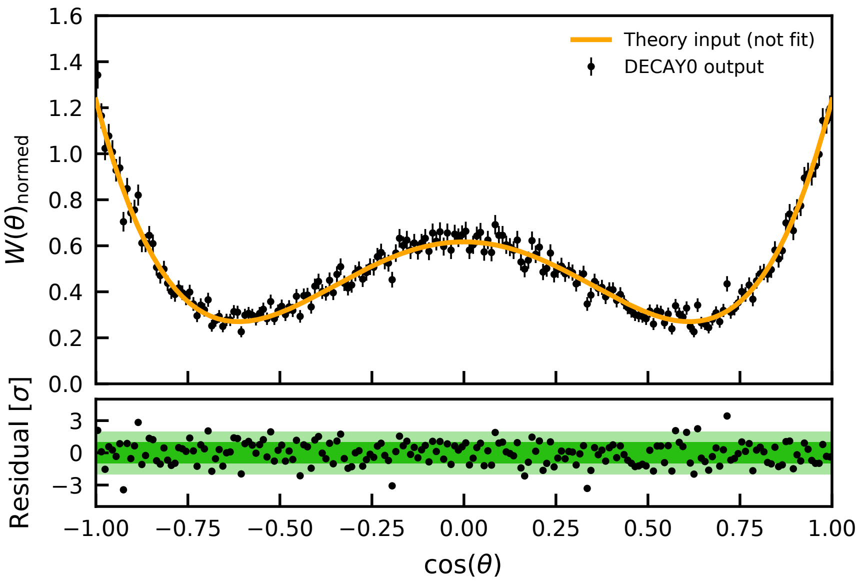

Figure 5.3: Probability distribution $W(\theta)_{\text{normed}}$ for the angle θ between the two γ-rays emitted in a $0^+ \to 2^+ \to 0^+$ transition. The black points are taken from the momentum vectors of 10^5 0νECEC events generated with DECAY0. Only events with the $0^+ \to 2^+ \to 0^+$ transition have been selected. The uncertainties represent Poisson counting uncertainties. The orange curve indicates the theory expectation that has been implemented in the DECAY0 Fortran code.

5.2.1 Signal simulations

The emitted quanta and their initial momentum vectors for each decay channel are generated with the DECAY0 event generator [271]. The version used here has been modified previously for the simulation of the positronic ^{124}Xe decay modes [272]. In the scope of this work, the implementation was verified and the resonant 0νECEC decay mode with double-K capture was added. The angular correlations for the γ-cascades under the assumption of $J^P = 0^+$ for the resonantly populated [273, 274] state were implemented. In this case the J^P sequences of the γ-cascades are either $0^+ \to 2^+ \to 0^+$ or $0^+ \to 2^+ \to 2^+ \to 0^+$ for two- and three-γ transitions, respectively. For illustration, the angular correlation parametrisation for the $0^+ \to 2^+ \to 0^+$ transition is shown in figure 5.3. The angle θ is defined as the angle between the momentum vectors of the two γ-rays. These vectors are generated for each emitted particle in the respective decay and are handed to Geant4 as an input.

The particles generated for each decay are propagated through simplified models of the detectors under investigation using the XeSim package [275], based on Geant4 [276]. These detector models consist of a cylindrical liquid xenon volume in which we uniformly place the primary positions of the ^{124}Xe decay events. In order to evaluate the efficiency, at least 10^4 events per decay channel were used. The liquid xenon volume is surrounded by a thin shell of copper which is used for modelling the impact of external γ-backgrounds.

Two different detector sizes are simulated and correspond to two classes of future experiments: The *Generation 2* (G2) experiments have the approximate dimensions of the LZ [17] and XENONnT [18] Dark Matter detectors, which will use dual-phase TPCs filled with natural xenon. The future nEXO neutrinoless double-β decay experiment [150] can also be grouped in this category. It will use a single-phase liquid TPC filled with xenon enriched to > 90% in ^{136}Xe. All G2 experiments are modelled as a right-cylinder of liquid

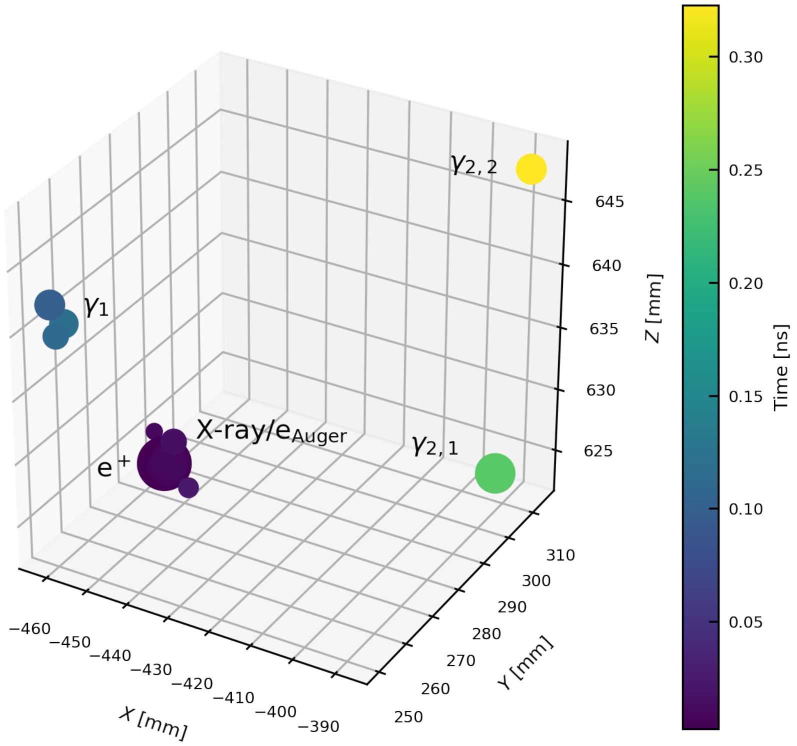

Figure 5.4: Simulated $0\nu EC\beta^+$ event with a signature similar to the one described in figure 5.2. The x-y-z axes mark the positions of energy depositions within a given detector. The origin of the coordinate system is at the centre of the bottom face of the cylinder. The size of each marker indicates the magnitude of the energy deposition. The colour signifies the time difference of each energy deposition with respect to the first energy deposition in the event. Accordingly, the positron was stopped close to the nucleus where also the atomic deexcitation was registered. The first γ-ray underwent multiple Compton scatters within a ~ 5 mm radius before photoabsorption (γ_1). The second γ's Compton scatters occured further from the nucleus. The location of the first Compton scatter of ($\gamma_{2,1}$) and the ultimate photoabsorption ($\gamma_{2,2}$) are separated by ~ 20 mm.

xenon with a height and diameter of 120 cm[3]. A *Generation 3* (G3) experiment with the dimensions of the proposed DARWIN Dark Matter experiment [277] is also simulated. Here, the height and diameter are each increased to 250 cm. Experiments using ^{nat}Xe targets contain approximately 1 kg of ^{124}Xe per tonne of target material. Therefore, G2 Dark Matter experiments would reach ^{124}Xe-exposures of ~ 50 kg-yr in 10 years of continuous operation. Scaling the target mass up to 50 tonnes, the G3 experiment DARWIN will amass a ~ 500 kg-yr exposure. For nEXO, the ^{124}Xe would have to added into the target again. Approximately 50 kg of ^{124}Xe could be extracted from the ^{136}Xe-depleted xenon that is left over from the initial enrichment. These could be mixed back into the target. Thus, in a 10 year run time it could compete with the ~ 500 kg-year exposure of a G3 natural xenon experiment.

Figure 5.4 shows an exemplary simulated $0\nu EC\beta^+$ event from Geant4. The structure of this event is similar to the one discussed in figure 5.2. The position of the markers in x-y-z gives the position of energy depositions within the simulated geometry. The origin of the geometry is located at the centre of the bottom face of the cylinder. The

---

[3] LZ and XENONnT will be slightly larger than this, but this assumption has a negligible impact on the efficiency estimation as shown below.

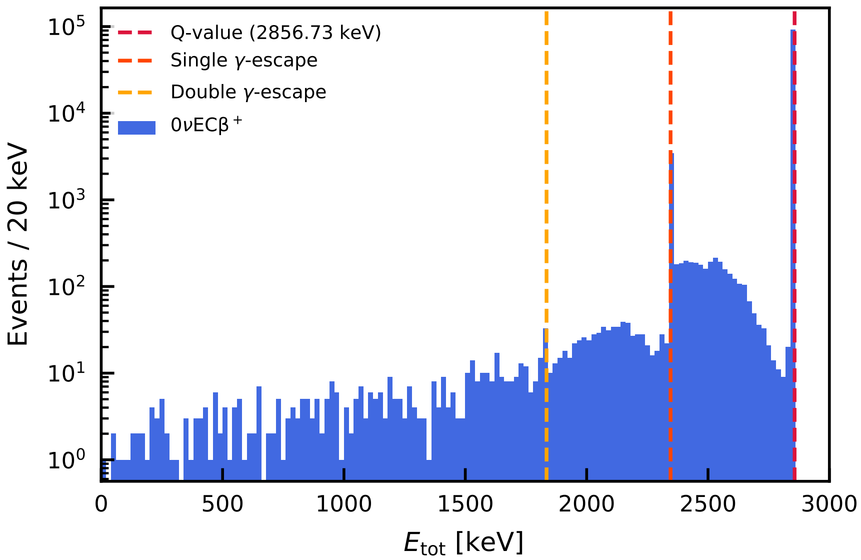

Figure 5.5: Total energy deposition histogram from 10^6 $0\nu EC\beta^+$ events directly from Geant4 output and not yet smeared with the energy resolution. In the majority of cases the total energy deposition is equal to the Q-value (dashed red line). If a lower total energy deposition occurs, individual quanta have left the detector before depositing their full energy. This is more likely in proximity to the edges of the detector volume and no fiducial cuts have been applied to the data. As prominent examples the single- and double-γ escape lines are indicated by the orange and gold dashed lines. The reconstruction algorithm outlined in section 5.2.2 would remove all events except those within a $1\sigma_E$ energy-resolution interval (after smearing) around the Q-value.

marker size is proportional to the magnitude of the energy deposition and the marker colour contains timing information: Energy depositions early in an event are coloured blue while late energy depositions are coloured yellow. Accordingly, the positron and atomic deexcitation quanta from the $0\nu EC\beta^+$ were contained within a few mm from the nucleus. The first γ-ray (γ_1) undergoes multiple scatters within a short ~ 5 mm distance before photoabsorption in vicinity of the annihilation vertex of the positron. The second γ-ray undergoes a single Compton scatter further from the nucleus ($\gamma_{2,1}$) and travels another ~ 20 mm before photoabsorption[4] ($\gamma_{2,2}$). An experiment with a spatial resolution of 10 mm in all directions would be able to reconstruct a single S1 and four S2s: one for the positron and atomic quanta, one for γ_1, and the remaining two for $\gamma_{2,1}$ and $\gamma_{2,2}$.

A histogram of the total energy depositions of 10^6 $0\nu EC\beta^+$ events is shown in figure 5.5. Most events exhibit an expected energy deposition equal to the Q-value. Since no fiducial selections have been applied, events with only partially contained energy are present in the spectrum. Here, quanta emitted in the decay have left the detector before depositing their full energy. As prominent examples the peaks where a single or two γ-rays leave the detector are shown as dashed orange and gold lines. The total energy spectra and reconstructed energies of individual energy depositions are highly dependent on detector properties and reconstruction. They are discussed in the next section.

---

[4] The first energy depositions of the two γ-rays and the annihilation site of the positron cannot be connected by a straight line because one of the γ-rays also Compton-scattered close to its origin.

5.2.2 Reconstruction algorithm

Within this study all simulated detectors use the energy dependence of the resolution on the combined signal as reported in [31] and detailed in section 3.1. The parametrisation of the resolution is

$$\frac{\sigma_E}{E} = \frac{a}{\sqrt{E}} + b \tag{5.11}$$

with σ_E as the standard deviation of a Gaussian peak centred at the energy E. The reconstruction parameters are $a = 0.34\,\mathrm{keV}^{1/2}$ and $b = 0.0017$. With this, an energy resolution of $\sim 1\,\%$ is expected at the Q-value. This is similar to the energy resolution achieved by the EXO-200 experiment in this energy range [149]. Since the individual energy depositions can only be distinguished by their S2 signals, the anti-correlation improvement of the energy resolution is not applicable here. In order to model the deterioration of the charge-only energy resolution compared to the combined light+charge reconstruction, the factor b in equation (5.11) is scaled up to a value of $b_{\text{S2-only}} = 4.4$. The charge-only energy resolution resolution then is 6 % at the annihilation γ-energy of 511 keV. This is consistent with measurements reported in [278] and [279].

In order to reconstruct and validate the detection efficiencies for the unique event signatures, several filtering and clustering steps are performed. The algorithm outlined in the following is classical in the sense that all selections in an analysis step are based on a single variable and a predefined cut value. The application of machine learning techniques using highly multidimensional information in these filtering and clustering steps would likely enhance the signal efficiencies and background rejection. As an example, boosted decision trees could be used to distinguish signal event characteristics from background. This has been applied in a search for $2\nu\beta^-\beta^-$ of ^{136}Xe into the first excited 0^+ state of ^{136}Ba with the EXO-200 experiment [280]. The decay in question also features a multi-coincidence signature with a combination of two electrons and a γ-cascade. However, the application of machine learning models exceeds the scope of this work and would require simulations with a significantly higher degree of realism. Accordingly, the conventional analysis outlined here can be regarded as a baseline scenario.

In the first step, the events are filtered based on the total energy deposited in the detector. This is supposed to remove events with only partially contained energy. For the neutrinoless modes a total energy deposition within $1\sigma_E$ around the Q-value is required. Due to the continuous spectra, this criterion is relaxed for the two-neutrino decays. Here, a broad energy range with a maximum cut-off at the Q-value is used. The decay-dependent lower thresholds are 1022 keV and 2044 keV for for $2\nu\mathrm{EC}\beta^+$ and $2\nu\beta^+\beta^+$, respectively.

The individual interaction positions in each of the remaining events are sorted by their depth (z-coordinate). Individual energy depositions are grouped within a spatial range which is determined by the assumed axial position resolution of the detector. If a separation in the radial direction is also possible, the grouping algorithm also takes the radial separation into account. In this direction a different position resolution is assumed because the radial position resolution is driven by the signal readout and reconstruction algorithms. In the axial direction diffusion dominates the position resolution. The energies of all clustered interactions are summed. In a real detector these clusters would be measured as individual S2 signals.

After the clustering the further filtering targets the reconstruction of the γ-rays that are either emitted in positron annihilation or in the resonant 0νECEC. All clusters in an event are permuted to test each possible interaction combination. The energy sum of each combination is compared to the expected value, e.g. 511 keV for a single γ from positron annihilation. The combination with the smallest difference to the expected energy is removed from the list of energy depositions. Under the condition that it lies within the energy resolution around the expected value, the counter of measurable signatures in the event is raised by one. The procedure is repeated until all desired signatures have been found. If the energy condition cannot be met, the event is discarded right away. For example, in a $2\nu\beta^+\beta^+$ four signatures, one for each γ, have to be identified. Any left-over clusters are checked if they resemble a point-like energy deposition which would be expected from a positron and/or the electron capture atomic cascade. For $0\nu\text{EC}\beta^+$ as well as $2\nu\text{EC}\beta^+$ a single merged energy deposition of the positron and atomic relaxation processes is expected. While one requires a fixed maximum value for a single signature in case of the neutrinoless mode, a range of values is allowed for the two-neutrino decays – between zero or the single K-shell energy and a maximum cutoff depending on the Q-value. If multiple expected signatures are merged to a single cluster due to the limited spatial and time resolution in an experiment, the corresponding events are discarded. If signatures are otherwise missing or if energy criteria cannot be fulfilled, the events are also removed. The efficiency ϵ is then given as the ratio of all events surviving the filtering algorithm and the original number of generated events.

5.2.3 Selection efficiencies

Even though the signals discussed above are generally at energies of $\mathcal{O}(100-1000)$ keV, individual energy depositions are lost to the reconstruction if they fall below the energy threshold of a detector [155]. Accordingly, signal events would be discarded by the reconstruction algorithm due to missing energies in one or several expected signatures. Effectively, an energy threshold would be given by the capability of measuring small individual S2s for the detectors and signals considered here. The S2 threshold is in the keV range for Dark Matter detectors owed to the charge amplification in the gas phase. For an experiment like nEXO the situation is different because it will measure charge directly. Here, the energy treshold would be driven by electronic noise in the readout circuit. The impact of the energy threshold on the efficiency is visualised in Figure 5.6 for three decay modes.

The threshold effect was invesigated for a single 1 cm position resolution in the radial and axial direction. If an energy cluster was below a sharp cutoff energy, it would be ignored in the filtering, so its information would be lost in the analysis. It is evident that the efficiency decreases with an increasing energy threshold. As the above analysis focused on decays involving electron captures from the K-shell, a threshold below this minimum energy has to be achieved for maximum efficiency. Accordingly, for an experiment without charge amplification, an improvement from $\mathcal{O}(100\,\text{keV})$ as achieved in EXO-200 [147] would be required for nEXO. Especially, in order to look for unambiguous evidence of the $0\nu\text{ECEC}$ decay, a threshold below $E_{2\text{k}}$ would be necessary. From here on it is assumed that the achieved energy threshold is low enough in order to be negligible.

In a next step the impact of axial (z) and radial (x-y) position resolution[5] for multiple energy depositions was investigated [155]. The results for several fixed radial resolutions in G2 (black) and G3 (dark red) detectors are shown in Figure 5.7 for $0\nu\text{EC}\beta^+$ as a function of z-resolution. The efficiencies for all decays are summarized in table 5.4. For any detector with an axial resolution better than ~ 50 mm a higher efficiency can only be achieved by an improved radial resolution. At an achieved cluster separration of 10 mm in z, an x-y resolution of also 10 mm would improve the efficiency by more than a factor of two compared to the case of no radial cluster separation. In case of nEXO the radial resolution is determined by the pitch of the charge readout strips [127]. Accordingly a radial cluster separation of few mm is plausible. For dual-phase detectors the axial reconstruction is more complex since it is determined by the electrode geometry, such as the pitch of wire

---

[5] The term position resolution is used as a synonym of cluster separation capability, i.e. the distance at which a separation of individual energy depositions within one event can be resolved.

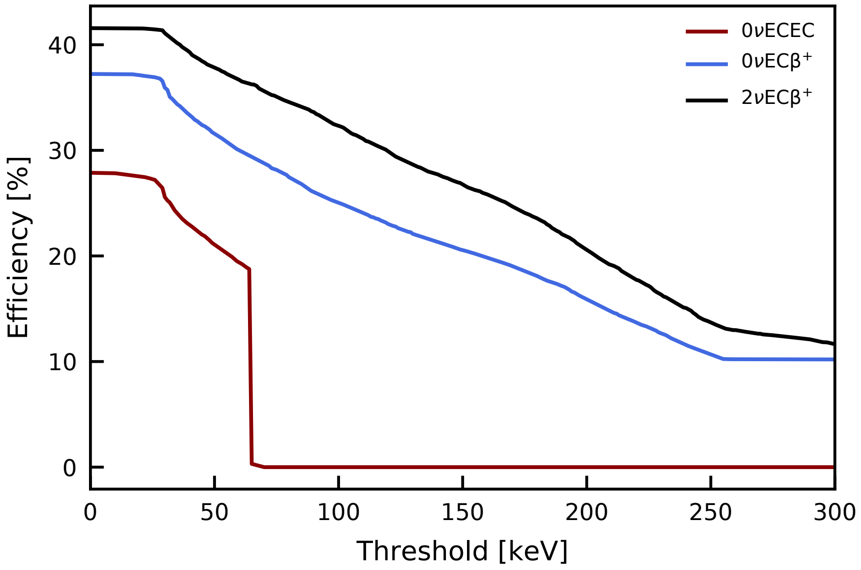

Figure 5.6: Dependence of the charge-only energy threshold on the detection efficiency for selected decay channels. The efficiency for the 0νECβ^+ (blue) and 2νECβ^+ (black) show a decrease with energy up to about 250 keV with efficiencies ranging from about 41 % to 10 %. The 0νECEC (red), features a sharp cutoff as soon as the double electron capture energy (64.3 keV) is below the threshold. Since this signature is required within this analysis in order to provide a clear evidence and necessary background suppression, the efficiency drops to zero in this case. A fixed position resolution of 10 mm has been used in both directions. Taken from [155].

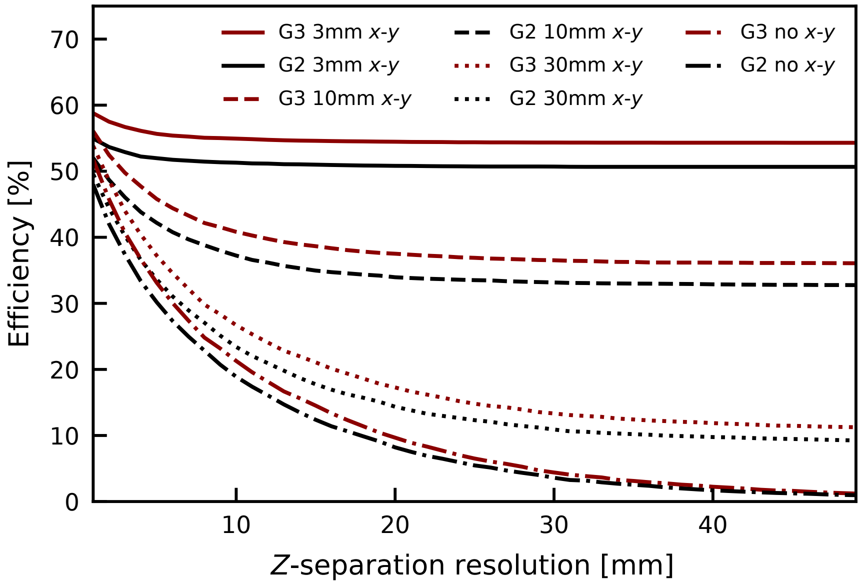

Figure 5.7: Comparison of reconstruction efficiencies for the 0νECβ^+ decay, for different radial resolutions and detector sizes as a function of the axial resolution. The black (red) lines show the efficiencies for a G2 (G3) detector with 3 mm (solid), 10 mm (dashed), 30 mm (dotted) and no (dashdotted) x-y cluster separation capability. Taken from [155].

Table 5.4: Efficiencies for all evaluated decay channels in a G2 and a G3 experiment assuming three different radial resolutions and an axial position resolution of 10 mm. Threshold effects are considered to be negligible. We only considered the most probable branch (57.42%) for 0νECEC with a three-fold γ-signature. An analysis using the two-fold signatures would yield higher efficiency but can add coincidental γ-backgrounds, which would weaken the sensitivity of a given search. Taken from [155].

Decay	**Only z [%]**		**30 mm x-y [%]**		**10 mm x-y [%]**	
	G2	**G3**	**G2**	**G3**	**G2**	**G3**
$2\nu EC\beta^+$	22	24	27	31	42	47
$2\nu\beta^+\beta^+$	4	4	14	17	31	35
$0\nu ECEC$	4	5	15	19	28	33
$0\nu EC\beta^+$	19	21	23	27	37	41
$0\nu\beta^+\beta^+$	2	2	8	10	25	29

electrodes [281], but also by signal saturation [201] and reconstruction algorithms [70, 281]. To this day, no xenon Dark Matter detector has reported its x-y resolution for multiple energy depositions arriving at the charge detection plane simultaneously. For single energy depositions the reported position resolutions depend on S2 size and are on the order of 1 cm [70, 281]. In principle, a similar resolution should be achievable if the aforementioned factors are under control.

Comparing a nEXO-like detector with a G2 geometry (black) and a G3 Dark Matter experiment (dark red) in figure 5.7, both could have the same amount of ^{124}Xe within different-sized detector volumes. The influence of the detector size on the efficiency, here for $0\nu EC\beta^+$, is only on the order of a few percent. This is due to the marginally larger number of events with only partially contained energy in a smaller detector that features a larger surface to volume ratio. Factoring in a possibly better radial reconstruction a smaller detector using enriched xenon could compete with a larger detector using natural xenon. However, the larger surface to volume ratio also makes a G2 detector more susceptible to external backgrounds. Accordingly, possible background sources have to be evaluated in order to properly assess the discovery potential of G2 and G3 detectors [155].

5.3 Background sources

Factoring in the expected half-lives and efficiencies, $0\nu/2\nu EC\beta^+$ are the most accessible decays to experiments. The key characteristic of these decays is their positron-emission which is supposed to enable efficient background rejection. Possible sources of backgrounds are discussed in this section with estimates on the expected rates of events passing the topological selection criteria described in section 5.2.2. The considered background sources are radiogenic backgrounds from detector construction materials, intrinsic backgrounds from ^{222}Rn, the charged-current scattering of neutrinos, and neutron-induced backgrounds. As comparison points, the expected numbers of ^{124}Xe decays per tonne-year exposure of ^{nat}Xe (0.95 kg-year of ^{124}Xe) are calculated using the half-lives estimated in table 5.1 and table 5.2. After including the respective efficiencies for a G2 experiment with 10 mm resolution in x-y-z and assuming a ^{nat}Xe target, 8.3 ± 2.9 decays per tonne-year are expected for $2\nu EC\beta^+$. Given the most optimistic assumptions on NME, PSF and effective neutrino mass, a rate of less than $2.6 \cdot 10^{-2}$ decays per tonne-year is expected for $0\nu EC\beta^+$.

5.3.1 Radiogenic backgrounds

Radioactivity from the environment and detector materials are ubiquitous γ-background sources. Two main concerns arise from this background: First, an MeV γ-ray undergoing multiple Compton-scatters can mimic the expected ^{124}Xe event signatures. Second, a γ-ray may create a positron by pair production. This positron will annihilate and produce a background event that the filtering algorithm has been designed to identify as a signal. Since they are present in most detector construction materials, γ-backgrounds from the ^{238}U and ^{232}Th decay chains are investigated. For each decay step in the respective chains, 10^7 events have been uniformly generated with Geant4 in a 1 cm copper shell surrounding the liquid xenon volume of a G2 detector[6]. The events with interactions in the liquid xenon volume were evaluated with the same reconstruction and filtering algorithm as outlined in section 5.2.2. It was found that the only relevant decays are β-decays into excited states due to the accompanying high-energy γ-emission [155].

For the neutrinoless decay, the β-decay of ^{214}Bi in the ^{238}U-chain is problematic [155]. It has a small branching ratio to the 2880 keV state of ^{214}Po. If this γ-ray interacts via pair production, it creates an event identical to the signal in energy. A number of $1.5 \cdot 10^{-6}$ events per ^{214}Bi primary decay pass the selection criteria. Another problematic transition is the decay of ^{208}Tl to ^{208}Pb in the ^{232}Th-chain [155]. Here, various transitions are available in which different γ-rays are detected in coincidence with the one from the 2614 keV state. Here, $4.5 \cdot 10^{-5}$ events per ^{232}Th primary decay pass the selection considering the 35.9 % branching fraction for creating ^{208}Tl. Both sources of background can be reduced by fiducialisation, as different γ-rays with energies below 300 keV are paired with a high energy γ in the ^{208}Tl decay. Due to LXe self-shielding these intermediate energy γ-rays cannot penetrate deeply into the detector. Cutting away the outer 10 cm of LXe reduces this background contribution by almost an order of magnitude. After doubling the radial cut to 20 cm none of the simulated background events for any isotope passes the selection criteria. Accordingly, these backgrounds can be eliminated by fiducialisation in a realistic experiment [155].

Due to the lack of a sharp total energy deposition and the correspondingly less strict selection criteria, radiogenic backgrounds impact $2\nu\mathrm{EC}\beta^+$ searches more strongly [155]. Three isotopes in the ^{238}U chain produce events that pass the selections [155]. Decays of ^{214}Bi into manifold ^{214}Po states are the major background component (>99 %) with $6.9 \cdot 10^{-3}$ events per ^{238}U primary decay. Fiducial volume selections with 10 cm and 20 cm cuts reduce the rates to $1.5 \cdot 10^{-3}$ and $1.1 \cdot 10^{-4}$ decays per primary, respectively. For the ^{232}Th-chain, ^{208}Tl β-decay is the main background (~ 75%) again. In addition, γ-rays from the β-decays of ^{228}Ac and ^{212}Bi also contribute (~ 23 %/2 %). For the whole chain one has $7.3 \cdot 10^{-3}$ (no fiducialisation), $1.5 \cdot 10^{-3}$ (10 cm cut), and $1.3 \cdot 10^{-4}$ (20 cm cut) events per primary ^{232}Th decay. The fiducial volume cuts are less efficient for the ^{208}Tl events in the case of $2\nu\mathrm{EC}\beta^+$, but still reduce the background significantly [155].

In conclusion both, the fiducial volume cut and the actual amount of contaminants surrounding the TPC, influence the radiogenic background. In order to provide an exemplary experimental setting, the reported contamination levels and experimental details projected for the nEXO experiment [150] are considered and presented in figure 5.8. The main source of external γ-ray backgrounds for nEXO is the copper cryostat, with projected ^{238}U and ^{232}Th concentrations of 0.26 ppt and 0.13 ppt, respectively. The resulting background rate amounts to $2.8 \cdot 10^5$ primary decays per year as indicated in Figure 5.8 by the dotted grey line. It is evident that it would only require a 10 – 20 cm fiducial volume cut in order to achieve a favourable signal to background ratio[7]. Dark matter experiments, in contrast to

---

[6] By simulating the same number of events for each decay, decay chain equilibrium is implicitly assumed.

[7] This assumes the ~ 650 kg copper TPC vessel as the sole background source.

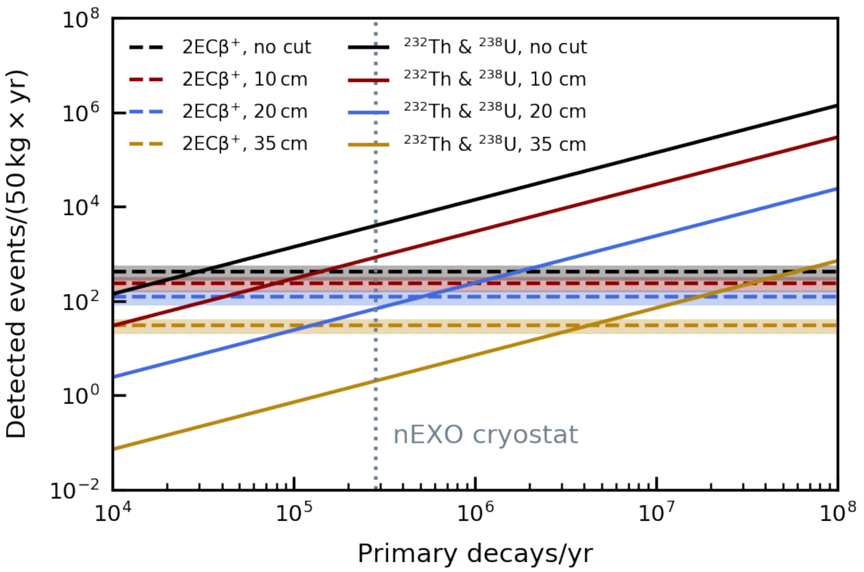

Figure 5.8: Expected events detected falsely as signal for a given number of primary decays per year for the ^{238}U and ^{232}Th decay chains. A reduction from the expectation in the full detector volume (solid black) is achieved by cutting the fiducial volume in all dimensions by 10 cm (red), 20 cm (blue) or 35 cm (gold). For reference the number of expected 2νECβ$^+$ signal events is shown for a 50 kg-year ^{124}Xe-exposure (dashed black) and for the respective fiducial volumes (dashed red, blue and gold) with correspondingly reduced exposures. The expected number of ^{232}Th and ^{238}U primary decays per year for the nEXO cryostat is indicated as the dotted gray line. Taken from [155].

nEXO, are optimised for the low-energy regime, and typically have higher background levels in the ∼ MeV range. They may therefore require more aggressive fiducial cuts in order to achieve a similar signal-to-background ratio. In any case, these results are a rough approximation. In a realistic experiment, a full likelihood analysis with a modelling of the events' spatial components and energy distributions should improve background discrimination. However, the detailed simulations for more precise estimates of these backgrounds are beyond the scope of this work.

5.3.2 ^{222}Rn

The β-decays of ^{222}Rn progeny within the LXe volume create backgrounds if there is coincident γ-emission [155]. The α-decay events can be easily rejected by the ratio of ionized charge to scintillation light [282]). Only two β-decays in the decay chain are energetic enough to produce relevant background: ^{214}Bi and ^{210}Bi. The decay of ^{214}Bi is accompanied by the subsequent α-decay of ^{214}Po within $T_{1/2} = 164\,\mu s$ [184]. This background can be rejected efficiently via a coincidence analysis. The Q-value of ^{210}Bi is well below the ROI for 0ν signals at 1.2 MeV. Moreover, it decays with no accompanying γ and does not pass the signal selection criteria.

5.3.3 (Anti)neutrino charged-current scattering

Charged-current (CC) scattering of neutrinos and antineutrinos is extremely rare. However, due to the rarity of the signals of interest, it may produce positrons which can exactly mimic them [155]. The CC scattering of antineutrinos with energies of a few MeV, such as reactor antineutrinos or geoneutrinos, produces a fast positron in the final state. The threshold for the charged-current reaction is given by the mass difference between the involved xenon isotopes and their iodine isobars. The cross-sections from [283] were obtained in tabular form from the authors.

The expected interaction rates for geoneutrinos were calculated for the two xenon isotopes with the lowest CC reaction thresholds (of those with > 1% abundance): ^{129}Xe and ^{131}Xe, which have thresholds of 1.2 MeV and 2.0 MeV, respectively. Convolving the energy spectra and flux with the cross section, interaction rates of 5.0×10^{-8} and 4.9×10^{-6} events per tonne-year of $^{\mathrm{nat}}$Xe exposure are found for ^{129}Xe and ^{131}Xe, respectively [155]. In a $^{\mathrm{nat}}$Xe G3 detector less than 0.01 events would be measured in a 10-year exposure. An experiment using xenon enriched in ^{134}Xe and ^{136}Xe will be completely insensitive to geoneutrinos due to their high thresholds for CC reactions at 5.1 MeV and 7.9 MeV, respectively [128]. There is an expected factor ~ 2 variation of geoneutrino flux across the globe. A similar calculation is carried out for reactor antineutrinos. Three possible locations were considered for an experiment: SNOLAB (in Sudbury, Ontario, CA), Sanford Underground Research Facility (in Lead, South Dakota, USA), and LNGS. The reactor antineutrino flux at each site was calculated using reactor power and location data in the Antineutrino Global Map reactor database [284]. The antineutrino flux and energy spectra were computed using the empirical models given in Ref. [285]. Neutrino oscillations were neglected for simplicity which leads to a slight overestimation of the interaction rate. At SNOLAB, the location with the highest flux due to nearby reactors, expected CC scattering rates of 9.1×10^{-7} and 3.6×10^{-6} events per tonne-year were calculated for scattering on ^{129}Xe and ^{131}Xe, respectively [155]. Accordingly, this background is negligible regardless of an experiment's location.

In contrast to antineutrinos, low-energy neutrino CC scattering does not create positrons directly. Here, backgrounds arise in the form of a prompt and a delayed component. The prompt component features the emission of a fast electron after a CC reaction and leaves a daughter nucleus in an excited state. This can emit γs and mimic the signal event topology. The delayed component stems from the creation of a daughter isotope that decays via β^+-emission. Solar ^{8}B neutrinos with energies of $\sim 1-15$ MeV may cause these two backgrounds. Consequently, they are the only solar neutrinos with enough energy to react above threshold *and* populate an excited state in the daughter nucleus. The energy-averaged cross-section for these reactions is of $\mathcal{O}\left(10^{-42}-10^{-41}\right)\mathrm{cm}^2$ [283], so 10's of events per tonne-year would occur for each isotope in a $^{\mathrm{nat}}$Xe detector [155].

In order to pass the selection criteria, prompt events would need to deposit a total energy below the ^{124}Xe Q-value. Due to the comparatively high energy of ^{8}B neutrinos, $\sim 90\,\%$ of neutrino CC events deposit more energy and are easily rejected. For $0\nu\mathrm{EC}\beta^+$, the narrow energy ROI reduces the impact of this background to a negligible level. For $2\nu\mathrm{EC}\beta^+$ the individual events with allowed energy depositions would still need to pass the further filtering steps. Therefore, this background is expected to be subdominant compared to the signal.

Delayed events would mainly occur in the form of ^{128}Cs and ^{130}Cs decays, which each have half-lives of < 1 hr and can decay via β^+-emission with Q-values of 3.9 MeV and 2.9 MeV, respectively. With the ^{8}B-averaged cross sections [283] a production rate of 0.02 nuclei of ^{128}Cs and 0.07 nuclei of ^{130}Cs per tonne-year of $^{\mathrm{nat}}$Xe exposure was calculated [155]. The resulting β^+ decays are distributed across a broad spectrum, and simulations indicate the expected background rates for the $2\nu\mathrm{EC}\beta^+$ process are an order of magnitude lower than the expected signal rate. The narrow ROI for 0ν searches renders these backgrounds negligible. Two isotopes of xenon feature CC reaction thresholds low enough to react with CNO, ^{7}Be, and pp neutrinos: ^{131}Xe and ^{136}Xe. Yet, the daughter isotopes either exclusively undergo electron capture (^{131}Cs) or β^--decay (^{136}Cs) with a Q-value of (2548.2 ± 1.9) keV

[286]. In turn, they are too low in energy for the $0\nu EC\beta^+$ selection and lack the positron signature to mimic the two-neutrino decays. Moreover, they have half-lives of $\mathcal{O}(10)$ days. Next-generation experiments plan to recirculate and purify the liquid xenon with a turnover time of ~ 2 days [127] which would remove these isotopes from the LXe before their decay [155].

5.3.4 Neutron-induced backgrounds

In neutron capture, the daughter nucleus is generally left in a highly-excited state leading to the emission of γ-rays. As the total energies in neutron capture are generally above the Q-value for ^{124}Xe decay, these events should be easy to reject and are not considered further. However, activated Xe-radioisotopes may decay via β^+ emission in the region of interest. The fast neutron scattering reaction $^{124}\mathrm{Xe}(n,2n)^{123}\mathrm{Xe}$ was identified as the only significant one. It has a neutron-energy threshold of 10.5 MeV with a cross-section of ~1.4 barn at ~ 20 MeV neutron energy [287]. Due to the high threshold radiogenic neutrons from (α,n) reactions cannot produce this background. It would be produced by muon-induced neutrons, which can extend in energy up to the GeV scale. The muon-induced neutron flux at Gran Sasso is 10^{-9} n/cm^2/s. It is downscaled by a factor of 10^{-2} to account for the expected reduction from shielding and veto typically employed in these experiments [82]. This yields an expected activation rate of ~10^{-3} nuclei per kg (^{124}Xe) per year. Each of these nuclei will produce a background event in a detector. However, the decay has a small β^+ branching ratio [288]. Moreover, the Q-value of 1228.6 keV [288] prevents it from passing the selection criteria for any of the signals except for the $2\nu EC\beta^+$. Here, the continuous spectra overlap between 1022 keV and 1228.6 keV. As the signal spectrum extends up to 2856.7 keV, an additional energy cut could fully remove this background with a minor signal efficiency loss.

In summary, the only significant background for $2\nu EC\beta^+$ originates from external γ-rays. With strong fiducial volume cuts, a likelihood-analysis utilising energy information and γ-background suppression, the G2 Dark Matter detectors XENONnT and LZ that are currently under commissioning may measure this decay mode in the near future. For $0\nu EC\beta^+$, the searches in G2 and G3 experiments will be virtually “background-free". Here, the experimental sensitivity will only be limited by the detection efficiencies and the achievable ^{124}Xe exposure.

5.4 Discovery potential and complementarity with other decay modes

The half-life measured by a detector with no expected background is calculated by rearranging equation (1.31) and inserting the reconstruction efficiency ϵ for the decay in question. If no events are observed in a background-free counting experiment, a 90 % C.L. lower limit on $T_{1/2}$ can be calculated by inserting $N = 2.3$. In the following a detector with 10 mm position resolution in the axial as well as the radial direction is discussed. The sensitivities for a G3 experiment with a 500 kg-year ^{124}Xe exposure are summarised in table 5.5 for all decay modes. A G2 detector enriched to 50 kg of ^{124}Xe would be approximately ~ 10% less sensitive due to the lower detection efficiency. With a $^{\mathrm{nat}}$Xe inventory the sensitivity of a G2 experiment is ~ 10 times smaller due to the exposure. The sensitivities are compared to the range of theoretical predictions from table 5.1 for 2ν-decays, and table 5.2 for 0ν-decays.

Among the two-neutrino decays, $2\nu EC\beta^+$ will likely be detected by a G2 Dark Matter experiment if the γ-background can be controlled. In this case a G2 experiment’s sensitivity would exceed the predicted $2\nu EC\beta^+$ half-life by more than an order of magnitude. A G3

Table 5.5: Theoretical predictions for the various decay channels of ^{124}Xe. The experimental sensitivity is calculated for a 500 kg-year ^{124}Xe exposure assuming a G3-experiment with 10 mm position resolution in all three dimensions, a negligible threshold, and no backgrounds. The range of theoretical predictions for neutrinoless decays is given between the weakest limit obtained with $\langle m_{\beta\beta}\rangle < 1.1\,\mathrm{eV/c^2}$ and the strongest limit obtained with $\langle m_{\beta\beta}\rangle < 0.061\,\mathrm{eV/c^2}$ (table 5.2). A G2 experiment with enrichment would have an approximately 10 % lower sensitivity due to the lower efficiency (table 5.4). Without enrichment the sensitivity of a G2 experiment would be reduced by an additional order of magnitude. Taken from [155].

Decay	**Exp. Sensitivity [10^{26} yr]**	**Exp. Sensitivity/Theory**
$2\nu EC\beta^+$	3.3	$(1.9 \pm 0.7) \cdot 10^3$
$2\nu\beta^+\beta^+$	2.5	$(1.3 \pm 0.4) \cdot 10^{-2}$
$0\nu ECEC$	2.4	$1.3 \cdot 10^{-3} - 6.2 \cdot 10^{-7}$
$0\nu EC\beta^+$	2.9	$6.0 - 5.5 \cdot 10^{-3}$
$0\nu\beta^+\beta^+$	2.4	$0.3 - 2.6 \cdot 10^{-4}$

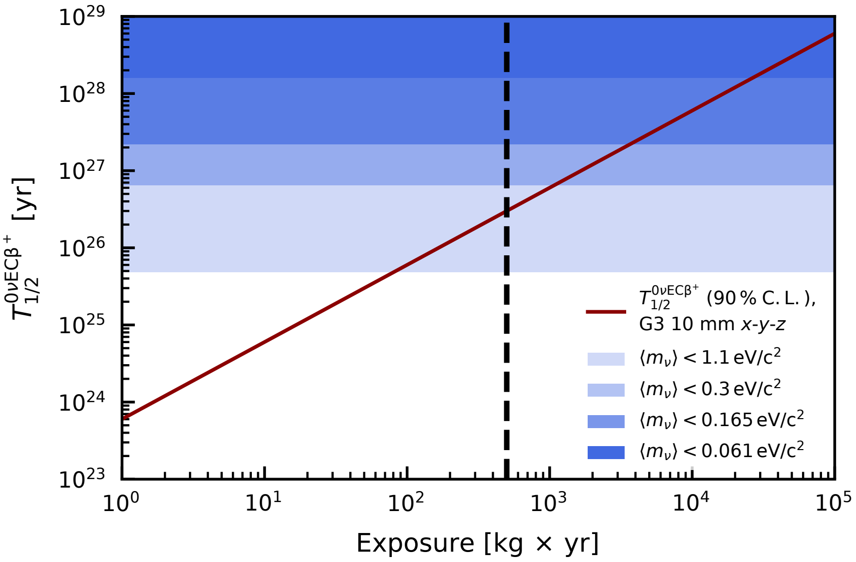

Figure 5.9: Projected 90 % C.L. lower limit on $T_{1/2}^{0\nu EC\beta^+}$ for a background-free experiment with 10 mm resolution in x-y-z, as a function of the exposure (red). This calculation assumes the G3 geometry; the sensitivity curve decreases by ~ 10 % for a G2 detector at all exposures. Four ranges of lower limits on the $0\nu EC\beta^+$-decay half-life are shown. They correspond to the upper and lower ends of the $\langle m_{\beta\beta}\rangle$ ranges in table 5.2: $\langle m_{\beta\beta}\rangle < 1.1,\mathrm{eV/c^2}$ (light blue) and $\langle m_{\beta\beta}\rangle < 0.3\,\mathrm{eV/c^2}$ (light medium blue), as well as $\langle m_{\beta\beta}\rangle < 0.165,\mathrm{eV/c^2}$ (dark medium blue) and $\langle m_{\beta\beta}\rangle < 0.061\,\mathrm{eV/c^2}$ (dark blue). The respective lower bounds are given by the weakest limit among the three NMEs for each $\langle m_\nu\rangle$. The dashed black line represents an exposure of 500 kg-year. Taken from [155].

Dark Matter experiment like DARWIN or an enriched nEXO-like detector could measure a few thousand signals. The $2\nu\beta^+\beta^+$ will likely be out of reach for all experiments discussed here. The same is true for $0\nu\beta^+\beta^+$ with half-lives inaccessible to experiments. As the 0νECEC half-life is similarly large in the absence of resonance enhancement it is also out of reach given current measurements of decay energies and ^{124}Te energy levels [27, 157]. Still, an independent measurement of the energy mismatch as recommended by the authors of [27] would be worthwhile in order to make a final verdict. This leaves $0\nu EC\beta^+$ as the most promising neutrinoless ^{124}Xe decay candidate.

For $0\nu EC\beta^+$ the experimental sensitivity is compared to the four different half-life scenarios from table 5.2. Scenarios one and two are based on the effective neutrino mass range of constraint 1 from equation 5.9. Scenarios three and four are based on constraint 2, using the KamLAND Zen effective neutrino mass limits from equation (5.10). The results are shown in figure 5.9 as a function of exposure. Within a 500 kg-year ^{124}Xe exposure, a background-free experiment would cover a significant portion of the parameter space given by the first constraint. Once this value is reduced, e.g. by phase cancellations in the PMNS-matrix, the lower limits on the half-life are an order of magnitude above the experimental sensitivity. Assuming light-neutrino exchange as the decay mechanism for ^{136}Xe and ^{124}Xe, the expected half-lives are two orders of magnitude above the experimental sensitivity taking into account the current limits placed by KamLAND Zen. Exposures larger than 10^4 kg-year would be needed to probe this parameter space [155].

5.4.1 Discussion

After calculating the half-lives for the second order weak decays of ^{124}Xe, investigating signal efficiencies of future detectors to the respective channels, and discussing possible background sources, the sensitivities of G2 and G3 experiments could be established. For a G2 Dark Matter detector a detection of $2\nu EC\beta^+$ is feasible. A background-free experiment is a realistic prospect for $0\nu EC\beta^+$, but only a G3 Dark matter detector or a nEXO-like detector enriched in ^{124}Xe would barely be sensitive enough to probe the most optimistic half-life predictions. This most optimistic predictions would require a mechanism that leads to a different decay mechanism in proton-rich and neutron-rich nuclei. Otherwise the accessible parameter space would already be excluded by existing constraints on $0\nu\beta^-\beta^-$.

In the case of extensions to the SM that predict exactly this effect, a measurement of $0\nu EC\beta^+$ would provide complementary information on the physical mechanism mediating the neutrinoless decay. Therefore, detectors with the capability of measuring ^{124}Xe and ^{136}Xe decays simultaneously would be an attractive proposition. An example mechanism are left-right symmetric models, in which a right-handed weak sector is added to left-handed SM neutrinos [28]. By adding right-handed terms to the Standard Model Lagrangian, a new expression for the half-life of neutrinoless second-order weak decays can be derived:

$$\begin{aligned}[T^{\alpha}_{1/2}(0^+_i \to 0^+_f)]^{-1} = &\\ & C^{\alpha}_{mm}\left(\frac{\langle m_\nu\rangle}{m_e}\right)^2 + C^{\alpha}_{\eta\eta}\langle\eta\rangle^2 + C^{\alpha}_{\lambda\lambda}\langle\lambda\rangle^2 + \\ & C^{\alpha}_{m\eta}\frac{\langle m_\nu\rangle}{m_e}\langle\eta\rangle + C^{\alpha}_{m\lambda}\frac{\langle m_\nu\rangle}{m_e}\langle\lambda\rangle + C^{\alpha}_{\eta\lambda}\langle\eta\rangle\langle\lambda\rangle.\end{aligned} \tag{5.12}$$

Here, α represents the decay mode ($0\nu\beta^-\beta^-$, $0\nu EC\beta^+$, etc.), $\langle m_{\beta\beta}\rangle$ is the effective neutrino mass, and $\langle\eta\rangle$ and $\langle\lambda\rangle$ are newly introduced effective coupling parameters that contain right-handed currents from the new interaction. The coefficients C^{α}_{ij} are decay-mode specific, and contain nuclear matrix elements and phase space factors. The λ terms are significantly enhanced in the case of the mixed-mode decays [28], so the shape of the parameter space

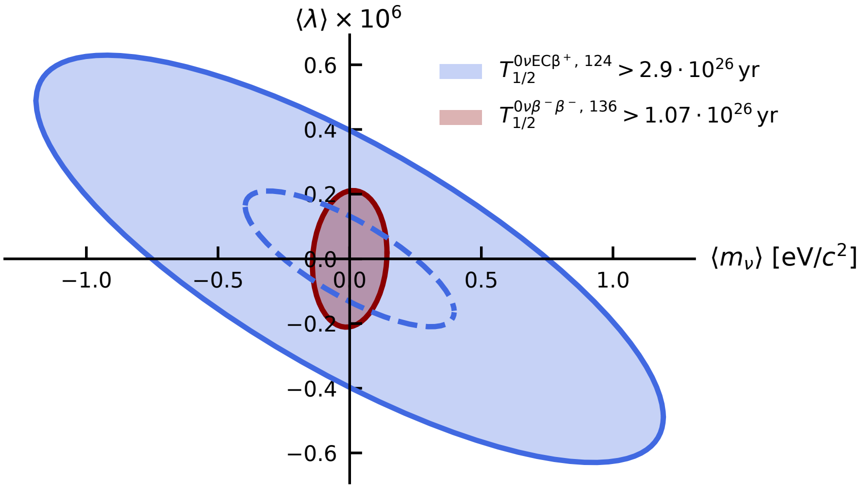

Figure 5.10: Comparison of exclusion limits at 90 %C.L. for left-right symmetric models, in the $\langle m_{\beta\beta}\rangle$ vs. $\langle\lambda\rangle$ plane. Parameter space outside the colored regions is excluded. Here we assume $\langle\eta\rangle = 0$. The exclusion limits compare the present limits on the $0\nu\beta^-\beta^-$-decay of ^{136}Xe [25] with the possible limits on $0\nu EC\beta^+$ derived in this work. We assume the full 500 kg-year exposure for the ^{124}Xe search – comparable to the 504 kg-year exposure used for the ^{136}Xe measurements. The dashed line represents the boundary of the excluded zone after arbitrarily scaling the NMEs for ^{124}Xe by a factor of three, to mimic uncertainties in NME calculations. Taken from [155].

explored by $0\nu EC\beta^+$ searches differs from that explored by $0\nu\beta^-\beta^-$ experiments. This is illustrated in figure 5.10. The possible limit for $0\nu EC\beta^+$ derived above for a G3 experiment is compared to the current limit for the $0\nu\beta^-\beta^-$ of ^{136}Xe decay from Kamland-Zen [25].

As observed earlier, the sensitivity of $0\nu EC\beta^+$ in ^{124}Xe to the $\langle m_\nu\rangle$ is significantly weaker due to the reduced phase space in the positron-emitting decay mode. Still, the sensitivity of the mixed-mode decay for the right-handed coupling $\langle\lambda\rangle$ is within a factor of two of that of ^{136}Xe decay. This is within the factor ~ 3 uncertainties typically assumed for nuclear matrix element calculations. Consequently, the ^{124}Xe measurement would provide complementary information in the event of a discovery of a 0ν decay mode in either isotope. Future experiments expect to reach sensitivities considerably larger than those shown in figure 5.10. Unless the $0\nu\beta^-\beta^-$ decay of ^{136}Xe is discovered with a half-life just beyond the existing limits, the ^{124}Xe mixed-mode decays will not be competitive in constraining left-right symmetric models with a G3 experiment's exposure. Still, proton-rich isotopes could still play a role in determining the mechanism of lepton number violation. Examples would be a discovery of neutrinoless decays in either only ^{124}Xe or in *both* ^{124}Xe and ^{136}Xe. This would indicate that neither the light neutrino exchange nor right-handed currents mediate neutrinoless second order weak decays, which would point towards alternative BSM physics. In light of these possible surprises, future xenon-based TPC experiments should explore $0\nu EC\beta^+$ in ^{124}Xe.

6 Sensitivity of XENON1T to the Neutrinoless Double-β Decay of ^{136}Xe

Although XENON1T was designed for the detection of low-energy nuclear recoils of WIMP Dark Matter it can be used as a demonstrator for high-energy searches in xenon dual-phase TPCs. Dedicated high energy reconstruction algorithms provide excellent energy reconstruction linearity and resolution for electronic recoils in the MeV range [201]. This chapter presents a sensitivity study for ^{136}Xe neutrinoless double-β decay that was carried out as a prerequisite of an unblinding of the XENON1T $0\nu\beta\beta$ data. This study showcases the physics potential in this channel for upcoming experiments such as XENONnT and DARWIN with their lower background and larger exposure. It also sets an example for other high-energy signal searches, e.g. those for $0\nu EC\beta^+$ in ^{124}Xe. The contents of this chapter represent the work of the XENON1T high-energy analysis group that has been headed by C. Capelli (reconstruction, data selections and fiducial volume as published in [201] and [289]), F. Gao (reconstruction and general coordination) and the author of this work (background model and statistical inference). The data has been unblinded recently, but due to the XENON publication policy the unblinded data cannot be shown in this work. A publication by the XENON collaboration containing the contents of this chapter and chapter 4 is in preparation.

6.1 Event reconstruction, fiducial volume and data selections

Several improvements in the reconstruction of high-energy events, i.e. the treatment of signals from energy depositions in the MeV-range, in PAX version 6.10.1 enabled the search for neutrinoless double-β decay with XENON1T [201]. Although the author of this work was only involved in the analysis as an internal reviewer, the improvements are outlined here in order to appreciate the results and their impact on the analysis. The primary concern when measuring signals in the MeV-range with a detector designed to probe nuclear recoils of few keV energy is saturation. While a WIMP interaction is expected to result in S2s with $\mathcal{O}(10^3)$ pe, signals and backgrounds in the blinded $0\nu\beta\beta$ signal region will produce S2s of $\mathcal{O}(10^6)$ pe (cf. figure 3.3). Accordingly, the PMTs themselves as well as the readout electronics are susceptible to saturation from large S2 signals. Saturation leads to information loss in affected PMT channels and adversely affects energy- and radial position-reconstruction. S1 signals are not expected to cause saturation since they lack gas-amplification and are more evenly distributed among the PMT channels in both arrays [201].

Figure 6.1 shows two typical single-PMT waveforms in high-energy events before and after saturation corrections. The uncorrected waveforms are denoted as W_S in the figure. The left waveform from a $\sim 2 \cdot 10^5$ pe S2 is truncated at the 2.25 V upper bound of the digitiser's

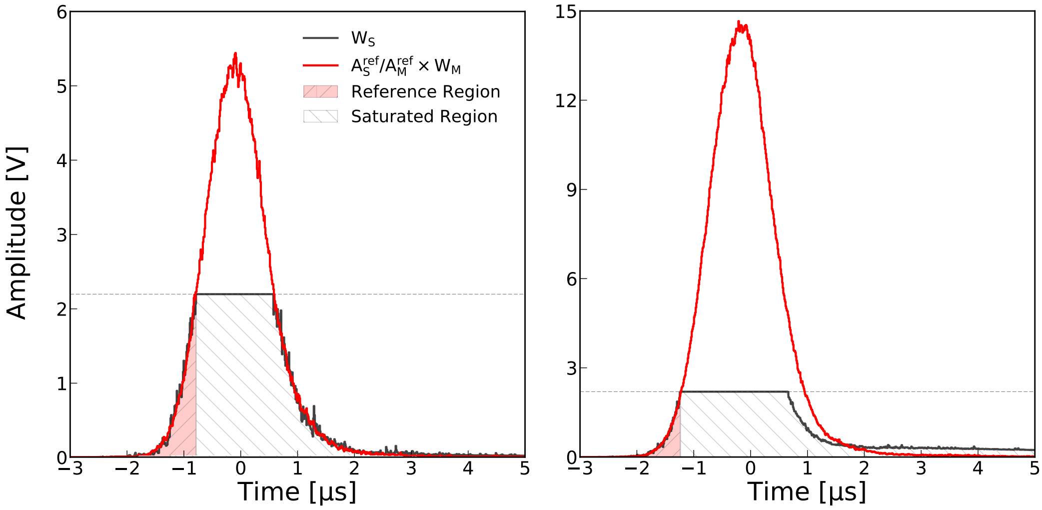

Figure 6.1: Example single PMT waveforms from S2s with a size of ~ $2 \cdot 10^5$ pe (**left**) and ~ 10^6 pe (**right**) before and after saturation corrections. The uncorrected waveforms W_S as measured by the digitiser are shown as solid grey lines. They are centred around zero in time. Both waveforms are truncated at the upper end of the digitiser's dynamic range. The corrected waveform model $A_S^{ref}/A_M^{ref} \cdot W_M$ is overlaid as the solid red line. The red shaded region in each panel marks the 1 µs reference region before the first truncated sample that is used to define the saturated waveform and model waveform areas A_S^{ref} and A_M^{ref}, respectively. The hatched region stretches from the first truncated sample to the end of the pulse and indicates the range where the waveforms are corrected. Modified from [201].

dynamic range. The right waveform originates from a ~ 10^6 pe S2 and is similarly truncated. In addition the tail of the waveform exhibits the effects of pre-digitiser saturation caused by a non-linear response of the PMT's voltage divider circuit and amplifier [201]. Since the S2 signals are highly localised in the radial direction, PMT channels that are further away from the S2s centre of gravity do not exhibit saturation. The sum waveform of the unsaturated PMT's is used as a waveform model W_M which is treated as the hypothetical shape of the total sum waveform in absence of saturation [201]. Each of the saturated waveforms is corrected using this model. The correct per-PMT scaling of W_M is derived by integrating the pulse areas A_S^{ref} and A_M^{ref} of the saturated and model waveforms, respectively, within a 1 µs reference region before the first saturated pulse. These reference areas are indicated by the red shaded regions in the figures and the corrected waveforms are shown as solid red lines. The corrections are applied up to the first pulse in the waveform that does not exceed the dynamic channel-specific threshold anymore.

Apart from saturation, high-energy waveforms contain signals that are not directly caused by particle interactions: light and electron emissions triggered by the primary S1 and S2 signals. The two main types of these secondary signals are photoionisation (PI) and PMT afterpulses (AP) [201]. If a PMT's vaccuum seal is imperfect, gas can enter the PMT body. It can subsequently be ionised by accelerated electrons between the photocathode and the first dynode when a PMT measures a photon signal. The drifted ions produce AP signals with a specific delay caused by the mass over charge ratio of the respective gas [204]. Scintillation light impinging on exposed metal surfaces or electronegative impurities creates individual electrons that cause PI signals in the form of spurious small S2s. Due to the magnitude of the primary signals both AP and PI are abundant in high-energy waveforms

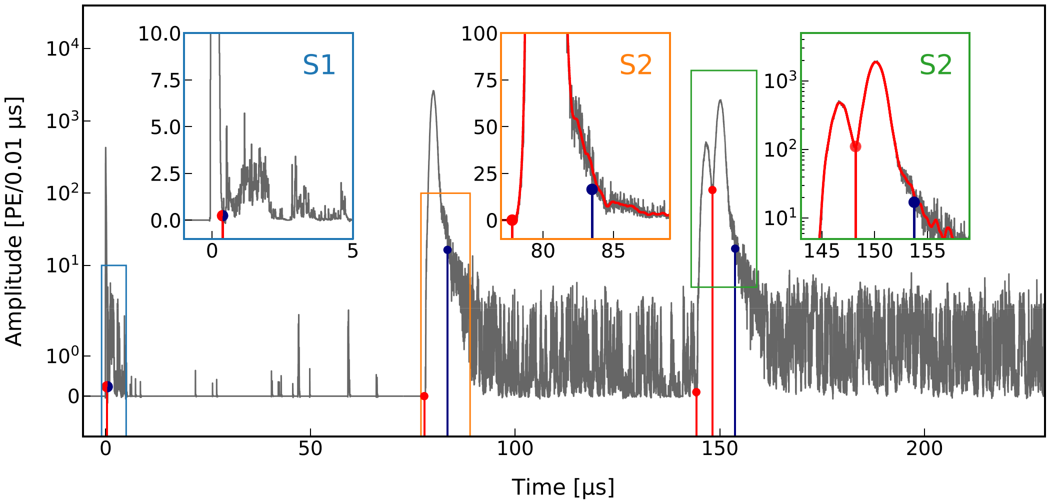

Figure 6.2: Exemplary sum waveform from a high-energy multiple Compton-scatter event. The raw sum waveforms in the main plot and insets are shown as solid grey lines while the smoothed waveforms are the solid red lines. The physical narrow S1 and wide S2 peaks are followed by AP and PI secondaries. The effects of the two clustering algorithms on each peak are shown in the insets. The left and right peak edges are indicated by red and blue circle markers. These mark the local minima and 3σ cutoff points. Taken from [201].

and have to be separated from the primary S1s and S2s. Otherwise they would bias the primary signals towards larger areas and consequently larger reconstructed energies.

Figure 6.2 shows a typical high-energy sum waveform caused by multiple Compton scatters inside the detector after saturation corrections. A single S1 peak and three S2 peaks are identified. All these primary peaks are followed by AP and PI secondaries and the S2 peaks overlap with one another. In order to separate the secondaries from the primaries and to distinguish the individual primaries, two complementary algorithms were incorporated in the PAX peak clustering plugin. In the first algorithm, the sum waveform (solid grey) from all PMTs is smoothed in order to minimise the impact of noise. Local minima in the smoothed waveform, indicated for the S2 peaks by the solid red lines, define the end of the S1 peak and the onset of each new S2 peak [201]. The local minima are indicated by the red circle markers in the figure. At this point the left boundary of each peak is set. The second algorithm sets the right peak boundaries in the form of an amplitude cutoff. The cutoff threshold on the falling edge of each peak is placed at the amplitude of a Gaussian function at a 3σ distance from the peak centre. The maximum amplitude of the Gaussian matches that of the respective peak. The Gaussian peak model is motivated by the longitudinal diffusion of the electron cloud during the drift [290]. For a Gaussian peak, the 3σ falling edge cutoff leads to a loss of only 0.13 % of the peak area while removing most of the secondary signals [201]. The cutoff points are indicated by the blue circle markers and vertical lines.

As the interaction position in the radial direction is reconstructed from the S2 hit pattern on the top PMT array, the saturation correction causes an improvement in position reconstruction. This is shown in figure 6.3 for 2614.5 keV ^{208}Tl γ-events from an external ^{228}Th source. The reconstructed radial positions from a neural network with four hidden layers shows good agreement between the reconstructed and the true TPC edge (black dashed) in the corrected data (solid red). In the uncorrected data (solid blue) the radial position reconstruction shows an inward bias due to the information loss from saturation. In the figure drift-field inhomogeneity is taken into account as in [70].

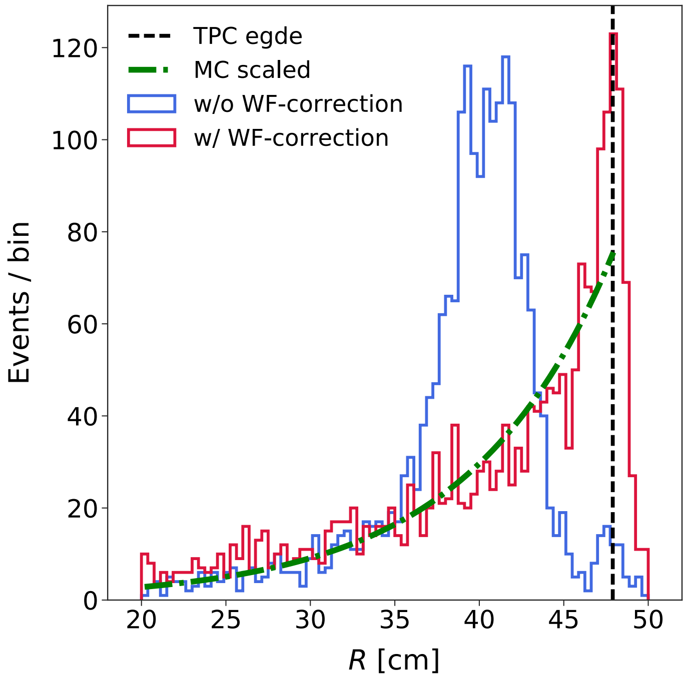

Figure 6.3: Radial position distributions of ^{208}Tl events from external ^{228}Th calibration source. Data processed with waveform saturation corrections (solid red) reproduces the true TPC edge (dashed black) as well as the expected distribution – scaled to match the data – from MC simulations (dash-dotted green). The uncorrected data (solid blue) exhibits an inward bias due to saturation affecting the PMT hit patterns which are used by a neural network for radial position reconstruction. Taken from [201].

The energy reconstruction of high-energy events works by the same principle as outlined in section 3.1 and the code developed in the scope of that analysis was used by the high-energy reconstruction team. Figure 6.4 shows the reconstructed energy spectra, energy resolution and deviation of the reconstructed energies from the true peak energies for events with a single (blue) and multiple S2 signals (red). These are referred to as single- and multi-site events, respectively. For the latter population the energy is reconstructed from the sum of corrected S2 signals within the event. The separation of the individual S2s allows to reconstruct the interaction position for each S2 individually, so the correct position-dependent S2 corrections can be used. A fit of both single- and multi-site light and charge yields resulted in consistent energy reconstruction parameters [201]

$$\begin{aligned} g_1 &= (0.147 \pm 0.001)\ \mathrm{pe/ph}, \\ g_2 &= (10.53 \pm 0.04)\ \mathrm{pe/e}. \end{aligned} \tag{6.1}$$

The z-dependence of these parameters was determined in the same fashion as in section 3.1, but parametrised such that one has $cS1(z)$ and $cs2_\mathrm{b}(z)$ while g_1 and g_2 are constant [201]. Figure 6.4 shows the reconstructed energy spectra, the relative energy resolution and the relative deviation of the reconstructed energies from the true peak energies. These observables are given for single-site (blue) and multi-site (red) events in a cylindrical 1 t fiducial volume.

Starting with the spectra in the top panel of figure 6.4, the fiducial volume selection leads to a lower rate of multi-site events at low energies. Single site events in the low energy region are still mainly caused by the ^{85}Kr, ^{214}Pb and ^{136}Xe single- or double-β

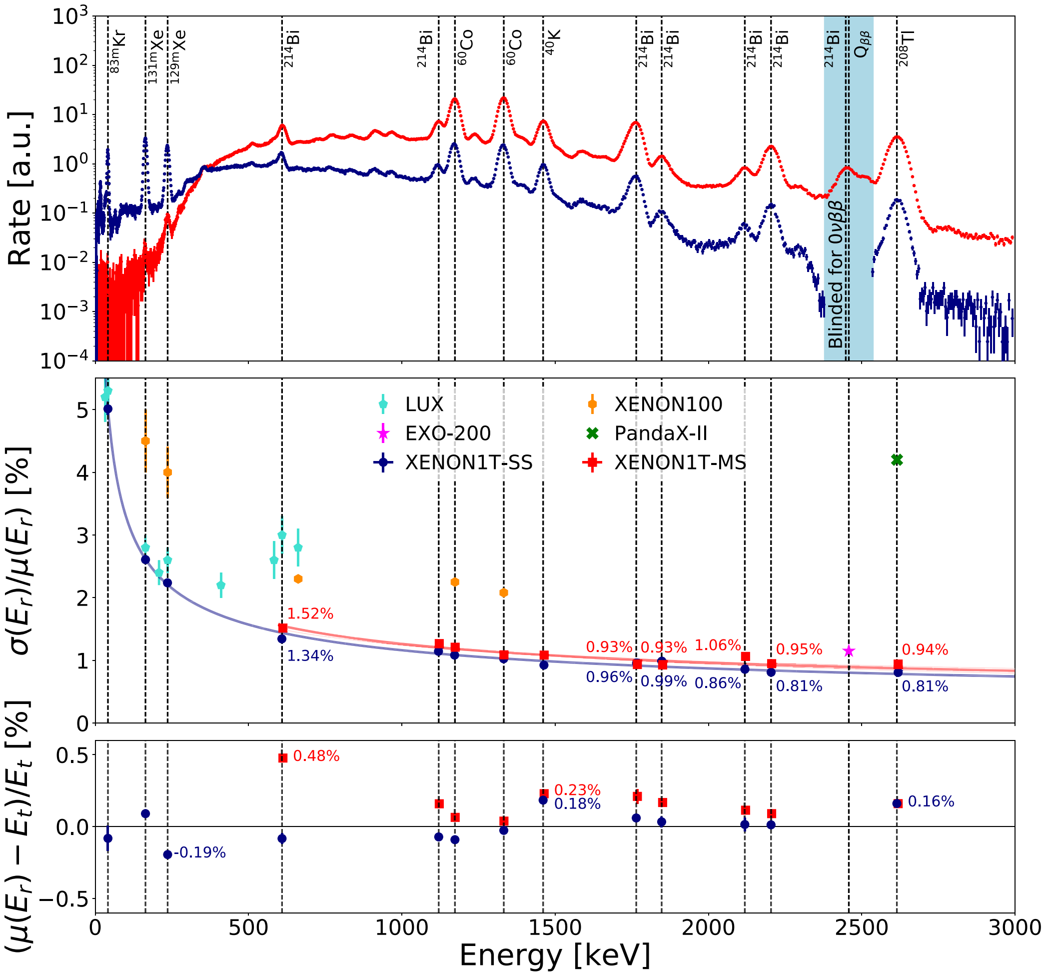

Figure 6.4: Energy reconstruction observables as a function of the reconstructed energy after high-energy enhancements of PAX. **Top:** Electronic recoil energy spectra for single-site (blue) and multi-site (red) events in a central cylindrical 1 t fiducial volume of XENON1T with the rate in arbitrary units. The light blue shaded region marks the blinding of the energy region around the ^{136}Xe Q-value $Q_{\beta\beta}$ for single-site events. Black dashed lines mark mono-energetic peaks and are labelled with the source isotopes. The fiducial volume selection leads to a lower rate of multi-site events at low energies while the increasing Compton-scattering cross-section leads to a higher multi-scatter rate above ~ 350 keV. **Middle:** Relative energy resolution for single- and multi-site events in XENON1T derived from the standard deviation $\sigma(E_r)$ and mean $\mu(E_r)$ of Gaussian fits to mono-energetic lines. The data points are fitted with the empirical function from equation 5.11. Results from XENON100 [197], LUX [227], EXO-200 [138] and PandaX-II [291] are included for comparison. **Bottom:** Relative deviation of the reconstructed mean energies $\mu(E_r)$ from the expected values E_t for single- and multi-site events. Taken from [201].

emitters. External γ-rays only contribute here if they have undergone Compton-scattering outside of the sensitive volume and if they are absorbed in the fiducial volume in a single resolvable interaction. Above ~ 350 keV the multi-site events dominate over single-site events due to the increasing Compton-scattering cross-section in LXe. With regard to the energy resolution, a 4σ-region around the ^{136}Xe Q-value $Q_{\beta\beta}^{^{136}\mathrm{Xe}} = 2458.7(0.6)$ keV [154] was blinded. The blinding cut was implemented before the high-energy enhancements in data processing. Accordingly, the energy reconstruction and resulting resolution have changed afterwards. This can cause fringe-effects: Events that had reconstructed energies outside of the blinded region with the preliminary energy reconstruction can move into the blinded region with the new energy reconstruction and vice versa. Accordingly, for the present analysis a larger energy window from 2300 to 2600 keV is excluded from the analysis before unblinding.

Among the xenon TPCs shown in figure 6.4, XENON1T offers the best energy resolution for single-site events. The resolution was determined by fitting mono-energetic peaks in the measured spectrum with Gaussian functions where the ratio of the fitted standard deviation $\sigma(E_\mathrm{r})$ and mean $\mu(E_\mathrm{r})$ gives the relative energy resolution. The resulting resolution data points were then fitted with the phenomenological function from equation (5.11). The parametrisation for the single-site energy resolution as a function of the reconstructed energy E_r is

$$\frac{\sigma(E_\mathrm{r})}{\mu(E_\mathrm{r})} = \frac{(0.313 \pm 0.007)\,\mathrm{keV}^{1/2}}{\sqrt{E_\mathrm{r}}} + (0.0017 \pm 0.0002). \tag{6.2}$$

With this, the single-site energy resolution $Q_{\beta\beta}^{^{136}\mathrm{Xe}}$ is $(0.80 \pm 0.02)\,\%$ [201]. For comparison, the dedicated double-β decay experiment EXO-200 achieved $(1.15 \pm 0.02)\,\%$. The energy resolution for multi-site events is slightly worse at $(0.90 \pm 0.03)\,\%$ [201]. Multi-site events are not considered further in the analysis since the majority of $0\nu\beta\beta$-events are expected to be single-site due to the few-mm range of the emitted electrons. In XENONnT a consideration of multi-site events would allow to place stronger constraints on backgrounds. Since the XENON1T study is a proof-of-principle analysis and since it is not expected to yield a limit that can compete with EXO-200 [138] and Kamland-Zen [25], it was decided to analyse the single-site energy spectrum only.

The single-site energy spectra will be fitted with MC simulations as in section 3, so the linearity of the energy reconstruction is a central concern. For the fitted monoenergetic peaks it is evident that the reconstructed mean energies $\mu(E_\mathrm{r})$ show relative deviations from the expected values E_t that are below 0.2 % for single-site events [201]. This would translate to an absolute 5 keV deviation from the expected energy at $Q_{\beta\beta}^{^{136}\mathrm{Xe}}$.

6.1.1 Fiducial volume and cuts

At MeV energies – depending on the fiducial volume already at 500 keV [66] – the background energy spectrum is dominated by γ-rays from detector construction materials. As the background composition differs from the radon-dominated Dark Matter and double-electron capture searches, the optimal fiducial volume is expected to be different. In order to obtain the optimal fiducial volume, a similar method as in section 3.1.2 was applied [289]. The total active volume of the detector was segmented into 64 bins with 8 bins each in the squared radius R^2 and depth Z directions. The sensitivity figure of merit $S_\mathrm{vol,\,i}$ from equation (3.5) was calculated for each bin, denoted by the index i, using events within $4\sigma_E$ energy-resolution windows of the 2.2 MeV ^{214}Bi and 2.6 MeV ^{208}Tl peaks. The resulting grid of sensitivity values was smoothed to 100 contour levels of S_vol. The result is shown in figure 6.5. The optimal fiducial volume is not centred in Z, but shifted towards the bottom of the sensitive volume. This is expected, as the LXe layer between the bottom

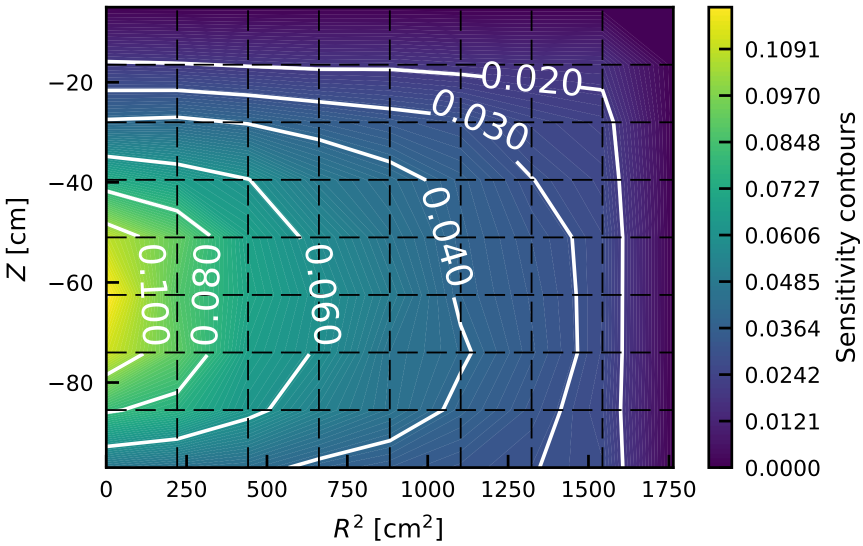

Figure 6.5: Sensitivity figure of merit contours in the active volume of the XENON1T detector. The TPC was segmented into $8 \cdot 8$ bins in the R^2 and Z directions (dashed black). The sensitivity figure of merit for each bin was calculated according to equation (3.5) using events within 4σ energy-resolution windows of the 2.2 MeV ^{214}Bi and 2.6 MeV ^{208}Tl peaks. The resulting 2D histogram was then smoothed to 100 figure of merit contours shown in the plot by the colour scale. Six exemplary contours are indicated by the white solid lines. Modified from [289].

PMT array and the cathode offers more shielding from material backgrounds, especially from the PMTs, than the GXe layer at the top of the detector. Accordingly, the contours of equal S_{vol} were fitted with an asymmetric shape function. This function consists of two semi-superellipsoids from the top and bottom. The bottom superellipsoid is constrained to Z-values above −94 cm in order to maintain a minimum clearance from the cathode. The resulting total figure of merit values $\sum_i S_{\mathrm{vol,\,i}}$ for the fitted contours were then contrasted with the enclosed fiducial mass. The optimal volume with a mass of $(741 \pm 9_{\mathrm{sys}})$ kg was identified by fitting a parabola to the resulting distribution 6.6 [289]. The shape of the optimal volume is shown in figure 6.6.

The data selection cuts are conceptually similar to those outlined in section 3.1.1. They are summarised in table 6.1 together with the methods used to derive the cut acceptances. Since most cuts were previously not defined up to the MeV range, they had to be updated for the $0\nu\beta\beta$ analysis [289]. These cuts are marked in the table with the suffix *_HE*. Cuts that were not previously discussed are outlined in the following. The *MuonVeto* cut is used in this analysis and removes events which were coincident with a trigger from the muon veto. This cut effectively reduces the live time of the measurement, so the acceptance loss is treated in the same fashion as for the *DAQVeto* and *S2Tails* cuts. The analysis uses PAX version 6.10.1 which only requires a two-fold PMT coincidence for S1 signals in order to achieve a lower energy threshold. Since this is not needed for the high-energy analysis discussed here, the previous three-PMT coincidence criterion was reintroduced with a cut that has unity acceptance in the MeV energy range. The *ERband* cut targets a different event population than in the double-electron capture analyses. There, the cut was supposed to remove NR and wall background events. Here, the cut is supposed to remove γ-X events. These events occur at the bottom of the detector when a γ-ray interacts in the LXe volume between the bottom PMT array and the cathode. Ionisation electrons from this region cannot reach

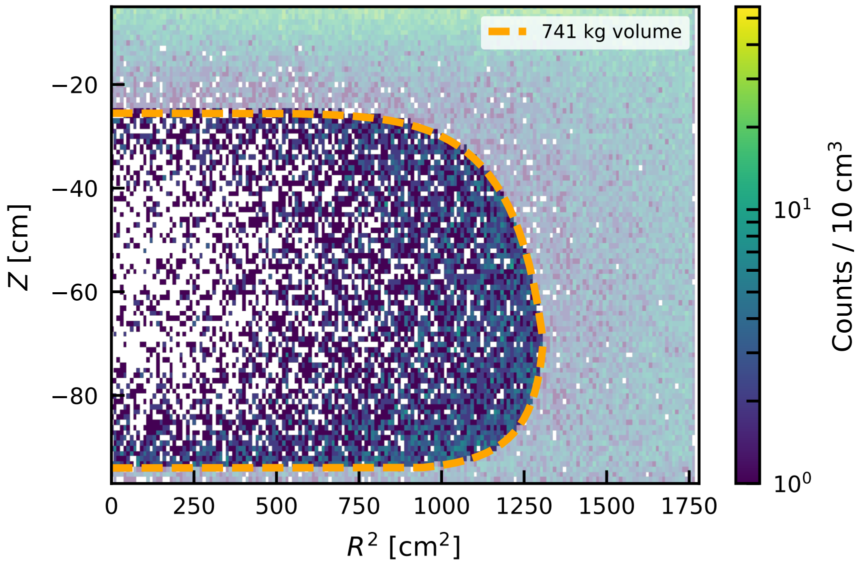

Figure 6.6: Optimal 741 kg fiducial volume for the 0νββ analysis constructed from two semi-superellipsoids and constrained to $Z \geq -94$ cm (dashed orange). The volume is offset downwards from the centre of the TPC due to the lower background at the bottom of the detector. The 2D histogram shows the background data underlying the optimisation. Modified from [289].

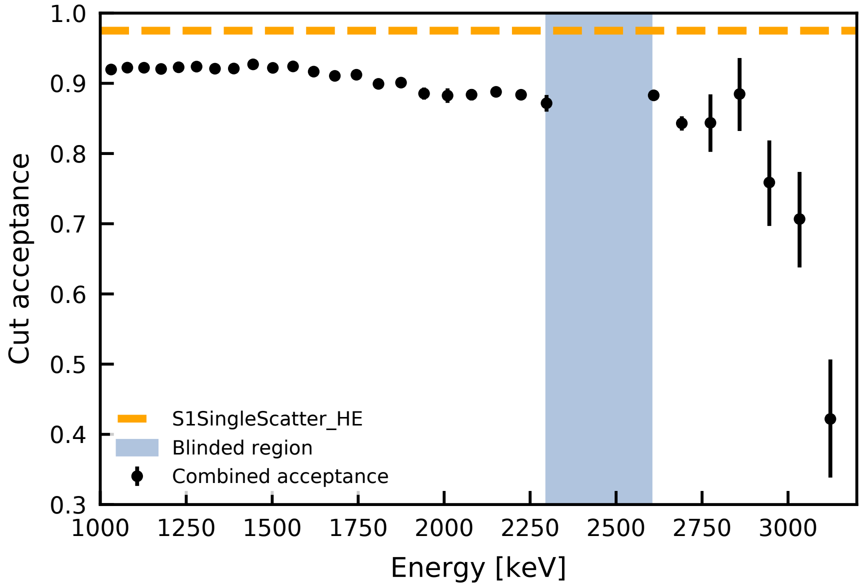

Figure 6.7: Cut acceptance for the 0νββ analysis. The *S1SingleScatter_HE* cut features a 97.5 % acceptance by definition (dashed orange). The combined acceptance of the remaining cuts was calculated iteratively. Multiplying this with the *S1SingleScatter_HE* acceptance yields the black points. The vertical uncertainties are the Gaussian-propagated binomial uncertainties of the single cut acceptances. The horizontal uncertainties from the variable binning with the energy resolution are not shown in the plot. Since the acceptance of the *ERband* cut was determined on background data, the blinded region was excluded from the determination of the total acceptance. Modified from [289].

Table 6.1: Data quality criteria (cuts) for the $0\nu\beta\beta$ search with their acceptance derivation method and a short description. The different methods of determining the cut acceptance have been outlined in section 3.1.1.

Cut name	**Acceptance derivation**	**Description**
DAQVeto	Live time	Correct for DAQ deadtime
S2Tails	Live time	Remove high rate periods following large S2s
MuonVeto	Live time	Remove events coincident with muon veto trigger
S1PMT3fold	Analytic	Require threefold S1 coincidence
S2SingleScatter_HE	Analytic	Remove multi-site events
S1SingleScatter_HE	Analytic	Remove signals with multiple S1s from consecutive nuclear decays or pileup
ERband_HE	Analytic, $N-1$	Remove events with anomalous S2/S1 ratio
CS2AreaFractionTopExtended	Iterative (^{220}Rn)	Remove events with anomalous relative PMT array contributions to the S2
S1AreaFractionTop_HE	Iterative (^{220}Rn)	Remove events with anomalous relative PMT array contributions to the S1
S2PatternLikelihood	Iterative (^{220}Rn)	S2 signal distribution among PMTs
S2Width_HE	Iterative (^{220}Rn)	Correlate S2 signal width and interaction depth
PosDiff_HE	Iterative (^{220}Rn)	Remove signals where PMT pattern fit and neural network yield different positions

the top of the detector, so only S1 signals from these interactions are measured. If the γ interacts a second time, but this time in the active volume between cathode and gate, it will display an anomalous S2/S1 area ratio due to the additional S1 from the first interaction. Accordingly, a selection of the ER band removes such events. Since γ-X events do not occur at the top of the detector, the cut is defined on the central 98 % interval of the ER band from events occurring in the top half of the effective volume. In addition to the cut definition, this also gives the analytic acceptance of 98 %. The *CS2AreaFractionTopExtended* cut is conceptually similar to the *S2AreaFractionTop* cut from the double-electron capture analysis, but was redefined after the reconstruction updates in order to achieve a higher acceptance. The *PosDiff_HE* cut compares the reconstructed interaction positions of two different reconstruction algorithms, namely a likelihood fit of the top PMT array hit pattern and a neural network [292]. Events with a difference in the reconstructed radial interaction positions above a threshold value are discarded.

The combined cut acceptance was determined in the same fashion as in section 3.1.1 using the analytic, $N-1$ and iterative acceptances [289]. The combined acceptance is shown in figure 6.7. The dashed orange line shows the acceptance of the *S1SingleScatter_HE* cut. This is the only cut with an analytic acceptance different from unity. Since it removes 2.5 % of the data by definition, the upper bound of the cut acceptance is $a_{\mathrm{up}} = 97.5\,\%$. The combined cut acceptance of the remaining cuts is multiplied with a_{up} which yields the black data points. The uncertainties represent the Gaussian-propagated binomial uncertainties of the single acceptances derived in [289]. The combined acceptance from these points can be interpreted as a lower limit on the cut acceptance since the method assumes that all events removed by the cut under investigation are signal events.

6.1.2 Exposure and neutron generator γ-background

Initially it was planned to use the same 247 d dataset as in the SI-WIMP analysis [12]. This dataset had to be reduced to 202.7 d because of an additional external high-energy γ-background from the neutron generator. During SR1 the NG was immersed in the water tank and next to the TPC for extended periods of time, namely from 10th February 2017 to 13th April 2017 and from 1st May 2017 to 8th June 2017. In the first period several tests of the NG were carried out and the second period was used for more tests and a neutron calibration. During most of these periods, the NG was not in operation. The live time of science data with the neutron generator next to the TPC is 44.5 d while there are 202.7 d of data without the NG. Figure 6.8 shows the exposure-corrected event rate per tonne and day in an energy range from 300 to 3200 keV in the 741 kg fiducial volume for each of the 6362 data taking runs of 247 d dataset from [12]. The upper bound of the energy range is the upper analysis bound for $0\nu\beta\beta$ in this analysis. The lower bound has been chosen in order to remove the time-varying rate of neutron-activated xenon isotopes (cf. table 3.2). Periods with the NG next to the detector (red) exhibit a clear increase in event rate compared to periods with the neutron generator removed (blue)[1]. Moreover, the rate in the blue data without NG is stable while it varies in the red data. This could be attributed to moving the neutron generator to different positions in the water tank. However, these positions cannot be reconstructed from the entries in the XENON1T runs database or electronic logbook. Since neutron calibration data is excluded in the data shown in the figure, the additional rate must stem from γ-rays emitted from the inactive NG.

The energy-dependence of the rate increase can be inferred from comparing the rate in the blue periods alone with that from the red periods. The corresponding spectra in the

---

[1] The neutron generator was not extracted from the water tank in these periods, but pulled towards the top of the tank. Thus, a few metres of water shielded the TPC from the NG. Next to the TPC this shielding is reduced to a few centimetres.

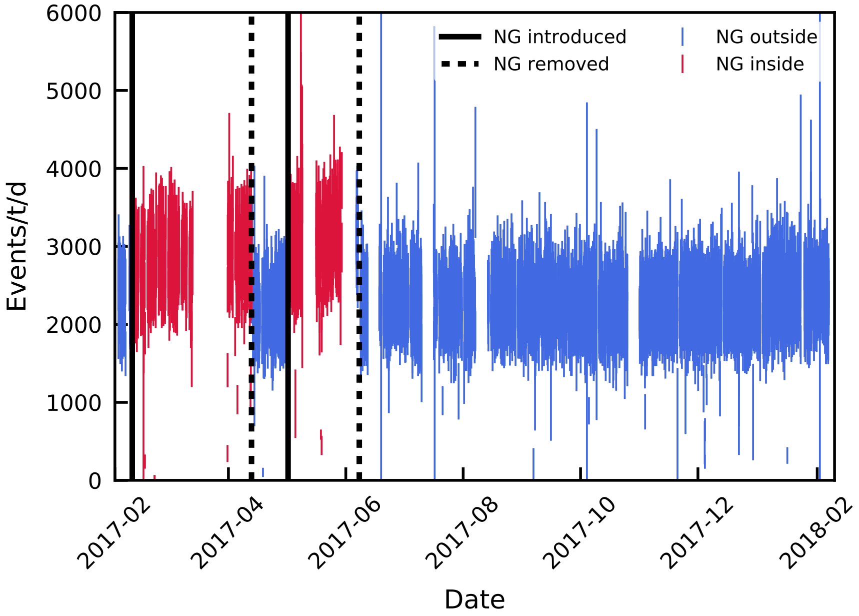

Figure 6.8: Exposure-corrected event rate per tonne and day in an energy range from 300 to 3200 keV in the 741 kg fiducial volume for each of the 6362 data taking runs in the 247 d dataset from [12]. Only background and no calibration data is shown in the plot. Data with the inactive NG next to the TPC is indicated by the red data points, data with the NG removed is shown in blue. The introduction and removal dates of the NG are illustrated by the solid and dotted black lines. Uncertainties on the data are Poissonian for each data taking run.

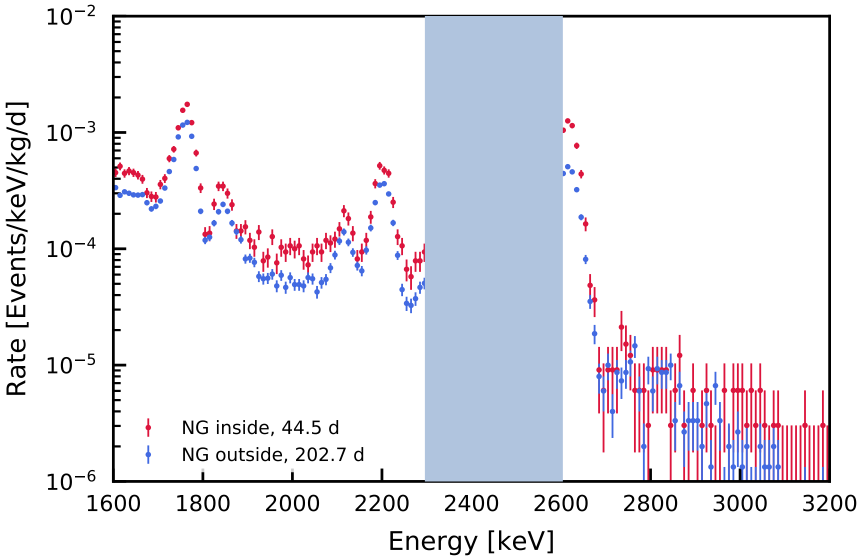

Figure 6.9: Energy spectra in the 741 kg fiducial volume from 1600 to 3200 keV. The data with the NG next to the TPC is shown in red. The live time of this data is 44.5 d. The 202.7 d of data with the NG removed are shown in blue. The binning of the data is 10 keV and uncertainties are Poissonian. The blinded region is shown in light blue.

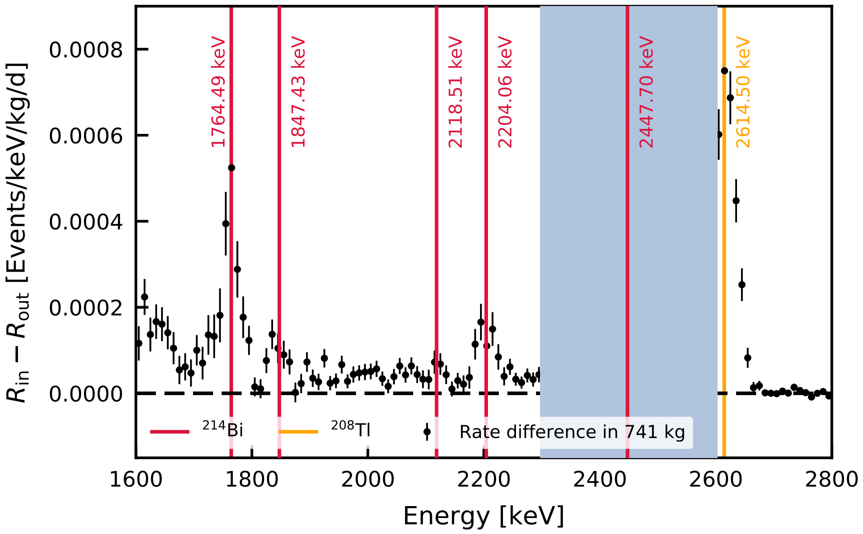

Figure 6.10: Absolute rate difference between the data with the neutron generator inside, R_{in}, and the data with the neutron generator outside, R_{out}, of the water tank (black points). The energy region is 1600 to 2800 keV. The binning of the data is 10 keV and uncertainties are Gaussian-propagated Poissonian uncertainties from the datasets with and without the NG. Several γ-lines of ^{214}Bi and ^{208}Tl are marked by the vertical red and orange lines, respectively. The mean energies are given next to the lines [183, 184]. The blinded region is shown in blue.

energy range relevant for $0\nu\beta\beta$ of ^{136}Xe in the 741 kg fiducial volume are shown in figure 6.9 with the same colour-coding as before. A clearly increased event rate in the data with NG is found. In the ^{208}Tl peak at 2614.5 keV [183] the rate in the red data is almost twice as high as in the blue data. Going higher in energy, the event rates in both datasets are the same since no γ-rays above the ^{208}Tl energy are expected. The absolute rate difference from 1600 to 2800 keV is shown in figure 6.10. Several γ-lines from ^{214}Bi (red lines) [184] can be identified in addition to the aforementioned line of ^{208}Tl (orange). This points to the presence of of ^{238}U and ^{232}Th in the NG. Other regions of increased background around 1600 keV and 2000 keV cannot be easily identified with isotopes from those decay chains and could be related to neutron-activation of the NG's aluminium casing itself [293]. Since it was not considered as a permanent background source, the NG had not been screened and eventual backgrounds from its construction materials had not been considered in the XENON1T MC simulation[2]. Since ^{214}Bi peaks are present in the measured spectrum, the 2447.70 keV line [184] is expected to appear in the blinded region. According to the MC simulations presented in the next section, this is the main background line for ^{136}Xe $0\nu\beta\beta$. With this, the NG-inside data contains a significant background that cannot be modeled sufficiently. Consequently, the data with the NG next to the TPC is removed from the final analysis dataset resulting in a final exposure of 0.41 t-yr.

A final concern arises from the fact that data with the NG next to the TPC is present in both, the clean and dirty, datasets used for the double-electron capture searches in chapters 3 and 4. In these analyses the fiducial volumes extend further outwards, so external backgrounds have a larger impact. The event rate per run from 300 to 600 keV in

---

[2] Internal studies on the background impact of the NG next to the TPC were carried out during SR1. None of these studies used the full SR1 background dataset and all analyses targeted the low-energy WIMP search region. There, the rate increase was found to be unproblematic. The energy region relevant for $0\nu\beta\beta$ was not considered.

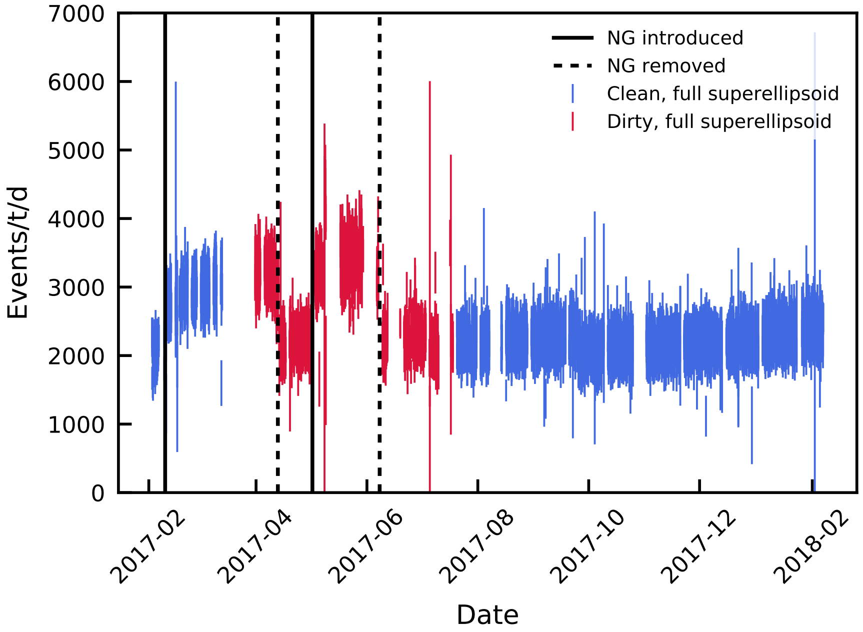

Figure 6.11: Event rate per run from 300 to 600 keV in the full 1.5 t superellipsoid for the clean (blue) and dirty (red) 2νECEC data from chapter 4. The introduction and removal dates of the NG are illustrated by the solid and dotted black lines. Uncertainties on the data are Poissonian for each data taking run.

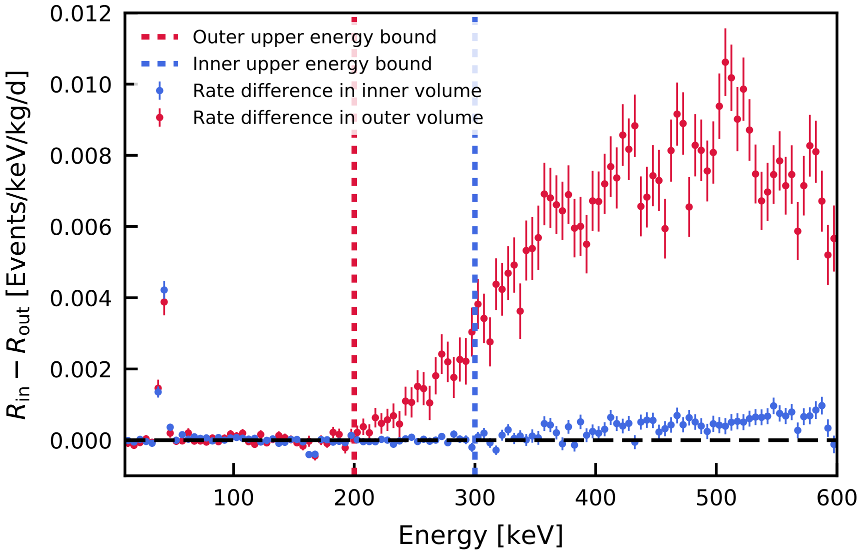

Figure 6.12: Rate difference as a function of energy between data with and without the neutron generator next to the TPC for the inner (blue) and outer (red) fiducial volumes from chapters 3 and 4. The energy range is 10 to 600 keV in 5 keV bins. Uncertainties are Gaussian propagated Poisson uncertainties for the datasets with and without the NG. In order to avoid neutron-activations, only NG-inside data from before the first neutron calibration in SR1 is used (15.7 d). For the NG-outside data, 155.4 d from the clean partition from [14] are used. The energy bounds for both fiducial volumes from chapter 3 are shown by the dashed lines in the respective colours.

the full 1.5 t superellipsoid for the clean and dirty 2νECEC data from chapter 4 is shown in figure 6.11. Although the energy region is smaller, the rate increase with the NG is more pronounced due to the larger fiducial volume.

The spectral shape of the NG-induced γ-background is again investigated by looking at the rate difference between NG-inside and NG-outside data. Since the effect of the γ-background from the NG could be obscured by neutron-activated xenon, only NG-inside data before the first neutron calibration in SR1 is used, which amounts to 15.7 d of data. For the NG-outside data, the remaining 155.4 d of clean data according to [14] are used. The rate differences for the inner (blue) and outer (red) fiducial volumes from the 2νECEC analyses in chapters 3 and 4 are shown in figure 6.12. As expected, the absolute background contribution is more pronounced in the outer volume and the continuous shape can be attributed to Compton-scatters. At low energies, the rate difference fluctuates around zero in both volumes, so the 2νECEC peaks are not affected by additional background. The onset of NG-background occurs at ~ 200 keV in the outer and at ~ 350 keV in the inner volume. This is just above the energy range used for the 2νECEC analysis in chapter 3 and [31] and the relative fraction of NG-inside data in the 177.7 d dataset was small. In conclusion, there is no impact on this analysis. For the analysis in chapter 4 the NG-background was already known and the energy ranges used in the fits were reduced accordingly. It should be noted that this background would not manifest itself as a peak at the 2νKK and 2νKL energies, but as a Compton continuum that would increase the overall background level.

6.2 Background model

This study uses the same simulations and fitting framework as the 2νECEC searches in chapters 3 and 4, albeit in a different energy range from 1600 to 3200 keV and with a stronger emphasis on material over intrinsic backgrounds. The numbers of simulated events for each background can be found in table 3.4 for material backgrounds and in table 3.5 for intrinsic backgrounds. Only two isotopes are expected to produce background for the 0νββ search from inside the LXe: ^{136}Xe and ^{214}Bi. The former has been discussed in detail in section 3.2 and the corresponding simulations and background constraints are also used in this analysis.

The background from ^{214}Bi was not relevant for the former analyses and two separate contributions have to be considered. First, ^{214}Bi decays inside the active volume of the detector. This background can be rejected due to the second S1 from ^{214}Po decay in so-called BiPo events (cf. section 3.2). Assuming an equilibrium of ^{214}Bi with the ~ 10 μBq/kg activity concentration of ^{214}Pb and a 90 % BiPo rejection efficiency, a residual ^{214}Bi activity concentration of 1 μBq/kg is expected in the active volume. The spectrum after the selection of single-site events consists of the continuous ^{214}Bi β-spectra from decays to various excited states of ^{214}Po. These are merged with the energy depositions of the ^{214}Po γ-rays where the individual scatters could not be distinguished from one another and the β-interaction. The second ^{214}Bi background originates from the uninstrumented LXe shell surrounding the TPC. For this background the α- and β-particles emitted in the ^{214}Po decay cannot be measured, so BiPo coincidences cannot be used to reject these events. With this the activity concentration in the LXe shell contributing to the background spectrum is ~ 10 μBq/kg. Only γ-rays from the ^{214}Bi decay can reach the fiducial volume and produce multiple peaks.

The expected intrinsic and material background spectra are shown in figure 6.13. At the expected activity levels, the intrinsic backgrounds are subdominant to the material backgrounds. In addition, an exemplary 0νββ-peak from ^{136}Xe is shown. The decay rate leading to the displayed peak assumes the measured ^{136}Xe abundance of $\eta_{^{136}\mathrm{Xe}} = 8.49\,\%$ and

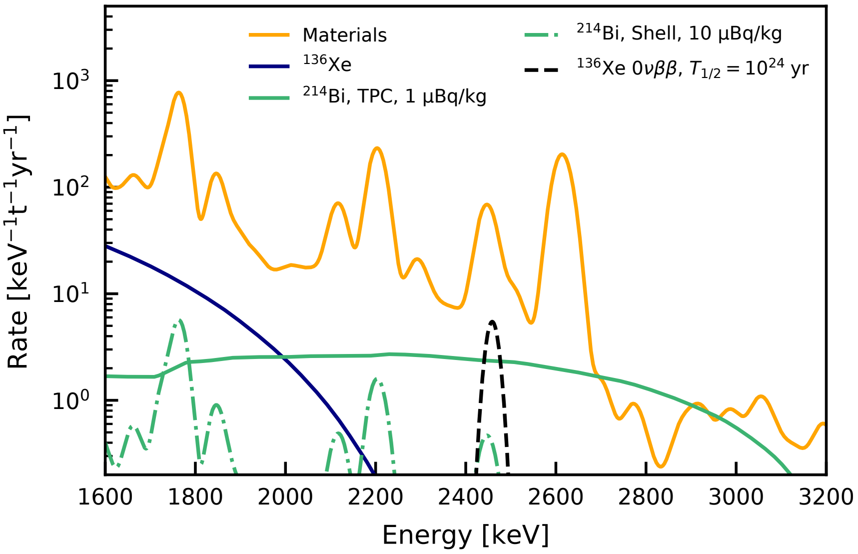

Figure 6.13: Expected intrinsic and material background energy spectra for the ^{136}Xe 0$\nu\beta\beta$ search. The intrinsic backgrounds are comprised of ^{136}Xe (solid blue, cf. table 3.2), ^{214}Bi from the active volume of the detector (solid green, 1 µBq/kg with BiPo rejection) and ^{214}Bi from the uninstrumented LXe shell around the TPC (dash-dotted green, 10 µBq/kg). The sum of material backgrounds is indicated by the solid orange line (cf. table 3.3 and section 6.2.1). An exemplary 0$\nu\beta\beta$ peak is shown for $\eta_{^{136}\mathrm{Xe}} = 8.49\,\%$ and $T_{1/2}^{^{136}\mathrm{Xe}} = 10^{24}$ yr as the dashed black line. All energy spectra have been smeared with the parametrisation of the energy resolution for single-site events from [201].

a half-life of 10^{24} yr. This would correspond to 111 decays in the 0.41 t-yr exposure. Note that the most stringent lower limit on this half-life by KamLAND-Zen is two orders of magnitude higher at $T_{1/2}^{^{136}\mathrm{Xe}} > 1.07 \cdot 10^{26}$ yr (90 % C.L.). Even at the much shorter half-life shown here, the signal peak is still an order of magnitude lower in rate than the background. Taking the KamLAND-Zen limit as the central half-life value would yield a single 0$\nu\beta\beta$ event in the exposure used in this analysis. Accordingly, the XENON1T exposure and background level render the achievement of a competitive sensitivity challenging. Especially the material background – even in the optimised fiducial volume – is expected to adversely affect the achievable limit. The derivation of the absolute material background expectation from figure 6.13 will be discussed now.

6.2.1 Absolute material background constraints from screening

While in chapter 3 the screening expectations from table 3.3 were merely used to fix the relative contributions from each detector component to the background caused by each isotope, in this analysis they are also used to formulate absolute activity constraints. As the high-energy spectrum exhibits a multitude of γ-peaks, the degeneracy of the different background components, which is caused by the featureless Compton-continua at low energy, is partly overcome. Particular care is given to the absolute normalisation of the material backgrounds. In order to derive and use absolute activity constraints from the material screening, the first MC simulation normalisation from [66] has to be extended with two more considerations: The decay chain treatment of the XENON1T MC simulation based on Geant4 and the decay of ^{60}Co after the screening and during the science run.

Table 6.2: Screening dates, time difference to the start of SR1 and decay correction factors for ^{60}Co material screening measurements. In addition to the exponential decay before SR1, the correction factors include a downscaling for the activity reduction over SR1 with $S_{\mathrm{SR1}} = 0.938$. If no exact screening date could be determined, it was assumed that the screening measurements were made on the 15th of the respective month. The PTFE is not considered since no significant ^{60}Co activity was found in this material [68].

Component	Screening date	Time to SR1 [yr]	Correction factor
Cryostat shell	July 2013	3.56	0.59
Cryostat flanges	December 2012	4.14	0.54
Copper	October 2015	1.30	0.79
Steel	October 2013	3.30	0.61
PMT bases	23rd September 2013	3.36	0.60
PMTs	23rd September 2013	3.36	0.60

The screening measurements give the activity concentrations of the respective parent isotope for the ^{238}U and ^{232}Th decay chains. The total activity from the decay chain is in fact higher due to the additional decays of the daughter isotopes. In the XENON1T MC simulation, a new decay event is generated for each α- and β-decay within a chain while the associated γ-rays are written into the same event. Accordingly, the number of simulated events does not correspond to the number of parent isotope decays for a decay chain. In order to obtain the correct target normalisation of 1 µBq/kg for the activity concentration of the parent isotope, the spectrum has to be scaled up by the number of decay steps within the chain. The ^{238}U was split at ^{226}Ra in the simulation. The first part of the chain has 5 steps and the part starting at ^{226}Ra has 9 steps. The ^{232}Th chain was simulated in full with 10 steps. The ^{228}Th part of the chain with 7 steps can then be added or subtracted in order to account for chain disequilibrium. The ^{40}K and ^{60}Co decays are considered as single-step decays in the scope of this analysis.

While the activity for almost all screened isotopes does not change significantly over the operation time of the experiment, the half-life of ^{60}Co is $T_{1/2}^{^{60}\mathrm{Co}} = 5.27$ yr [182] leading to a relative activity decrease of 12.3 % per year. Some screening measurements were made as early as 2012 [68] while the analysed data was taken mostly in 2017. Therefore, the screening predictions on the activity concentration $A_{\mathrm{screening}}^{^{60}\mathrm{Co}}$ have to be reduced by the amount of decayed ^{60}Co in the time t between the start of the measurement campaign:

$$A^{^{60}\mathrm{Co}}(t) = A_{\mathrm{screening}}^{^{60}\mathrm{Co}} \cdot e^{-\frac{\ln(2)\cdot t}{T_{1/2}^{^{60}\mathrm{Co}}}} . \tag{6.3}$$

Table 6.2 gives the dates of the screening measurements and the corresponding correction factors. Since the isotope also decays during the measurement, the correction factors already include an additional downscaling $S_{\mathrm{SR1}} = 0.938$ for the activity reduction over SR1. These factors are multiplied with the ^{60}Co screening expectations and their uncertainties from table 3.3. This treatment assumes that the samples had reached saturation activity from cosmogenic activation at the time of the screening [78] and that underground activation can be neglected due to reduction in muon flux [294].

With this it is possible to fit the data directly with the simulated MC spectra using the screening uncertainties. Screening measurements that only yielded upper limits on the activity are not considered in the fit (cf. table 3.3). In the following the background contributions from these isotopes in the respective components are fixed to zero. For the remaining isotopes and components the absolute constraints can then be taken directly from table 3.3 after the application of the correction factors from table 6.2 for ^{60}Co. Here, the screening activity concentration is the expected mean fit value and the uncertainty is the expected 1σ deviation from the mean.

6.2.2 Modification of the ^{60}Co screening constraint in the cryostat shell

Before discussing the background fit with the final constraints, ^{60}Co is considered once more. It was found during the analysis outlined in chapter 4 that the ^{60}Co best-fit with fixed component ratios was lower than expected. Since the material spectra are largely degenerate at low energy, it has to be checked if this is also the case at high energy. Two ^{60}Co lines at 1173.2 keV and 1332.5 keV [182] are accessible and outside of the planned fit range from 1600 to 3200 keV. The merged peak of both γ-rays is within the blinded ROI at 2505.7 keV. Therefore, the expected background from this peak is solely based on the screening. Since the fit of the background model discussed in this section will be used in order to derive the sensitivity before unblinding, an overestimation and overconstraint of ^{60}Co could lead to a too low sensitivity estimation. This would then manifest itself in a stronger final limit than predicted before the unblinding. Enlarging the fit range to include the ^{60}Co peaks was tested, but the residual peak energy shift could not be corrected sufficiently over a 2 MeV energy range (cf. section 6.2.3). Instead, for now only a small 300 keV fit range from 1100 to 1400 keV containing both ^{60}Co peaks is considered. Only the ^{136}Xe $2\nu\beta\beta$-spectrum and the material backgrounds are fitted to the data using the screening constraints. No other backgrounds are expected to contribute significantly to the background in this energy range. Notably, the ^{214}Bi background rate is expected to be two orders of magnitude smaller than the material background rate. Owed to the high rate in this energy region, the fit is a χ^2 fit with a 1 keV binning.

The fit with $\chi^2/\mathrm{ndf} = 420/300$ and the residuals are shown in figure 6.14. The parameter pulls are shown in figure 6.15. Apart from slight mismodelling around the peaks at 1173.2 keV and 1332.5 keV the residuals are symmetrically distributed. The mean and width of the residual distribution are $\mu = 0.04$ and $\sigma = 1.09$ in units of the data Poisson uncertainty. Accordingly, the data is well-described by the model. The χ^2/ndf is largely driven by the single 6.5σ pull of ^{60}Co in the cryostat shell. No other anomalous pulls are observed. As expected for 28 constrained parameters, 5 further pulls exceed 1σ, but are within 2σ of the expectation. The best fit for ^{60}Co in the cryostat shell is 2.46 ± 0.09 mBq/kg while the expected activity is 5.7 ± 0.5 mBq/kg. Since no other large material background pulls, e.g. for the ^{214}Bi peaks in the ^{226}Ra chain, are observed and since the pulls go in both directions, it is unlikely that an overestimation of the cut acceptance or single-scatter reconstruction efficiency lead to this result[3]. A similar behaviour would be observed if the activity concentration of ^{60}Co were overestimated or if the systematic uncertainty of the screening measurement were underestimated. This is a likely explanation for the following reasons: The mass of the cryostat shell is 870 kg. For the screening, 10.1 kg of NIRONIT AISI 304L stainless steel – 1.1 % of the total component mass – were screened for 6.7 d with the GeMPI II germanium detector [68]. It can be reasoned that the sample featured an activity concentration for ^{60}Co that is not representative for the whole cryostat shell. The uncertainty given in the paper does not take the systematic effect from the sample selection into account. The mean of the original screening expectation and the best-fit activity concentration from above is used in the following. The semi-difference between both values gives the systematic uncertainty. The new constraint for ^{60}Co in the cryostat shell is (4.1 ± 1.6) mBq/kg.

---

[3] This would require an overestimation of the efficiency by more than a factor of two.

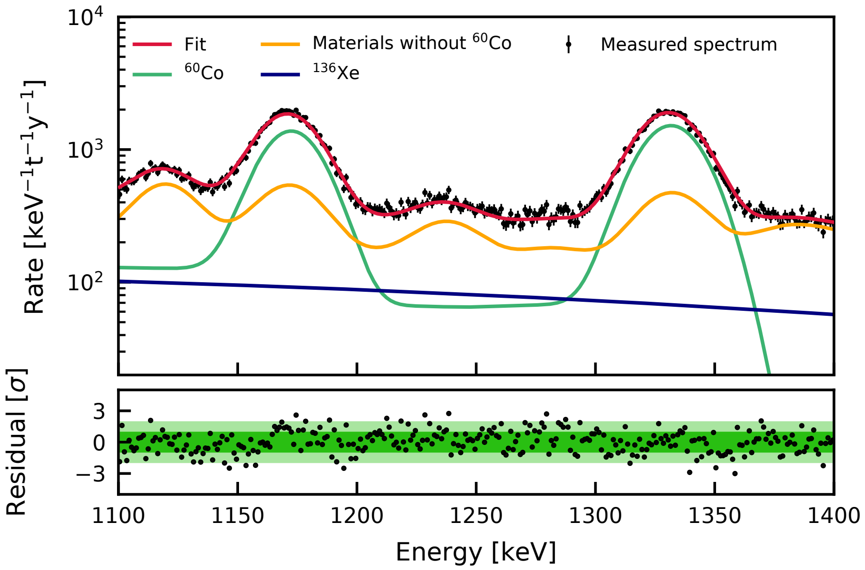

Figure 6.14: **Top:** Fit of the ^{60}Co background peaks in the 741 kg fiducial volume with $\chi^2/\mathrm{ndf} = 420/300$. The fit range is 1100 to 1400 keV with a 1 keV binning. Uncertainties on the measured data (black) are Poissonian. The total fit (red) consists of intrinsic ^{136}Xe background (blue), ^{60}Co from materials (green) and the remaining material backgrounds (orange) according to table 3.3. Only the red curve is scaled with the best-fit cut-acceptance and has the energy-shift correction applied. **Bottom:** Residuals of the fit in units of the measured data Poisson uncertainties. The 1σ and 2σ bands are indicated in dark and light green, respectively.

Looking at the pulls further it is evident that the fit components for the PMT bases and stainless steel components inside the TPC exhibit near zero deviations from the expectations[4]. Since no convergence issues for the fits were found, this is an indicator that some parameters are underconstrained. This is due to the fact that the material background spectra are still degenerate. The fit components with low absolute background contributions, due to their low component mass or large distance from the active volume, have only little effect on the shape of the background fit function. Thus, they are fitted to their constrained mean value. Consequently, the relative contribution of each component to a given isotope's background will be fixed using the screening inputs, as it was done in chapters 3 and 4. Here, each MC simulation is normalised and weighted such that the expected activity concentration corresponds to a fit value of unity. The only exception is ^{228}Th, as it is either subtracted from or added to the ^{232}Th chain. Here, the baseline expectation is decay chain equilibrium corresponding to a fit value of zero. Table 3.3 is used for the weighting. Components with only an upper limit for the activity concentration of a given isotope from the screening have been excluded, i.e. set to zero activity. In the screening their activity was too small to be measured, so no significant background is expected from them. The screening activities for ^{60}Co were decay-corrected using table 6.2. The uncertainties are the Gaussian propagated relative screening uncertainties of the individual components per isotope. The absolute constraints for the fixed-ratio fits are summarised in table 6.3 together with the constraints on intrinsic backgrounds and systematic parameters.

---

[4] The pulls also contain systematic uncertainty parameters for the residual energy shift of peaks and the cut acceptance. These will be discussed next in section 6.2.3.

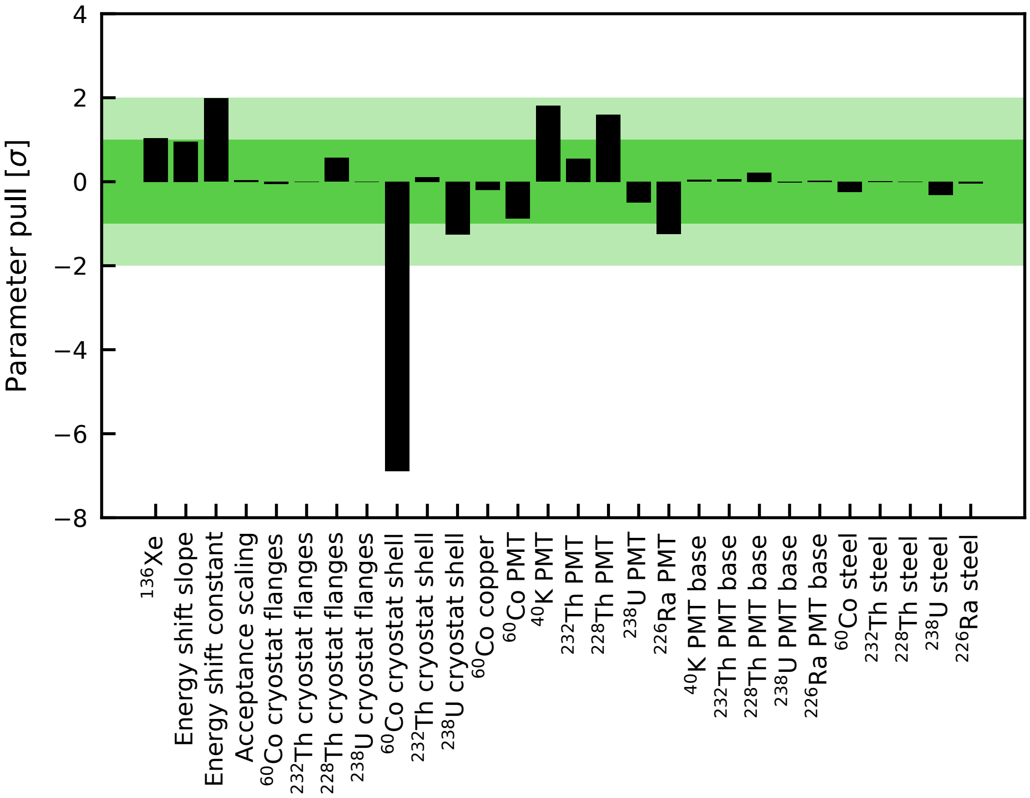

Figure 6.15: Parameter pulls for the ^{60}Co fit (black bars) in units of the constraints' standard deviations. The 1σ and 2σ bands are indicated in dark and light green, respectively. The systematic uncertainty parameters for the energy shift and acceptance are discussed in section 6.2.3. The material background constraints have been taken from table 3.3 and scaled for ^{60}Co with the correction factors from table 6.2. The constraint for ^{136}Xe was taken from table 3.2.

6.2.3 Systematic uncertainties from residual peak energy shift and cut acceptance

The cut acceptance and bias of the energy reconstruction have to be considered as systematic uncertainties in the background model. The latter manifests itself in an apparent shift of mono-energetic peaks from their expected positions. It has been shown in [201] that the absolute shift in the energy range considered here is expected to be smaller than 5 keV. Figure 6.16 shows the measured energy spectrum in the 741 kg fiducial volume in the upper panel and the fitted peak means in the lower panel. Several γ-peaks of ^{214}Bi (red), ^{60}Co (blue), ^{40}K (green) and ^{208}Tl (orange) can be identified and by eye no significant bias of the energy reconstruction can be discerned. A selection of lines in the shown energy range was fitted with Gaussian peaks in order to quantify an eventual energy shift, namely the ^{60}Co line at 1173.2 keV [182], the ^{214}Bi lines at 1120.3 keV, 1238.1 keV, 1764.5 keV, 2118.5 keV and 2204.1 keV [184], and the ^{208}Tl line at 2614.5 keV [183]. The remaining peaks were not used because either they contained unidentified smaller peaks in their flanks, which lead to a bias of peak position and width, or they displayed a strong residual z-dependence of the energy reconstruction. The latter is the case for ^{40}K which is primarily located in the PMTs. Even after the z-dependent energy reconstruction, the full peak still consists of two slightly offset peaks in energy, one originating from the bottom PMTs, the other from the top PMTs

Table 6.3: Fit parameter constraints for the MC-background model. Ten out of the 11 fit parameters are constrained. The table is horizontally divided into sections for the material backgrounds, intrinsic backgrounds and systematic parameters for acceptance and energy reconstruction bias. The only unconstrained parameter is ^{214}Bi inside the TPC since the BiPo removal efficiency of the single scatter cut is not known. The activity concentration is expected to be lower than ∼ 10 µBq/kg. For the material backgrounds, the relative contributions of the detector components to the background from each isotope have been fixed using table 3.3 with the ^{60}Co decay corrections from table 6.2. The uncertainties originate from the Gaussian-propagated relative screening uncertainties. Components with only an upper limit for the activity concentration of a given isotope from the screening have been excluded, i.e. set to zero activity.

Parameter	**Constraint/Limit**	**Unit**
^{60}**Co**	1.00 ± 0.42	Scaling factor
^{232}**Th**	1.00 ± 0.59	Scaling factor
^{228}**Th**	0.00 ± 0.59	Scaling factor
^{238}**U**	1.00 ± 0.58	Scaling factor
^{226}**Ra**	1.00 ± 0.48	Scaling factor
^{136}**Xe**	1.00 ± 0.03	Scaling factor
^{214}**Bi (TPC)**	$\lesssim 10$	µBq/kg
^{214}**Bi (shell)**	10 ± 5	µBq/kg
$\mathbf{p_a}$	5 ± 5	Scaling factor
Δ_E **slope**	$(1.5 \pm 0.2) \cdot 10^{-3}$	-
Δ_E **constant**	-4.4 ± 0.3	keV

(cf. left plot in figure 3.7). Therefore, the peak width and position of ^{40}K are not suitable for determining energy reconstruction bias. The data points are fitted with a linear function as an effective model that describes the trend of the data well in the chosen energy range, which it is limited to. The linear model yields $\chi^2/\mathrm{ndf} = 14.8/5.0$ which is almost exclusively driven by the 3σ deviation of the ^{214}Bi line at 2204.1 keV [184]. Still, the model describes the remaining data points well. Moreover, the peak fits used a simple linear background parametrisation that could lead to systematic uncertainties that are currently not included in the fit. All in all, the peak shift is at the expected level from [201] also in the 741 kg fiducial volume. The remaining shift is included in the background model by allowing the simulated energies E_MC to shift with

$$
\begin{aligned}
E_\mathrm{fit} &= E_\mathrm{MC} + \Delta E, \\
\Delta E &= (1.5 \pm 0.2) \cdot 10^{-3} \cdot E_\mathrm{r} - (4.4 \pm 0.3)\ \mathrm{keV}.
\end{aligned}
\tag{6.4}
$$

Here, E_MC is the energy of the MC simulation. Ideally the shift would be applied on an event-by-event basis. However, the linear slope and constant in ΔE are optimised during the background-model fit, so an event by event energy shift for $> 10^9$ events per fit step is not feasible computationally. Instead, in each iteration of the fit the MC spectra are first

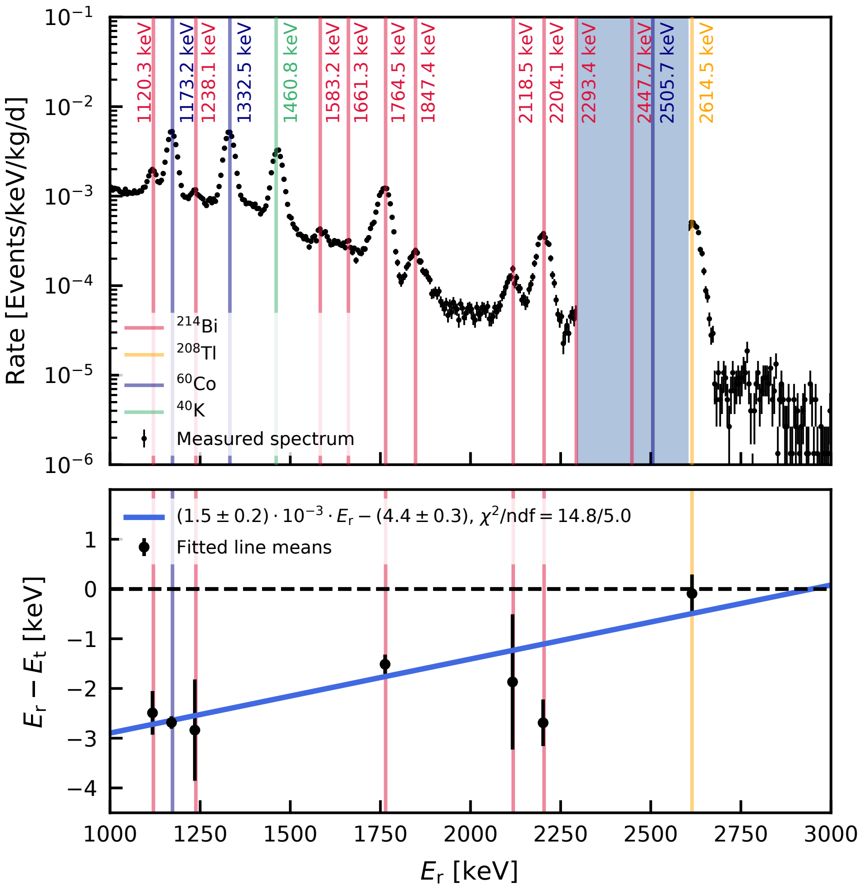

Figure 6.16: **Top:** Measured energy spectrum from 1000 to 3000 keV in the 741 kg fiducial volume (black). The bin size is 5 keV and the uncertainties on the data points are Poissonian. The blinded region is shaded blue. The γ-lines of ^{214}Bi (red), ^{60}Co (blue), ^{40}K (green) and ^{208}Tl (orange) can be identified. The expected peak energies are given next to the solid vertical lines [182–184]. **Bottom:** Linear fit of the difference between the reconstructed mean energy E_r and the expected energy E_t of selected γ-lines with $\chi^2/\mathrm{ndf} = 14.8/5$. The means and their uncertainties were extracted from Gaussian fits of the peaks with linear backgrounds.

binned to 0.1 keV. After the shift within each fit step, a coarser binning is applied to the spectrum before comparing it with the binned measured data.

The cut acceptance from [289] (cf. figure 6.7) is implemented by allowing it to float between the lower limit given by the combined acceptance data points and the upper bound given by the analytic cut acceptances. As there is no obvious parametrisation of the total acceptance, it is interpolated with a univariate quadratic spline as implemented in the SciPy package [295]. The corresponding SciPy function allows to assign weights to the data points. The symmetrised biomial uncertainties $\sigma_{a,i}$ for the acceptance a_i from [289] are implemented as weights w_i for each energy bin E_i with

$$w_i = \frac{1}{\sigma_{a,i}}. \tag{6.5}$$

The smoothing factor s of the spline $f_s(E_i)$ is set to the number of acceptance data points

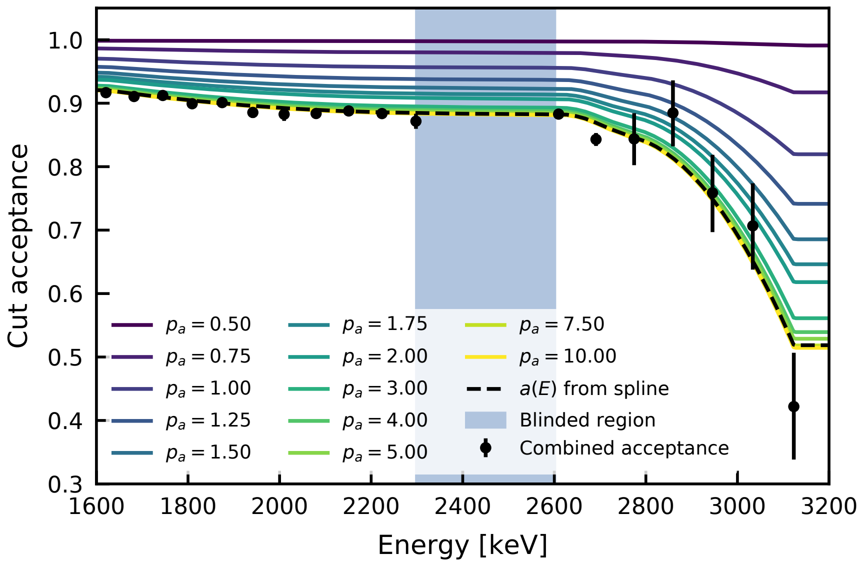

Figure 6.17: Cut acceptance implementation in the background fit. The quadratic univariate spline fit $a(E)$ (dashed black) to the combined acceptance (black markers) represents the lower limit of the acceptance. The uncertainties on the data points are the Gaussian-propagated binomial uncertainties from [289]. The scaling function $g(E, p_a)$ from equation 6.8 is used to vary the fitted acceptance $a_{\mathrm{fit}}(E, p_a)$ between the lower acceptance bound $a(E)$ and the upper bound a_{up}. Above a_{up} was set to unity for illustration. The fitted acceptance $a_{\mathrm{fit}}(E, p_a)$ is shown for different p_a (coloured solid lines). At energies beyond the last combined acceptance data point, the spline $a(E)$ is fixed to the value it assumed at that last point. An extrapolation would yield unphysical negative values.

N_{i}. With the smoothing condition

$$\sum_{\mathrm{i}=0}^{N_{\mathrm{i}}} w_{\mathrm{i}}^2 \cdot (a_{\mathrm{i}} - f_{\mathrm{s}}(E_{\mathrm{i}}))^2 < s \tag{6.6}$$

this approximates a χ^2 fit where the quadratic spline is defined such that $s/N_{\mathrm{i}} \simeq \chi^2/\mathrm{ndf} \approx 1$. The resulting continuous function

$$a(E) = f_{\mathrm{s}}(E) \tag{6.7}$$

is solely determined by s and can now be included in the fit by binwise multiplication with the summed energy spectrum. In order to let it float between the lower and upper bounds in the fit, it is scaled using the function

$$g(E, p_a) = a(E) + \left(a_{\mathrm{up}} - a(E)\right) \cdot \left(1 - e^{-p_a^{-2}}\right) \tag{6.8}$$

with the fit parameter p_a and the upper bound of the accepptance a_{up}. The fitted acceptance then is

$$a_{\mathrm{fit}}(E, p_a) = a(E) \cdot g(E, p_a) \tag{6.9}$$

and the asymptotic behaviour of $g(E, p_a)$ leads to the fitted acceptance approaching the upper and lower limits when going to zero or infinity, respectively:

$$\lim_{p_a \to \pm\infty} a_{\mathrm{fit}}(E, p_a) = a(E),$$
$$\lim_{p_a \to 0} a_{\mathrm{fit}}(E, p_a) = a_{\mathrm{up}}. \tag{6.10}$$

The fitted acceptance $a_{\text{fit}}(E, p_a)$ is shown in figure 6.17 for several values of p_a with $a_{\text{up}} = 1$ for illustration. In practice, the lower limit is reached at $p_a \gtrsim 10$. Going closer to the upper bound, the acceptance is also continuously flattened and becomes featureless at unity. Within the blinded region, the acceptance is expected to be flat with the lower limit at $\sim 88\,\%$. One data point with a fairly large uncertainty is located below the spline. In the fit, the acceptance is constrained such that it can reach both limits within a 1σ pull with $p_a = 5 \pm 5$.

6.2.4 Background model fit to the blinded data

The measured background spectrum from 1600 to 3200 keV is fitted using the MC-based background model. The blinded region from 2300 to 2600 keV is excluded from the fit. As in chapter 4 (cf. equation (4.25)) the likelihood is a binned χ^2_λ likelihood [263]. A 5 keV binning is chosen and will also be used after the unblinding in order to always have > 20 events per bin in the blinded region based on the background expectation from figure 6.13[5]. The fit result and the residuals from the summands of χ^2_λ are presented in figure 6.18. The data is well described by the fit with $\chi^2_\lambda/\text{ndf} = 311/319 \approx 0.98$. A χ^2 distribution with the same number of degrees of freedom would have a standard deviation of $\sqrt{2/\text{ndf}} = 0.08$.

The residuals are the square-roots of the summands of χ^2_λ where the sign of the residual is given by the positive or negative difference between the rate of the measured data and the rate predicted by the model. The visualised uncertainties are based on Feldman & Cousins 68.3 % confidence intervals [262]. Taking a closer look at the distribution of the residuals in figure 6.19 reveals that over the full fit range (orange), the residual distribution is asymmetric with the mean at -0.16 and a standard deviation of 1.07. This asymmetry is induced by the low-count tail of the energy spectrum that comes above the ^{208}Tl peak. In this region, each bin contains less than five events and the uncertainties are highly asymmetric. Since the fit function can only assume physically meaningful values that are positive, a symmetric residual distribution is not possible in this region. In the energy region between 1.6 MeV and 2.3 MeV (black) the higher count rates lead to symmetric uncertainties. A symmetric residual distribution centred around zero with a standard deviation of 1.05 is found here.

The best-fit parameters together with their constraints are summarised in table 6.4 and the associated parameter pulls are shown in figure 6.20. No pulls above 3σ are observed while two pulls exceed 2σ as expected for ten pull terms. Both ^{238}U and ^{226}Ra exhibit downward pulls hinting to an overestimation of this background. Moreover, their fit parameters assume the same value suggesting decay chain equilibrium. The antipodal pulls for the two parts of the thorium chain hint at decay chain disequilibrium. Since its rate is two orders of magnitude below the other fit components and since it has a loose constraint, the pull for the LXe shell contribution of ^{214}Bi is near zero. Another near zero pull is observed for ^{60}Co since it is mostly contained in the blinded part of the spectrum. The squared sum of all ten pulls is 4.8. The acceptance scaling in the fit prefers the lower bound.

The best fit activity concentration for the fraction of ^{214}Bi contributing to the energy spectrum is 1.72 ± 0.11 μBq/kg which is mostly constrained by the low-count tail of the energy spectrum. This suggests a BiPo tagging efficiency of approximately $(82.8 \pm 1.1)\,\%$ for an assumed ^{214}Bi activity concentration of 10 μBq/kg. Since the S1 single-scatter cut is the only cut applied in this analysis that targets BiPo events, the tagging requires that the ^{214}Po decay occurs in the same event and that the S1 can be identified. This would not be possible if it is obscured by the S2 from the ^{214}Bi decay. The ^{214}Po half-life is 164.3 μs, so approximately

---

[5] It is noted that an unbinned likelihood should offer a better sensitivity. However, the background level is the main factor limiting the sensitivity of this analysis. An unbinned likelihood would only offer a marginal benefit and require substantial changes of the fitting framework originally developed for the analysis in chapter 4.

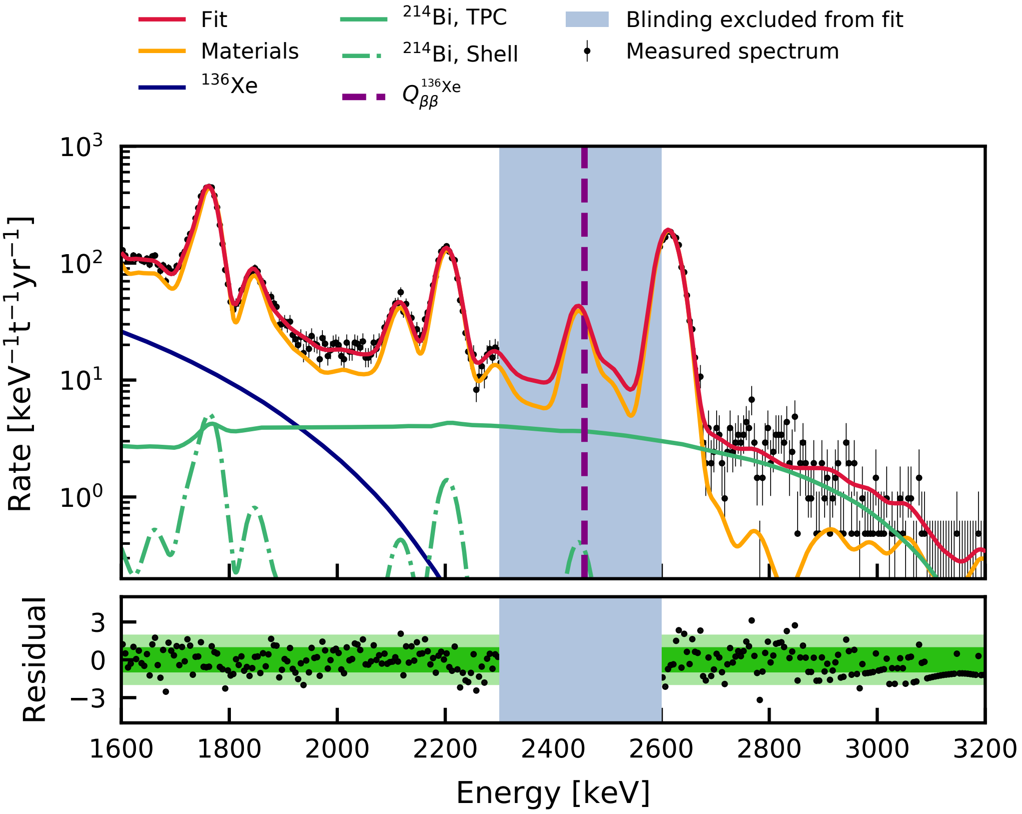

Figure 6.18: **Top:** Fit of the MC-based background model to measured data with $\chi^2_\lambda/\text{ndf} = 311/319 \approx 0.98$. The fit range is 1600 to 3200 keV in 5 keV bins (black points). The displayed uncertainties for each bin are Feldman & Cousins 68.3 % confidence intervals [262]. The blinded region (blue) is excluded from the fit. The ^{136}Xe double-β decay Q-value is marked by the dashed purple line. The best-fit model, is indicated by the solid red line. It consists of the sum of material backgrounds (solid orange), ^{136}Xe (solid blue), ^{214}Bi inside the TPC (solid green), and ^{214}Bi in the uninstrumented LXe shell (dash-dotted green). **Bottom:** Residuals from the square-roots of the summands of χ^2_λ (black points). The 1σ and 2σ regions are marked by the light and dark green bands.

93.6 % of ^{214}Po decays occur within a 650 µs time window – the maximum drift time inside XENON1T [88] for events occurring near the cathode. For events in the middle of the TPC with half this drift time the fraction is 74.6 %. Since the fiducial volume is not centred in the TPC, larger drift times are favoured. Taking into account that high-energy S2s can have widths of tens of microseconds (cf. figure 6.2) the detection efficiency should be less than 100 % due to S2s overlapping the S1s. With these assumptions, an efficiency of 82.8 % is plausible enough that a detailed analysis on this subject can be forgone. However, it is noted that the BiPo tagging efficiency could be improved by cuts that identify S1s over multiple events. Moreover, the high ratio of S1 over S2 for α-events could be used to identify the ^{214}Po S1s if they are obscured by S2s.

For the sensitivity estimation, the best-fit background model is used for the production of toy-MC energy spectra. To this end the model uncertainty has to be determined. Since the fit parameters are correlated, the model uncertainties have to be propagated using the covariance matrix [4]. The uncertainty propagation is based on a modified implementation

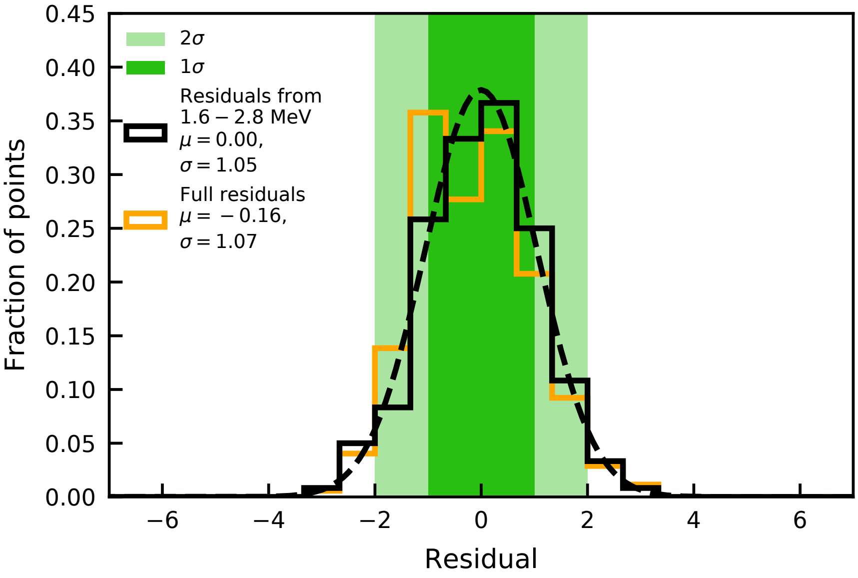

Figure 6.19: Residual distributions from the bottom panel of figure 6.18 in two energy ranges: for the full energy range (solid orange) and the reduced energy range from 1.6 to 2.8 MeV (solid black). Thirty bins from -7 to 7 are used for both distributions and the histograms are normalised such that the area under each histogram is unity. A unit Gaussian with $\mu = 0.00$ and $\sigma = 1.05$ of the reduced energy range is drawn as a dashed black line.

Table 6.4: Fit parameters for the fit of the MC-background model to the blinded $0\nu\beta\beta$ data with the best-fit results, the parameter constraints and the corresponding units from the parameter definitions (cf. table 6.3).

Parameter	**Fit result**	**Constraint/Limit**	**Unit**
^{60}Co	0.96 ± 0.31	1.00 ± 0.42	Scaling factor
^{232}Th	1.61 ± 0.13	1.00 ± 0.59	Scaling factor
^{228}Th	-0.79 ± 0.15	0.00 ± 0.59	Scaling factor
^{238}U	0.62 ± 0.10	1.00 ± 0.58	Scaling factor
^{226}Ra	0.620 ± 0.007	1.00 ± 0.48	Scaling factor
^{136}Xe	1.006 ± 0.030	1.00 ± 0.03	Scaling factor
^{214}Bi (TPC)	1.72 ± 0.11	$\lesssim 10$	μBq/kg
^{214}Bi (shell)	10 ± 5	10 ± 5	μBq/kg
p_a	7.3 ± 3.4	5 ± 5	Scaling factor
Δ_E slope	$(1.48 \pm 0.10) \cdot 10^{-3}$	$(1.5 \pm 0.2) \cdot 10^{-3}$	-
Δ_E constant	-4.63 ± 0.18	-4.4 ± 0.3	keV

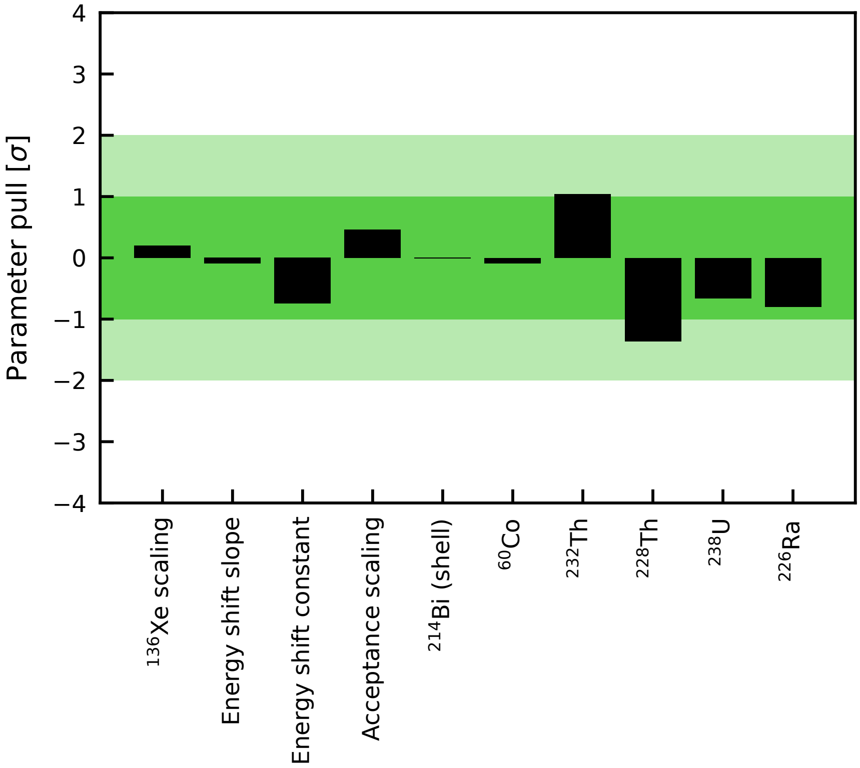

Figure 6.20: Parameter pulls for the background model fit of the ^{136}Xe 0νββ search before unblinding. The pulls (black bars) are given in units of their uncertainty σ. The 1σ and 2σ bands are shown in dark green and light green, respectively. The sum of the squared pulls, as they contribute to the cost function of the fit, is 4.8. The best-fit values and constraints together with their respective uncertainties are summarised in table 6.4.

from the *kafe* data analysis package [296] which was provided by V. Hannen. Here, the numerical derivatives of the model with respect to the fit parameters are used together with the covariance matrix in order to derive a model uncertainty band. The best-fit model and the associated uncertainty band are shown in figure 6.21. While the band is narrow over a large part of the fit range, it is widened at the ^{60}Co peak in the blinded region. This reflects the enlargement of the fit constraint in section 6.2.2. The background rate within a symmetric $2\sigma_E$ window around $Q_{\beta\beta}^{^{136}\mathrm{Xe}}$ is (2297 ± 53) events/t/yr or (942 ± 22) events in the 0.41 t-yr exposure. With this, the sensitivity for the 0νββ peak can be investigated.

6.3 Sensitivity to 0νββ of ^{136}Xe

The sensitivity for setting a 90 % C.L. lower limit on the ^{136}Xe neutrinoless double-β decay half-life $T_{1/2}^{0\nu\beta\beta}$ was determined in collaboration with M. Pierre and T. Wolf. M. Pierre determined the single-site event fraction of 0νββ events with MC simulations [297]. T. Wolf made the toy-MCs from the background model derived in this work and fitted these with the framework described above. The Poisson likelihood $\mathscr{L}$ for the construction of the log-likelihood ratio (LLR) test statistic is defined as

$$\mathscr{L}(A_{0\nu}, \vec{N}_{\mathrm{toy}}, \vec{p}) = \prod_{\mathrm{i}}^{N_{\mathrm{bins}}} \mathrm{Poisson}\left(N_{\mathrm{i}}, \lambda_{\mathrm{i}}(A_{0\nu}, \vec{p})\right) \cdot \prod_{\mathrm{j}}^{N_{\mathrm{constraints}}} \mathrm{Gauss}(p_{\mathrm{j}}, \mu_{\mathrm{j}}, \sigma_{\mathrm{j}}), \tag{6.11}$$

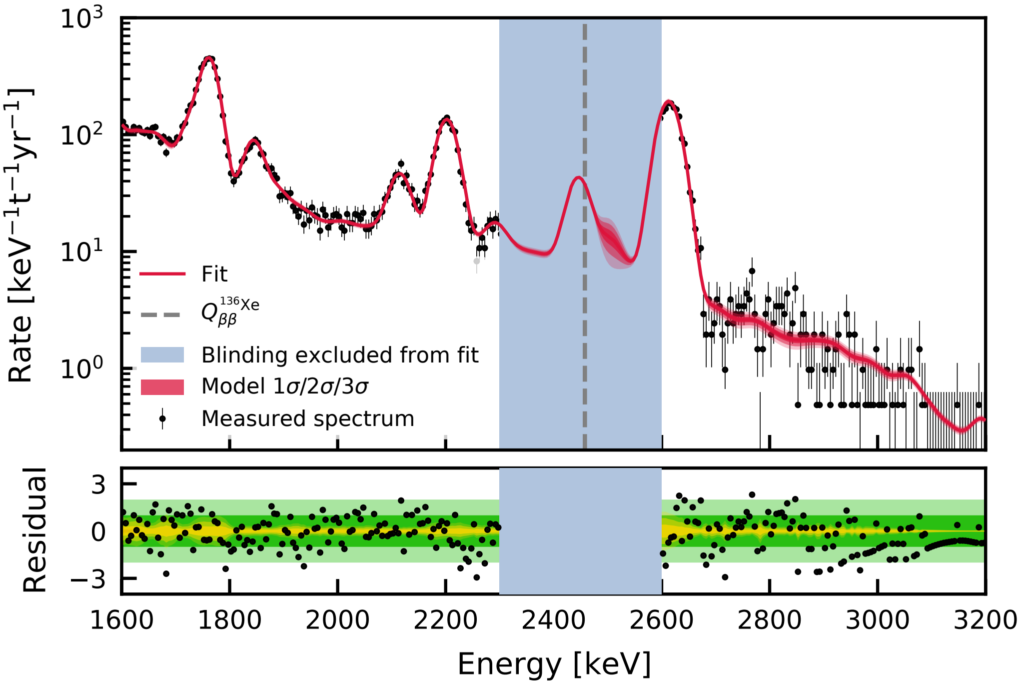

Figure 6.21: **Top:** Fit of the MC-based background model to measured data with model uncertainties as in figure 6.18. The 1σ, 2σ and 3σ model uncertainty bands are indicated by the red shaded bands around the best fit (solid red). **Bottom:** Residuals as in figure 6.18. The 1σ, 2σ and 3σ model uncertainty bands after subtraction of the best-fit model are indicated by the orange shaded bands centred around zero.

where $A_{0\nu}$ is the amplitude, i.e. the decay rate, of the $0\nu\beta\beta$ peak, $\vec{p}$ are the nuisance parameters, and $\vec{N}$ is the energy histogram of the toy dataset with N_{bins} bins. Then N_{i} are the toy-MC counts in a single bin and λ_{i} is the expectation value given by the fit function. The constraints are again added as Gaussian terms for the constrained parameters p_{j} with the mean μ_{j} and the uncertainty σ_{j}. Apart from the normalisation this binned likelihood function is equivalent to the χ^2_λ defined in equation (4.17). The test statistic is then constructed as

$$-2\,\text{LLR} = \begin{cases} 0 & \text{for } A_{0\nu} < 0 \\ -2\log\left(\frac{\mathscr{L}(A_{0\nu},\vec{p}_{\text{fixed}})}{\mathscr{L}(A_{0\nu,\text{fit}},\vec{p}_{\text{fit}})}\right) & \text{for } A_{0\nu} \geq 0. \end{cases} \tag{6.12}$$

Here, $A_{0\nu}$ is the tested rate and $\vec{p}_{\text{fixed}}$ are the best-fit nuisance parameters for the fixed value of the tested $A_{0\nu}$. These are contrasted with the likelihood for the best-fit rate $A_{0\nu,\text{fit}}$ and the remaining best-fit parameters $\vec{p}_{\text{fit}}$.

Figure 6.22 shows the result from the evaluation of $-2\,\text{LLR}$ for a large ensemble of toy-MCs. In a first step, only toy datasets without artificially injected signal have been generated (blue points). Each point for a tested $A_{0\nu}$ represents the median of the $-2\,\text{LLR}$ distribution for 10^4 toy fits. In the asymptotic case, where $A_{0\nu}$ follows a χ^2 distribution, the limit sensitivity would be given by the 90 % confidence interval of a χ^2-distribution with one degree of freedom. This is indicated in the figure by the dashed black line. Since no signal is present in the toys, the negative log-likelihood ratio continuously grows, indicating a deteriorating goodness of fit in the enumerator of $-2\,\text{LLR}$. The asymptotic case is not necessarily realised, so a second likelihood scan is performed in order to identify the asymptoticity threshold.

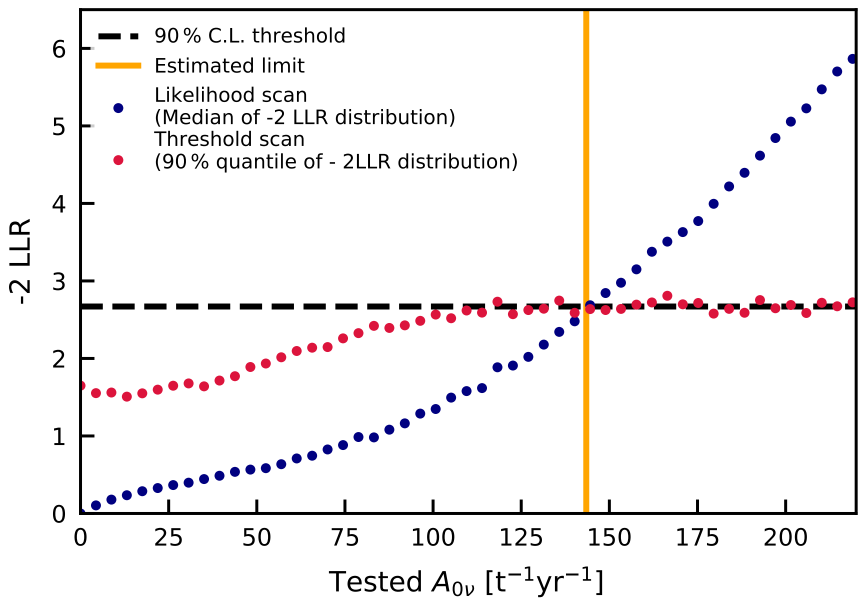

Figure 6.22: Sensitivity estimation before unblinding based on toy-MCs using the negative double ratio between the log-likelihoods with the tested and the best-fit rate for 0νββ. The blue points represent the median of the log-likelihood distribution from 10^4 toy experiments at each tested rate without signal injected into the toy-MCs. The red points stem from the 90 % quantile of the log-likelihood distribution from 10^4 toy experiments at each tested rate with the tested signal injected into the toy-MCs. At larger rates they approach the 90 % quantile of a χ^2 distribution with one degree of freedom (dashed black). The crossing point of the likelihood and threshold scans gives the estimated upper limit on the 0νββ decay rate (solid orange) $A_{0\nu} < 144$ events/t/yr at 90 % confidence level.

Here, the peak for the tested $A_{0\nu}$ is injected into the toy MCs (red points). Every point represents the 90 % quantile of the −2 LLR distribution for 10^4 toy fits. With increasing signal, i.e. larger $A_{0\nu}$, the points are flatly distributed around the asymptotic limit. The crossing point of the red and blue data points is in the asymptotic limit and gives the upper limit on the decay rate with $A_{0\nu} < 144$ events/t/yr at 90 % confidence level.

Since only single-site events are selected from data and MC, the fraction of single-site events in the 0νββ peak was determined using MC simulations [297]. The initial momenta of 10^6 electron pairs were generated with DECAY0 [271]. The decay positions were uniformly distributed in the whole LXe volume of XENON1T. Then, the electrons were propagated using the XENON1T MC simulation framework and the energy depositions were clustered with *nSort* [66]. Figure 6.23 shows the simulated two-electron energy spectrum from the neutrinoless decay before single-site and fiducial volume selections. At the edge of the TPC quanta may leave the detector before depositing their full energy, so a small fraction of the spectrum is continuous down to low energies[6]. The major part of the spectrum is concentrated in the Gaussian peak at $Q_{\beta\beta}^{^{136}\mathrm{Xe}}$. After the fiducial cut, only this peak is left. The single-site selection removes events with multiple distinguishable energy depositions. Since the range of electrons is rather small these occur when a Bremsstrahlung photon, which features an absorption length considerably longer than the range of the

---

[6] The peak at low energy is likely caused by atomic relaxation since its energy is in the region of the Xe and Ba K-edges [156].

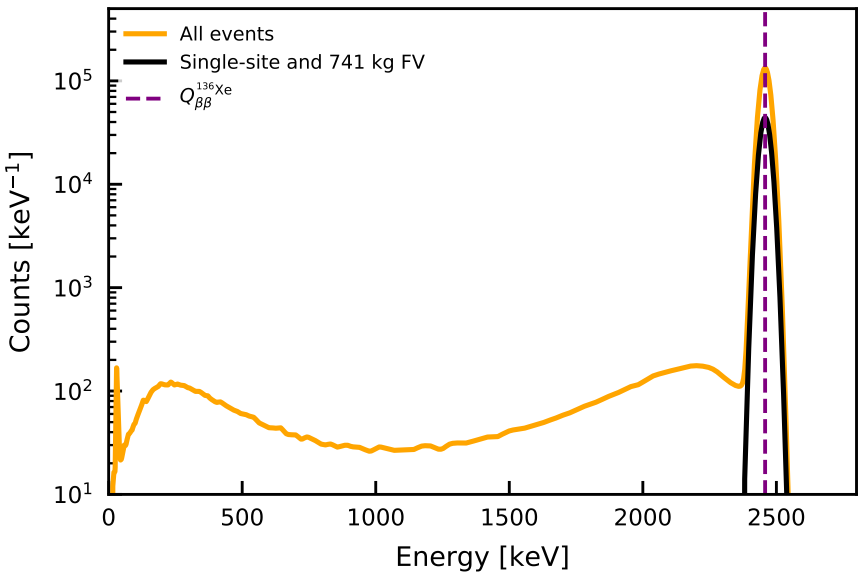

Figure 6.23: Simulated two-electron energy spectra for the single-site efficiency estimation. The spectrum before selections (solid orange) stretches down to low energies owed to events with only partially contained energy. After the 741 kg fiducial volume and single scatter selections only a Gaussian peak (solid black) centred around $Q_{\beta\beta}^{^{136}\text{Xe}}$ (dashed purple) remains. Taken from [297].

charged electron, is emitted by one of the electrons. The single site spectrum is indicated by the solid black line and the fraction of single-site events in the fiducial volume is 90.9 %. Including the single-site fraction and using equation 1.31 with the ^{136}Xe isotopic abundance $\eta_{\text{meas}}^{^{136}\text{Xe}} = (8.49 \pm 0.04_{\text{stat}} \pm 0.13_{\text{sys}}) \cdot 10^{-2}$ mol/mol, the decay rate is translated into a half life. With this, the expected sensitivity is

$$T_{1/2}^{0\nu\beta\beta} > 1.7 \cdot 10^{24}\,\text{yr} \quad (90\,\%\,\text{C. L.}). \tag{6.13}$$

Upon completion of the sensitivity study the XENON collaboration decided to remove the blinding in the energy region of interest. The unblinded data and analysis results cannot be shown in this work, but a publication by the XENON collaboration is in preparation with active participation of the author.

With $T_{1/2}^{0\nu\beta\beta} > 1.7 \cdot 10^{24}$ yr at 90 % confidence level, XENON1T's expected sensitivity is between one and two orders of magnitude below the sensitivities of dedicated xenon-based experiments such as EXO-200 and Kamland-Zen [25, 138]. With regard to Dark Matter direct detection experiments the most stringent lower limit on the $0\nu\beta\beta$ half-life has been set by the PandaX-II experiment at $T_{1/2}^{0\nu\beta\beta} > 2.3 \cdot 10^{23}$ yr at 90 % confidence level with a 0.24 t-yr exposure [298]. With its lower background, factor 1.7 larger exposure and four times better energy resolution, XENON1T achieves an order of magnitude better sensitivity. The achieved energy resolution, fulfilled background goals and stable long-term operation of XENON1T lend credibility to the projected sensitivities of LZ, XENONnT and DARWIN [18, 151, 152].

Conclusion and Outlook 7

This work investigated neutrino physics in the context of direct Dark Matter detection with a focus on the second-order weak decays of two isotopes: ^{124}Xe and ^{136}Xe. The analysis presented in chapter 3 was carried out in collaboration with A. Fieguth [207] and targeted the two-neutrino double-K capture of ^{124}Xe in 0.73 t-yr of XENON1T data. In the scope of this work an energy calibration method based on the anti-correlation of light and charge signals was applied. A relative energy resolution of 4.1 % could be achieved for the 2νKK signal at 64.3 keV. Before the unblinding of the data, a background model based on MC simulations with the XENON1T geometry was developed and successfully fitted to the blinded data. Here, systematic uncertainties and external constraints were considered in the fit. A model for the neutron-activated ^{125}I background peak at 67.3 keV could only be developed after an unblinding of the data. To this end, the decay of the ^{125}Xe parent isotope was tracked over time and converted into an expected ^{125}I decay rate evolution that was fitted to the measured rate in the unblinded ^{125}I energy region. The model suggested a removal of iodine from the detector by the gas purification system, it lead to the reduction of the dataset to the final 0.73 t-yr exposure, and it yielded the ^{125}I background expectation with $N_{^{125}\mathrm{I}} = (10 \pm 7)$ events. The constrained ^{125}I background and the 2νKK peak were added to the background model and a final fit was applied to the unblinded data. This culminated in the first direct observation of two-neutrino double-K capture in ^{124}Xe with a 4.4σ significance and a half-life of

$$T_{1/2}^{2\nu\mathrm{KK}} = (1.8 \pm 0.5 \pm 0.1) \cdot 10^{22}\ \mathrm{yr}. \tag{7.1}$$

This value is in excellent agreement with those predicted in recent NME calculations. The results were published in [31].

In chapter 4, additional data, extended signal and background models, as well as improved analysis techniques brought a 5σ discovery of ^{124}Xe 2νECEC with XENON1T in reach. Using the XENON1T low-energy ER analysis [14] as a stepping stone, the exposure was increased by 33 % to 0.93 t-yr. An updated position reconstruction algorithm required a reassessment of the systematic uncertainties on the fiducial mass using homogeneously distributed $^{83\mathrm{m}}$Kr calibration events. Refined analysis cuts allowed to include the KL- and LL-capture peaks in the signal model. This also required an extension of the ^{125}I modelling in the extended data periods under the consideration of additional background peaks. Beyond providing background constraints for the four different datasets considered in the extended analysis, the model indicated that the ^{125}I removal from the detector was indeed proportional to the gas flow in the purification system.

The fit method from the initial analysis was updated in order to handle the lower statistics in the SR2 dataset and improved constraints on several background components were implemented. The fit framework itself was optimised, generalised and made available to the XENON collaboration and has since been used in several analyses. A fit of the extended

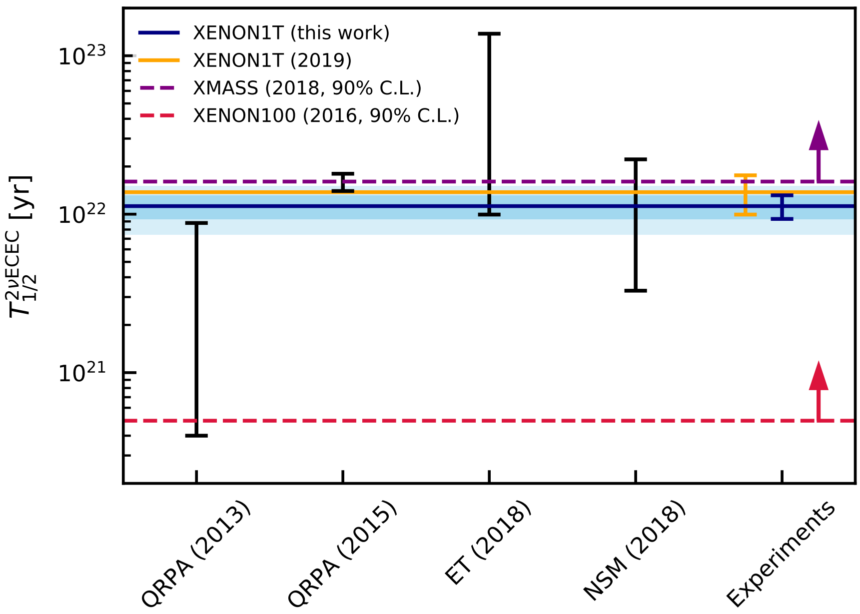

Figure 7.1: Comparison of the 2νECEC half-life from this work with theoretical predictions and the experimental 90 % C.L. lower limits from XMASS [145] (dashed purple) and XENON100 [254] (dashed red). The published result from the previous XENON1T analysis is indicated by the solid orange line [31]. The value was scaled down by $f_{2\nu\mathrm{KK}}$ [89]. The uncertainty is given by the error bars on the right of the plot. The updated central value of the measured half-life is shown as the solid blue line. The 1σ and 2σ uncertainty bands are indicated in blue and light blue, respectively. Four results from nuclear structure calculations [106, 108, 110] are indicated by the black uncertainty bars. An agreement within 2σ is found for all measurements.

signal and background model to the data yielded a 2νECEC decay rate of

$$A_{2\nu\mathrm{ECEC}} = (280 \pm 45)\ \mathrm{events/t\times yr}. \tag{7.2}$$

This translates to a fractional KK-capture half-life of

$$T_{1/2}^{2\nu\mathrm{KK}} = (1.47 \pm 0.24_{\mathrm{stat}} \pm 0.07_{\mathrm{sys}}) \cdot 10^{22}\ \mathrm{yr} \tag{7.3}$$

and a total double-electron capture half-life of

$$T_{1/2}^{2\nu\mathrm{ECEC}} = (1.13 \pm 0.18_{\mathrm{stat}} \pm 0.05_{\mathrm{sys}}) \cdot 10^{22}\ \mathrm{yr}. \tag{7.4}$$

At a significance of 6.8σ this marks the first significant detection of 2νECEC in any isotope. It is also the first result on the full double-electron capture half-life under the consideration of KK-, KL- and LL-capture. Consistency with the previous result could be demonstrated under the consideration of the added exposure, the inclusion of additional signal peaks, systematic uncertainties, and the improved energy reconstruction from [201] that was applied to the extended data. The decreased uncertainties provide nuclear theorists with a benchmark from the proton-rich side of the nuclide chart for their NME calculations (figure 7.1 from section 4.4). In its planned exposure of 20 t-yr XENONnT will measure ~ 5600 events from 2νECEC. This will reduce statistical uncertainties to the percent level. A publication by the XENON collaboration that contains the extended XENON1T 2νECEC results is in preparation.

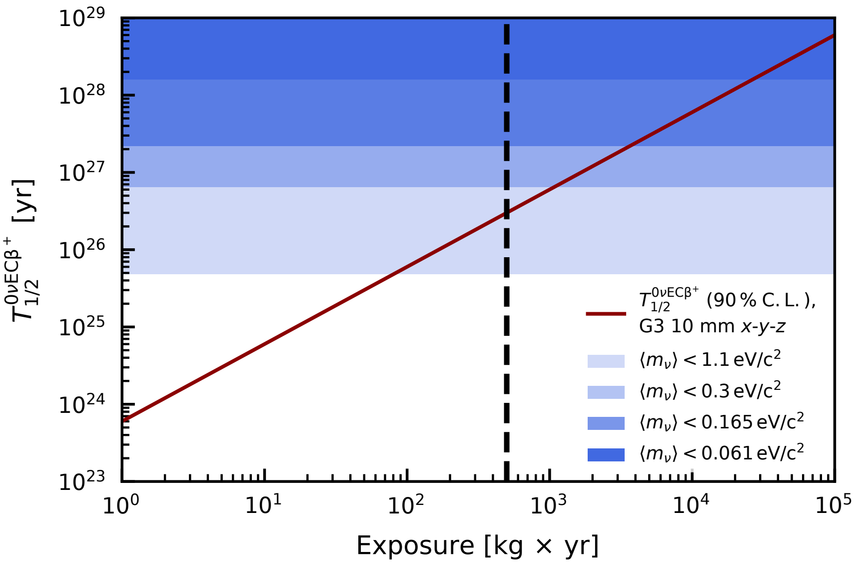

Figure 7.2: Projected 90 % C.L. lower limit on $T_{1/2}^{0\nu EC\beta^+}$ for a background-free experiment with 10 mm resolution in x-y-z, as a function of the exposure (red). This calculation assumes the G3 geometry; the sensitivity curve decreases by ~ 10 % for a G2 detector at all exposures. Four ranges of lower limits on the $0\nu EC\beta^+$-decay half-life are shown. They correspond to the upper and lower ends of the $\langle m_{\beta\beta} \rangle$ ranges in Table 5.2: $\langle m_{\beta\beta} \rangle < 1.1, \mathrm{eV/c^2}$ (light blue) and $\langle m_{\beta\beta} \rangle < 0.3\,\mathrm{eV/c^2}$ (light medium blue), as well as $\langle m_{\beta\beta} \rangle < 0.165, \mathrm{eV/c^2}$ (dark medium blue) and $\langle m_{\beta\beta} \rangle < 0.061\,\mathrm{eV/c^2}$ (dark blue). The respective lower bounds are given by the weakest limit among the three NMEs for each $\langle m_\nu \rangle$. The dashed black line represents an exposure of 500 kg-year. Taken from [155].

Chapter five presented a comprehensive study on the future detection prospects of the yet undetected two-neutrino and hypothetical neutrinoless second-order weak decays of ^{124}Xe. In a first step PSFs and NMEs were used in order to calculate the half-lives of the decays. The mixed $2\nu EC\beta^+$ and $0\nu EC\beta^+$ decays are favoured over double-β^+ decays due to the larger available phase-space. The 0νECEC would only be viable in the presence of a resonant enhancement, but this is discouraged by existing measurements. The signal efficiencies of future detectors to the respective decay channels were investigated for a coincidence-based reconstruction technique on the basis of MC simulations of G2 and G3 experiments. Such simulations were also used in order to investigate how such searches would be affected by background. It was found that the detection of $2\nu EC\beta^+$ with a half-life of $(1.7 \pm 0.6) \cdot 10^{23}$ yr is feasible in G2 Dark Matter detectors if backgrounds are sufficiently controlled. Moreover, a search for $0\nu EC\beta^+$ would likely be background-free. However, even a G3 experiment such as DARWIN [152] would likely not be able to measure this decay considering current limits on the effective neutrino mass by Kamland-Zen [25] (figure 7.2 from section 5.4). In this context, alternative left-right symmetric models were discussed. In these the detection of both decays would allow to disentangle the mechanism that mediates the neutrinoless decay. The results presented in this study have been published in [155].

Finally, the sensitivity of XENON1T to the neutrinoless double-β decay of ^{136}Xe was investigated. This analysis in the MeV range presented a considerable challenge since XENON1T was designed for the detection of keV-range NR interactions. Therefore, the high-energy reconstruction improvements by XENON collaborators [201] and the data selection

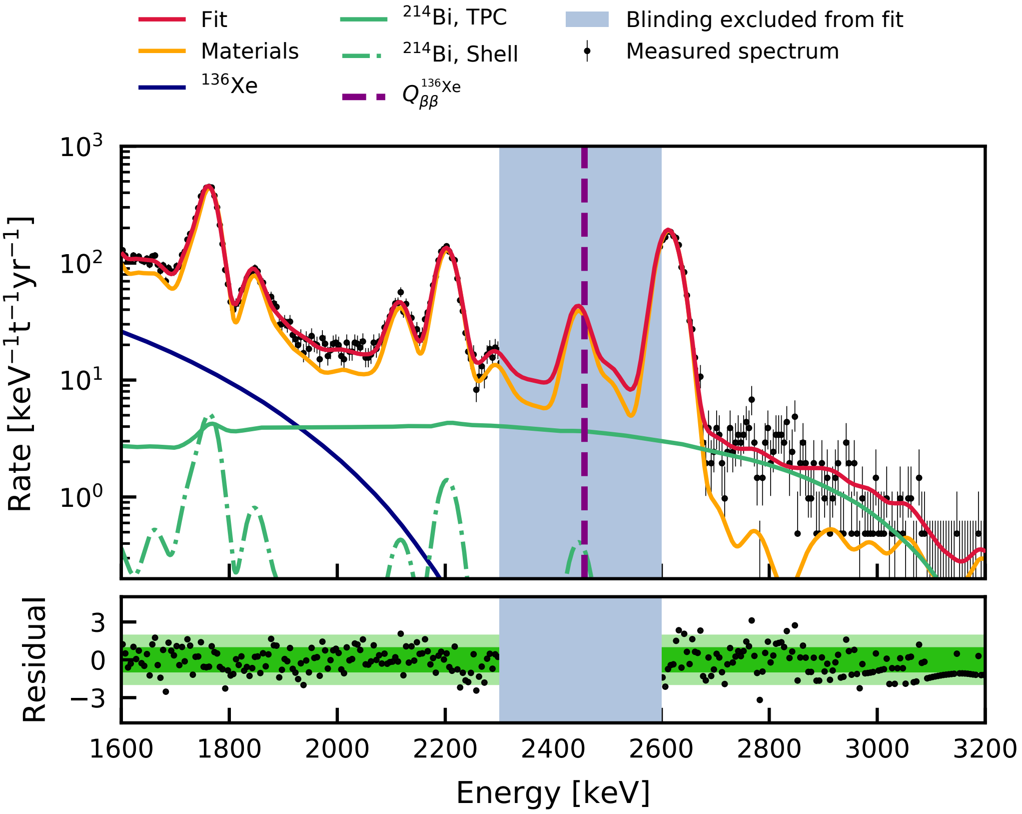

Figure 7.3: **Top:** Fit of the MC-based background model to measured data with $\chi^2_\lambda/\text{ndf} = 311/319 \approx 0.98$. The fit range is 1600 to 3200 keV in 5 keV bins (black points). The displayed uncertainties for each bin are Feldman & Cousins 68.3 % confidence intervals [262]. The blinded region (blue) is excluded from the fit. The ^{136}Xe double-β decay Q-value is marked by the dashed purple line. The best-fit model, is indicated by the solid red line. It consists of the sum of material backgrounds (solid orange), ^{136}Xe (solid blue), ^{214}Bi inside the TPC (solid green), and ^{214}Bi in the uninstrumented LXe shell (dash-dotted green). **Bottom:** Residuals from the square-root of the summands of χ^2_λ (black points). The 1σ and 2σ bands are shown in dark and light green.

and cut acceptance studies by C. Capelli [289] were presented in detail. In the scope of this work a previously disregarded γ-ray background induced by the inactive neutron generator was discovered and quantified. The increased background rate resulting from the neutron generator being submerged next to the TPC lead to a removal of 44.5 live-days of data. It was also shown that this background did not adversely affect the two-neutrino double-electron capture analyses due to the chosen energy ranges.

As for the ^{124}Xe analyses, a background model based on MC simulations was developed. This required the simulation of ^{214}Bi decays in the active and inactive LXe volumes of the detector. Moreover, absolute constraints on radioactive contaminations of detector construction materials were derived on the basis of screening measurements [68] and under the consideration of ^{60}Co decay during the construction and operation of the detector. It was found that the ^{60}Co activity concentration in the cryostat shell of the detector was likely overestimated by approximately a factor of two. This was attributed to the factor ~ 100 difference between the masses of the screened material sample and the installed component. Although the energy reconstruction and resolution were drastically improved in [201], residual energy-dependent shifts of mono-energetic peaks from their expected energies were observed. This was quantified and incorporated into the fit of the background model to the blinded $0\nu\beta\beta$ data (figure 7.3 from section 6.2.4). The best-fit background model was then used to draw toy MCs for the sensitivity estimation. Using a binned log-likelihood ratio test-statistic a sensitivity of

$$T_{1/2}^{0\nu\beta\beta} > 1.7 \cdot 10^{24}\,\mathrm{yr} \quad (90\,\%\,\mathrm{C.\,L.}) \tag{7.5}$$

was found and the data was unblinded. While the results cannot be shown in this work, a publication by the XENON collaboration is in preparation. Although the XENON1T sensitivity that was found in this work would not yield a competitive limit compared to dedicated experiments such as EXO-200 [138] and Kamland-Zen [25], it would be the most stringent limit on $T_{1/2}^{0\nu\beta\beta}$ by a xenon Dark Matter experiment. Moreover, the achievement of percent level energy resolution at $Q_{\beta\beta}^{^{136}\mathrm{Xe}}$ and a full background description, based on material screening and MC simulations, showcases the high-energy potential of future xenon dual-phase TPCs for direct Dark Matter detection.

The next-generation xenon Dark Matter detectors LZ [151] and XENONnT [18] are in commissioning and will reach $\mathcal{O}(10^{26})$ yr sensitivities for $0\nu\beta\beta$ of ^{136}Xe. This puts them at a similar sensitivity level as the current dedicated experiments EXO-200 [138] and KamLAND Zen [25]. The following generation represented by DARWIN [152] could directly compete with dedicated experiments such as nEXO [150]. This also holds true for the potential detection of $2\nu\mathrm{EC}\beta^+$ and the search for the neutrinoless ^{124}Xe decay modes. In contrast to the dedicated double-β decay experiments their low thresholds will allow the Dark Matter detectors to also investigate signals in the few keV range such as CEνNS, axions, neutrino magnetic moments and WIMP Dark Matter. This makes them versatile observatories for physics within and beyond the Standard Model.

Bibliography

[1] L. M. Brown, M. Riordan, M. Dresden, and L. Hoddeson, *The Rise of the Standard Model: 1964–1979* (Cambridge University Press, 1997), p. 3–35.

[2] G. Aad *et al.*, Physics Letters B **716**, 1 (2012).

[3] S. Chatrchyan *et al.*, Physics Letters B **716**, 30 (2012).

[4] Particle Data Group, P. A. Zyla *et al.*, Progress of Theoretical and Experimental Physics **2020** (2020), 083C01.

[5] M. E. Peskin, Proceedings of the National Academy of Sciences **112**, 12256 (2015).

[6] H. Nilles, Physics Reports **110**, 1 (1984), https://doi.org/10.1016/0370-1573(84)90008-5.

[7] A. Ringwald, Exploring the Role of Axions and Other WISPs in the Dark Universe, 2012, arXiv:1210.5081.

[8] T. M. Undagoitia and L. Rauch, Journal of Physics G: Nuclear and Particle Physics **43**, 013001 (2015).

[9] E. Aprile and T. Doke, Review of Modern Physics **82**, 2053 (2010).

[10] M. Schumann, Journal of Physics G: Nuclear and Particle Physics **46**, 103003 (2019).

[11] E. Aprile *et al.*, Physical Review D **100**, 052014 (2019).

[12] XENON Collaboration, E. Aprile *et al.*, Physical Review Letters **121**, 111302 (2018), arXiv:1805.12562.

[13] XENON Collaboration, E. Aprile *et al.*, Physical Review Letters **122**, 141301 (2019), arXiv:1902.03234.

[14] XENON Collaboration, E. Aprile *et al.*, (2020), arXiv:2006.09721.

[15] XENON Collaboration, E. Aprile *et al.*, Physical Review Letters **122**, 071301 (2019), arXiv:1811.12482.

[16] XENON Collaboration, E. Aprile *et al.*, Physical Review Letters **123**, 241803 (2019), arXiv:1907.12771.

[17] LZ, D. S. Akerib *et al.*, The LUX-ZEPLIN (LZ) Experiment, 2019, arXiv:1910.09124.

[18] XENON Collaboration, E. Aprile *et al.*, Projected WIMP sensitivity of the XENONnT dark matter experiment, 2020, arXiv:2007.08796.

[19] Super-Kamiokande Collaboration, Y. Fukuda *et al.*, Physical Review Letters **81**, 1562 (1998).

[20] SNO Collaboration, Q. R. Ahmad *et al.*, Physical Review Letters **89**, 011301 (2002).

[21] KATRIN Collaboration, M. Aker *et al.*, Physical Review Letters **123**, 221802 (2019).

[22] KATRIN, M. Aker *et al.*, Physical Review Letters **123**, 221802 (2019), arXiv:1909.06048.

[23] M. J. Dolinski, A. W. Poon, and W. Rodejohann, Annual Review of Nuclear and Particle Science **69**, 219 (2019).

[24] W. Buchmüller, R. Peccei, and T. Yanagida, Annual Review of Nuclear and Particle Science **55**, 311 (2005).

[25] KamLAND-Zen Collaboration, A. Gando *et al.*, Physical Review Letters **117**, 082503 (2016).

[26] R. G. Winter, Physical Review **100**, 142 (1955).

[27] D. A. Nesterenko *et al.*, Physical Review **C86**, 044313 (2012).

[28] M. Hirsch, K. Muto, T. Oda, and H. V. Klapdor-Kleingrothaus, Zeitschrift für Physik A Hadrons and Nuclei **347**, 151 (1994).

[29] M. Goeppert-Mayer, Physical Review **48**, 512 (1935).

[30] R. Saakyan, Annual Review of Nuclear and Particle Science **63**, 503 (2013), https://doi.org/10.1146/annurev-nucl-102711-094904.

[31] XENON Collaboration, E. Aprile *et al.*, Nature **568**, 532 (2019), arXiv:1904.11002.

[32] J. C. Kapteyn, The Astrophysical Journal **55**, 302 (1922).

[33] J. H. Oort, Bulletin of the Astronomical Institutes of the Netherlands **6**, 249 (1932).

[34] F. Zwicky, Helvetica Physica Acta **6**, 110 (1933).

[35] V. Rubin, N. Thonnard, and J. Ford, The Astrophysical Journal **225**, L107 (1978).

[36] A. Bosma, The Astronomical Journal **86**, 1825 (1981).

[37] E. E. Richards *et al.*, Monthly Notices of the Royal Astronomical Society **449**, 3981 (2015), arXiv:1503.05981.

[38] C. T. Slater, D. L. Nidever, J. A. Munn, E. F. Bell, and S. R. Majewski, The Astrophysical Journal **832**, 206 (2016).

[39] D. Clowe *et al.*, The Astrophysical Journal **648**, L109 (2006), arXiv:astro-ph/0608407.

[40] G. Hinshaw *et al.*, The Astrophysical Journal Suppl. **208**, 19 (2013), arXiv:1212.5226.

[41] N. Aghanim *et al.*, Astronomy & Astrophysics **641**, A6 (2020).

[42] Planck, P. A. R. Ade *et al.*, Astronomy & Astrophysics **594**, A13 (2016), arXiv:1502.01589.

[43] M. Vogelsberger *et al.*, Monthly Notices of the Royal Astronomical Society **444**, 1518 (2014), arXiv:1405.2921.

[44] J. E. González, C. G. Lacey, C. M. Baugh, C. S. Frenk, and A. J. Benson, Monthly Notices of the Royal Astronomical Society **397**, 1254–1274 (2009).

[45] BOSS, L. Anderson *et al.*, Monthly Notices of the Royal Astronomical Society **441**, 24 (2014), arXiv:1312.4877.

[46] Liddle, A.R. and Otterstein, S., *Einführung in die moderne Kosmologie,* Lehrbuch Physik (Wiley-VCH, 2008).

[47] D. N. Schramm and M. S. Turner, Review of Modern Physics **70**, 303 (1998).

[48] D. Hooper and S. Profumo, Physics Reports **453**, 29–115 (2007).

[49] L. Roszkowski, Pramana **62**, 389 (2004), https://doi.org/10.1007/BF02705097.

[50] K. M. Zurek, Physics Reports **537**, 91–121 (2014).

[51] H. Baer, K.-Y. Choi, J. E. Kim, and L. Roszkowski, Physics Reports **555**, 1–60 (2015).

[52] J. D. Lewin and P. F. Smith, Astroparticle Physics **6**, 87 (1996).

[53] M. C. Smith *et al.*, Monthly Notices of the Royal Astronomical Society **379**, 755–772 (2007).

[54] R. H. Helm, Physical Review **104**, 1466 (1956).

[55] M. Hoferichter, P. Klos, J. Menéndez, and A. Schwenk, Physical Review D **99**, 055031 (2019).

[56] M. Hoferichter, P. Klos, J. Menéndez, and A. Schwenk, Physical Review D **94**, 063505 (2016).

[57] A. Fieguth *et al.*, Physical Review D **97**, 103532 (2018).

[58] L. Vietze, P. Klos, J. Menéndez, W. Haxton, and A. Schwenk, Physical Review D **91**, 043520 (2015).

[59] D. Akerib *et al.*, Physical Review Letters **118**, 021303 (2017).

[60] PandaX-II, X. Cui *et al.*, Physical Review Letters **119**, 181302 (2017), arXiv:1708.06917.

[61] R. Agnese *et al.*, Physical Review D **97**, 022002 (2018).

[62] A. Abdelhameed *et al.*, Physical Review D **100**, 102002 (2019).

[63] P. Agnes *et al.*, Physical Review Letters **121**, 081307 (2018).

[64] XENON Collaboration, E. Aprile *et al.*, Physical Review Letters **123**, 251801 (2019), arXiv:1907.11485.

[65] D. Akerib *et al.*, Astroparticle Physics **62**, 33–46 (2015).

[66] E. Aprile *et al.*, Journal of Cosmology and Astroparticle Physics **2016**, 027–027 (2016).

[67] LUX Collaboration, D. S. Akerib *et al.*, Discrimination of electronic recoils from nuclear recoils in two-phase xenon time projection chambers, 2020, arXiv:2004.06304.

[68] XENON Collaboration, E. Aprile *et al.*, The European Physical Journal C **77**, 890 (2017), arXiv:1705.01828.

[69] D. Akerib *et al.*, Astroparticle Physics **96**, 1 (2017).

[70] XENON Collaboration, E. Aprile *et al.*, Physical Review D **99**, 112009 (2019), arXiv:1906.04717.

[71] K. Abe *et al.*, Astroparticle Physics **31**, 290–296 (2009).

[72] XENON Collaboration, E. Aprile *et al.*, The European Physical Journal C **77**, 275 (2017), arXiv:1612.04284.

[73] M. Murra, *Intrinsic background reduction by cryogenic distillation for the XENON1T dark matter experiment*, PhD thesis, WWU Münster, 2019.

[74] S. A. Brünner, *Mitigation of*^{222}*Rn induced background in the XENON1T dark matter experiment*, PhD thesis, Universität Heidelberg, 2017.

[75] J. Street *et al.*, AIP Conference Proceedings **1921**, 050002 (2018), https://aip.scitation.org/doi/pdf/10.1063/1.5018995.

[76] E. Aprile *et al.*, ^{222}Rn emanation measurements for the XENON1T experiment, 2020, arXiv:2009.13981.

[77] E. Aprile *et al.*, The European Physical Journal C **77**, 358 (2017), arXiv:1702.06942.

[78] L. Baudis, A. Kish, F. Piastra, and M. Schumann, The European Physical Journal C **75**, 485 (2015).

[79] B. J. Mount *et al.*, LUX-ZEPLIN (LZ) Technical Design Report, 2017, arXiv:1703.09144.

[80] A. Wright, P. Mosteiro, B. Loer, and F. Calaprice, Nuclear Instruments and Methods in Physics Research Section A: Accelerators, Spectrometers, Detectors and Associated Equipment **644**, 18–26 (2011).

[81] D. M. Poehlmann *et al.*, Characterization of gadolinium-loaded plastic scintillator for use as a neutron veto, 2018, arXiv:1812.11267.

[82] E. Aprile *et al.*, Journal of Instrumentation **9**, P11006–P11006 (2014).

[83] J. Billard, L. Strigari, and E. Figueroa-Feliciano, Physical Review D **89**, 023524 (2014), arXiv:1307.5458.

[84] J. Aalbers *et al.*, Journal of Cosmology and Astroparticle Physics **2016**, 017 (2016).

[85] E. Aprile *et al.*, Astroparticle Physics **34**, 679–698 (2011).

[86] XENON Collaboration, J. Angle *et al.*, Physical Review Letters **100**, 021303 (2008), arXiv:0706.0039.

[87] XENON Collaboration, E. Aprile *et al.*, Physical Review D **94**, 122001 (2016).

[88] XENON Collaboration, E. Aprile *et al.*, The European Physical Journal C **77**, 881 (2017), arXiv:1708.07051.

[89] M. Doi and T. Kotani, Progress of Theoretical Physics **87**, 1207 (1992).

[90] E. Majorana, Il Nuovo Cimento (1924-1942) **14**, 171 (1937).

[91] J. Bernabeu, A. De Rujula, and C. Jarlskog, Nuclear Physics **B223**, 15 (1983).

[92] M. Doi, T. Kotani, H. Nishiura, K. Okuda, and E. Takasugi, Progress of Theoretical Physics **66**, 1739 (1981).

[93] M. Doi, T. Kotani, H. Nishiura, and E. Takasugi, Progress of Theoretical Physics **69**, 602 (1983).

[94] T. Tomoda, Reports on Progress in Physics **54**, 53 (1991).

[95] J. Kotila and F. Iachello, Physical Review C **85**, 034316 (2012).

[96] J. Barea, J. Kotila, and F. Iachello, Physical Review C **87**, 057301 (2013).

[97] S. Stoica and M. Mirea, Frontiers in Physics **7**, 12 (2019).

[98] B. Povh, K. Rith, C. Scholz, F. Zetsche, and W. Rodejohann, *Teilchen und Kerne. Eine Einführung in die physikalischen Konzepte*, 9th ed. (Springer Spektrum, Berlin, Heidelberg, 2014).

[99] R. Arnold *et al.*, The European Physical Journal C **79**, 440 (2019).

[100] KamLAND-Zen, A. Gando *et al.*, Physical Review Letters **122**, 192501 (2019), arXiv:1901.03871.

[101] F. Iachello, *The Interacting Boson Model* (Springer US, Boston, MA, 1979), pp. 23–35.

[102] J. Kotila, J. Barea, and F. Iachello, Physical Review C **89**, 064319 (2014).

[103] J. Barea, J. Kotila, and F. Iachello, Physical Review C **91**, 034304 (2015).

[104] E. Caurier, G. Martínez-Pinedo, F. Nowacki, A. Poves, and A. P. Zuker, Review of Modern Physics **77**, 427 (2005).

[105] J. Menéndez, Journal of Physics **G45**, 014003 (2018), arXiv:1804.02105.

[106] E. A. Coello Pérez, J. Menéndez, and A. Schwenk, Physics Letters B **797**, 134885 (2019), arXiv:1809.04443.

[107] J. Toivanen and J. Suhonen, Physical Review Letters **75**, 410 (1995).

[108] J. Suhonen, Journal of Physics **G40**, 075102 (2013).

[109] F. Šimkovic, V. Rodin, A. Faessler, and P. Vogel, Physical Review C **87**, 045501 (2013).

[110] P. Pirinen and J. Suhonen, Physical Review C **91**, 054309 (2015).

[111] J. Hyvärinen and J. Suhonen, Physical Review C **91**, 024613 (2015).

[112] P. Gysbers *et al.*, Nature Physics **15**, 428 (2019).

[113] T. Kajita, Review of Modern Physics **88**, 030501 (2016).

[114] A. B. McDonald, Review of Modern Physics **88**, 030502 (2016).

[115] A. de Gouvêa, Annual Review of Nuclear and Particle Science **66**, 197 (2016).

[116] K. Abe *et al.*, Nature **580**, 339 (2020).

[117] J. Kotila and F. Iachello, Physical Review C **87**, 024313 (2013).

[118] S. R. Choudhury and S. Hannestad, Journal of Cosmology and Astroparticle Physics **2020**, 037 (2020).

[119] J. Engel and J. Menéndez, Reports on Progress in Physics **80**, 046301 (2017).

[120] S. Pascoli and S. Petcov, Physics Letters B **544**, 239–250 (2002).

[121] I. Esteban, M. C. Gonzalez-Garcia, A. Hernandez-Cabezudo, M. Maltoni, and T. Schwetz, Journal of High Energy Physics **2019**, 106 (2019).

[122] M. Agostini, G. Benato, and J. Detwiler, Physical Review D **96**, 053001 (2017), arXiv:1705.02996.

[123] J. Schechter and J. W. F. Valle, Physical Review D **25**, 2951 (1982).

[124] V. I. Tretyak and Y. G. Zdesenko, Atomic Data and Nuclear Data Tables **80**, 83 (2002).

[125] S. Rahaman *et al.*, Physics Letters B **662**, 111 (2008).

[126] M. Redshaw, E. Wingfield, J. McDaniel, and E. Myers, Physical Review Letters **98**, 053003 (2007).

[127] nEXO Collaboration, S. A. Kharusi *et al.*, (2018), arXiv:1805.11142.

[128] G. Audi, F. G. Kondev, M. Wang, W. Huang, and S. Naimi, Chinese Physics C **41**, 030001 (2017).

[129] Majorana Collaboration, C. E. Aalseth *et al.*, Physical Review Letters **120**, 132502 (2018).

[130] S. Umehara *et al.*, Physical Review C **78**, 058501 (2008).

[131] GERDA, M. Agostini *et al.*, Physical Review Letters **125**, 252502 (2020), arXiv:2009.06079.

[132] A. S. Barabash, V. B. Brudanin, and N. Collaboration, Physics of Atomic Nuclei **74**, 312 (2011).

[133] J. Argyriades *et al.*, Nuclear Physics A **847**, 168 (2010).

[134] NEMO-3 Collaboration, R. Arnold *et al.*, Physical Review D **92**, 072011 (2015).

[135] A. S. Barabash *et al.*, Physical Review D **98**, 092007 (2018).

[136] C. Arnaboldi *et al.*, Physics Letters B **557**, 167 (2003).

[137] D. Adams *et al.*, Physical Review Letters **124**, 122501 (2020).

[138] EXO-200 Collaboration, G. Anton *et al.*, Physical Review Letters **123**, 161802 (2019).

[139] NEMO-3 Collaboration, R. Arnold *et al.*, Physical Review D **94**, 072003 (2016).

[140] M. Agostini *et al.*, Science **365**, 1445 (2019), 1909.02726.

[141] GERDA Collaboration, M. Agostini *et al.*, Physical Review Letters **120**, 132503 (2018).

[142] CUORE Collaboration, C. Alduino *et al.*, Physical Review Letters **120**, 132501 (2018).

[143] T. Brunner and L. Winslow, Searching for $0\nu\beta\beta$ decay in ^{136}Xe – towards the tonne-scale and beyond, 2017, arXiv:1704.01528.

[144] A. Barabash, AIP Conference Proceedings **2165**, 020002 (2019), arXiv:1907.06887.

[145] XMASS, K. Abe *et al.*, Progress of Theoretical and Experimental Physics **2018**, 053D03 (2018), arXiv:1801.03251.

[146] EXO-200 Collaboration, J. Albert *et al.*, Physical Review D **96**, 092001 (2017), arXiv:1704.05042.

[147] EXO-200 Collaboration, J. B. Albert *et al.*, Physical Review **C89**, 015502 (2014), arXiv:1306.6106.

[148] W. Feldmeier, *Search for neutrinoless double beta decay in* ^{136}*Xe with EXO-200*, PhD thesis, Munich, Tech. U., 2015.

[149] EXO-200 Collaboration, J. B. Albert *et al.*, Physical Review Letters **120**, 072701 (2018).

[150] nEXO Collaboration, J. B. Albert *et al.*, Physical Review C **97**, 065503 (2018).

[151] LZ, D. Akerib *et al.*, Physical Review C **102**, 014602 (2020), arXiv:1912.04248.

[152] DARWIN, F. Agostini *et al.*, The European Physical Journal C **80**, 808 (2020), arXiv:2003.13407.

[153] J. Meija *et al.*, Pure and Applied Chemistry **88**, 293 (01 Mar. 2016).

[154] P. M. McCowan and R. C. Barber, Physical Review C **82**, 024603 (2010).

[155] C. Wittweg, B. Lenardo, A. Fieguth, and C. Weinheimer, The European Physical Journal C **80**, 1161 (2020), arXiv:2002.04239.

[156] R. D. Deslattes *et al.*, Review of Modern Physics **75**, 35 (2003).

[157] J. Katakura and Z. Wu, Nuclear Data Sheets **109**, 1655 (2008).

[158] D. Z. Freedman, Physical Review D **9**, 1389 (1974).

[159] D. Akimov *et al.*, Science **357**, 1123 (2017).

[160] M. Hoferichter, J. Menéndez, and A. Schwenk, Physical Review D **102**, 074018 (2020).

[161] CONUS Collaboration, H. Bonet *et al.*, Physical Review Letters **126**, 041804 (2021).

[162] D. Akimov *et al.*, Physical Review D **100**, 115020 (2019).

[163] J. Barranco, O. G. Miranda, and T. I. Rashba, Journal of High Energy Physics **2005**, 021 (2005).

[164] B. Dutta, S. Liao, L. E. Strigari, and J. W. Walker, Physics Letters B **773**, 242 (2017).

[165] J. Liao and D. Marfatia, Physics Letters B **775**, 54 (2017).

[166] Particle Data Group, M. Tanabashi *et al.*, Physical Review D **98**, 030001 (2018).

[167] E. Vitagliano, I. Tamborra, and G. Raffelt, Review of Modern Physics **92**, 045006 (2020).

[168] M. Agostini *et al.*, Nature **587**, 577 (2020).

[169] SNO+ Collaboration, M. Anderson *et al.*, Physical Review D **99**, 012012 (2019).

[170] M. Agostini *et al.*, Nature **562**, 505 (2018).

[171] N. Vinyoles *et al.*, The Astrophysical Journal **835**, 202 (2017), arXiv:1611.09867.

[172] J. N. Bahcall, Physical Review C **56**, 3391 (1997).

[173] W. T. Winter, S. J. Freedman, K. E. Rehm, and J. P. Schiffer, Physical Review C **73**, 025503 (2006).

[174] J. N. Bahcall *et al.*, Physical Review C **54**, 411 (1996).

[175] XENON Collaboration, E. Aprile *et al.*, Search for coherent elastic scattering of solar ^{8}B neutrinos in the XENON1T dark matter experiment, 2020, arXiv:2012.02846.

[176] LUX-ZEPLIN, D. Akerib *et al.*, Physical Review D **101**, 052002 (2020), arXiv:1802.06039.

[177] B. Dutta and L. E. Strigari, Annual Review of Nuclear and Particle Science **69**, 137 (2019), arXiv:1901.08876.

[178] XENON Collaboration, E. Aprile *et al.*, Physical Review Letters **118**, 101101 (2017).

[179] XMASS Collaboration 3, K. Abe *et al.*, Physical Review D **97**, 102006 (2018).

[180] P. Linstrom, NIST Chemistry WebBook, NIST Standard Reference Database 69, 1997.

[181] NIST, PML, Radiation Physics Division, M. Berger *et al.*, XCOM: Photon Cross Sections Database. NIST Standard Reference Database 8 (XGAM), 2016.

[182] E. Browne and J. Tuli, Nuclear Data Sheets **114**, 1849 (2013).

[183] M. Martin, Nuclear Data Sheets **108**, 1583 (2007).

[184] S.-C. Wu, Nuclear Data Sheets **110**, 681 (2009).

[185] S. Rosendahl, *Gas purification of the XENON dark matter search*, PhD thesis, WWU Münster, 2015.

[186] D. Akerib *et al.*, Physical Review D **97**, 112002 (2018).

[187] S. Kubota *et al.*, Physical Review B **17**, 2762 (1978).

[188] EXO-200 Collaboration, E. Conti *et al.*, Physical Review **B68**, 054201 (2003), arXiv:hep-ex/0303008.

[189] E. Aprile, K. L. Giboni, P. Majewski, K. Ni, and M. Yamashita, Physical Review B **76** (2007).

[190] M. Szydagis *et al.*, Journal of Instrumentation **6**, P10002–P10002 (2011).

[191] XENON100, E. Aprile *et al.*, Astroparticle Physics **54**, 11 (2014), arXiv:1207.3458.

[192] J. Lindhard, M. Scharff, and H. E. Schiøtt, Det Kongelige Danske Videnskabernes Selskab. Matematisk-fysiske Meddelelser **33** (1963).

[193] G. Plante *et al.*, Physical Review C **84**, 045805 (2011), arXiv:1104.2587.

[194] B. Lenardo *et al.*, Measurement of the ionization yield from nuclear recoils in liquid xenon between 0.3 - 6 keV with single-ionization-electron sensitivity, 2019, arXiv:1908.00518.

[195] NEST Collaboration, M. Szydagis, G. Rischbieter, and K. Kozlova, A Comprehensive, Exhaustive, Complete Analysis of World LXe NR Data With a Final Model, Public analysis note, http://nest.physics.ucdavis.edu.

[196] NEST Collaboration, M. Szydagis *et al.*, Noble element simulation technique, https://doi.org/10.5281/zenodo.3905382.

[197] E. Aprile *et al.*, Astroparticle Physics **35**, 573–590 (2012).

[198] C. L. Brown, *Light Propagation and Reflection off Teflon in Liquid Xenon Detectors for the XENON100 and XENON1T Dark Matter Experiment*, PhD thesis, WWU Münster, 2014.

[199] F. Neves *et al.*, Journal of Instrumentation **12**, P01017 (2017).

[200] L. Althueser, Light collection efficiency simulations of the XENON1T experiment and comparison to data, Master's thesis, WWU Münster, 2017.

[201] XENON Collaboration, E. Aprile *et al.*, The European Physical Journal C **80**, 785 (2020), arXiv:2003.03825.

[202] XENON Collaboration, E. Aprile *et al.*, Physical Review Letters **119**, 181301 (2017), arXiv:1705.06655.

[203] R. Lang *et al.*, Journal of Instrumentation **11**, P04004 (2016).

[204] XENON Collaboration, E. Aprile *et al.*, The European Physical Journal C **75**, 546 (2015), arXiv:1503.07698.

[205] A. Fieguth, Investigations of impurities in xenon gas with a cold-trap-enhanced quadrupole mass spectrometer., Master's thesis, WWU Münster, 2014.

[206] S. Lindemann and H. Simgen, The European Physical Journal C **74**, 2746 (2014), arXiv:1308.4806.

[207] A. Fieguth, *First observation of double electron capture in* ^{124}*Xe and detection prospects for underlying nuclear interaction mechanisms in direct dark matter search*, PhD thesis, WWU Münster, 2018.

[208] E. Brown *et al.*, The European Physical Journal C **78**, 604 (2018).

[209] E. Boulton *et al.*, Journal of Instrumentation **12**, P08004 (2017).

[210] L. Baudis *et al.*, The European Physical Journal C **80**, 477 (2020).

[211] E. Browne, Nuclear Data Sheets **104**, 427 (2005).

[212] A. Manalaysay *et al.*, Review of Scientific Instruments **81**, 073303 (2010).

[213] M. Zbořil *et al.*, Journal of Instrumentation **8**, P03009–P03009 (2013).

[214] E. McCutchan, Nuclear Data Sheets **125**, 201 (2015).

[215] XENON Collaboration, E. Aprile *et al.*, Journal of Instrumentation **14**, P07016–P07016 (2019).

[216] XENON Collaboration, E. Aprile *et al.*, The PAX data processor v6.8.0, https://doi.org/10.5281/zenodo.1195785.

[217] D. Remenska *et al.*, Journal of Physics: Conference Series **898**, 042003 (2017).

[218] C. R. Harris *et al.*, Nature **585**, 357 (2020).

[219] J. Reback *et al.*, pandas-dev/pandas: Pandas 1.0.3, 2020, https://doi.org/10.5281/zenodo.3715232.

[220] F. Rademakers *et al.*, root-project/root: v6.18/02, 2019.

[221] C. Wittweg, XENON100 Dark Matter Search with the PAX Raw Data Processor for XENON1T, Master's thesis, WWU Münster, 2016.

[222] K. Ni *et al.*, Nuclear Instruments and Methods A **582**, 569 (2007), arXiv:0708.1976.

[223] J. Timar, Z. Elekes, and B. Singh, Nuclear Data Sheets **121**, 143 (2014).

[224] Y. Khazov, I. Mitropolsky, and A. Rodionov, Nuclear Data Sheets **107**, 2715 (2006).

[225] J. Chen, Nuclear Data Sheets **140**, 1 (2017).

[226] LUX Collaboration, D. S. Akerib *et al.*, Physical Review D **102**, 112002 (2020).

[227] LUX Collaboration, D. S. Akerib *et al.*, Physical Review D **95**, 012008 (2017).

[228] D. Cullen, Lawrence Livermore National Laboratory Report No. UCRL-ID–110438, 1992 (unpublished), https://www.osti.gov/servlets/purl/5360235.

[229] R. Harnik, J. Kopp, and P. A. N. Machado, Journal of Cosmology and Astroparticle Physics **2012**, 026–026 (2012).

[230] Y. Khazov, A. Rodionov, and F. Kondev, Nuclear Data Sheets **112**, 855 (2011).

[231] J. Katakura, Nuclear Data Sheets **112**, 495 (2011).

[232] XENON Collaboration, N. Rupp, Summary note on Radon concentration for SR0 and SR1, Internal note, 2018.

[233] M. Shamsuzzoha Basunia, Nuclear Data Sheets **121**, 561 (2014).

[234] A. K. Jain and B. Singh, Nuclear Data Sheets **107**, 1027 (2006).

[235] S. Singh, A. Jain, and J. K. Tuli, Nuclear Data Sheets **112**, 2851 (2011).

[236] J. Ahlswede, S. Hebel, J. O. Ross, R. Schoetter, and M. B. Kalinowski, Journal of Environmental Radioactivity **115**, 34 (2013).

[237] B. Singh and J. Chen, Nuclear Data Sheets **116**, 1 (2014).

[238] XENON Collaboration, M. Vargas and Z. Greene, Summary note on Kr-85 concentration for SR1, Internal note, 2018.

[239] J. Kotila and F. Iachello, Physical Review C **85**, 034316 (2012).

[240] F. Toschi, Study of the electronic recoil background of the XENON1T experiment, Master's thesis, University of Bologna, 2018.

[241] S. Agostinelli *et al.*, Nuclear Instruments and Methods in Physics Research Section A: Accelerators, Spectrometers, Detectors and Associated Equipment **506**, 250 (2003).

[242] J. Allison *et al.*, IEEE Transactions on Nuclear Science **53**, 270 (2006).

[243] J. Allison *et al.*, Nuclear Instruments and Methods in Physics Research Section A: Accelerators, Spectrometers, Detectors and Associated Equipment **835**, 186 (2016).

[244] D. Adams, *The Hitchhiker's Guide to the Galaxy* (Random House Publishing Group, 2007).

[245] M. Be *et al.*, Table of Radionuclides (Vol. 6 - A = 22 to 242). I-125, 2011, https://nucleide.org/DDEP_WG/Nuclides/I-125_tables.pdf.

[246] A. Rindi, F. Celani, M. Lindozzi, and S. Miozzi, Nuclear Instruments and Methods in Physics Research Section A: Accelerators, Spectrometers, Detectors and Associated Equipment **272**, 871 (1988).

[247] P. Belli *et al.*, Il Nuovo Cimento A (1965-1970) **101**, 959 (1989).

[248] H. Wulandari, J. Jochum, W. Rau, and F. von Feilitzsch, Astroparticle Physics **22**, 313–322 (2004).

[249] Z. Debicki *et al.*, Nuclear Physics B - Proceedings Supplements **196**, 429 (2009), Proceedings of the XV International Symposium on Very High Energy Cosmic Ray Interactions (ISVHECRI 2008).

[250] A. Best *et al.*, Nuclear Instruments and Methods in Physics Research Section A: Accelerators, Spectrometers, Detectors and Associated Equipment **812**, 1 (2016).

[251] S. F. Mughabghab, Thermal neutron capture cross sections resonance integrals and g-factors, 2003, http://inis.iaea.org/search/search.aspx?orig_q=RN:34020739, INDC(NDS)–440.

[252] J. H. Hubbell *et al.*, Journal of Physical and Chemical Reference Data **23**, 339 (1994), https://doi.org/10.1063/1.555955.

[253] S. S. Ratkevich *et al.*, Physical Review C **96**, 065502 (2017).

[254] XENON Collaboration, E. Aprile *et al.*, Physical Review C **95**, 024605 (2017), arXiv:1609.03354.

[255] H. Zhang *et al.*, Science China Physics, Mechanics & Astronomy **62** (2018).

[256] XENON Collaboration, D. Winkler, Analysis of Xe1T RGMS Data, Internal note, 2020.

[257] XENON Collaboration, H. Schulze-Eißing, Energy reconstruction in SR2, Internal note, 2020.

[258] E. Shockley, *Study of Excess Electronic Recoil Events in XENON1T*, PhD thesis, University of Chicago, KICP, 2020.

[259] XENON Collaboration, A. Bismark, S2PatternLikelihood Cut for SR2 DEC Analysis, Internal note, 2020.

[260] XENON Collaboration, A. Bismark, CS2AreaFractionTop Cut for SR2 DEC Analysis, Internal note, 2020.

[261] M. Paterno, FERMILAB-TM-2286-CD (2004), https://lss.fnal.gov/archive/test-tm/2000/fermilab-tm-2286-cd.pdf.

[262] G. J. Feldman and R. D. Cousins, Physical Review D **57**, 3873–3889 (1998).

[263] S. Baker and R. D. Cousins, Nuclear Instruments and Methods in Physics Research **221**, 437 (1984).

[264] A. Thompson *et al.*, X-ray Data Booklet, 2009, https://xdb.lbl.gov/xdb.pdf.

[265] H. Dembinski *et al.*, scikit-hep/iminuit: v1.5.4, 2020, https://doi.org/10.5281/zenodo.4283509.

[266] I. Esteban, M. C. Gonzalez-Garcia, A. Hernandez-Cabezudo, M. Maltoni, and T. Schwetz, JHEP **01**, 106 (2019), arXiv:1811.05487.

[267] Majorana Collaboration, S. I. Alvis *et al.*, Physical Review C **100**, 025501 (2019).

[268] E. Caurier, J. Menéndez, F. Nowacki, and A. Poves, Physical Review Letters **100**, 052503 (2008).

[269] M. Doi and T. Kotani, Progress of Theoretical Physics **89**, 139 (1993), http://oup.prod.sis.lan/ptp/article-pdf/89/1/139/5207768/89-1-139.pdf.

[270] J. Menéndez, private communication.

[271] O. A. Ponkratenko, V. I. Tretyak, and Y. G. Zdesenko, Physics of Atomic Nuclei **63**, 1282 (2000).

[272] N. Barros, J. Thurn, and K. Zuber, Journal of Physics **G41**, 115105 (2014), arXiv:1409.8308.

[273] T. Yamazaki, Nuclear Data Sheets. Section A **3**, 1 (1967).

[274] J. Smith *et al.*, Nuclear Instruments and Methods in Physics Research Section A: Accelerators, Spectrometers, Detectors and Associated Equipment **922**, 47–63 (2019).

[275] L. Althueser, l-althueser/xesim: v0.1.0, 2019, https://doi.org/10.5281/zenodo.3541115.

[276] S. Agostinelli *et al.*, Nuclear Instruments and Methods in Physics Research Section A: Accelerators, Spectrometers, Detectors and Associated Equipment **506**, 250 (2003).

[277] DARWIN, J. Aalbers *et al.*, Journal of Cosmology and Astroparticle Physics **1611**, 017 (2016), arXiv:1606.07001.

[278] XENON100, E. Aprile *et al.*, Astroparticle Physics **35**, 573 (2012), arXiv:1107.2155.

[279] M. Jewell *et al.*, Journal of Instrumentation **13**, P01006 (2018).

[280] EXO-200 Collaboration, J. B. Albert *et al.*, Physical Review C **93**, 035501 (2016).

[281] D. Akerib *et al.*, Journal of Instrumentation **13**, P02001–P02001 (2018).

[282] EXO-200 Collaboration, J. B. Albert *et al.*, Physical Review C **92**, 045504 (2015).

[283] P. Pirinen, J. Suhonen, and E. Ydrefors, Physical Review C **99**, 014320 (2019).

[284] S. Usman, G. Jocher, S. Dye, W. McDonough, and J. Learned, Nature Scientific Reports **5**, 13945 (2015).

[285] P. Huber, Physical Review C **84**, 024617 (2011).

[286] A. Sonzogni, Nuclear Data Sheets **95**, 837 (2002).

[287] D. Brown *et al.*, Nuclear Data Sheets **148** (2018).

[288] S. Ohya, Nuclear Data Sheets **102**, 547 (2004).

[289] C. Capelli, *Search for Dark Matter and Neutrinoless Double Beta Decay in XENON1T and Calibration of the Photosensors in XENONnT*, PhD thesis, University of Zürich, 2020.

[290] P. Sorensen, Nuclear Instruments and Methods in Physics Research Section A: Accelerators, Spectrometers, Detectors and Associated Equipment **635**, 41 (2011).

[291] K. Ni *et al.*, Chinese Physics C **43**, 113001 (2019).

[292] B. E. J. Pelssers, *Enhancing Direct Searches for Dark Matter: Spatial-Temporal Modeling and Explicit Likelihoods*, PhD thesis, Stockholm University, 2020.

[293] R. Lang *et al.*, Nuclear Instruments and Methods A **879**, 31 (2018), arXiv:1705.04741.

[294] E. V. Bugaev *et al.*, Physical Review D **58**, 054001 (1998).

[295] P. Virtanen *et al.*, Nature Methods **17**, 261 (2020), arXiv:1907.10121.

[296] D. Savoiu, G. Quast, and J. Schindler, kafe, v1.3.2, 2020, http://www-ekp.physik.uni-karlsruhe.de/ quast/kafe/htmldoc/.

[297] M. Pierre, *Neutrinoless Double Beta Decay Search with XENONnT and Future Prospects*, PhD thesis, Institut Mines Telecom Nantes, 2022 (in preparation).

[298] PandaX-II, K. Ni *et al.*, Chin. Phys. C **43**, 113001 (2019), arXiv:1906.11457.

List of Abbreviations

$0\nu ECEC$ Neutrinoless double electron capture

$0\nu EC\beta^+$ Neutrinoless electron capture with positron emission

$0\nu\beta^+\beta^+$ Neutrinoless double-β decay (with double-positron emission)

$2\nu ECEC$ Two-neutrino double electron capture

$2\nu EC\beta^+$ Two-neutrino electron capture with positron emission

$2\nu\beta^+\beta^+$ Two-neutrino double-β decay (with double-positron emission)

ECEC Double electron capture

$EC\beta^+$ Electron capture with positron emission

$\beta^+\beta^+$ Double-β^+ decay

$\beta^-\beta^-$ Double-β^- decay

ALP Axion-like particle

AP Afterpulse (PMT)

BSM Beyond the Standard Model of particle physics

CC Charged-current (interaction)

CEνNS Coherent elastic neutrino-nucleus scattering

CMB Cosmic microwave background

DAQ Data acquisition system

DSNB Diffuse supernova neutrino background

ER Electronic recoil

G2 Second generation (experiment)

G3 Third generation (experiment)

GUT Grand unified theory

HSD Higher-state dominance

IBM Interacting boson model

IC Internal conversion

IO Inverted ordering (of neutrino masses)

LLR Log-likelihood ratio

LNGS Laboratori Nazionali del Gran Sasso

LSS Large scale structure (of the Universe)

MC Monte Carlo (simulation)

NEST Noble Element Simulation Technique

NG Deuterium-deuterium fusion neutron generator

NME Nulcear matrix element

NO Normal ordering (of neutrino masses)

NR Nuclear recoil

NSM Nuclear shell model

PAX Processor for Analysing Xenon

pe Photoelectron

PI Photoionisation

PMNS Pontecorvo–Maki–Nakagawa–Sakata

PMT Photomultiplier tube

PSF Phase-space factor

PTFE Polytetrafluoroethylene

QCD Quantum chromodynamics

QRPA Quasiparticle random phase approximation

RGA Residual gas analyser

RGMS Rare gas mass spectrometry

ROI Region of interest

SD Spin-dependent (interaction)

SI Spin-independent (interaction)

SM Standard Model of particle physics

SR Science run

SSD Single-state dominance

SUSY Supersymmetry

TPC Time projection chamber

WIMP Weakly interacting massive particle

Nomenclature

$cS1$	Area of the S1 signal corrected for the position-dependent light-collection efficiency and field-distortion effects
$cS2_\mathrm{b}$	Area of the S2 signal as seen by the bottom PMT array and corrected for the x-y-dependent light-collection efficiency and charge aplification, electron lifetime, and position-depedent field-distortion effects

Appendix

A1 Energy reconstruction bias from α-decay electron lifetimes

The results presented in this section were obtained in collaboration with Z. Greene who performed the electron-lifetime model fits and the scaling of the α-based electron-lifetime model to the $^{83\mathrm{m}}$Kr electron-lifetime data points. The author of this work created the energy spectrum plots and determined the energy resolution with fits of the Gaussian γ-lines in the energy spectrum.

Figure A-1 shows the XENON1T ER energy spectrum in a 1 t cylindrical fiducial volume along the z-coordinate of the TPC. The electron-lifetime correction for $cS2_\mathrm{b}$ has been derived using S2s from the α-decays of ^{222}Rn progeny inside the TPC [70]. The energies have been derived using equation (2.9) with $g_1 = 0.1472\,\mathrm{pe/ph}$ and $g_1 = 10.99\,\mathrm{pe/e}$. One can clearly see that the mono-energetic lines from decays of radioactive impurities contained in the LXe target and detector construction materials are not straight along the depth of the TPC. The tilt of the lines appears to increase with energy. This points to an energy- and depth-dependent bias of a correction.

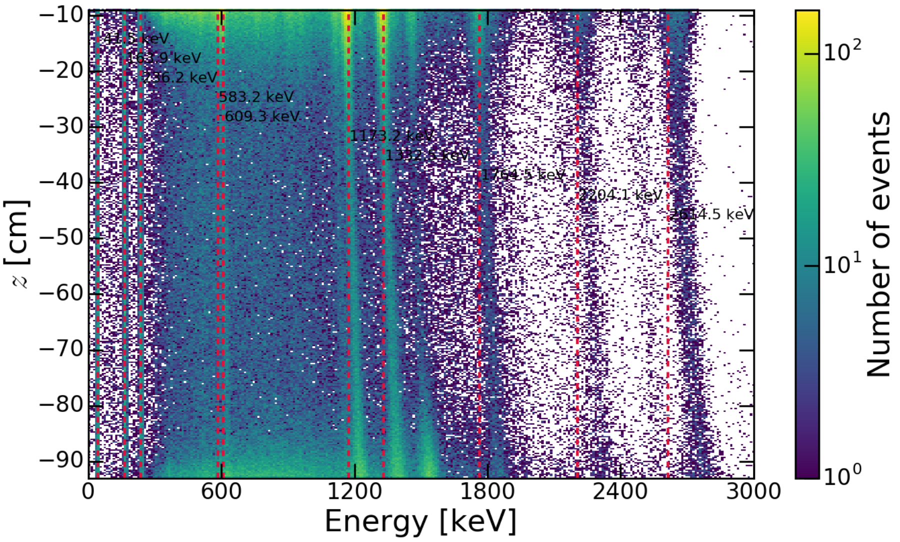

Figure A-1: Energy spectra of ER events in a cylindrical 1 t fiducial volume in XENON1T. The electron-lifetime correction for $cS2_\mathrm{b}$ was derived using α-decays of ^{222}Rn progeny inside the detector. Positions of mono-energetic lines are indicated by the dashed red lines.

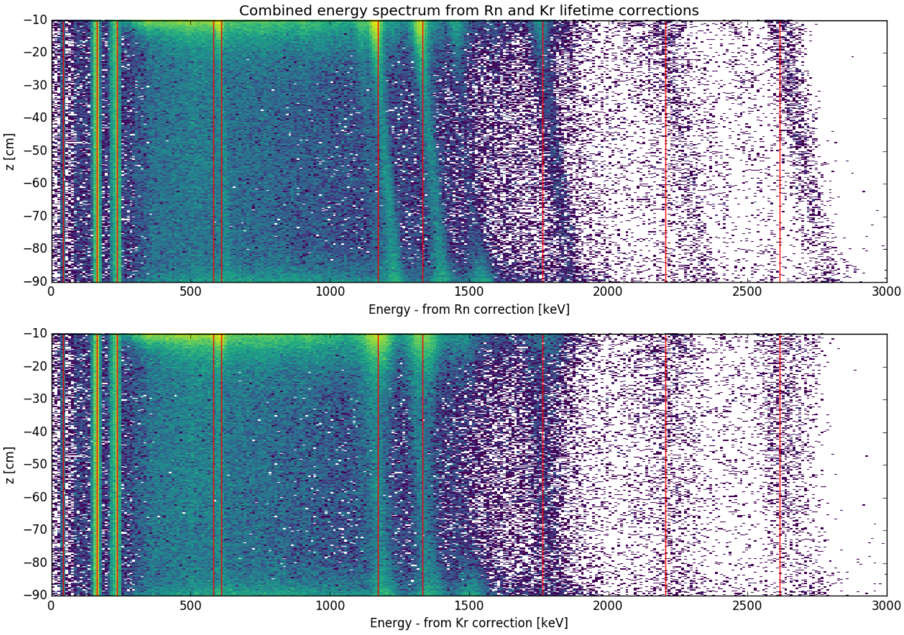

Figure A-2: Comparison of depth-dependent energy spectra with α-correct (**top**) and $^{83\mathrm{m}}$Kr-corrected (**bottom**) electron lifetimes. Positions of mono-energetic lines are indicated by the dashed red lines.

The corrections for S1 as well as S2 are depth-dependent. However, the relative contribution of the S2 to the energy reconstruction increases with energy while that for S1 diminishes. This points towards an issue with the electron-lifetime correction on S2. The electron-lifetime were also determined with $^{83\mathrm{m}}$Kr. The data points suggested a larger value of the electron lifetime than those from the α-decays. This fits the observation that with increasing depth mono-energetic lines are shifted towards larger energies. Here, the underestimation of the electron-lifetime leads to an overestimation of $cS2_\mathrm{b}$ as well as of the reconstructed energy. Consequently, the α-based electron lifetime model was scaled to the $^{83\mathrm{m}}$Kr data points. This is illustrated in figure 2.10 in the main text. Figure A-2 shows the energy spectra for both corrections. New energy calibration parameters $g_1 = 0.1445\,\mathrm{pe/ph}$ and $g_1 = 10.80\,\mathrm{pe/e}$ were determined for the data with the krypton-corrected electron-lifetime. The tilt of the mono-energetic lines is almost fully reduced. The increased sharpness of peaks in the energy spectrum is shown in figure A-3. Even without the high-energy optimisations introduced later (cf. chapter 6) this allowed for energy resolutions at the 1 % level in the MeV energy range. This is shown in figure A-4.

The origin of this bias can be attributed to the inhomogeneity of the electric field inside the detector [201]. A field-gradient is present between the top and bottom of the TPC. Since the field affects recombination depending on the interaction type and energy [67, 190], the S2 signals from $^{83\mathrm{m}}$Kr and α-decays are affected differently over the depth of the TPC. More recombination occurs in the presence of a weaker field that separates the electrons and the ions. In turn, a weaker field at a given position leads to a larger S1 signal and a smaller S2. If due to recombination S2s at the bottom are systematically smaller for one source than for the other, an apparently larger loss of electrons is observed. This leads to a systematic underestimation of the electron lifetime for that source. Since the charge yield observed in α-decays is very sensitive to field effects [9] this explanation is plausible.

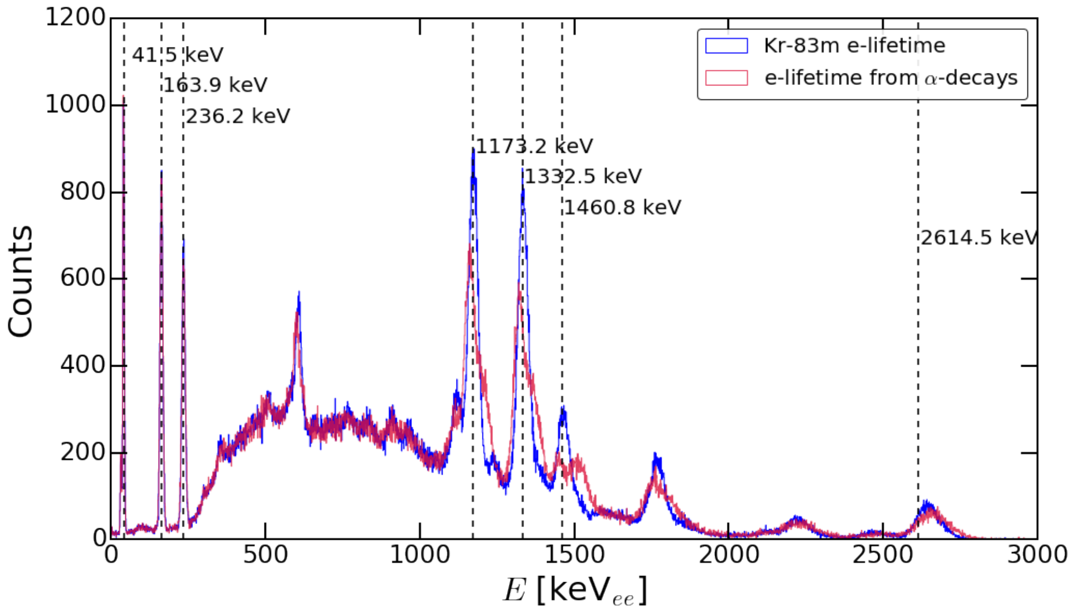

Figure A-3: Comparison of energy spectra with α-correct (red) and ^{83m}Kr-corrected (blue) electron lifetimes. Expected positions of mono-energetic lines are indicated by the dashed black lines.

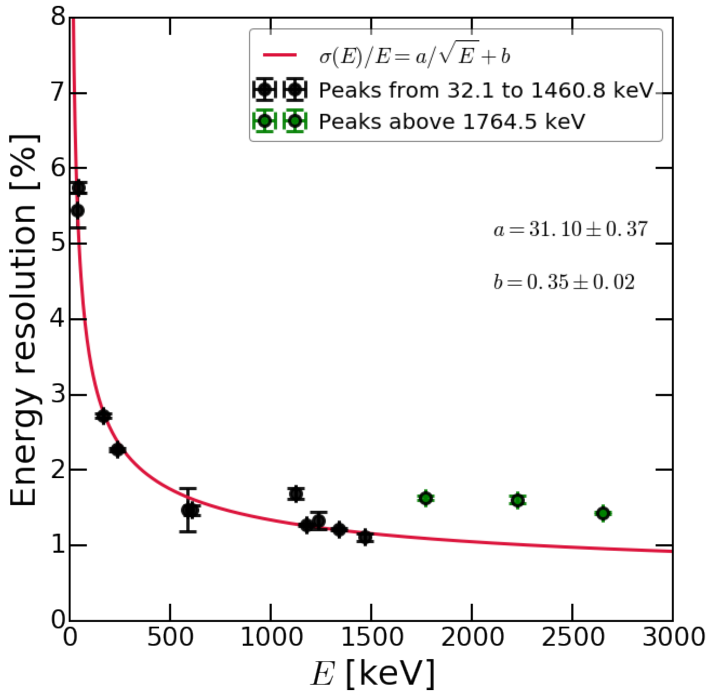

Figure A-4: Energy resolution from fits of mono-energetic lines in the energy spectrum derived from S1 and S2 using the Kr-based electron-lifetime correction. Data points above the ^{40}K line were excluded from the fit since they do not follow the trend of the other datapoints due to missing high-energy optimisations of the data processor.

A2 Exemplary fits of mono-energetic lines for energy calibration

This section shows the 2D fits of the mono-energetic lines of $^{83\text{m}}$Kr, $^{131\text{m}}$Xe, $^{129\text{m}}$Xe, ^{60}Co and ^{40}K in $cS1$-$cS2_\text{b}$ space. The $^{83\text{m}}$Kr peak has been fitted with the function in equation (3.6) and is shown in the top panel of figure A-5. The metastable xenon peaks have been fitted with the sum of two ellipses and are shown in the bottom panel of figure A-5. The ^{60}Co and ^{40}K peaks have been fitted with the sum of four ellipses; the fourth ellipse was supposed to model the 1120.3 keV peak of ^{214}Bi which is just below the lower energy peak of ^{60}Co. The four-ellipse fit is shown in figure A-6. All fits are binned likelihood fits. The data range used for the fits of the $^{83\text{m}}$Kr and activated xenon line fits corresponds to the full $cS1$-$cS2_\text{b}$ range in the plots. For the fits of the ^{60}Co and ^{40}K lines the fit range was restricted to $cS1 > 6000$ pe and $cS2_\text{b} > 370000$.

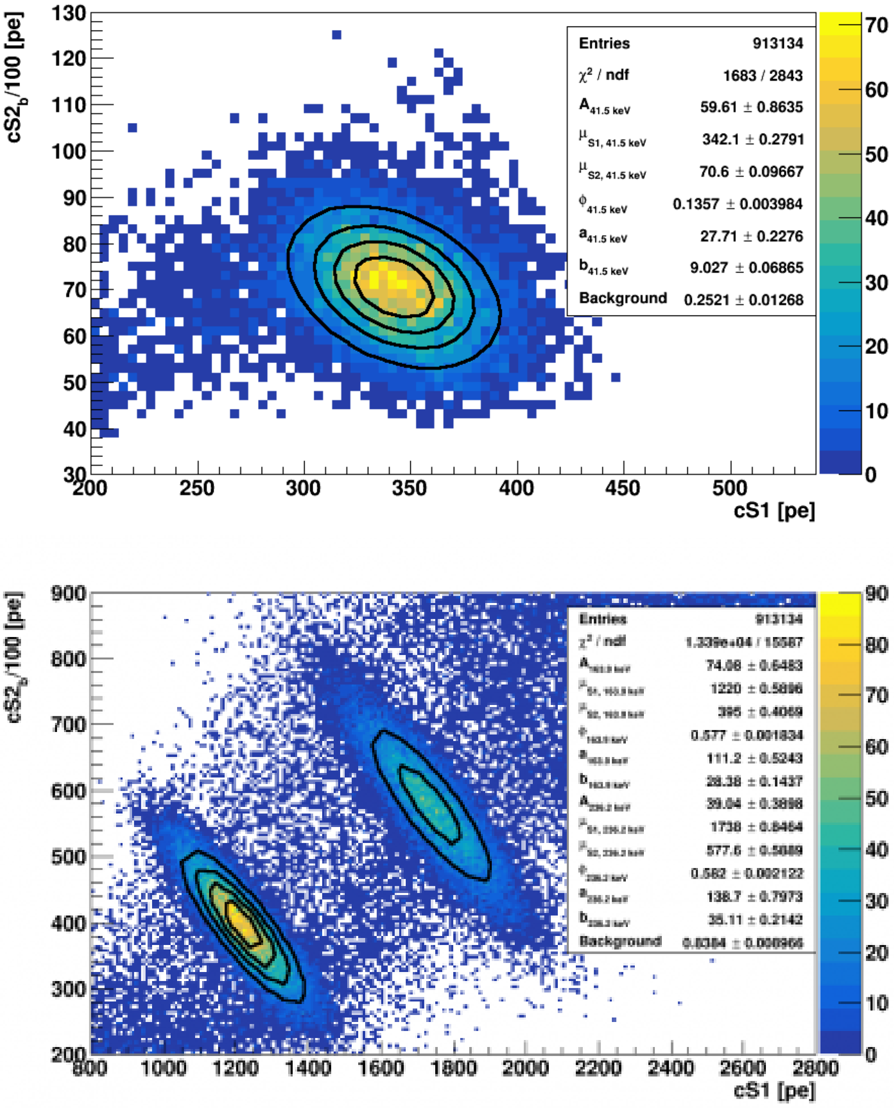

Figure A-5: **Top:** Elliptical fit of the $^{83\text{m}}$Kr peak at 41.5 keV. **Bottom:** Simultaneous two-ellipse fit of the $^{131\text{m}}$Xe and $^{129\text{m}}$Xe peaks at 163.9 keV and 236.2 keV, respectively.

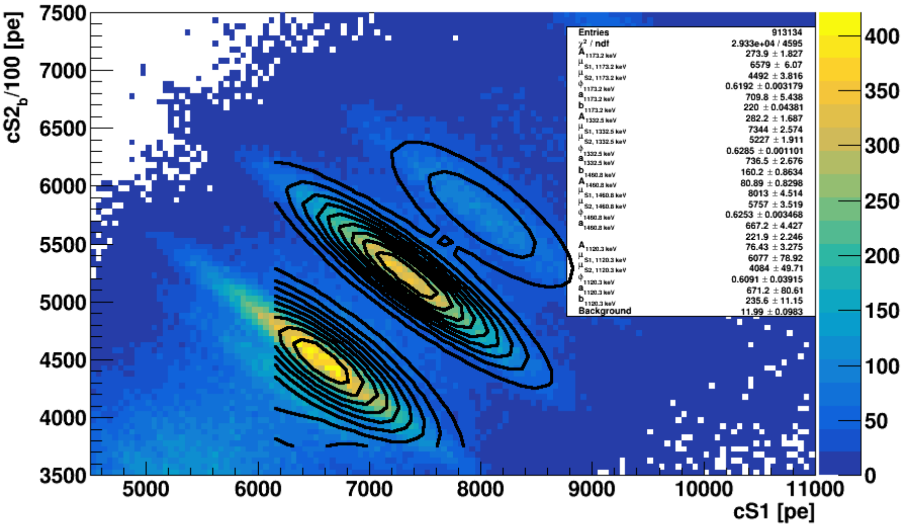

Figure A-6: Simultaneous four-ellipse fit of the ^{214}Bi, ^{60}Co and ^{40}K peaks. The ^{214}Bi line has an energy of 1120.3 keV, the ^{60}Co lines are at 1173.2 keV and 1332.5 keV, and the ^{40}K line is at 1460.8 keV.

A3 Acceptance of the S2 width cut for the outer detector volume in the original 2νKK analysis

The behaviour of the S2 width cut acceptance in the outer detector volume was parametrised as unity below a freely fitted threshold energy E_{var} and with the phenomenological function

$$\mathrm{Acceptance}_{\mathrm{S2Width}} = \begin{cases} 1 & \text{for } E \leq E_{\mathrm{var}}, \\ (E - E_{\mathrm{var}}) \cdot a + (E - E_{\mathrm{var}})^3 \cdot b & \text{for } E > E_{\mathrm{var}}. \end{cases} \tag{A-1}$$

In a χ^2 fit using the mean symmetrised uncertainty one obtains

$$\begin{aligned} E_{\mathrm{var}} &= (155 \pm 1)\ \mathrm{keV}, \\ a &= (1.60 \pm 0.02) \cdot 10^{-3}, \\ b &= (1.9 \pm 0.2) \cdot 10^{-9} \end{aligned} \tag{A-2}$$

with $\chi^2/\mathrm{ndf} = 1.00$.

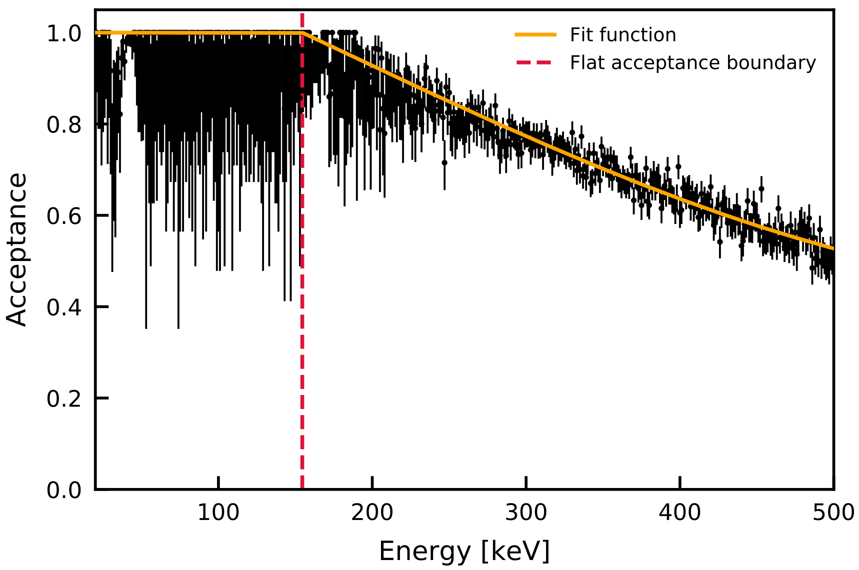

Figure A-7: The $N-1$ acceptance of the S2 width cut as a function of energy in bins of 1 keV width between 10 and 500 keV in the outer volume of the original 2νKK search. All other event selections for the 2νECEC search have been applied. Binomial uncertainties are shown for the data points. The dashed red line indicates the 155 keV energy up to which a flat unity acceptance is assumed. The orange line shows the fitted model with the flat behaviour up to this point and the subsequent acceptance decrease.

A4 Studies on neutron activation

Due to large ^{124}Xe thermal neutron capture cross-section of (165 ± 11) b [251], ^{125}Xe is produced during neutron calibrations. This was first identified by comparing the event rates before and after neutron calibrations. Figure A-8 shows the rate difference between 2.55 t-d of post-NG data and 27.4 t-d of pre-NG data. The positive ^{129m}Xe ^{131m}Xe indicate activation by the NG while the negative ^{83m}Kr peak decays over time and is not reactivated. An increase in rate starting at ~ 80 keV can be attributed to the activation of ^{133}Xe. The peak to the right of the ^{129m}Xe peak can be identified as the merged energy deposition from the ^{125}I K-edge at 33.2 keV [156] and the 243.4 keV γ-ray from the EC-decay of ^{125}Xe [231]. A secondary peak from this decay is present in the left flank of the ^{129m}Xe peak originating from the 33.2 keV X-ray being merged with a 188.4 keV γ-ray [231]. The relative frequencies of the 243.4 keV and 188.4 keV nuclear transitions in ^{125}Xe EC are 66.6 % and 25.4 %, respectively [231]. Figure A-9 shows a combined fit of the three lines. The area ratio $r_{A,\mathrm{measured}} = 0.31 \pm 0.10$ of the two ^{125}Xe lines matches the expected ratio of the nuclear transitions $r_{A,\mathrm{expected}} = 0.254/0.666 = 0.383$.

The activation rate from the NG was determined by including the data taken during the NG calibration in the difference spectrum and refitting the peaks. The same was done for the AmBe source. As the half-life of ^{125}Xe is 16.8 h [231], a few days after the end of the calibration suffice in order to measure the total number of calibration-induced decays. In these fits the peak from ^{125m}Xe at 252.2 keV [231] also has to be considered. The neutron-activated isomer undergoes a transition to the ground state before decaying via electron-capture with a half-life of 57 s [231]. Considering the nuclear branching fraction

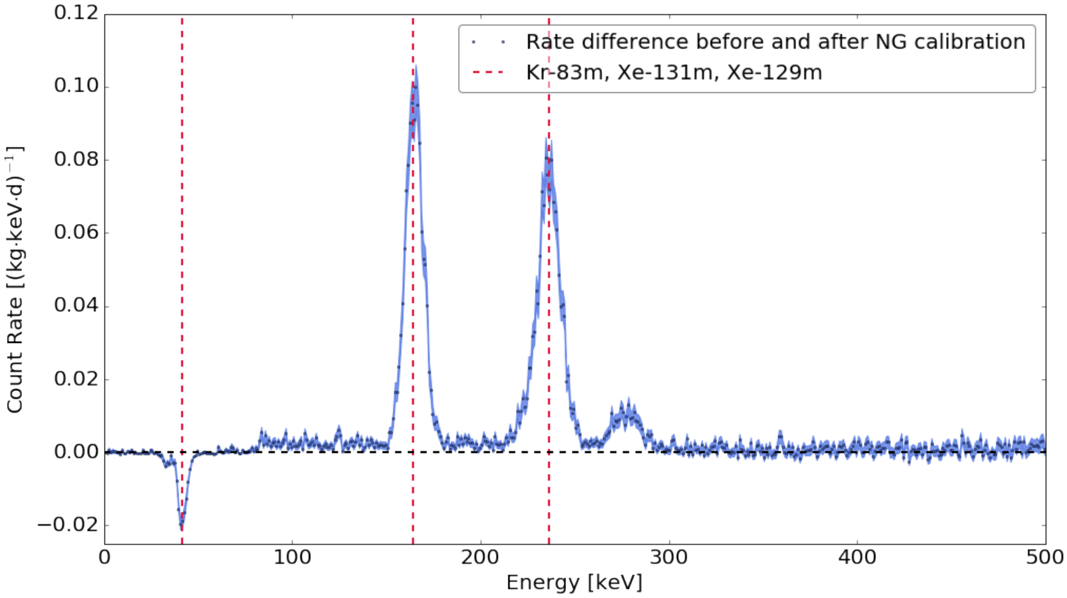

Figure A-8: Rate-difference between 2.55 t-d of post-NG data and 27.4 t-d of pre-NG data. The metastable xenon and krypton lines are marked by the dashed red lines. The blue band around the data points indicates the Gaussian-propagated $\sqrt{N}$ counting uncertainties on the data points.

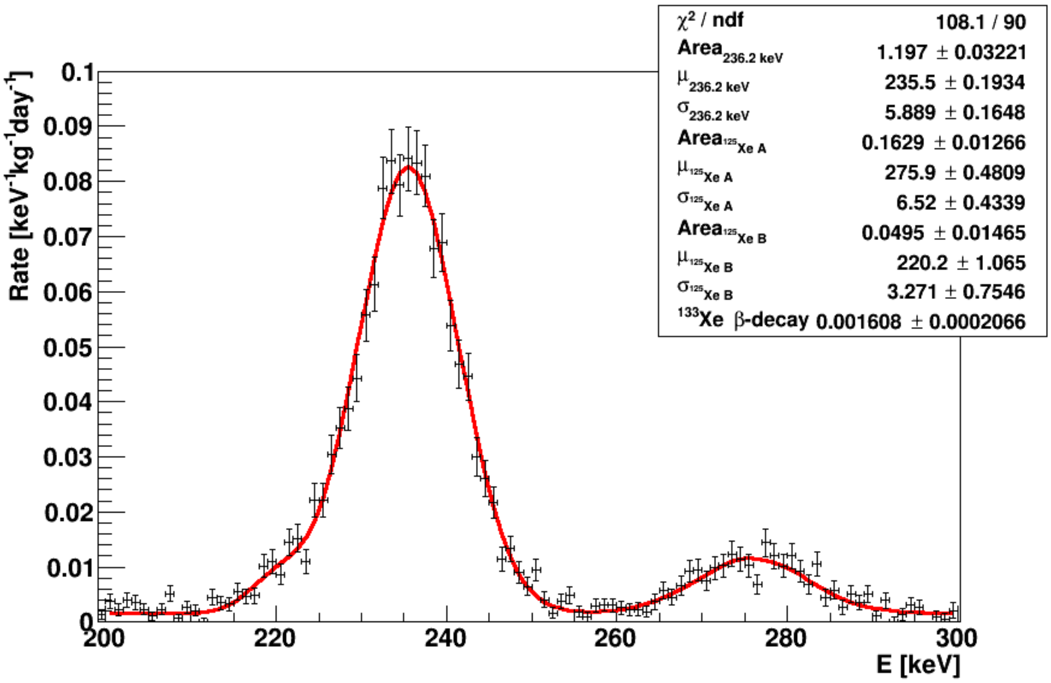

Figure A-9: Fit of the ^{125}Xe lines and the ^{129m}Xe line in the rate-difference spectrum. The rate difference is between 2.55 t-d of post-NG data and 27.4 t-d of pre-NG data.

and the K-capture intensity, activation rates of

$$\begin{aligned} \mathscr{A}_{^{241}\mathrm{AmBe}} &\approx (60 \pm 7)\ \mathrm{t}^{-1}\mathrm{d}^{-1}, \\ \mathscr{A}_{\mathrm{NG}} &\approx (411 \pm 35)\ \mathrm{t}^{-1}\mathrm{d}^{-1} \end{aligned} \tag{A-3}$$

were determined. These results were used in order to plan a neutron-generator run in SR2 aimed at determining the ^{125}I removal efficiency. This study is described in [207].

A5 Background subtraction for ^{125}Xe in the construction of the ^{125}I model

For the background subtraction, the ^{125}Xe data is rebinned such that more than 20 events are contained in each bin. This leads to a bin size of 5 d. The data is then scaled up by the coverage of the $2\sigma_E$ interval 0.954, the nuclear branching ratio 0.664 and the K-capture fraction 0.882 [231, 245]. The resulting data is shown in figure A-10. For the background subtraction only data before or sufficiently long after neutron calibrations is used. The red datapoints in the plot are excluded since they were recorded during or shortly after NG or AmBe calibrations. A linear function is fitted to the black data points and yields

$$R_{\mathrm{bg}}(t_{\mathrm{d}}) = (25.3 \pm 1.2)\,\frac{\text{events}}{\mathrm{t \cdot d}} - (0.019 \pm 0.005)\,\frac{\text{events}}{\mathrm{t \cdot d^2}} \cdot t_{\mathrm{d}} \tag{A-4}$$

with $\chi^2_{\mathrm{ndf}} = 49.6/44 \approx 1.12$. The background-subtracted data in 1-day bins is shown in figure A-11. In the ^{125}Xe data empty bins occur in periods without activation. This is mainly due to calibrations or unfavourable detector conditions. An empty bin at $t_{\mathrm{d,i}}$ bins can be filled by taking the rate in the preceding bin at $t_{\mathrm{d,i-1}}$ and applying an exponential decay with the ^{125}Xe decay lifetime τ_{Xe}:

$$R_{\mathrm{Xe}}(t_{\mathrm{d,i}}) = R_{\mathrm{Xe}}(t_{\mathrm{d,i-1}}) \cdot e^{-\frac{1\mathrm{d}}{\tau_{\mathrm{Xe}}}}.$$

This way one obtains a continuous ^{125}Xe decay rate that can be translated into the ^{125}I decay rate.

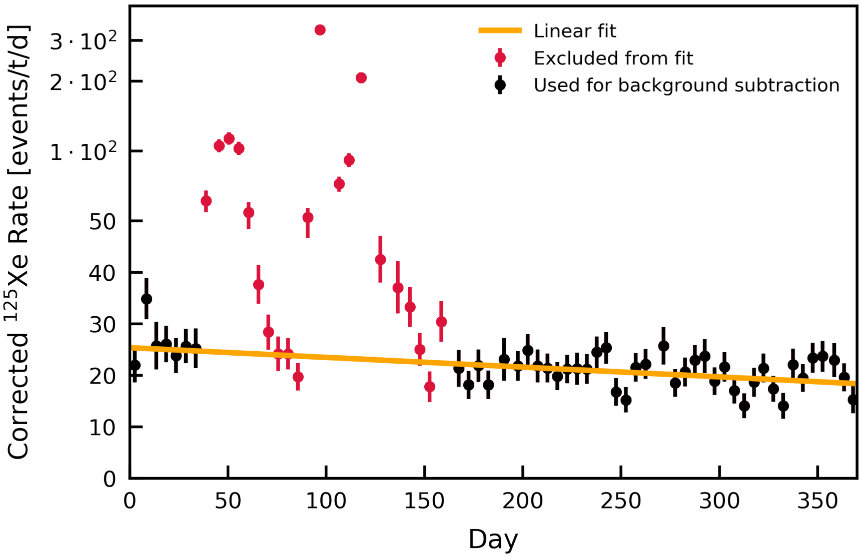

Figure A-10: Corrected ^{125}Xe rate over time in a $2\sigma_E$ interval around 276.4 keV before background subtraction. The bin size is 5 d. A linear function (solid orange) is fitted to the data sufficiently far away from calibrations (black). The data indicated by the red markers was taken during or shortly after calibrations and is excluded from the fit. The error bars show $\sqrt{N}$ Poisson uncertainties. Note that the y-axis is logarithmic above 50 events/t/d and linear below.

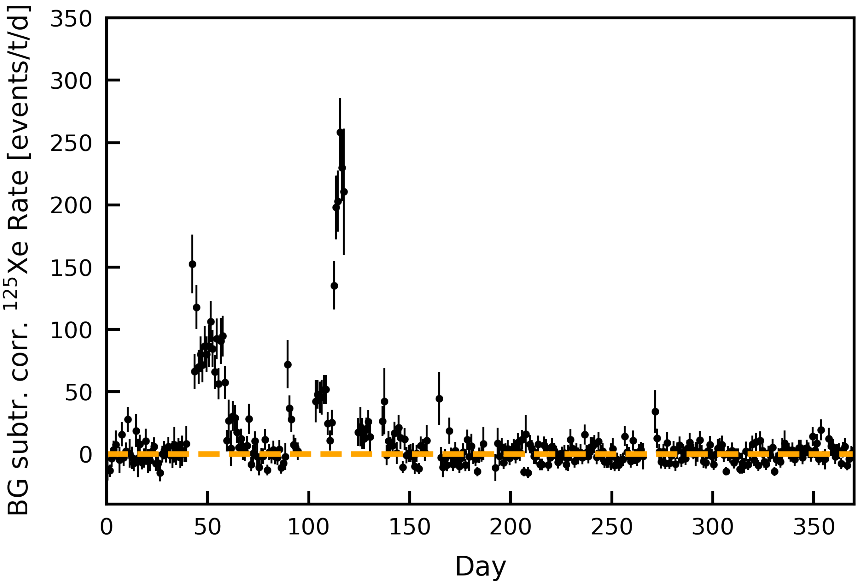

Figure A-11: Background-subtracted ^{125}Xe data in 1-day bins. The rate has been corrected for the nuclear and K-capture ratios as well as the $2\sigma_E$ interval coverage. Error bars indicated $\sqrt{N}$ Poisson uncertainties.

A6 Uncertainty propagation of the ^{125}I model

As outlined in section 3.3, the uncertainties of the ^{125}I model that are induced by the counting uncertainties on the ^{125}Xe data are propagated using toy datasets that are generated from the measured ^{125}Xe data points after background subtraction and the filling of empty bins. A toy dataset is drawn by sampling the content of each ^{125}Xe bin from a Poisson distribution with the bin content of that bin in the measured data as the expectation value. An ^{125}I model is constructed from this data and fitted to the measured ^{125}I data points. The integration of the model over the actual data-taking periods gives the number of expected iodine events considering the underlying toy dataset. Accordingly, an ensemble of 1000 toy datasets yields an ensemble distribution for the number of fitted ^{125}I events $N_{\mathrm{I,\,DEC}}$. Figure A-12 shows the ensemble distribution for 1000 toy datasets where the ^{125}I data was fitted in with a binned Poisson likelihood fit in 10-day bins. Fitting the distribution with a Gaussian distribution yields

$$\mu_N = (44 \pm 6)\ \text{events}. \tag{A-5}$$

$N_{\mathrm{I,DEC}}$ has an additional uncertainty from the counting uncertainties in the ^{125}I data. This is investigated by varying the four fit parameters (A, τ and linear background variables) of the I-125 model fit in a 1σ interval around the best fit. Due to the model uncertainty one has to multiply the 1 sigma uncertainties of the data points such that the reduced χ^2 becomes unity. Therefore, one actually probes a 1.2σ interval for each parameter. The resulting distribution of $N_{\mathrm{I,DEC}}$ is shown in figure A-13. The final expectation for the artificial activation in the 1.5 t fiducial volume and 214.3 live-days is

$$N_{\mathrm{I,DEC}} = (44 \pm 9)\ \text{events}. \tag{A-6}$$

This prompted the reduction of the dataset to 177.7 live-days. The corresponding ensemble distributions for the ^{125}Xe with 1000 toy-datasets and for the ^{125}I uncertainties are shown in figure A-14.

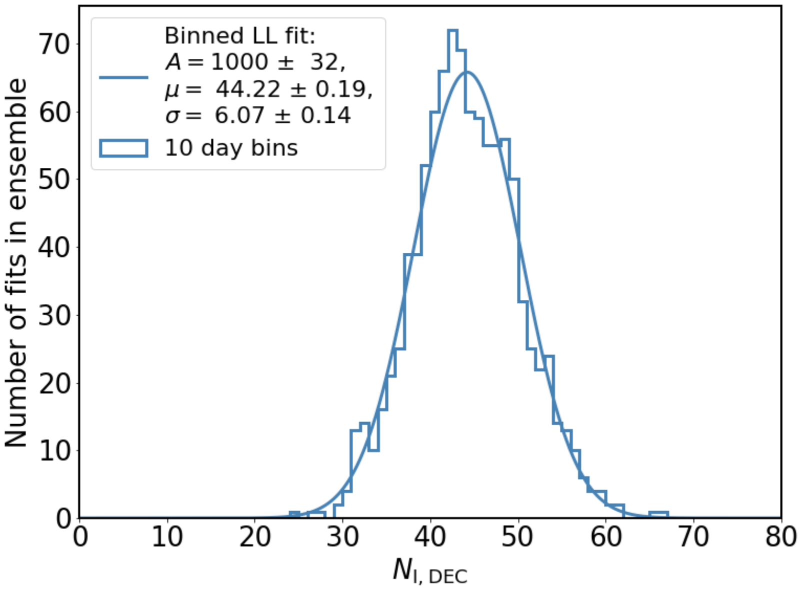

Figure A-12: Ensemble distribution for 1000 toy datasets where the ^{125}I data from 214.3 live-days in 1.5 t was fitted with a binned Poisson likelihood fit in 10-day bins. The distribution has been fitted with a Gaussian (solid blue).

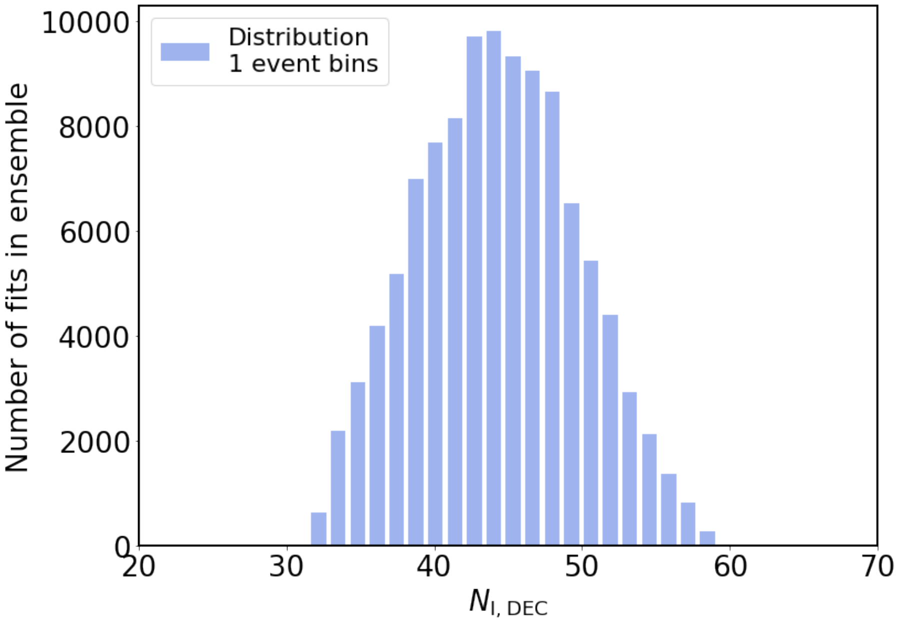

Figure A-13: Distribution of $N_{\mathrm{I,DEC}}$ in 214.3 live-days and 1.5 t obtained from varying the fit parameter uncertainties.

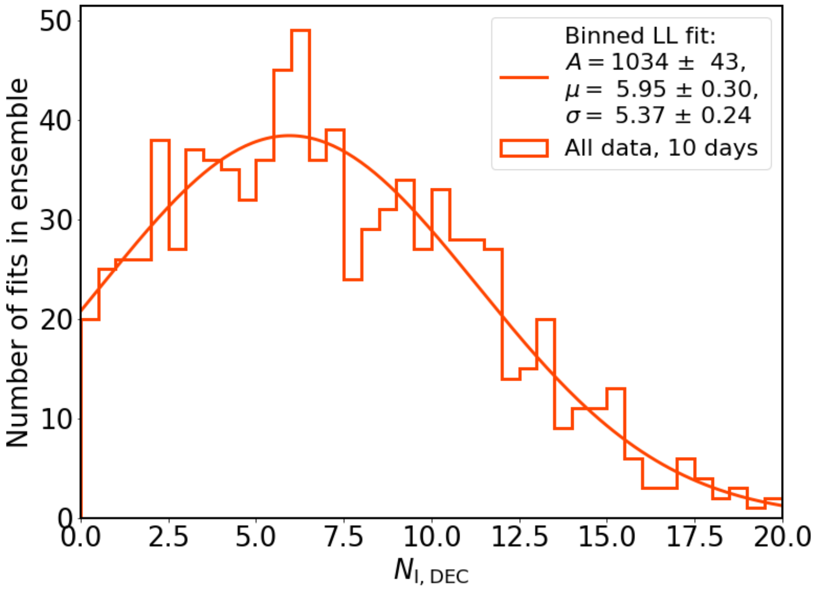

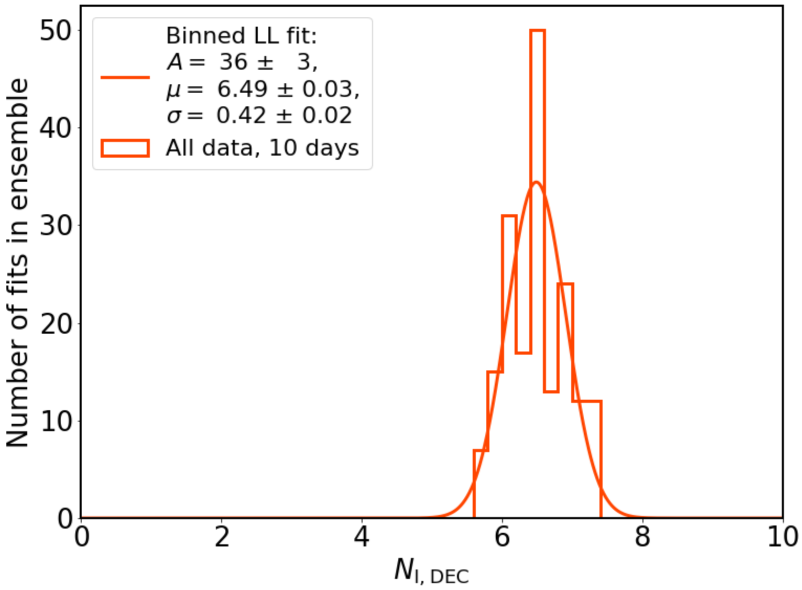

Figure A-14: **Top:** Ensemble distribution for 1000 toy datasets where the ^{125}I data from 177.7 live-days in 1.5 t was fitted with a binned Poisson likelihood fit in 10-day bins. The distribution has been fitted with a Gaussian (solid orange). **Bottom:** Distribution of $N_{\mathrm{I,DEC}}$ in 177.7 live-days and 1.5 t obtained from varying the fit parameter uncertainties.

A7 Fiducial volume plots for the extended 2νECEC analysis

The distributions of $^{83\mathrm{m}}$Kr events inside the active volume of the TPC are shown for the different data partitions used in chapter 4. All respective analysis cuts have been applied and the 41.5 keV line was selected in $cS1$-$cS2_\mathrm{b}$ space. The R^2-Z and X-Y plots have 500 bins in each direction. Accordingly, the bin volume for the R^2-Z plots is 1 cm^3. The bin area in the X-Y plots is 0.04 cm^2. The R^2-Z plot for the clean partition of SR 1 is shown in chapter 4 as figure 4.6

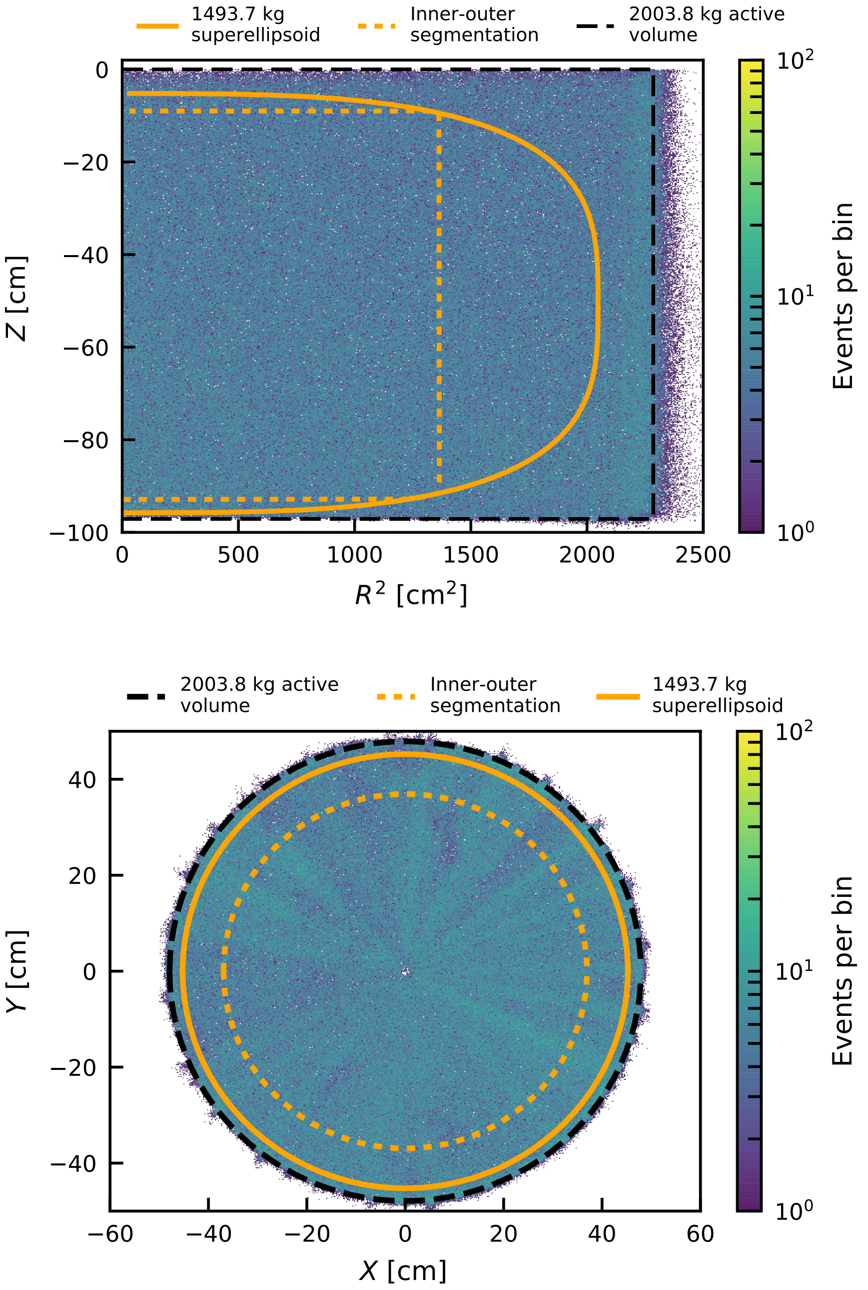

Figure A-15: **Top:** Distribution of 41.5 keV $^{83\mathrm{m}}$Kr events in the R^2- and Z-directions for the dirty partition of SR1. **Bottom:** Distribution of the same data in X and Y. The edges of the active volume are marked by the dashed black line. The superellipsoid fiducial volume is indicated by the solid orange line. The dotted orange line marks the segmentation between the inner and outer volumes.

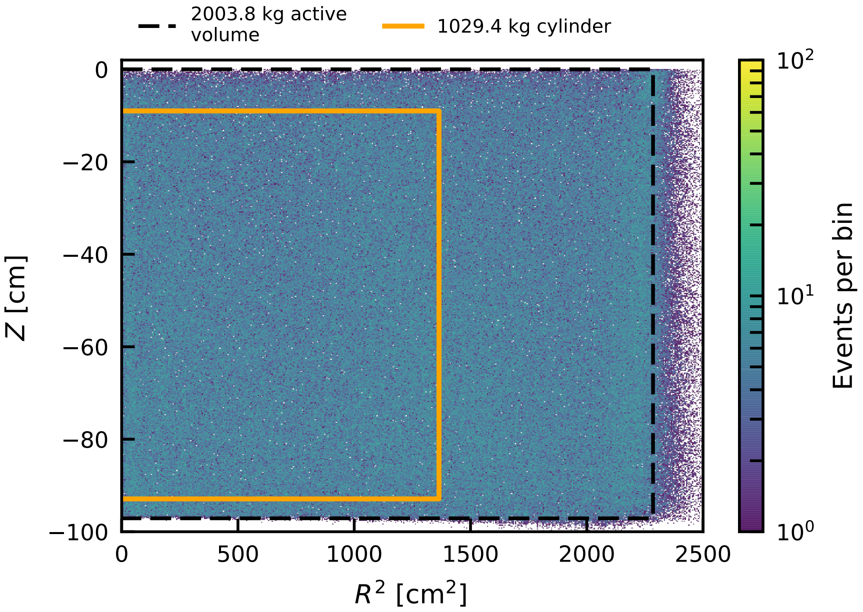

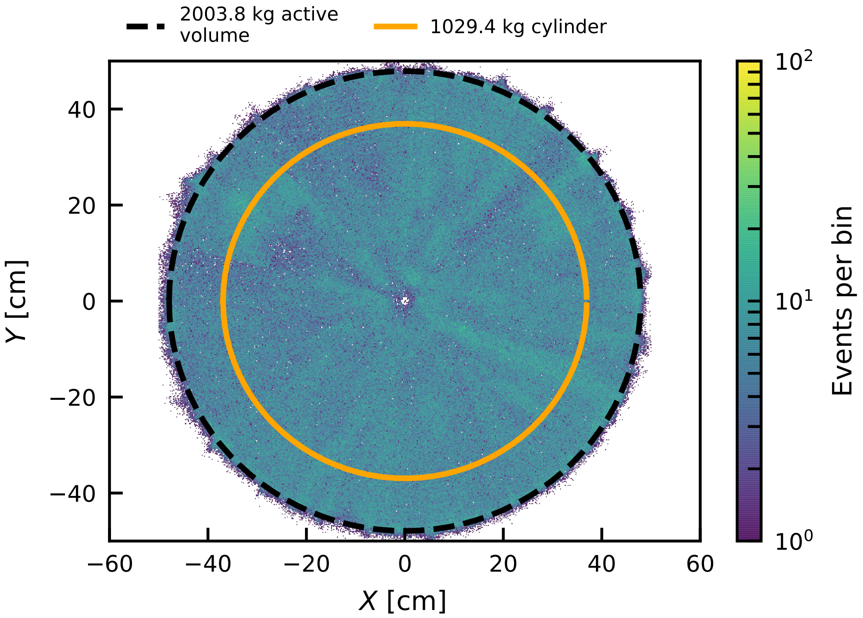

Figure A-16: **Top:** Distribution of 41.5 keV $^{83\mathrm{m}}$Kr events in the R^2- and Z-directions for the dirty partition of SR1. **Bottom:** Distribution of the same data in X and Y. The edges of the active volume are marked by the dashed black line. The superellipsoid fiducial volume is indicated by the solid orange line. The dotted orange line marks the segmentation between the inner and outer volumes.

A8 Details on the ^{125}I model for the extended double-electron capture search

The expected numbers of ^{125}I events for SR1 were obtained by integrating the model introduced in section 3.3 over the respective data periods. Figure A-17 shows the model for the duration of SR1 with the respective 1σ and 2σ uncertainty bands obtained by propagation of the correlated parameter uncertainties with the covariance matrix. The clean and dirty data partitions are represented by the square blue and purple markers, respectively.

In a second step, the uncertainty induced by the ^{125}Xe data was assessed by drawing 10^4 toy datasets. Here, the measured number of events in each ^{125}Xe bin was drawn from a Poisson distribution with the actual measured number of ^{125}Xe events as the expectation value. Then the respective ^{125}I model was constructed from this data and fitted to the ^{125}I data. The best-fit model was then integrated over the data-taking periods. The sample distributions for the numbers of expected ^{125}I events from 10^4 samples are shown in figure A-18. The distribution means are taken as the central values for the ^{125}I expectations with the standard deviations as the uncertainties associated with ^{125}Xe.

Notably, the distribution for the dirty partition is narrower. This is owed to the higher event rates in the dirty partition, so the Poisson uncertainties on the ^{125}Xe data points are smaller. Accordingly there is less variation on the model shape in these areas. On the other hand less ^{125}I datapoints are available in the dirty partition, so the model uncertainty is larger than for the clean data. The central values and uncertainties for the expected ^{125}I events from artificial activation are

$$\begin{aligned} N^{^{125}\mathrm{I}}_{\text{art, clean}} &= (5.2 \pm 2.8_{\text{model}} \pm 3.5_{^{125}\mathrm{Xe}})\ \text{events/t}, \\ N^{^{125}\mathrm{I}}_{\text{art, dirty}} &= (102.7 \pm 18.7_{\text{model}} \pm 2.1_{^{125}\mathrm{Xe}})\ \text{events/t}. \end{aligned} \tag{A-7}$$

The uncertainties are added in quadrature in order to obtain the total uncertainty.

SR2 model data preparation

For science run 2 additional data had to be prepared beforehand. The energy calibration from [257] could be used on most of the additional data. There is an exception for the July 2018 NG data where the anode tripped during the neutron generator calibration. Therefore, the data was taken with two different anode voltages, namely 3 kV after the trip and the nominal 4 kV. This affects the amount of extracted electrons at the liquid gas interface as well as the charge amplification in the gas-phase. Thus, the events taken in the lower voltage period feature smaller S2 areas. This is shown in figure A-19. Since the statistics in the July 2018 NG data were insufficient to derive an energy calibration from ellipse fits – especially not in a Z-dependent fashion – the optimal calibration parameters g_1 and g_2 were determined by iterating through different pairs of values. And checking the positions of the $^{131\mathrm{m}}$Xe and $^{129\mathrm{m}}$Xe peaks in the reconstructed spectrum. The parameter pair with the best match was kept leading to:

$$\begin{aligned} g_{1,3\,\text{kV, July}} &= 0.137, \\ g_{2,3\,\text{kV, July}} &= 10,7 \\ g_{1,4\,\text{kV, July}} &= 0.143, \\ g_{2,4\,\text{kV, July}} &= 11.6. \end{aligned} \tag{A-8}$$

Figure A-20 shows the energy spectra in the three calibration campaigns in early March, late March and July. The July data is separated into the data with two different anode voltages. It is evident that the lines for all NG datasets are now at their expected positions. The

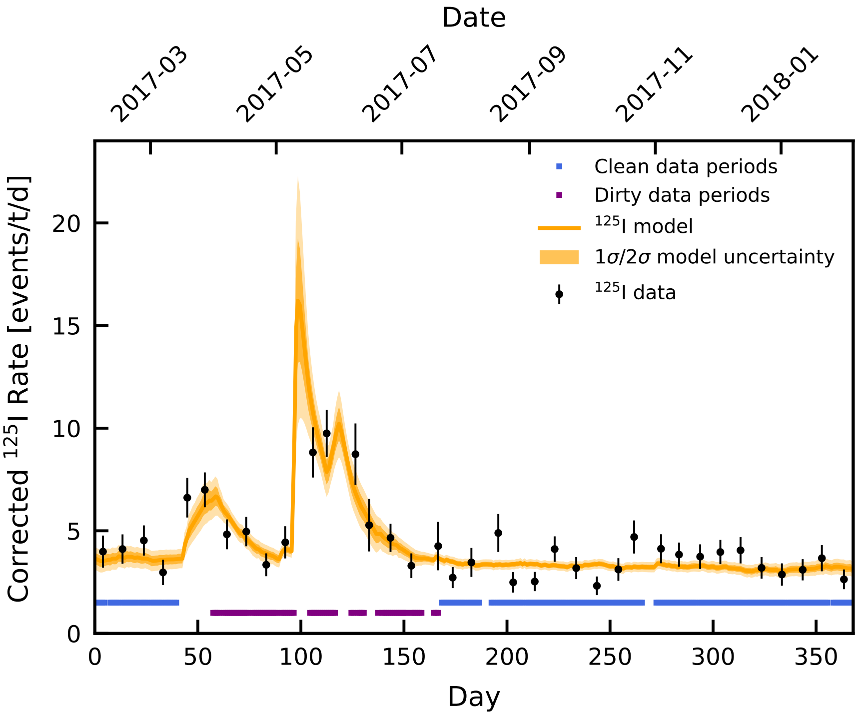

Figure A-17: Model for ^{125}I background (orange) with data from the ^{125}I energy region in 14-day bins (black markers). The clean and dirty partitions of SR1 are indicated by the square blue and purple markers, respectively. The 1σ and 2σ model uncertainties are shown as the dark and light orange bands around the best-fit model.

^{125}Xe data selection interval of $2\sigma_E$ is shaded in orange. The ^{131m}Xe and ^{129m}Xe peaks for fixing the energy calibrations are indicated by the dotted and dashed red lines, respectively.

Figure A-21 shows the rate in a $2\sigma_E$ region around the 276.6 keV peak of ^{125}Xe. Each 1-day bin has been corrected for its actual data live time. A clear increase in rate is observed in periods with the NG in operation. Before using this data for model construction six bins with an exposure of less than 0.1 d are removed. The live times for all bins are shown in figure A-22. Moreover, bins between 23rd July and 8th August 2018 are removed because they exhibit an unusually large background rate that cannot originate from ^{125}Xe decay due to its prolonged presence. The increased rate is attributed to a preceding ^{220}Rn calibration as well as the start-up of the radon distillation. In this process closed-off volumes in the gas circulation systems were opened to the detector. It is possible that ^{222}Rn was collected in these volumes at a higher equilibrium activity concentration than in the TPC. Thus, the equilibrium in the detector would have been disturbed.

In a next step, the ^{125}Xe data is background-subtracted. For this, three different background periods have to be observed: period one before the MagPump installation, period two after the MagPump installation and before radon distillation, and period three after the start of the radon distillation. The background rate in the second two periods is expected to be lower due to the reduced ^{222}Rn level. For the background subtraction, constant functions are fitted to data outside of increased ^{125}Xe rate periods. With the installation of the MagPump on 15th June and the start of the radon distillation on 30th July 2018, these

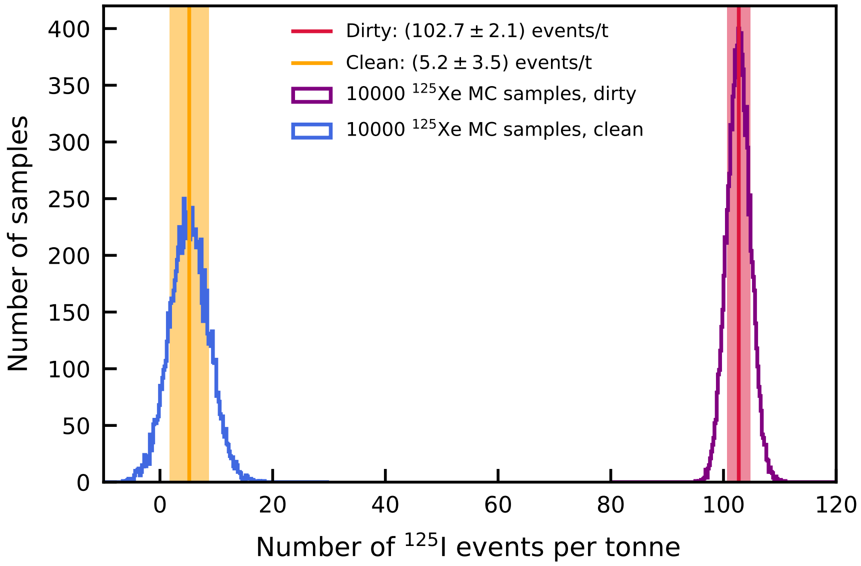

Figure A-18: Distributions for the expected numbers of ^{125}I events in the clean (blue histogram) and dirty (purple histogram) partitions of SR1. The distributions originate from 10^4 ^{125}Xe toy datasets underlying the same number of fitted and integrated ^{125}I models. The means of both distributions are indicated by the vertical solid lines. The colour-shaded areas represent the $\pm 1\sigma$ standard deviation bands around the mean.

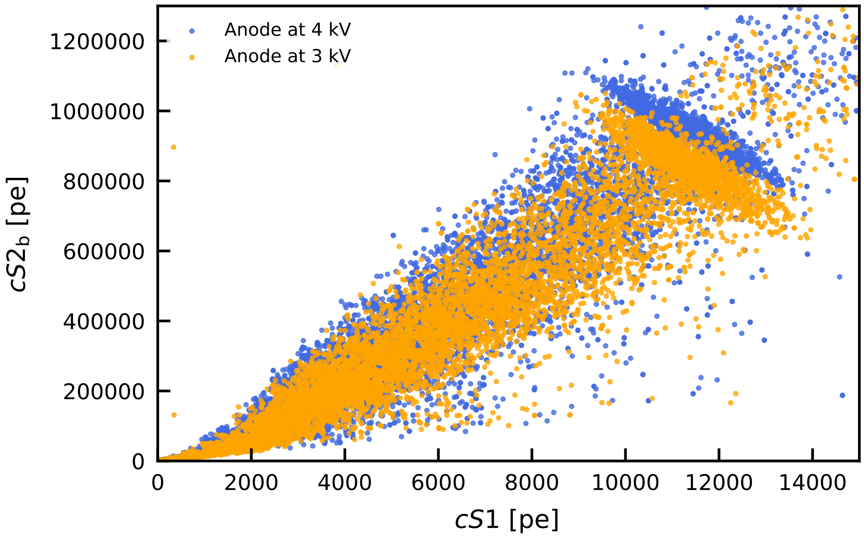

Figure A-19: Areas of the corrected S1 ($cS1$) and bottom S2 ($cS2_b$) signals for all NG events in the July 2018 NG data. Due to an anode trip the data was taken at two different anode voltages: 3 kV (orange) and 4 kV (blue). Due to the lower anode voltage, the 3 kV data features smaller S2 signals.

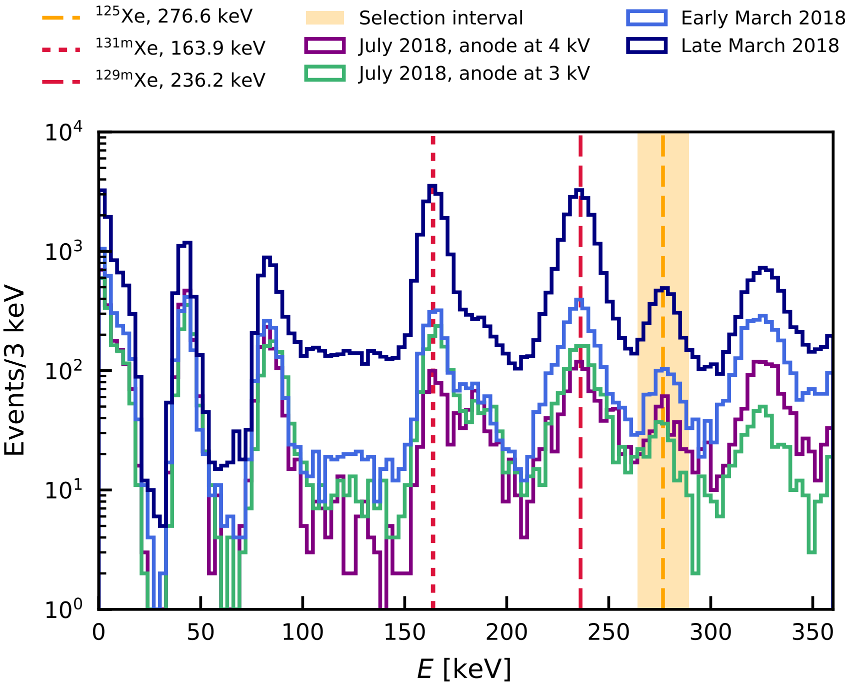

Figure A-20: Energy histograms of the early March (light blue), late March (dark blue) and July neutron calibrations in SR2. The July 2018 NG data has been subvided into the 3 kV (green) and 4 kV (purple) anode voltage periods. The g_1 and g_2 energy reconstruction parameters for the July 2018 datasets were determined with the ^{131m}Xe and ^{129m}Xe peaks. These are indicated by the red dotted and dashed lines, respectively. The ^{125}Xe peak at 276.6 keV for the ^{125}I model is marked with the dashed orange line and the selection interval for the model is coloured in orange.

periods are defined as

Period 1: 7th February – 12th March,
16th April – 31st May,
Period 2: 16th June – 13th July,
Period 3: 9th August – 30th September. (A-9)

The first period is subdivided into the data before and after the NG calibrations in March, but should feature the same background level. The background levels are:

$$\begin{aligned}\text{Period 1:}&\quad (13.5\pm6.6)\ \text{events}\cdot\text{t}^{-1}\text{d}^{-1},\\ \text{Period 2:}&\quad (13.8\pm6.9)\ \text{events}\cdot\text{t}^{-1}\text{d}^{-1},\\ \text{Period 3:}&\quad (14.2\pm5.0)\ \text{events}\cdot\text{t}^{-1}\text{d}^{-1}.\end{aligned} \tag{A-10}$$

With the large uncertainties no significant change in background rate can be discerned. Due to the increasing background contribution from TPC construction materials this change is expected to be smaller than at lower energies where the increased ^{85}Kr activity and the reduced ^{222}Rn activity should lead to a background reduction of ~ 20 %. Figure A-23 shows the background-subtracted ^{125}Xe rate. Here, the background level from the second period was subtracted from data up to the 22nd July 2018. For all other periods, data within the

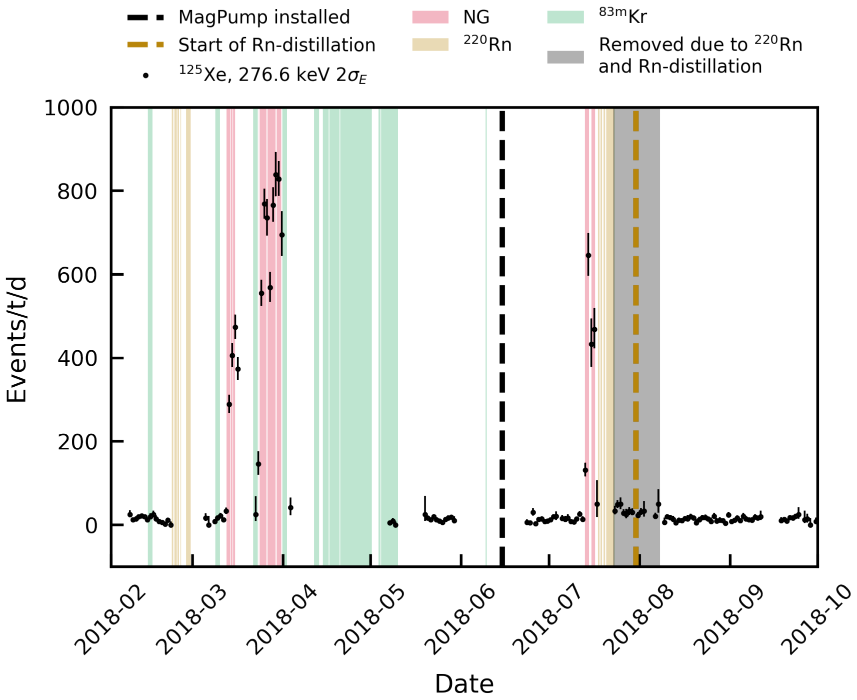

Figure A-21: Measured event rate over SR2 in a $2\sigma_E$ interval (264.0 to 289.2 keV) around the 276.6 keV peak of ^{125}Xe. The black markers show the rate before background-subtraction. The data from the cylindrical SR2 fiducial volume after cuts has been corrected by the live time per bin. Uncertainties are based on Feldman & Cousins 68.3 % confidence intervals [262]. NG, ^{83m}Kr and ^{220}Rn calibration data are shaded in red, green and gold, respectively. Data points outside these regions are from clean and dirty SR2 background data. The data points inside the May 2018 krypton data are isolated dirty background runs. The MagPump installation is indicated by the dashed black line. The start of the radon distillation is indicated by the gold dashed line. Data between 23rd July and 8th August 2018, shaded in dark grey, is removed due to an abnormally increased rate.

smallest and largest dates were subtracted with the respective background. The rate has been scaled up by the 95.4 % coverage of the $2\sigma_E$ interval, the nuclear branching ratio of 66.6 % [231] and the K-capture branching ratio. For the model construction, the empty bins are filled in the same fashion as in section 3.3.

Taking purification flow into account

The purification flow over SR2 changed multiple times. Since the removal time constant of ^{125}I should scale with the purification flow this has to be considered in the model. Figure A-24 shows the rate in a $2\sigma_E$ interval around the 67.3 keV ^{125}I peak over SR2 on the left y-axis and the purification flow from the XENON1T slow control on the right y-axis. Two main periods where ^{125}I removal takes place have to be considered. These are marked in orange. In all other purification flow periods, the decay rate has returned to the background level. Accordingly, the purification flow in these periods does not affect the model. As outlined in section 4.2, the purification flow ratio of the marked periods is used in the ^{125}I model.

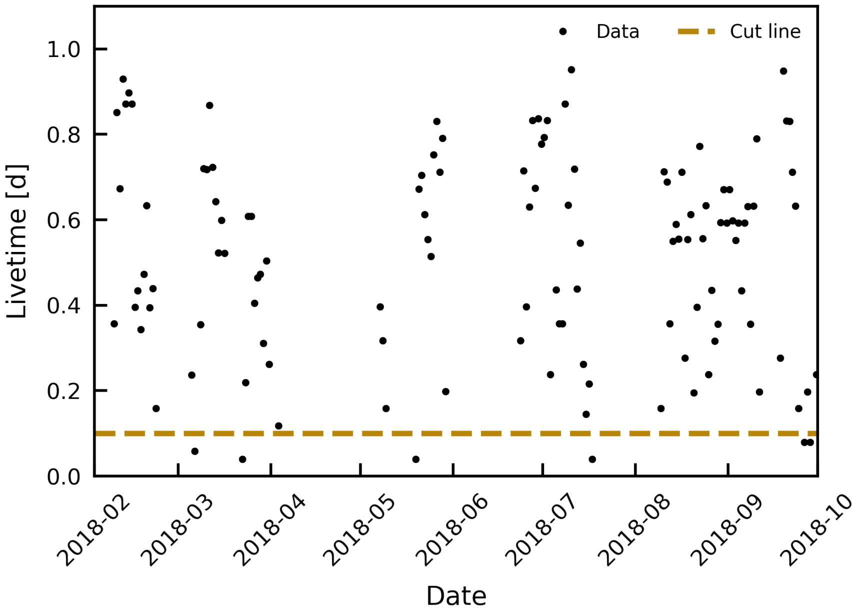

Figure A-22: Livetime in each 1-day bin of the SR2 data for ^{125}I model construction indicated by black markers. Bins with a live time of less than 0.1 d are removed. The boundary is marked by the dashed gold line.

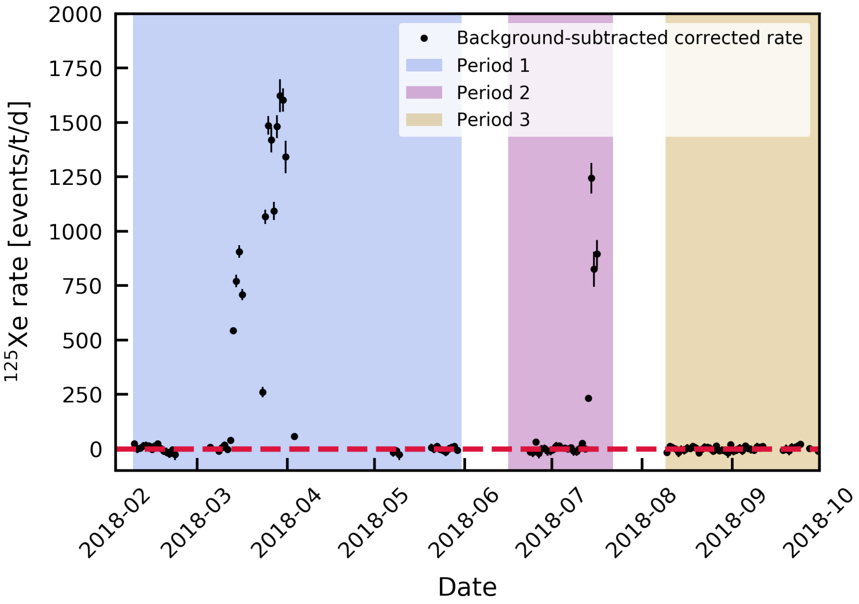

Figure A-23: Rate from ^{125}Xe after background subtraction corrected for the 95.4 % coverage of the $2\sigma_E$ selection interval as well as for the nuclear and atomic branching ratios of the 276.6 keV peak. The different periods considered in the background subtraction are shaded blue, purple and gold for periods 1, 2 and 3, respectively.

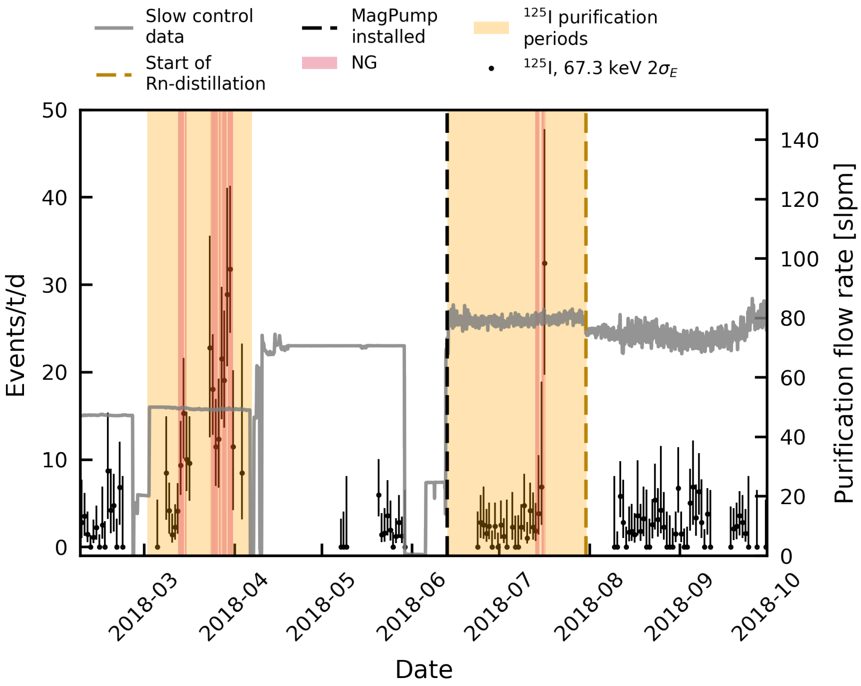

Figure A-24: Rate in a $2\sigma_E$ interval around the 67.3 keV ^{125}I peak over SR2 on the left y-axis and purification flow from the XENON1T slow control in standard-litres per minute (slpm) on the right y-axis. NG data is shaded red. Purification flow periods considered in the ^{125}I model are shaded orange.

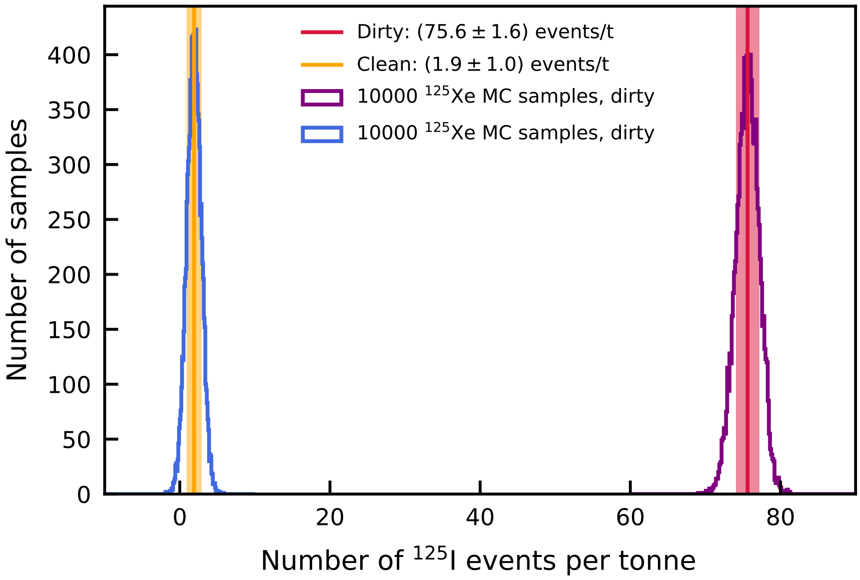

Figure A-25: Distributions for the expected numbers of ^{125}I events in the clean (blue histogram) and dirty (purple histogram) partitions of SR2. The distributions originate from 10^4 ^{125}Xe toy datasets underlying the same number of fitted and integrated ^{125}I models. The means of both distributions are indicated by the vertical solid lines. The colour-shaded areas represent the $\pm 1\sigma$ standard deviation bands around the mean.

Taking the mean and standard deviation of the flows in both periods one obtains

$$r_{\mathrm{flow}} = 1.59 \pm 0.08. \tag{A-11}$$

Uncertainties of the SR2 model predictions

The uncertainties on the numbers of ^{125}I events are derived and propagated in the same fashion as for the SR1 model. Figure A-25 shows the distributions for the expected numbers of ^{125}I events per tonne in the clean and dirty SR2 data. Only the clean data is used in the analysis, the dirty data is shown in order to illustrate the grounds for its exclusion. The distributions originate from the fits of 10^4 ^{125}I models based on the same number of ^{125}Xe toy datasets. The means and standard deviations of both distributions are used to infer the central value and the uncertainty associated with the ^{125}Xe data underlying the model. The model uncertainties from the fit are obtained by integrating the model uncertainty bands. These bands were derived using numerical partial derivatives of the model and the covariance matrix in order to take parameter correlations into account. The resulting ^{125}I expectations from artificial activation are:

$$\begin{aligned} N^{^{125}\mathrm{I}}_{\mathrm{art,\,clean\,SR2}} &= (1.9 \pm 1.0_{\mathrm{model}} \pm 1.0_{^{125}\mathrm{Xe}})\ \mathrm{events/t}, \\ N^{^{125}\mathrm{I}}_{\mathrm{art,\,dirty\,SR2}} &= (75.6 \pm 38.1_{\mathrm{model}} \pm 1.6_{^{125}\mathrm{Xe}})\ \mathrm{events/t}. \end{aligned} \tag{A-12}$$

The uncertainties are added in quadrature in order to obtain the total uncertainty.

A9 Validation of the extended double-electron capture signal and background model

This section shows the fits of the extended 2νECEC signal and background model from chapter 4 to the data from [31] that is described in chapter 3. The best-fit parameters are given in table A-2. The best fit spectra for the inner and outer volume are shown in the top and bottom panels of figure A-26, respectively. The relevant goodness of fit measures, significance and half-lives are given in table A-1. Figure A-27 shows the parameter pulls and the χ^2_λ-profile of $A_{2\nu\text{ECEC}}$ can be found in figure A-28.

The fit quality is improved in comparison to the published analysis ($\chi^2/\text{ndf} = 527.3/462 \approx 1.14$ [31]). This improvement can be attributed mostly to the reduced fit range. Especially in the outer volume, the goodness of fit deteriorated towards higher energies in the published analysis [31]. More importantly, two immediate effects of including the KL-peak become apparent. First, the significance from the profile of $A_{2\nu\text{ECEC}}$ is increased to 5.0σ. Second, the best-fit half-life for the KK-capture is decreased to $T^{2\nu\text{KK}}_{1/2} = (1.72 \pm 0.42_{\text{stat}} \pm 0.07_{\text{sys}}) \cdot 10^{22}$ yr. Removing the KL- and LL- peaks from the fit yields the same result as [31] with $T^{2\nu\text{KK}}_{1/2,\text{KK-only}} = (1.77 \pm 0.45_{\text{stat}} \pm 0.07_{\text{sys}}) \cdot 10^{22}$ yr. Accordingly, leaving out the KL- and LL-peaks biased the former half-life estimate to larger values. This is notable since it was assumed that XENON1T would not be sensitive to these peaks due to the $^{83\text{m}}$Kr contamination and the larger half-life predicted by XMASS [145].

Table A-1: Fit results for the fit of the extended 2νECEC signal and background model to the data from [31].

$\mathbf{n_{data}}$	340
$\mathbf{n_{par}}$	29
$\mathbf{n_{constrained}}$	18
ndf	329
χ^2_λ	319.1
$\sqrt{\frac{\mathbf{2}}{\mathbf{ndf}}}$	0.08
Σ	10.1
$\frac{\chi^2_\lambda}{\mathbf{ndf}}$	0.97
$\frac{\chi^2_\lambda - \Sigma}{\mathbf{n_{data}} - \mathbf{n_{par}}}$	0.99
$\sqrt{\Delta\chi^2_\lambda}$	5.0
$\mathbf{N}_{2\nu\text{ECEC}}$ [**events**]	176 ± 43
$\mathbf{T}^{2\nu\text{ECEC}}_{\mathbf{1/2}}$ [10^{22} **yr**]	$1.31 \pm 0.32_{\text{stat}} \pm 0.06_{\text{sys}}$
$\mathbf{T}^{2\nu\text{KK}}_{\mathbf{1/2}}$ [10^{22} **yr**]	$1.72 \pm 0.42_{\text{stat}} \pm 0.07_{\text{sys}}$

Table A-2: Best-fit parameters for the fit of the extended 2νECEC signal and background model to the data from [31].

Parameter	**Value**	**Unit**
Solar ν	1.00 ± 0.02	scaling
^{136}Xe	0.993 ± 0.029	scaling
^{238}U	1.0 ± 0.6	scaling
^{226}Ra	0.66 ± 0.35	scaling
^{232}Th	0.9 ± 0.6	scaling
^{228}Th	-0.7 ± 1.3	scaling
^{60}Co	0.58 ± 0.31	scaling
^{40}K	0.97 ± 0.26	scaling
$\mu_{^{83\mathrm{m}}\mathrm{Kr,misID}}$	32.8 ± 0.4	keV
$\sigma_{^{83\mathrm{m}}\mathrm{Kr,misID}}$	2.2 ± 0.6	keV
$f_{^{83\mathrm{m}}\mathrm{Kr,misID,inner}}$	$(0.017 \pm 0.004) \cdot 10^{-4}$	-
$f_{^{83\mathrm{m}}\mathrm{Kr,misID,outer}}$	$(0.014 \pm 0.006) \cdot 10^{-4}$	-
$A_{^{83\mathrm{m}}\mathrm{Kr,inner}}$	$(0.420 \pm 0.006) \cdot 10^{-4}$	-
$A_{^{83\mathrm{m}}\mathrm{Kr,outer}}$	$(0.398 \pm 0.008) \cdot 10^{-4}$	-
$\mu_{2\nu\mathrm{KK}}$	64.31 ± 0.13	keV
$\mu_{2\nu\mathrm{KL}}$	37.2 ± 0.7	keV
$\mu_{2\nu\mathrm{LL}}$	10.01 ± 0.13	keV
$A_{2\nu\mathrm{ECEC}}$	$(6.6 \pm 1.6) \cdot 10^{-4}$	events/kg·d
^{214}Pb	8.9 ± 0.4	μBq/kg
$^{85}\mathrm{Kr}_{\mathrm{SR1}}$	6.7 ± 1.1	0.1 ppt
^{133}Xe	$(-0.2 \pm 1.3) \cdot 10^{-2}$	μBq/kg
$A_{^{125}\mathrm{I}}$	$(3.8 \pm 3.2) \cdot 10^{-5}$	events/kg·d
$A_{^{131}\mathrm{Xe}}$	$(5.93 \pm 0.26) \cdot 10^{-3}$	events/kg·d
κ_{slope}	$(-14.8 \pm 1.0) \cdot 10^{-5}$	keV^{-1}
κ_{const}	0.942 ± 0.007	-
a_{res}	0.3202 ± 0.028	keV$^{1/2}$
b_{res}	$(4.01 \pm 0.28) \cdot 10^{-3}$	-
a_{shift}	$(13.7 \pm 2.1) \cdot 10^{-3}$	-
b_{shift}	43.3 ± 1.9	keV

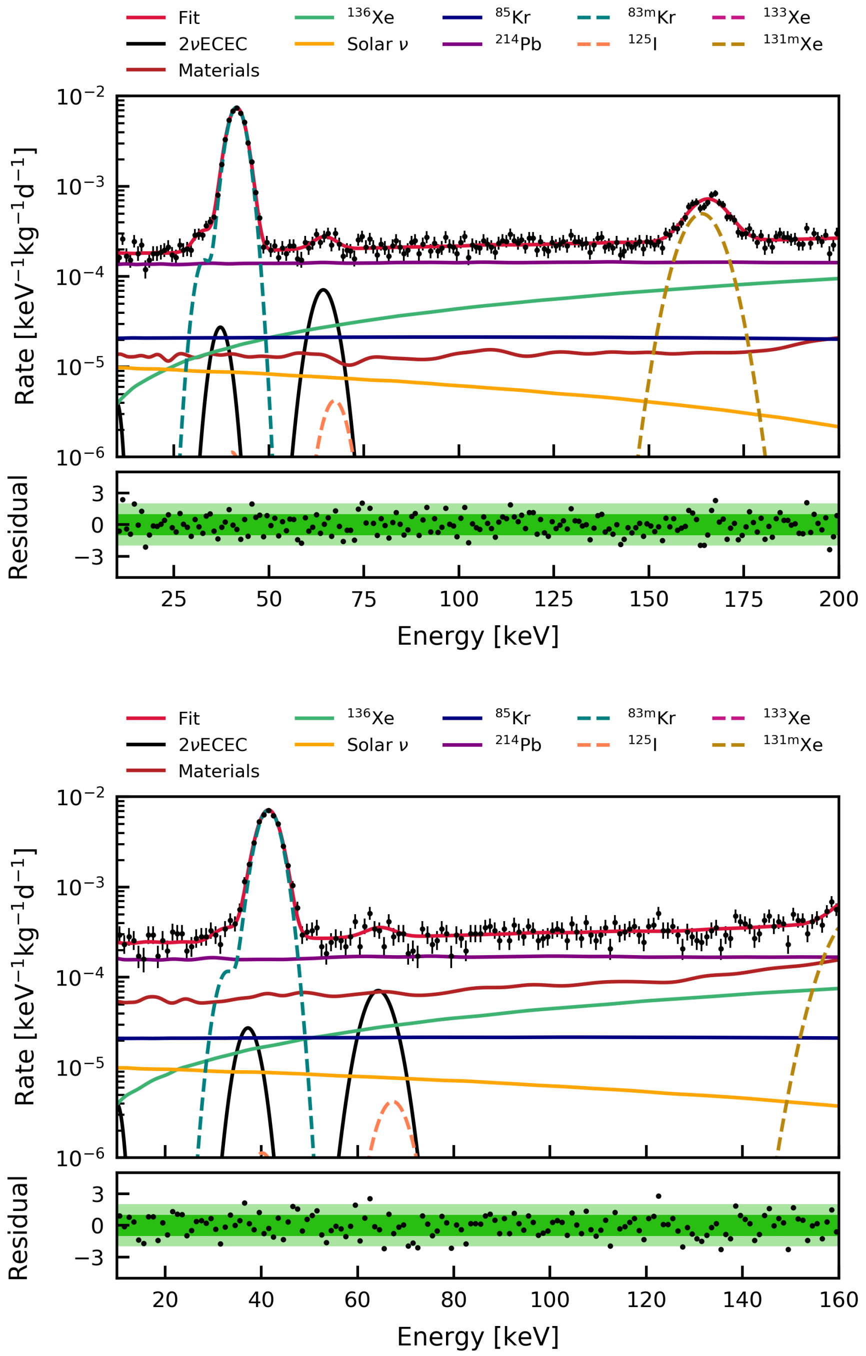

Figure A-26: Fit of the signal and background models to the measured energy spectra from [31] in the inner (**top**) and outer (**bottom**) detector volume. Residuals were calculated from the square-roots of the χ^2_λ summands. Uncertainties on the datapoints are 68.3 % Feldman & Cousins confidence intervals [262]. The datasets of the inner and outer sub-volumes of the 1.5 t superellipsoid were fitted simultaneously.

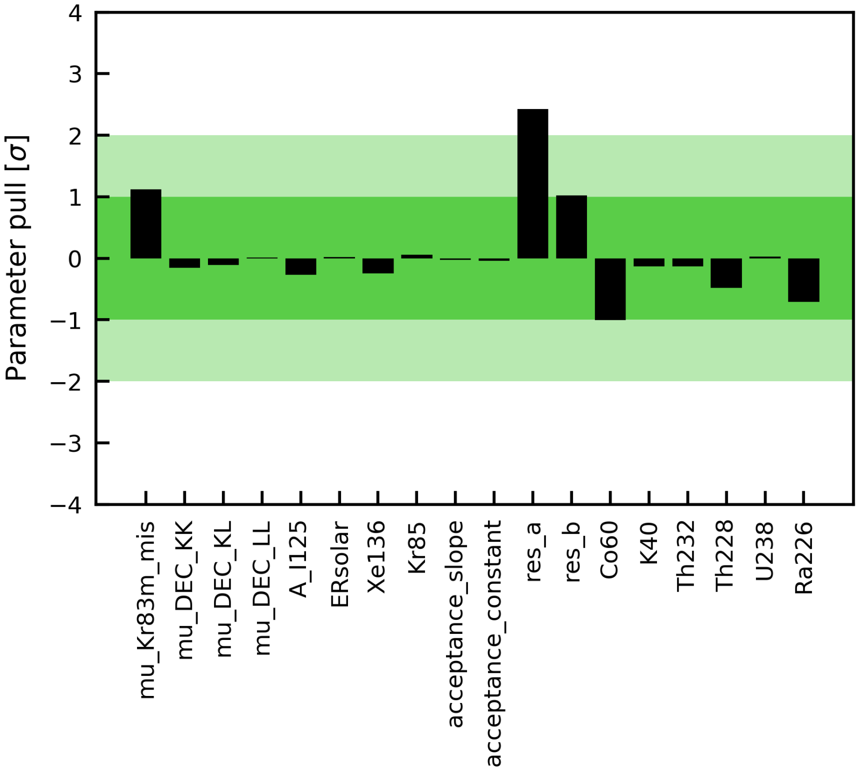

Figure A-27: Parameter pulls for the fit of the extended 2νECEC signal and background model to the data from [31].

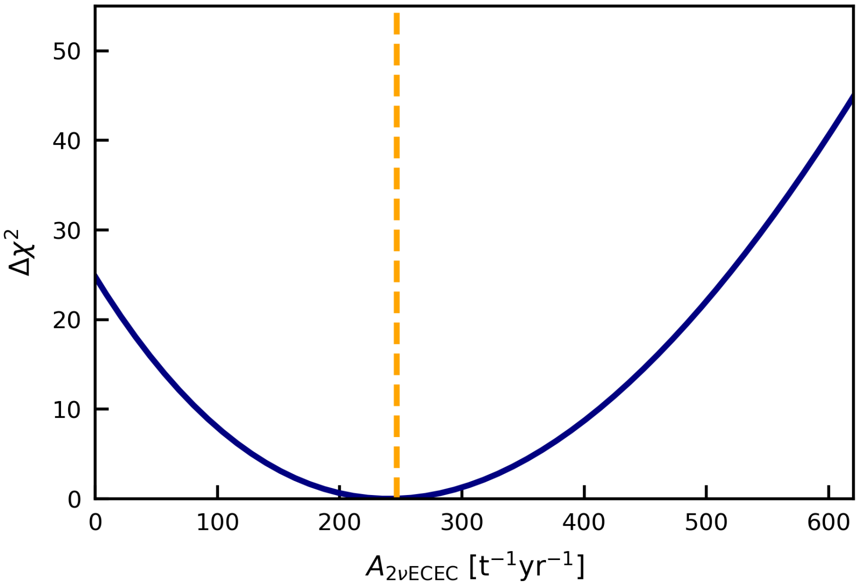

Figure A-28: χ^2_λ-profile of $A_{2\nu\mathrm{ECEC}}$ for the fit of the extended 2νECEC signal and background model to the data from [31].

A10 Constraints on the residual peak from misidentified $^{83\mathrm{m}}$Kr events

The *MisIDS1SingleScatter* cut removes $^{83\mathrm{m}}$Kr events where the S1 of the second 9.4 keV decay is misidentified as an S2. These are important for the double-electron capture analysis because they are not removed by the S1SingleScatter cut and form a low-energy shoulder on the 41.5 keV peak. The cut identifies these events based on the largest S2 before the main S2. However, since the 41.5 keV and the misidentified peak slightly overlap, a small fraction of misidentified events remains in the shoulder of the peak. Moreover, the cut deforms the misID peak. The mean, width and fraction with respect to the 41.5 keV peak are determined using $^{83\mathrm{m}}$Kr calibration data from the full SR1. This is done independently for the inner and outer volume of the 1.5 t superellipsoid. Fitting the Kr-83m peak with a double-Gaussian and a constant background, one finds the parameters summarised in table A-3. The fits are shown in the figure A-29. The residuals show that the 41.5 keV peak is not fully Gaussian. However, this is only visible in the high statistics of the calibration data. In the data used for the analysis the statistics per bin are reduced by a factor of > 100. The fraction of surviving misID events is on the 0.01 % level. Considering uncertainties it is the same in both volumes. Additionally, the peaks are narrower than physical peaks in both volumes due to the cut. These parameters are used as constraints for the fits in section 4.4.

Table A-3: Fit parameters of the misidentified $^{83\mathrm{m}}$Kr peak in the inner and outer volume of the 1.5 t superellipsoid after the *MisIDS1SingleScatter* cut in SR1 calibration data.

Parameter	**Inner**	**Outer**
$f_{^{83\mathrm{m}}\mathrm{Kr}_{\mathrm{misID}}}$	$(2.51 \pm 0.26) \cdot 10^{-4}$	$(2.6 \pm 0.4) \cdot 10^{-4}$
$\mu_{^{83\mathrm{m}}\mathrm{Kr}_{\mathrm{misID}}}$ [keV]	31.74 ± 0.27	32.03 ± 0.26
$\sigma_{^{83\mathrm{m}}\mathrm{Kr}_{\mathrm{misID}}}$ [keV]	1.28 ± 0.10	1.36 ± 0.10

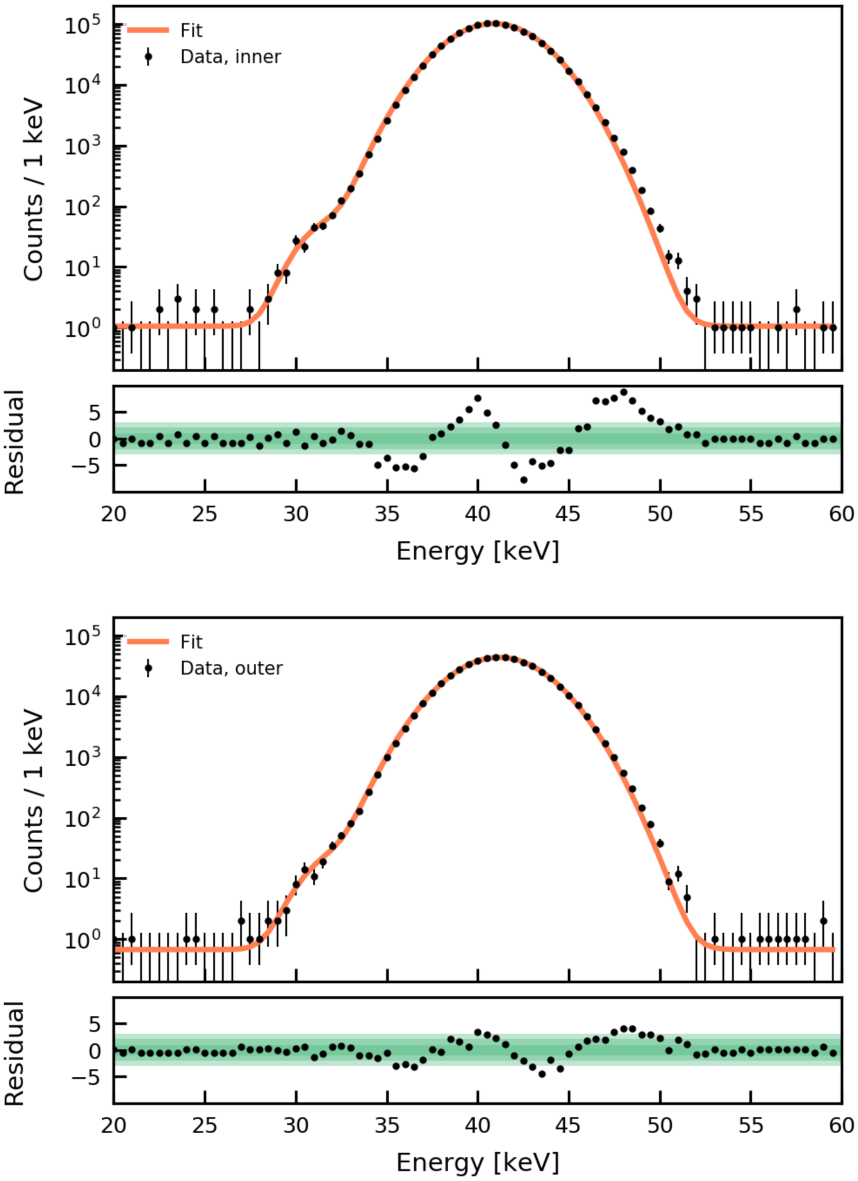

Figure A-29: Spectra of the misidentified and 41.5 keV $^{83\mathrm{m}}$Kr peaks in the inner (**top**) and outer (**bottom**) volume of the 1.5 t superellipsoid after the *MisIDS1SingleScatter* cut in SR1 calibration data. The bin size is 1 keV. Double-Gaussian binned likelihood fits with a constant background are indicated by the solid orange lines in the respective top panels. Residuals are shown in the lower panels of both figures. Uncertainties represent 68.3 % Feldman & Cousins confidence intervals [262]. The mean of the upper and lower uncertainty is used in the residual calculation.

A11 Fit plots for the event overlap in PAX 6.8.0 and PAX 6.10.1 data

See section 4.5 for the discussion of the fits in the figures below.

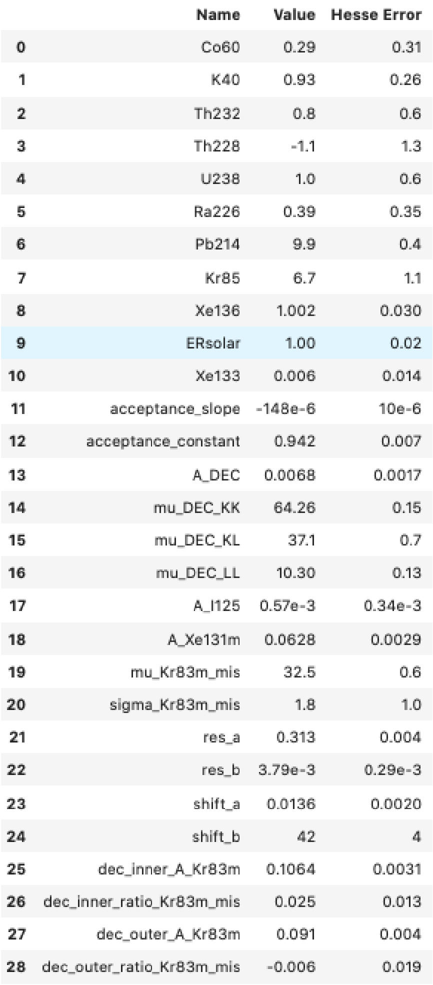

	Name	Value	Hesse Error
0	Co60	0.29	0.31
1	K40	0.93	0.26
2	Th232	0.8	0.6
3	Th228	-1.1	1.3
4	U238	1.0	0.6
5	Ra226	0.39	0.35
6	Pb214	9.9	0.4
7	Kr85	6.7	1.1
8	Xe136	1.002	0.030
9	ERsolar	1.00	0.02
10	Xe133	0.006	0.014
11	acceptance_slope	-148e-6	10e-6
12	acceptance_constant	0.942	0.007
13	A_DEC	0.0068	0.0017
14	mu_DEC_KK	64.26	0.15
15	mu_DEC_KL	37.1	0.7
16	mu_DEC_LL	10.30	0.13
17	A_I125	0.57e-3	0.34e-3
18	A_Xe131m	0.0628	0.0029
19	mu_Kr83m_mis	32.5	0.6
20	sigma_Kr83m_mis	1.8	1.0
21	res_a	0.313	0.004
22	res_b	3.79e-3	0.29e-3
23	shift_a	0.0136	0.0020
24	shift_b	42	4
25	dec_inner_A_Kr83m	0.1064	0.0031
26	dec_inner_ratio_Kr83m_mis	0.025	0.013
27	dec_outer_A_Kr83m	0.091	0.004
28	dec_outer_ratio_Kr83m_mis	-0.006	0.019

Figure A-30: Fit parameters for the fit of the overlap data in PAX 6.8.0. Note that all peak areas (DEC, ^{125}I, $^{83\text{m}}$Kr, $^{131\text{m}}$Xe), have to be divided by 10 in order to obtain $^{\text{events}}/_{\text{kg}\cdot\text{d}}$. This is a feature of the internal 0.1 keV binning of the fit.

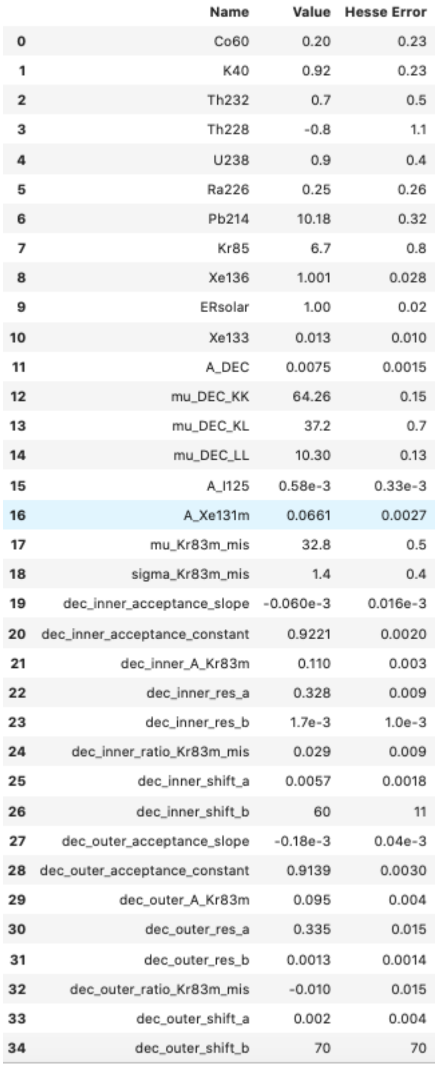

	Name	Value	Hesse Error
0	Co60	0.20	0.23
1	K40	0.92	0.23
2	Th232	0.7	0.5
3	Th228	-0.8	1.1
4	U238	0.9	0.4
5	Ra226	0.25	0.26
6	Pb214	10.18	0.32
7	Kr85	6.7	0.8
8	Xe136	1.001	0.028
9	ERsolar	1.00	0.02
10	Xe133	0.013	0.010
11	A_DEC	0.0075	0.0015
12	mu_DEC_KK	64.26	0.15
13	mu_DEC_KL	37.2	0.7
14	mu_DEC_LL	10.30	0.13
15	A_I125	0.58e-3	0.33e-3
16	A_Xe131m	0.0661	0.0027
17	mu_Kr83m_mis	32.8	0.5
18	sigma_Kr83m_mis	1.4	0.4
19	dec_inner_acceptance_slope	-0.060e-3	0.016e-3
20	dec_inner_acceptance_constant	0.9221	0.0020
21	dec_inner_A_Kr83m	0.110	0.003
22	dec_inner_res_a	0.328	0.009
23	dec_inner_res_b	1.7e-3	1.0e-3
24	dec_inner_ratio_Kr83m_mis	0.029	0.009
25	dec_inner_shift_a	0.0057	0.0018
26	dec_inner_shift_b	60	11
27	dec_outer_acceptance_slope	-0.18e-3	0.04e-3
28	dec_outer_acceptance_constant	0.9139	0.0030
29	dec_outer_A_Kr83m	0.095	0.004
30	dec_outer_res_a	0.335	0.015
31	dec_outer_res_b	0.0013	0.0014
32	dec_outer_ratio_Kr83m_mis	-0.010	0.015
33	dec_outer_shift_a	0.002	0.004
34	dec_outer_shift_b	70	70

Figure A-31: Fit parameters for the fit of the overlap data in PAX 6.10.1. Note that all peak areas (DEC, ^{125}I, ^{83m}Kr, ^{131m}Xe), have to be divided by 10 in order to obtain events/kg·d. This is a feature of the internal 0.1 keV binning of the fit.

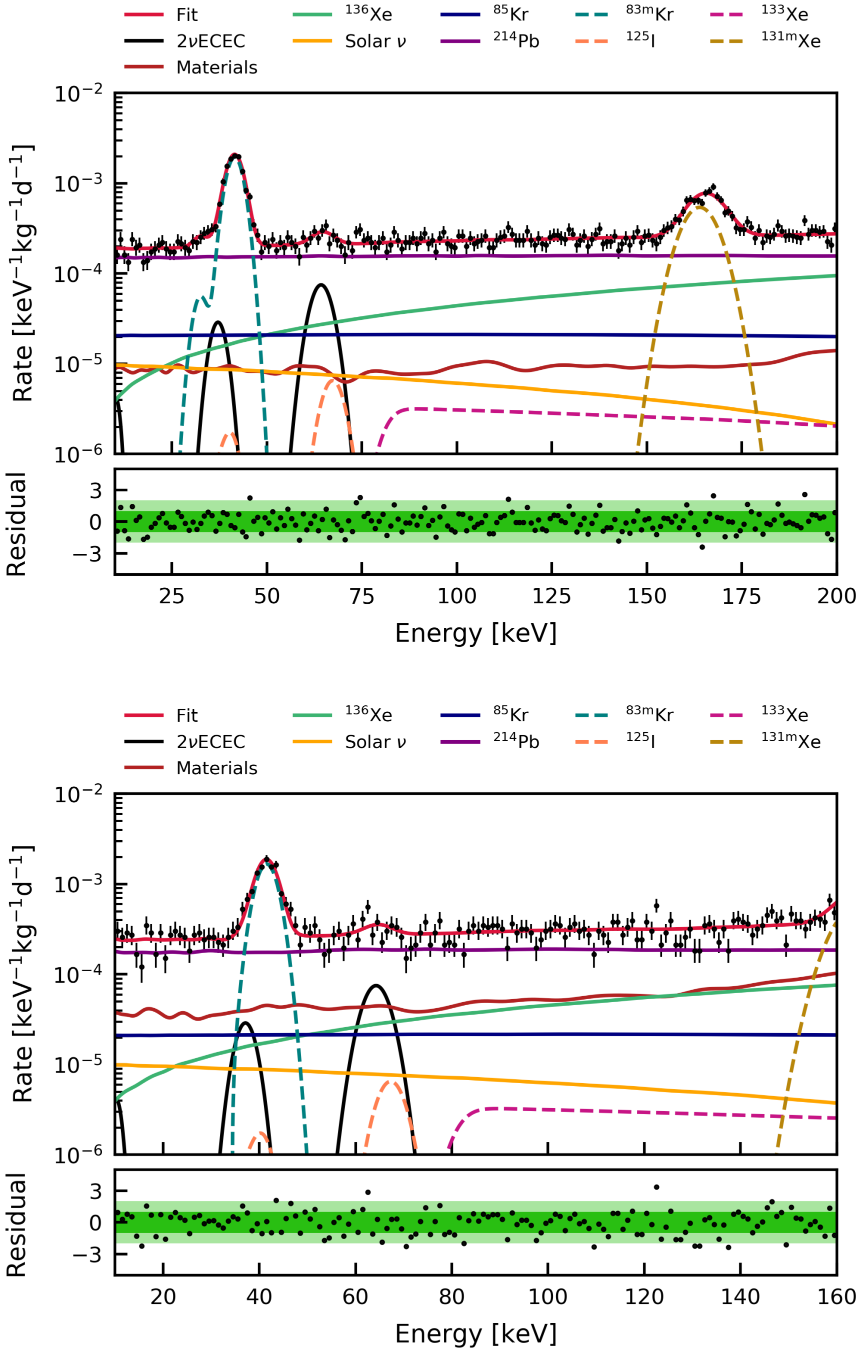

Figure A-32: Fit of the signal and background models to the measured energy spectra in PAX 6.8.0 data from the event overlap present in the analyses from chapter 3 and chapter 4. The best-fit spectra are shown for the inner (**top**) and outer (**bottom**) detector volume. Residuals were calculated from the square-roots of the χ^2_λ summands. Uncertainties on the datapoints are 68.3 % Feldman & Cousins confidence intervals [262]. The datasets of the inner and outer sub-volumes of the 1.5 t superellipsoid were fitted simultaneously.

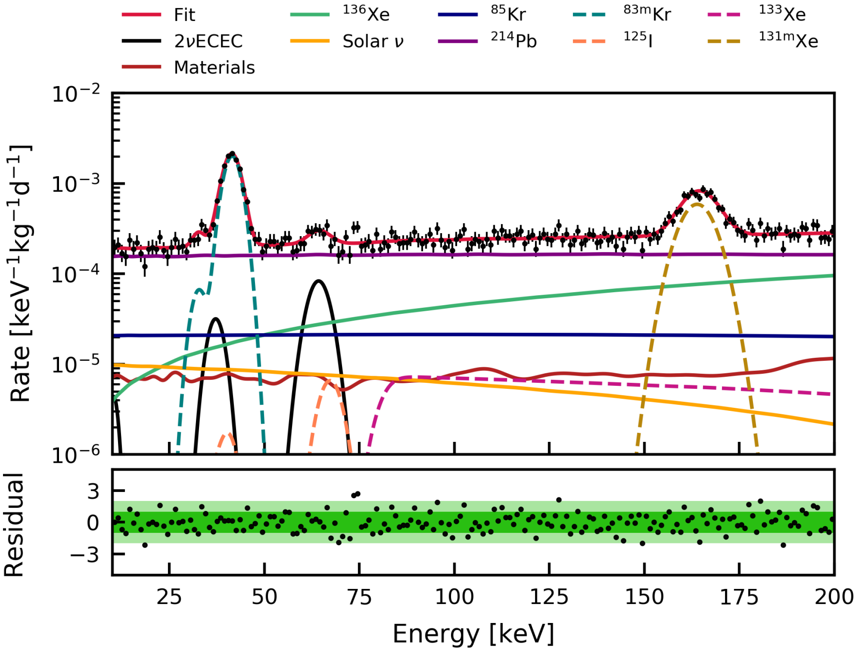

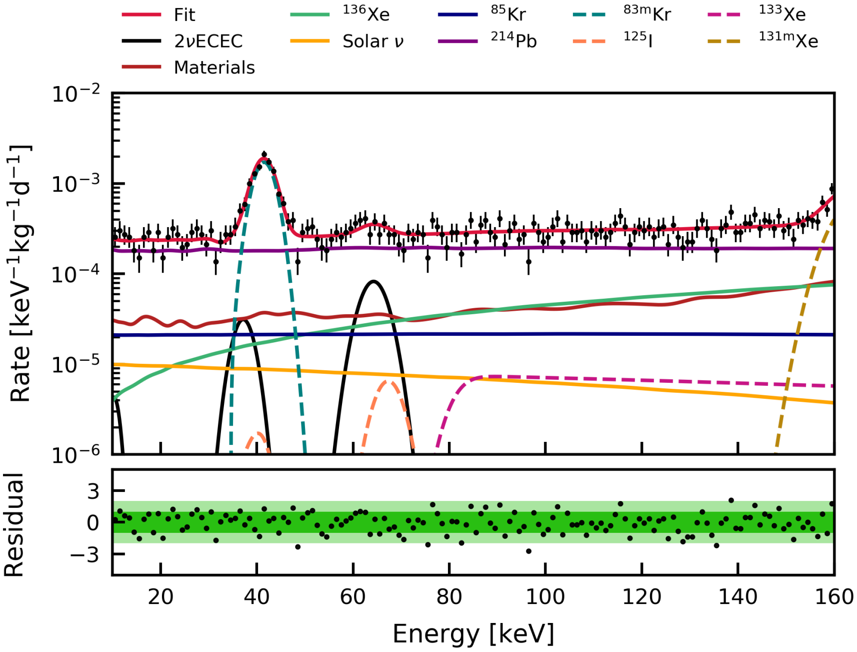

Figure A-33: Fit of the signal and background models to the measured energy spectra in PAX 6.10.1 data from the event overlap present in the analyses from chapter 3 and chapter 4. The best-fit spectra are shown for the inner (**top**) and outer (**bottom**) detector volume. Residuals were calculated from the square-roots of the χ^2_λ summands. Uncertainties on the datapoints are 68.3 % Feldman & Cousins confidence intervals [262]. The datasets of the inner and outer sub-volumes of the 1.5 t superellipsoid were fitted simultaneously.

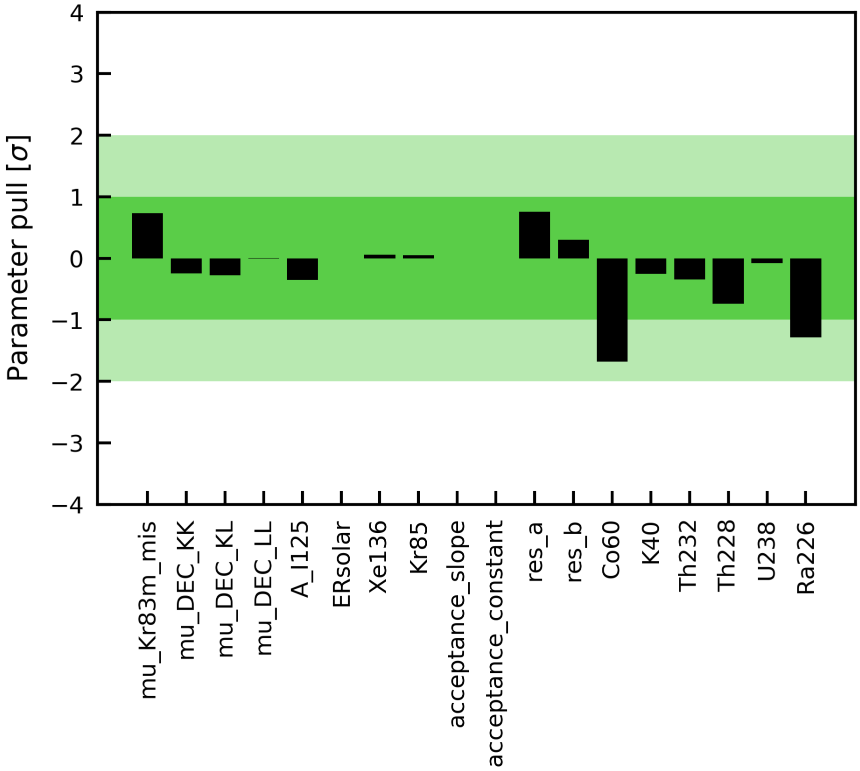

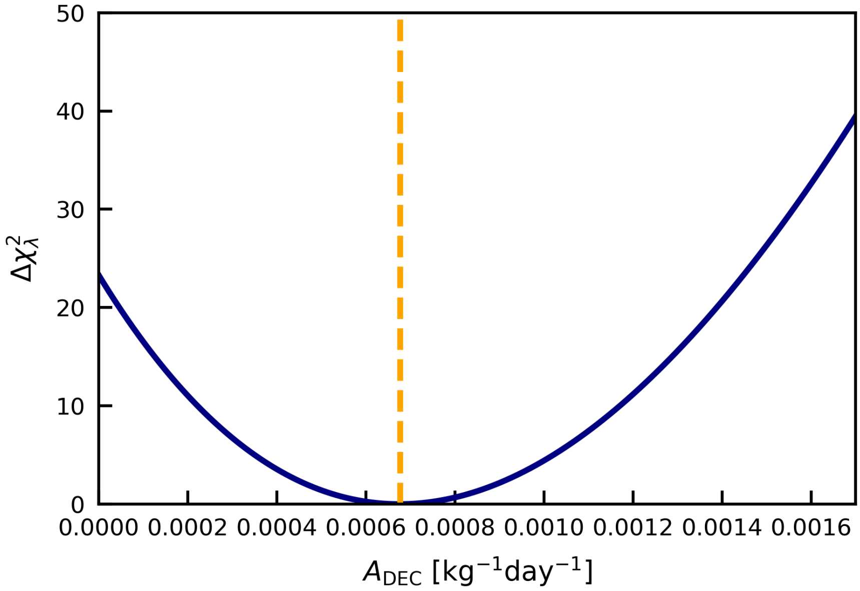

Figure A-34: Parameter pulls (**top**) and χ^2_λ-profile of $A_{2\nu\mathrm{ECEC}}$ (**bottom**) for the fit of the overlap data in PAX 6.8.0.

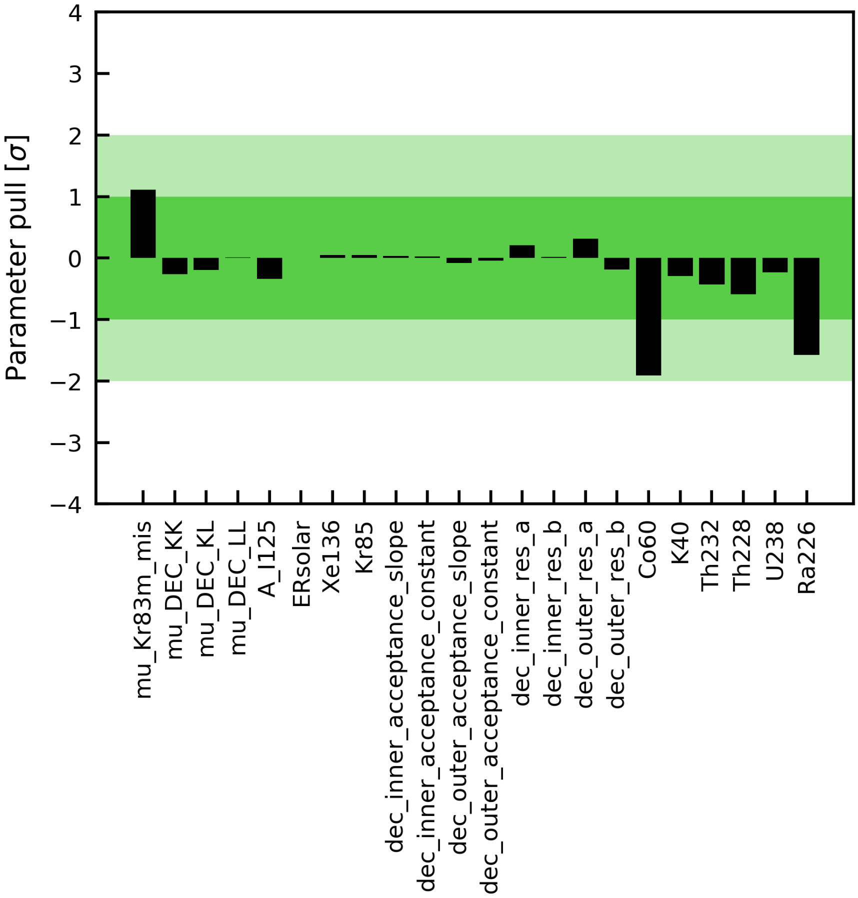

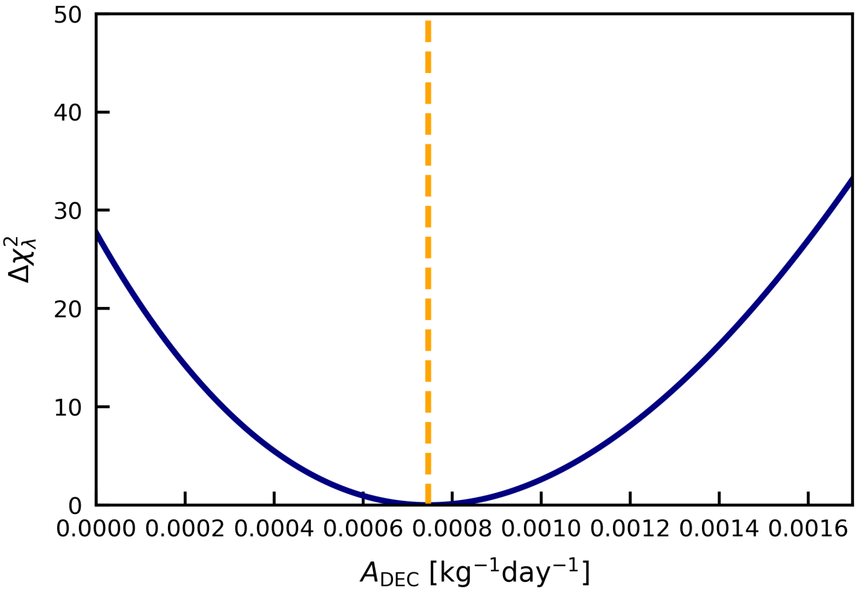

Figure A-35: Parameter pulls (**top**) and χ^2_λ-profile of $A_{2\nu\mathrm{ECEC}}$ (**bottom**) for the fit of the overlap data in PAX 6.10.1.

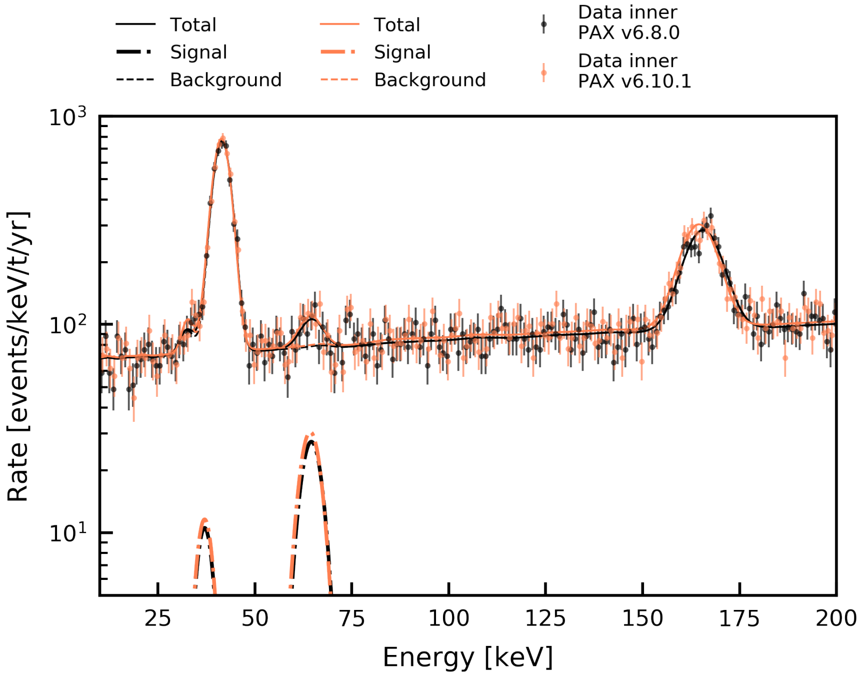

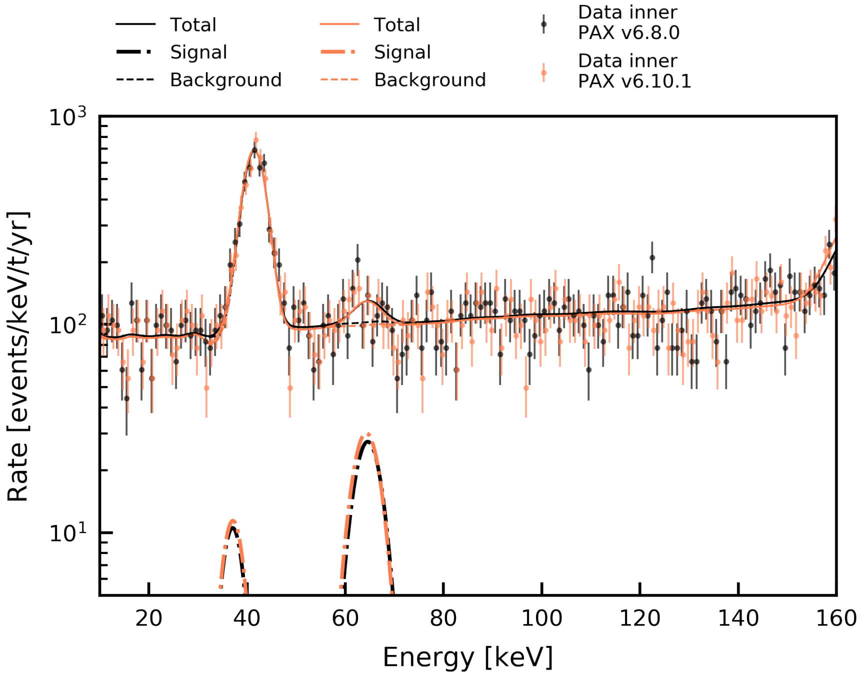

Figure A-36: Energy spectra for the fit of the overlap in events between the published PAX 6.8.0 data (black markers) from [31] and the updated PAX 6.10.1 data (orange markers) from this work. Spectra are shown separately for the inner (**top**) and outer (**bottom**) sub-volumes of the 1.5 t fiducial superellipsoid. The best-fit total spectra for the PAX 6.8.0 and the PAX 6.10.1 data are indicated by the solid black and orange lines, respectively. The background-only spectrum und the KK-peak are indicated by the dashed and dash-dotted lines of the same color. Uncertainties on the data points resemble 68.3 % Feldman & Cousins confidence intervals and are used for illustration only.

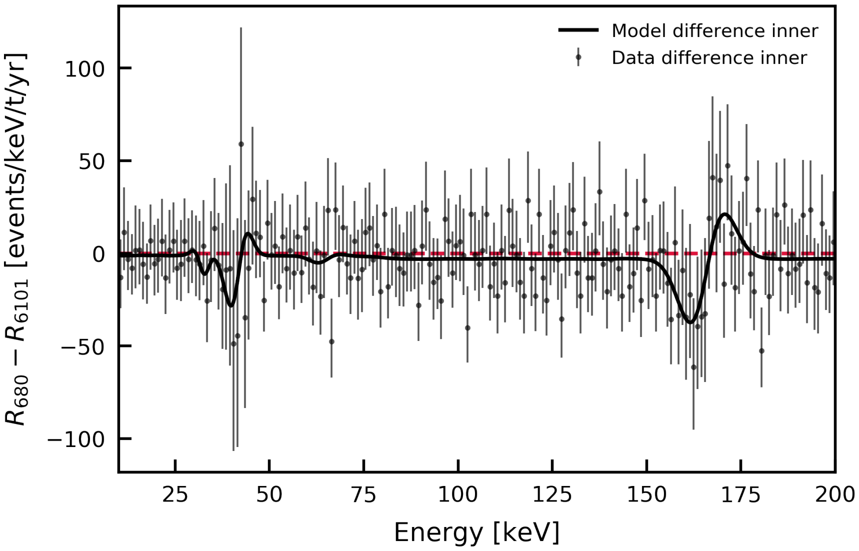

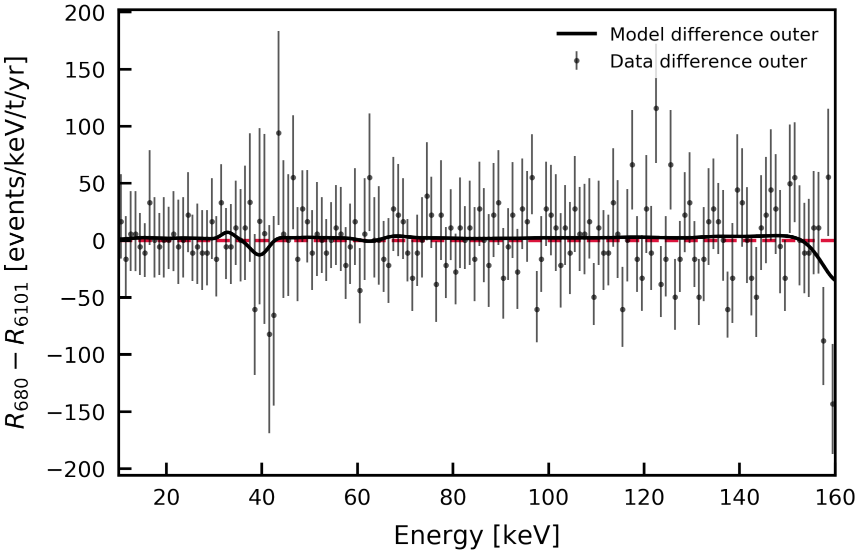

Figure A-37: Rate difference in energy spectra for the fit of the overlap in events between the published PAX 6.8.0 data from [31] and the updated PAX 6.10.1 data from this work. Difference spectra are shown separately for the inner (**top**) and outer (**bottom**) sub-volumes of the 1.5 t fiducial superellipsoid. The difference of the data is indicated by the black markers. The model-difference is indicated by the solid black line. The dashed red line marks the zero-difference. The uncertainties of the data points in both datasets have been added in quadrature. This overestimates the actual uncertainty due to the partial, but unknown correlation between the datasets.

Danksagung

Am Ende von etwas mehr als drei Jahren Doktorarbeit bleibt vor allem eins zu sagen: Danke! Vielen Dank an alle, die beim Gelingen dieser Arbeit geholfen haben und ohne die es die Arbeit in dieser Form gar nicht gäbe. Da ich abgabebedingte Scheuklappen trage, bitte ich um Nachsicht von allen, deren namentliche Erwähnung ich an dieser Stelle vergessen habe. Ihr wisst, wer Ihr seid. Vielen Dank!

Der größte Dank gilt Prof. Dr. Christian Weinheimer, der mir nicht nur die Arbeit an einem Weltklasseexperiment ermöglicht, sondern auch selbstlos viele Türen geöffnet hat. Für seine starke Förderung, die schier unaufhörliche Expertise und die aufopferungsvolle Hilfe bei der Überwindung von Hindernissen kann ich mich kaum genug bedanken. Für die stetige Motivation, immer noch etwas mehr herauszuholen, die wissenschaftliche wie auch menschliche Integrität und das sich Einbringen, wenn es mal schwierig wurde, bin ich zutiefst dankbar!

Prof. Dr. Anton Andronic möchte ich dafür danken, dass er die Zweitkorrektur dieser Arbeit übernommen hat! Das Wiedersehen in Münster nach der Zeit als GSI Sommerstudent hat mich sehr gefreut. Vielleicht gibt es ja in Zukunft einen IKP Filmclub.

Prof. Dr. Michael Klasen danke ich für seine Betreuung im Rahmen des GRK 2149 und für die gute Zusammenarbeit im GRK Board! Die Verlängerung des Graduiertenkollegs war ein persönliches Highlight. Ich bin sehr dankbar dafür, dass ich diese Teamanstrengung von Lehrenden und Studierenden aus erster Hand miterleben durfte.

Dank gebürt auch denen, die den Laden am laufen halten, also Uta Mayer, Michaela Erdmann und Petra Voss. Ein großes Dankeschön für die Unterstützung bei Verträgen, Anträgen, Reports, Dienstreisen, der Organisation des Astroseminars und all den administrativen Nebenschauplätzen einer Promotion!

Für die tolle Atmosphäre in meinen rund sechs Jahren in der AG Weinheimer möchte ich allen jetzigen und ehemaligen Gruppenmitgliedern danken: Volker, Nicho, Alex Fulst, Kevin, Alexey, Stephan Dyba, Jan, Oliver, Mariia, Rudolf, Simon, Caroline, Sonja, Nils, Ken, Benedikt, Björn, Hans-Werner und Daniel. Ob Institutsgrillen, Mensa, Weihnachtsfeier oder ein zufälliger gemütlicher Abend: Es war eine richtig gute Zeit! An der Stelle auch noch ein doppelter Genziana auf die XENON-Gruppe mit Michael, Alex, Stephan Rosendahl, Christian Huhmann Denny, Miguel, Lutz, Kevin, Axel, Henning, Johanna und Sergej(100). Danke, für das gemeinsame Lernen und (rein)Arbeiten.

Tausend Dank an die fleißigen Korrekturleser dieser Arbeit also an Kevin, Alexey, Michael, Henning, Lutz und Alex. Ihr habt großen Anteil daran, dass am Ende ein halbwegs lesbares Textstück herausgekommen ist. Merci beaucoup!

Ein Shout-out geht raus ans Astroseminar Team: Daniel, Alex, Fabian, Lutz, Stephan, Laura, Jan, Simon, Alex Fulst, Laura, Henning, Peter, Pia und die zahllosen anderen, die in den letzten Jahren mitgemacht haben. Es war mir eine Ehre, von euch zu lernen, mit euch zu planen, zu eilen, aufzuräumen und am Ende zu feiern. Viel Erfolg der nächsten Generation!

A big thank you to all the members of the XENON collaboration that I had the privilege to work with. Thanks to David, Jelle, Fei, Chiara, Tim, Maxime, Arianna, Rafael, Marc, Darryl, Jacques, Theresa, Sander, Knut, Jingqiang, Patrick de Perio, Ludwig, Junji, Auke Pieter, Ale, Dominick, Constanze, Guillaume E., Evan and Michelle – just to name a few. I would also like to thank Brian for cooperating on my very first few-author paper. Thank you, dankesehr und gracias also to Achim, Martin and Javier for starting an experiment-theory cooperation. I am looking forward to exciting projects in the future!

Nicht zu vergessen sind auch die Kaffeegruppen. Da wäre einmal das AG Khoukaz Espressobüro mit Nils, Christopher, Johannes, Michael, Alex, Sergej und Olli. Danke für die erfrischenden Kaffeepausen, Lasertag, gemeinsame Suchen nach dem Impostor und das geduldige Erklären von Abseitsregeln. Und dann ist da noch der inoffizielle zweite Kaffeeraum im zugigsten Raum des ganzen Instituts. Cheers an die Kaffeerunde mit Simon, Kevin, Lutz, Michael und Henning für viele wertvolle Stunden und Diskussionen zum optimalen Mahlgrad. Don’t swirl. Stir!

Grazie mille gebührt Michael, der mir als Wahlitaliener die dortige Lebensart nähergebracht hat. Kaum etwas fasst die häufigen Widrigkeiten des wissenschaftlichen Arbeitens so gut zusammen wie sein lakonisches: "Is ok."

Einen unerschöpflichen Fundus an administrativem und technischem Wissen konnte ich bei Lutz anzapfen. Danke für deine geduldige Kompetenz, die ihresgleichen sucht.

Bei Alexander Fieguth möchte ich mich im speziellen bedanken, weil er nicht nur nach wie vor fragt, wie es gerade läuft und es dann auch wirklich wissen will, sondern weil er mich an Bord geholt hat für die Analysen in seiner Doktorarbeit. Ohne ihn wäre diese Arbeit nicht so entstanden. Vielen Dank für die Riesenchance, die unzähligen Stunden gemeinsamer Arbeit und den Spaß dabei! Besonders hoch anzurechnen ist ihm das alles, weil er dafür mit meinem Humor leben musste. Respekt!

Danke an Dennis, Alina und Benedikt! Für die Musik, die gemeinsamen Wochenenden und Abende. Für das Rechnen und Lernen im Grundstudium. Ohne euch wäre das alles nicht nur viel schwieriger gewesen, es hätte auch einfach nicht so viel Spaß gemacht. Das gilt auch für alle Freunde hier in Münster und alle, die (mittlerweile) weit verstreut über Deutschland, Europa und die Welt leben. Ihr habt mir die mittlerweile fast 12 Jahre in dieser Stadt mit einer dicken Schicht Zuckerguss überzogen!

Ein gesonderter Dank gilt Rafael Lang, ohne den ich vielleicht gar keine Promotion angefangen hätte. Tausend Dank für den guten Rat, die Zeit an der Purdue University, die Begeisterung für die Forschung und die Unterstützung in den letzten Jahren!

Ganz besonders möchte ich mich bei meiner Familie bedanken; bei meinen Eltern Beate und Volker Wittweg sowie bei meiner Oma Ursula Wehrmann. Durch eure Unterstützung konnte ich ein Studium anfangen, zwischendurch noch einmal den Kurs korrigieren und jetzt hier herauskommen. Dafür kann ich mich in Worten gar nicht genug bedanken!

Bei Juliane bedanke ich mich zum Schluss. Für die letzten Jahre, jetzt und immer.